LBNL-41658
UC-411

Advanced Light Source

Compendium of User Abstracts and Technical Reports 1997

July 1998

Ernest Orlando Lawrence Berkeley National Laboratory
University of California
Berkeley, California 94720

The material in this Compendium is also available on the World Wide Web (http://alspubs.lbl.gov/compendium).
The Web version provides a full-text search of user abstracts as well as searches by beamline, author name, subject area, and other parameters.

The Compendium is intended to complement the Advanced Light Source Activity Report, which presents an overview of the scientific program, ongoing research and development efforts, and operations.

Related publications available from ALS User Administrator

ALS Activity Report 1996/97

ALS Compendium of User Abstracts and Technical Reports 1993–1996

Workshop on Scientific Directions at the Advanced Light Source: Summary and Reports of the Working Groups

Soft X-Ray Spectromicroscopy: Materials Characterization on a Microscale

ALS Users' Handbook

Editors: Deborah J. Dixon, Arthur L. Robinson, Annette Greiner, and Constance Silva
Cover Design: Flavio Robles, Jr.

The editors gratefully acknowledge the assistance of the ALS User Services Office staff in compiling this volume, as well as the contributions of ALS users and staff to its contents.

Advanced Light Source

Compendium of User Abstracts and Technical Reports 1997

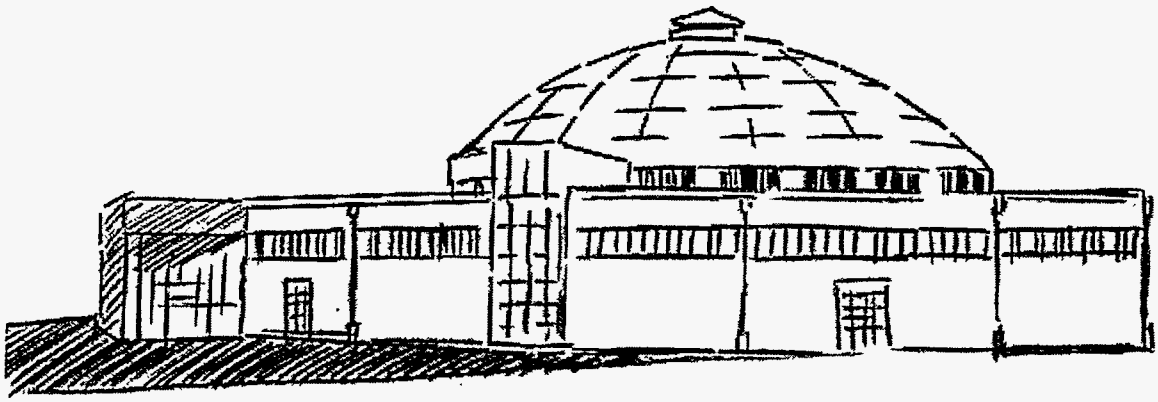

July 1998

Ernest Orlando Lawrence Berkeley National Laboratory
University of California
Berkeley, California 94720

Prepared for the U.S. Department of Energy under Contract DE-AC03-76SF00098

Welcome to our second annual Compendium of research abstracts and technical reports from the Advanced Light Source (ALS). Unlike last year's volume, which covered research conducted from the onset of ALS operations in 1993 through all of 1996, this year the Compendium covers just one year, 1997, yet the number of abstracts included is about the same (122 compared to 137 for 1993-96). The increase is easily explained by a steadily growing number of station-hours (the number of beamline stations times the hours of operation). This figure will surely continue to swell in coming years. We now have 21 beamlines in operation for users, and thanks in part to a boost from the Department of Energy (DOE) Scientific Facilities Initiative that began in 1996, there will be 6 more by the end of 1998. This augurs well for a larger and larger Compendium as new experimental facilities come to fill more and more of the ALS experimental floor.

The reports in this compendium show that we were already well on the way to achieving our goal of a robust scientific program at the ALS. The research summarized in the abstracts is both broad and deep, with topics distributed among such major scientific areas as complex materials, nanostructures/semiconductors, magnetic materials, environmental and earth sciences, polymers and soft matter, protein crystallography, biomicroscopy and spectroscopy, catalytic materials and surface science, atomic and molecular (AMO) physics, and chemical dynamics, as well as major technology development effort in extreme ultraviolet (EUV) lithography. These abstracts, then, constitute the latest snapshots in a growing family album that documents our collaborative march with the user community toward a scientific program characterized by both excellence and scope.

A further expression of our scientific goals will appear in a report documenting forefront research ideas by top-notch scientists. As I write these words, we are hard at work on just this assignment. Many of you may have been among the 325 or so participants at our three-day workshop on Scientific Directions at the Advanced Light Source that was held at the Berkeley Lab from March 23-25, 1998, with Yves Petroff, Director-General of the European Synchrotron Radiation Facility, as the chair. With DOE and Berkeley Lab, we organized the workshop with the goals of formulating a vision for the ALS scientific program into the twenty-first century and of making recommendations that will result in a road map for the implementation of that program. A workshop report will compile the findings of breakout groups concentrating on specific areas of scientific research and will lay the groundwork for a new ALS roadmap.

In concert with this renewal of the scientific vision, the internal organization of the ALS has been restructured to emphasize our principal mission of providing the means for our users to do the very best science. On the scientific side of the house, we now

have three groups: the Experimental Systems Group, reporting as previously to Howard Padmore, plus two new groups—the User Services Group led by Gary Krebs, and the Scientific Support Group led by Zahid Hussain. In the User Services Group, we have consolidated some of the functions that were previously dispersed throughout the ALS. We have given Gary and the User Services Group the mission of assisting users to come to the ALS and establish their experiments on the floor in a seamless and user-friendly fashion. The mission of Zahid and the Scientific Support Group is to provide, as requested, assistance to users in the execution and interpretation of their experiments. Gary and Zahid both have seats in the ALS group leaders "cabinet," which is resulting in a shift at the ALS to a greater emphasis on users and their science. We trust that these changes will be reflected in next year's Compendium, where we expect the abstracts and technical reports to be even more adventurous and innovative than those reported here!

Neville Smith
Deputy Director for
Scientific Program

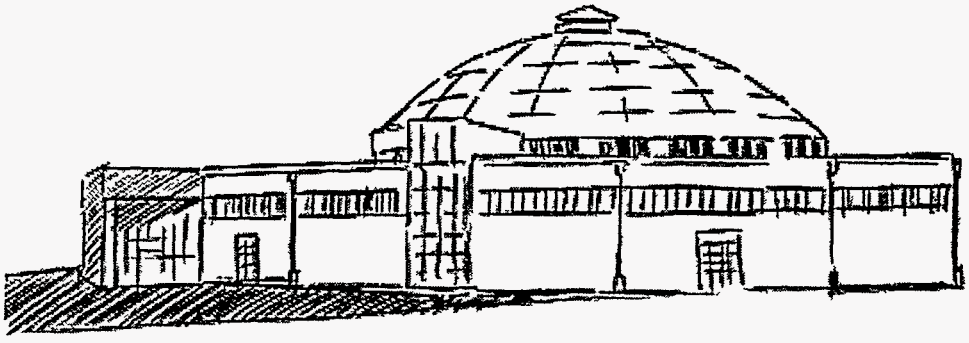

Advanced Light Source

Compendium of User Abstracts and Technical Reports 1997

The Advanced Light Source (ALS), a national user facility located at Ernest Orlando Lawrence Berkeley National Laboratory of the University of California, is available to researchers from academia, industry, and government laboratories. Operation of the ALS is funded by the Department of Energy's Office of Basic Energy Sciences.

This Compendium contains abstracts written by users summarizing research completed or in progress during 1997, ALS technical reports describing ongoing efforts related to improvement in machine operations and research and development projects, and information on ALS beamlines planned through 1998.

Two tables of contents organize the user abstracts by beamline and by area of research, and an author index makes abstracts accessible by author and by principal investigator. Technical details for each beamline, including whom to contact for additional information, can be found in the beamline information section. The most current information on ALS beamlines can be found on the ALS web pages (http://www-als.lbl.gov/).

Available to DOE and DOE Contractors from the
Office of Scientific and Technical Communication
P.O. Box 62, Oak Ridge, TN 37831
Prices available from (615) 576-8401

Available to the public from the
National Technical Information Service
U.S. Department of Commerce
5285 Port Royal Road, Springfield, VA 22161

User Abstracts
Table of Contents by Beamline

Abstracts are organized first by beamline, then by title. Abstracts associated with two beamlines are listed under both. Some beamlines that began operations in late 1997 or in 1998 have few or no abstracts listed.

Beamline 1.4: Visible and Infrared Spectroscopy and Microscopy, Ultraviolet Photoluminescence

Beamline 5.0.2: Multiple-Wavelength Anomalous Diffraction (MAD) and Monochromatic Protein Crystallography

Beamline 6.1.2: High-Resolution Zone-Plate Microscopy

Beamline 6.3.2: Calibration and Standards; EUV Optics Testing; Atomic, Molecular, and Materials Science

Beamline 7.0.1: Surface and Materials Science, Spectromicroscopy, Spin Resolution, Photon-Polarization Dichroism

Beamline 7.0.2: Coherent Optics Experiments

Beamline 7.3.1: Surface and Materials Science, Magnetic Microscopy, Spectromicroscopy, Micro X-Ray Photoelectron Spectroscopy

Beamline 8.0.1: Surface and Materials Science, Spectromicroscopy, Imaging Photoelectron Spectroscopy

Beamline 9.0.1: Atomic, Molecular, and Optical Physics; High-Resolution Gas-Phase Spectroscopy

Beamline 9.0.2: Chemical Reaction Dynamics, Photochemistry, High-Resolution Photoelectron and Photoionization Spectroscopy

Beamline 9.3.1: Atomic, Molecular, and Materials Science

Beamline 9.3.2: Chemical and Materials Science, Circular Dichroism, Spin Resolution

Beamline 10.3.1: X-Ray Fluorescence Microprobe

Beamline 10.3.2: X-Ray Optics Development, Materials Science

Beamline 12.0.1: Surface and Materials Science, Spectromicroscopy, EUV Lithography Optics Testing, Interferometry

Beam Test Facility

User Abstracts
Table of Contents by Subject Area

Abstracts are organized by subject area, as assigned by the abstracts' authors. The main subject areas are Atomic Physics; Beamlines, Instrumentation, and Techniques; Biosciences; Chemical Dynamics; Condensed Matter Science; Earth and Environmental Sciences; Molecular Physics; Surface Science; and Technology. Abstracts in some areas are further divided into subcategories, then alphabetized by title. Abstracts associated with more than one subject area are listed under each. Beamlines associated with the abstracts appear at right.

Atomic Physics

Beamlines, Instrumentation, and Techniques

Beamline Optics

Experimental Apparatus

Experimental Techniques

Biosciences

Macromolecular Crystallography

Soft X-Ray Biomicroscopy

Spectroscopy

Chemical Dynamics

Condensed Matter Science

Dynamics

Electronic Structure

Geometric Structure

Magnetic Structure

Micro/Nanostructure

Earth and Environmental Sciences

Molecular Physics

Surface Science

Electronic Structure

Geometric Structure

Magnetic Structure

Micro/Nanostructure

Technology

Alloys and Composites

Magnetic Structures

Microelectronic Structures

Optical Properties Characterization and Metrology

Polymers

User Abstracts Author Index

If an author is the principal investigator for an abstract, that abstract's page number appears in bold type.

Beamline 1.4 Abstracts

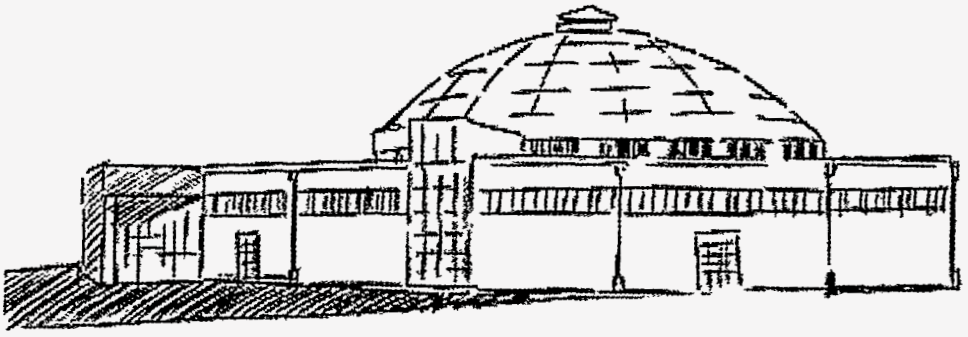

BL1.4.2: Time-resolved FTIR spectroscopy at up to 5 nanosecond resolution demonstrated

Michael C. Martin and Wayne R. McKinney
Advanced Light Source Division, Ernest Orlando Lawrence Berkeley National Laboratory,
University of California, Berkeley, California 94720, USA

INTRODUCTION

Synchrotron-based infrared (IR) beamlines provide a unique opportunity for doing time-resolved IR spectroscopy. Synchrotrons operate with electrons travelling in bunches around the storage ring. Each bunch emits a pulse of synchrotron radiation every time the electrons are forced to turn via a bending magnet. The time structure of the light pulses is therefore determined by the filling pattern of the electron bunches. The ALS typically operates in multi-bunch mode with 288 bunches spaced 2 nanoseconds apart, followed by an 80nsec gap. The individual pulse width is 44psec (FWHM). This electron filling pattern is schematically drawn in Figure 1.

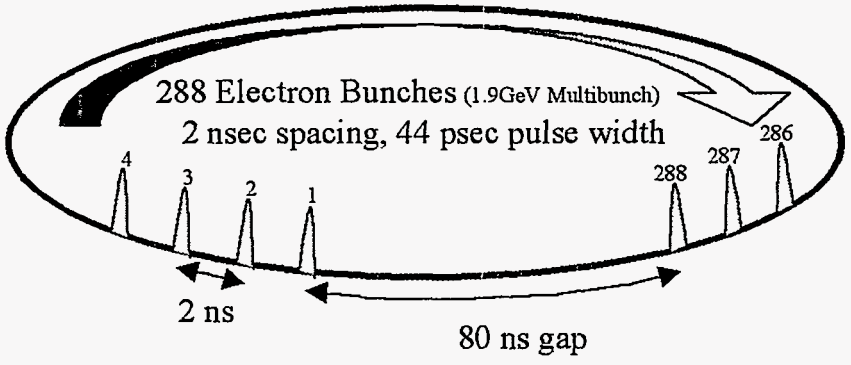

Figure 1. The ALS produces pulses at intervals of 2nsec, expect for a single long gap of 80ns. We use this time structure to demonstrate the fast timing capabilities of BL1.4.2.

Standard rapid-scan Fourier Transform Infrared Spectroscopy (FTIR) acquires scans on the time scale of one second, so the very fast pulses of a synchrotron source are not noticed. However, using the step-scan capabilities and fast electronics of the Bruker IFS66v/S FTIR spectrometer on BL1.4.2, we can measure IR spectra with a time resolution as fast as 5nsec. This means that processes which occur on the nanosecond all the way up to hour time scales can be probed spectroscopically on this beamline.

TIMING DEMONSTRATION

To demonstrate the fast-timing capabilities of this beamline, we synchronized the detection electronics with the ALS ring timing structure (one trigger per complete revolution of the electrons). IR spectra were then obtained at 5nsec time slices for a total of 650nsec. We plot the measured IR intensity as a function of time in Figure 2.

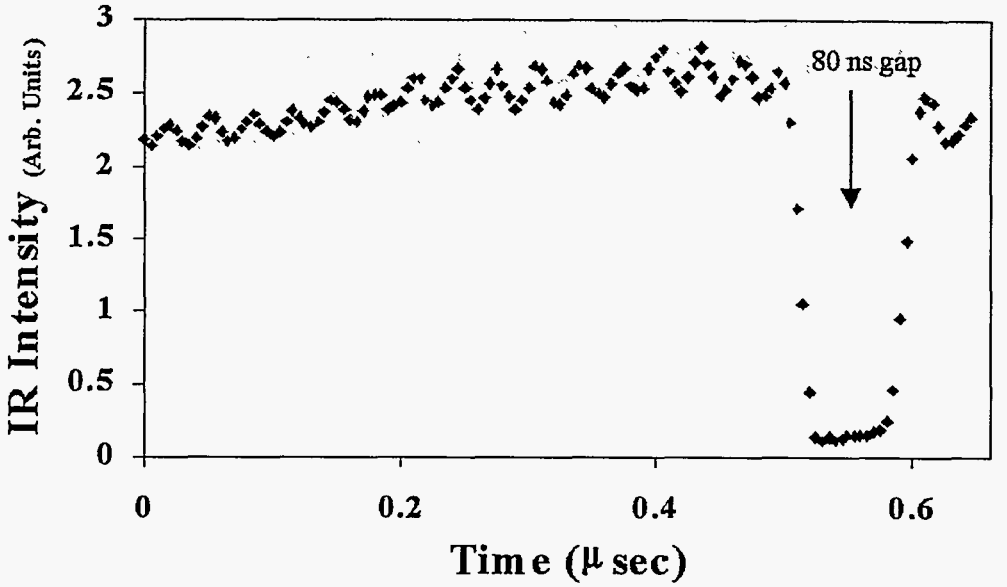

Figure 2. Time-resolved measurement of the IR intensity showing the 80 nsec gap in the ALS synchrotron filling pattern. The time resolution of the current electronics does not yet fully separate the 2 nsec spacing between pulses.

Figure 2 clearly shows that we can observe the 80 nsec gap in the synchrotron light pulses. The IR detector and digitization electronics are not yet fast enough to observe the 2 nsec pulse spacing, but forthcoming enhancements should allow sub-nanosecond timing enabling the use of individual synchrotron pulses to serve as the probe in very fast time-resolved experiments.

Typical applications for this beamline will include pump-probe measurements (semiconductors, metastable states), environmental science (adsorbates, bacteria, soil chemistry, bioremediation), biological materials (identification of biomolecules, time-resolved chemical reactions), high-pressure systems (materials in diamond anvil cells), and measurements in high-magnetic fields (reflectivity from high-T_c and other correlated electronic systems).

CONCLUSION

The step-scan capabilities of the IFS66v/S FTIR spectrometer on BL1.4.2 allow for very fast time-resolved IR spectroscopy. This instrument, in conjunction with the ALS synchrotron's pulsed nature, makes possible a host of new time-resolved and pump-probe spectroscopic experiments.

ACKNOWLEDGMENTS

This work was supported by the Director, Office of Energy Research, Office of Basic Energy Sciences, Materials Science Division, of the U.S. Department of Energy under Contract No. DE-AC03-76SF00098.

Principal investigator: Michael C. Martin, Advanced Light Source, Mail Stop 7-222, Ernest Orlando Lawrence Berkeley National Laboratory. Email: mcmartin@lbl.gov. Telephone: 510-495-2231.

BL1.4.3: 10-micron spot size achieved for high spatial resolution FTIR spectromicroscopy

Michael C. Martin and Wayne R. McKinney
Advanced Light Source Division, Ernest Orlando Lawrence Berkeley National Laboratory,
University of California, Berkeley, California 94720, USA

INTRODUCTION

Synchrotron-based infrared (IR) beamlines provide considerable brightness advantages over conventional IR sources. This brightness advantage manifests itself most beneficially when measuring very small samples. In the commissioning of ALS beamline 1.4.3, we have experimentally measured the small spot-size obtained by our IR microscopy system when using the synchrotron beam and we compare it to the internal Globar source. Here we demonstrate this tight focus and the factor of ~100's improvement over conventional sources in measured signal through very small apertures.

ACHEIVED SPOT SIZE

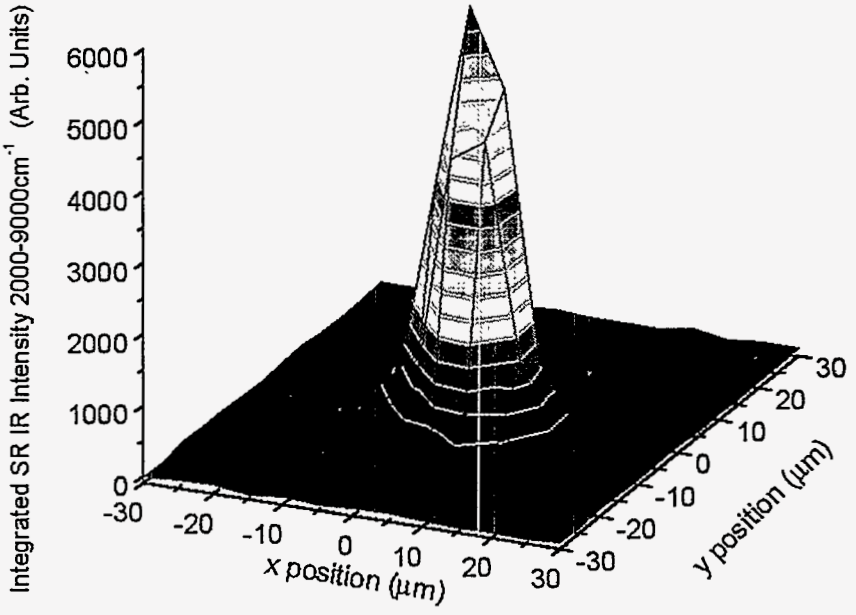

Figure 1. Integrated IR signal intensity from 2000 - 9000cm^{-1} through a 10μm pin hole being scanned on microscope stage. There are no other apertures in the optical path. This graph demonstrates the small spot size achieved using the synchrotron IR beam

We have made measurements to determine the small spot sizes achievable with the infrared microspectroscopy set-up on Beamline 1.4.3. The spectrometer software can take an area scan by moving the sample stage with 1 micron spatial resolution under the focused IR beam and acquiring FTIR spectra at each point. To determine the actual focused spot size of the synchrotron beam and compare it to the internal Globar IR source, we used a 10μm pin hole and measured the transmitted spectra as a function of the pin hole position. No other beam-defining apertures were used.

By integrating over the measured energies, we obtain an intensity number. The intensity as a function of pin hole position is shown above in Figure 1. We clearly have a nice small spot being produced by our optics. In Figure 2 (below) we plot the x and y profiles of this spot along with fits to a Gaussian line-shape. The data fits very well to a Gaussian line-shape with resultant widths of 10μm in x and 8μm in y. This spot size is becoming roughly diffraction-limited for the low-energy end of our detection capabilities (1000cm^{-1} = 10μm wavelength).

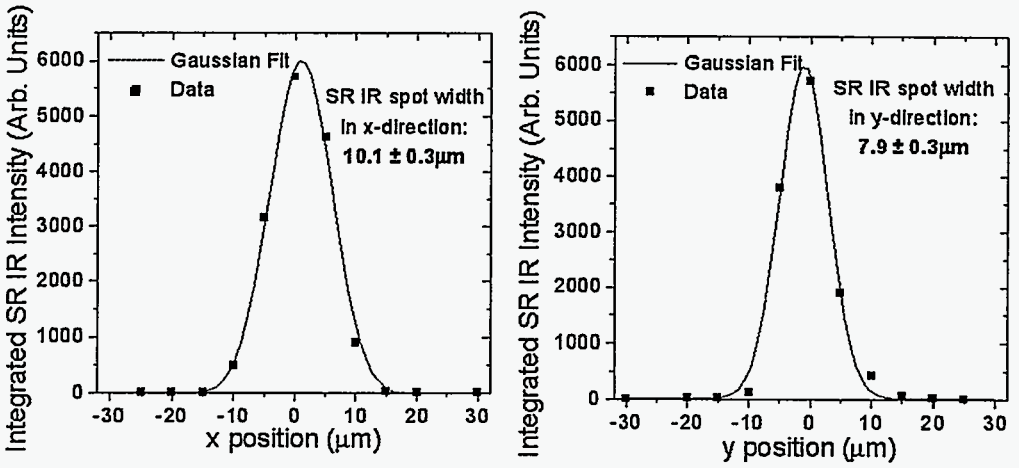

Figure 2. Peak shape profiles in the x (left panel) and y (right panel) directions. We observe a well-defined Gaussian peak shape with widths of 10μm in x and 8μm in y.

When we compare the above measurements to similar measurements made with a conventional Globar IR source, the brightness advantages of the synchrotron become readily apparent. The Globar has a much broader peak profile of around 100μm in width simply due to the large source size of this glowing filament source making a better focus impossible. Therefore, while the overall amount of light passing through the optical system from the Globar and the synchrotron sources is comparable, nearly all of the synchrotron light can be focused onto a 10μm spot. To achieve a similar spot size using the conventional Globar source, one must simply mask down the apertures and throw away a factor of lot of signal intensity. We measure improvements of several hundred in intensity through small pin-holes (5μm and smaller) for the synchrotron source compared to the Globar.

CONCLUSION

When high spatial resolution infrared experiments are of interest, Beamline 1.4.3 provides a huge gain in the available signal.

ACKNOWLEDGMENTS

This work was supported by the Director, Office of Energy Research, Office of Basic Energy Sciences, Materials Science Division, of the U.S. Department of Energy under Contract No. DE-AC03-76SF00098.

Principal investigator: Michael C. Martin, Advanced Light Source, Mail Stop 7-222, Ernest Orlando Lawrence Berkeley National Laboratory. Email: mcmartin@lbl.gov. Telephone: 510-495-2231.

The First Infrared Beamline at the ALS: Design, Construction, and Commissioning

Wayne R. McKinney, Michael C. Martin, Carol J. Hirschmugl, Howard A. Padmore
Advanced Light Source Division, Lawrence Berkeley National Laboratory
MS 2-400, One Cyclotron Road, Berkeley, California 94720-0001 USA

Ted Lauritzen, Nord Andresen, Greg Andronaco, Rob Patton, Martin Fong, Noel Kellogg
Engineering Division, Lawrence Berkeley National Laboratory
MS 46-161, One Cyclotron Road, Berkeley, California 94720-0001 USA

INTRODUCTION

The bright continuous spectrum of radiation from all storage rings extends into the infrared (IR) region of the spectrum. In fact, within about two orders of magnitude, all synchrotron radiation sources provide an essentially similar source of IR light. While synchrotrons do not provide as much flux as a typical laboratory source, the highly collimated nature of the light allows more light to be routed through a smaller pinhole than when using any other continuum source. The cross-over point when the use of synchrotron radiation (SR) for microscopy becomes advantageous is at pinhole sizes of approximately 50 to 75 microns depending on the storage ring.

Figure 1 shows the brightness in watts/mm/str/2cm^{-1}/ampere at the ALS with respect to a 1200 degree K blackbody. 2cm^{-1} is a typical bandwidth of a Fourier transform IR spectrometer (FTIR). It is quoted per ampere to allow for comparison with other rings. The maximum current at the ALS is 400 ma. Clearly, for microscopy, the SR source is on the order of two to three orders of magnitude brighter than the blackbody source.

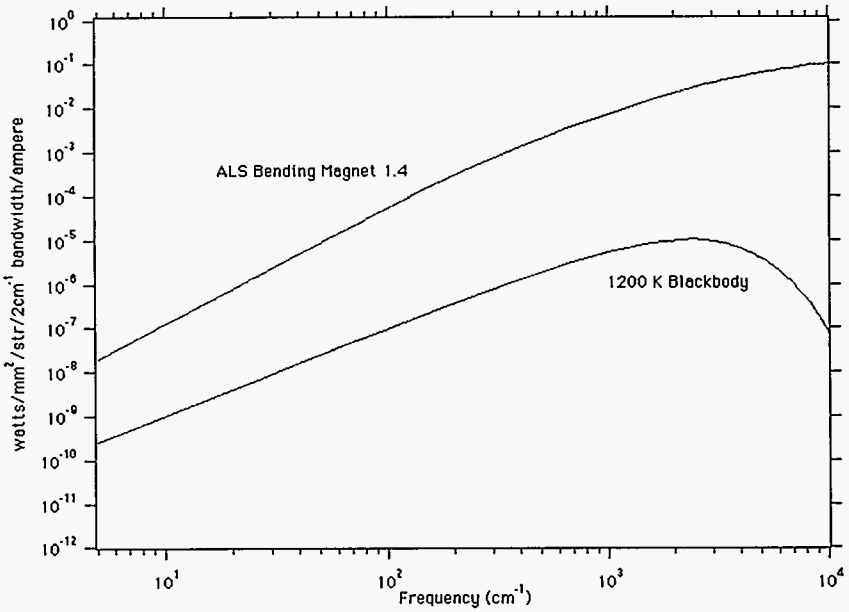

Figure 1.

This abstract provides the overall layout of the beamline, and a description of the commissioning of the beamline.

OVERALL LAYOUT

Figure 2 shows the layout of the beamline. The physical aperture in the storage ring is approximately 10 mr vertical by 80 mr horizontal. Only half of the horizontal aperture can be used, due to interference with a magnet downstream of the bending magnet. A water-cooled Glidcop™ aperture plate absorbs half of the radiation and passes the 10 mr vertical by 40 mr horizontal beam. The aperture plate is followed by a bellows and an all-metal valve which can shut only when the

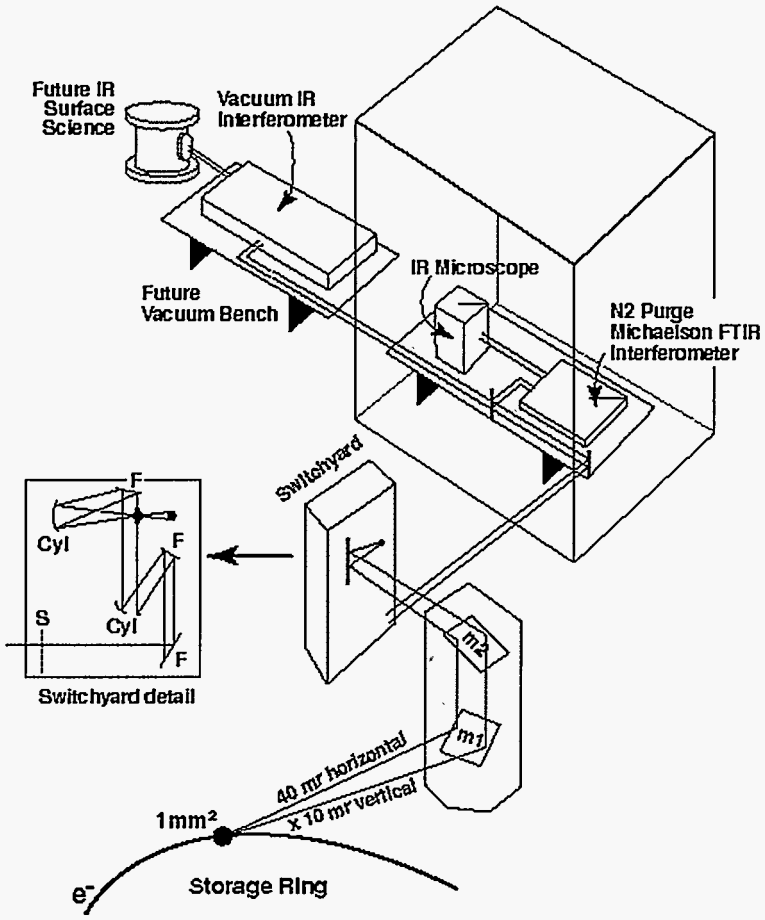

Figure 2. Layout of IR Beamline 1.4

storage ring is not running. (It would quickly overheat if closed during operation.) The first mirror (M1) is a water-cooled mirror of brazed Glidcop™ with an electroless nickel polished layer. The mirror is located three meters from the tangent point in the bending magnet. The mirror was fabricated at LBNL, and ground and polished by SESO of France. It is novel in that most of it is located outside the UHV chamber, and the mirror body itself forms the seal with the chamber, with an Helicoflex seal. Space considerations drove these choices, and there is considerable advantage to being able to change the mirror for coating and inspection. With proper tenting and dry nitrogen purge, the mirror can be removed during shutdown periods without the need to bake the system after re-installation. The incidence angle on the mirror (M1), 45 degrees, directs the radiation vertically upward onto an ellipsoidal mirror (M2). This is a Zerodur mirror made by conventional techniques, also by SESO. It is placed in the same UHV chamber as M1, and directs the light 90 degrees tangentially to the storage ring and outside of the shielding wall. The 0.5 meter rise will allow future x-ray lines from the previous two bending magnets to pass under the IR beam. A five-inch hole in the shielding wall permits the beam pipe to pass without any lead shielding because of the 0.5 meter vertical difference between the hole and the ring. Measurements show essentially no radiation outside the hole during operation of the ring, and only minimal radiation during injection. The beam passes through a large ion pump just inside the shield wall.

Immediately outside the wall is a large, low vacuum box: the "switchyard." It can be positioned by a six-strut system. Only one rotation is motorized. The UHV extends a short distance into the switchyard. A small, flat mirror turns the radiation towards the microscopy hutch and a diamond window. The diamond window, manufactured by Druker and sold by Harris corporation, is rated to withstand three atmospheres, and is the last UHV component. For additional protection, a small fused-silica-windowed valve with a Viton o-ring seal just before the switchyard shuts automatically if the vacuum fails in the switchyard. The diamond window is 12 mm in diameter and is placed at the focus of the ellipsoidal mirror. It is sealed in indium foil on both sides, and is polished with a one-degree wedge to remove possible extraneous interference fringes in the FTIR spectra caused by multiple reflections.

The M1/M2 chamber has two motions which can be controlled remotely using DC servo-motors. The chamber can be rotated about a vertical axis through the centers of the two mirrors, and the chamber can be moved up and down vertically to center M1 on the height of the radiated beam. M2 has pitch, roll, and yaw which can be adjusted only from inside the chamber.

Within the switchyard the radiation is allowed to expand four times as far in the 10 mr direction than in the 40 mr direction to allow the beam to be collimated by two separate cylindrical mirrors. This "squares up" the beam to a size which optimally fills one of two microscope objectives of 32x and 15x. There are two separate collimating/squaring sets of optics which can be moved in and out by motorized control under vacuum. Parallel beams approximately 6 mm square and 12 mm square leave the switchyard in the vacuum pipe which leads to the hutch. The cylindrical mirrors are precision optics from a vendor specializing in cylindrical optics.

In the hutch, plane mirrors inside the vacuum pipe lead to a KBr window or another wedged diamond window of 20 mm diameter. The low vacuum stops here and the radiation enters a dry air purged Nicolet 760 FTIR bench. The use of low vacuum all the way to the bench prevents noise from moving purge gas in the long run from the switchyard to the hutch. The bench is followed by a Nic-Plan all-reflective IR microscope with LN_2 cooled detector. The hutch has a small positive pressure from a HEPA filtered air source to keep some degree of cleanliness near the microscope and to provide a secure and isolated environment. Both instruments are supported by an optical table mounted on an interoferometrically stable "six strut" kinematic support system which is successfully in use in throughout the ALS. A hand crank provides rotation of the entire table about the center of the first steering mirror in the transfer pipe at the corner of the table nearest the entrance of the beam, without sacrificing interferometric stability.

For pump-probe timing and IR surface science experiments we have obtained a vacuum FTIR bench from Bruker which will be placed on another table outside the hutch, identical to the one in the hutch which supports the microscope and FTIR bench. The vacuum plumbing is being extended through the hutch wall, onto this table, and into the vacuum instrument. Additional optical components will transfer the beam into an IR surface science experiment.

COMMISSIONING

The M1/M2 chamber was connected to the ring during a two-day shutdown. Synchrotron IR is now routinely in the IR microscope, producing a 10 μm spot size. Synchrotron light has been admitted to the vacuum FTIR bench, and the timing and step-scan abilities of the instrument have been demonstrated with a timing signal from the storage ring. Formal operation of the beamline will commence on June 3. 1998.

SUMMARY

A state-of-the-art beamline for the extraction of IR radiation from a bending magnet at the ALS has been constructed, and is being commissioned. FTIR microscopy at higher spatial resolution than is available in the normal laboratory environment will be available to users. In addition, timing experiments and IR surface science experiments will be able to share the beamline after minimal further construction.

ACKNOWLEDGMENTS

Greg Vierra drew the layout of the beamline. At all stages of the development, Gwyn Williams and Larry Carr of the NSLS have generously provided the advantages of their extensive experience in IR beamline design and commissioning.

REFERENCES

[1] Hirschmugl, C.J., PhD Thesis Yale University, 1994.

This work was supported by the Director, Office of Energy Research, Office of Basic Energy Sciences, Materials Science Division, of the U.S. Department of Energy under Contract No. DE-AC03-76SF00098.

Principal investigator: Wayne R. McKinney, Advanced Light Source, Ernest Orlando Lawrence Berkeley National Laboratory. Email: wrmckinney@lbl.gov. Telephone: 510-486-4395.

Surface-Enhanced Infrared Absorption-Reflectance (SEIRA) Microspectroscopy – A Chemical/Biological Probe for Bacteria Localization in Geologic Materials

Hoi-Ying N. Holman, Dale L. Perry, Michael C. Martin, Wayne R. McKinney, and Jennie C. Hunter-Cevera
E.O. Lawrence Berkeley National Laboratory, University of California, Berkeley, CA 94720 USA

INTRODUCTION

Pollution of subsurface geologic zones and the possibility of using the intrinsic endolithic (rock/mineral-inhabiting) bacteria to either detoxify or immobilize the pollutants have stimulated new interests in the exploration of endolithic bacteria and their long-term survival in the geologic environment. The location of bacteria within rocks and minerals affects the type and intensity of environmental stresses the bacteria are exposed to and thus affects their long-term survival potential. Localization of bacteria within rocks has been the subject of many ongoing research programs. Strategies must be devised to answer the question of relationships between the microbial localization and the microstructure of rocks. One approach is a microscopic system approach [1], using microscopy techniques to visually enumerate the distribution of microorganisms on an intact environmental sample. The distribution is related to the microscale physical and geochemical features measured on the same intact environmental sample. Other approaches include a global system [2], which uses different molecular probes to identify the presence of microorganisms in crushed rocks and conventional methods to identify the physical and geochemical properties of the rock materials.

The purpose of this study is to present the use of surface-enhanced infrared absorption-reflectance (SEIRA) microspectroscopy as a chemical/biological probe to analytically study — quickly and with minimum sample preparations — relationships between the microbial localization and the microstructure of geologic materials such as rocks. Specifically, it was to investigate if spatially resolved SEIRA microspectra, when recorded with a proper spatial scale and infrared beam area, could successfully illustrate the micro-scale spatial composition differences and to provide further insights into factors that control localization of bacteria in the specimen. The fundamental goal of our selecting spatially resolved SEIRA microspectroscopy was to identify qualitatively highly localized differences in the chemical composition and structure of clusters of living-bacteria within rocks that inherently have low infrared reflective surfaces.

PRINCIPLE OF SEIRA MICROSPECTROSCOPY

SEIRA microspectroscopy combines the traditional light-reflecting microscopy with the more recent but well-documented SEIRA spectroscopy technique. The fundamental working concept of SEIRA microspectroscopy is to use visible light and reflecting optics to view a magnified image of the sample and to select a microscopic surface area on the sample for infrared reflection-absorption spectroscopic analysis [3]. The selection of the area is relatively subjective and relies on a number of physical properties and other material-specific features of the sample surface. Once the sample area is selected, the molecular information of the selected surface area can be recorded spectroscopically in the infrared spectral region. For samples with surfaces of low infrared reflection, such as rock surfaces or surfaces with low analyte concentrations, such as those typically encountered in studies of environmental pollution, the measured spectra often do not have sufficient sensitivity for obtaining molecular information of the surface. Several researchers [e.g., 4-5] have found that SEIRA spectroscopy can increase the spectral sensitivity tremendously by

using different enhancement techniques that are commonly employed for chemical analyses for extremely small amounts of chemicals on surfaces. The increase is due to the enhancement of the incident infrared field at the surface. Recent literature has demonstrated that SEIRA spectroscopy has been successfully used in a wide variety of the analysis of water and thin organic films on semi-conductors, glasses, and polymers [6-10].

RESULTS AND DISCUSSION

The space-resolved SEIR microspectroscopy analysis was a line analysis conducted along axis BAB' inside a 400×500-μm study area, as shown in Fig. 1. Fig. 2 shows confocal micrograph images of the x-y section of bacterial microcolonies along axis BAB' under simultaneous excitation at 488 and 510 nm. Additionally, confocal micrograph images of the y-z section (not shown here) indicate that most microcolonies were less than 1 μm thick from the basalt surface, except for the colony "A". Fig. 3 shows the SEM (scanning electron microscopy) micrograph images of endolithic

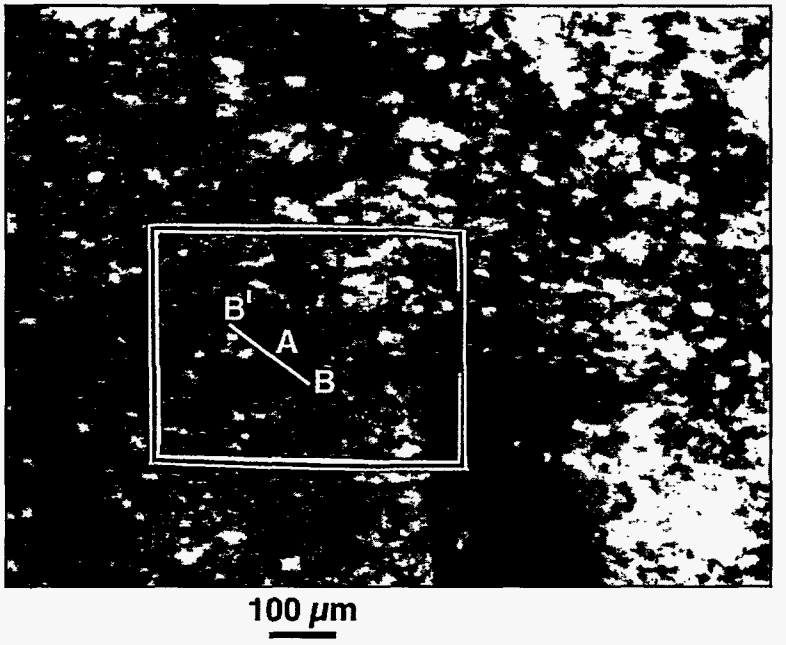

Figure 1. Microphotography of the study area. Bar = 100 μm.

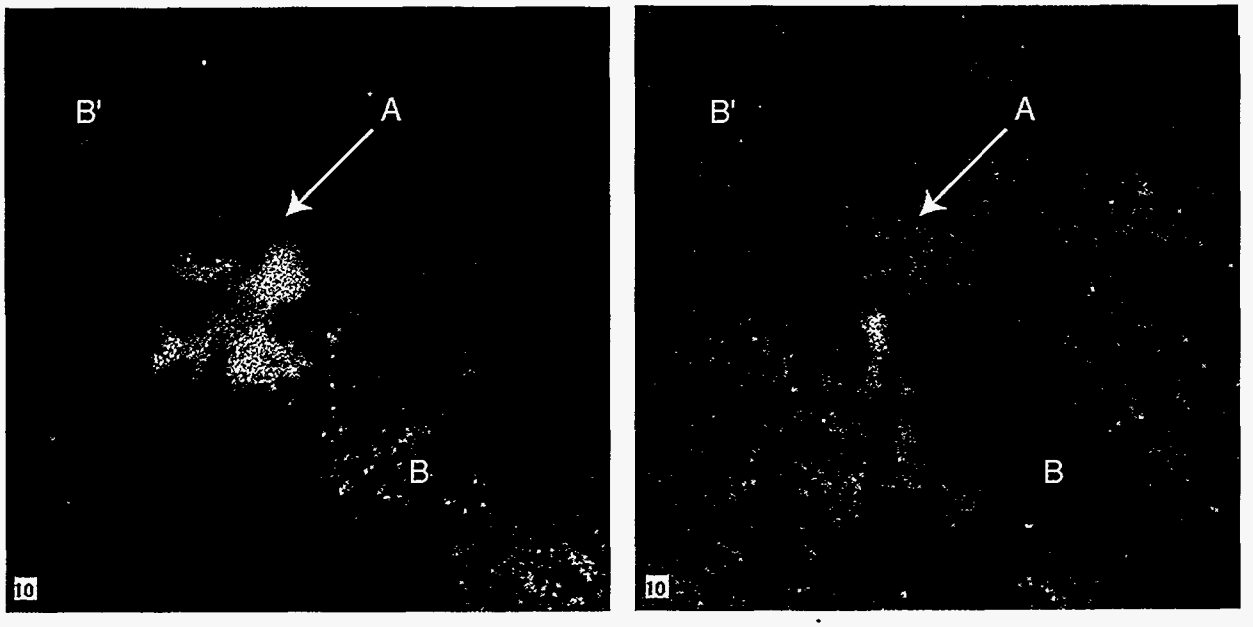

TOP BOTTOM

Figure 2. Confocal fluorescence micrograph of x-y sections showing images of microbial clusters "A" at two different optical depths on the vesicular basalt sample: 8.8 μm (top) and 1.1 μm (bottom) from the base of the brightest microbial cluster. The microbes were observed with simultaneous excitation at 488 and 514 nm. Microcolonies fluoresced naturally under simultaneous excitation at 488 and 510 nm. The fluorescence color was mostly pale yellow to yellow-green. Scale bar =10 μm.

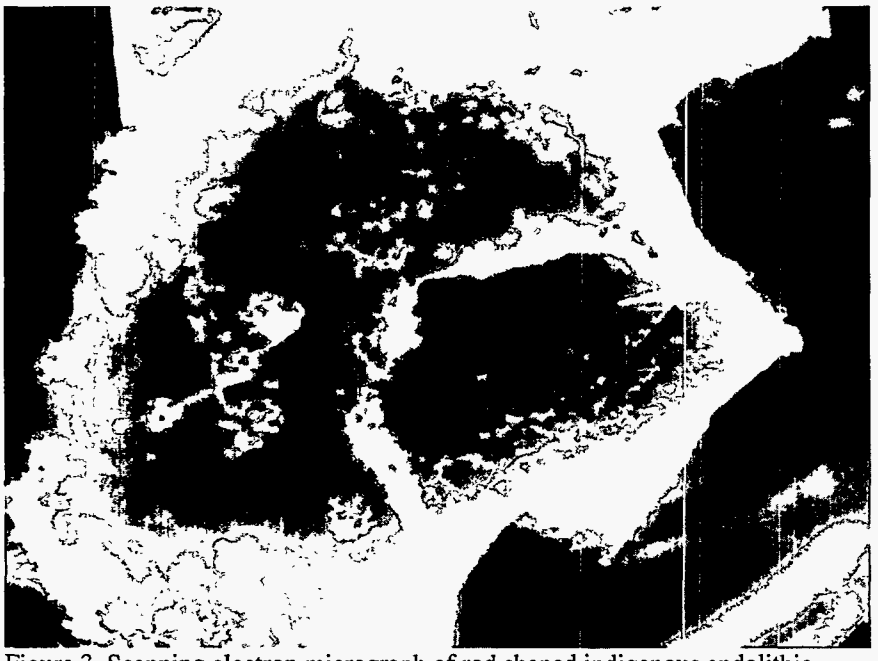

Figure 3. Scanning electron micrograph of rod shaped indigenous endolithic bacteria on the mineral surface inside a vesicle. (9,500x)

microbial populations on a mineral surface inside a basalt vesicle within the study area. Notice that the visible bacteria were rod shaped with approximate dimensions of 0.4-0.5 μm and were smaller than bacteria commonly found in the soil and aquatic environment.

All SEIRA microspectroscopic data were collected along the measurement axis BAB', starting at Point B and moving pass the edge of the fluorescent microcolony clusters. Fig. 4 shows the spectroscopic differences of FTIR scans as the sampling point was moved along BAB'. Notice the infrared spectral characteristics changed abruptly by scan 24 as the transition into the bacteria-free area was made. The continuous presence of biomolecule spectral peaks way into the dark area in the confocal micrograph (Fig.2) indicated that not all the indigenous bacteria naturally fluoresced under simultaneous excitation at 488 and 510 nm. The decrease of biomolecules marker peaks between scans 21 and 24 coincided with a change of mineral marker peaks. With this experimental effort, the practical aspects and the usefulness of SEIRA as a promisingly simple and fast analytical tool for studying the localization of living bacteria within rocks have been demonstrated.

ACKNOWLEDGMENTS

The authors wish to acknowledge the support of this research by the Directors, Office of Energy Research, Offices of Health and Environmental Sciences, Biological and Environmental Research Program and Basic Energy Sciences, Materials Science Division, of the United States Department of Energy under Contract No. DE-AC03-76SF00098. Special thanks are also extended to the Dr. S.E. Ruzin of the Center for Biological Imaging (University of California, Berkeley) for providing us with the molecular dynamics confocal laser scanning microscope, and Dr. R. Cowell of the Idaho National Engineering Laboratory for supplying us with the samples.

REFERENCES

1. Ferris, F.G., and Lowson, E.A. (1997) Ultrastructure and geochemistry of endolithic microorganisms in limestone of the Niagara Escarpment. Can. J. Microbiol. **43**, 211-219.
2. Fredrickson, J.K., McKinley, J.P., Bjornstad, B.N. (1997) Pore-size constraints on the activity and survival of subsurface bacteria in a late cretaceous shale-sandstone sequence, Northwestern New Mexico. Geomicrobiology J. **14**, 183-202.
3. Reffner, J.A., and Martoglio, P.A. (1995) Uniting microscopy and spectroscopy. In: Practical Guide to Infrared Microspectroscopy (Brame, E.G., Ed.), pp. 41-84, Marcel Dekker, Inc., New York.
4. Kellner, R., Mizaikoff, B., Jakusch, M., Wanzenböck, H.D, and Weissenbacher, N. (1997) Surface-enhanced vibrational spectroscopy: a new tool in chemical IR sensing? Appl. Spectrosc. **51**, 495-503.

5. Hartstein, A., Kirtley, J.R., and Tsang, J.C. (1980) Enhancement of the infrared absorption from molecular monolayers with thin metal overlayers. Phys. Rev. Lett. **45**, 201-204.
6. Hattta, A., Suzuki, Y., and Suëtaka W. (1984) Infrared absorption enhancement of monolayer species on thin evaporated Ag films by use of a Kretschmann configuration: Evidence for two types of enhanced surface electric fields. Appl. Phys. A. **35**, 135-140.
7. Ataka, K.-I., Yotsuyanagi, T., and Osawa, M. (1996) Potential-dependent reorientation of water molecules at an electrode/electrolyte interface studied by surface-enhanced infrared absorption spectroscopy. J. Phys. Chem. **100**, 10664-10672.
8. Johnson, E., and Aroca, R. (1995) Surface-enhanced infrared spectroscopy of monolayers. J. Phys.Chem. **99**, 9325-9330.
9. Wanzenböck, H.D., Mizaikoff, B., Weissenbacher, N., and Kellner, R. (1997) Multiple internal reflection in surface enhanced infrared absorption spectroscopy (SEIRA) and its significance for various analyte groups. J. Molecular Structure **411**, 535-538.
10. Nishikawa, Y., Fujiwara, K., Ataka K.-I., and Osawa M. (1993) Surface-enhanced infrared external reflection spectroscopy at low reflective surfaces and its application to surface analysis of semi-conductors, glasses, and polymers. Anal. Chem. **65**, 556-562.

Principal investigator: Hoi-Ying N. Holman, Mail Stop 70A-3317, Ernest Orlando Lawrence Berkeley National Laboratory. E-mail: hyholman@lbl.gov. Telephone: 510-486-5943.

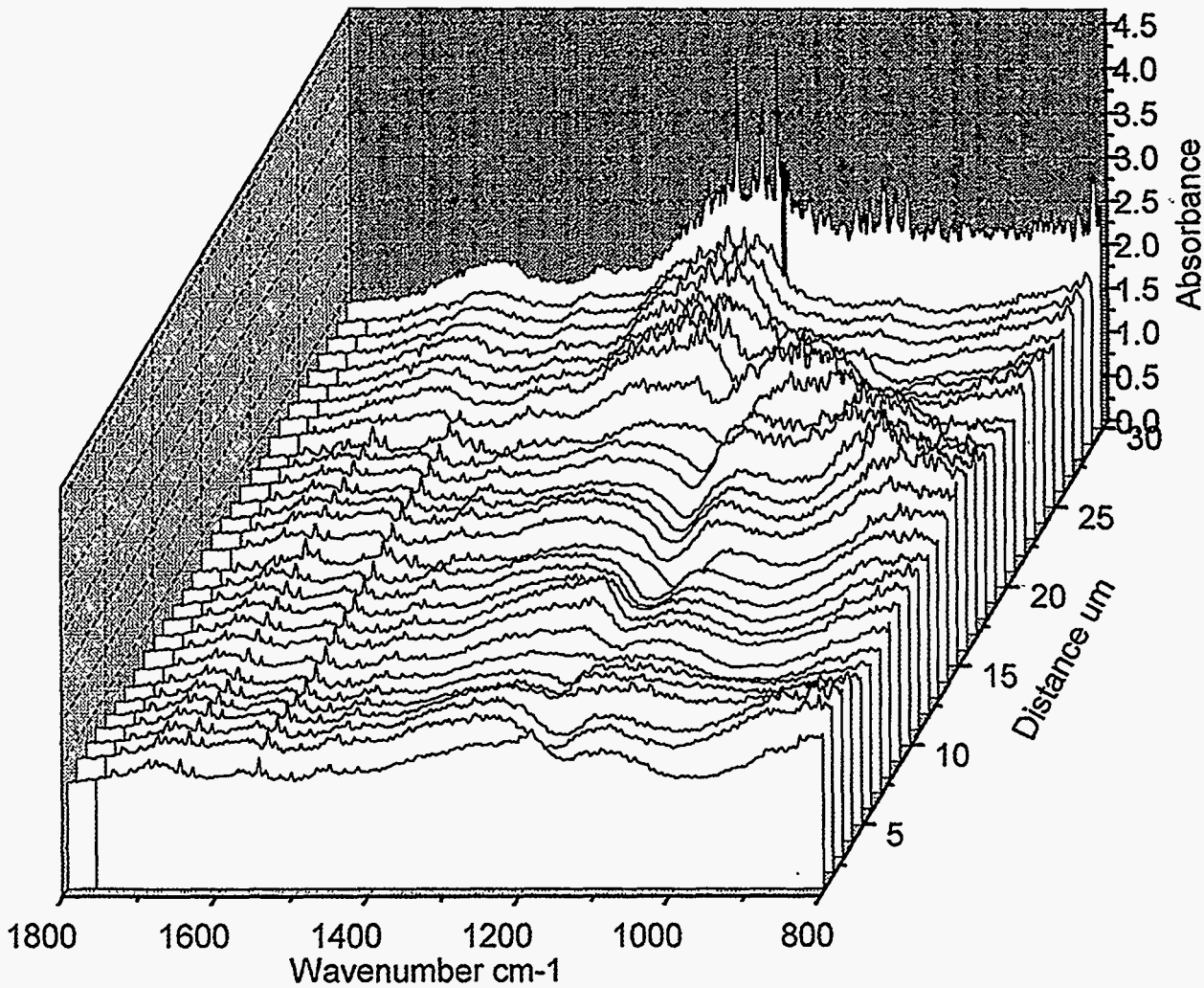

Figure 4. A series of SEIRA spectra showing the transition from bacteria-containing to bacteria-free basalt surface. Each step = 5 μm.

Beamline 5.0.2 Abstracts

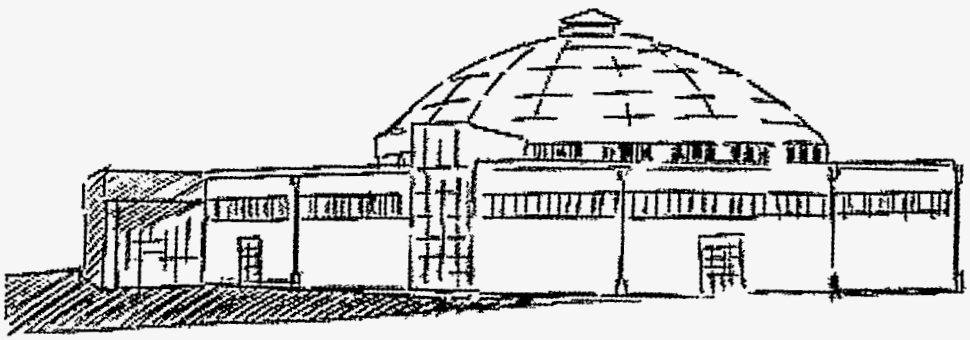

Crystallographic Analysis of Active-Site Mutants of Photoactive Yellow Protein

Ronald Brudler, Ulrich K. Genick, Ilona L. Canestrelli, Elizabeth D. Getzoff
The Scripps Research Institute, Department of Molecular Biology MB-4,
10550 North Torrey Pines Road, La Jolla, CA 92037 USA

Photoactive Yellow Protein (PYP) is a small cytoplasmic photoreceptor (14 kDa) from the halophilic purple bacterium *Ectothiorhodospira halophila*. PYP has been also found in several other photosynthetic bacteria and is proposed to mediate negative phototaxis.

Similar to the retinal binding membrane proteins like rhodopsin, bacteriorhodopsin or sensory rhodopsin, PYP enters a photocycle upon absorption of blue light (λ_{max} = 446 nm). PYP's chromophore is a *p*-hydroxycinnamyl anion covalently bound to C69 via a thioester linkage and undergoes *trans-cis* photoisomerization around its double bond. A red-shifted intermediate I_1 (460 nm) is formed in < 10 ns and decays with a time constant of 200 µs to a blue-shifted intermediate I_2 (355nm) which is proposed to be the signalling state. I_2 reacts back to the ground state P in 140 ms.

The ground state structure of PYP has been determined with 1.4 Å resolution [1] which was recently improved to 0.82 Å [2]. In addition, the structures of an early photocycle intermediate [2] and of I_2 [3] were solved by cryo-trapping and time-resolved Laue crystallography, respectively. This makes PYP a unique model for studying the molecular basis of light detection, signal transduction and dynamic structural changes in proteins.

The overall structure of PYP consists of a central, 6-stranded, antiparallel β-sheet flanked on each side by a hydrophobic core. The chromophore's aromatic ring, conjugated double bond, and thioester linkage are completely buried in the major hydrophobic core. Based on the structural information, we have constructed and crystallized the mutants E46Q and T50V in order to investigate the interplay of the chromophore and the protein environment in creating the photocycle. In the ground state, the phenolate oxygen of the chromophore hydrogen bonds with the hydroxyl group of E46. The other carboxyl oxygen of E46 has no hydrogen-bonding partner. An unsaturated hydrogen-bonding valence is unusual and may contribute to the increase of the pK_a of E46 (pK_a ~ 4.5 in solution) and the decrease of the pK_a of the chromophore (pK_a ~ 9 in solution). Thr 50 has a central role: its side-chain oxygen hydrogen bonds with the main-chain oxygen of E46 and with the OH group of Y42, which forms a second hydrogen bond to the phenolate oxygen of the chromophore; its main-chain carbonyl oxygen hydrogen bonds with R52, which shields the chromophore from solvent and undergoes major rearrangement during the photocycle [3]. All together, these amino acids are essential for maintaining the negative charge of the chromophore and to produce its yellow colour.

The mutations E46Q [4] and T50V shift the ground state absorption maximum from 446 nm to 462 and 458 nm, respectively. In addition, the photocycle kinetics are altered. For E46Q the largest effect is a 700-fold increase in the rate of recovery to the ground state (I_2 --> P) in response to a change in pH from 5 to 10 [4]. The photocycle kinetics for T50V are also altered. These changes indicate that hydrogen bonding between the chromophore, E46 and T50 is important for the fine

tuning of PYP's absoption maximum and the specific rates of its photocycle kinetics. We also have started FTIR spectroscopic investigations on wild-type and the mutants. Since FTIR spectroscopy is highly sensitive to even minor structural changes, the structural integrity of the mutants has to be determined by X-ray crystallography to very high accuracy.

Crystals of native and mutated PYP grow as long hexagonal rods and belong to the space group $P6_3$. The unit cell dimensions of the wild-type crystals (a = 66.9 Å, b = 66.9 Å, c = 40.8 Å) are slightly modified for the mutants (E46Q: a = 66.3 Å, b = 66.3 Å, c = 40.7 Å; T50V: a = 67.8 Å, b = 67.8 Å, c = 39.4 Å). Data collection at ALS in December 1997 allowed us to obtain data with 1.7 Å resolution (3.9 % complete to 1.5 Å). The obtained resolution was limited by the crystal-detector distance at beamline 5.0.1 which could not be decreased beyond 152 mm. We hope that an improved setup will allow the collection of higher resolution data.

REFERENCES

1. Borgstahl, G.E.O., Williams, D.R., and Getzoff, E.D., Biochemistry **34**, 6278 (1995).
2. Genick, U.K., Soltis, S.M., Kuhn, P., Canestrelli, I.L., and Getzoff, E.D., Nature, in press (1998).
3. Genick, U.K., Borgstahl, G.E.O., Ng, K., Ren, Z., Pradervand, C., Burke, P.M., Srajer, V., Teng, T.-Y., Schildkamp, W., McRee, D.E., Moffat, K., and Getzoff, E.D., Science **275**, 1471 (1997a).
4. Genick, U.K., Devanathan, S., Meyer,T.E., Canestrelli, I.L., Williams, E., Cusanovich, M.A., Tollin, G., and Getzoff, E.D., Biochemistry **36**, 8 (1997b).

This work was supported by a grant from NIH (GM37684 to E.D.G.) and fellowships from Boehringer Ingelheim Fonds (U.K.G.) and Deutsche Forschungsgemeinschaft (R.B.).

Principal investigator: Elizabeth D. Getzoff, The Scripps Research Institute, Department of Molecular Biology. Email: edg@scripps.edu. Telephone: 619-784-2878.

Crystal Structure of Free Human Growth Hormone

Mark Ultsch & Abraham M. de Vos
Department of Protein Engineering, Genentech, Inc., 460 Point San Bruno Boulevard,
South San Francisco, CA, 94080, USA

INTRODUCTION

Human growth hormone (hGH) is a pituitary hormone exhibiting a wide variety of biological effects, including growth and differentiation of muscle, bone, and cartilage [1]. These functions are mediated through binding of hGH to the human growth hormone receptor (hGHR) and the prolactin receptor (PRLR). The growth hormone system is well characterized by mutagenesis, structural and functional studies. Crystal structures of free hGH [2] and hGH bound to each of its receptors have been determined [3,4]. These studies seem to imply that hGH undergoes surprisingly large structural changes upon receptor binding.

However, the crystal structure of free hGH is only of moderate quality despite the reported resolution of 2.5 Å. The data set used for refinement was merely 67% complete with only 37% of all reflections measured in the highest resolution shell between 2.5 Å and 2.75 Å. No free-R value was used to monitor refinement progress and several criteria, such as the stereo chemistry and Ramachandran plot which are commonly used to assess the quality of a refined structure, indicate that the model is partially inaccurate. The present study was initiated to provide an independent assessment of the structural changes of hGH upon receptor binding.

RESULTS AND DISCUSSION

Crystals of hGH were obtained under the same conditions reported by Chantalat et al. [2]. A single frozen crystal was used to collect a data set with 99.7% completeness at a maximum resolution of 2.7 Å at ALS, beamline 5 in December 1997. The data set is of good quality with an R-sym of 6.1% and 7-fold redundancy. The tetragonal space group $P4_12_12$ of Chantalat et al. was confirmed with cell parameters of a=b=56. 1 Å and c=129.8 Å. Molecular replacement using program AMoRe and the coordinates of the free hGH structure (pdb-entry 1hgu) resulted in an initial R-factor of 46% using all reflections between 10 Å and 3.0 Å. Refinement is in progress.

REFERENCES

1. Chawla, R.K., Parks, J.S. & Rudman, D. (1983). Structural variants of human growth hormone: biological, genetic and clinical aspects. Annu. Rev. Med. **34**, 519-547.
2. Chantalat, L., Jones, N.D., Körber, F., Navaza, J. & Pavlovsky, A.G (1995). The crystal structure of wild-type growth hormone at 2.5 Å resolution. Prot. Pep. Lett **2**, 333-340.
3. De Vos, A.M, Ultsch, M. & Kossiakoff, A.A. (1992). Human growth hormone and extracellular domain of its receptor: crystal structure of the complex. Science **255**, 306-311.
4. Somers, W., Ultsch, M., De Vos., A.M. & Kossiakoff., A.A. (1994). The X-ray structure of a growth hormone-prolactin receptor complex. Nature **372**, 478-481.

All funding for this work was provided by Genentech, Inc.

Principal investigator: Abraham M. de Vos, Genentech, Inc. Email: devos@gene.com. Telephone: (650) 225-2523. Fax: (650) 225-3734.

Crystal Structures of Vascular Endothelial Growth Factor in Complex with Fab Fragments

Christian Wiesmann, Hans W. Christinger, Yvonne Chen, Henry B. Lowman & Abraham M. de Vos
Department of Protein Engineering, Genentech, Inc., 460 Point San Bruno Boulevard, South San Francisco, CA, 94080, USA

INTRODUCTION

Vascular endothelial growth factor (VEGF) is a cell-selective mitogen for vascular endothelial cells [1]. As a potent angiogenic factor it is required for the development of the vascular system and has been implicated in pathological processes such as tumor growth, metastasis, diabetic retinopathy and rheumatoid arthritis [2]. Neutralizing antibodies against VEGF are capable of suppressing tumor growth in a murine model [3] and will potentially be very useful therapeutic agents to regulate excessive vascularization.

VEGF is a homodimeric glycoprotein, which occurs naturally in four different isoforms consisting of 121, 165, 189 or 206 residues. The three longer isoforms are capable of binding to heparin and are found in complex with heparan sulfate containing proteoglycans in the extracellular matrix. Plasmin cleavage of $VEGF_{165}$, the most abundant isoform, yields an N-terminal fragment consisting of 110 amino acids. This 'receptor-binding' fragment is capable of binding to the two receptors of VEGF, the fms-like tyrosine kinase (flt-1) and the kinase domain receptor (KDR), with wild type affinity [4].

Recently, the structures of a truncated receptor binding fragment covering residues 8 to 109 has been solved in its unbound state [5], in complex with the second domain of the flt-1 receptor [6], and in complex with the humanized version of antibody A4.6.1. [7]. Based on the structure of VEGF in complex with the Fab-fragment, two affinity improved antibodies (Y0313 and Y0317) were derived using phage display.

RESULTS AND DISCUSSION

The receptor binding domain of VEGF in complex with Y0317 crystallizes in spacegroup $P2_1$ with cell parameters of a=89.1 Å, b=66.4 Å, c=138.8 Å, and β=94.7°. A full dataset with a maximum resolution of 2.5 Å and an R_{sym} of 7.6% was collected at ALS, beamline 5, in December 1997. The previously solved structure of VEGF in complex with an antibody fragment was used to solve the structure. The current R-value is 25.3% with a R-free of 30.1% and refinement is in progress.

The first X-ray quality crystals of $VEGF_{165}$, the most abundant isoform of VEGF, were obtained by forming a complex with the Fab fragment Y0313. These crystals diffract to a maximum resolution of 2.8 Å and belong to space group P2 with cell parameters of a=107.6 Å, b=65.8 Å, c=123.8 Å, and β=93.4°. A complete dataset of good quality with a R-sym of 7.4% was collected in December 1997 at ALS, beamline 5. One complex consisting of one Fab fragment bound to each side of a VEGF dimer was expected in the asymmetric unit. The structure was solved by molecular replacement, using the constant domains and the variable domains of an Fab fragment as a search model. A model of the receptor binding domain of VEGF could be placed unambiguously in a resulting difference density map. Refinement of the structure is in progress, the current R-value is 27% with an R-free of 34% using all data between 2.8 Å and 20 Å.

These two structures, together with the structure of the parent Fab in complex with the receptor binding domain of VEGF [7], will help us to understand the different binding affinities towards VEGF of the three different Fab fragments.

REFERENCES

1. Dvorak, H.F., Brown, L.F., Detmar, M. & Dvorak, A.M. (1995). Vascular permeability factor/vascular endothelial growth factor, microvascular hyperpermeability and angiogenesis. *Am. J. Pathol.. 146,* 1029–1039.
2. Ferrara, N. (1995). The role of vascular endothelial growth factor in pathological angiogenesis. *Breast Cancer Res. Treat.* **36**, 127–137.
3. Kim, J.K., Li, B., Winer, J., Armanini, M., Gillet, N., Phillips, H.S. & Ferrara, N. (1993). Inhibition of vascular endothelial growth factor-induced angiogenesis suppresses tumor growth in vivo. *Nature* **362**, 841–844.
4. Keyt, B.A., Berleau, L.T., Nguyen, H.V., Chen, H., Heinsohn, H., Vandlen, R., & Ferrara, N. (1996). The carboxyl-terminal domain of vascular endothelial growth factor is critical for its mitogenic potency. *J. Biol. Chem.* **271**, 7788–7795.
5. Muller, Y.A., Li, B., Christinger, H.W., Wells, J.A., Cunningham, B.C., & de Vos, A.M. (1997). Crystal structure at 1.7 Å resolution of VEGF in complex with domain 2 of the flt-1 receptor. *Cell* **91**, 695–704.
6. Muller, Y.A., private communication.

All funding for this work was provided by Genentech, Inc.

Principal investigator: Abraham M. de Vos, Genentech, Inc. Email: devos@gene.com. Telephone: (650) 225-2523. Fax: (650) 225-3734.

DNA homing site recognition and cleavage by I-*Ppo*I, a nuclear intron-encoded homing endonuclease

Karen E. Flick[1], Raymond J. Monnat, Jr.[2], and Barry L. Stoddard[1]

[1] Fred Hutchinson Cancer Research Center A3-023 1100 Fairview Ave. N
Seattle, WA 98019, USA

[2] Department of Pathology, University of Washington Box 357705
Seattle WA 98195, USA

INTRODUCTION

Homing endonucleases are a diverse family of proteins encoded by open reading frames in mobile self-splicing introns. Similar homing endonucleases have also been identified as optional, independently folded domains in self-splicing protein introns, termed 'inteins', and as free-standing open reading frames (ORFs). Homing endonucleases promote the lateral transfer of their encoding introns or open reading frames by a targeted transposition mechanism termed intron mobility or homing. This process is initiated and targeted by the endonuclease, which makes a highly site-specific DNA double strand break at a homing site that lacks the self-splicing intron or open reading frame (an "intron- or ORF-less" allele). The endonuclease ORF is subsequently transferred to the cleaved recipient allele by a double strand break repair/gene conversion event (Figure 1). Homing endonucleases have been identified in a diverse collection of unicellular eukaryotes, *Archea*, and eubacteria, with the largest number having been identified in organellar genomes. These comparatively small endonucleases (18 to 22 kDa per subunit for active dimers, 32 to 44 kDa for active monomers) share the ability to recognize and cleave long DNA target or "homing" sites of 15 to 40 bp with high specificity *in vivo* and *in vitro* [1-5] .

Four homing endonuclease families have been identified on the basis of conserved protein motifs. These include the LAGLIDADG, His-Cys box, GIY-YIG and HNH endonucleases. The His-Cys box endonucleases contain two conserved histidines and three conserved cysteines within a 30 residue region of protein (Figure 1).The first His-Cys box homing endonuclease identified, as well as the first nuclear homing endonuclease, was I-*Ppo*I [6-8]. The intron encoding I-*Ppo*I is one of three mobile introns known to reside in a eukaryotic nucleus. The other two nuclear-encoded endonucleases were identified in nuclear introns of the slime mold *Didymium iridis,* and in the amoeba *Naegleria andersoni* ssp *andersoni* [9]. The His-Cys box endonucleases, like the LAGLIDADG homing endonucleases, cleave their homing site DNAs to generate 4 base, 3' extended cohesive ends. The remaining two families of homing endonucleases consist of the bacteriophage-encoded GIY-YIG endonucleases that cleave homing site DNA to generate 2 base, 5' extended cohesive ends; and the catalytically diverse H-N-H homing endonucleases, that cleave their homing site DNAs to generate 2 base or 10 base, 5' extended cohesive ends, or that cleave only one of the strands of homing site DNA.

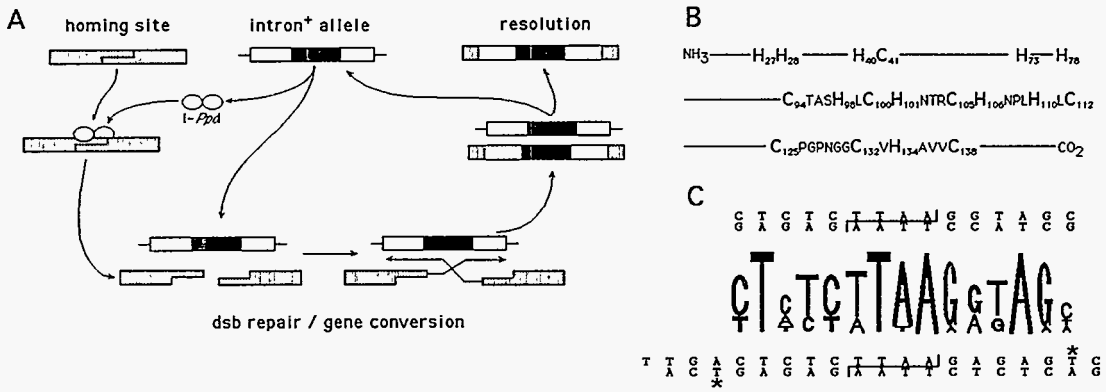

Figure 1. **The I-*Ppo*I intron homing cycle and sequences of the I-*Ppo*I homing site and His-Cys box motif.** A: Intron mobility or homing is initiated and targeted by a site-specific DNA double strand break made in an intron-less allele B: Diagrammatic representation of the primary structure of the I-*Ppo*I protein. The conserved His-Cys boxes are found between residues 73 and 138. C: Sequence of the wild-type, pseudo-palindromic I-*Ppo*I homing site (above), and the synthetic DNA palindrome used for cocrystallization (below). The position of the thymine nucleotides derivatized to iodinated uracils is shown by asterisks; the cleavage pattern (which produces 4 base, 3' extended ends) is indicated by the staggered underline. Aligned in between the wild type and synthetic homing site sequences is a code denoting relative invariance of positions in the I-*Ppo*I homing site.

We have expressed, purified and crystallized recombinant I-*Ppo*I homing endonuclease with a 20 base pair synthetic I-*Ppo*I DNA homing site (Figure 1) [10]. Preliminary X-ray studies indicated that the protein contains two bound zinc ions per subunit that are essential for protein folding. A requirement for zinc to allow I-*Ppo*I folding or activity was suggested by the presence of the potential zinc binding His-Cys protein motif.

METHODS AND THE USE OF ALS FACILITIES

Crystals were grown of I-*Ppo*I complexed with a synthetic DNA duplex (Oligos, Etc., Inc.) that contains a variant of the 15 bp I-*Ppo*I homing site (Figure 1). The DNA construct forms a palindromic sequence of 20 bp and contains a single 5' deoxythymidylate overhang at each end. A high resolution native data set, used to refine the I-*Ppo*I structure to its current resolution value of 1.8 Å, was collected on an ADSC 4 panel CCD area detector at beamline 5.0.2 at the Advanced Light Source (LBNL, Berkeley, CA) with the assistance and advice of Thomas Earnest, using a wavelength of 1.0 Å. This data set, which extends to 1.6 Å resolution, represents a dramatic improvement from a previous best of 2.4 Å, which was collected earlier on a rotating anode generator equipped with mirrors. All RAXIS data were reduced using the DENZO/SCALEPACK crystallographic data reduction package [11], while the ALS CCD data were reduced using MOSFLM 5.5 [12]. Two isomorphous derivatives were prepared for structure determination. The first was prepared by synthetic incorporation of an iododeoxyuridine in the DNA duplex (Figure 1). A second derivative was prepared by a 1 hour soak of the native crystals in a 1 mM $Hg(CN)_2$ solution prior to flash-cooling. All initial MIR phase calculations and phase refinements were done using the CCP4 package [13], with phases calculated using the program MLPHARE. Phases calculated using these data yielded an interpretable electron density map that was further improved by solvent flattening, histogram matching, and phase extension. Phase-combined maps were calculated using SFALL and SIGMAA to resolve ambiguous regions of the orginal DM electron density map The resolution used for the refinement of the final models extends to 1.8 Å. There is a single I-*Ppo*I dimer and DNA duplex in the asymmetric unit of the crystal.

RESULTS

I-*Ppo*I monomer folds into a single extended domain, of dimensions 25 Å x 35 Å x 55 Å, that contains three separate, anti-parallel β-sheets flanked by two long α-helices. The extended fold of the enzyme monomer is stabilized by two covalently bound, independently coordinated zinc ions located 15 Å apart and on the protein face opposite the DNA binding surface. The homodimer contains four bound zinc ions.

The I-*Ppo*I endonuclease dimer forms an extended DNA binding surface that is approximately 80 Å long and oriented along the DNA-binding axis (Figure 2). The homodimer is stabilized by an unusual combination of a very small, highly solvated central interface, and an extended C-terminal tail that extends 34 Å across the adjacent monomer. I-*Ppo*I, in contrast to the LAGLIDADG homing endonucleases, does not exhibit a tightly packed dimer interface that facilitates homing site cleavage across the minor groove.

The two bound zinc ions in each protein monomer are tetrahedrally coordinated in different motifs composed of cysteine and histidine residues. The two motifs are distinct from one another, and are also differ from previously described zinc binding motifs. The first zinc ion is coordinated by a Cys_3-His_1 ligand cluster from the N-terminal end of the protein, with a single side chain contributed by β2 (Cys 41) and the remaining three side chains by a short loop between β7 and β8 (Cys 100, Cys 105,and His 110). The binding motif for this metal is therefore C-X_{58}-C-X_4-C-X_4-H. The second zinc ion is coordinated by a cluster of four closely spaced protein side chains (Cys_2-His_1-Cys_1 coordination), all donated from a short buried protein loop (Cys 125, Cys 132, His 134, and Cys 138) near the C-terminal end of the enzyme. The motif for the second bound zinc ion is C-X_6-C-X_1-H-X_3-H.

The 15 bp I-*Ppo*I homing site is one of the shortest DNA homing sites characterized to date. This is nonetheless a large target for sequence-specific recognition and binding by the 163 residue I-*Ppo*I protein. An important part of the DNA recognition strategy of I-*Ppo*I is to use a homodimer as the active form of the endonuclease to recognize the limited two-fold sequence symmetry within the homing site. The primary contacts made by I-*Ppo*I to homing site DNA are between the second β-sheet (β3–β4–β5) of each monomer and base pairs in the major groove to either side of the cleavage site at positions -5 to -9 and +5 to +9. Additional contacts are made in the center of the complex, across the minor groove, and between residues in the active site and DNA atoms in the cleavage site. The I-*Ppo*I homodimer also strongly bends homing site DNA to facilitate cleavage across the minor groove with the generation of 4 base, 3' extended cohesive ends.

The structure determined with ALS data clearly indicates a divalent cation is bound in the active site and the scissile phosphate has been cleaved. The metal ion is coordinated in both structures to the 3' hydroxyl leaving group of the phosphate backbone and the side chain oxygen of Asn 119, and has four easily visible coordinating water molecules, one of which directly contacts an oxygen atom of the cleaved 5' phosphate group. The distance between the 3' hydroxyl oxygen leaving group and the 5' phosphorus atom refines to 3.5 to 4.3 Å in all of the structures. Apart from the active site divalent cation and its coordinating asparagine residue, the other groups within potential chemical interaction distance of the scissile phosphate group are His 98 (which is absolutely conserved in the SHLC sequence found in the His-Cys box endonucleases), Arg 61 (which contacts oxygen atoms on the cleaved phosphate and its immediate phosphate neighbor through its two guanidinyl nitrogens), and His 78.

Figure 2. Stereo ribbon diagram of the endonuclease dimer in complex with the DNA homing site. The substrate is dramatically deformed in the complex, with a sharp pair of kinks near the cleavage site opening the major groove, and a pair of shallower opposing bends to either side giving an overall bend of approximately 50 degrees. This figure made with program SETOR [14].

REFERENCES

1. M. Belfort and R. Roberts, Nucleic Acids Res. **25** (17), 3379 - 3388 (1997).
2. A. M. Lambowitz and M. Belfort Ann. Rev. Biochem. **62,** 587 - 622 (1993).
3. J. E. Mueller, M. Brysk, N. Loizos and M. Belfort, in Nucleases, 2nd Ed., edited by S. M. Linn, R. S. Lloyd, and R. J. Roberts (Cold Spring Harbor Laboratory Press, Cold Spring Harbor, NY), pp. 111-143 (1993).
4. M. Belfort and P. S. Perlman, J. Biol. Chem. **270,** 30237 - 30240 (1995).
5. M. Belfort, M. E. Reaban, T. Coetzee, and J. Z. Dalgaard J. Bacter. **177,** 3897 - 3903 (1995).
6. D. E. Muscarella and V. M. Cell **56,** 443 - 454 (1989).
7. D. E. Muscarella, E. L. Ellison, B. M. Ruoff, and V. M. Vogt, Mol. and Cell. Biol. **10**(7), 3386 - 3396 (1990).
8. S. Johansen and V. M. Vogt, Cell **76**(4), 725 - 734 (1994).
9. S. Johansen, T. M. Embley and N. P. Willassen, Nuc. Acids Res. **21** (18), 4405 (1993).
10. K. E. Flick, D. McHugh, J. D. Heath, K. M. Stephens, R. J. Monnat, Jr. and B. L. Stoddard, Protein Science **6**, 1 - 4 (1997).
11. Z. Otwinowski and W. Minor, Methods in Enzymology **276**,307-326 (1997).
12. A. G. W. Leslie in Joint CCP4 and ESF-EACMB Newsletter on Protein Crystallography No. 26 (Daresbury Laboratory, Warrington, U.K.) (1992).
13. CCP4 The SERC (UK) Collaborative Computing Project No. 4, a suite of programs for protein crystallography. (Daresbury Laboratory, Warrington WA4 4AD, UK) (1979).
14. Evans, S. V. J. Mol. Graphics **11**, 134-138 (1993).

This work was supported by the National Institutes of Health under grant No. GM49857.

Principal investigator: Barry L. Stoddard, Fred Hutchinson Cancer Research Center. Email: bstoddar@fred.fhcrc.org. Telephone: 206-667-4031.

Membrane Protein Crystallization at the Advanced Light Source

Gerry McDermott, Trey Simmons, Anjali Gupta, Natasha Khlebtsova & Thomas N. Earnest

Macromolecular Crystallography Facility at the Advanced Light Source, Physical Biosciences Division, Lawrence Berkeley National Laboratory, University of California, Berkeley, California CA 94720, USA

INTRODUCTION

Proteins are ubiquitous in Nature. Typically, they function as the principle components and/or the controlling agents of biological systems. All protein molecules are comprised of one or more chains of polymerized amino acids. As such, these linear chains must 'fold' into particular spatial conformations to be fully functional [1]. Constructing an accurate model of a protein's molecular topology is an essential step on the path towards understanding its *in vivo* function [2]. In recent years, advances in the technology of gene cloning and sequencing have resulted in an exponential increase in the number of identified genes; however, understanding the functions of these genes products at the molecular level has not kept pace [3]. Although it is possible to determine the amino acid sequence of a protein given the DNA sequence, it is not possible to predict how the protein will fold: this can only be determined experimentally. For some years now, the technique that has been most successfully used to obtain this information is protein X-ray crystallography [3].

In recent years, the crystallization of proteins has moved from being the exclusive domain of the specialist crystallographer to become a routine practice in most laboratories that study protein biochemistry [4]. Several thousand proteins have now been crystallized and their corresponding crystallographic structures established. In fact, the technique has now evolved to the extent that a new protein structure is currently being deposited in the protein structure databank every five hours. In spite of this fact, one class of biologically important proteins remains underrepresented in terms of available structural information: The molecular structure of only a few integral membrane proteins has been established. Primarily, this paucity of structural information can be attributed to the particular biochemical and biophysical properties of membrane proteins [5].

MEMBRANE PROTEINS

Integral membrane proteins are proteins that are vectorially inserted into the lipid bilayer of biological membranes [6]. A typical membrane protein has three topologically distinct domains: two hydrophilic extra-membranous domains and the hydrophobic domain that spans the lipid bilayer. *In vitro,* it is possible to 'release' membrane proteins into solution by treating membranes with suitable surfactants, such as non-ionic detergents [6]. However, the strong amphipathic character of the resultant molecule makes it insoluble in both polar and apolar solvents. To render the protein soluble in aqueous solution, the hydrophobic region must be covered with a 'jacket' that interacts readily with the bulk solute [7]. In practice, this is achieved by constantly maintaining the protein in a solution containing detergent at a concentration above its critical micelle concentration. Under these conditions the protein molecules are incorporated into detergent micelles, and hence present a mostly hydrophilic surface to the solvent [7].

CRYSTALLIZATION OF MEMBRANE PROTEINS: BACKGROUND

Proteins crystallize according to the principles that govern the crystallization of simple salts; i.e. by making a solution of the protein supersaturated, nucleation and crystal growth may occur [8]. In practice, the method used to crystallize proteins takes advantage of the way protein solubility varies as a function of ionic strength: for example, adding increasing amounts of ammonium sulfate will

cause most protein solutions to become saturated, and if the conditions are favorable, supersaturated. Unfortunately, increasing ionic strength of a membrane protein solution can cause the detergent to partition into a separate phase. When this occurs, the protein rapidly migrates into the detergent enriched phase, where depletion of the protein's solvation water results in its rapid denaturation [7].

To overcome this problem, Michel pioneered a method of employing 'amphiphilic additives' to prevent detergent phase separation. This allowed membrane proteins to be crystallized in a manner similar to globular proteins [7]. This was a landmark event in the history of X-ray crystallography. Accordingly, for this feat Michel, Deisenhofer and Huber were awarded the Nobel prize in 1988. Unfortunately, optimism that this work would result in the elucidation of many more membrane protein structures proved short-lived.

Protein crystallization is fundamentally an empirical process. In most instances, a set of parameters successfully used to crystallize one protein will not be applicable to other proteins. *A priori* there is no way of formulating such conditions; they must be determined experimentally for each protein [8]. It was found that, in addition to the other parameters that can affect the success of crystallization experiment, the choice of detergent and additive is crucial [9]. Hence, for membrane proteins the number of parameters that must be permuted is much greater than for soluble globular proteins, which has the effect that typically many more experiments must be carried out to establish the conditions that lead to the crystallization of a membrane protein. This exacerbates yet further an inherent problem of membrane protein crystallization, the generally limited availability of starting material. Most membrane proteins are only present *in vivo* in small quantities, making purification directly from tissue impractical. Unfortunately, when membrane proteins are overexpressed in heterologous expression systems, protein yields tend to be comparatively low [10]. This obviously restricts the number of crystallization trials that can be conducted, and consequently reduces the likelihood of ever obtaining crystals.

PROTEIN CRYSTALLIZATION AT THE ALS

This prompts the question: why is the ALS an ideal place to conduct membrane protein crystallization trails? The answer lies in the fact that en route to obtaining 'good' quality crystals one often goes through various stages of getting poor quality ones; i.e. crystals whose internal order is such that they only diffract X-rays to low resolution. Although these can't be used for data collection, information on their diffraction properties can be used in the iterative process of optimizing the crystal growth conditions [11]. In this context, it is essential to use a highly collimated, intense synchrotron beam, such as beamline 5.0.2 at the ALS. Having ready access to such a facility means that we are able to get rapid and quantifiable feedback on the effect protocol changes have on the resultant crystal's diffraction properties, and hence greatly speed up the process of optimizing diffraction and minimize the amount of protein used in the process. In addition, by testing 'sub-optimal' crystals, such as microcrystals (i.e. those with dimensions of less than 50 μm) we are stretching the limits of the data collection facilities on BL 5.0.2. By doing so, the data collection capabilities of this beamline will, as a matter of course, be further developed and enhanced.

CURRENT PROJECTS

The proteins we are currently crystallizing are either integral membrane proteins or proteins which interact with membrane proteins. In particular we are interested in proteins involved in process of signal transduction across biological membranes. In general, the components of these systems

include integral membrane proteins such as receptors or ion channels, as well as extracellular ligands such as hormones or cytokines and intracellular effectors like kinases. A particular focus of the laboratory is the erythropoietin system. Erythropoietin is a cytokine involved in the proliferation and differentiation of the erythroid progenitor cells that eventually form red blood cells [12]. Its effects are transmitted to the interior of the cell via the erythropoietin receptor and a number of downstream effectors such as the kinase JAK2. We are currently conducting crystallization trials using erythropoietin receptor, and are beginning to conduct trials with JAK2.

Other projects in the lab, which are at various stages along the pathway from isolating the gene to conducting crystallization trials, include the membrane protein PMP-22, which is involved in several hereditary peripheral nervous system neuropathies [13], and MOMP, the Chlamydia surface antigen, whose crystallographic structure may hold the key to a successful vaccine against the world's most common sexually transmitted disease [14].

ACKNOWLEDGMENTS

Work on the erythropoietin receptor is in collaboration with Amgen Inc., Thousand Oaks, CA; PMP-22 with Prof. E. Shooter of Stanford University School of Medicine and MOMP with Prof. Rick Stevens, UC Berkeley School of Pubic Health.
This work was supported by the Department of Energy, and Amgen Inc.

REFERENCES

[1] Creighton, T.E. (1983) *Proteins* W.H. Freeman & Co.
[2] Blundell, T.L. & Johnson, L.M. (1976) *Protein Crystallography.* Academic Press, London.
[3] Pennisi, E. (1998) X-ray Crystallography: Taking a Structured Approach to Understanding Proteins. *Science* **279**, 978.
[4] McPherson, A. Malkin, A.J. & Kuznetsov, Y.G (1995) The science of macromolecular crystallization. *Structure* **3**, 759-768.
[5] Kühlbrandt, W. (1992) Two-dimensional crystallization of membrane proteins. *Quart. Rev. Biophs.* **25**, 1-49.
[6] Singer, S.J. & Nicholson, G.L. (1972) The Fluid Mosaic Model of Cell Membranes. *Science* **175**, 720-731.
[7] Michel, H. (1983) Crystallization of membrane proteins. *TiBS* **8**, 56-59.
[8] McPherson, A. (1985) The crystallization of macromolecules: General principles. *In*: Methods in Enzymology: Diffraction Methods. (Hirs, M., Timasheff, S. N. & Wykoff, H. ed.s) Academic Press, New York.
[9] Garavito, R.M. & Picot, D. (1990) The Art of Crystallising Membrane Proteins. *Methods: A companion to Methods in Enzymology*, **1**, 57-69.
[10] Gould, G. W. (ed.). (1994) "Membrane protein expression systems, A users guide" Portland Press, London.
[11] McDermott, G. (1993) Crystallisation of membrane proteins. *In*: Data collection and processing. Proccedings of the CCP4 study weekend (Sawyer, L., Isaacs, N.W. & Bailey, S. ed.s).
[12] Ohashi, H., Maruyama, K., Liu, Y-C & Yoshimura, A. (1994) Ligand-induced activation of chimeric receptors between the erythropoietin receptor and receptor tyrosine kinases. *Proc. Natnl. Acad. Sci.* **91**, 158-162.USA.

[13] Suter, U; Welcher, AA; Snipes, GJ. (1993) Progress in the molecular understanding of hereditary peripheral neuropathies reveals new insights into the biology of the peripheral nervous system. *Trends in Neurosciences*, **16**, 50-56.
[14] Brunham, RC; Peeling, RW. (1994) Chlamydia trachomatis antigens: role in immunity and pathogenesis. *Infectious Agents and Disease*, **3,** 218-233

Principal investigator: Thomas Earnest, Macromolecular Crystallography Facility at the Advanced Light Source, LBNL. E-mail: TNEarnest@lbl.gov.

Toward the High Resolution Structures of DNA Repair Enzymes: Endonuclease IV and Manganese Superoxide Dismutase

Yue Guan,[1] David N. Silverman,[2] Richard P. Cunningham,[3] John A. Tainer[1]
[1]The Scripps Research Institute, Department of Molecular Biology MB-4,
10550 N. Torrey Pines Road, La Jolla, CA 92037 USA;
[2]University of Florida, Department of Pharmacology & Therapeutics,
1600 S W Archem Road, Gainesville, FL 32610-0267 USA;
[3]State University of New York at Albany, Department of Biological Sciences,
1400 Washington Avenue, Albany, NY 12222 USA.

Endonuclease IV (endoIV) is a damage-inducible apurinic/apyrimidinic (AP) endonuclease in the base-excision repair (BER) pathway (Cunningham *et al.*, 1986). Its activity is to catalyze the cleavage of an abasic site created by DNA glycosylases such as MutY after the removal of damaged bases. Exonuclease III and endoIV are responsible for most of the AP endonuclease activity in the cell. To address the structural basis for the DNA base-excision repair pathway in damaged base recognition and removal, and backbone cleavage we have been focusing on the determination of three-dimensional structures of endonuclease IV in its uncomplexed form and in complex with a mononucleotide and oligonucleotide substrates.

We are working on two different kinds of endoIV, namely *E. coli* endoIV and *Thermotoga M* endoIV. The *E. coli* endoIV crystallized in monoclinic crystal form with the space group P21. The unit cell dimensions are a=50 Å , b=60 Å , and c=51 Å , and β=110°. With a complete 1.4 Å resolution native data set collected we have been scanning extensively heavy atom derivatives. During the December 1997 ALS run, we have collected one potential gold derivative data set to 1.7 Å resolution with flash cooling cryogenic device. The crystal was well frozen. We recently found a new crystal form with the unit cell dimensions of a=49 Å, b=59 Å, and c=94 Å, and β =96°. The crystallization conditions make it easier for the heavy atom derivative scan.

MAD phasing with selenium-methionine (SeMet) has been proven to be a powerful tool in protein crystallography. We have obtained the isomorphous crystals for selenium-methionine endoIV which diffract poorly (~5 Å resolution). It's so critical for us to collect better than 3 Å data of SeMet endoIV to do MIR/MAD phasing. During the December run, we have, for the first time, collected a complete 2.6 Å resolution SeMet endoIV data set from a tiny crystal with the bright synchrotron X-ray beam at ALS. This data set greatly improved the MIR/MAD phasing of endoIV. We are in the progress of solving the structure of this key DNA repair enzyme.

The function of MnSOD is to protect mitochondria against oxidative damage. The 2.2 Å resolution crystal structure of human MnSOD reveals a homotetrameric assembly and the active site of hMnSOD ligates the manganese with three histidines (His 26, 74, 163), one aspartate (Asp 159), and a water molecule (hydroxyl anion) as the fifth ligand in a trigonal bipyramidal arrangement (Borgstahl *et al.*, 1992). Azide, a competitive inhibitor of MnSOD, is thought to bind to the active site Mn ion in a manner similar to the superoxide substrate. We have recently obtained co-crystals of azide-MnSOD and collected a 2.8 Å resolution data set from a crystal flash frozen at liquid nitrogen temperature using a Rigaku rotating anode generator and a MAR image plate detector. This resolution has been extended considerably when we collected a 2.0 Å resolution data set during the December 1997 ALS run. These data enable us to derive a more accurate model for azide-inhibited MnSOD and help to understand the function of this enzyme. Great efforts have

been made to functional mutants to further our understanding on the mechanism of MnSOD (Guan *et al.*, 1997).

REFERENCES

1. R. P. Cunningham, S. M. Saporito, S. G. Spitzer, and B. Weiss (1986) *J. Bacteriol.* **168**:1120-1127.
2. G. E. O. Borgstahl, H. E. Parge, M. J. Hickey, M. J. Johnson, M. Boissinot, R. A. Hallewell, J. R. Lepock, D. E. Cabelli, and J. A. Tainer (1996) *Biochemistry* **35**:4287-4297.
3. Y. Guan, M. J. Hickey, G. E. O. Borgstahl, R. A. Hallewell, J. R. Lepock, D. O'Connor, Y. Hsieh, H. S. Nick, D. N. Silverman, and J. A. Tainer (1997) *Biochemistry*, submitted.

This work was supported by the National Institutes of Health under grant nos. GM46312 (DNA repair enzyme work) and GM48495 (superoxide dismutase work).

Principal investigator: John A. Tainer, Scripps Research Institute. Email: jat@scripps.edu.

Beamline 6.1.2 Abstracts

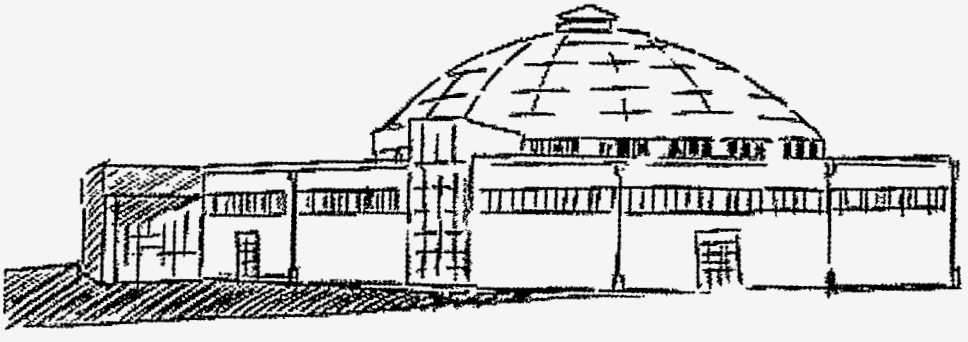

Analysis of the Spatial Variation of Crosslink Density in Superabsorbent Polymers

G. E. Mitchell*, S. G. Urquhart**, L. Wilson*, M. Dineen*, E. G. Rightor*, A. P. Hitchcock‡, U. Neuhaeusler‡‡, H. W. Ade **, W. Meyer-Ilse†, J. Brown†, and T. Warwick††

* The Dow Chemical Company, Midland, MI, 48667

** Department of Physics, North Carolina State University, Raleigh, NC, 27695-751

‡ Brockhouse Institute for Materials Research, McMaster University, Hamilton, ON, L8S 4M1

‡‡ Department of Physics, State University of New York - Stoney Brook, 11794 and Forschungseinrichtung Roentgenphysik, Universitaet Goettingen, Goettingen Germany

†Center for X-ray Optics, E. O. Lawrence Berkeley National Laboratory, Berkeley, California 94720, USA

††Advanced Light Source · E. O. Lawrence Berkeley National Laboratory, Berkeley, California 94720, USA

INTRODUCTION

Superabsorbent polymers are often designed with increased density of crosslinking in the outer layer of the particles in order to improve liquid retention under load. For efficient product design, it is desirable to directly measure the spatial variation in crosslink density. Typically employed techniques (solvent uptake or measuring the changes in various mechanical properties such as the modulus) do not normally provide spatially resolved crosslink density information. We have applied Scanning Transmission X-ray Microscopy (STXM) to examine the swelling of inhomogenously crosslinked superabsorbent polymers in deionized water and salt water solution.

STXM is an effective way to study the chemical and morphological character of polymers on a sub micron spatial scale.[1] STXM image contrast is based on core electron excitation by x-ray absorption; an interaction that has remarkable chemical sensitivity.[1,2] Beam damage is less than in TEM microscopes [2] and samples can be examined in wet and in ambient conditions.

EXPERIMENTAL

The XM-1 conventional (BL 6.1) as well as the scanning transmission x-ray microscopes (STXM) at the Advanced Light Source (BL 7.0)[3] and the National Synchrotron Light Source (X1A) were used in this study.

The super absorbent polymer samples were approximately 0.3 mm diameter spherical beads of polyacrylic acid lightly crosslinked throughout. Samples A and B were 80% neutralized with NaOH. All three samples were more heavily crosslinked in the outer shell by reaction of the spheres with ethylene glycol diglycidyl ether (EGDE). Sample A was reacted with half as much crosslinking agent (EGDE) as the other samples.

RESULTS

Figure 1 presents a simplified schematic of the wet cell used for this work. Similar wet cells have been used in X-ray microscopes for examining biological materials, clay particles and manganese nodules in wet environments.[5] The hydrated sample is sandwiched between two ~100 nm thick Si_3N_4 windows, and the water thickness is controlled by compression of the front and back cell halves.

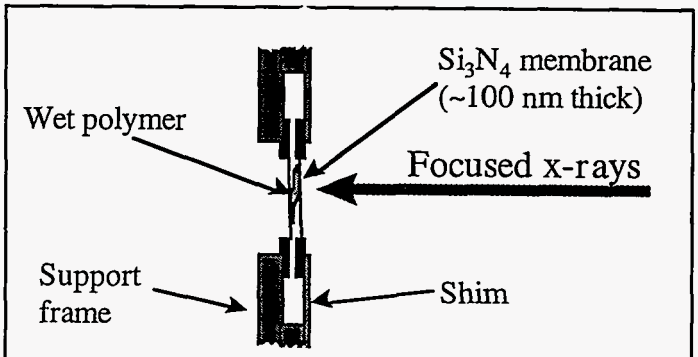

Fig. 1. Simplified schematic of the wet cell design.

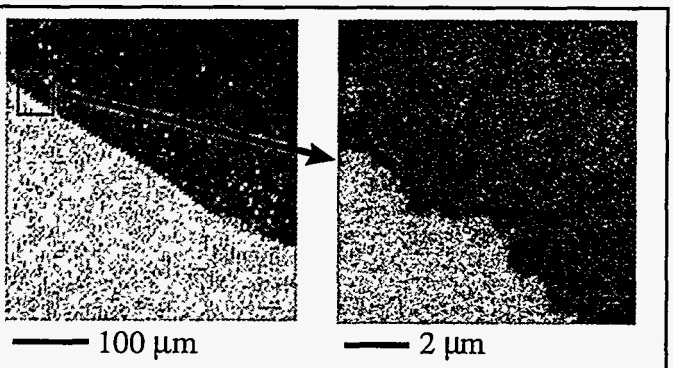

Fig. 2. STXM micrographs of the edge of SAP sample A, hydrated with deionized water

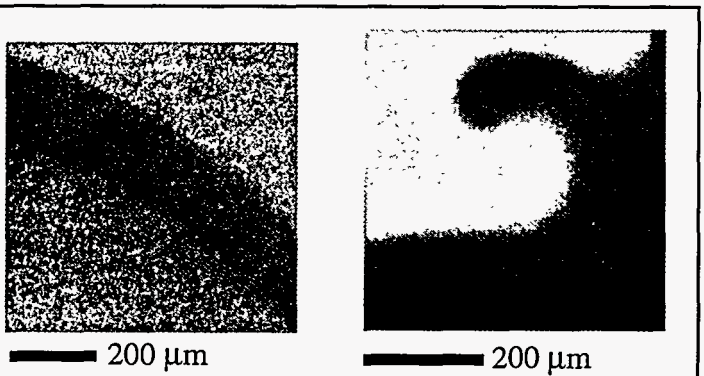

Fig. 3. STXM micrograph of the edge of two samples of SAP B, hydrated with deionized water (left) and 0.9% salt water (right)

The results for two different SAP polymers are presented in Figures 2 and 3. In both polymers, the surface region of the SAP sections were crosslinked, but twice as much crosslinker was used for sample B than for sample A. Figure 2 presents a STXM image of the edge of SAP section A, hydrated with deionized water. In the higher resolution image, small dark features are observed near the edge of the section. In this instance, the decreased x-ray transmission corresponds to an increased polymer density, which is a consequence of a higher crosslink density. Figure 3 (left-hand image) presents the edge of water-hydrated SAP section B, which has twice the crosslinker as section A. In this image, a ~150 µm wide band of higher density polymer is observed at the section edge. The image on the right-hand side of Figure 3 is of the edge of a sample of SAP B hydrated with 0.9% salt-water solution. A narrower band of higher density is observed at the edge of this polymer and has broken loose from the core polymer. Both the center and the more crosslinked edge of this polymer do not expand as much in salt solution as in deionized water solution.

We have also had success in analyzing core / shell structured SAP material which has been wetted and dried onto an Si_3N_4 window using the XM-1 microscope at the ALS. The advantages in using XM-1 include the facile sample mounting and ease and speed in obtaining images. Since one is

constrained to relatively large magnifications on this microscope compared to STXM, several images in a line across the edge of the sample were obtained and pasted together in a montage to cover the interesting area of the sample.

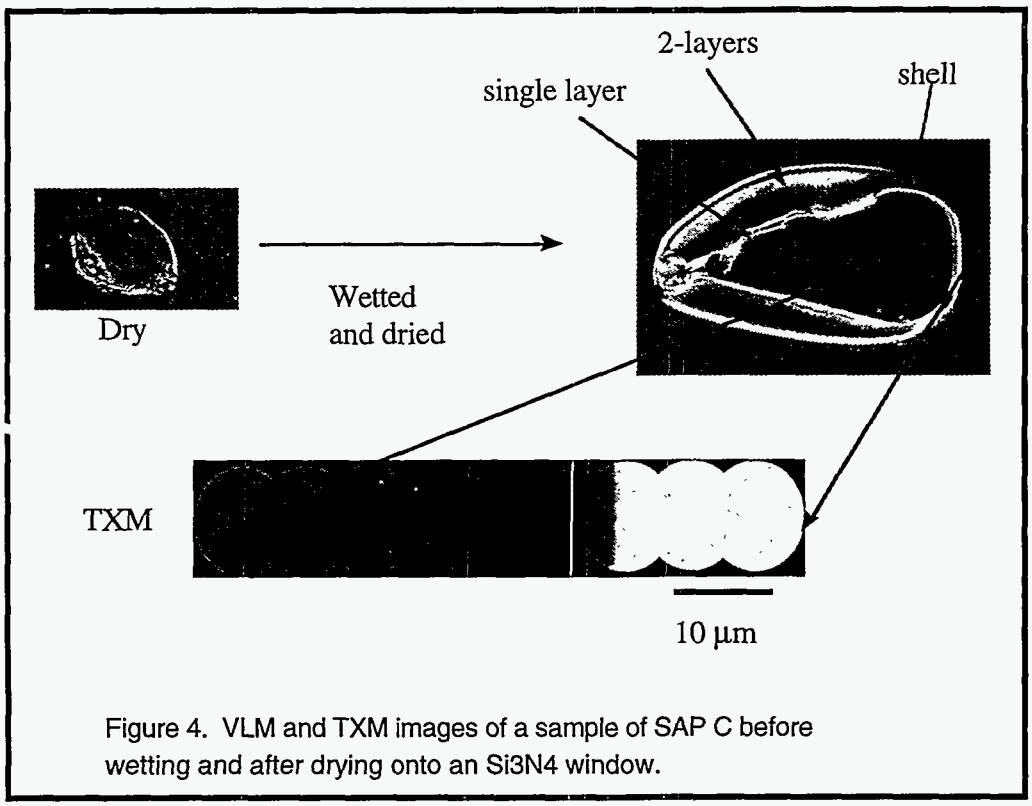

Figure 4. VLM and TXM images of a sample of SAP C before wetting and after drying onto an Si3N4 window.

Figure 4 presents the VLM and the TXM results for a thin section of an acid form core/shell bead which was wetted with de-ionized water and dried on a Si_3N_4 window. At top left is a VLM image of the section prior to wetting it. The section is oblong in shape because of a small amount of compression which occurred in the direction of cutting during microtoming. There was some debris on the window before the section was added and which we were not able to remove. A montage of TXM images obtained from this sample is shown at the bottom. The VLM image collected before the TXM imaging is presented in the upper right.

The wetted and dried section in Figure 4 had an interesting shape. Because the outer shell of the sample was crosslinked, it did not swell as much as the central part of the section. When the inner part of the sample disk swelled, it apparently expanded past the shell. The shell can be seen as the band closest to the middle of the sample. The sample is shaped something like a bedroom slipper with polymer folded over and therefore forming two layers (one atop the other) on each side at the toe end. Although there was a good deal of variation in shape from one sample to another after sections were wetted and dried, shapes similar to this with the shell remaining much less expanded than the core polymer were seen fairly often.

From the VLM images in Figure 4 one can see that the polymer section remains at least partly expanded (radially) after wetting and drying. It is difficult to determine by VLM the size of the wet polymer after swelling because of the refraction effects of the water. If the polymer does not shrink laterally during dehydration, then the thickness of the polymer after being wetted and dried

is also a useful measure of the polymer density in the swollen polymer gel. In the TXM montage in Figure 4 there is a band about 16 μm wide of material which is more x-ray absorbing, near the center of the image and at the edge of the sample which we identify as the shell.

CONCLUSIONS

We have shown that STXM can be used to visualize the core / shell structure of hydrated SAP prepared by chemically crosslinking the surface of SAP beads. Conventional and scanning TXM can provide information on the internal structure (or strength) of thin sections of SAP materials which have been wetted in DI water, as well as those wetted and allowed to dry.

ACKNOWLEDGMENTS

The x-ray microscope XM-1 at the Advanced Light Source is supported by the United States Department of Energy, Office of Basic Energy Sciences under contract DE-AC 03-76SF00098. The ALS STXM and the Advanced Light Source are supported by the United States Department of Energy, Office of Basic Energy Sciences under contract DE-AC 03-76SF00098. The X-1A STXM was developed by the group of Janos Kirz and Chris Jacobsen at SUNY Stony Brook with support from the Office of Biological and Environmental Research, U.S. DoE under contract DE-FG02-89ER60858, and the NSF under grant DBI-9605045. U. Neuhaeusler would like to thank the German Academic Exchange Service for financial support.

REFERENCES

1. H. Ade et al., *Science* 258 (1992) 972
2. E.G. Rightor et al., *Journal of Physical Chemistry B.*, 101 (1997) 1950
3. T. Warwick et al., *Journal of Electron Spectroscopy and Related Phenomena*, 84 (1997) 85
4. X. Zhang et al., *Instruments and Methods in Physics Research A*, 347 (1994) 431
5. J. Kirz et al., *Quarterly Reviews of Biophysics* 28 (1995) 1

Principal Investigator:
Gary E. Mitchell, Analytical Sciences, Dow Chemical, 1897E Building, Midland, MI 48667 USA.
Email: gemitchell@dow.com. Tel: (517)636-3666.:

High Resolution Soft X-Ray Microscopy of Micronodules produced by Biomineralization

J. Rothe[1], W. Meyer-Ilse[3], T. Grundl[2], K. H. Nealson[2] and B. P. Tonner[1]
[1]Dept. of Physics, University of Wisconsin-Milwaukee, PO Box 413, Milwaukee, WI 53201, USA
[2]Center for Great Lake Studies, University of Wisconsin-Milwaukee, PO Box 413, Milwaukee, WI 53201, USA
[3]Center for X-ray Optics, Ernest Orlando Lawrence Berkeley National Laboratory,
University of California, Berkeley, CA 94720, USA

INTRODUCTION

The study of the production of inorganic Mn compounds by one-cell micro-organisms is of great importance for the further understanding of the bacterial metabolism based on the respiration of transition metal oxides. The attachment of bacterial cultures to and subsequent modification of inorganic surfaces, as well as the precipitation of inorganic microparticles by these bacteria is a fundamental process in environmental chemistry. Bacterial strains have been discovered which use Mn or Fe compounds as part of their energy transport cycle by oxidizing transition metal compounds to higher valence states, while others will reduce the metal ions [1,2]. An inherent characteristic of the metabolic activity of bacteria is the fact that the chemical processes involved are spatially inhomogeneous. Soft x-ray microscopy is an ideal tool for the investigation of bacterial reaction products. It offers the spatial resolution required, for instance, for the imaging of micro-scale precipitates ('micronodules'). Additionally, by means of the variation of the wavelength (energy) of the incident radiation, the absorption contrast may be adjusted to reveal the spatial distribution of a particular element in the sample. Finally, liquid state imaging of the microorganisms within the so-called 'water window' is possible, giving direct insight into the location of the bacterial activity.

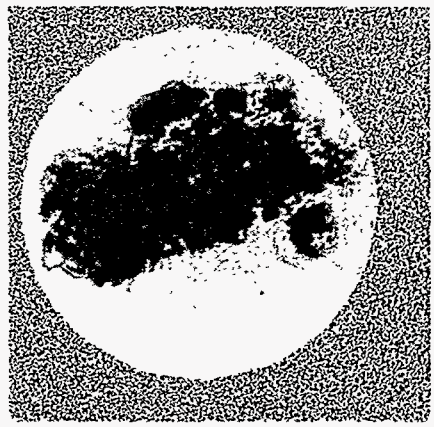

Fig. 1: XM-1 image of micronodules (normalized)

This article is a report on the results obtained for natural Mn nodules (from sediment core samples of Green Bay) produced by the bacterium *S. putrefaciens* using high resolution soft x-ray imaging at the x-ray microscope XM-1, operated by the CXRO at ALS beamline 6.1. The differential energy contrast at the Mn L_{III} absorption edge has been found sufficient to clearly reveal the Mn distribution in a variety of agglomerates of micronodules.

EXPERIMENT

Soft x-ray microscopic images of Mn containing micronodules have been taken at the x-ray micro-scope XM-1, both within the water window (2.4 nm ≅ 516.5 eV) and in the vicinity of the Mn L_{III} absorption edge. As expected from microspectroscopic x-ray absorption measurements performed on these samples [3], the +2 valence state of Mn is predominant. To establish the exact position of the corresponding absorption maximum ('white line') at the given calibration of the XM-1 pinhole monochromator, a sequence of images of a $Mn(II)SO_4$ crystal has been taken between 620 and 646 eV (1.5 eV steps). The ratio of the averaged intensities of two arrays of image pixels (one on top and one next to the edge of the imaged crystal) allows the direct calculation of the absorption coefficient as function of the photon energy.

Fig. 2 shows the resulting x-ray absorption spectrum in the vicinity of the Mn L_{III} edge ($2p_{3/2} \rightarrow 3d_{5/2}$ core transitions). Correspondingly, microscopic images of Mn containing micronodules have been taken at 629.3 eV (1.97 nm), 635.7 eV (1.95 nm), 639.0 eV (1.94 nm - strongest absorption contrast expected) and 642.3 eV (1.93 nm).

One of the major advantages of high resolution soft x-ray microscopy is the possibility to image biological samples in their naturally aqueous environments. For imaging within the water window 2 µl of the centrifuged suspension containing the micronodules have been sandwiched between two Si_3N_4 membranes of 120 nm thickness. All samples have been checked by DIC optical microscopy prior to x-ray imaging.

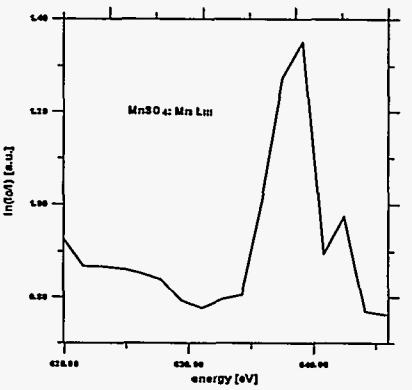

Fig. 2: BL6.1-XM-1 xray absorption spectrum of crystalline $MnSO_4$; absorption maximum at 639 eV.

RESULTS

A typical image of a micronodule of about 10 µm diameter is shown in Fig. 1 (dry sample, 1.97 nm, magnification 2400×). The particles generally tend to form agglomerates of various sizes and shapes, nevertheless the network of needle-shaped structures turned out to be a common characteristic. The image has been normalized by division through a background image, taken at the same wavelength at an 'empty' area of the Si_3N_4 membrane. In Fig. 3 a sequence of images taken at four different wavelengths in the vicinity of the Mn L_{III} absorption edge is presented. By relating to the low energy image (calculation of I_0/I), the Mn distribution appears as bright area in these images. As expected from the sulfate reference measurement, there is no contrast at 1.95 nm (below the white line), maximal contrast at 1.94 nm (on top of the white line, image 3c) and diminishing contrast at 1.93 nm. These images can be seen as a clear visualization of the inhomogeneous action of the Mn reducing bacteria. In all agglomerates, which have been investigated by this technique, the Mn distribution appears to be concentrated in diffuse zones sur-

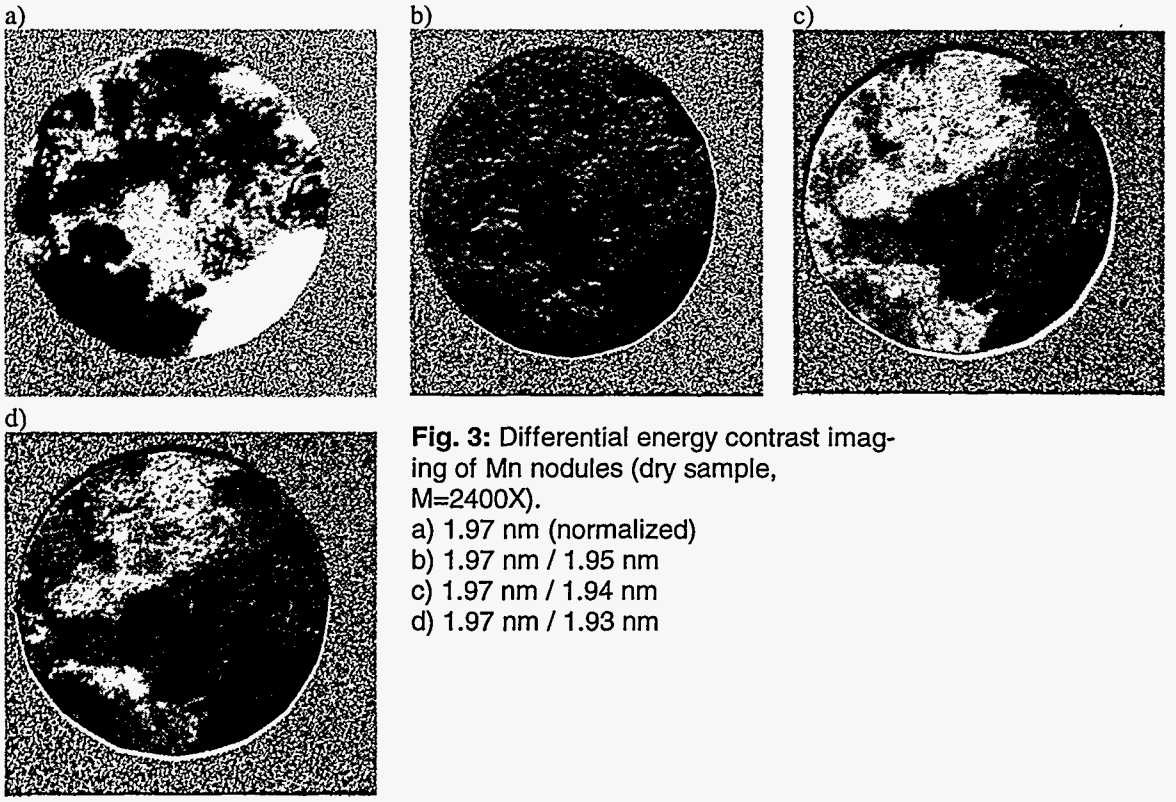

Fig. 3: Differential energy contrast imaging of Mn nodules (dry sample, M=2400X).
a) 1.97 nm (normalized)
b) 1.97 nm / 1.95 nm
c) 1.97 nm / 1.94 nm
d) 1.97 nm / 1.93 nm

rounding larger, regular shaped particles. Here the function of silicate particles as 'anchors' for the bacterial attachment and subsequent precipitation of Mn oxides may be observed.

Finally, Fig. 4 shows a wet-cell image of a micro- nodule taken at 2.4 nm inside the water window. The exposure time has been 6.4 sec. The arrow marks a bacterium of the size of about 1 μm still attached to the particle.

Fig. 4: XM-1 image of micro-nodule taken in the water window (2.4 nm)-the hexagonal structure is an impurity on one of the membranes.

CONLUSIONS

Differential energy contrast imaging at the Mn L_{III} absorption edge has been used to reveal the distribution of Mn in inorganic precipitates produced by one-cell micro-organisms. It has been shown that the investigation of reference compounds helps to establish the energy position of the maximum absorption contrast. The energy resolution of XM-1 turned out to be sufficient to differentiate, in principle, between +2 and +3 Fe species. This may enable valence state selective imaging of transition metal compounds in future work.

REFERENCES

1. C. Meyers and K. Nealson, 1988. "Bacterial manganese reduction and growth with manganese oxide as the sole electron acceptor." Science 240: 1319-1321
2. D. Lovely and E. Phillips, 1988. "Novel mode of microbial energy metabolism: organic carbon oxidation coupled to dissimilatory reduction of iron or manganese." Appl. Environ. Microbiol. 51: 683-689
3. J. Rothe, E.M. Kneedler, B.P. Tonner and K.H. Nealson, 1998. "Spectromicroscopy of Mn distributions in micronodules produced by Bacterial Biomineralization." This compendium.

This work was supported by the Department of Energy, OBER, NABIR program ER62474.

Principal investigator: Brian Tonner, Department of Physics, Laboratory for Surface Studies, University of Wisconsin-Milwaukee. Email: tonner@csd.uwm.edu.

Mechanisms of Concrete Damage Caused by Sulfate Attack Examined through Transmission X-ray Microscopy

K.E. Kurtis[1], P.J.M. Monteiro[1], J.T. Brown[2], and W. Meyer-Ilse[2]

[1]Department of Civil and Environmental Engineering,
University of California, Berkeley, California 94720, USA

[2]Center for X-ray Optics, Ernest Orlando Lawrence Berkeley National Laboratory,
University of California, Berkeley, California 94720, USA

INTRODUCTION

Increasingly often, concrete is the material of choice for the construction of structures exposed to extreme conditions whether it be offshore oil platforms in icy water or hazardous waste containment vessels buried in the earth. As demand for construction in harsh environments increases, so do the desired service lives of these structures. Typically, concrete structures are designed to perform, with minimal maintenance, 50 to 100 years. Concrete containment vessels, which may be hold chemical and radioactive waste, are designed for 500 year service lives and a desire exists to extend the expected service life to 1000 years.

Sulfates present in soils, groundwater, sea water, decaying organic matter, and industrial effluent surrounding a concrete structure pose a major threat to the long term durability of the concrete exposed to these environments. Sulfate attack of concrete may lead to cracking, spalling, increased permeability, and strength loss. Thus, resistance of concrete to sulfate attack is integral to ensure satisfactory performance over long periods.

While the objective is the avoidance of sulfate-related durability problems, this goal is difficult to achieve oftentimes because the mechanisms of expansion caused by sulfate attack in concrete are not well understood. The aim of an ongoing research investigation at XM-1, a transmission x-ray microscope owned and operated by the Center for X-ray Optics (CXRO) at beamline 6.1, is to gain knowledge about the means by which sulfate attack damages concrete.

ETTRINGITE FORMED BY SULFATE ATTACK OF CONCRETE

Sulfates present in soils, groundwater, sea water, decaying organic matter, and industrial effluent surrounding a concrete structure may permeate the concrete and react with existing hydration products. In the presence of calcium hydroxide (CH) and water (H), monosulfate hydrate ($C_3A{\cdot}C\${\cdot}H_{18}$) and calcium aluminate hydrate ($C_3A{\cdot}C\${\cdot}H_{18}$) react with the sulfate ($) to produce ettringite ($C_3A{\cdot}3C\${\cdot}H_{32}$) [1]:

$$C_3A{\cdot}C\${\cdot}H_{18} + 2CH + 2\$ + 12H \rightarrow C_3A{\cdot}3C\${\cdot}H_{32}$$

$$C_3A{\cdot}CH{\cdot}H_{18} + 2CH + 2\$ + 12H \rightarrow C_3A{\cdot}3C\${\cdot}H_{32}$$

In hardened concrete, the formation of ettringite by sulfate attack *can*, but does not always, result in expansion and lead to cracking of the concrete. The conditions under which ettringite formation produces damage in the concrete are uncertain.

It should be noted that ettringite produced by the reactions described above occupies a smaller volume than the reactants occupied. Therefore, the reaction described above must not be responsible for the expansion. It is generally accepted that the expansion caused by sulfate attack is the result of a particular mechanisms associated with the ettringite reaction or is the result of reaction other than the formation of ettringite. Gypsum, in addition to ettringite, can be produced during sulfate attack and is capable of producing expansion.

Two particular mechanisms for expansion associated with the formation of ettringite have been widely published - the topochemical reaction mechanism [2] and the swelling mechanism [3]. According to the topochemical reaction theory of expansion, sulfate and calcium ions in the concrete pore fluid react with dissolving aluminate ions near the surface of the solid phase, and the ettringite produced by this reaction grows perpendicular to the original solid surface. Since the sulfate and calcium ions are in solution, only the volume of the aluminate phase is considered when

comparing volume of reactants to the volume occupied by the ettringite produced. In an open system where the concrete is permeable to water present in the environment, water may then occupy the newly formed pore space, producing an expansion.

According to the swelling theory of expansion, poorly crystalline ettringite produces expansion by adsorption of water. In a system containing sufficient concentrations of sulfate, hydroxyl, and calcium ions, small, nearly colloidal ettringite is believed to form. Water from the environment outside the concrete member is adsorbed by the poorly crystalline ettringite, generating an osmotic pressure. If the elastic modulus of the concrete is sufficiently low, a volumetric expansion of the member results.

Thus, the mechanism responsible for expansion caused by sulfate attack in concrete is uncertain. It is possible that both theories described above are valid under certain conditions. An improved understanding of behaviors occurring at the ettringite/pore solution interface is critical in developing a total appreciation for the mechanisms responsible for expansion of concrete from sulfate attack. Because interest in the reaction is focused upon the adsorption of water and the effect of ion concentration on the ettringite produced, the use of an instrument that allows the microscopic study of the reaction and the reaction product in a wet environment is integral for understanding the reaction and conditions required for expansion.

EXPERIMENT

The morphology of the ettringite resulting from the reaction*,

$$C_4A_3\$ + 8C\$ + 6C + 96H \rightarrow 3(C_3A{\cdot}3C\${\cdot}32H)$$

was examined through transmission x-ray microscopy. The $C_4A_3\$$ was made by heating a blended mixture of calculated amounts of calcium carbonate, alumina, and gypsum to 1300C in a furnace. The C$ was obtained by heating gypsum to 150C. The C was obtained by decomposing calcium carbonate at 600C. A calcium sulfoaluminate mixture containing 30.0% C4A3$, 53.5% C$, and 16.5% C by weight was prepared and stored at 150C.

In addition, O.1M $CaCl_2$ solution was substituted for water (H) in the above equation. The purpose of this substitution was to study the effect of increased concentrations of Ca^{++} on the product morphology. The images can be analyzed with respect to the theories described above to impart information concerning the expansive behavior of ettringite in some concrete systems. The reaction product of the calcium sulfoaluminate mixture in water is shown in Fig.1, and the reaction product of the calcium sulfoaluminate mixture in O.1M $CaCl_2$ solution is shown in Fig. 2.

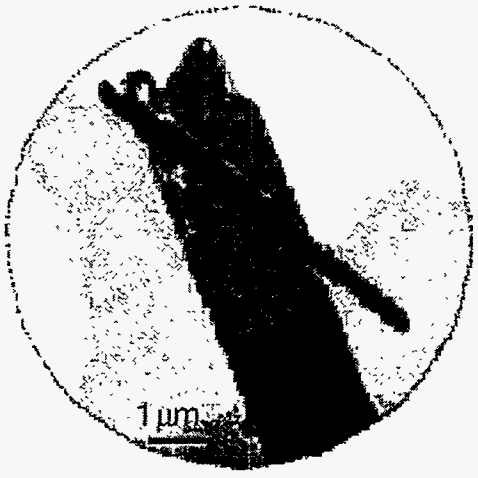

Figure 1
Calcium sulfoaluminate mixture in water.
80121063

Figure 2
Calcium sulfoaluminate mixture in 0.1M $CaCl_2$ solution. 80131011

* In cement chemistry notation: C=CaO, A=Al_2O_3, $=$SO_3$. H=$H_2O$.

CONCLUSION

Variations in the morphology of the products of the calcium sulfoalumiate reaction in water and in 0.1M $CaCl_2$ are readily apparent. Comparison of the x-ray diffraction pattern and surface charge density of each reaction product will provide further information as to the expansive nature of these products. These investigations are currently underway.

ACKNOWLEDGEMENTS

The first-named author wishes to acknowledge financial support by the National Science Foundation graduate research fellowship. Research at XM-1 is supported by the United States Department of Energy, Office of Basic Energy Sciences under contract DE-AC 03-76SF00098.

REFERENCES

1. Mehta, P.K. and Monteiro, P.J.M. *Concrete: Structure, Properties and Materials*, Prentice Hall, New Jersey, 1993.
2. Odler, I. and Jawed, I., "Expansive Reactions in Concrete", *Materials Science of Concrete II*, Eds. J. Skalny and S. Mindness, The American Ceramic Society, Westerville, OH, 1991, p.221-247.
3. Mehta, P.K., "Sulfate Attack on Concrete - A Critical Review", *Materials Science of Concrete III*, Ed. J. Skalny, The American Ceramic Society, Westerville, OH, 1992, p.105-130.

Principal investigator: Paulo J.M. Monteiro, Professor, Department of Civil and Environmental Engineering, University of California, Berkeley. Email: monteiro@ce.berkeley.edu Telephone:(510)643-8251.

Soft X-Ray Microscopy of Precipitates Resulting from Reductive Dissolution of Hematite by *Shewanella alga* BrY

B.L. Cox[2] and W. Meyer-Ilse[1]
[1]Center for X-ray Optics, Ernest Orlando Lawrence Berkeley National Laboratory, University of California, Berkeley, California 94720, USA
[2]Earth Sciences Division, Ernest Orlando Lawrence Berkeley National Laboratory, University of California, Berkeley, California 94720, USA

INTRODUCTION

Hematite and other iron oxide minerals can be dissolved by iron-reducing bacteria under anaerobic conditions. The resulting suspensions from hematite dissolution experiments with *Shewanella alga* BrY [1] contained aggregates of solids with dimensions less than 1 μm under phase contrast optical microscopy. The composition, structure, oxidation state, and distribution of these aggregates is unknown. Imaging these suspensions with soft-X-Ray microscopy allows the examination of the sizes and shapes of these precipitates. In addition, by imaging above and below the iron edge, it is possible to determine which of the solids contain iron. The purpose of this preliminary study is to obtain images of these precipitates and to examine the iron distribution.

METHODS

Synthetic hematite crystals were dissolved by *Shewanella alga* BrY in anaerobic tubes [1]. The initial concentration of hematite was 1.65 g/l (7.2 mM Fe(III)). Macroscopic observation of the tubes suggested that the hematite had been totally dissolved. These tubes were transported to the Center for X-ray Optics soft-X-Ray microscope XM-1 (Beamline 6.1.2) [2] at the Advanced Light Source (ALS). Samples were removed from the anaerobic tube by syringe, and 2 μl of the suspension was placed between two 120nm thick Si_3N_4 windows.

PRELIMINARY RESULTS

Images of the suspensions (Fig. 1) show bacteria surrounded by a lattice of material, probably a biofilm. In another image (Fig. 2) precipitates with diverse morphologies are present. It is possible to obtain a map of the iron distribution. This procedure requires images to be taken below and above the iron edge. The dark shapes that appear on the image taken above the iron edge should appear on the image taken below the iron edge only if they contain iron. Three pairs of these images are shown in Figure 3. Most of the dark shapes shown at 705 eV are present as bright shapes when imaged at 696 eV. This suggests that most of the shapes do contain iron. However, there are some dark shapes in the middle and left pairs which do not appear to contain iron. Surface plots of the mass and iron distributions are shown in Figure 5. These plots show that spatial distributions of mass and iron are similar but not identical. Two broad shapes at the top and bottom of the mass distribution are missing in the iron distribution.

The next step in this research is to obtain spectroscopic data (micro-XAS) and elemental analyses to determine the oxidation state and spatial distribution of the iron species, local atomic structure, and composition. Crystals, if present, could be the minerals vivianite, siderite, or magnetite.

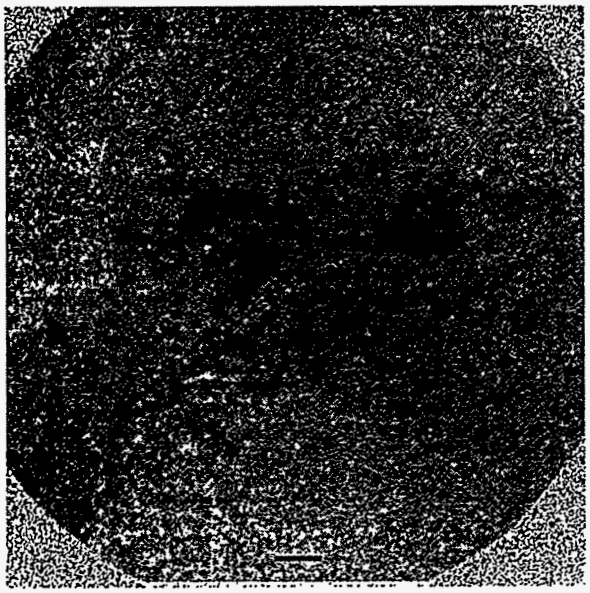

Figure 1: Bacteria, bar is 1 μm.

Figure 2: Precipitates, bar is 1 μm.

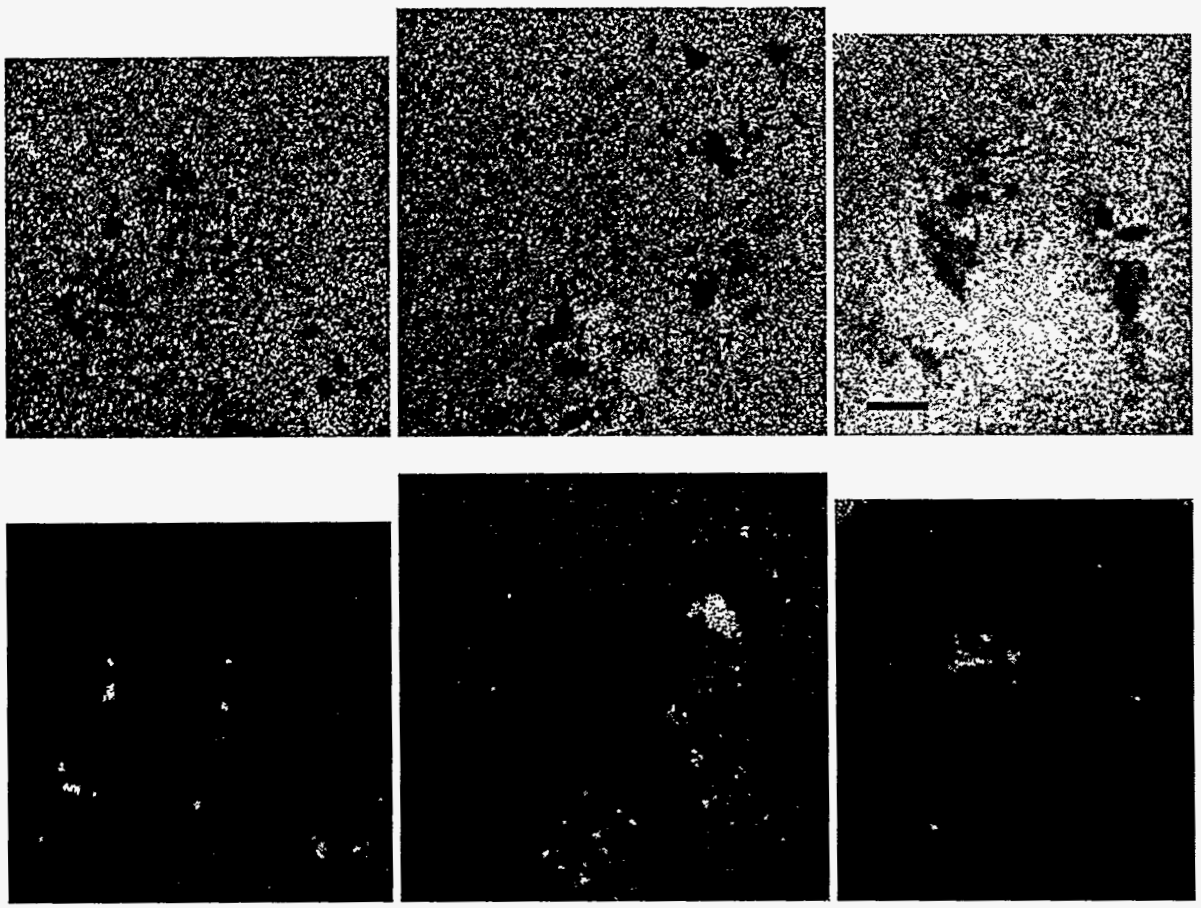

Figure 3: Mass (top; 705 eV) and iron (bottom, 705 eV) distributions; bar is 1 μm.

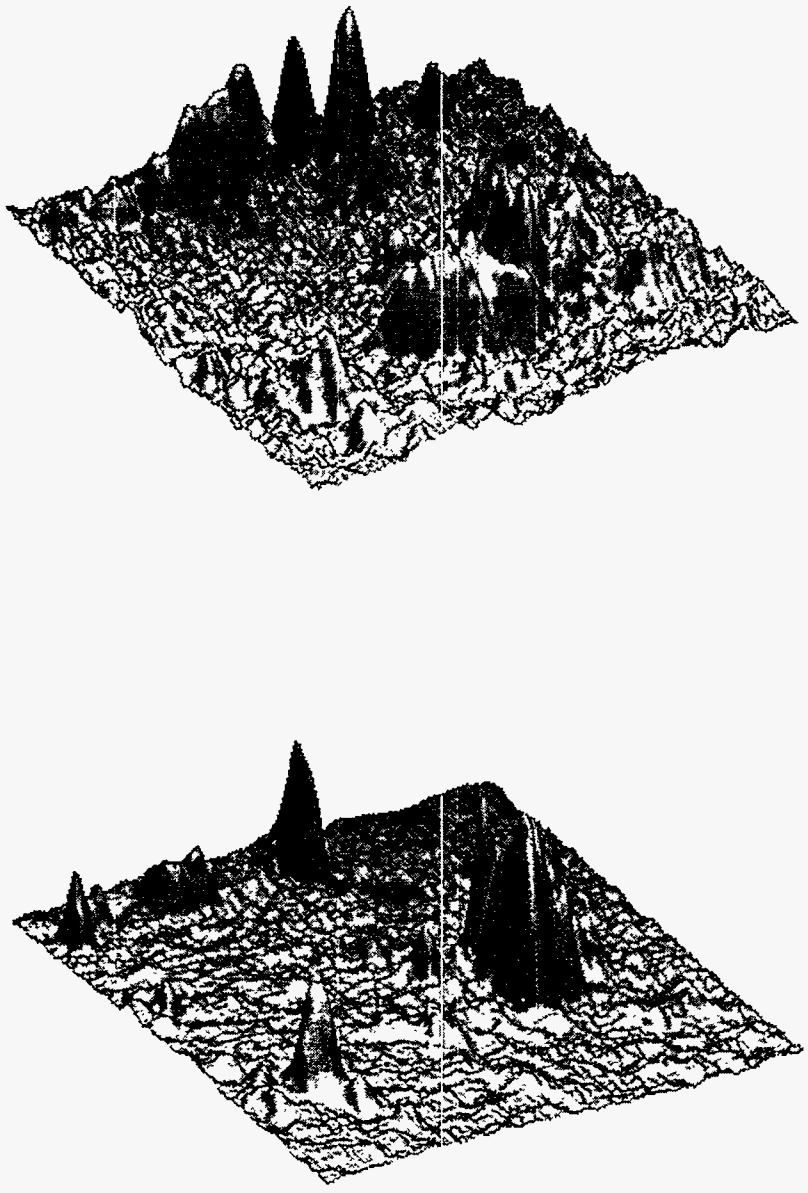

Figure 4: Surface plots of mass (705 eV; top) and iron (696 eV; bottom).

ACKNOWLEDGMENTS

Thanks to Dr. Geraldine Lamble for encouraging and facilitating collaboration between the Earth Sciences Division and the ALS.

REFERENCES

1. B. Lea Cox, Reductive Dissolution of Iron Oxide Minerals by *Shewanella putrefaciens* BrY, PhD Dissertation, University of California, Berkeley, CA (1995).
2 Meyer-Ilse, W., H. Medecki, L. Jochum, E. Anderson, D. Attwood, C. Magowan, R. Balhorn, M. Moronne, and D.R. Schmahl, "New High-Resolution Zone-Plate Microscope at Beamline 6.1 of the ALS", *Synchrotron Radiation News*, 8 (3), 29-33, (1995).

This work was supported by the Office of Energy Research of the U.S. Department of Energy under Contract No. DE-AC03-76SF00098.

Principal investigator: Lea Cox, Jet Propulsion Laboratory/California Institute of Technology. Email: blcox@mail1.jpl.nasa.gov. Telephone: 818-354-0527.

X-Ray Microscopic Visualization of Specific Labeling of Adhesive Molecule CD36 and Cytoadherence by *Plasmodium falciparum* Infected Erythrocytes

Jackson Yeung[1], John T. Brown[2], Ajit Nair[2], Narla Mohandas[1], Werner Meyer-Ilse[2], and Cathleen Magowan [1]

[1]Life Sciences Division, Ernest Orlando Lawrence Berkeley National Laboratory, University of California, Berkeley, California 94720, USA

[2]Center for X-ray Optics, Ernest Orlando Lawrence Berkeley National Laboratory, University of California, Berkeley, California 94720, USA

Cytoadherence between *Plasmodium falciparum* malarial infected red blood cells and venular endothelium results in sequestration of mature parasites in the microvasculature, a condition that contributes to cerebral malaria, the most frequently fatal complication of malaria. Cytoadherence, a biological phenomenon of critical importance to the survival of *P. falciparum* malarial parasites, is the result of specific interaction between receptors on endothelium, including CD36 [1,2], and adhesive ligands that the parasite inserts into the infected erythrocyte membrane, including the antigenically variant family of molecules known as PfEMP1 [3,4]. CD36 is a member of a family of integral membrane glycoproteins that functions both as a cell adhesion molecule and as a scavenger receptor. It is expressed on several cell types, including platelets, monocytes/macrophages, adipocytes, and microvascular endothelial cells.

We used high resolution soft x-ray microscopy to investigate the interactions between target cells that express CD36, malarial infected red blood cell membranes, and intraerythrocytic parasites. We examined surface and internal structures of intact, hydrated, fixed infected erythrocytes and target cells during *in vitro* cytoadherence. We detected 0.2-3m fibrillar structures projecting from the surface of both melanoma and endothelial cells (Figure 1).

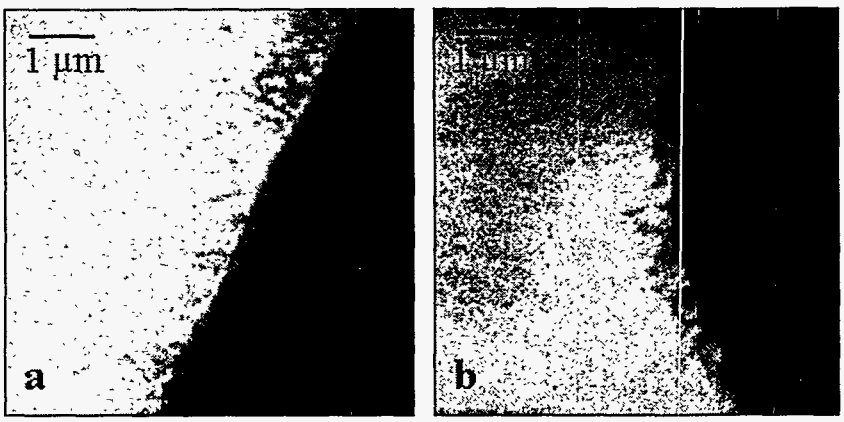

Figure 1. Fibrillar structures projecting from the surface of intact, 1% glutaraldehyde fixed, cultured melanoma cells (a) and endothelial cells (b) are detected by x-ray microscopy.

We investigated the distribution of CD36 on target cells using an immunogold labeling technique that has previously been used in dark-field x-ray microscopy [5]. We examined the orientation of intraerythrocytic parasites in relation to the contact between the erythrocyte membrane and the target cell, and whether membranes of either the erythrocyte or the target cell are detectably altered during cytoadherence. We observed infected erythrocytes in direct contact with the plasma membrane of the target cell, but most interestingly, in some instances the 0.2-3.0 µm fibrillar extensions from the surface of melanoma and endothelial cells appeared to be involved in specific adherence of infected red blood cells. (Fig 2).

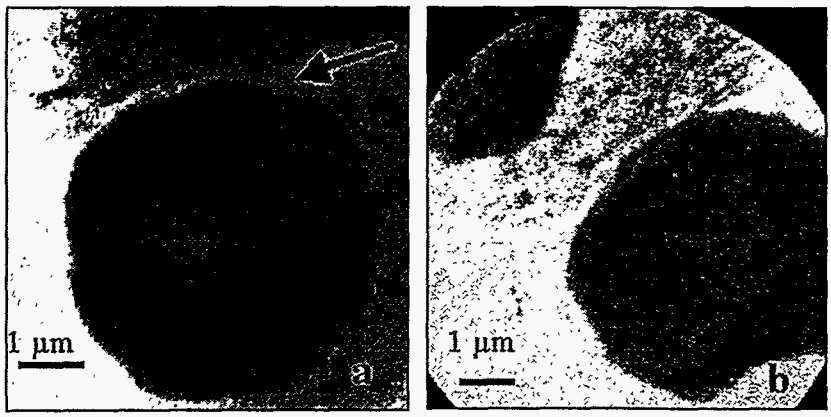

Figure 2. In vitro cytoadherence of *P. falciparum* infected erythrocytes to melanoma or endothelial cells imaged by x-ray microscopy. a) Infected erythrocyte binding to an endothelial cell. Arrow indicates an apparent tether between the cells. Note the vesicular structure adjacent to the intraerythrocytic parasite. b) Infected erythrocyte binding to a melanoma cell.

In our cytoadherence assays, infected erythrocytes tended to bind along the edges of the target cells, so we examined surface distribution of CD36 on melanoma and endothelial cells using monoclonal antibody OKM5 and silver enhanced immunogold labeling. We showed that OKM5 is distributed particularly heavily along the growing edge of melanoma cells (Fig 3). Labeling of CD36 by silver enhanced immunogold beads on endothelial cells was also concentrated along the edges of the cells, but it was very light compared with melanoma cells (data not shown).

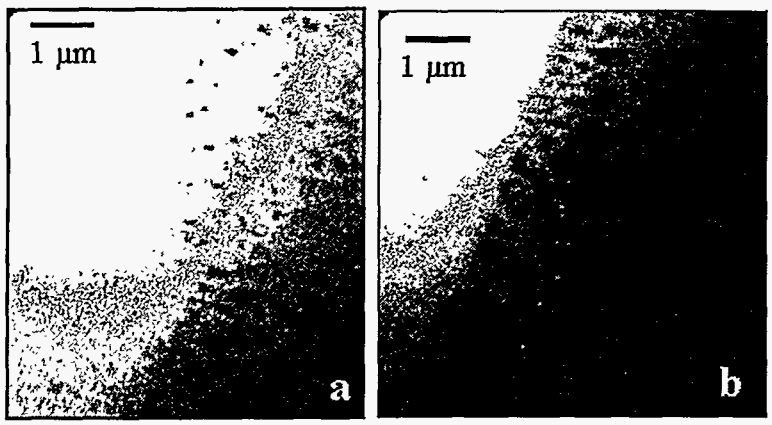

Figure 3. Labeling of CD36 with mAb OKM5 for x-ray microscopic analysis. a,b) Edges of a melanoma cell incubated with OKM5 are heavily decorated with silver enhanced 30nm immunogold beads in these x-ray micrographs. Silver enhancement proceeded under experimentally determined conditions to ensure a high degree of enhancement and low self-nucleation-induced background. For x-rays with 517 eV photon energy (2.4 nm wavelength), the 1/e attenuation length of water, organic material, and silver is about 10m, 0.5m, and 0.05m respectively.

Triton X-100 extracted cells [6] were incubated with OKM5 and a series of images were collected and tiled. Distribution of CD36 throughout the extracted cell can be visualized (Fig 4).

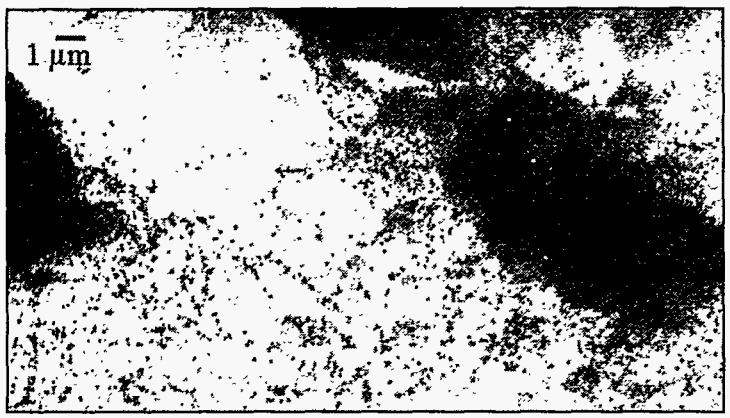

Figure 4. Tiled x-ray image of a Triton X-100 extracted C32 melanoma cell. Extracted cell was incubated with OKM5, followed by immunogold beads enhanced with silver.

Our work provides the first x-ray microscopic images of cytoadherent infected red cells and their interactions with the plasma membrane and surface structures of cells that express CD36. We have

demonstrated that parasites may be oriented in various positions within the red cell cytoplasm during cytoadherence, and that fibrillar structures on the surface of the target cells may be involved in cell-cell adherence. Except for an occasional tether (Fig 2a), changes coincident with cytoadherence were not consistently detected in either the parasite, the red cell membrane, or the target cells. Most alterations of red blood cells, particularly membrane alterations that occur coincident with parasitization and specifically in association with cytoadherence, occur at the biochemical and molecular levels and cannot be detected by microscopy [7,8]. Likewise, potential changes in the membranes of target cells occur at the molecular level [9].

The interaction between *P. falciparum* infected erythrocytes and cells that express CD36, such as venular endothelium in the microvasculature or cultured melanoma cells or endothelial cells, has been studied extensively because *in vivo* it is both critical for survival of the parasite, and potentially fatal for the infected individual. Disruption of the association between infected erythrocytes and the host's venular endothelium is considered a promising vaccine strategy [10]. An eventual understanding of the complex biological interactions and mechanisms which result in cytoadherence and sequestration of malarial infected red cells will contribute to prevention and/or reversal of adherence associated with cerebral malaria.

REFERENCES

1. C. F. Ockenhouse, N. N. Tandon, C. Magowan, G. A. Jamieson and J. D. Chulay (1989) Identification of a platelet membrane glycoprotein as a falciparum malaria sequestration receptor. *Science* **243**, 1469-1471.
2. J. W. Barnwell, A. S. Asch, R. L. Nachman, M. Yamaya and M. Aikawa (1989) A human 88-kD membrane glycoprotein (CD36) functions in vitro as a receptor for a cytoadherence ligand on Plasmodium falciparum-infected erythrocytes. *J Clin Invest* **84**, 765-772.
3. D. I. Baruch, B. L. Pasloske, H. B. Singh, X. H. Bi, X. C. Ma, M. Feldman, T. F. Taraschi and R. J. Howard (1995) Cloning the P. falciparum gene encoding Pfemp1, a malarial variant antigen and adherence receptor on the surface of parasitized human erythrocytes. *Cell* **82**, 77-87.
4. C. Magowan, W. Wollish, L. Anderson and J. Leech (1988) Cytoadherence by Plasmodium falciparum-infected erythrocytes is correlated with the expression of a family of variable proteins on infected erythrocytes. *J Exp Med* **168**, 1307-1320.
5. H. N. Chapman Jacobsen, C., Williams, S. (1996) A characterization of dark-field imaging of colloidal gold labels in a scanning transmission x-ray microscope. *Ultramicroscopy* **62**, 191-213.
6. E. Fey, KM Wan, S. Penman. (1984) Epithelial cytoskeletal framework and nuclear matrix-intermediate filament scaffold: three dimensional organization and protein composition. *J Cell Biol* **98**, 1973-1984.
7. M. Foley and L. Tilley (1995) Home Improvements: Malaria and the red blood cell. *Parasitol Today* **11**, 436-39.
8. I. W. Sherman (1985) Membrane structure and function of malaria parasites and the infected erythrocyte. *Parasitology* **91**, 609-645.
9. C. F. Ockenhouse, C. Magowan and J. D. Chulay (1989) Activation of monocytes and platelets by monoclonal antibodies or malaria-infected erythrocytes binding to the CD36 surface receptor in vitro. *J Clin Invest* **84**, 468-475.
10. R. S. Nussenzweig and C. A. Long (1994) Malaria vaccines: multiple targets. *Science* **265**, 1381-1383.

ACKNOWLEDGMENTS

This work was supported by the Office of Energy Research of the U.S. Department of Energy under Contract No. DE-AC03-76SF00098 and NIH Grant No. DK32094-10. OKM5 was kindly provided by Ortho Diagnostics and EA.hyb926 endothelial cells were provided by Dr.Cora-Jean Edgell.

Principal investigator: Cathleen Magowan, Ernest Orlando Lawrence Berkeley National Laboratory.
Email: Cathie_Magowan@macmail2.lbl.gov. Telephone: 510-486-6439.

Beamline 6.3.2 Abstracts

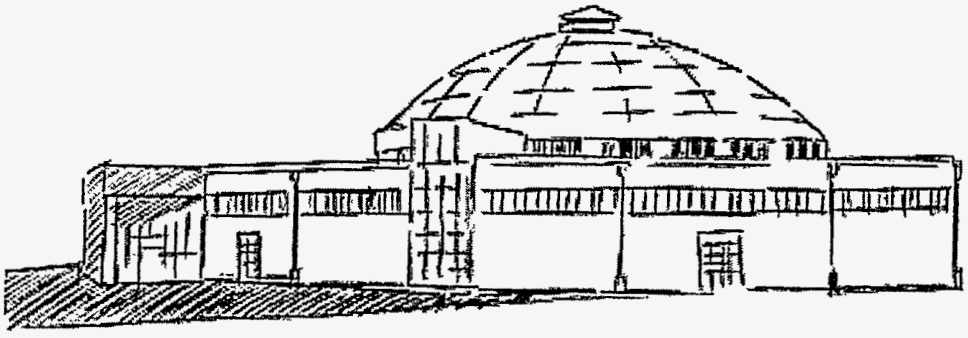

Absolute Photoabsorption Measurements of Molybdenum in the Range 60 to 930 eV for Optical Constant Determination

R. Soufli[1,2] and E. M. Gullikson[2]

[1] Department of Electrical Engineering and Computer Sciences, University of California, Berkeley, California 94720, USA

[2] Center for X-ray Optics, Ernest Orlando Lawrence Berkeley National Laboratory, University of California, Berkeley, California 94720, USA

INTRODUCTION

In recent years there has been increased interest in the optical properties of Mo in the extreme ultraviolet (EUV)/soft x-ray region, due to its implementation as the absorber layer for Mo/Si and Mo/Be multilayer mirrors. These optics are becoming essential elements in applications such as lithography, astronomy and synchrotron research; they operate at energies below the Si $L_{2,3}$ edge (99.8 eV) and the Be K edge (111.5 eV) respectively, where silicon and beryllium exhibit low absorption. Information on the dispersive and absorptive behavior of each material can be obtained from the real and imaginary part of the energy dependent refractive index $n = 1 - \delta + i\beta$, which has to be measured to a great degree of accuracy. A comprehensive compilation of published data for Mo was published [1] by Henke, Gullikson and Davis in 1993 and will be referred to as the "1993 atomic tables" throughout this abstract. These tables use interpolations between all published experimental data for the absorption (for all elements with atomic number $Z = 1$ to $Z = 92$) combined with a theoretical model [2], in order to determine the imaginary part of the refractive index in the range 10 - 30,000 eV. The real part is then calculated through dispersion (Kramers-Kronig) analysis. It should be noted that the values for n in these tables have been determined according to the independent atom approximation, in the long wavelength and/or small scattering angle regime. The optical constants δ, β of Mo from the 1993 tables are tested for accuracy and self-consistency through a series of sum rules. This evaluation reveals inaccuracies originating in the quality of experimental results. For instance, reflectance data included in the 1993 tables may have been severely influenced by surface oxide, contamination and roughness, in the EUV and soft x-ray regions. New transmission measurements for the refractive index of Mo are presented in this work, in the region of interest for EUV applications. The new compilation of optical constants is evaluated through a series of sum rules and applied in the calculation of the Bragg reflectivity of multilayer optics.

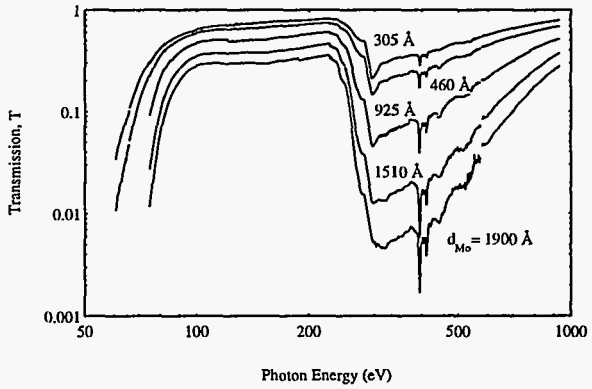

Figure 1. Transmission data from the five C/Mo/C films are shown, corresponding to molybdenum layers of 305, 460, 925, 1510 and 1900 Å each, deposited between two 145 Å thick carbon layers.

SUM RULES

The accuracy of a set of optical data from $\omega = 0$ to $\omega = \infty$ may be tested through the sum rules

$$Z^* = \frac{2}{\pi}\frac{m\epsilon_0}{n_a e^2}\int_0^\infty u\, A_i(u)\, du \qquad i = 1,2,3, \tag{1}$$

where the optical data are obtained in one of the following forms: $A_1 = \epsilon_2$, $A_2 = \beta$, $A_3 = Im\{-\epsilon^{-1}\}$ (the "energy-loss function"). $\epsilon = n^2 = \epsilon_1 + i\,\epsilon_2$ represents the dielectric

function of the material and Z^* is the atomic number reduced by the relativistic correction $(Z/82.5)^{2.37}$. For materials with well separated absorption levels, Eq. (1) may be written in its partial form

$$N_{eff,i}(\omega) = Z^* - \frac{2}{\pi}\frac{m\epsilon_0}{n_a e^2}\int_\omega^\infty u\, A_i(u)\, du, \qquad i = 1,2,3, \tag{2}$$

where the quantity under the integral is known as "oscillator strength" and $N_{eff,i}(\omega)$ represents the effective number of electrons contributing to the absorption up to frequency ω. For the energies above the first core absorption level of the material, all 3 sum rules should give identical results. At the lower energies, below the first core absorption level, it is expected from the theory that $N_{eff,1} > N_{eff,2} > N_{eff,3}$. The reason for this behavior is that, for the valence electrons, each of $A_{1,2,3}$ is subject to a different degree of "shielding" from the polarizable background of the core states [3]. At $\omega = 0$, if accurate optical constants are used, Eq. (2) should give $N_{eff,1}(0) = N_{eff,2}(0) = N_{eff,3}(0) = 0$. Eq. (2) yields identically $N_{eff,1}(\infty) = N_{eff,2}(\infty) = N_{eff,3}(\infty) = Z^*$ regardless of the accuracy of the data. The sum rule for $A_2 = \beta$ can be used to characterize absorption data only, while A_1, A_3 involve both real and imaginary parts of the refractive index. Thus, it is often useful to plot all 3 $N_{eff,i}$s of Eq. (2) in order to assess the self-consistency of a set of optical constants. $N_{eff,2}(\omega)$ for Mo was calculated and it was found that 2.3 electrons are missing from the absorption values for Mo in the 1993 atomic tables. The errors in the experimental absorption data are most likely to come from the EUV range, where measurements are particularly difficult and sensitive, as explained in the Introduction. The EUV includes the region around 100 eV, where the optical constants of Mo are of particular importance for multilayer mirror applications.

EXPERIMENT

C/Mo/C free-standing foils were fabricated by sputtering on photoresist coated Si wafers. Five different thicknesses of Mo were deposited, ranging from 305 Å to 1900 Å and the C layer thickness was maintained the same ($\approx$ 145 Å) for all five samples. Prior to removal, Mo layer thicknesses were verified to an accuracy of $\pm$ 2% by fitting Cu K_α (8047.8 eV) and Al K_α (1486.7 eV) reflectance data. Fitting was not possible for the 1900 Å sample, due to low visibility of the interference fringes. The C thickness was fitted to values between 140 and 145 Å. For the removal process, support rings were attached to the sample surface using an acetone resistant glue, and the foils were removed by soaking in acetone, resulting in free-standing films with an open area of 7 mm^2. Transmission measurements on the five C/Mo/C foils were performed at beamline 6.3.2., in the energy range 60 - 930 eV, as shown in Fig. 1. The results were fitted for the absorption coefficient μ (cm^2/g) of Mo at each energy, using the expression

$$T = T_0\, e^{-\mu\rho x}, \tag{3}$$

where $T = I/I_0$ is the measured transmission (I, I_0 are the transmitted and incident intensities respectively), ρ = 10.22 g/cm^3 is the Mo density and x is the Mo thickness in the foil. T_0 represents the transmission from layers of other materials present in the foil (in this case the two layers of carbon). Thus, the fitting procedure yields μ and T_0 at each energy. An analysis of the results for T_0 vs. energy revealed $\sim$ 2% atomic content of Ar in the samples, coming from the Ar^+ ions in the sputtering chamber. Moreover, the presence of $\sim$ 400 Å overlayer of photoresist, left from the removal process, was found on the samples. The effect of any overlayers is included in T_0 and therefore cancels out in the fitting procedure for the absorption coefficient of Mo, as explained above.

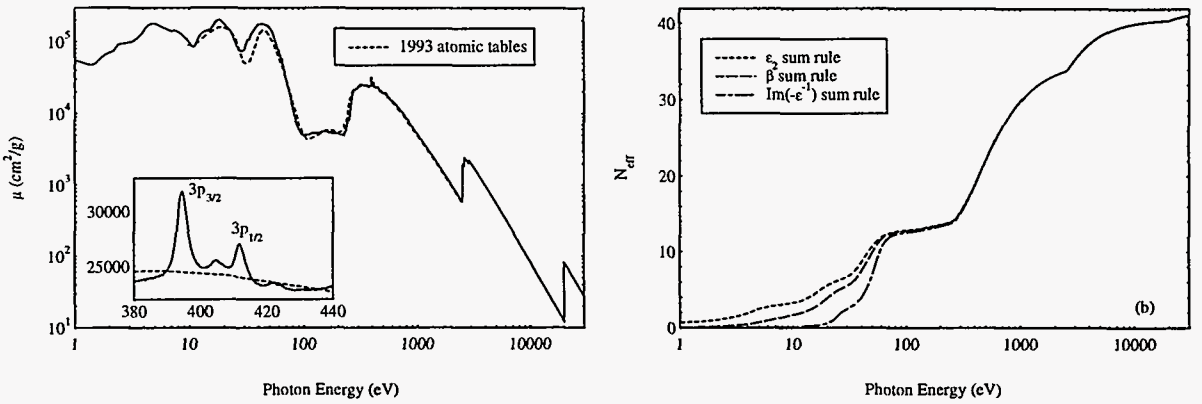

Figure 2. Left: A new compilation of data for μ of Mo from 1 eV to 30 keV is shown with the solid line. The values in the range 60 - 930 eV are obtained from the present measurements. Data from previous workers, compiled in Ref. 4, are used in the low energy region (1 - 35 eV). In the rest of the spectrum, the values of the 1993 atomic tables are used with small corrections around the energy region of the present work. In the inset, the molybdenum $M_{2,3}$ structure and its deviation from the smoothed tabulated values are shown in detail. Right: The sum rules for ϵ_2, β, $\mathrm{Im}\{-\epsilon^{-1}\}$ are shown, calculated using the new compilation of optical constants for Mo. The results demonstrate accuracy and self-consistency.

RESULTS AND DISCUSSION

The absorption coefficient μ for Mo derived from the measurements in this work in the energy range 60 - 930 eV is plotted in Fig. 2 (left), combined with the tabulated values [1] and experimental data at the low energies [4] in order to form a set of values for the absorption in the complete spectrum (1 - 30,000 eV). In the inset, it is shown that the structure due to the splitting of the Mo $3p_{1/2}$, $3p_{3/2}$ peaks, which was absent from the simplified calculations in the 1993 atomic tables, is revealed in the new absorption measurements. In the region of operation of Mo/Si normal incidence mirrors (around 92.5 eV, or 13.4 nm in wavelength units), the new experimental data yield lower values for the absorption, while at the Mo/Be mirror regime (around 109 eV, or 11.4 nm), the new values for the absorption appear higher than the 1993 atomic tables. The imaginary (absorptive) part β of the refractive index was obtained in the energy range 1 - 30,000 eV, through the expression $\beta = \mu(\lambda\rho/4\pi)$. Then, δ was calculated from the Kramers-Kronig relations, using the above set of absorption data. The sum rules with the revised set of optical constants for Mo are shown in Fig. 2 (right). The result of the sum rule for β at $\omega = 0$ is $N_{eff,2}(0) = 0$. This demonstrates that the new set of absorption data is accurate, as opposed to the missing oscillator strength of 2.3 electrons found in the absorption values from the 1993 atomic tables. All three $N_{eff,i}$s fall off at the low energies as predicted by the theoretical model discussed in the Sum Rules section. Finally, the Bragg reflectivities for typical Mo/Si and Mo/Be multilayer mirrors for EUV lithography were calculated vs. wavelength, in Fig. 3. It is shown that the new set of data yields 2% higher theoretical peak reflectivity for Mo/Si at 13.4 nm, compared to the 1993 atomic tables. The calculated reflectivity for Mo/Be mirrors with the revised data becomes a few percent lower, for wavelengths longer than the Be edge. These results become significant when one attempts to fit experimental results for the reflectance of a multilayer optic to a theoretical model. Two different sets of optical constants would yield two different sets of fitted parameters (multilayer period, ratio of Mo thickness in the period, interfacial roughness, etc.) for the mirror. Thus, using accurate optical constants is essential for the understanding of the experimental conditions during the multilayer deposition and the prediction of the mirror performance.

CONCLUSIONS

Precise transmission measurements in the range 60 - 930 eV for the determination of the optical constants of molybdenum are presented in this work. Compared to the 1993 tables, the new

results yield different values for the absorption of Mo in the wavelength range 11 - 14 nm, which is important for normal incidence Mo/Be and Mo/Si multilayer mirror applications; the new measurements also reveal the fine structure in the absorption coefficient of Mo around the $M_{2,3}$ edge. Sum rule tests show that the missing oscillator strength from the absorption coefficient in the 1993 tables is recovered and that the new set of optical constants is self-consistent. The results presented have been published [5] and have been used to revise the optical constants files for Mo, which are available on the World Wide Web [6].

ACKNOWLEDGMENTS

The authors are indebted to Chris Walton for his invaluable help in depositing the samples. We are also thankful to J. H. Underwood for his support in carrying out these measurements.

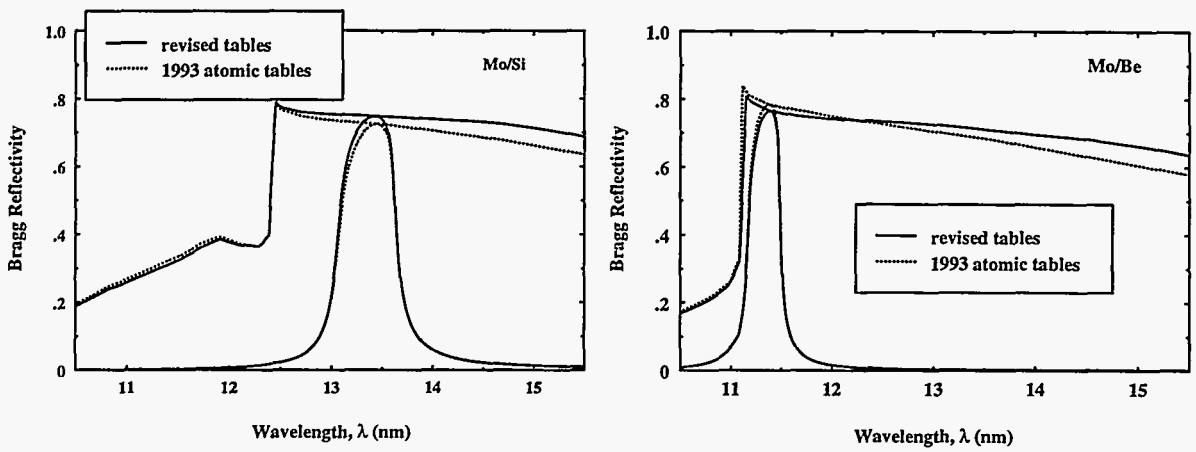

Figure 3. Calculated peak (Bragg) reflectivities at normal incidence, for an infinite multilayer stack of Mo/Si (left) and Mo/Be (right), plotted vs. wavelength. The ratio of Mo thickness to the multilayer period was 0.4 and the period was optimized at each wavelength. The Bragg peak is shown in detail for a Mo/Si mirror with 6.87 nm period (left) and a Mo/Be mirror with 5.75 nm period (right). For comparison, the same calculations are performed using the optical constants in the 1993 atomic tables.

REFERENCES

1. B. L. Henke, E. M. Gullikson and J. C. Davis, Atomic Data and Nuclear Data Tables **54**, 181-343 (1993).
2. G. Doolen and D. A. Liberman, Phys. Scripta **36**, 77-79 (1987).
3. D. Y. Smith and E. Shiles, Phys. Rev. B **17**, 4689-4694 (1978).
4. D. W. Lynch and W. R. Hunter, in *Handbook of Optical Constants of Solids*, edited by E. D. Palik, (Academic Press, San Diego, CA, 1985), pp. 303-313.
5. R. Soufli and E. M. Gullikson, Appl. Opt., to appear in the April 1, 1998, issue.
6. E. M. Gullikson, "X-ray interactions with matter," *http://www-cxro.lbl.gov/optical_constants.*

This work was supported by the Director, Office of Basic Energy Sciences, Materials Sciences Division, of the U.S. Department of Energy under Contract No. DE-AC03-76SF00098.

Principal Investigator: Regina Soufli, currently with the Smithsonian Astrophysical Observatory, 60 Garden Str., Cambridge, MA 02138. Email: regina@head-cfa.harvard.edu. Telephone: 516-344-8029.

Characterization of Cathode/Electrolyte Interfacial Impurities in a Solid Oxide Fuel Cell by Soft X-Ray Spectroscopy

Y. Muramatsu[1]*, M. Arakawa[2], M. Grush[1], T. A. Callcott[1], J. H. Underwood[3], E. M. Gullikson[3], and R. C. C. Perera[3]
[1]University of Tennessee, Knoxville, TN 37996
[2]NTT Integrated Information and Energy Systems Laboratories, Tokyo 180-8585, Japan
[3]Advanced Light Source, Lawrence Berkeley National Laboratory, Berkeley, CA 94720
*permanent address: NTT Integrated Information and Energy Systems Laboratory, Tokyo 180-8585, Japan

INTRODUCTION

Solid Oxide Fuel Cells (SOFC) have been expected to be clean and high energy conversion power sources [1, 2]. From the viewpoint of SOFC fabrication, control of the electrodes/ electrolyte interfaces could be critical because interface impurities generally cause interfacial resistance and decrease the stability of SOFCs. In the interface of $La_{0.8}Sr_{0.2}MnO_3$ (LSM) cathode and ZrO_2 (8-mol% stabilized Y_2O_3) (YSZ) electrolyte, it has been suggested from x-ray diffraction (XRD) measurements that $La_2Zr_2O_7$ may be formed in the annealed LSM/YSZ interface [3]. However, the interfacial impurities have not been clearly identified because XRD provides only information about crystal structure, and none about chemical/electronic states.

Soft x-ray emission/absorption spectroscopy is a powerful tool for determining the chemical/electronic states of materials. It can be used not only for conductive materials but also for insulators, because the x-ray emission/absorption process is generally unaffected by static electricity on the materials. Therefore, soft x-ray emission/absorption spectroscopy has great potential for characterizing SOFC materials. This paper describes the characterization of interfacial impurities in LSM/YSZ by soft x-ray emission/absorption spectroscopy.

EXPERIMENTAL

The interfacial sample was made by the annealing a mixture of LSM and YSZ powder at 1000 °C. Powder samples of LSM, YSZ, and $La_2Zr_2O_7$ were also prepared as references. Soft x-ray spectral measurements of these samples were carried at BL-8.0 [4] in ALS for emission measurements and BL-6.3.2 [5] for absorption measurements with a total electron yield method. We used the O*K* absorption edge because O*K* emission/absorption spectra may reflect the environmental chemical states more strongly than Zr*L* or *M* spectra.

RESULTS AND DISCUSSION

Before x-ray absorption measurements, O*K* x-ray emission spectra of the interfacial sample, YSZ, LSM, and $La_2Zr_2O_7$ were measured. Although energy shifts of the emission peaks were clearly observed among these samples, it may be difficult to identify the interfacial species because the individual spectral shapes were broad with FWHM of 3.5 eV.

Figure 1 (a) shows the O*K* x-ray absorption spectra of the interfacial sample, YSZ, LSM, and $La_2Zr_2O_7$. The spectral shape of LSM (manganese oxide compound) is quite different from those of YSZ and $La_2Zr_2O_7$ (zirconium oxide compounds). Even in these Zr compounds, energy shifts can be observed in the sharp peaks (assigned B, C, D, and E in the figure) between YSZ and $La_2Zr_2O_7$. Therefore, we may analyze the interfacial species from these absorption spectra to see whether $La_2Zr_2O_7$ is formed in the LSM/YSZ interface. Figure 1 (b) shows the absorption spectrum of the interfacial sample minus the LSM fraction: the LSM spectrum was subtracted from the original interfacial sample spectrum up to the disappearance of the 529-eV peak (assigned A) in the original spectrum. Comparing the spectral shape of

YSZ and $La_2Zr_2O_7$, we see that the interfacial sample spectrum with the LSM fraction subtracted looks like a mixture of YSZ and $La_2Zr_2O_7$. To confirm this, we compared the interfacial sample spectrum with the synthesized spectra of YSZ and $La_2Zr_2O_7$ in Figure 2. The fractions of YSZ and $La_2Zr_2O_7$ were varied from 0% to 100 % in a 10% steps in the synthesized spectra. Spectral shape and individual peak energy of the interfacial sample with LSM fraction subtracted agree with those of the synthesized spectra of YSZ:$La_2Zr_2O_7$ = 0.6:0.4. This confirms that $La_2Zr_2O_7$ is formed in the LSM/YSZ interface, which agrees with the XRD analysis [3].

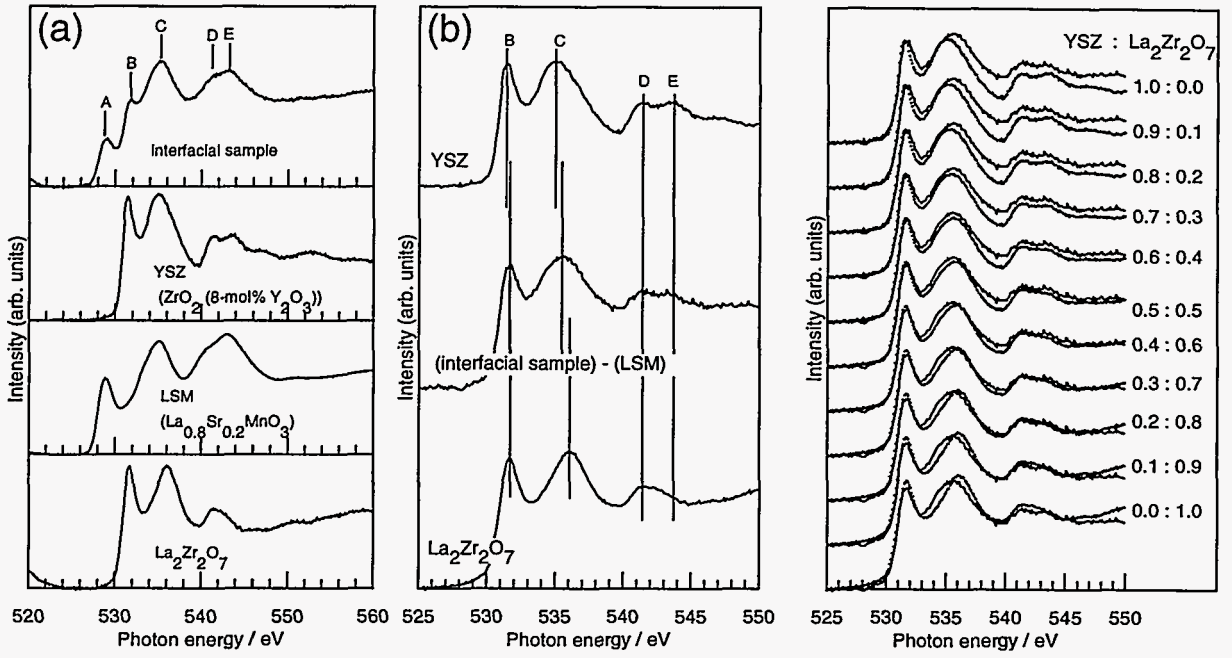

Fig. 1 (a) O*K* x-ray absorption spectra of LSM/YSZ interfacial sample, YSZ, LSM, and $La_2Zr_2O_7$. (b) Absorption spectrum of the interfacial sample minus the LSM fraction. Spectra of YSZ and $La_2Zr_2O_7$ are also shown as references.

Fig. 2 Comparison of the interfacial sample spectra with the LSM fraction subtracted (solid line) with the synthesized spectra of YSZ and $La_2Zr_2O_7$ (dotted line).

CONCLUSION

Chemical species in a 1000-°C annealed LSM/YSZ interface were analyzed from O*K* x-ray absorption measurements using $La_2Zr_2O_7$ as a reference sample. Since the spectral shape of the interfacial sample agreed with the mixture of LSM, YSZ, and $La_2Zr_2O_7$, we conclude that $La_2Zr_2O_7$ is formed in the annealed LSM/YSZ interface. This indicates that suppressing the formation of $La_2Zr_2O_7$ in the LSM/YSZ interface is a critical point in advanced SOFC fabrication.

REFERENCES

1. N. Q. Minh, *J. Am. Ceram. Soc.*, 76, 563 (1993).
2. S. E. Veyo, A. Kusunoki, S. Takeuchi, S. Kaneko, and H. Yokoyama, *US DOE REP., DOE-MC-28055-94-C-0334*, p. 9 (1994).
3. D. Ikeda, M. Arakawa, T. Matsushima, and T. Hirai, *Extended Abstracts of 190th Electrochemical Society Meeting,* San Antonio, Texas, p. 143 (1996).
4. J. J. Jia, T. A. Callcott, J. Yurkas, A. W. Ellis, F. J. Himpsel, M. G. Samant, J. Stohr, D. L. Ederer, J. A. Carlisle, E. A. Hudson, L. J. Terminello, D. K. Shuh, and R. C. C. Perera, *Rev. Sci. Instrum.*, 66, 1394 (1995).

5. J. H. Underwood, E. M. Gullikson, M. Koike, P. J. Batson, P. E. Denham, K. D. Franck, R. E. Tackaberry, and W. F. Steele, *Rev. Sci. Instrum.*, 67, 1 (1996).

This work was supported by the Office of Basic Energy Sciences of the U.S. Department of Energy under contract Nos. DE-AC03-76SF00098 and W-7405-Eng-48, and by National Science Foundation Grant No. DMR-9017996 to the University of Tennessee.

Principal investigator: Yasuji Muramatsu, University of Tennessee. Currently at NTT Integrated Information and Energy Systems Laboratories. Email: murama@ilab.ntt.co.jp. Telephone: +81-422-59-2521.

Chemical effect on resonant inelastic *L* x-ray emission spectra in Cr compunds

Y.Ito, T.Tochio, A.M.Vlaicu, D.Ohsawa, T.Mukoyama, Y.Muramatsu[1], R.C.C.Perera[2], M.M.Grush[3], and T.A. Callcott[3]

Institute for Chemical Research, Kyoto University, Uji, Kyoto 611, Japan

[1] NTT Integrated Information and Energy Systems Laboratory, Tokyo 180, Japan

[2] Lawrence Berkley National Laboratory, University of California, 1 Cyclotron Road MS 2-400, Berkley, CA 944720 USA

[3] Department of Physics, University of Tennessee, 401, Nielson Physics Bldg. Knoxville, TN 37996, USA

ABSTRACT

We have measured and analysed the resonant enhancement of photo-emission in the energy region of the Cr 2p threshold on Cr compounds using tunable synchrotron radiation. The Raman scattering peak is resonantly enhanced at excitation energies corresponding to Cr 2p absorption peaks. The x-ray absorption and emission spectra (XAES) of Cr(VI) are very different from those of Cr(III). The difference by the resonant photo-emission may be attributed to the effect of the covalency in bonding. Moreover, it is followed that XAES are very sensitive to ligand environment in Cr compounds and relatively insensitive to metal oxidation state, as Grush *et al.* suggested in Mn complexes [7].

KEYWORDS: Resonant; Soft X-ray; Emission; Fluorescence; Absorption; Transition metal; Chromium compounds.

INTRODUCTION

It was investigated by some workers [1-3] that the Kα/Kβ x-ray intensity ratios for chemical compounds of Cr and Mn elements with tetrahedral symmetry were larger than those with octahedral symmetry. It is necessary to carry out further the studies of the chemical effect for L-x-ray spectra so as to elucidate the valence electronic structures of the 3d compounds.

There are three L subshells and the vacancy produced by the primary ionization process can move between subshells through Coster-Kronig transitions. In the vicinity of the absorption edges strong emission components, which are actually multiple-ionization satellites, can be misinterpreted as part of the parent emission band. This fact indicates that for the study of the L-x-ray emission spectra, it is absolutely required to tune the energy of the incident photons and excite each subshell selectively.

Much effect has inquired into using x-ray absorption spectroscopy (XAS) for the investigation [4-6]. The benefit of using soft x-rays to study 3d transition metals is the longer core hole lifetime of the L-edge transitions which occur in this region, compared to the corresponding K-edges in the hard x-ray regime. This decrease in the linewidth leads to better-resolved features in the spectra; that is, the resonant emission phenomenon involves the excitation of core electrons to a localized, empty state. If the core hole lives long enough, the electron may recombine with the core hole and subsequently emit a photon . A resonant feature is observed only if a localized unoccupied state exists. Thus selective excitations to the localized state provide an important opportunity to study the localized states.

Grush et al.[7] have recently showed that L-edge x-ray absorption spectroscopy is a sensitive probe of the oxidation and spin state of metal sites and soft x-ray fluorescence very sensitive to ligand environment and relatively insensitive to electronic geometry and metal oxidation state in Mn complexes.

In the present study we investigate the emission spectra of Cr compounds in the energy region of *L*-subshell absorption edges with Total Electron Yield method in BL 6.3.2 to elucidate the *d* character effect in the chemical binding.

EXPERIMENTAL

Soft x-ray absorption experiments were performed on Beamline 6.3.2 at the Advanced Light Source. This is a bend magnet beamline with a Hettrick-Underwood type monochromator capable of high resolution, as has been previously described [8]. A 1200 l/mm grating with an exit slit of less than 20 microns resulted in a resolving power (E/δE) of better than 1200 at the Cr L-edge.

The absorption was monitored by collecting the total current from the sample as a function of exciting energy. The incident intensity (Io) of the x-ray beam was recorded as the current from either a gold mesh in the beampath or refocusing mirror. Spectra were recorded over a 60 eV range with a step size of about 0.1 eV. The spectra were divided by Io. All samples were finely powdered and identified by x-ray diffraction method, respectively. Both spectra have a 9.2 eV separation between L_3 and L_2 , in spite of the differences in geometry and ligand. The Cr (VI) spectra occur at 1.7 eV higher than the corresponding Cr (III) spectra, are much sharper, and decrease in broadness with increasing oxidation state has been observed in Cr compounds (Fig.1 and Table 1). Large differences in the ligand coordination can cause changes in electronic geometry and spin state which are often readily observable in the absorption spectra. The sample slide was then mounted perpendicular to the incoming x-ray beam.

Soft x-ray fluorescence spectra were recorded on Beamline 8.0 at the Advanced Light Source. This is an undulator beamline with a spherical grating monochromator, as has been previously described [9]. A 925 l/mm grating was used to monochromatize the excitation energy for these measurements The incident beam intensity was monitored as the current from a gold mesh in the beampath.

The soft x-ray fluorescence end station [9] consists of a Rowland circle - type emission spectrometer with a fixed 100 micron entrance slit and a 1500 l/mm grating mounted on a 10 m Rowland circle. The x-ray fluorescence is refocused onto a multichannel plate area detector which enables the entire emission spectrum to be obtained without scanning the detector. Samples for emission measurements were finely powdered, pressed into pellets, and mounted in the chamber at 22 degree to the incoming beam.

Table 1 Cr $L_{2,3}$ peaks in Cr compounds

Compound	L_3 [eV]	L_2 [eV]	$L_2 - L_3$
Cr atom	574.5	583.7	9.2
Cr metal	575.8	585.0	9.2
Cr_2O_3	575.8	585.0	9.2
$FeCr_2O_4$	575.8	585.0	9.2
$K_2Cr_2O_7$	577.5	586.7	9.2
Line	Lα	Lβ	
	573	583	10

RESULTS

The soft x-ray absorption and emission spectra of two oxidation state pairs are shown in Fig. 2. The Cr centers in Cr(VI) and Cr(III) have oxygen ligands with tetrahedral and octahedral geometry, respectively. In both cases, the x-ray absorption spectrum of Cr(VI) is strikingly different from that of Cr(III) as seen in Figures 1a. The L_3 peak occurs at 575.8 eV and 577.5 eV for the $Cr(III)_2O_3$ and $K_2Cr(III)_2O_7$. The appearance of the Lα and Lβ spectra to the ligand environment is shown in Figure 2. Cr L-emission spectra were recorded for Cr compounds. In the case of the Cr compounds with oxygen ligands: Cr metal, $Cr(III)_2O_3$, $FeCr(III)_2O_4$, $Cr(IV)O_2$, and $K_2Cr(VI)_2O_7$ the Lα and Lβ peaks maintain similar energy position for the same oxidation state. No difference in broadness was observed for any of the ligands in the Lα region .

The observed spectra will be compared and interpreted with DV-Xα theoretical calculations to clarify valence electronic structures of the compounds and the calculations are currently in progress.

REFERENCES

1. Y.Tamaki, T.Omori, and T.Shiokawa, Radiochem. Radioanal. Lett. **20**, 255(1975); ibid. **37**, 39 (1979); Jpn.J.Appl.Phys.**17**, S245(1978)
2. T.Mukoyama, K.Taniguchi, and H.Adachi, Phys.Rev.**B34**,3710 (1986).
3. M.C.Lepy, J.Plagnard, and J.Morel, Nucl.Instrum.Meth., **A339**,241(1994).
4. J.Nordgren and N.Wassdahl, J.Electron Spectros.Relat.Phenom. **72**,273(1995).
5. J.Nordgren, Physica Scripta **T61**, 32(1996).
6. M.M.Grush, J.Chen, T.L.Stemmler, S.J.George, C.Y. Ralston, R.T.Stibrany, A.Gelasco, G.Christou, S.M.Gorun, J.E.Penner-Hahn, S.P.Cramer, JACS, **118**, 65 (1996).
7. M.M.Grush, Y.Muramatsu, J.H.Underwood, E.M.Gullikson, D.L.Ederer, R.C.C.Perera, T.A.Callcott, J.Electron Spectros. Relat. Phenom., in press.
8. J.H.Underwood, E.M.Gullikson, M.Koike, P.J.Batson, SPIE, **3113,** 214(1997).
9. J.J.Jia, T.A.Callcott, J.Yurkas, A.W.Ellis, F.J.Himpsel, M.G.Samant, J.Stohr,D.L.Ederer, J.A.Carlisle, E.A.Hudson, L.J.Terminello, D.K.Shuh, R.C.C.Perera, Rev.Sci.Instr., **66,** 1394 (1995)

Funding: Ministery of Education, Japan

Principal investigator: Yoshiaki ITO

Kyoto University, Institute for Chemical Research
Gokasho, 611-Uji, Kyoto, JAPAN
fax: ++81-774-38-3045; phone: ++81-774-38-3045
email: yosi@elec.kuicr.kyoto-u.ac.jp

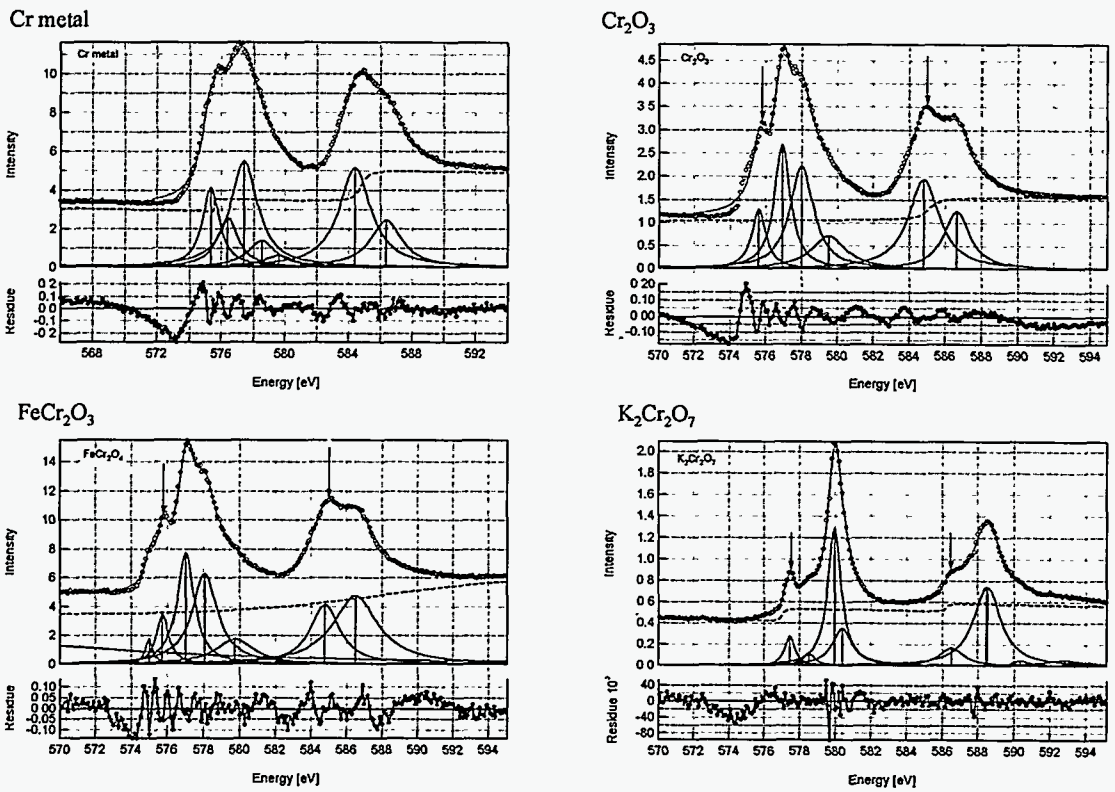

Figure 1. The Cr $L_{2,3}$ absorption spectra for the Cr compounds. The arrows on the absorption spectra indicate excitation energies used for fluorescence

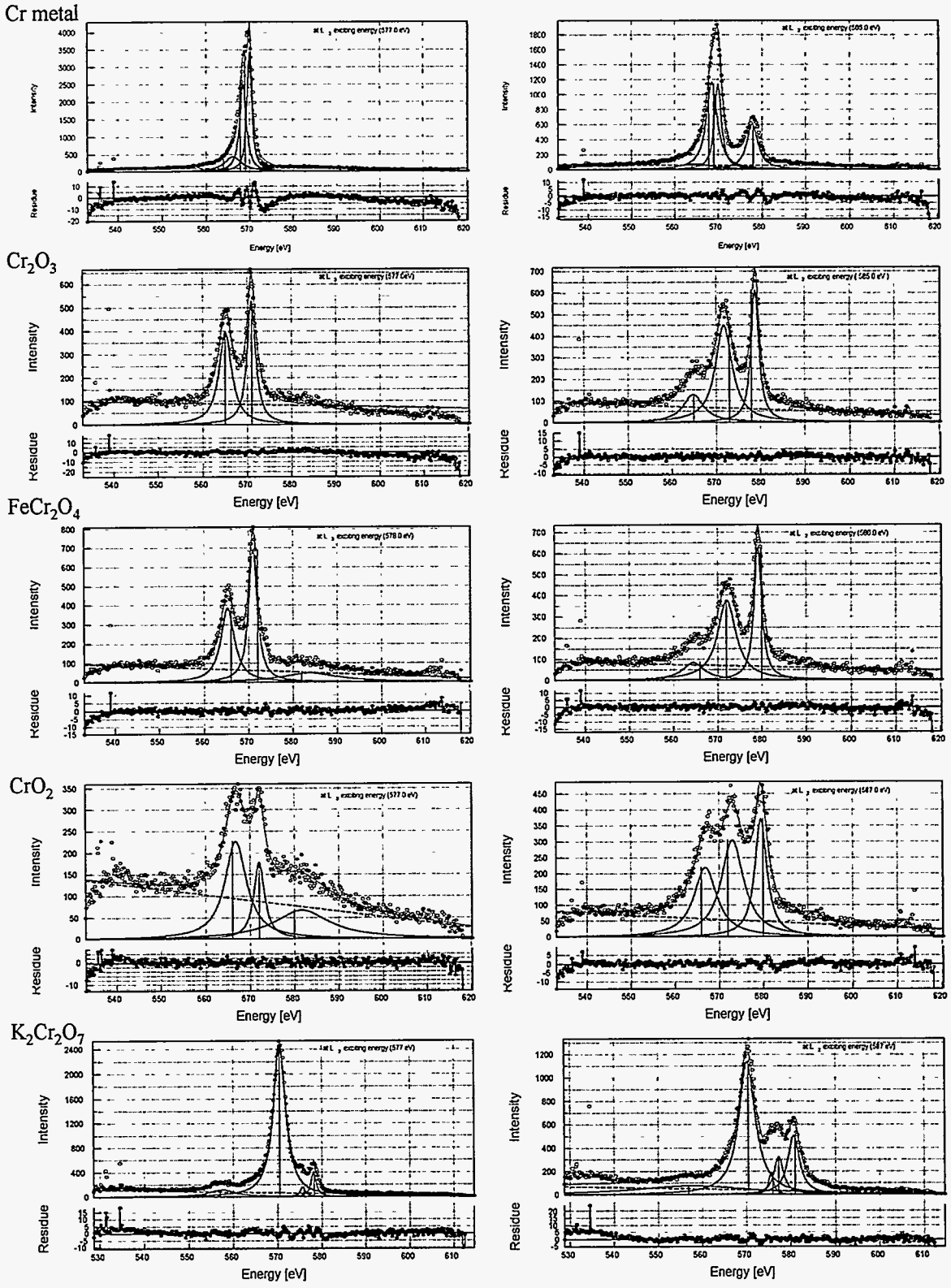

Figure 2 The Cr 2p x-ray fluorescence spectra in the Cr compounds at theshold energies

Evolution of Boron K Near Edge Structure in Ultra-Short Period W/B_4C Multilayers: Differences in Transmission and Photocurrent Measurements

C. C. Walton and J. B. Kortright
Materials Science Division
Ernest Orlando Lawrence Berkeley National Laboratory
Berkeley, California, 94720 USA

INTRODUCTION

In a larger study of the microstructure/performance relationships of ultra-thin W/B_4C multilayer x-ray interface structures,[1] we measured near-edge absorption spectra across the B K edge for multilayer periods ranging from 5-50 Å. Near-edge absorption measurements were chosen because of their potential sensitivity to changes in local bonding environment[2] that might shed light on questions concerning the changing extent of intermixing between the W- and B_4C-rich layers as a function of multilayer period. Absorption spectra were collected in both transmission and photocurrent modes for samples with a range of multilayer periods and for pure B_4C films. While subtle, systematic changes were observed between samples, very significant differences were observed between transmission and photocurrent data sets, which are clearly the result of bulk vs. surface sensitivity, respectively, of the different measurement techniques. These results thus have important implications for ALS experimenters whose goal is to study soft x-ray absorption features from the bulk of samples.

EXPERIMENT

The multilayers were deposited by conventional magnetron sputtering techniques at the Center for X-Ray Optics, LBNL, on Si_3N_4 membranes about 1500Å thick. The number of periods was adjusted for a constant overall thickness of the multilayer of another 1500Å, to give an absorption drop near $1/e$ at the B edge (188eV). Absolute transmission was measured by a GaAs photodiode behind the sample, and electron total yield (photocurrent) with a Keithley picoammeter attached to the samples, otherwise electrically isolated.

RESULTS

Absolute absorption measurements were normalized with the I_0 of the full incident beam, then plotted as $\mu \propto -ln(I/I_0)$ to show the edge as an increase in absorption. Both measurements were also normalized by the photocurrent from the beamline M3 mirror to remove the decay of the beam over time. The curves have been scaled to show the same change in height from 180eV to 220eV, and have been displaced vertically by arbitrary factors for comparison.

DISCUSSION

For both techniques, only subtle changes with multilayer period are observed. A π^* shoulder near 192eV is seen in all the curves and does not change much with period. The curves also show a broad σ^* feature near 200eV which shows a slight narrowing as the period decreases. The most distinct difference between any of the curves is the sharp peaks appearing for all samples in the photocurrent measurements, which are totally absent in the transmission measurements. Since the measurements were made during the same experiment the difference cannot be attributed to any change of the specimens over time. However, the two techniques are quite different in their surface sensitivity. The photocurrent measures only those electrons which escape the sample completely, so it is dependent on the energy distribution of the excited electrons and their proximity to the

surface. The energy distribution is complex, with contributions from photoelectrons and secondary and Auger electrons, but is dominated by a low-energy tail below 20eV. Since these electrons have escape depths from a few atomic diameters to 50Å, the photocurrent represents absorption by atoms very near the surface. By contrast the transmission measurement averages through the bulk of the specimen.

Similar photocurrent measurements by Jia[3] on a variety of metal borides show peaks at 193.9eV, very close to the peak at 193.8eV in this study. Results by Jia[3] on several other B compounds also show this peak, and it appears most strongly in a specimen of B_2O_3. Its presence in every scan suggests that surface oxidation of the specimens is responsible. A peak at 192.3eV in B compounds has been identified Chaiken and Terminello[4] as a quasi-bound π^* state consistent with an sp^2 bonding state of B, and is absent in the case of full sp^3 hybridization.

The absence of these sharp peaks in our transmission results suggests they result from a surface phase that is too thin to give a significant signal above the bulk. The multilayers are expected to contain a highly disordered bonding state of the B atoms, since they are amorphous sputtered layers of high-melting-point compounds that have strong chemical bonding and little mobility on the growing film surface. The sharp peaks in the photocurrent results are consistent with a better-defined chemical state, such as might be formed in an equilibrium process like surface oxidation. Based on the signal-to-noise ratio of the absorption measurement and the maximum contribution from the surface phase that would not appear above the noise, the thickness of the surface phase can be estimated as 50Å or less, consistent with the escape depth available to the electrons giving the sharp peaks in the TEY results.

In the transmission absorption results, several trends with d-spacing can be observed. A subtle pre-edge feature at 189eV (which can be elaborated in a derivative plot) becomes stronger with shorter multilayer period. The π^* feature at 192eV also becomes stronger with shorter period, measured as absolute height or relative to the post-edge jump height at 220eV. Third, the broad σ^* feature changes shape with decreasing period, from a broader, two-lobed shape similar to that in B_4C, at d = 30Å, to a narrower single-lobed shape at d = 6Å.

The stronger π^* feature is consistent with more unhybridized p-orbitals as the layers get thinner. Microstructural studies by HRTEM show that the thinner B_4C layers are more mixed with the adjacent W layers. Since W forms very stable borides and carbides it is reasonable to expect more bonding with W to introduce some d-character in the boron bonding environment, which would reduce the sp^3 hybridization in B_4C. This is also consistent with the σ^* feature evolving to a different shape from that found in B_4C. Further study including single films of WB and WB_2, the expected end products of increasing intermixing at the mole ratios present, would allow more a conclusive interpretation.

CONCLUSIONS

The transmission absorption spectra show changes consistent with a greater degree of intermixing with shorter multilayer period. Though the multilayers retain separate W-rich and B-rich phases even at the shortest periods, as demonstrated in other parts of this study,[1] the thinner layers and greater interface area in the thinner layers cause a closer average proximity of W and B atoms. These trends in the boron bonding can be observed with a relatively simple experiment, though a fuller set of standard specimens is needed for a more complete interpretation.

Distinct differences between boron K-edge absorption spectra taken by transmission or by photocurrent show that the high surface sensitivity of the photocurrent measurement can significantly distort the results, which should not be interpreted as representing the bulk without careful consideration of the sampling depth and possible surface contamination.

REFERENCES

1. C.C. Walton, "Ultra-Short-Period W/B_4C Multilayers for X-Ray Optics—Microstructure Limits on Reflectivity," Ph.D., University of California, 1997.
2. Joachim Stohr, *NEXAFS spectroscopy* (Springer-Verlag, Berlin New York, 1992).
3. J.J. Jia, J.H. Underwood, E.M. Gullikson *et al.*, "Soft X-ray absorption spectroscopy in 100-1000 eV region at the ALS," presented at the 11th International Conference on Vacuum Ultraviolet Radiation Physics, Tokyo, Japan, 1995 (unpublished).
4. A. Chaiken, L.J. Terminello, J. Wong *et al.*, "Electronic and atomic structure of metastable phases of boron nitride using core-level photoabsorption," Applied Physics Letters **63** (15), 2112-14 (1993).

Acknowledgments: This work was supported by the Director, Office of Energy Research, Office of Basic Energy Sciences, Materials Sciences Division, of the U.S. Department of Energy under Contract No. DE-AC03-76SF00098.

Author Affiliations:
contact author: CCW now at Advanced Microtechnology Program, L-395, Lawrence Livermore National Laboratory, Livermore, CA 94550 USA. e-mail walton9@llnl.gov, phone 510-423-2834.

PI when experiments were done: JBK at Materials Science Division, MS 2-100, Lawrence Berkeley National Laboratory, Berkeley, CA 94720. e-mail jbkortright@lbl.gov, phone 510-486-5960.

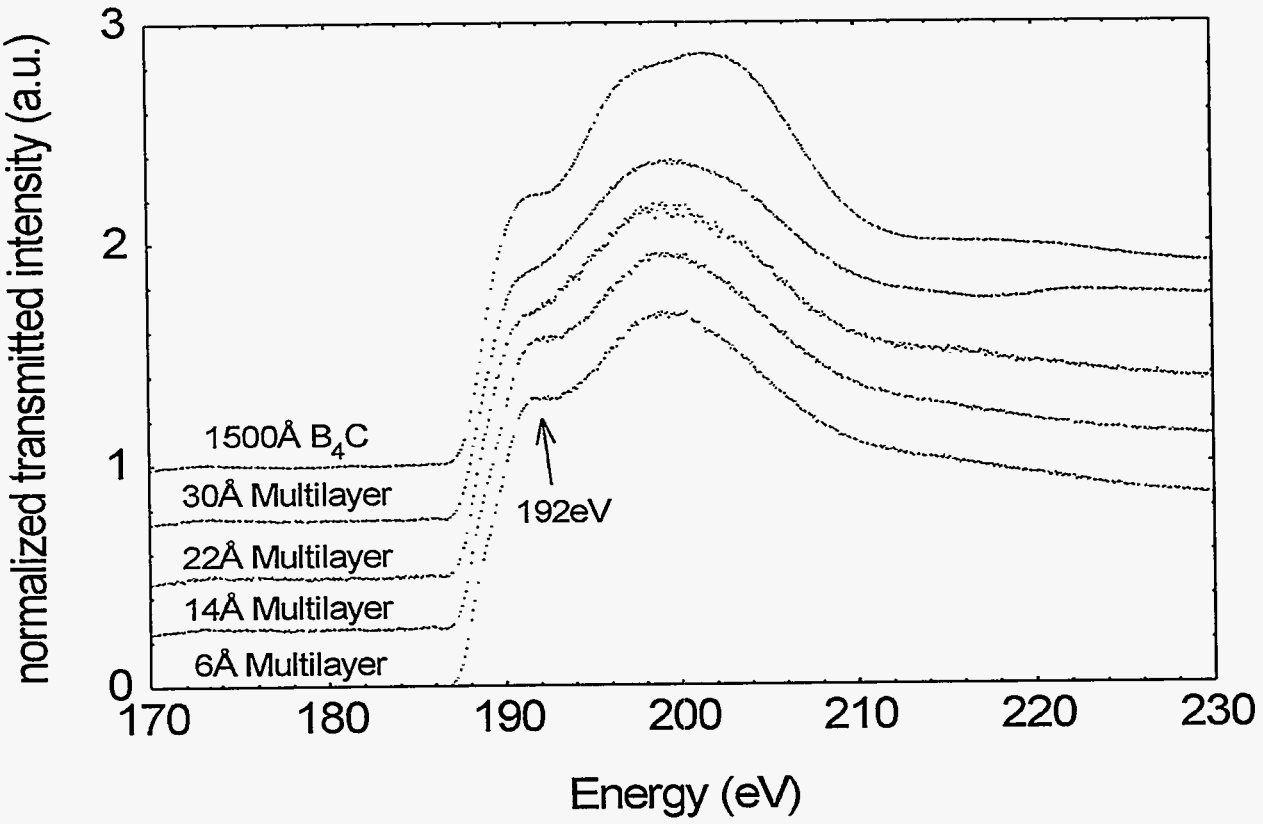

Fig. 1. Near-edge absorption spectra at the boron K edge (188eV)of four W/B_4C multilayers and of a single film of B_4C, measured in transmission. Note smooth curves near the edge, despite the high energy resolution of the measurement (< 0.1eV). Curves have been displaced vertically for comparison.

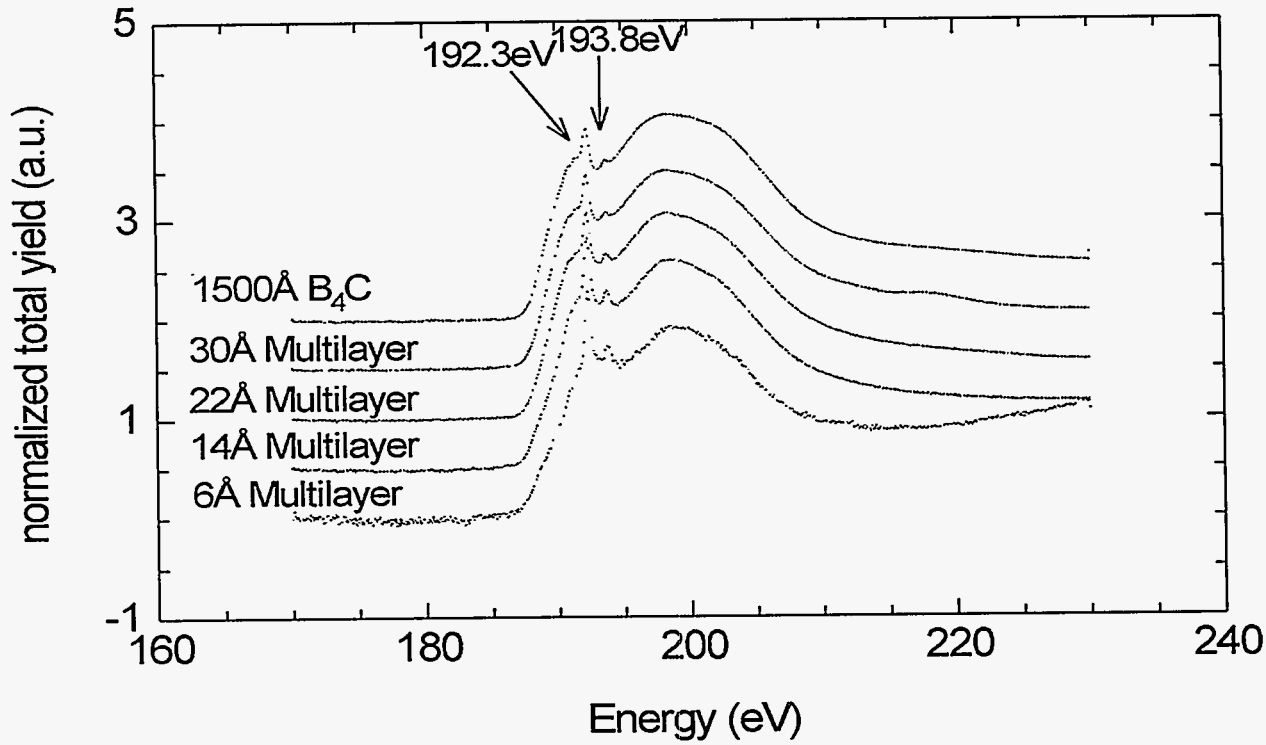

Fig. 2. Same spectra measured by photocurrent, taken in the same experiment as results above. Discrepancy in sharp peaks near the absorption edge underscores high surface sensitivity of the photocurrent measurements.

Ferromagnetic to Antiferromagnetic Transition in Fe_xCr_{1-x} Films with Composition: A Transmission MCD Study

J.B. Kortright and Sang-Koog Kim
Materials Sciences Division, Lawrence Berkeley National Laboratory
University of California, Berkeley, California 94720 USA

INTRODUCTION

The ability to study element-resolved magnetism using magnetic circular dichroism (MCD) and other soft x-ray magneto-optical techniques enables a variety of studies of both homogeneous and inhomogeneous magnetic thin film systems. The goal of this study is to better understand the transition from ferromagnetism to antiferromagnetism with composition in the Fe_xCr_{1-x} alloy system. This system is especially interesting for reasons both fundamental and practical. Ferromagnetic Fe and antiferromagnetic Cr both take the bcc crystal structure with less than one percent difference in lattice constant, so that the magnetic transition with X at first glance might be thought to involve purely electronic rather than structural effects. This system forms one boundary of the Slater-Pauling curve representing the evolution of magnetic moments with d electron concentration in 3d transition metal alloys, and has been a prototypical system for studying magnetic and structural correlations in alloys with neutron [1,2] and x-ray scattering [3] techniques. More recently, magnetic ordering of Cr monolayers on Fe has been much studied [4,5], as have Fe/Cr multilayer [6,7] and granular alloy [8] films for their magneto-resistive properties. Even with this extensive background on FeCr alloys and related systems, alloy thin films have not been the subject of systematic element-resolved MCD studies that should offer new insight into these systems.

Polycrystalline alloy films ranging from 55 - 75 nm thick were grown by magnetron co-deposition onto silicon nitride membrane substrates and capped with several nm of silicon carbide to prevent oxidation. Transmission MCD measurements were made with magnetization saturated in-plane and circular polarization from out-of-plane radiation on bending magnet beamlines 9.3.2 and 6.3.2. The use of transmission measurements stems from our interest to study the bulk of thin film specimens rather than their near-surface regions.

RESULTS AND DISCUSSION

Thickness effects in transmission x-ray absorption spectra in the vicinity of the sharp white lines manifest themselves as apparent reductions in absorption at white lines, or equivalently as enhanced transmission [9]. This results from unwanted spectral components in the incident beam that fall outside the fundamental energy resolution to enhance apparent transmission at the white line when transmission of the fundamental becomes comparable to that of the spectral impurities. Thickness effects become more problematic as the optical thickness of samples increases, and can be safely ignored only for samples which are optically thin at white line peaks. We made absorption measurements vs. film thickness in pure Fe films (having 1/e length of only 17 nm at the L_3 line) revealing significant thickness effects that varied with the grating used in the monochromator and hence from beamline to beamline. We attribute the thickness effects in the soft x-ray primarily to higher order contamination in the incident beam originating from the gratings. Since MCD signals are the difference of two white line intensities that are distorted differently by thickness effects, great care must be exercised in attempting to obtain quantitative MCD results (sum rules, etc.) from transmission spectra. Since not all samples studied here were optically thin at the Fe and Cr L_2 and L_3 edges, we do not attempt to quantify elemental moments based on these

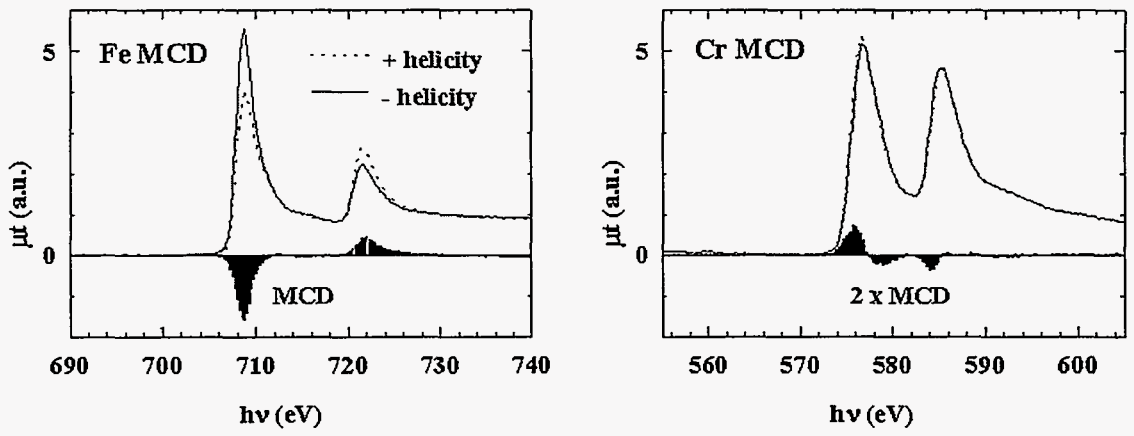

Figure 1. Transmission absorption spectra for a saturated $Fe_{0.85}Cr_{0.15}$ film taken with opposite helicity and the difference yielding the MCD are shown across the Fe (left) and Cr (right) $L_{2,3}$ edges. Cr has a net moment oriented opposite to that of Fe, and a very different spin polarization from that of Fe.

spectra. However, we do believe that the qualitative trends in elemental moments are generally correct. In the conclusions we indicate how we plan to avoid thickness effects in the future.

Absorption and MCD spectra for an alloy film with X = 0.85 are shown at the Fe and Cr $L_{2,3}$ edges in Figure 1. Absorption spectra taken with opposite helicity relative to the magnetization are each normalized to have edge jump of 1 and then subtracted to give the MCD signal. The Fe results are typical of elemental Fe, with strong MCD peaks of opposite signs at the L_3 and L_2 peaks. The Cr MCD spectrum is very different from that of Fe, with a bipolar feature at the L_3 edge and a weaker feature of opposite sign at the L_2 edge. The different shapes of the Fe and Cr MCD are qualitatively understood by realizing that Cr has a lower d-band occupancy than Fe of roughly 2 electrons, and Fe has a roughly half-filled d band. The strong exchange splitting in Fe results in nearly complete spin-polarization characterized by a nearly full spin up (majority) band and nearly empty spin down (minority) band. The absorption is dominated by transitions into the minority band. The spin polarization in Cr is very different from Fe, and can be interpreted as containing empty states of both spins with different energy dependencies. The striking differences between Fe and Cr MCD spectra reveal that a theoretical description in terms of a single spin-polarized band structure describing both Fe and Cr spin polarizations is not possible.

Just the MCD spectra at both the Fe and Cr $L_{2,3}$ edges are shown in Figure 2, and reveal three distinct magnetization regions as a function of composition. In the region from pure Fe to roughly X = 0.58 Fe retains its distinct MCD spectrum. The apparent increase in Fe MCD intensity may indicate a real increase in Fe moment, or may be the result of thickness effects.

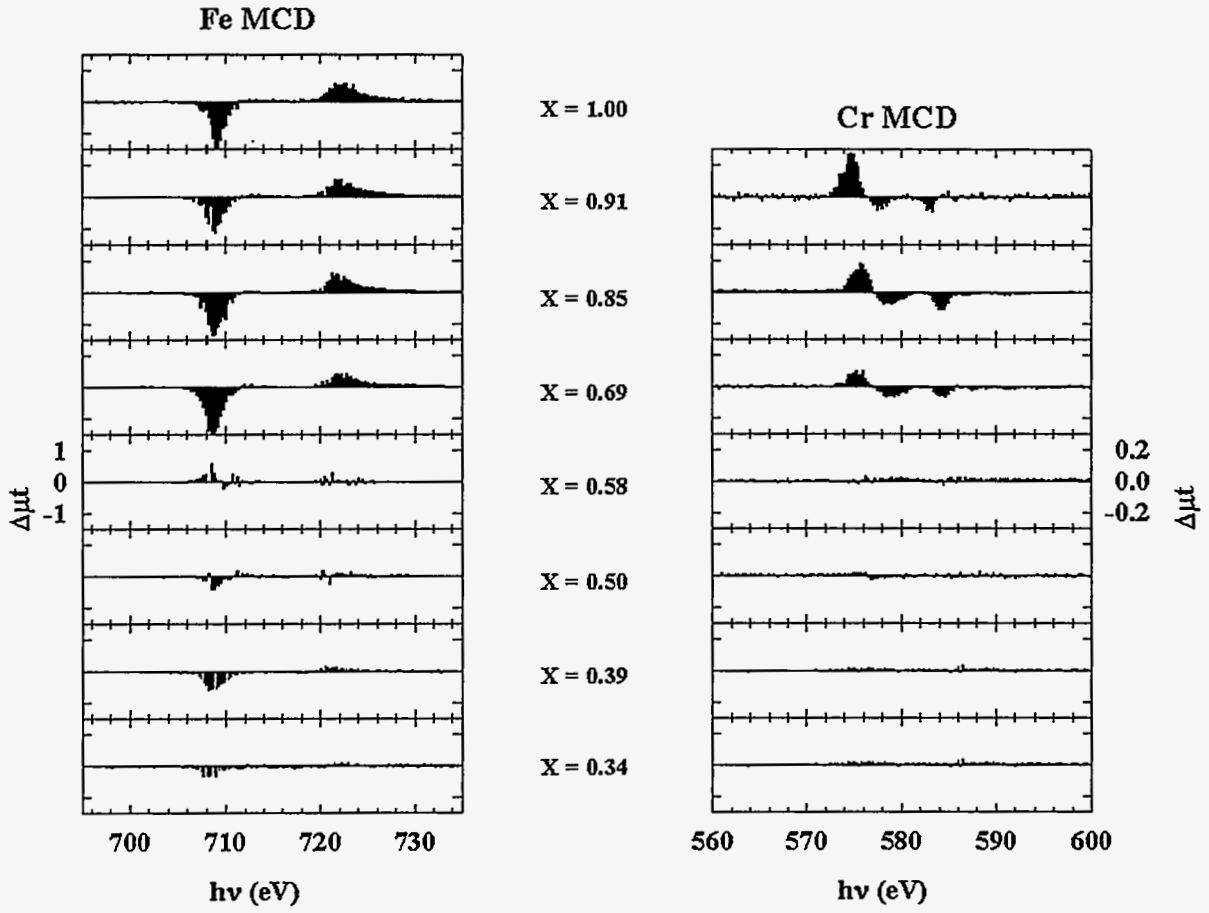

Figure 2. Fe (left) and Cr (right) MCD spectra for a range of alloy compositions reveal three distinct ranges of magnetization as discussed in the text.

The Cr MCD spectra in this range resembles that in Figure 1 but with decreasing intensity as Cr content increases. Evidently at the lowest Cr concentrations Cr atoms have predominantly Fe neighbors, and order ferrimagnetically with respect to the Fe. As more Cr is added in this range, the decreasing Cr moment can be interpreted assuming that Cr is segregating. In this case Cr atoms adjacent to Fe will tend to have moments opposite to those of Fe, while Cr atoms adjacent to Cr in clusters will order antiferromagnetically with respect to the adjacent Cr, resulting in a decrease in net Cr moment. Such a chemical short range order inversion in bulk FeCr alloys has been reported based on neutron scattering [2].

The second region is from $0.58 > X > 0.50$, in which neither Fe or Cr exhibit a significant moment. This composition range corresponds closely to that of a slow-forming σ phase in the equilibrium phase diagram for bulk alloys, although this phase has never been reported in thin films. X-ray diffraction results of films in this region reveal a shift in the 110 Bragg peak to higher angles, indicating a structural distortion characterized by an increased interatomic spacing accompanies the loss of magnetism in this composition range. This may be evidence of incipient σ phase formation, and at least indicates a strong link between structure and magnetism in this system, possibly related in to the invar transition in other binary transition metal alloys. Further experiments will determine if the films in this intermediate composition range are paramagnetic or possibly antiferromagnetic with Fe and Cr sharing the two sublattices.

The third region comprises the Cr-rich samples, and shows the re-emergence of an Fe moment that then disappears with increasing Cr content and no clear Cr moment. This behavior can be interpreted as representing a ferrimagnetic arrangement in which the Fe moments ultimately vanish as the antiferromagnetism of Cr dominates the magnetic behavior.

CONCLUSIONS

This transmission MCD study of Fe_xCr_{1-x} alloys reveals qualitative changes in magnteism with composition that are similar to but somewhat different than those reported in bulk alloys. The element-resolved sensitivity of the x-ray techniques provides information in all three composition ranges that is not possible by most techniques, and the L edge spectroscopies provide very direct information on the changing average spin polarization around Fe and Cr atoms with composition. The evident thickness effect that precludes determination of absolute moments and their resolution into spin and orbital moments for these transmission measurements will be overcome by future measurements of the Faraday rotation spectra, which are free from thickness effects and can also yield the moment information via Kramers-Kronig transformation analysis [10]. Several other studies using soft x-rays suggest themselves based on these early results, including a diffuse scattering study of the alloy films especially in the Fe-rich region where chemical segregation is suspected. Tuning to the Fe and Cr edges will significantly enhance diffuse small angle scattering [11] from such segregation if it exists.

REFERENCES

1. C.G. Shull and M.G. Wilkinson, Phys. Rev. **97**, 304 (1955).
2. I. Mirebeau, M. Hennion and G. Parette, Phys. Rev. Lett. **53**, 687 (1984).
3. L. Reinhard, J.L. Robertosn, S.C. Moss, G.E. Ice, P. Zschack and C.J. Sparks, Phys. Rev. B **45**, 2662 (1992).
4. L.E. Klebanoff, S.W. Robey, G. Liu, and D.A. Shirley, Phys. Rev. B **30**, 1048 (1984).
5. A. Davies, J.A. Stroscio, D.T. Pierce, and R.J. Celotta, Phys. Rev. Lett. **76**, 4175 (1996).
6. S.S.P. Parkin, N. More and K.P. Roche, Phys. Rev. Lett. **64**, 2304 (1990).
7. E.E. Fullerton, S.D. Bader and J.L. Robertson, Phys. Rev. Lett. **77**, 1382 (1996).
8. K. Takanashi, T. Sugawara, K. Hono and H. Fujimori, J. Appl. Phys. **76,** 6790 (1994).
9. L.G. Parratt, C.F. Hempstead, and E.L. Jossem, Phys. Rev. **105**, 1228 (1957).
10. J.B. Kortright, M. Rice and R. Carr, Phys. Rev. B **51**, 10240 (1995).
11. Walton and J.B. Kortright, this compendium, and C.C. Walton, Ph.D. Thesis U.C. Berkeley and LBNL Report LBNL-41425 (December, 1997).

Data were collected on bending magnet beamlines 9.3.2 and 6.3.2. We thank M. LeGros and S. Cramer for use of equipment. This work was supported by the Director, Office of Energy Research, Office of Basic Energy Sciences, Division of Materials Sciences, of the U.S. Department of Energy under Contract No. DE-AC03-76SF00098.

Principal Investigator: Jeffrey Kortright, Materials Sciences Division, Lawrence Berkeley National Laboratory, Email:jbkortright@lbl.gov, Telephone: 510-486-5960.

Generation and characterization of femtosecond x-ray pulses

R.W. Schoenlein,[2] T.E. Glover,[2] P.A. Heimann,[1] A.A. Zholents,[3] and M.S. Zolotorev[3]

[1]Advanced Light Source, Accelerator and Fusion Research Division, Lawrence Berkeley National
[2]Materials Sciences Division, Lawrence Berkeley National Laboratory, Berkeley, CA 94720
[3]Center for Beam Physics, Accelerator and Fusion Research Division, Lawrence Berkeley National Laboratory, Berkeley, CA 94720

Applying powerful x-ray techniques such as EXAFS and XANES on a femtosecond time scale will enable one to directly probe the atomic motion associated with phase transitions, coherent vibrational motion and ultrafast chemical reactions. However, the current temporal resolution of synchrotron sources is several orders of magnitudes lower than the fundamental time scale for atomic motion, which is on the order of one vibrational period (~100 fs). We are developing a technique to generate ~200 fs x-ray pulses using synchrotron radiation from a bending magnet of the ALS.

The duration of ALS x-ray pulses (~30 ps) can be reduced by more than two orders of magnitude by selecting radiation which originates from only a thin (~100 fs) temporal slice of an electron bunch. [1] Such a slice can be created through the interaction of a femtosecond laser pulse co-propagating with an electron bunch in an appropriate wiggler (Figure 1a). The high electric field present in the femtosecond laser pulse produces an energy modulation in the electrons as they traverse the wiggler. The accelerated and decelerated electrons are then spatially separated from the rest of the electron bunch in a dispersive section (bend magnet) of the storage ring which follows the wiggler (Figure 1b). Finally, by imaging the displaced beam slice to the experimental area, and by placing an aperture radially offset from the focus of the beam core, we will be able to separate out the radiation from the offset electrons (Figure 1c). Since the spatially offset electrons result

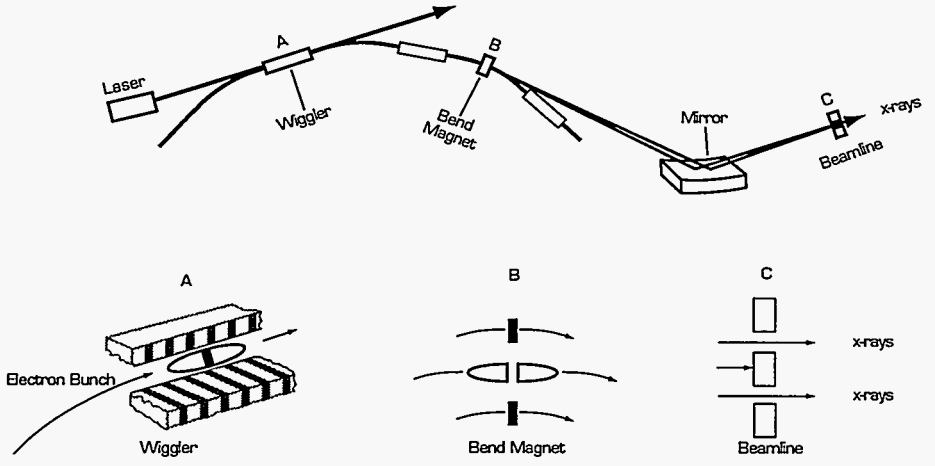

Figure 1. Schematic illustration of the technique for generating femtosecond pulses of synchrotron radiation.

from interaction with the laser pulse, the duration of the synchrotron radiation produced by these electrons will be approximately the same as the duration of the laser pulse, and will be absolutely synchronized.

The necessary components of the femtosecond x-ray source are installed at the ALS. A Ti : sapphire laser system generates 800 nm radiation with ~ 50 fs pulse duration and 2 kHz repetition rate. The femtosecond laser pulses co-propagate with electron bunches through the wiggler W16 in sector 5. The laser beam is injected into the ALS vacuum chamber through a window on the back-tangent port. After passing along the straight, the laser light (as well as the wiggler radiation) is deflected by water-cooled mirrors toward diagnostics, which monitor the spatial and temporal overlap of the laser and electron beams. X-rays are produced by bend magnet 6.3 and imaged by beamline 6.3.2.

The interaction of the laser field with the electrons can be observed in two ways. The electron bunch heated by the laser shows an increase in the spatial wings because of the increased energy spread. In the horizontal focus of the x-rays at beamline 6.3.2, a 10 % intensity increase was measured at a position 300 - 500 μm horizontally offset from the optical axis. The magnitude of this effect is less than the predictions of calculations and further improvement is required in matching the mode of the laser operating at a high average power and the spontaneous radiation from the electrons in the wiggler. Secondly, the laser field is amplified as a result of the free electron laser process in the wiggler. This gain was observed in a preliminary measurement at low laser power. The size of this effect was in a good agreement with predictions (see Figure 2).

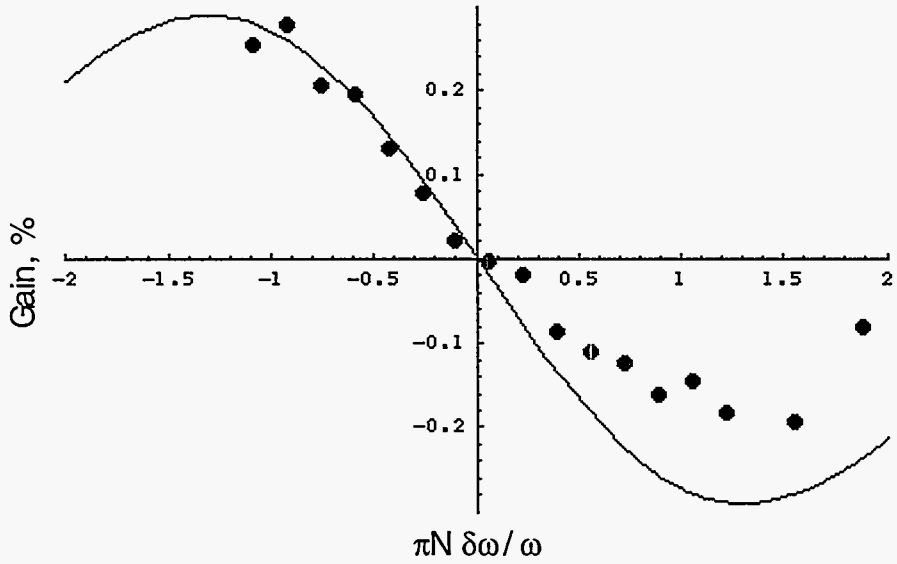

Figure 2. FEL gain measured at the beam line 5.0. Solid line is a theoretical prediction. Dots show data points. N=19 is the number of wiggler periods and $\delta\omega/\omega$ is wiggler detuning with respect to the laser frequency.

Methods are being developed to measure the duration of the femtosecond x-ray pulses created by slicing technique. Using the visible synchrotron radiation, a cross-correlation can be performed with 100 fs laser pulses in a non-linear crystal. To date, the synchrotron radiation pulse has been measured in the absence of laser-electron beam interaction. In addition, a gating detector is under construction to determine the duration of the x-ray pulse directly. This detector is based on laser-assisted photoemission, which has been demonstrated with high laser harmonics at 320 Å wavelength. [2]

REFERENCES

1. A. A. Zholents and M. S. Zolotorev, Phys. Rev. Lett. **76**, 916 (1996).
2. T. E. Glover, R. W. Schoenlein, A. H. Chin, and C.V. Shank, Phys. Rev. Lett. **76**, 2468 (1996).

This work was supported by the Director, Office of Energy Research, Office of Basic Energy Sciences, Materials Science Division, of the Department of Energy under Contract No. DE-AC03-76SF00098.

Principal investigator: Robert Schoenlein, Lawrence Berkeley National Laboratory. Email: rwschoenlein@lbl.gov.

Iridium Reflectivity Calibrations in the Region 50-1100 eV for the AXAF Telescope Mirror

D.E. Graessle[1], R.L. Blake[1], A.J. Burek[1], J.J. Fitch[1], E.M. Gullikson[2], R. Soufli[1] and A. Stonas[3],
[1] Smithsonian Astrophysical Observatory,
60 Garden Street, Cambridge, Massachussets 02138, USA
[2] Center for X-ray Optics, Ernest Orlando Lawrence Berkeley National Laboratory,
University of California, Berkeley, California 94720, USA
[3] Oxford Research Group,
5737 Clinton Avenue, Richmond, California 94805, USA

INTRODUCTION

In December 1998 NASA will launch the Advanced X-ray Astrophysics Facility (AXAF) into earth orbit for the next generation studies of radiation from cosmic x-ray sources, in the energy range 0.1-10 keV. For the past seven years our team at the Smithsonian Astrophysical Observatory has been conducting a program to calibrate the reflectivity of the x-ray telescope mirrors, so that the observed intensities may be converted to an absolute scale required for quantitative scientific analysis. The program has been carried out on synchrotron beamlines, where witness flats, coated simultaneously with the telescope mirrors, are measured for reflectivity as a function of energy and angle of incidence over the range of energies and angles that are applicable to the telescope in orbital observations . In July 1996 we obtained our first beamtime at the ALS beamline 6.3.2, which allows us to calibrate the mirrors over the range 50-1100 eV that is not available to us elsewhere. Beamline 6.3.2 not only covers the needed energy range, but also has a reflectometer built into the end position . It was sufficient to make a revised sample holder for our AXAF mirror samples and to adapt a foil holder for transmission samples that we use to augment the determination of optical constants. Witness flats (samples) consist of glass optical substrates that have been coated with about 100 Å of Cr and 330 Å of Ir - the reflecting surface for the telescope. During the coating process, these flats were located either along the locus of the AXAF mirror element surface (qualification coating runs), or just off the ends of the AXAF mirrors (production coating runs). Since the curved telescope mirrors will have some figure errors and roughness variations over their surfaces, both of which cause differences in reflectivity, it is necessary to determine the optical constants of the Ir coatings from the calibration data and subsequently derive the AXAF mirror efficiency by a complex modeling process. We report here the results of our third run on beamline 6.3.2, in July 1997.

MEASUREMENTS

Two types of measurements are required to completely characterize each witness sample. First, one measures the reflectivity versus angle at some energy where the beam can penetrate deeply enough into the Ir-Cr layers to make the reflectivity sensitive to the layer thicknesses. Then, the reflectivity versus angle shows interference oscillations at large grazing angles. The Fresnel equation, which gives the reflectivity versus angle from electromagnetic theory, may then be used to adjust the Ir and Cr layer thicknesses until the measured oscillations best match the calculated ones. Simulations showed that the best sensitivity is at the higher energies on this beamline. Fig. 1 (left) shows measured data for a particular sample. One can see that the oscillations at reflectivities below 1% have a distinctive pattern. The details of this pattern determine the Ir and Cr layer thicknesses, while the average amplitude versus angle determines the sample roughness. The second type of measurement required is the reflectivity versus angle, at closely spaced energies over the entire range of operation of the mirrors. This permits application of the Fresnel equation at each energy to derive the Ir optical constants from fits to the data. The reflectivity varies strongly with energy, especially in the vicinity of x-ray absorption edges. Furthermore, the

AXAF mirror elements have one of four fixed grazing angles, each less than one degree. It is therefore more relevant to measure the reflectivity versus energy at selected angles. From earlier runs we have been able to determine an optimum choice of angles for each energy sub-range between 50 and 1400 eV. We try to achieve an approximately uniform distribution of steps in reflectivity between 10% and 100% by choice of angles in each energy sub-range. Therefore, the angles may not be the same from one sub-range to the next. Table 1 lists the angles and the optimized beamline parameters for each sub-range.

Energy Range (eV)	Grating (lines/ mm)	Order Sorter (mirror, angle in deg)	Filter	Grazing Sample Angles (deg)	# of energy steps
50-72	300	C, 10	Al	0.864, 3, 6, 11, 15, 19, 23, 27, 35	88
66-100	300	C, 14	Si	0.864, 3, 6, 11, 15, 19, 23, 27, 35	68
94-112	300	C, 8	Be	0.864, 3, 6, 11, 15, 19, 23, 27, 35	36
107-187	300	C, 6	B	0.864, 1.5, 2.5, 4, 6, 9, 12, 15, 20	40
181-285	600	Ni, 8	C	0.696, 1.33, 2, 3, 4, 5, 6, 7.5, 9, 12	52
260-454	600	Ni, 6	Ti	0.614, 0.864, 1.33, 2.2, 3, 3.8, 4.5, 6, 7.5, 9, 10.5	194
440-574	1200	Ni, 6	Cr	0.614, 0.864, 1.33, 2, 2.7, 3.4, 4.2, 5.2, 6.5, 8	134
558-778	1200	none	Co	0.614, 0.864, 1.33, 2, 2.7, 3.4, 4.2, 5.2, 6, 7	220
752-932	1200	none	Cu	0.614, 1, 2, 2.7, 3.4, 4.1, 4.8, 5.6, 6.3	90
900-1400	1200	none	none	0.614, 1, 2, 2.7, 3.4, 4.1, 4.8, 5.6, 6.3	50

Table 1. Measurement parameters for the Ir mirror calibrations at the ALS beamline 6.3.2. The monochromator grating chosen for each energy region is indicated in the 2nd column. A filter (4th column) is used in order to block second harmonic wavelengths and scattered light from the monochromator; in upcoming measurements, a Mg filter will be used for the energy range 900-1300 eV. Furthermore, a triple-reflection low-pass filter (order sorter, 3rd column) is used for suppression of higher harmonics.

TENTATIVE RESULTS

Partial results for a particular sample are shown in Fig. 1 (right) for the lowest four energy sub-ranges and part of the fifth. A measure of beam purity and freedom from systematic errors is the overlap of reflectivities between segments for different sub-ranges. From Table 1 the grazing angle of 6° is seen to be common to all five of the energy subranges plotted in Fig. 1 (right). The overlaps are within the data noise. Of special interest is the region from 50 to 72 eV, where one can see the well defined profiles of the Ir N_{VII} and N_{VI} absorption edges in the reflectivity. Fine scans reveal the convolved presence of the Ir O_{II} edge between the N_{VII} and N_{VI} edges. The amplitude of reflectivity jumps across Ir absorption edges is important because the calibrations can be done in lower resolution, with higher signal to noise ratio, when the jumps are less than 1%. We have the following preliminary results from the data obtained thus far:

(i) Ir N_{VII} and N_{VI} edges are well observed with large jumps. High resolution scans are required in this energy region.

(ii) N_V and N_{IV} edges (296.3 and 311.9 eV) are in the vicinity of the C K edge (284.2 eV); the presence of carbon contamination on the witness flats makes it necessary to utilize special procedures for studies in this energy region.

(iii) N_{III}, N_{II} is a well defined doublet feature requiring fine scans in the region 480-520 eV. Especially the range 440-574 eV requires high resolution due to the Cr underlayer and the presence of oxygen contamination on the samples.

(iv) N_{II}, N_I, and O_{II} edge regions have reflectivity jumps of less than 1%, thus they may be

scanned in a low resolution mode.
(v) The ranges 94-112, 107-187, 181-285, 752-932, and 900-1400 eV may be scanned with lower resolution and improved signal to noise ratio in future runs.
(vi) Both angle scans at 925 eV and energy scans 558-778 eV may be used in the future to evaluate the Cr and Ir layer thicknesses and simultaneously improve the optical constants of these two elements in the low energy range, especially around the Cr L_{III}, L_{II} edge.

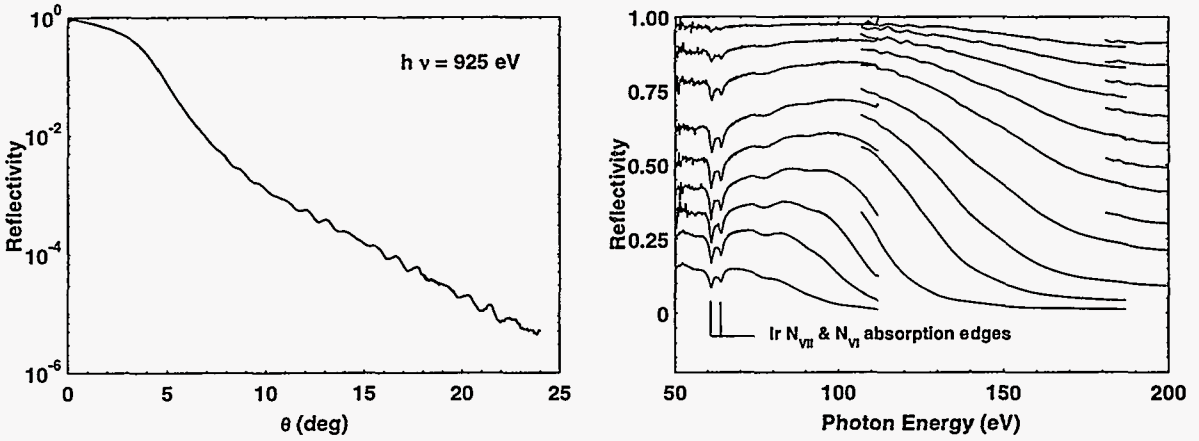

Figure 1. Left: Reflectivity data (shown on a logarithmic axis) versus grazing angle θ (in degrees), from one of the AXAF witness mirrors. This type of measurement aids in the determination of the Cr and Ir layer thicknesses on the mirror. Right: Reflectivity data versus energy at selected angles (see Table 1). Data obtained in five energy sub-ranges within the region 50-200 eV, are shown in this plot. After converting the above data to reflectivity versus angle at each energy point, the optical constants δ, β of the refractive index $n = 1 - \delta + i\beta$ of Ir are derived by means of least-squares curve fitting. Angles in each energy sub-range are selected so as to give a uniform sampling for the curve fitting.

ACKNOWLEDGEMENTS

We thank Jim Underwood for arranging initial beamtime at 6.3.2 to get this program started and for continuing to upgrade the beamline. Thanks to John Cobuzzi and John Bowers for technical assistance. Stan Mrowka was especially generous in his efforts to keep the computers updated and to implement new beamline electrometers.

REFERENCES

1. D. E. Graessle, A. J. Burek, J. J. Fitch, B. Harris, D. A. Schwartz, and R. L. Blake, in *Grazing Incidence and Multilayer X-Ray Optical Systems*, edited by R. B. Hoover and A. B. C. Walker II, (Proceedings of SPIE Vol. 3113, San Diego, CA, 1997), pp. 52-64.
2. J. H. Underwood, E. M. Gullikson, M. Koike, P. J. Batson, P. E. Denham, K. D. Franck, R. E. Tackaberry, and W. F. Steele, Rev. Sci. Instrum. **67**, available in CD ROM only.

This work was supported by the US D.O.E. and by NASA under contract number NAS8-40224.

Principal Investigator: Dale E. Graessle, Smithsonian Astrophysical Observatory, 60 Garden Str., Cambridge, MA 02138. Email: graessle@head-cfa.harvard.edu. Telephone: 617-495-7041.

Optical constants of ferromagnetic iron at the 2p resonances

Maurizio Sacchi [1], Coryn Hague [1,2], Stan Mrowka [3], Eric Gullikson [3], James Underwood [3]

[1] LURE, Bât. 209d, Centre Universitaire Paris-Sud, 91405 Orsay (France)
[2] Laboratoire de Chimie Physique - Matière et Rayonnement, 11, rue P. et M. Curie, 75231 Paris (France)
[3] Center for X-ray Optics, Materials Sciences Division, Lawrence Berkeley Laboratory, Berkeley CA 94720

The energy dependence of optical constants at resonance represents a priviledged standpoint for comparing theory and experiment in terms of structural, electronic and magnetic properties of materials. In the X-ray range, this comparison is usually performed only over the imaginary part β of the complex refractive index $n = 1 - \delta - i\,\beta$, i.e. over the absorption. For decades, extended or near edge X-ray absorption spectra served as a reference for refining parametrized models of the local structure and of chemical environment. Over the last ten years the use of polarized x-rays has widened this field to include the study of anisotropic systems, and in particular of magnetic materials [1]. Model calculations, on the other hand, may deal with both the real and imaginary parts of the index at resonance. The real part is seldom exploited, due to a lack of experimental data, even if it contains as much information as the latter. It has even been shown that the interference between the two (as in resonant reflectivity) can facilitate the investigation of spectroscopy features, like satellites, that are weak but of major importance for understanding some ground state properties [2]. X-ray magneto-optics effects, related to the off-diagonal terms of the dielectric tensor, are stronger when the core excitations produce transitions to a final state that directly involves the "magnetic" orbitals, e.g. 3d for the transition metals of the first row or 4f for rare-earths. The largest cross-sections are observed for dipolar transitions, which implies that the most interesting resonances for studying magneto-optics effects (2p,3p -> 3d or 3d,4d -> 4f) are all located in the soft x-ray range. Most of the few direct experimental determinations of δ at resonance (i.e. without using Kramers-Kronig relations) have been performed on crystals by measuring the Bragg peak displacement when the photon energy is scanned through an absorption edge. The Bragg law imposes the relation between the photon wavelength λ and the crystal spacing 2d, hence, in order to match the 2d values for typical crystals (a few A), x-ray resonant magnetic scattering (XRMS) has been performed mainly at high energy. Recently, XRMS experiments have been performed with soft x-rays [3] using metallic multilayers as artificial periodic structures of adequate 2d spacing. We have determined the real part δ of the index of Fe across its 2p resonances by analysing the Bragg diffraction from an epitaxially grown Fe/V superlattice (2d = 30.6 A) prepared by sputter deposition of the metallic layers on an MgO (001) crystal [4]. We have compared our results to the only previous direct determination of δ obtained by measuring the Faraday rotation of x-rays transmitted by ferromagnetic iron [5]. X-ray scattering and absorption measurements were performed on the reflectometer of the soft x-ray metrology beamline 6.3.2 at ALS (Berkeley) [6]. We used the radiation emitted by a bending magnet between 110 and 200 μrad above the orbit plane, which gives elliptically polarized photons with a circular polarization rate of 40 % over the energy range 650-780 eV. The sample was magnetized parallel to its surface and in the scattering plane by means of a permanent magnet located behind the sample holder and mounted on a stepper motor used to reverse the field direction. Absorption spectra, recorded by measuring the photocurrent on the sample, were scaled to the non resonant values at 650 and 780 eV to give the imaginary part of the index $\beta^{\pm}$, where + and - signs refer to opposite magnetization/helicity orientations. Resonant

scattering spectra are reported in Fig.1(a,b) as a function of θ and photon energy, for the two magnetization/helicity orientations. These are raw data, simply normalized to the incoming photon flux. Fig.1c shows the difference between the curves in a) and b). The decrement to the real part of the index, $\delta^{\pm}$, is obtained from the Bragg peak displacement versus energy following the model of Rosenbluth and Lee [7]. The four real functions ($\beta^{\pm}$ and $\delta^{\pm}$) allow to determine the helicity dependent refractive index $n^{\pm}$ for ferromagnetic iron at the 2p resonances in a strictly experimental way. The diagonal elements of the dielectric tensor are then given by $1/2[(n^{+})^2 + (n^{-})^2]$, and the off diagonal elements by $\pm i/2[(n^{+})^2 - (n^{-})^2]$. We consider that the experimental determination of the dielectric tensor including its off-diagonal elements is an important step towards a better refinement of theoretical and calculational models that describe the electronic and magnetic ground state properties of materials. To this end, it is essential to develop several independent experimental methods in addition to the standard Kramers-Kronig approach. Polarization rotation (upon transmission or reflection), interferometry and resonant magnetic scattering together constitute a sound basis for future work.

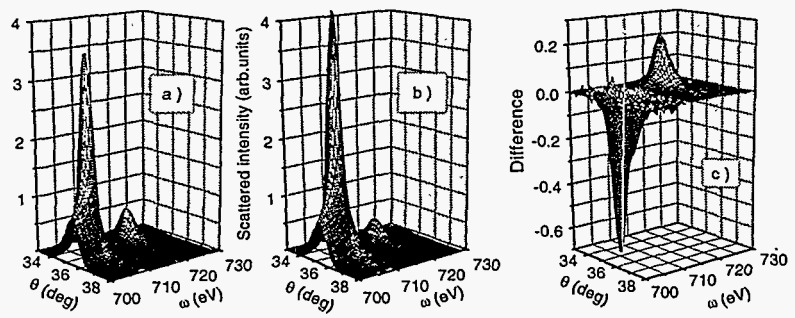

Fig.1. θ/2θ scans at various photon energies (2p edges of Fe) for parallel (a) and antiparallel (b) magnetization/helicity orientations. Panel (c) reports the corresponding difference curves.

REFERENCES

1. see e.g. N.Mainkar, D.A.Browne and J.Callaway, Phys.Rev.B53, 3692 (1996)
2. C.C.Kao et al., Phys.Rev.Lett. 65, 373 (1990); M.Sacchi and A.Mirone, Phys.Rev.B57(1998)
3. J.-M.Tonnerre et al., Phys.Rev.Lett. 75, 740 (1995); M.Sacchi, C.F.Hague, E.M.Gullikson and J.H.Underwood, Phys.Rev.B57, 108 (1998)
4. P.Isberg et al., Vacuum 48, 483 (1997)
5. J.B.Kortright, M.Rice and R.Carr, Phys.Rev.B51, 10240 (1995)
6. J.H.Underwood et al., Rev.Sci.Instrum. (1997)
7. A.E.Rosenbluth and P.Lee, Appl.Phys.Lett. 40, 466 (1982)

This work was supported by the Centre National de la Recherche Scientifique (France) and by Istituto Nazionale per la Fisica della Materia (Italy)

Principal investigator: Maurizio Sacchi, Laboratoire pour l'Utilisation du Rayonnement Electromagnétique, Centre Universitaire Paris-Sud, 91405 Orsay (France)
tel. -33-1-64468089; fax -33-1-64464148; email: sacchi@lure.u-psud.fr

Oxygen K Edge Total Electron Yield Spectra

M. Uda[1,2], T. Yamamoto[1], H. Osawa[2], T. Tatebayashi[2], A. Kanai[2], H. Wakita[3], K. Taniguchi[4], J. H. Underwood[5] and R. C. C. Perera[5]
[1]Laboratory for Materials Science and Technology, Waseda University, Nishiwaseda, Shinjuku-ku, Tokyo 169, Japan
[2]Department of Materials Science and Engineering, Waseda University, Ohkubo, Shinjuku-ku, Tokyo 169, Japan
[3]Department of Chemistry, Fukuoka University, Nanakuma, Jonan-ku, Fukuoka 814-01, Japan
[4]Osaka Electro Communication University, Hatsucho, Neyagawa, Osaka 572, Japan
[5]Center for X-ray Optics Lawrence Berkeley National Laboratory, Berkeley, California 94720, USA

INTRODUCTION

X-ray transmission measurements give in general important information on chemical bonding or chemical reactivity because unoccupied molecular orbitals localized above valence bonds are characteristic of chemical species. If the number of emitted secondary electrons is proportional to the number of electron holes produced by incident X-rays, or the fluorescence X-ray is dominant in decay processes of the holes, the total electron yield (TEY) or fluorescence yield (FY) is a good measure of X-ray absorption. Then the transmission measurements are frequently replaced by TEY or FY experiments[1] due to simplicity of the latters. K edge absorption spectra obtained from light elements such as B, C, N, O and F are expected to have characteristic shapes of chemical compounds if chemical environments of the atoms of interest are different. In this investigation a series of oxides are studied to clarify their electronic structures experimentally and theoretically.

EXPERIMENTAL RESULTS

Experiments were carried out at ALS beamline 6.3.2. TEY spectra were recorded using pulverized specimens embedded in In foil. Surface of In was in general covered with its oxide and then gave a TEY spectrum, as shown in Fig. 1. Thickness of the specimens was chosen to be thick enough to avoid contamination of TEY from In foil, but to be thin enough to prevent surface charging of the specimen. Examples of TEY are shown in Fig. 2, which are characterized by easily distinguishable shapes even for the same metal oxides if valence states of the metal are different (PbO and PbO_2), and even for the same valence states if species of cations are different (Cr_2O_3 and Fe_2O_3). Such dramatic charge in spectral shapes is expected to be explained by the molecular orbital theory.

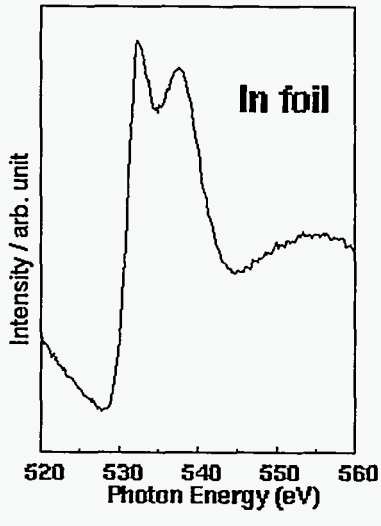

Fig. 1. TEY of In foil covered with its oxide

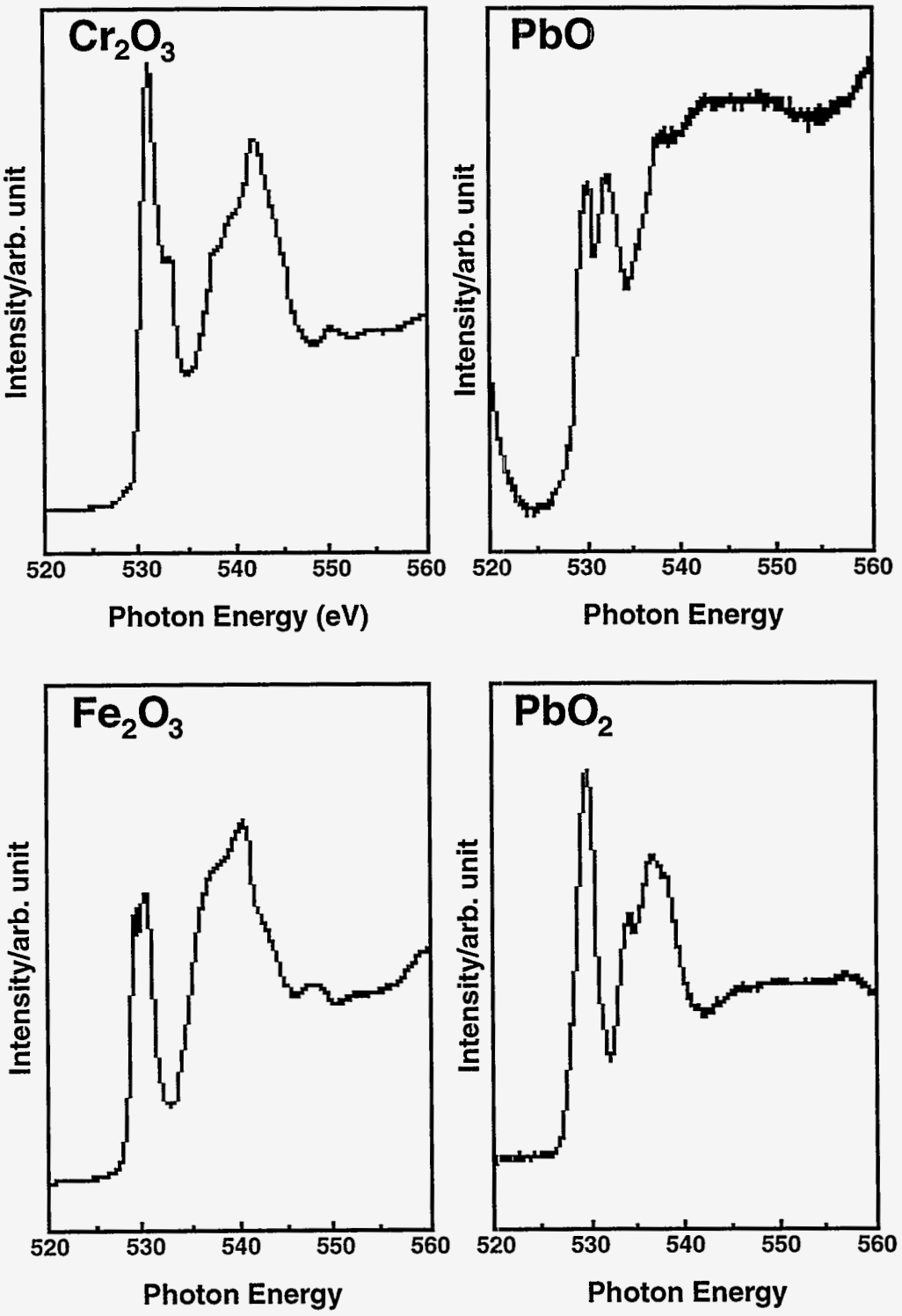

Fig. 2. TEY of Cr_2O_3, Fe_2O_3, PbO and PbO_2

MOLECULAR ORBITAL CALCULATION

Molecular orbital (MO) calculations were performed using the discrete-variational (DV) Xα method[2,3] in which a linear combination of numerically generated atomic orbitals were used to describe the MOs. The basis functions for MgO were 1s~3p for O and Mg. Sample points of 2000 for numerical integration were distributed three-dimensionally in a manner described elsewhere[3]. A diameter and depth of the potential to confine wave functions were chosen to be $0.7a_0$ and

-3.0 Hartree, respectively where a_0 was an interatomic distance between O and Mg atoms. In the present study, a cluster model of $(Mg_6O_{19})^{26-}$ was employed, as shown in Fig. 3. If we assume that TEY or FY is described by photo-absorption originated from electronic excitation from O 1s to O 2p and 3p, an observed spectrum of TEY or FY near the O K edge for MgO, as shown in Fig. 4, can be explained approximately by unoccupied partial density of states (PDOS) of O 2p and 3p. The PDOS calculated here is compared with TEY and FY spectra in Fig. 4. This suggests that further discussions are indispensable whether or not the X-ray absorption can mostly be written by the dipole approximation. Comparison between observed TEY and calculated PDOS is in due course for several oxides.

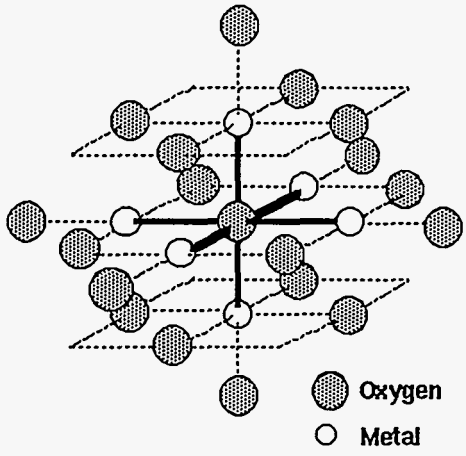

Fig.3. A $(Mg_6O_{19})^{26-}$ cluster used in DV-Xα calculation

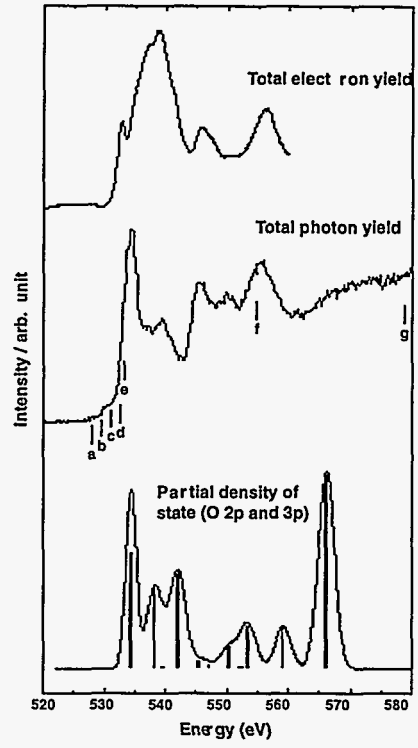

Fig. 4. Comparison among TEY, FY and PDOS for MgO

REFERENCES

1. F. M. F. de Groot, M. A. Arrio, Ph. Sainctavit, Ch. Cartrier, C. T. Chem, Physica B 208/209 (1995) 84.
2. D. E. Ellis, H. Adachi, F. W. Averill, Surf. Sci. 58 (1976) 497.
3. H. Adachi, M. Tsukada, C. Satoko, J. Phys. Soc. Jap. 45 (1978) 875.

This work was supported by Waseda University, Rigaku, and Hitachi.

Principal investigator: Masayuki Uda, Laboratory for Materials Science and Technology, Waseda University.
Email: muda@mn.waseda.ac.jp.

Resonant scattering of polarized soft x-rays for the study of magnetic oxide layers

Maurizio Sacchi [1], Coryn F. Hague [1,2], Eric Guiot [3], Martine Gautier-Soyer [3], Susana Gota [3], Eric M. Gullikson [4] and James H. Underwood [4]

[1] LURE, Bât. 209d, Centre Universitaire Paris-Sud, 91405 Orsay (France)
[2] Laboratoire de Chimie Physique - Matière et Rayonnement, 11, rue P. et M. Curie, 75231 Paris (France)
[3] CEA-DRECAM, Centre d'Etudes de Saclay, Bât.462, 91191 Gif-sur-Yvette (France)
[4] Center for X-ray Optics, Materials Sciences Division, Lawrence Berkeley Laboratory, Berkeley CA 94720

Magnetic oxides, particularly in the form of thin films, are the object of intense study in both fundamental and applied research[1]. The epitaxial growth of magnetic iron oxides on oxides allows to obtain high quality single crystal thin films that serve as a reference for the investigation of the fundamental characteristics of these systems in terms of electronic and magnetic properties, covering the thickness range from the monolayer to the bulk[2]. Spectroscopic techniques which are appropriate for these investigations are often based on electron detection (e.g. LEED, XPS, spin analysis and even absorption performed in electron yield mode on thick samples), hence affected by the insulating nature of both sample and substrate. As a complement to electron based spectroscopies, we have applied resonant scattering of polarized soft x-rays[3] (a photon-in / photon-out technique) to the study of epitaxial oxide layers. Experiments were performed on the reflectometer of beamline 6.3.2 at ALS, using linearly and elliptically polarized light. Test samples were epitaxial Fe_2O_3 and Fe_3O_4 layers grown on sapphire.

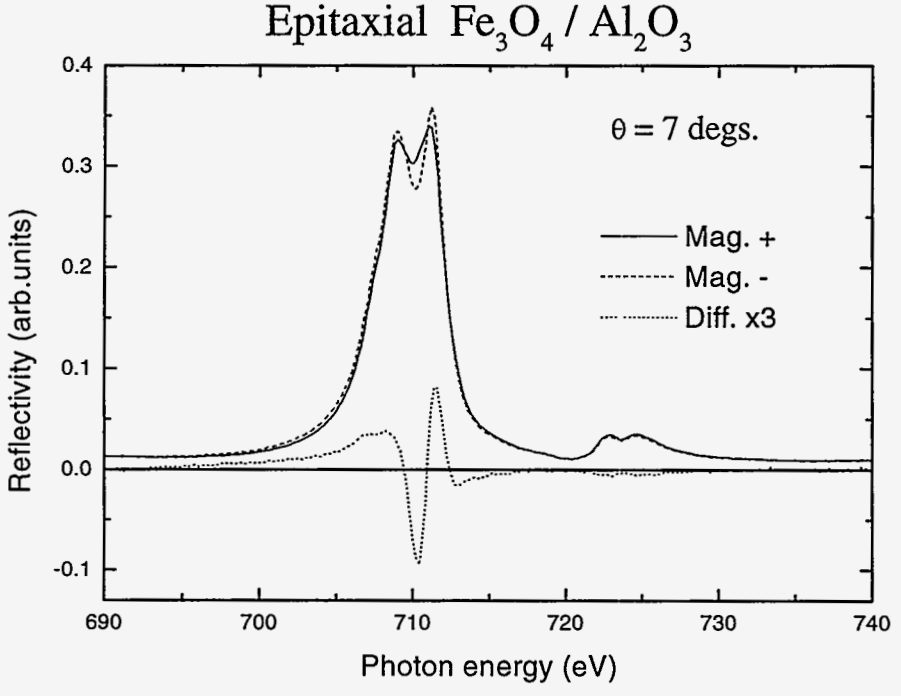

Fig. 1. Resonant magnetic scattering of elliptically polarised x-rays at the Fe 2p edges in an epitaxial iron oxide film. The two curves refer to opposite magnetization/helicity orientations.

The experimental geometry allowed to search for both linear dichroism related to antiferromagnetic ordering in Fe_2O_3 and circular dichroism coming from the ferrimagnetic ordering in Fe_3O_4 (see Fig. 1). Elastic x-ray scattering can be used at the same time for a structural analysis on the layers, studying the angular dependence of the reflectivity (Fig. 2).

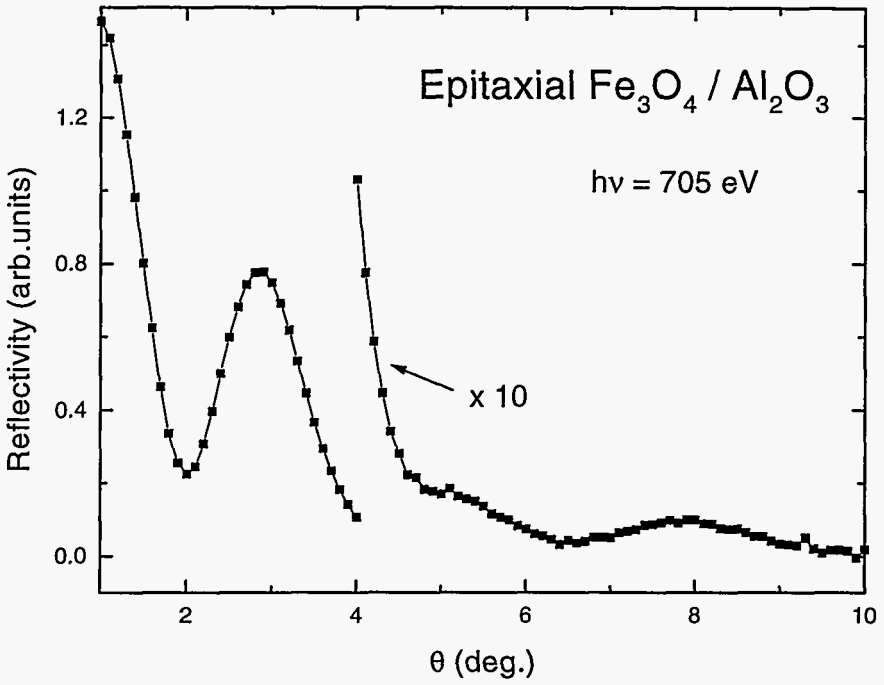

Fig. 2. Reflectivity versus scattering angle at 705 eV. Three structures can be identified, related to the thickness of the iron oxide layer.

We have then a technique that can give spectroscopic as well as microstructural information with very high sensitivity, capable of working on insulating samples and in presence of high magnetic fields. Moreover, the well defined relation between resonant scattering and absorption allows a natural extension to the former of dichroism sum rules for an element selective and quantitative evaluation of the magnetic moments.

REFERENCES

1. e.g. R.L.Kurtz and V.E.Henrich, Phys.Rev.B36 3413 (1987); J.P.Crocombette et al., Phys.Rev. B52 3143 (1995); Z.Y.Wu et al., Phys.Rev. B55 2570 (1997)
2. Eric Guiot, Susana Gota and Martine Gautier-Soyer, unpublished
3. Maurizio Sacchi, Coryn F. Hague, Eric M. Gullikson and James H. Underwood, Phys.Rev. B57 108 (1998)

This work was supported by the Centre National de la Recherche Scientifique and by the Commisariat à l'Energie Atomique (France)

Principal investigator: Maurizio Sacchi, Laboratoire pour l'Utilisation du Rayonnement Electromagnétique, Bât. 209d, Centre Universitaire Paris-Sud, 91405 Orsay (France)
tel. -33-1-64468089; fax -33-1-64464148; email: sacchi@lure.u-psud.fr

Small-Angle X-ray Scattering at Large Angles in the Soft X-ray Range: Layer Discontinuity in Ultra-Short Period W/B_4C Multilayers

C. C. Walton and J. B. Kortright
Advanced Light Source and Materials Science Division
Ernest Orlando Lawrence Berkeley National Laboratory
Berkeley, California, 94720 USA

INTRODUCTION

Recent novel applications of multilayer x-ray mirrors, for example as linear polarizers in the soft x-ray,[1] have brought with them new interest in multilayers of ultra-short periods (d < 15Å). Most materials combinations show a severe loss of reflectivity at periods below 30-40Å, but W/B_4C has been shown[2,3] to maintain useful reflectivities (1-2% or better) for periods down to 12Å. To optimize performance at these periods, we have studied the microstructure of W/B_4C multilayers with Small-Angle X-ray Scattering (SAXS) experiments at Beamline 6.3.2 at ALS. Measurements usually performed at 0.1°-5°in the hard x-ray range correspond to angles up to 60° at soft x-ray energies (700eV). While not generally applied to x-ray multilayers, this technique provides valuable information on in-plane inhomogeneities not easily accessible to other techniques. Discontinuity of the films at early stages of growth contributes to reflectivity loss and can be directly measured by this technique.

EXPERIMENT

The multilayers in this study were grown by standard magnetron sputtering techniques described elsewhere, on free-standing Si_3N_4 membranes about 1500Å thick. There were examined in transmission at BL 6.3.2 at E = 700eV and on a rotating-anode source at CuK_α (λ = 1.54Å) The scattered signal was measured by a detector at angle 2θ, and the sample was rotated by θ to keep the scattering vector in the plane of the films. Background signal from the tails of the incident beam was measured separately and subtracted, and the remaining signal divided by the full beam intensity I_0 to yield an absolute scattered intensity vs. angle. Multilayers of period d = 6, 14, 22 and 30Å were measured.

ANALYSIS

The scattered signal was compared to a simple SAXS model based on earlier work by Rice.[4] The model assumes spherical particles of one composition in a homogeneous matrix of another. Using the known overall multilayer composition, the size of the particles and the volume fraction they occupy were varied to fit the experimental results. Within plausible ranges of these parameters a unique fit was obtained.

RESULTS AND DISCUSSION

The experimental data (points) and fits (smooth curves) are shown in Fig. 1. For the shortest d-spacing, a broad peak is present at both incident energies. At d = 14Å a weak peak at a smaller angle (corresponding to larger particles) is present, and at d = 22Å and d = 30Å no SAXS signal is observed. This is consistent with a transition from discontinuous to continuous multilayers between d = 14Å and D = 22Å. Because the scattering factor for W is more than ten times that of B or C at both wavelengths, the SAXS signal represents almost exclusively the W-W correlations. For a continuous multilayer the scattering vector lies parallel to the layers and measures only weak in-plane density fluctuations, while for a discontinuous multilayer the sizes and separations of the islands in the film give a strong in-plane signal.

The fit parameters agree well for the two incident energies used – particles of about 25Å diameter for the d = 6Å multilayer and 32Å diameter for the d = 14Å multilayer. The results are corroborated by plan-view HRTEM of other W/B_4C specimens grown under the same conditions – Fig. 2. shows a d = 6Å multilayer with a clear islanded structure. The islands are of irregular shape, consistent with a broad distribution of widths indicated by the peak width in the SAXS signal, and show diameters about 25Å.

CONCLUSIONS

W/B_4C forms layered structures with separate phases for periods as short as 6Å, though for periods below 14-22Å the layers are discontinuous. This work demonstrates that scattering measurements in the soft x-ray can probe inhomogeneities in materials on the nm scale and greater. Coupled with the strong anomalous dispersion (in charge and possibly magnetic scattering) associated with many soft x-ray core levels, this capability can be readily extended to study a variety of materials and problems.

REFERENCES

1. J. B. Kortright, M. Rice, and R. Carr, "Soft-X-ray Faraday rotation at Fe L2,3 edges," Physical Review B (Condensed Matter) **51** (15), 10240-3 (1995).
2. J. F. Seely, G. Gutman, J. Wood *et al.*, "Normal-incidence reflectance of W/B4C multilayer mirrors in the 34-50A wavelength region," Applied Optics **32** (19), 3541-3 (1993).
3. C.C. Walton and J.B. Kortright, to be published.
4. M. B. Rice, "Anomalous Small Angle X-Ray Scattering Studies of Amorphous Metal-Germanium Alloys," Ph.D., Stanford University, 1993.

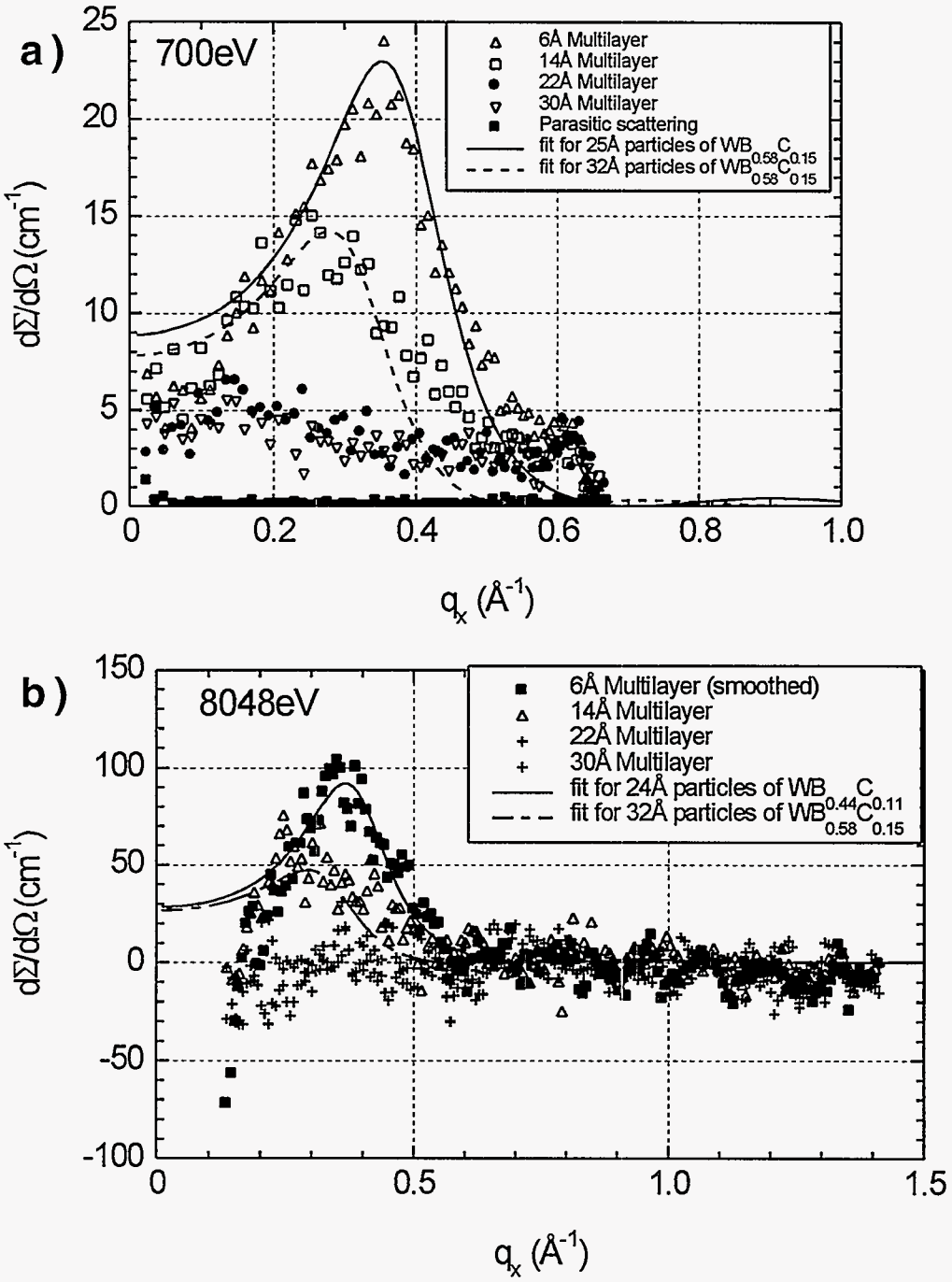

Fig. 1. *a)* Small-Angle X-Ray Scattering (SAXS) data (points) and fits (smooth curves) for W/B_4C multilayers of four periods, taken at E = 700eV. Fits are consistent with the W-rich layers in the shortest-period multilayers (6Å and 14Å) consisting of islands of about 24Å and 32Å diameter rather than continuous layers. The islands are not bulk W but compounds near the composition W_2B. *b)* Similar results taken at E = 8048eV (CuK_α).

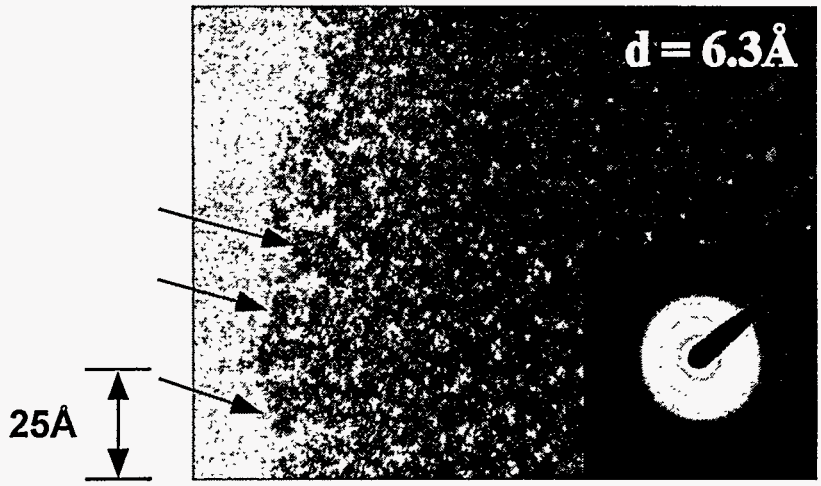

Fig. 2. Plan-view HRTEM of d = 6Å W/B_4C multilayer. Island structure of W-rich layers is clearly visible.

This work was supported by the Director, Office of Energy Research, Office of Basic Energy Sciences, Materials Sciences Division, of the U.S. Department of Energy under Contract No. DE-AC03-76SF00098.

Author Affiliations:
Contact author: CCW now at Advanced Microtechnology Program, L-395, Lawrence Livermore National Laboratory, Livermore, CA 94550 USA. e-mail walton9@llnl.gov, phone 510-423-2834.

Principal investigator when experiments were done: JBK at Materials Science Division, MS 2-100, Lawrence Berkeley National Laboratory, Berkeley, CA 94720. e-mail jbkortright@lbl.gov, phone 510-486-5960.

Soft X-ray Emission and Absorption - A Comparative Study on The Sensitivity to Oxidation State and Ligand Environment of Transition Metal Complexes

M.M. Grush[a,*], Y. Muramatsu[a,b], J.H. Underwood[d], E.M. Gullikson[d], D.L. Ederer[c], R.C.C. Perera[d], T.A. Callcott[a]

[a]University of Tennessee, Knoxville, TN 37996 USA
[b]NTT Integrated Information and Energy Systems Laboratory, Tokyo 180, Japan
[c]Tulane University, New Orleans, Louisiana 70118 USA
[d]Lawrence Berkeley National Laboratory, Berkeley, CA 94720 USA

INTRODUCTION

Transition metals are a necessary part of many catalytic cycles. They play a major role in biological redox reactions (e.g. iron in nitrogenase and manganese in Photosystem II) as well as in material science applications. For example, manganese has been proposed as a less toxic and less expensive alternative to nickel-based electrodes in rechargeable batteries [1]. In order to understand these systems, it is necessary to obtain information about oxidation states, ligand environment, and local structure surrounding the metal centers. L-edge XAS, which probes the *unoccupied* 3d levels, has been shown to be a sensitive probe of the oxidation and spin state of transition metal sites in proteins [2,3,4]. As soft x-ray fluorescence (SXF) instead probes the *occupied* states, an investigation of how this complimentary technique can be used to probe transition metals was conducted and the results are presented here.

EXPERIMENTAL

Soft x-ray absorption experiments were performed on Beamline 6.3.2 at the Advanced Light Source [5]. A 1200 l/mm grating with an exit slit of less than 20 microns resulted in a resolving power (E/ΔE) of better than 1200 at the Mn L-edge. Soft x-ray fluorescence spectra were recorded on Beamline 8.0 at the Advanced Light Source [6]. A 925 l/mm grating was used to monochromatize the excitation energy for these measurements. Throughout the series of Mn emission scans, the monochromator and undulator were fixed at 672.58 eV and 23.78 mm, respectively. The monochromator was energy calibrated by setting the L_{III} peak of MnF_2 to 639.36 eV. Spectra were normalized to unit intensity at the L_{II} peak.

The soft x-ray fluorescence endstation [6] consists of a Rowland circle - type emission spectrometer with a fixed 100 micron entrance slit and a 1500 l/mm grating mounted on a 10 m Rowland circle. The x-ray fluorescence is refocused onto a multichannel plate area detector, enabling the entire emission spectrum to be obtained without scanning the detector. Emission spectra were calibrated relative to the L_β emission of MnO [7]. Spectra were normalized to unit intensity at the L_β peak.

RESULTS AND DISCUSSION

The soft x-ray absorption and emission spectra of two oxidation state pairs are shown in Figure 1. The Mn centers in Mn(II)$(acac)_2$ and Mn(III)$(acac)_3$ have oxygen ligation with tetrahedral and octahedral geometry, respectively. The Mn in Mn(II)(pc) is square planar with nitrogen ligation. Mn(III)(pc)Cl adds a chloride to the ligation sphere and the resulting complex is square pyramidal. In both cases, the x-ray absorption spectrum of Mn(II) is strikingly different from that of Mn(III) (Figure 1, left). The L_{III} peak occurs at 639.35 eV and 639.37 eV for the Mn(II)$(acac)_2$ and Mn(II)(pc), respectively. Both spectra have an ~11.3 eV separation between L_{III} and L_{II} and have similar multiplet structure, in spite of the differences in geometry and ligation. The Mn(III) spectra

occur ~1.4 eV higher than the corresponding Mn(II) spectra, are much broader, and have a more equal distribution in intensity between the L_{III} and L_{II} regions of the spectrum. This increase in energy, decrease in the ratio of L_{III} to L_{II}, and increase in broadness with increasing oxidation state has been observed in Mn complexes previously [8]. These spectral differences can be used to determine the average oxidation state in an unknown manganese compound [3]. Although large differences in the ligand coordination can cause changes in electronic geometry and spin state which are often readily observable in the absorption spectra [8], relatively small differences appear as a result of minor changes in ligation. Determining the relative percentages of oxygen or nitrogen, for example, can be quite difficult.

In contrast to x-ray absorption, the x-ray emission spectra of complexes with different oxidation states but similar ligation are remarkably similar in both the broadness and the energy position of the L_α and L_β peaks, neither of which show resolved multiplet features (see Figure 1, right). The L_β peak occurs at 648.2 eV and 649.0 eV for the Mn(II)$(acac)_2$ and Mn(II)(pc) spectra, respectively, 9-10 eV higher in energy than the L_α peak. An increase to higher oxidation state results in no change to the L_β region of the Mn(III)$(acac)_3$ and a slight increase in broadness for the Mn(III)(pc)Cl. The major difference between Mn(II) and Mn(III) spectra with similar ligation is not a change in energy position but instead an increase in the ratio of the integrated area of the L_α region divided by that of the L_β.

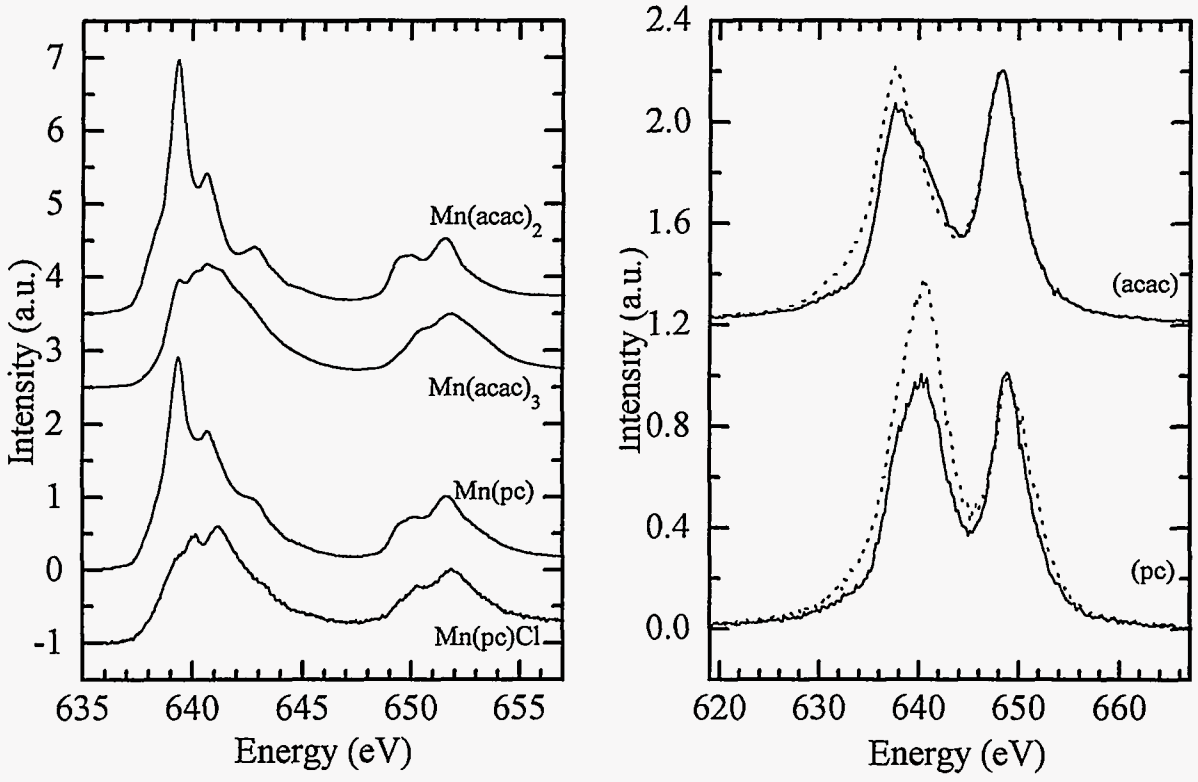

Figure 1. Soft X-ray Absorption and Emission Spectra of Mn complexes. Left (from top to bottom): Mn L-absorption spectra of Mn(II)$(acac)_2$, Mn(III)$(acac)_3$, Mn(II)(pc), and Mn(III)(pc)Cl. Right: Mn L-emission spectra of Mn(II)$(acac)_2$ (top, solid line), Mn(III)$(acac)_3$ (top, dotted line), Mn(II)(pc) (bottom, solid line), and Mn(III)(pc)Cl (bottom, dotted line).

Mn L-emission spectra were recorded for two sets of Mn complexes. The first group had oxygen ligation and varying Mn oxidation states while the second was a series of divalent Mn complexes with varying ligation. The L_α / L_β ratios and the energies of the zero crossings from the first derivative of the emission spectra are tabulated in Table 1 (emission spectra not shown). In the case of the four Mn complexes with oxygen ligation: Mn(II)$(acac)_2$, Mn(II)O, Mn(III)$(acac)_3$, and λ-Mn(IV)O_2, the L_α and L_β peaks maintain similar energy position throughout the oxidation state range. The spectra do, however, show an increase in both broadness and branching ratio with increasing oxidation state. Although the second two zero crossings are relatively independent of ligation for the series of Mn(II) complexes, an increase in broadness in the L_α region (by ~3 eV) is seen for ligands with an atomic group number of 6 and higher. This is shown by the lower energy position of the first zero crossing for these spectra. In addition, a strong correlation ($r^2 = 0.998$) is seen between the L_α / L_β ratio and the atomic group number of the ligands to the manganese. Increasing the group number from 5 to 7 results in a linear decrease in the L_α / L_β ratio. This inverse dependence on the ionicity of the compound has been noted previously in copper complexes [9].

Although atomic multiplet calculations can successfully simulate manganese soft x-ray absorption spectra [3,8], the application of these calculations to soft x-ray emission spectra measured with above threshold excitation is more difficult. Efforts to use these and other types of calculations to simulate manganese soft x-ray emission spectra and reproduce the experimental findings reported here are currently in progress.

Table 1: Spectral parameters of Mn compounds.

Ligand Group Number	Compound	L_α / L_β Ratio	First Zero Crossing*	Second Zero Crossing*	Third Zero Crossing*
5	Mn(II)(pc)	1.57	640.70 eV	645.07 eV	648.97 eV
5.5	Mn(III)(pc)Cl	2.19	640.64	645.14	649.03
6	Mn(II)$(acac)_2$	1.18	637.75	644.13	648.50
	Mn(III)$(acac)_3$	1.43	637.75	644.13	648.50
	Mn(II)O	1.14	637.61	644.13	648.50
	λ-Mn(IV)O_2	3.13	638.08	644.13	648.97
	Mn(II)S	1.20			
< 7	Mn(II)Cl_2*xH_2O	1.05	638.38	644.90	648.97
7	Mn(II)F_2	0.78	638.08	644.77	648.80

*Zero crossings are reported for the first derivative of the Mn emission spectra.

CONCLUSIONS

Mn L-edge absorption is known to be a sensitive probe of both oxidation and spin state. In contrast, L-edge emission has been shown here to be very sensitive to ligand environment and less sensitive to the electronic geometry and oxidation state of the manganese. The linear dependence of the L_α / L_β ratio on the group number of the ligands to the manganese suggests a method of determining the ligand environment of a transition metal of known oxidation state. This is especially exciting for metalloproteins in cases where the percentage of oxygen versus nitrogen ligation is not known. Other x-ray techniques such as EXAFS are not sensitive enough to distinguish between two elements of such close proximity in the periodic table as oxygen and nitrogen. In addition, the L_α / L_β ratio offers a probe of the covalency of the complex. As mentioned earlier, rechargeable batteries based on $LiMn_2O_4$ electrodes have been suggested as an alternative to the traditional nickel-based systems. Substitutions of other metals in small quantities have resulted in improvement in the cycling properties of these materials [10,11]. However, the

relationship between metal substitution and cycling enhancement is not well understood. By measuring the x-ray emission spectra on these components, it will be possible to probe the occupied states to gain an understanding of the difference in performance as dependent on electrode composition. These two examples show the potential of soft x-ray emission to be a powerful tool in examining transition metal catalytic systems.

ACKNOWLEDGMENTS

This work has been accepted for publication in the Journal of Electron Spectroscopy and Related Phenomena. $Mn(acac)_2$ (acac=acetylacetonate), $Mn(acac)_3$, Mn(pc) (pc=phthalocyanine), Mn(pc)Cl, MnF_2, and $MnCl_2$ were used as obtained from Aldrich Chemical Company; λ-MnO_2 from Covalent Associates, Inc. The MnO and MnS samples were provided by C.R. Horne and K. Lawniczak-Jablonska, respectively. This research was supported by the National Science Foundation, Grant No. DMR-9017996. The Advanced Light Source is supported by the Office of Basic Energy Science, U.S. Department of Energy Contract No. DE-AC03-76SF00098.

REFERENCES

1. J.M. Tarascon, D. Guyomard, Electrochem. Acta., 38 (1993) 1221.
2. S.J. George, J. van Elp, J. Chen, Y. Ma, C.T. Chen, J.-B. Park, M.W.W. Adams, B.G. Searle, F.M.F. de Groot, J.C. Fuggle, S.P. Cramer, JACS, 114 (1992) 4426.
3. M.M. Grush, J. Chen, T.L. Stemmler, S.J. George, C.Y. Ralston, R.T. Stibrany, A. Gelasco, G. Christou, S.M. Gorun, J.E. Penner-Hahn, S.P. Cramer, JACS, 118 (1996) 65.
4. J. van Elp, G. Peng, B.G. Searle, S. Mitra-Kirtley, Y.-H. Huang, M.K. Johnson, Z.H. Zhou, M.W.W. Adams, M.J. Maroney, S.P. Cramer, JACS, 116 (1994) 1918.
5. J.H. Underwood, E.M. Gullikson, M. Koike, P.J. Batson, SPIE, 3113 (1997) 214.
6. J.J. Jia, T.A. Callcott, J. Yurkas, A.W. Ellis, F.J. Himpsel, M.G. Samant, J. Stohr, D.L. Ederer, J.A. Carlisle, E.A. Hudson, L.J. Terminello, D.K. Shuh, R.C.C. Perera, Rev. Sci. Instr., 66 (1995) 1394.
7. S.M. Butorin, J.-H. Guo, M. Magnuson, P. Kuiper, J. Nordgren, Phys. Rev. B, 54 (1996) 4405.
8. S.P. Cramer, F.M.F. deGroot, Y. Ma, C.T. Chen, F. Sette, C.A. Kipke, D.M. Eichhorn, M.K. Chan, W.H. Armstrong, E. Libby, G. Christou, S. Brooker, V. McKee, O.C. Mullins, J.C. Fuggle, JACS, 113 (1991) 7937.
9. S.M. Butorin, V.R. Galakhov, E.Z. Kurmaev, V.I. Glazyrina, Solid State Commun., 81 (1992) 1003.
10. R. Bittihn, R. Herr, D. J. Hoge, Power Sources, 43-44 (1993) 223.
11. R.J. Gummow, A. de Kock, M.M. Thackeray, Solid State Ionics, 69 (1994) 59.

Principal Investigator: Thomas A. Callcott, University of Tennessee. E-mail: tcallcott@utk.edu. Telephone: (423) 974-6765.

Studies of Electronic Structure for $Ti_{1-x}V_xO_2$

B. Song[1], J. Tsuji[1], Y. Tsuji[1], Y. Nakane[1], R.C.C. Perera[2], J.H. Underwood[2], M. Uda[3], H. Wakita[4], T.A. Callcott[5], D.L. Ederer[6], and K. Taniguchi[1]

[1]Division of Electronics and Applied Physics, Osaka Electro-Communication University, 18-8, Hatsu-machi, Neyagawa, Osaka 572, Japan

[2]Center for X-Ray Optics, Lawrence Berkeley Laboratory, Berkeley, California 94720, USA

[3]Department of Materials Science and Engineering, Waseda University, Ohkubo, Shinjuku-ku, Tokyo 169, Japan

[4]Department of Chemistry, Fukuoka University, Nanakuma, Jonan-ku, Fukuoka 814-01, Japan

[5]Department of Physics, University of Tennessee, Knoxville, TN 37996, USA

[6]Department of Physics, Tulane University, New Orleans, LA 70118, USA

INTRODUCTION

Titanium vanadium oxides, including $Ti_{1-x}V_xO_2$ rutile solid solution have been attracting much attention because of their application in display devices, color filters, smart windows, lithium cells and many oxidation and reduction reactions. They are used as electrodes [1], electrochromic materials [2], and catalysts [3]. In order to explain the electronic, electrochromic, and optical properties of titanium vanadium oxides, it is very important to study their electronic structure. So far, there is neither theoretical nor experimental studies for electronic structure of titanium vanadium oxides, has been reported.

X-ray spectroscopy is a powerful technique for the study of the electronic structure of solids and the characterization of materials. The soft x-ray emission spectra (SXES) are capable of yielding occupied partial density of states in valence band for solid systems, whereas the x-ray absorption spectra reflect the unoccupied partial density of states. The disadvantage of SXES spectroscopy is the typically low fluorescence yields for many core levels, particularly for light elements. However, nowadays, the synchrotron radiation sources has stimulated the interest in the study of soft x-ray emission using photon excitation [4]. Advanced Light Source can overcome many of the disadvantages of electron spectroscopies. For example, it not only offer the high brightness that makes high resolution SXE experiments practical, but also allows a detailed investigation of defined materials by changing the excitation energy.

EXPERIMENTAL RESULTS

The SXES for $Ti_{1-x}V_xO_2$ were excited by photons from undulator beamline 8.0 at the Advanced Light Source in Lawrence Berkeley Laboratory, and the x-ray absorption spectra were measured from beamline 6.3.2. The Ti $L_{2,3}$ x-ray emission spectra from $Ti_{0.8}V_{0.2}O_2$ are shown in Fig. 1. It can be seen that the spectra are almost the same as that of TiO_2 (rutile) [5]. An elastic peak, a main peak and Raman scattering peak can be found in Fig. 1. The main peak located a energy about 453 eV should be a L_3 spectrum which results from transitions from the valence band to the 2p3/2 core hole of Ti atom. The Ti $L_{2,3}$ x-ray absorption spectrum is shown in Fig. 2. For comparison, the Ti $L_{2,3}$ x-ray absorption spectrum from TiO_2 (rutile) is also projected. Comparing the Ti $L_{2,3}$ x-ray absorption spectra from TiO_2 and $Ti_{0.8}V_{0.2}O_2$, it is found that peak positions are almost the same, however, the intensity ratio of the peaks are very different. This result indicates that quantity of the unoccupied Ti 3d states is different between TiO_2 and $Ti_{0.8}V_{0.2}O_2$. More detail experiments and theoretical calculations are necessary to clarify the electronic structure of $Ti_{0.8}V_{0.2}O_2$.

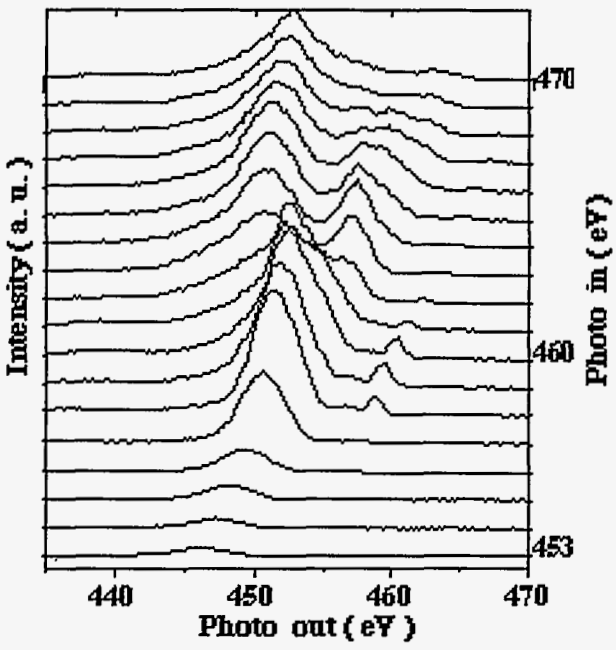

Figure 1. Evolution of the Ti $L_{2,3}$ emission spectra from $Ti_{0.8}V_{0.2}O_2$. All curves show the normalized x-ray emission as a function of the emission energy plotted as the abscissa. The scale on the right give the excitation energy.

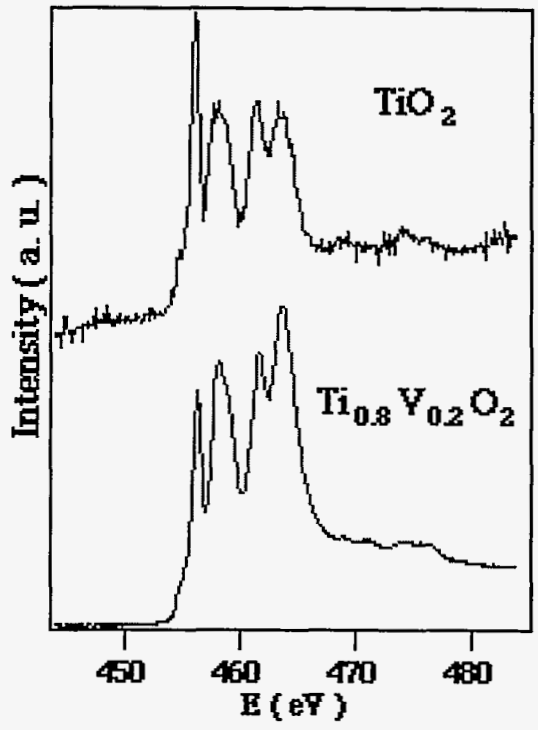

Figure 2. Comparison of the Ti $L_{2,3}$ x-ray absorption spectra between TiO_2 and $Ti_{0.8}V_{0.2}O_2$.

REFERENCES

1. M.G. Minett and J.R. Owen, J. Power Sources, 32, 81 (1990).
2. K. Nagase, Y. Shimizu, N. Miura and N. Yamazoe, Appl. Phys. Lett., 61, 243 (1992).
3. J. Ph. Nogier, J. Thoret, N. Jammul and J. Fraissard, Appl. Surf. Sci., 47, 287 (1991).
4. J.J. Jia, T.A. Callcott, A. Asfaw, J.A. Carlisle, L.J. Terminello, D.L. Ederer, F.J. Himpsel, and R.C.C. Perera, Phys. Rev. B52, 4904 (1995).
5. D.L. Ederer, J.A. Carlisle, J. Jimenez, J.J. Jia, Ling Zhou, T.A. Callcott, R.C.C. Perera, A. Moewes, L.J. Terminello, E. Shirley, A Asfaw, J. Van Ek, E. Morikawa and F.J. Himpsel; X-Ray and Inner-shell Processes, 17th International Conference, Hamburg Germany, 764 (1996).

This work was supported by the Division of Electronics and Applied Physics, Osaka Electro-Communication University, Japan.

Principal investigator: Bin Song, Division of Electronics and Applied Physics, Osaka Electro-Communication University. Email: d95101@isc.osakac.ac.jp. Telephone: 0720-25-4690.

Studies of Electronic Structures for α-Al_2O_3 and $AlPO_4$ by Al-L and O-K Absorption Spectra

H. Wakita[1], T. Kurisaki[1], S. Matsuo[1], H. Ichihashi[1], K. Koga[1],
M. Uda[2], K. Taniguchi[3], J.H. Underwood[4], R.C.C. Perera[4], and T. Yokoyama[5]

[1]Department of Chemistry, Fukuoka University, Nanakuma, Jonan-ku, Fukuoka 814-01, Japan
[2]Department of Material Science and Engineering, Waseda University,
Ohkubo, Shinjuku-ku, Tokyo 169, Japan
[3]Division of Electronics and Applied Physics, Osaka Electro-Communication University,
18-8 Hatsucho, Neyagawa, Osaka 572, Japan
[4]Center for X-ray Optics, Lawrence Berkeley National Laboratory, Berkeley, California 94720, USA
[5]Department of chemistry, Kyushu University, Hakozaki, Higashi-ku, Fukuoka 812, Japan

INTRODUCTION

Aluminum atoms in aluminosilicates are coordinated by oxygen atoms in many silicate net-works and have four-, five-, or six-coordinated structure, and sometimes have their mixed coordinated structure, however, it is not so easy to determine the coordination structures. We analyzed the coordination structures of mullite precursors by Al MAS-NMR[1] and XAFS[2], and the results show the existence of the five-coordinated structure in the precursors. But the XAFS spectra by our laboratory XAFS spectrometer was not so distinct. To analyze the structures of mullite and mullite precursors clearly, we measured X-ray absorption spectra for some aluminum silicates and reference samples such as α-alumina α-Al_2O_3 and aluminum phosphate $AlPO_4$, and analyzed the spectra by a molecular orbital calculation method, a DV-Xα method.

RESULTS AND DISCUSSION

The absorption spectra were measured by the spectrometers at UVSOR beamline 7A and at ALS beamline 6.3.2. The UVSOR and ALS beamlines are bend magnet beamlines and the energy range for the UVSOR beamline is 100eV-1500eV, and that for the ALS beamline is 50eV-1000eV. Absorption spectra were obtained by collecting total electrons from the samples.

Al-K absorption spectra of some aluminosilicates and reference samples obtained by the UVSOR beamline are shown in Fig. 1. There are some differences of the spectra from α-alumina having a six-coordinated structure to aluminum phosphate having a four-coordinated structure. However, by the absorption spectra of Al-K for reference samples shown in Figs. 2 & 4 obtained by the ALS beamline, the spectra differences between the reference samples are quite distinct. Figures. 3 & 5 show also distinct differences between the reference samples for O-K edges.

Molecular orbital calculations were performed by using a discrete-variational(DV) Xα method[3]. The basis functions for α-Al_2O_3 were 1s-4p for O and 1s-5p for Al, and for $AlPO_4$ they were 1s-4p for O, 1s-3d for P, and 1s-5p for Al. For numerical Integration sample points of 10000 for α-Al_2O_3 and 13000 for $AlPO_4$ were distributed three-dimensionally in a manner described elsewhere[4]. In the present study, models of $(Al_{14}O_6)^{20+}$, and $(AlO_{16}P_4)^{29-}$ were employed for the calculations of α-Al_2O_3 and $AlPO_4$, respectively. In case of α-Al_2O_3, an aluminum atom is surrounded by 6 oxygen atoms in the first coordination sphere and 13 aluminum atoms in the second sphere, and in case of $AlPO_4$ an aluminum atom is surrounded by 4 oxygen atoms in the first sphere, 4 phosphorous atoms in the second sphere, and 12 oxygen atoms in the third sphere. Using these models the calculated transition probabilities for each transition give good fits with observed spectra in Figs. 2-5. Comparing the result of Tanaka and Adachi[5], the fit between observed and calculated spectra in Fig. 3 is good enough though the model is simpler than that of

them in the observed region. The calculation of the Al-K spectra of aluminosilicate samples and the comparison of the results with those obtained from reference samples are in due course.

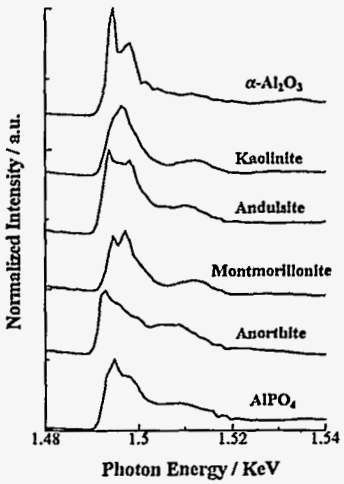

Fig.1 Al *K* XANES Spectra of a Series of Al Compounds

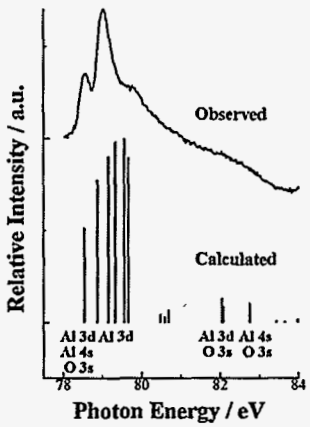

Fig. 2 Observed and Calculated Al-$L_{II,III}$ XANES Spectra of α-Al_2O_3

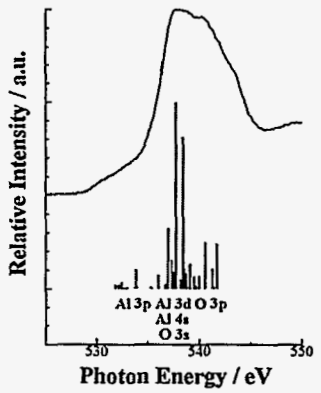

Fig.3 Observed and Calculated O-*K* XANES Spectra of α-Al_2O_3

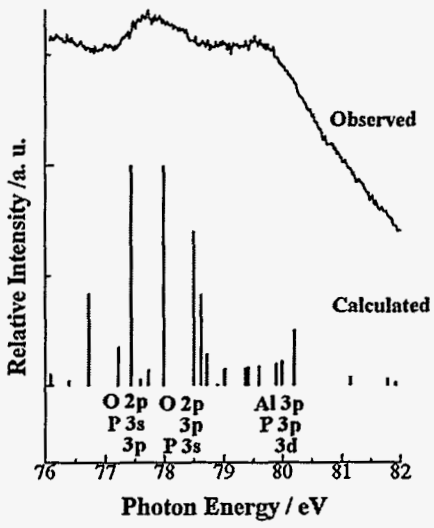

Fig.4 Observed and Calculated Al-$L_{II,III}$ XANES Spectra of $AlPO_4$

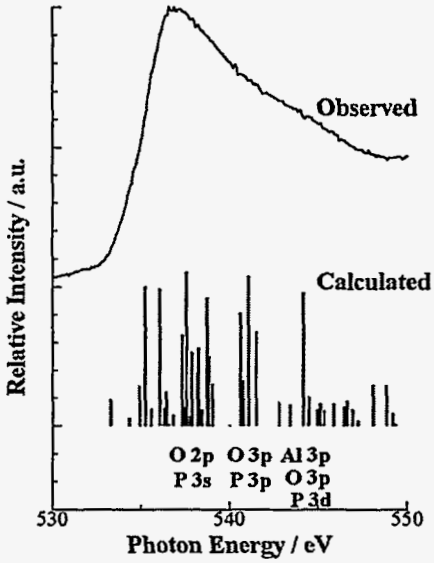

Fig.5 Observed and Calculated O-*K* XANES Spectra of $AlPO_4$

REFERENCES

1) Y.Ikeda,T.Yokoyama, S.Yamashita, and H.Wakita, Jpn. J. Appl. Phys. Suppl.32, 670(1993).
2) Y.Ikeda,T.Yokoyama, S.Yamashita, T.Watanabe, and H.Wakita, Adv. in X-ray Chem. Anal. Jpn., 26, 211 (1995).
3) D.E.Ellis, H.Adachi, F.W.Averill, Surf.Sci., 58, 497(1976).
4) H.Adachi, M.Tsukada, C.Satoko, J.Phys.Soc.Jpn., 45, 875(1978).
5) I.Tanaka, H.Adachi, Pys.Rev.B, 54, 4604(1996).

This work was supported by the authors institutions, and was carried out at the Advanced Light Source at Lowrence Berkeley National Laboratory operated under Contract No.DE-AC03-76SF00098 with the U.S. Department of Energy.

Principal investigator: H.Wakita, Department of Chemistry, Fukuoka University.
E-mail: wakita@sunsp1.sc.fukuoka-u.ac.jp

Sulfur L Absorption Spectra Observed by Total Electron Yield Method

J. Tsuji [1], Y. Tsuji [1], Y. Nakane [1], B. Song [1], R. C. C. Perera [2], J. H. Underwood[2], M. Uda [3], H. Wakita [4] and K. Taniguchi [1]

[1] Division of Electronics and Applied Physics, Osaka Electro-Communication University, 18-8 Hatsucho, Neyagawa, Osaka 572, Japan

[2] Center for X-ray Optics, Lawrence Berkeley National Laboratory, Berkeley, California 94720, USA

[3] Department of Materials Science and Engineering, Waseda University, Ohkubo, Shinjuku-ku, Tokyo 169, Japan

[4] Department of Chemistry, Fukuoka University, Nanakuma, Jonan-ku, Fukuoka 814-01, Japan

INTRODUCTION

The valence band x-ray emission and absorption spectra are very useful technique for the studies of valence band structure. The absorption spectra give the information about the unoccupied orbital of valence band structure. K and L x-ray absorption spectra for molecules such as SO_4^{2-},[1)] SF_6 [1),2)] and SiF_4,[3)] where electronegative ligand atoms surround a central atom, show resonance-like bands below and above the ionization threshold and quite weak Rydberg series.The resonance in x-ray absorption spectra has been interpreted through the concept of the effective potential barrier created by surrounding atoms. In this work, S-L x-ray absorption spectra of sulfate compounds have been measured by total electron yield method(T.E.Y.).

EXPERIMENTAL RESULTS

The absorption spectra were measured by used ALS beamline 6.3.2. This beamline is bend magnet beamline and energy range is 50eV-1000eV. Absorption spectra were obtained by collecting total electrons from the sample which has been embedded in indium metal.

S-L absorption spectra of Na_2SO_4, Na_2SO_3, $Na_2S_2O_3$ and $Na_2S_2O_5$ are shown in Fig. 1. As total structure, there is a big absorption peak at about 174eV. This peak is L absorption. The other L absorption peak is at about 182eV. For L absorption peak in high energy side, Na_2SO_4, Na_2SO_3, $Na_2S_2O_3$ and $Na_2S_2O_5$ is the same energy position. S-L absorption spectrum of Na_2SO_4 compare with the other three compounds, it is simple. SO_4^{2-} ion is T_d point group. Therefore, the absorption spectrum of Na_2SO_4 is very simple. The absorption spectrum of Na_2SO_3 is not complexity so well, too. SO_3^{2-} ion is C_{3V} structure. As total structure, the absorption peak is from about 170eV to about 175eV. The S-L absorption spectrum of Na_2SO_3 is complexity a little. $S_2O_3^{2-}$ ion is a molecule which combined SO_3^{2-} ion with another sulfur. One sulfur is electronegative of 2-, another sulfur is electropositive of 6+. The electronegative atom's electron is not influenced by surrounding atoms, but the electropositive atom's electron is influenced by surrounding atoms. Therefore this spectrum is complexity a little. The S-L absorption spectrum of $Na_2S_2O_5$ is shown in Fig. 1. This spectrum is simple, too. The S-L absorption spectra of ZnS, K_2S and NiS is shown in Fig. 2. The absorption spectra of these sulfide is not complexity so well. Because these compound's electron is not influenced so well by metal ion. It is necessary to discuss to analysis of these all spectra.

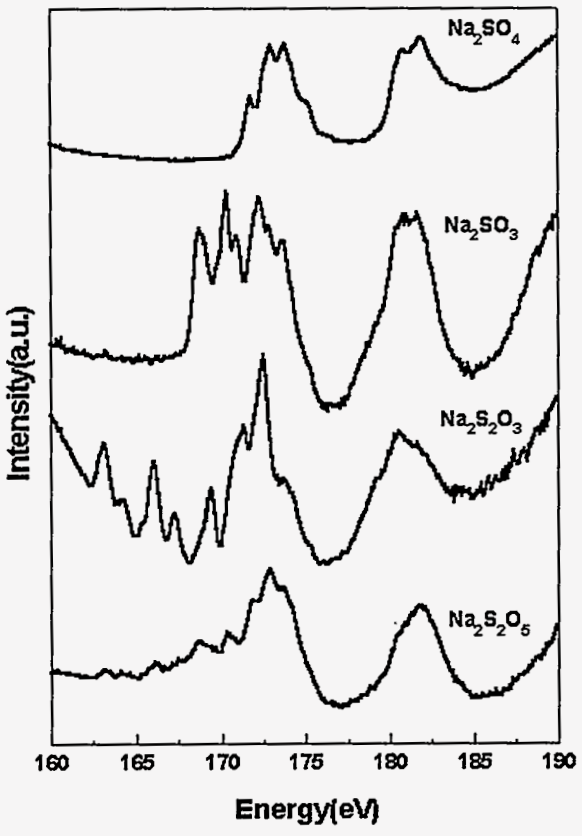

Figure 1. S-L absorption spectra for Na_2SO_4, Na_2SO_3, $Na_2S_2O_3$, and $Na_2S_2O_5$ measured by T.E.Y.

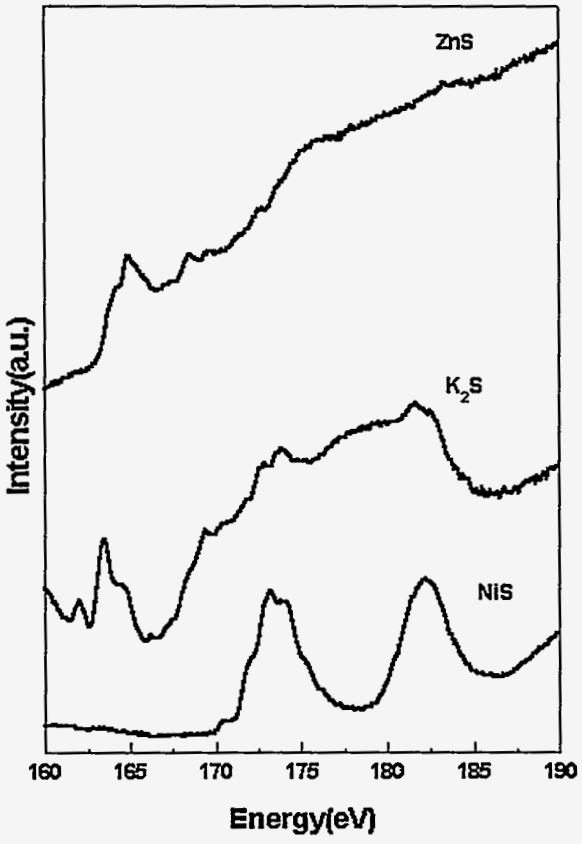

Figure 2. S-L absorption spectra for ZnS, K_2S and NiS measured by T.E.Y.

REFERENCES

1. V. I. Nefedov, V. A. Fomichev : *J. Struct. Chem.*, **9**, 107, 217(1968)
2. A. P. Hitchcock, C. E. Brion : *Chem. Phys.*, **33**, 55(1978)
3. H. Friedrich, B. Pittel, P. Rabe, W. H. E. Schwarz, B. Sonntag : *J. Phys. B*, **13**, 25(1980)

This work was supported by Osaka Electro-Communication University, 18-8 Hatsucho, Neyagawa, Osaka 572, Japan.

Principal investigator : Junichi Tsuji, Division of Electronics and Applied Physics, Osaka Electro-Communication University, 18-8 Hatsucho, Neyagawa, Osaka 572-8530, Japan
Email : m96110@mailserv.isc.osakac.ac.jp, Telephone & FAX : 81-720-25-4690

Beamline 7.0.1 Abstracts

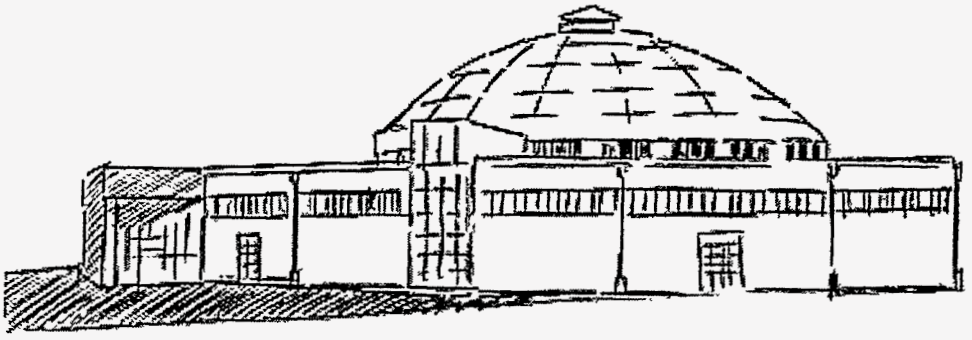

Angle-Resolved Photoemission Study of Galena

E.M. Kneedler[1], S. Banerjee[1], E. Rotenberg[2], and B.P. Tonner[1]
[1]Dept. of Physics and Laboratory for Surface Studies, University of Wisconsin-Milwaukee, P.O. Box 413, Milwaukee, WI 53201, USA
[2]MS 2-400, Advanced Light Source, Lawrence Berkeley Laboratory, Berkeley, CA 94720, USA

INTRODUCTION

The importance of sulfide minerals in environmental issues has been recognized for decades[1], but there has been relatively little study of relevant model systems using surface science techniques[2]. Key issues include mining separation processes, aquifer contamination, and corrosion. Of the sulfides, PbS (galena) is particularly good as a starting point for conventional surface techniques; the (100) surface is easy to prepare by cleavage, and the bulk structure is simply the cubic NaCl lattice. S and Pb reduction can occur under certain aqueous conditions, contaminating (and possibly acidifying) the water, but the surface chemistry is not fully understood. Numerous studies have applied a variety of surface techniques to the PbS system over the last two decades including XPS, and STM in solution[3]. However, surface chemistry on PbS has not been extensively studied by structural techniques, leaving unanswered such fundamental questions as adsorption sites and modifications to substrate surface structure.

We have conducted angle-resolved photoemission (ARP) measurements of the valence bands and core-level emission of vacuum-cleaved natural galena single crystals, as a prelude to detailed studies of the adsorption of molecules from liquids using photoelectron diffraction and high resolution spectroscopy. Our k-space images of the valence bands are particularly useful for comparison with the several theoretical treatments of the PbS system. Other images exhibit a striking example of the relationship between resonant photoemission and an Auger multi-electron process. The synchrotron-based x-ray photoelectron diffraction (XPD) images show considerable fine structure as a function of electron kinetic energy, which will be used to determine the surface structure with high precision by comparison to theoretical simulations.

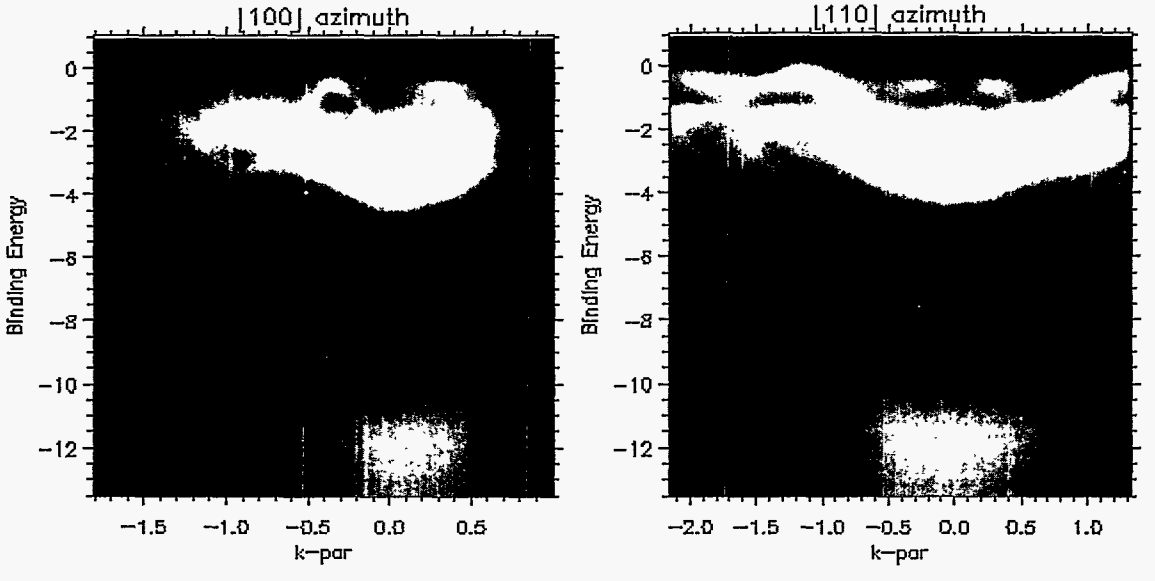

Fig. 1: Valence band spectra of PbS(001) as a function of polar emission angle taken at a photon energy of 100 eV in the [100] (left) and [110] azimuths (right). Data were collected at the UltraEsca endstation on BL7. Images were transformed to k-space coordinates (displayed in units of $Å^{-1}$). The binding energy (in units of eV) is relative to the valence band maximum.

RESULTS

Valence band spectra taken as a function of polar angle in the [100] (left panel) and [110] (right panel) azimuths are displayed in Fig. 1. These ARP images were produced by combining valence band spectra taken for a series of polar angles, then transforming to the corresponding k-space coordinates. The most obvious feature of these data is the PbS band structure, represented in the image as bright bands. The boundary of the first Brillouin zone can be seen in the symmetry of the bands near -1.0 $Å^{-1}$ ([100] azimuth) and -1.5 $Å^{-1}$ ([110] azimuth). In most respects, these results are similar to those of previous experiments[4].

In some previous discussions of PbS valence spectra, a careful distinction was made between those features due to bands and those resulting from density-of-states effects resulting from indirect transitions. Such a distinction can be difficult when viewing individual spectra. In the images of Fig. 1, however, the density-of-states effects are clearly visible as non-dispersive features. In particular, the flat "band" at 0.5 eV and the pronounced step at 1.25 eV binding energies are essentially independent of $\mathbf{k}_{\|}$.

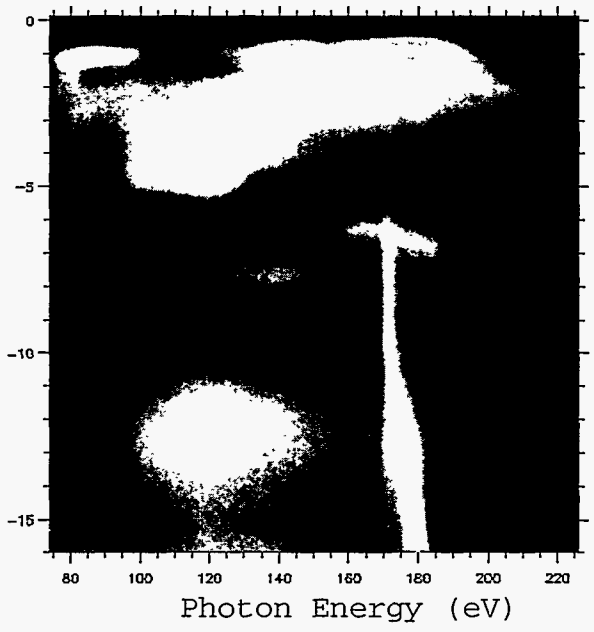

Figure 2: CIS series of raw spectra of normal-emission valence bands of PbS(001). The binding energy (in units of eV) is relative to the valence band maximum.

We have also probed the band structure in the $k_{\perp}$ direction. Figure 2 shows a series of normal emission valence spectra as a function of incident photon energy. If a free-electron approximation can be made about the final state of the photoelectron, this CIS series can be regarded as band map along $k_{\perp}$. This image of raw data will be analyzed in this vein, but in the present form serves to illustrate the dispersion of the valence bands. The density-of-states features discussed above are also evident in this image.

An additional feature of interest in Figure 2 is the significant intensity enhancement seen between 4 and 13 eV binding energy at a photon energy of 162 eV. The photon energy of the resonance is coincident with the measured binding energy of the S2p core level (not shown). According to theoretical calculations, this valence band range is predominantly a mixture of S3p and Pb6s character. These aspects indicate a photoemission resonance, which generally results from transitions between core and valence electronic levels. The image in Figure 3 displays a detailed CIS series in the photon energy region of the

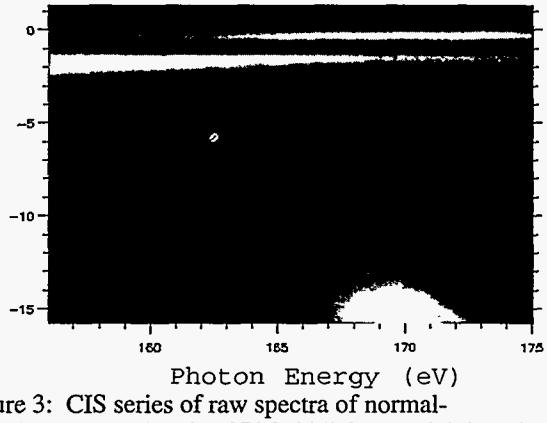

Figure 3: CIS series of raw spectra of normal-emission valence bands of PbS(001) in the vicinity of the S2p photoemission resonance.

resonance. The resonance appears as a doublet (vertical lines near 160 eV in Figure 2), directlycorresponding to the 1.2 eV separation of the S2p core level due to spin-orbit interaction. The prominent feature which "disperses" to lower binding energy for photon energies greater than the resonance is a constant kinetic energy peak due to the S LVV Auger level.

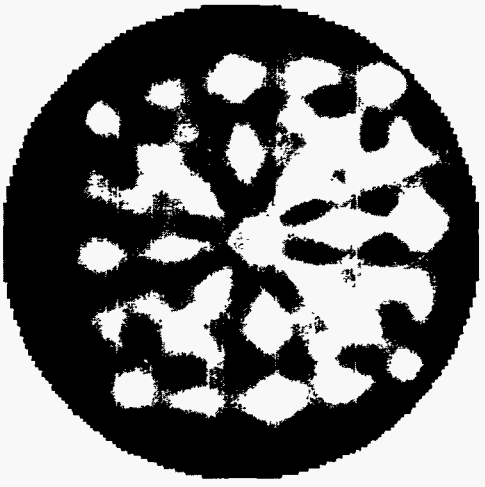

Figure 4: High energy XPD pattern (Al K) of the Pb 4f core-level.

Angle-resolved photoemission at high kinetic energies is dominated by structural effects, and is called x-ray photoelectron diffraction (XPD). We are measuring XPD patterns from galena substrates to understand the diffraction and surface structure of the clean, natural crystals, in preparation for studies of adsorption from liquids. At high kinetic energy, as shown in Figure 4, the XPD pattern of galena shows good fine structure from forward-scattering, correlated with chains of atoms in the bulk crystal structure.

At the ALS, we have the ability to change the outgoing XPD electron wavelength, by tuning the photon energy. We obtained a series of XPD images of the S2p and Pb4f core levels at several photon energies. A selection of these images for the S2p level is displayed in Figure 5. The final-

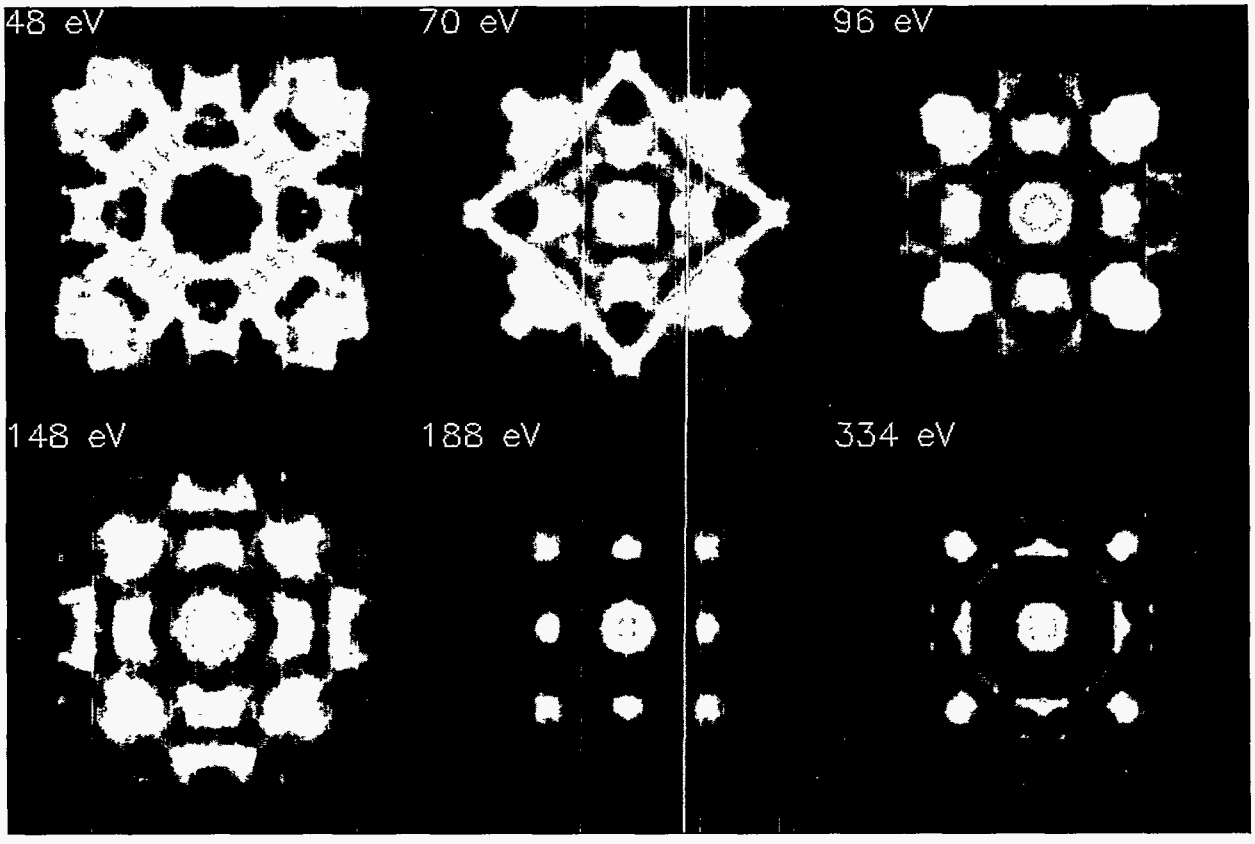

Figure 5: XPD images of the S2p core level of clean PbS(001). Data are plotted such that the radius is linear in polar emission angle, with the [100] azimuth horizontal. Data from a 90° sector were symmetrized by reflection about symmetry axes.

state kinetic energy of the photoelectron is indicated for each image. The high quality of the images indicates good crystal quality and purity. There is a strong variation in diffraction patterns as a function of kinetic energy, which is very sensitive to structural parameters in the theoretical simulations, leading to high precision in bond-length determinations. An additional advantage of low-energy XPD is the high sensitivity to surface atomic structure due to the intrinsic surface sensitivity and strong backscattering effects. Modelling parameters needed for the more complex systems (such as H_2O/PbS) can be established from these initial data.

CONCLUSION

We have studied the clean surface of natural PbS(001) using ARP and XPD. The ARP images are in good agreement with previous studies, although certain aspects such as density-of-states features are more readily apparent as a result of our image displays of the band structure. We have observed an interesting valence-band photoemission resonance related to the S2p core level. Both high and low-energy XPD images show high-quality diffraction patterns, which will be used as a basis for future experiments involving chemisorption of environmentally relevant substances, such as water.

REFERENCES

[1] D. K. Nordstrom and G. Southam, "Geomicrobiology of Sulfide Mineral Oxidation", Reviews in Mineralogy 35 (1997), 361-390.

[2] S. Chaturvedi, R. Katz, J. Guevremont, M. A. A. Schoonen and D. R. Strongin, Amer. Min. 81 (1996), 261.

[3] S. R. Higgins and R. J. Hamers, Geochim. Cosmochim. Acta 60 (1996), 3067-3073.

[4] V. Hinkel, H. Haak, C. Mariani, L.Sorba, K. Horn, and N.E. Christensen, Phys. Rev. B 40 (1989), 5549.

This work was supported by the Department of Energy, OBER, under Grant No. 97ER62474.

Principal investigator: Brian Tonner, Department Of Physics, University of Wisconsin-Milwaukee, Email: tonner@csd.uwm.edu. Telephone: 414-229-4626

Angle resolved photoemission study of Rh(111)

Choong Man Lee[1,2], Eli Rotenberg[2], Stephen, D, Kevan[1]
[1]Department of Physics, University of Oregon, Eugene, OR 97403
[2]Advanced light Source, Lawrence Berkeley Laboratory, Berkeley, CA 94720

I. INTRODUCTION

Transition metal surfaces have been a particular interest caused by their unfilled *d*-band induced phenomena and the importance of catalysts over hydrogenation and reduction reactions[1]. In particular, the late transition metals Pt and Rh are known for active catalysts in environmental science as reducing the exhausts, NO_x and CO. In metal surfaces, the 2-dimensional (2-D) Fermi contours have been increasingly interested because they play an important role on the electron-phonon interactions. It may be helpful to understand the surface electronic structure and electron-phonon interaction on Rh(111) surface. And it will help further understand on a catalytic behavior of transition metal surface, which is known for dominantly the charge transfer to the adsorbed reactive gas molecule.

II. RESULTS AND DISCUSSION

We focused on the observation of 2-D Fermi contours and determination of the k_F value. Fig.1 shows a typical ARP spectra collected from the clean Rh(111) and NO/Rh(111) surface along the $\overline{\Gamma K}$ symmetry line in the SBZ on Rh(111) surface. The photon energy is $h\nu$= 90 eV. So the free electron final state approximation is proper[2]. The range of surface parallel momentum of initial state is k = 0 ~ 2.0 $Å^{-1}$, which contains hexagonal first SBZ of Rh(111) with $\overline{K}$= 1.55 $Å^{-1}$ and $\overline{M}$=1.35 $Å^{-1}$.

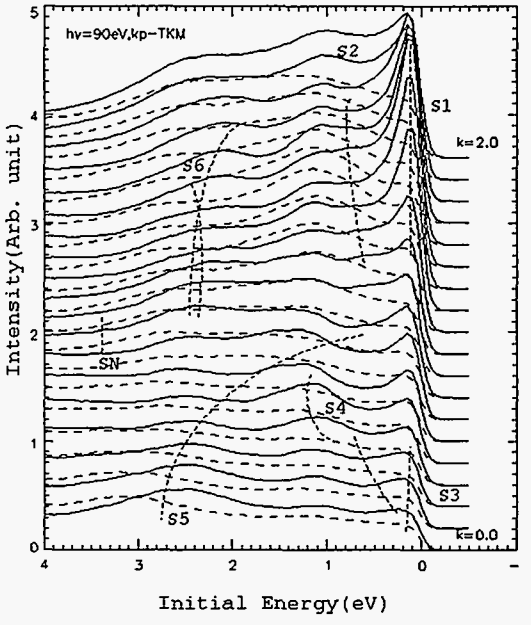

Fig. 1 ARP spectra of clean (solid curves) and NO-covered(dashed curves) Rh(111) collected along the azimuth $\overline{\Gamma K}$ at photon energy $h\nu$= 90 eV.

Three surface states of clean Rh(111) surface were identified near the Fermi level within 1 eV by crude test with NO adsorption in Fig. 1. The first is an intrinsic surface state located at binding energy 0.2 eV below E_F and shows almost no dispersion around $\overline{K}$. This state is labeled S1, and it is very similar to the one of Pt(111). The second is a large *sp* - disperse one labeled S5. This is a surface resonance and it has asymmetry between two $\overline{\Gamma M}$ symmetry lines, which is due to the bulk property. The third has a small dispersion near labeled S3 with binding energy 0.3 eV which shows low intensity and is hard to be distinguished clearly. One can see diffusive Fermi contours of Rh(111) made of six - triangular electron pockets centered at $\overline{K}$ and a small asymmetric-hexagon centered at $\overline{\Gamma}$ in Fig. 2. The features are so similar to the ones of Pt(111)[3]. This image was constructed by the interpolated normalized ARP spectra from the partial portion of the first SBZ area.

Fig. 2 shows dark semi-hexagon with low intensities near the point and bright triangles with high intensities at the zone boundary of SBZ. It consists of Γ5 dominant *d*-band electron pocket, Γ6 closed *sp*-band dispersion[4], *d*-band like X3, X4 hole pockets, and small hole pocket L*A*. So electron pocket has large Fermi velocity and free-electron like density. It means lower photoemission probability and resulting intensity of the hexagonal area than that of near the zone boundary. Since Γ5 sheet is composed of open *d*-band dominantly and locates near zone boundary, its strong intensity is reasonably assumed due to the localized *d*-band character at zone boundary and triangle electron pocket. The intensity of surface resonance about k = 0.8 Å^{-1} abruptly increased and it shows asymmetry. Thus the expected hexagon is distorted by bulk electronic structure. On the other hand, the diffusing triangle is composed of the *d*-band surface states, so it shows very flatness. It is possible to suppose that the valence band of Rh is very similar to that of Pt. It's right to assign the guess based from the paper of Rh(111) surface states. The predicted hole pocket by the rigid band property of Rh near $\overline{M}$ was not observed.

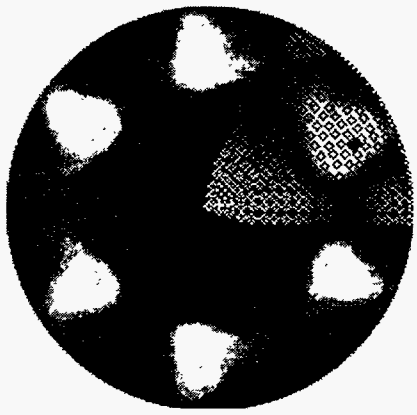

Fig. 2 Fermi edge of clean Rh(111).

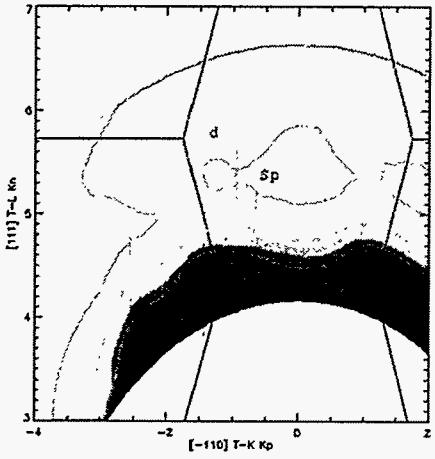

Fig. 3 ARP spectra of constant initial state mode(CIS) for the Fermi level crossing states on Rh(111) along the azimuth $\overline{\Gamma K}$ at photon energy $h\nu$ = 77 eV–210 eV

Fig. 3 shows $k_\perp$ dependence of surface Fermi contours on the high symmetry line of the SBZ. These arcs are the interpolation diagrams of states cross over Fermi edge. It measured ranging from k = 4.0 Å^{-1} to k = 7.0 Å^{-1} and Δk= 0.2 Å^{-1}. The solid line is the zone boundary of Rh bulk normal to the (111) orientation. If a surface state is an intrinsic, it doesn't depend on $k_\perp$. So it represents as a straight-line strip parallel to the $k_\perp$ axis as in Fig. 3. There are two very bright area k = 4.0 Å^{-1} and $\overline{K}$ = 1.55 Å^{-1}, $\overline{M}$ = 1.35 Å^{-1} respectively near the zone boundary at crossing area. We can find *sp*-band that forms a curvature from midpoint about 0.7 Å^{-1} to 0.9Å^{-1}. The surface resonance consisting of hexagonal electron pocket near zone center looks much nested even if it is free electron-like *sp*-band Γ6. Additionally weak strip footprints independent on k were observed at k = 0.2 Å^{-1} zone center and zone boundary. These are caused by the *d*-band surface states as reported in the previous theoretical calculation where a surface state near the zone center was flat band. This *d*-band shows wide hill parallel to the k axis. The large wide dark part of arc plane is due to Cooper minimum of Rh, about $h\nu$= 140 eV. From above we determine the 2-D Fermi contours of Rh(111). The hexagonal electron pocket crosses at k = 0.8 Å^{-1} on symmetry line and at k = 0.7 Å^{-1} on symmetry line. The triangular electron pocket crosses at k = 1.1 Å^{-1} on symmetry line. And hole pocket was not observed. But there remains an uncertainty of the k value for the boundary, as much as Δk = 0.1 Å^{-1}. This may be caused by the hybridization of

d-bands and *sp*-bands on the Fermi surface. It was also observed asymmetry on the $\overline{M}$ point. This is evidence of Rh(111) has fine edge.

III . CONCLUSION

The primary focus of this paper has been the mapping of 2-D Fermi contours on clean Rh(111) with ARPES experiment. Resultant 2-D Fermi contours are much similar to the ones of Pt(111) except the smaller hexagonal electron pocket size. And the flatness of triangular electron pocket is also observed. This flatness of Fermi contours induced by *d*-band and the hybridization of *sp* and *d* band relates the phonon softening of the metal. If Kohn anomaly is observed on Rh(111), it occurs at the twice of observed k_F.

ACKNOWLEDGMENT

This work was supported by the 97 post-Doc. program of Korean Research Foundation.

REFERENCES

1. H. L. Bonzel and J. H. Krebs, Surf. Sci. **91**, 499(1980).
2. P. Thiry, Ph. D Thesis, Université Pierre et Marie Curie (1979).
3. Wei Di ., Kevin E. Smith,and Stephen Kevan, Phys. Rev. **B 43**, 4,12062(1991).
4. O. K. Andersen and A. R. Mackintosh, Solid State Comm. **6**, 285 (1968).

Principal investigator: Stephen D. Kevan, University of Oregon. Email: kevan@oregon.uoregon.edu.

Angle-Resolved Photoemission Study of the Electronic Structures of $AuAl_2$ and $PtGa_2$

L.-S. Hsu,[1] J.D. Denlinger,[2] G-H. Gweon,[2] and J.W. Allen[2]
[1]Department of Physics, National Chang-Hua University of Education, Chung-Hua 50058, Taiwan, R.O.C.
[2]Randall laboratory, University of Michigan, Ann Arbor, Michigan 48109-1120, USA

INTRODUCTION

$AuAl_2$ and $PtGa_2$ are intermetallic compounds of both technological and scientific importance. The former has potential applications as a selective solar absorber [1], and the latter was proposed to be used as a thermodynamically stable conducting contact to GaAs [2]. They both crystallize in the fluorite structure, and superconduct at low temperatures [3]. They are also prototype materials for studying the Au and Pt 5d bands in intermetallic compounds, since group-III metals contribute only s-p states to the valence band (VB). The purple and gold colors of $AuAl_2$ and $PtGa_2$, respectively, also strongly motivated researchers to study the electronic structures of these two compounds. Many electronic and physical properties of these two compounds have been measured, and a majority of these works was recently reviewed by Hsu [3]. However, no angle-resolved photoemission study of these two materials has been reported so far. This paper will focus on just such a study.

EXPERIMENTS

Procedures for preparation of the (100) and (111) faces of $AuAl_2$ and the (111) face of $PtGa_2$ were the same as those reported in a previous paper [4]. Experiments were carried out on beam line 7.0 at the Advanced Light Source. Photon energies in the range of 80 to 220 eV were selected with a low spherical grating monochromator, and a Perkin-Elmer 137-mm hemispherical analyzer was used in the fixed-analyzer-transmission mode to collect photoemission spectra. With 900 lines/mm for grating setting and 3 eV for analyzer pass-energy setting, the energy resolution of the photons plus the electrons was 0.15 eV as estimated from the sharpness of the Fermi edge of the VB photoemission spectra. The pressure during the measurement was $2x10^{-10}$ Torr. The vacuum chamber was also equipped with a double-anode (Al and Mg) x-ray source for x-ray photoemisssion spectroscopy (XPS) and x-ray photoelectron diffraction (XPD) measurements, and with a low-energy electron diffraction (LEED) system.

The samples were cleaned by repeated cycles of sputtering with Ar ions and annealing to 500°C until XPS spectra showed no traces of O or C contamination on the sample surfaces. The observed XPD and LEED patterns also confirmed the cleanliness and ordering of the respective surfaces.

RESULTS AND DISCUSSION

Figs. 1 and 2 show a set of VB photoemission spectra from the (100) and (111) faces, respectively, of $AuAl_2$, and Fig. 3 shows that from the (111) face of $PtGa_2$ at normal emission. The photon energy ($h\nu$) was varied so as to probe the third to the fourth Brillouin zone (BZ) for the (100) face, and the fourth to the fifth BZ for the (111) face. The Fermi energy (E_F) was assigned at half height on the onset of a plateau, which is caused by photoemission from the Au or Pt s-p band. In general, the s-p bands disperse much more rapidly than the d bands, which accounts for the differing relative widths of the features seen in the photoemission spectra. For $PtGa_2$, there is a three-peak structure at higher binding energy (E_B) with mainly Pt 5d character. The crystal-field and spin-orbit parameters of $PtGa_2$ were determined to be 0.90 and 0.56 eV, respectively, in the same manner as was done in Ref. [4]. We note that the E_B values at the three

Γ points (at approximately hν=110 or 220 eV) for $PtGa_2$ are 3.40, 4.35, and 5.45 eV, which are essentially the same as those obtained from the density-of-states (DOS) features in the angle-integrated photoemission spectra [4]. This means that the Pt 5d bands in $PtGa_2$ are well localized and do not disperse more than 0.3 eV. We should also point out that these E_B values are within 10% of the corresponding values for elemental Au [5], which explains why $PtGa_2$ is gold-colored.

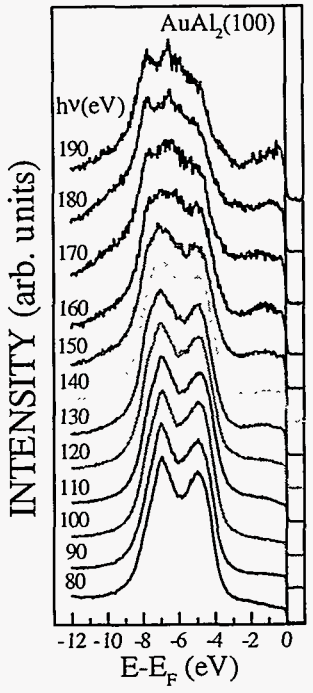

Figure 1. Angle-resolved photoemission spectra from the (100) face of $AuAl_2$ taken at normal emission.

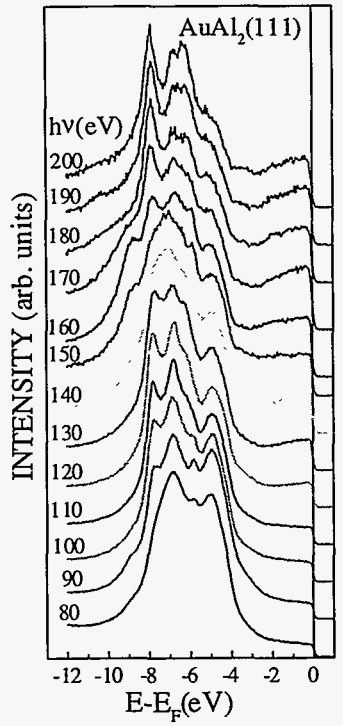

Figure 2. Angle-resolved photoemission spectra from the (111) face of $AuAl_2$ taken at normal emission.

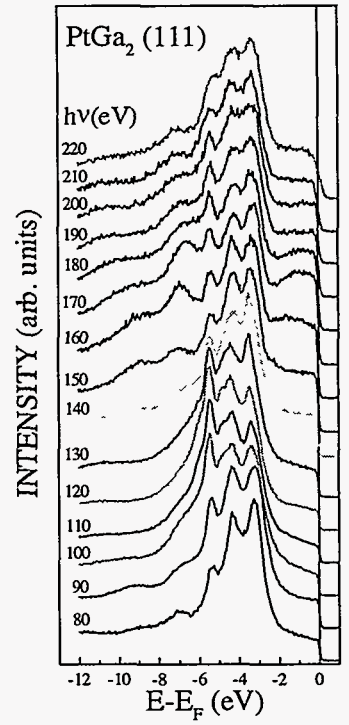

Figure 3. Angle-resolved photoemission spectra from the (111) face of $PtGa_2$ taken at normal emission.

By using a direct-transition model and assuming a free-electron conduction-band structure [6], the E vs. k curves can be plotted. The values of the inner potential used for $AuAl_2$ and $PtGa_2$ were estimated to be 12.1 and 10.8 eV, respectively. These values were taken to be the differences between the muffin-tin zeros of energy in the augmented-plane-wave calculations [7,8] and the vacuum level as determined from the work functions of the two compounds. In Fig. 4, the experimentally derived bands of $AuAl_2$ are compared with the bands obtained from a nonrelativistic band-structure calculation [7], while in Fig. 5, those of $PtGa_2$ are compared with the bands obtained from a semi-relativistic band-structure calculation [8]. The agreement between experiment and theory is very poor for $AuAl_2$, but rather good for $PtGa_2$, which indicates that the spin-orbit effect is important in calculating the band structures of these materials. The experimental band for $PtGa_2$ at roughly E_B=7 eV (indicated by diamonds in Fig. 5) probably involves the one-dimensional DOS effect [9], while that at roughly E_B=4.7 eV (indicated by squares in Fig. 5) probably involves a surface state.

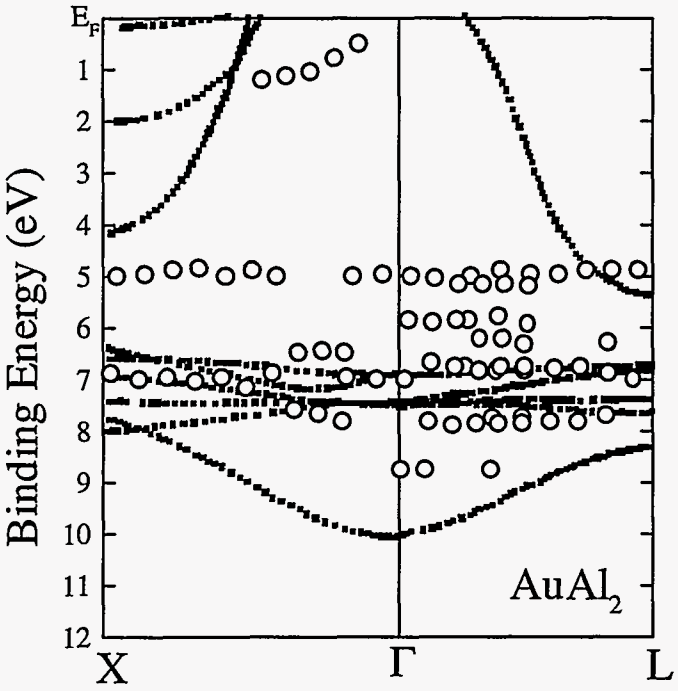

Figure 4. Band structure of $AuAl_2$ along X- Γ- L. Open circles are experimental dispersion curves.

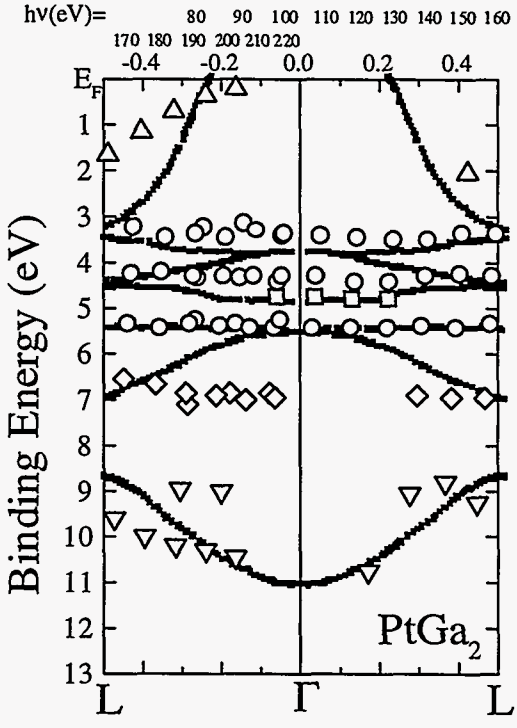

Figure 5. Band structure of $PtGa_2$ along Γ- L. Open circles, squares, diamonds, and triangles are experimental dispersion curves.

ACKNOWLEDGMENTS

We thank R.J. Baughman and R.S. Williams for supplying the samples.

REFERENCES

1. R.E. Hahn and B.O. Seraphin, Phys. Thin Films **10**, 1 (1978).
2. Y.K. Kim, D.A. Baugh, D.K. Shuh, R.S. Williams, L.P. Sadwick, and K.L. Wang, J. Mater. Res. **5**, 2139 (1990).
3. L.-S. Hsu, Mod. Phys. Lett. B **8**, 1297 (1994), and references therein.
4. L.-S. Hsu and K.-L. Tsang, Phys. Rev. B **56**, 6615 (1997).
5. K.A. Mills, R.F. Davis, S.D. Kevan, G. Thornton, and D.A. Shirley, Phys. Rev. B **22**, 581 (1980).
6. J.G. Nelson, W.J.Gignac, S. Kim, J.R. Lince, and R.S. Williams, Phys. Rev. B **31**, 3469 (1985).
7. A.C. Switendick and A. Narath, Phys. Rev. Lett. **22**, 1423 (1969).
8. K.J. Kim, B.N. Harmon, L.-Y. Chen, and D.W. Lynch, Phys. Rev. B **42**, 8813 (1990).
9. T. Grandke, L.Ley, and M. Cardona, Phys. Rev. B **18**, 3847 (1978).

This work was supported by the National Science Council, Taiwan, R.O.C., the U.S. Department of Energy under Contract No. DE-FG-02-90ER45416, and the U.S. National Science Foundation under Contract No. DMR-94-23741.

Principal investigator: Li-Shing Hsu, Department of Physics, National Chang-Hua University of Education, Chung-Hua 50058, Taiwan, R.O.C. Email: hsu@kondo.physics.lsa.umich.edu.

Assigning x-ray absorption spectra by means of soft x-ray emission spectroscopy

K. Gunnelin[1], P. Glans[2], P. Skytt[1], J.-H. Guo[1], J. Nordgren[1], and H. Ågren[3]
[1]Department of Physics, Uppsala University, Box 530, S-75121 Uppsala, Sweden
[2]Atomic Physics, Physics Department, Stockholm University, Frescativägen 24, 10405 Stockholm, Sweden
[3]Institute of Physics and Measurement Technology, Linköping University, S-58183, Linköping, Sweden

INTRODUCTION

X-ray absorption spectroscopy and electron-energy-loss spectroscopy are powerful techniques for obtaining information about the unoccupied orbitals of various systems. Yet, there are still uncertainties regarding the assignment of some absorption spectra, even those of some small molecules. Therefore, there is a need for a technique that can provide additional information in those cases. Here a simple method to distinguish between orbitals of different parity and spatial symmetry, using x-ray emission spectroscopy, is presented. To illustrate the usefulness of the method it is applied to the much debated Rydberg transitions in the x-ray absorption spectrum of CO_2.

SYMMETRY ASSIGNMENTS

I. Parity

According to the parity selection rule, the parities of the initial and the final states of a one-photon process have to be different. Thus, in a two-photon process the parities have to be the same. For the parity of the final state of the emission to be the same as that of the initial ground state, the electron filling the core hole has to come from an orbital of the same parity as the one to which the core electron was promoted.

This rule is valid for dipole transitions in homonuclear diatomics, where there is only one, totally symmetric, vibrational mode [1,2]. However, in polyatomic molecules vibrational modes of ungerade symmetry can couple nearly degenerate core-excited electronic states of different parity, thereby reducing the molecular symmetry. In this way parity-forbidden electronic transitions can borrow intensity of parity-allowed ones [3]. The intensity of a "forbidden" transition depends on the strength of the vibronic coupling and on the lifetime of the intermediate state relative to the period of vibration. If the parameters are such that the symmetry is completely broken, the intensity is the same as that of the corresponding transition in the nonresonantly excited molecule. In the general case the intensity of a "forbidden" transition is, however, lower than that of the corresponding transition following nonresonant excitation. The parity selection rule can therefore be thought of as a "propensity rule". This rule can be utilized to determine the parity of unknown absorption features. If there are two (or more) well-separated features in the emission spectra, each feature corresponding to electrons from either gerade or ungerade orbitals filling the core hole, then an intensity ratio of a "gerade feature" to an "ungerade feature" can be obtained. Comparing this ratio to the ratio of the corresponding transitions for nonresonant excitation will tell which transition is allowed and which is forbidden in the resonant case. From this information the parity of the unoccupied orbital can be deduced.

II. Spatial symmetry

When linearly polarized light is used for resonant excitation, the distribution of the emitted light is in general anisotropic. It depends on the spatial symmetries of the initial and final states. Therefore, it is possible to obtain spatial symmetry information by measuring the angular distribution of the

emitted photons. It is possible to make quantitative predictions of the angular distributions of the x-ray emission peaks [4]. The distributions can be accurately modeled for diatomic molecules, as a recent study of CO shows [5]. However, for polyatomic molecules vibronic coupling and the large number of close-lying final states make a quantitative analysis of x-ray emission spectra complicated. Because of these complications a simplified "two-step" model will be used to describe the angular distributions in a qualitative way.

Let us restrict the discussion, for simplicity, to linear molecules and *K*-shell resonant x-ray emission spectra. Then the absorption strength of a core excitation to an unoccupied orbital is determined by the local atomic *p*-type character of the orbital according to the one-center model [6]. For excitation to σ (p_z) orbitals the absorption rate is largest if the polarization vector ε_{in} is parallel to the molecular axis and, thus, the smaller the angle between the molecular axis and ε_{in} the more likely it is that the molecule gets core-excited. For excitation to a π (p_x, p_y) orbital the absorption rate is largest when the molecular axis is perpendicular to ε_{in}. In other words, an aligned ensemble of core-excited molecules is created by the linearly polarized photons and the preferential orientation of those molecules depends on the spatial symmetry of the unoccupied orbital.

The core-excited molecules may then decay by emitting x-ray photons. It should be noted that the lifetime of the core-excited molecules is much shorter than any rotational motion and the molecular axis can therefore be assumed to be frozen during the absorption-emission process. If a valence electron from a σ orbital fills the core hole the photons are mostly emitted perpendicular to the molecular axis with their polarization vector ε_{out} parallel to the molecular axis, whereas a transition from a π orbital gives maximum emission intensity parallel to the molecular axis.

Occupied orbital	Unoccupied orbital	Maximum emission intensity at
σ	σ	90°
	π	0°
π	π	90°
	σ	0°

In Table I we summarize in what direction we expect maximum intensity for different combinations of unoccupied and occupied orbitals. Using Table I and measuring how the relative intensities of the σ and π emission peaks change going from θ=0° to θ=90° the spatial symmetry of the unoccupied orbital can be obtained.

APPLICATION TO CO_2

The near-edge part of the O *K* x-ray absorption spectrum of CO_2 is shown in the lower part of Fig. 1. In order to study the absorption spectrum we have recorded x-ray emission spectra at two angles (θ=0° and θ=90°) for seven different excitation energies, five below the ionization threshold and two above. The arrows in Fig. 1 indicate the energy positions at which the x-ray emission spectra were recorded. The XES spectra are shown in Fig. 2. All the emission spectra show a high-energy feature and a low-energy feature. The upper part of Fig. 1 shows the intensity ratios of the high-energy to low-energy features, obtained from the emission spectra recorded at the corresponding excitation energies. The dashed line is the estimated intensity ratio in the case of an isotropic angular distribution and no parity selectivity, obtained as the average value of the experimental ratios from the spectra recorded at the energy position D, which is above the ionization threshold and the σ_g* shape resonance but below the shake-up transitions and the σ_u* shape resonance.

The intensity ratios presented in the upper part of Fig. 1 might be used to assign the symmetries of the absorption features A, B, and C. To do this we use our knowledge about the emission spectrum. Apart from a participator peak present in four of the emission spectra in Fig. 2, they consist of two main features caused by transitions involving the four outermost valence orbitals [7]. The high energy feature is due to an electron from the $1\pi_g$ orbital filling the core hole. The low-energy feature consists of three vibrationally and instrumentally broadened and overlapping peaks, $4\sigma_g$, $3\sigma_u$, and $1\pi_u$. In comparison to the other two, $4\sigma_g$ is small.

To determine the parities of the unoccupied orbitals we note that the high-energy feature is due to an occupied orbital of gerade parity, whereas the low-energy feature is mainly due to orbitals of ungerade parity. From the discussion above we expect the intensity ratios in Fig. 1 to be well above the value given by the dashed line if the excitation is to a gerade unoccupied orbital and well below the line if the unoccupied orbital has ungerade parity. It is clear from the figure that for both recording angles the ratios are below the dashed line at absorption peak A whereas the ratios are above the line at the other two features, B and C. The data, thus, indicate that peaks A, B, and C are due to unoccupied orbitals of ungerade, gerade, and gerade parities, respectively. The first assignment is in accordance with the fact that mainly the $2\pi_u$ resonance contributes to peak A.

The high-energy feature in the emission spectra is due to an occupied π orbital ($1\pi_g$) whereas the low-energy feature is due to occupied orbitals of both σ ($3\sigma_u$, $4\sigma_g$) and π ($1\pi_u$) symmetry, with the σ contribution on the low-energy side of the feature. The fact that the spatial symmetry character of the two emission features is different can be used to obtain the spatial symmetries of the unoccupied orbitals, as described above. To do that we consider how the intensity ratios in the upper part of Fig. 1 vary with the angle θ.

At absorption features B and C the intensity ratios are clearly different at the two angles. At both energies the ratios are smaller in the θ=90° spectra. Furthermore, it can be observed in Fig. 2 that the spectra primarily are different at the low-energy side of the low-energy feature. Since this side corresponds to σ emission peaks, the lower ratios at θ=90° are due to that the relative intensities of the σ peaks are larger at this angle. From these results and Table 1 it can be concluded that the absorption features B and C are mainly due to unoccupied orbitals of σ symmetry.

Calculations have been carried out to further test the validity of this method. The so called static exchange approach has been used to calculate the absorption spectra, and the results support our experimental findings. A complete description of this method for symmetry assignments and the analysis, briefly described in this report, can be found in ref. [8].

CONCLUSION

We can conclude that the experimental results and the assignments from the calculations agree well, giving more weight to the combined result. The symmetry of the transitions can thus be summarized as follows: The first absorption peak is dominated by an intense transition to the $2\pi_u$ orbital. The calculations give that the first Rydberg resonance, of σ_g symmetry, should appear on the high-energy side of the first absorption peak with about 1/15 intensity of the $2\pi_u$ resonance. At higher energy two groups of transitions are found below the ionization threshold. The experimental and calculated results show that these are predominantly due to excitations to σ_g orbitals. The results indicate a considerable valence-Rydberg mixing in the discrete region of the O *K* x-ray absorption spectrum of CO_2 similar to what is found for the O_2 molecule.

REFERENCES

1. P. Glans, K. Gunnelin, P. Skytt, J.-H. Guo, N. Wassdahl, J. Nordgren, H. Ågren, F.Kh. Gel'mukhanov, T. Warwick, and E. Rotenberg, Phys. Rev. Lett. **76**, 2448 (1996).
2. P. Glans, P. Skytt, K. Gunnelin, J.-H. Guo, and J. Nordgren, J. Electron Spectrosc. Rel. Phenom. **82**, 193 (1996).
3. L.S. Cederbaum, J. Chem. Phys. **103**, 562 (1995).
4. Y. Luo, H. Ågren, and F.Kh. Gel'mukhanov, Phys. Rev. A **53**, 1340 (1996).
5. P. Skytt, P. Glans, K. Gunnelin, J.-H. Guo, J. Nordgren, Y. Lou, and H. Ågren, Phys. Rev. A **55**, 134 (1997).
6. R. Manne, J. Chem. Phys. **52**, 5733 (1970).
7. J. Nordgren, et. al., J. Chem. Phys. **76**, 3928 (1982).
8. K. Gunnelin, P. Glans, P. Skytt, J.-H. Guo, J. Nordgren, and H. Ågren, Phys. Rev. A **57**, 864 (1998)

The experiments were performed at the ALS of Lawrence Berkeley National Laboratory operated by DOE under contract No. DE-AC03-76SF00098.

Principal investigator: Joseph Nordgren, Department of Physics, Uppsala University, Sweden. Email: joseph.nordgren@fysik.uu.se. Telephone:+46 18 4713554.

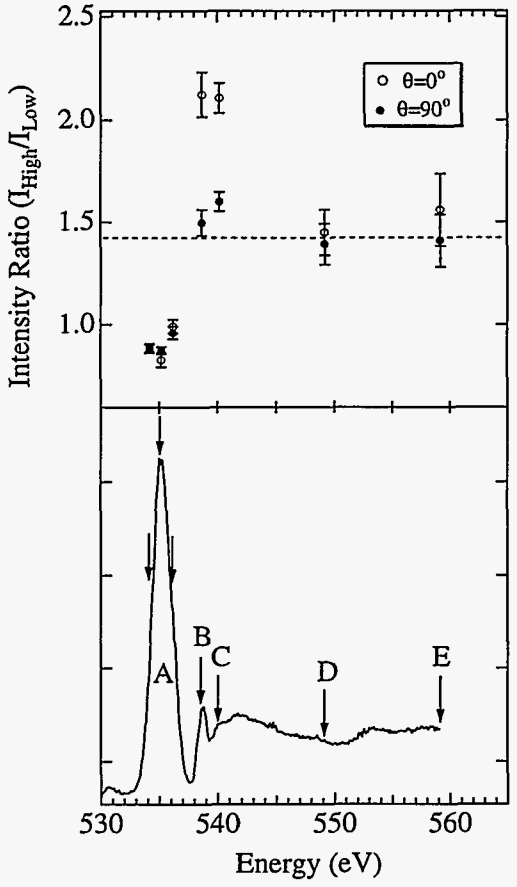

Figure 1. (bottom) X-ray absorption spectrum with arrows indicating at what excitation energies resonant x-ray emission spectra were recorded. (top) Intensity ratios between the high-energy peak (due to $1\pi_g$) and the low-energy peak (due to $1\pi_u$, $3\sigma_u$, and $4\sigma_g$) in x-ray emission spectra recorded at θ=0° and θ=90°.

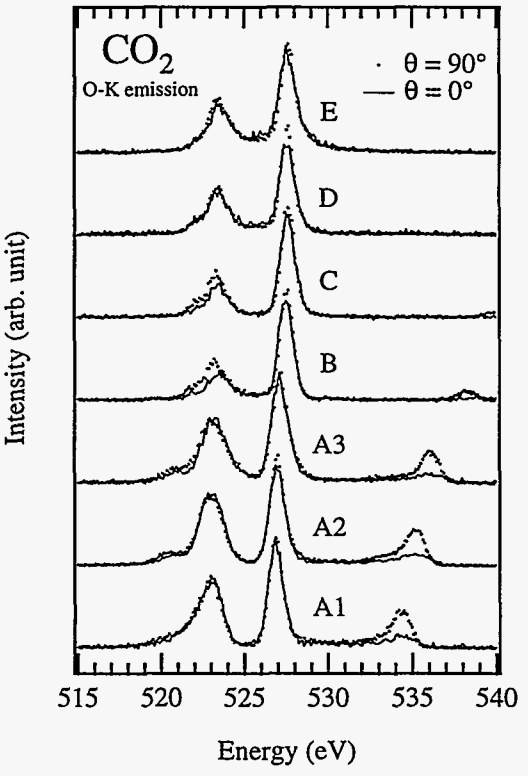

Figure 2. Resonant O *K* x-ray emission spectra excited at energy positions indicated in Fig. 1, detected perpendicular (θ=90°) and parallel (θ=0°) to the polarization vector of the exciting radiation.

Bond Formation at the Alkali-Metal/Metal Interface

Eli Rotenberg[1] and S. D. Kevan[2]

[1] Advanced Light Source, Ernest Orlando Lawrence Berkeley National Laboratory,Berkeley CA 94720
[2]Department of Physics, University of Oregon, Eugene OR 97403

Alkali metal growth on transition metals has very important applications in catalysis. Yet the interaction between isolated alkali metal atoms and metallic substrates is not completely understood, even without the complications of interactions between alkali atoms or alkali/gas molecules on these surfaces. For example, since the introduction of the Langmuir-Gurney model (LG) in 1935, the explanation of the large work function shift for metal substrates when covered by submonolayers of Alkali Metals (AM) was thought to be well understood in terms of a simple charge-transfer picture: at low coverages the AM donates its lone *s*-electron to the substrate, creating a large surface dipole layer, which lowers the work function. As coverage increases towards one monolayer (ML), the AM atoms interact, and the resulting dipole-dipole repulsion drives a charge transfer back from the substrate to the alkali *s*-level, a process called back-donation. This back-donation is thought to account for the characteristic minimum in the work function followed by recovery with higher coverage.

While providing a satisfactory explanation of experiment for over 50 years, this model has recently come under question from both experimental and theoretical work. While there is concensus that the work function change is due to a net surface dipole, the issue becomes: where is the dipole located? If the dipole is due to a complete charge transfer from the AM to the substrate, the AM is left with an unoccupied *s* valence level at low coverage, which becomes occupied at higher coverages. If, on the other hand, the dipole is localized withing the AM atom, there should be an occupied *s*-derived valence state observable at all coverages. A clear signature for *s*-derived valence band features has been lacking (at least for growth on transition metals), however, due to the presence of substrate *d*-bands.

To clarify these issues, we undertook a detailed study of the growth of Li on Mo(110) surface. The data were acquired using undulator-generated soft x-rays at beamline 7.0 of the ALS. By measuring the valence bands, work function, and Auger decay cross section as a function of coverage up to a monolayer of Li on Mo(110), we directly deduce the relative population of AM valence *s*-orbital *vs.* coverage. To first order, the LG model seems to be vindicated, although important questions remain.

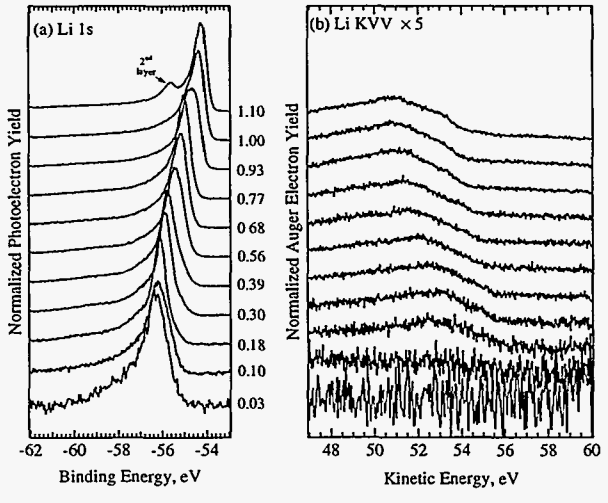

Fig. 1. (a) Core level and (b) Auger decay spectra as a function of Li coverage on Mo(110). The numbers in (a) indicate the approximate Li coverage in ML. The data are shown normalized to Li 1*s* intensity, in order that the Auger intensity is normalized per Li atom.

Fig. 1(a) shows a series of Li 1*s* core-level spectra as a function of Li coverage. The data have been normalized to Li 1*s* area, which is proportional to the number of Li atoms deposited. In (b) we show an additional peak,whose kinetic energy is independent of photon energy, which we identify as Li KVV (core - valence - valence) Auger

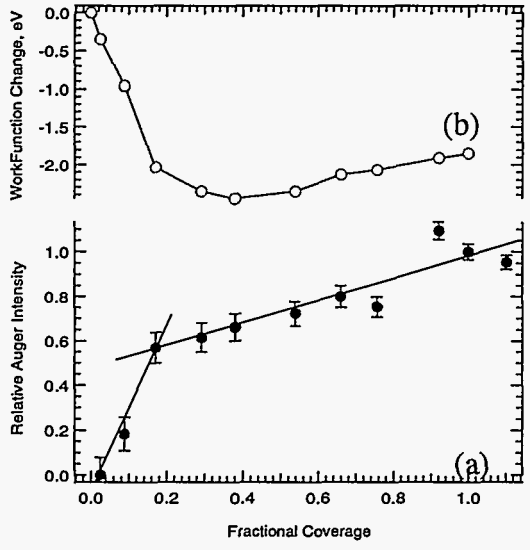

Fig. 2. (a) Normalized Auger yield per Li atom and (b) workfunction change as a function of Li coverage on Mo (110).

decay, and which we also show normalized to Li coverage. Clearly, the relative yield of this emission varies dramatically with coverage. Fig 2(a) shows how the Auger yield per Li atom varies with coverage. For comparison, the change in workfunction with coverage is shown in fig. 2(b). Since the Auger yield depends on occupation of the Li 2s level,our data gives a direct measure of the charge state of the Li atom. Hence, it would seem that the LG model is quite compatible with our data: while at low coverage, the 2s level is unoccupied (charge has transferred to the substrate), as the coverage increases, Li 2s valence states become occupied as charge is donated from the substrate back to the Li atom

We have also measured the valence bands as a function of growth, which gives independent confirmation of this picture. In fig. 3(a), we show angle-resolved valence band photoemission for the clean surface. The bands marked "*d*" are substrate *d*-like surface states. Fig. 3(b) shows that at 1 ML coverage, the *d*-states have moved significantly down in energy, due to the change in potential at the interface. In addition, a weak, broad band labeled "*s*" is observed. We identify this band with the Li 2*s* states, whose excitation in the presence of the Li 1*s* core hole accounts for the Auger decay intensity discussed above. For intermediate coverages, between clean and 1 ML, the *s*-level is observed to pass down from above the Fermi level. In fact, the first appearance of this band exactly coincides with the appearance of the Auger decay.

Significant questions remain, however, suggesting our interpretation is incomplete. First, the formation of the auger decay peak is essentially complete well before the minimum in the workfunction. Second, the width of the auger peak is significantly wider than the *s*- band we observe in fig. 3(b), suggesting a more atomic-like multiplet final state inconsistent with the band interpretation. Third, an alternate explanation of the Auger behavior is a transition from localized to delocalized Li 2*s* bands, which may be entirely unrelated to charge transfer to the substrate. We are currently working to further understand these issues.

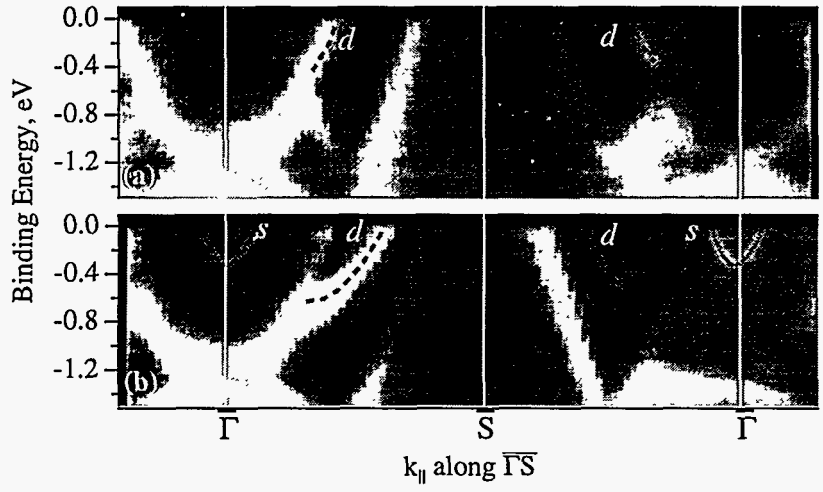

Fig. 3. Bandmaps for (a) clean and (b) 1 ML Li on Mo (110). The surface states *s* and *d* are assigned to Li 2*s*-like and Mo 4*d*-like states, respectively.

This work was supported by the U.S. Department of Energy under contract No. DE-FG06-86ER45275.

Principal investigator: Steve Kevan, Department of Physics, University of Oregon. Email: kevan@oregon.uoregon.edu.

Development of Scanning X-ray Microscopes for Materials Science Spectromicroscopy at the Advanced Light Source

T. Warwick[1], H. Ade[2], S. Cerasari[1,3], J. Denlinger[4], K. Franck[1], A. Garcia[1,2], S. Hayakawa[5], A. Hitchcock[6], J. Kikuma[7], S. Klingler[1], J. Kortright[1], G. Morisson[1], M. Moronne[1], E. Rightor[8], E. Rotenberg[1], S. Seal[1], H-J. Shin[1,9], W.F. Steele[1] and B.P. Tonner[10]

[1]Lawrence Berkeley National Lab., University of California, Berkeley, California, USA.

[2]Dept. of Physics, North Carolina State University, Raleigh, North Carolina, USA.

[3]Universita di Trieste, Trieste, Italy.

[4]University of Michigan, Ann Arbor, Michigan, USA.

[5]School of Engineering, University of Tokyo, Tokyo, Japan.

[6]Department of Chemistry, McMaster University, Hamilton, Ontario, Canada.

[7]ASAHI Chemical Industry Co., Fuji shi, Japan.

[8]DOW Chemical, Freeport, Texas, USA.

[9]Pohang Accelerator Laboratory, POSTECH, Pohang, Korea.

[10]Dept. of Physics, University of Wisconsin, Milwaukee, Wisconsin, USA.

INTRODUCTION

NEXAFS and XPS spectroscopies are applied in a pair of scanning zone-plate microscopes which have become operational at undulator beamline 7.0 at the ALS. Figure 1 shows this facility. The count rates in these microscopes are about ten times higher than previously available.

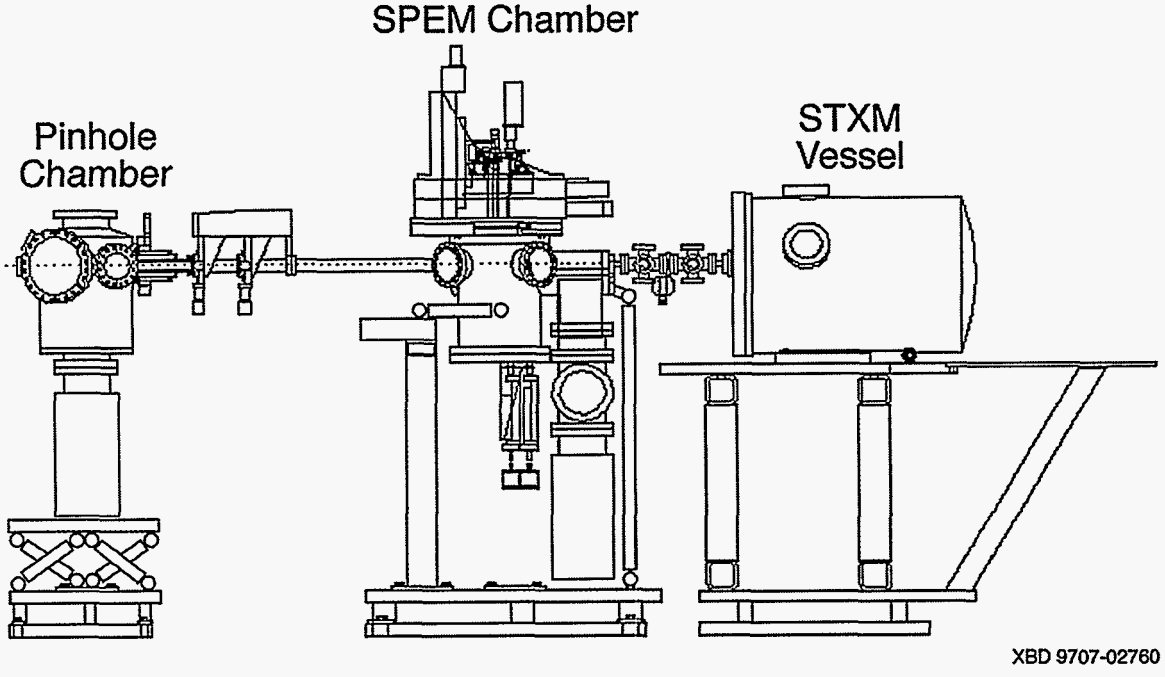

Figure 1. The tandem layout of the two microscopes. The upstream microscope is a UHV Scanning PhotoElectron Microscope (SPEM). The photon beam passes through the SPEM chamber to STXM, which is the last item in the beamline.

THE SCANNING TRANSMISSION X-RAY MICROSCOPE (STXM)

Figure 2 illustrates the zone plate scheme employed in STXM. The lens is outside a Si_3N_4 vacuum window 160nm thick. We are presently using lenses with 80nm outer zone width, and a corresponding diffraction limit to the spatial resolution of about 100nm. Images made of fractured

thin windows (100nm Si_3N_4) show blurring consistent with an x-ray spot size of 150nm FWHM. The order sorting aperture (OSA) is precisely positioned on the optical axis (+/-2 microns) to allow only the first order diffracted focus to reach the sample. This aperture is a photo-sensitive element which generates a signal (a few pA) proportional to the illumination intensity for spectral normalization against the effects of low frequency (<10Hz) beam motion in the beamline, which cannot be averaged over the counting interval (few hundred milliseconds). We have measured 2 x 10^7 photons/second with a spectral width 1/3000 in the zone plate first order focus spot at 300eV, with the storage ring running at 1.5 GeV, 400mA. At higher photon energies the intensity increases, as the windows become more transparent, until the beamline output decreases above 500eV. Images are typically acquired with a counting time of 10ms per pixel. NEXAFS spectra are acquired with a counting time of several hundred ms per energy point. Coordinated undulator and monochromator moves take about 250ms to complete, during which time a fast mechanical shutter closes to protect radiation sensitive samples from unnecessary exposure.

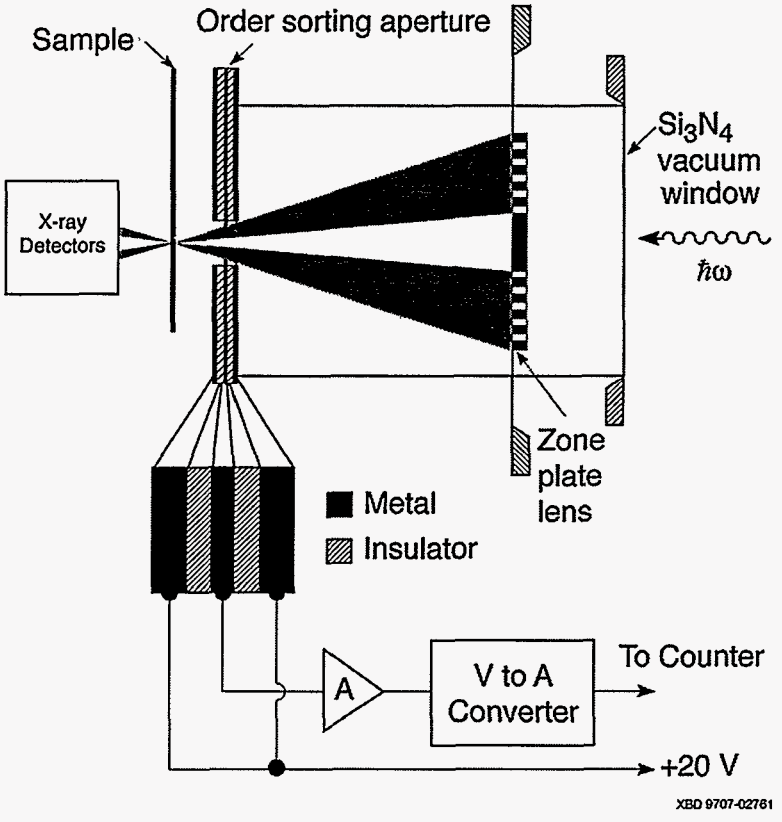

Figure 2. Schematic arrangement of the windows, lens, order sorting aperture (OSA), the sample and the detector in STXM.

The transmission geometry is the most efficient use of photons for an absorption spectrum, well suited to radiation sensitive organic samples.

Measurements in transmission are bulk sensitive, so that surface contamination is not a concern. This allows the operation of the microscope at atmospheric pressure, in air or helium, with hydrated samples for problems in environmental science.

The most difficult mechanism involved in this microscope is the flexure which translates the zone plate longitudinally through 0.5mm to remain in focus as the photon energy is changed during a NEXAFS scan. This mechanism inevitably has some unwanted sideways run-out (about 0.4 microns) which is reproducible and compensated by programmed sideways motion of the sample during the spectral scan. The resulting lock-in (0.2 microns) allows spectra to be measured with some confidence on features uniform over regions as small as 0.5 microns. We are presently making a transition to finer zone plates (spatial resolution improved by a factor of 2) with shorter focal lengths (by a factor of 4) so that the spatial resolution will be improved and this difficult translation will be smaller.

Photons are detected in transmission by one of two detectors.
1) An analog silicon photo-diode (from International Radiation Detectors, Torrance, CA90505, USA) for full intensity measurements. This detector is essentially 100% efficient above 100eV except for a thin oxide layer. It is typically used with a 10ms amplifier time constant.
2) A photo-multiplier tube collecting visible light from a phosphor (P43) behind the sample. This scheme is under development but shows overall x-ray counting efficiency of 25% and is linear beyond 1MHz counting rate.

Figure 3 shows a case study illustrating the STXM capabilities. In this case the polarization/orientation sensitivity is explored at the K edge of three atoms in the molecule; carbon, oxygen and nitrogen. The latter two measurements require a pure helium environment to remove atmospheric absorption effects.

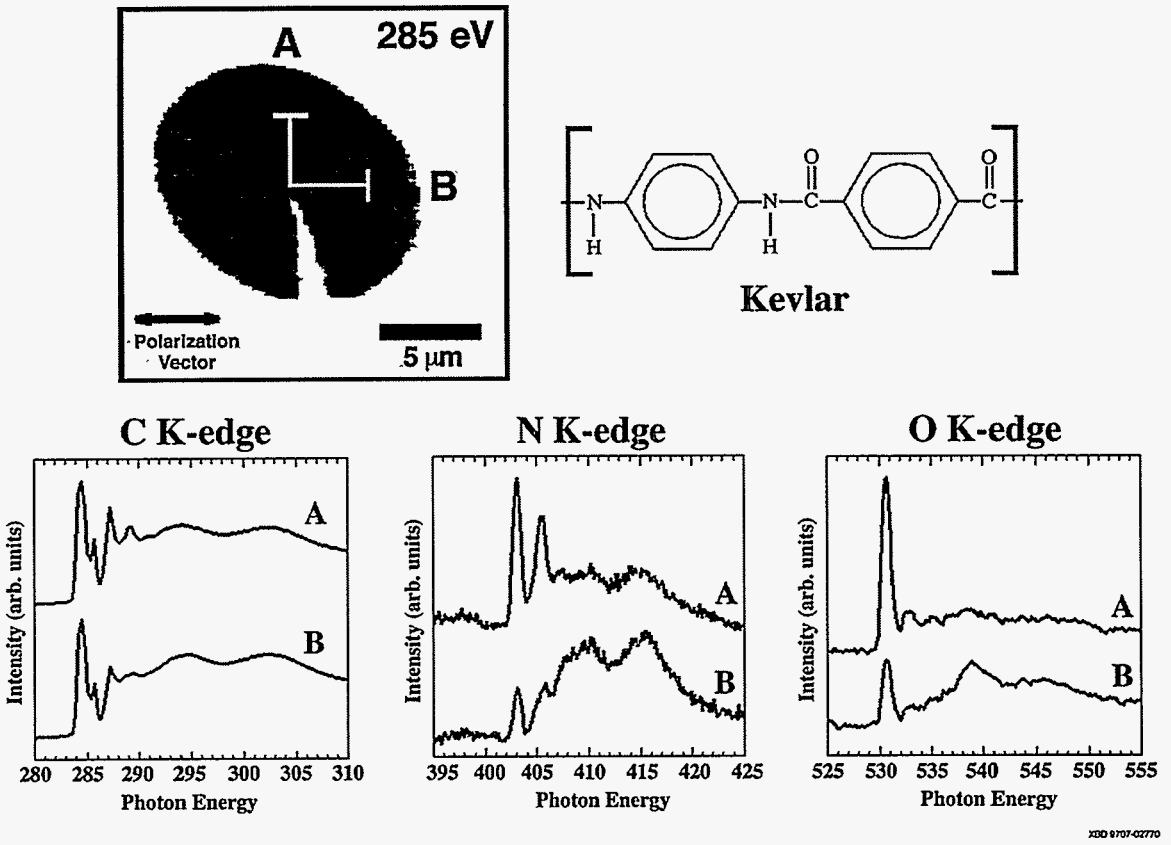

Figure 3. A sectioned Kevlar fiber measured in STXM. Absorption spectra are measured at points A and B, showing the dependence on the angle between the photon polarization vector (horizontal) and the radially oriented polymer chains. Spectra are shown for each of the main atomic species present. The polarization contrast reverses between the pi and sigma orbital peaks.

THE SCANNING PHOTO-EMISSION MICROSCOPE (SPEM)

Figure 4 illustrates the zone plate scheme employed in SPEM. Here the sample is stationary during imaging and the zone plate is rastered in the illumination field to carry the focused spot across the sample surface. The illumination is of the order of 1mm diameter and the raster range is 80x80 microns. The electron spectrometer can view the entire range of the image area and collects photo-electrons at 60 degrees from the sample normal. The OSA is within 0.5mm of the sample surface, and the zone plate assembly is cut back on one side to allow a line of sight for the spectrometer. NEXAFS capability is included by means of a flexure to carry the zone plate 0.5mm longitudinally

to retain the focus condition as the photon energy changes. The OSA moves away from its optimum longitudinal position during a NEXAFS scan but not so far as to intercept the first order light.

The OSA is fixed to the zone plate, with the focal length built in to the assembly. Different photon energies require different zone-plate/OSA combinations with different built-in focal lengths (e.g. 620eV for survey spectra including oxygen 1s photoelectrons, 270eV to 310eV for carbon K edge NEXAFS measurements). Five zone plates will be mounted together on a monolithic array with precisely parallel optical axes (to +/-1mrad), interchangeable under computer control. So far we have operated the microscope with three zone-plate/OSAs aligned in this way. SPEM allows us to perform quantitative XPS measurements of atomic concentration and core level chemical shifts over regions of the sample surface as small as the spatial resolution of the zone plate lens (currently x-ray spots smaller than 0.3 microns have been achieved). The zone plate array can be lowered out of the beam and the sample surface can be observed with the same video system, allowing visible fiducial marks on the sample to be used to position the region of interest within the 100x100 micron range of the scan stage. XPS spectra are measured with typical photo-peak count-rates of 70,000 counts/second (Au 4f at 420eV photon energy).

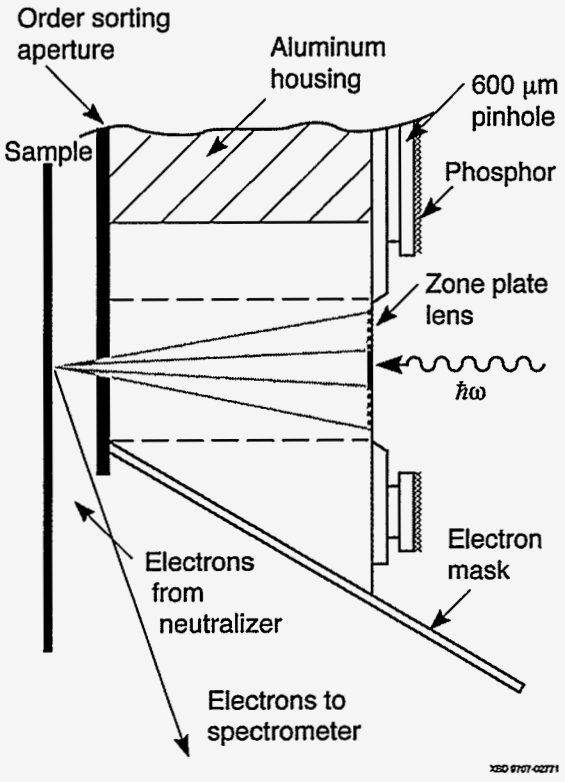

Figure 4. Schematic arrangement of the lens, order sorting aperture (OSA), the sample and the spectrometer in SPEM.

Sample charging is partially neutralized by the proximity of the zone plate assembly to the sample surface (which serves as a source of low energy electrons) and by an electron flood gun. Remaining charging shifts are corrected relative to the photo-emission peaks of contaminant carbon or to a Fermi edge. Sample sputtering and annealing is provided in a preparation chamber adjacent to the microscope chamber. The instrument operates at $5x10^{-10}$ Torr.

Figure 5 shows a SPEM case study in which an Al/Ti melt has been allowed to solidify on a graphite substrate. The image of the polished section shows the aluminum metal, precipitates of Al_3Ti alloy and the graphite interface, with carbide formation. Different core level chemical shifts are observed from the Al, the Al_3Ti alloy and the carbide region. Topography is visible in the image because of the sideways collection of electrons. The harder alloy precipitates are proud of the metal surface after polishing. In this case sputtering has removed the adventitious carbon contamination but the surface is still oxidized.

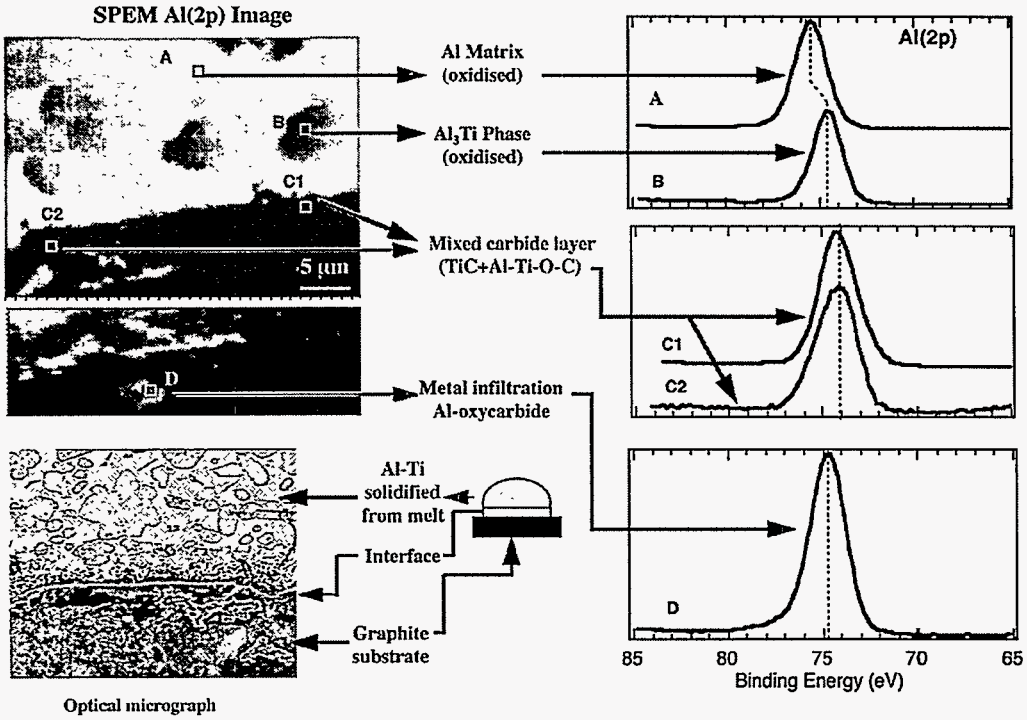

Figure 5. SPEM images and Al 2p XPS spectra from a metallurgical study of Al/Ti melt interactions with solid graphite. Early results provide quantitative chemical shifts and stoichiometry of alloy precipitates and carbide formation at the interface.

ACKNOWLEDGMENTS

Zone Plates were fabricated by Erik Andersen of the Center for X-ray Optics, LBNL and by Massimo Gentili with Gate Micro Technology, Rome, Italy.
Samples for SPEM were provided by N. Sobczak of the Foundry Res. Inst., Krakow, Poland.

This work was supported by the Director, Office of Energy Research, Office of Basic Energy Sciences, Materials Science Division, of the U.S. Department of Energy under Contract No. DE-AC03-76SF00098.

Principal investigator: Tony Warwick, Advanced Light Source, Ernest Orlando Lawrence Berkeley National Laboratory. Email: warwick@lbl.gov. Telephone: 510-486-5819.

Electronic Structure of Icosahedral AlPdMn

Eli Rotenberg[1], S.D.Barman[2], J.J.Paggel[3], K.Horn[2], Ph.Ebert[4], K.Urban[4]

[1]Advanced Light Source, Lawrence Berkeley Lab, Berkeley, CA 94720

[2]Fritz-Haber-Institut der Max-Planck-Gesellschaft, Berlin, Germany

[3]Fachbereich Physik der Philipps-Universität, Marburg, Germany

[4]Institut für Festkörperforschung, Forschungszentrum Jülich, Germany

Quasicrystals are a new class of materials with unexpected symmetry properties and a potential for applications in a wide range of fields [1]. The electronic structure of icosahedral quasicrystals is of great current interest, since in view of the unusual symmetry properties of these materials, conventional notions on electronic structure need to be adapted in order to provide a meaningful description of their properties. Among the striking features of quasicrystals are their high electrical resistivity and the low electronic contribution to the specific heat, compared to those of their metallic constituents. These features, and the specific heat finding in particular, still await an explanation in terms of the electronic structure of these materials. Here we report on a core and valence level photoemission study of icosahedral AlPdMn in order to assign regions of the valence band to the different atomic constituents, and to shed light on the atomic coordination in AlPdMn. Spectra were recorded from cleaved as well as sputter-annealed surfaces of surfaces with five-fold symmetry. A comparison of data from these different preparation methods can be used in order to investigate the possible influence of deviations from stoichiometry induced by sputter-annealing.

Figure 1 shows the core level spectrum of i-AlPdMn recorded at a photon energy of 400 eV, which shows the intense Al 2p and Pd 3d core levels, as well as a strong peak in the valence band region (also shown in the inset) which is ascribed contributions from the Pd 4d level. The satellite structure on the core level peaks, particularly prominent on the Al 2p, is due to plasmon losses.The atomic arrangement of the quasicrystal constituents is still a subject of intense research effort. We have therefore recorded the polar and azimuthal intensity variation of the strong core level lines. These patterns, which demonstrate that our quasicrystal surfaces exhibit good quasicrystalline order, are shown for the Al 2p and Pd 3d peaks in Figure 2. The left diagram shows the raw data of the Pd 4d peak, recorded over a polar angle range of about 250 degrees and an azimuthal range of 45 degrees. Even in the raw data the fivefold symmetry of the intensity distribution is clearly visible. The structures gain contrast when subjected to a smooth background subtraction and symmetrization procedure, as shown for both the Pd 3d and Al 2p levels in the center and on the right-hand side. These patterns, which arise from photoelectron diffraction, are currently being interpreted through multiple scattering diffraction calculations which are expected to yield information on the structure of the so-called pseudo-Mackay clusters which are thought to be the basic building blocks of quasicrystals, as suggested from recent scanning tunneling microscopy experiments [2], for example.

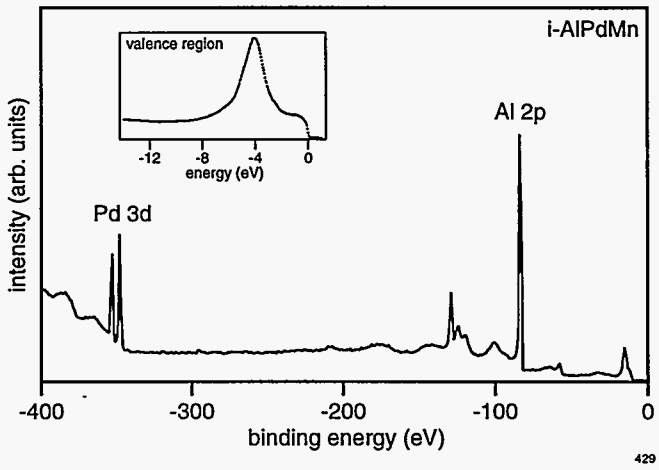

Figure 1: Core level spectrum of i-AlPdMn, displaying the intense Al 2p and Pd 3d lines. Inset: region of the valence band.

Spectra form the valence region of i-AlPdMn exhibit broad structure from which an assignment in terms of different atomic contibutions is not straightforward. The peak at about 4 eV below the Fermi level EF can be assigned to Pd 4d states because of its cross section upon photon energy variation, on account of the loss in intensity due to the Cooper minimum. The region of the valence band near EF can be attributed to Mn *s* states, from resonant photoemission experiments at the Mn 2p edge [3].

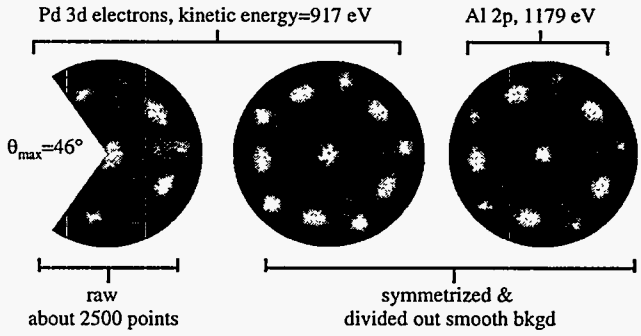

Figure 2: Angular variation of Pd 3d and Al 2p core level peak intensities, measured over a range of 250 ° polar and 45° azimuthal emission. The raw data (left) were subjected to a smooth background subtraction and symmetrization to yield the patterns in the center and on the right-hand side.

Many discussions of structure-induced features in the electronic spectra of quasicrystals are based on the concept of Brillouin zones, generalized in a vague way to quasicrystals. This generalization may actually be based on firm ground, by considering that the six-dimensional hypercubic lattice corresponds to a six-dimensional reciprocal lattice, in which the Brillouin zone may be defined in the usual way, being bounded by the planes bisecting the Q vectors that belong to the star of equivalent reciprocal lattice vectors. The special points in 6D reciprocal space can then be projected onto 3D reciprocal space to define quasiperiodically distributed special points. While the special points in this projection are dense everywhere, they are weighted by a generalized structure factor, and a quasi-Brillouin zone may be defined in terms of the strongest zone center and zone boundary special points[4]. The emission intensity as a function of angle from different regions of the valence band can give information on the symmetry of the states involved. This information has so far been lacking in conventional angle-resolved photoemission from quasicrystalline surfaces, since the features are rather broad and shifts upon variation of the parallel or normal component of the wave vector are difficult to detect. Thus, angular patterns from several regions of the valence band were recorded in a similar fashion to the ones shown in Figure 2. These also exhibit a marked angular pattern of fivefold symmetry, suggesting that the symmetry of the quasicrystal building blocks is indeed reflected in the valence states.

REFERENCES

[1] see the articles in the MRS Bulletin, Vol. **22**, November 1997.

[2] Ph.Ebert, M.Feuerbacher, N.Tamura, M.Wollgarten,K.Urban, Phys.Rev.Lett. **77**,3287 (1997).

[3] E.Rotenberg, S.D.Barman, J.J.Paggel, K.Horn, Ph.Ebert, K.Urban, to be published.

[4] M.Krajci, M.Windisch, J.Hafner, G.Kresse, and M.Mihalkovic, Phys.Rev.B**51**, 17355(1995)

This work was supported by Bundesministerium für Bildung, Forschung und Technologie under grant 05622 OLA 3. P.E. and K.U. thank the Deutsche Forschungsgemeinschaft for financial support under grant UR 51/3-1.

Principal investigator: Karsten Horn, Fritz-Haber-Institut der Max-Planck-Gesellschaft.
Email: horn@fhi-berlin.mpg.de.

High-energy ARPES of Low-Dimensional Molybdenum Bronzes

J. D. Denlinger,[1] G.-H. Gweon,[1] J. W. Allen,[1] J. Marcus,[2] and C. Schlenker[2]

[1]Randall Laboratory, University of Michigan, Ann Arbor, Michigan 98109-1120, USA
[2]Laboratoire d'Etudes des Propiétés Electroniques des Solides, CNRS, BP166, 38042 Grenoble Cédex 9, France

INTRODUCTION

The molydenum bronzes, $K_{0.3}MoO_3$ (blue bronze) and $A_xMo_6O_{17}$, (A=Li, K,Na; purple bronze), are a class of charge density wave (CDW) materials that exhibit quasi-one dimensional (1D) and quasi-2D transport properties [1]. The Fermi surface (FS) topology for each bronze is of fundamental importance for the understanding of the Fermi surface nesting that gives rise to the CDW instability and hence gives motivation for performing angle-resolved photoelectron spectroscopy (ARPES) on these materials. In addition, Luttinger liquid behavior replaces normal Fermi-liquid behavior in the theory of one-dimensional interacting electron systems and such results might apply to 1D materials. For example, near-vanishing Fermi energy (E_F) spectral weight in angle-integrated photoemission measurements of the metallic phase of quasi-1D bronzes [2,3] could be explained in this way. However, care has to be taken to distinguish between this and other competing effects, such as strong 1D CDW fluctuations toward an E_F gap. Sufficiently resolved near-E_F ARPES spectra have the potential to signal such non-Fermi liquid behavior and to discriminate models.

Previous ARPES measurements of the molybdenum bronzes have been performed in the low photon energy regime of (15-40 eV) at other synchrotrons [4-8]. The purpose of additional ARPES measurements at the ALS is to explore the advantages and challenges of using (a) higher photon energies ($h\nu$>70 eV) and (b) automated angular-dependent measurements of small samples in a rotating-sample/fixed-detector geometry. In this abstract, the Fermi surface topologies of the quasi-1D Li purple bronze and quasi-2D Na purple bronze are illustrated and contrasted.

EXPERIMENT

Angle resolved measurements were performed at Beamline 7.0.1.2 with an experimental end-station originally designed for highly-automated angular and energy-dependent photoelectron diffraction [9]. The apparatus includes a 137-mm hemispherical spectrometer with 16-channel multi-detection and has proven very successful in the application of ARPES and Fermi-surface contour mapping to elemental metals and surfaces [10]. Samples were measured at room temperature with a total instrumental resolution of ≈80 meV and full angular acceptance of ≈1.4°.

The molybdenum bronzes present additional challenges compared to elemental substrates due to (a) the small sizes of available single crystals, (b) the small Brilluoin zone (BZ) resulting from a larger more complicated unit cell, and (c) susceptibility to beam damage. The molybdenum bronzes are grown by an electrolytic reduction technique [1] and are produced in sizes not larger than a few mm square. Clean surfaces are produced by *in situ* cleaving where the layered structure of the material improves the chances of large uniform surfaces of size similar to the sample itself. While the focused photon beam size (<100 μm) is much less than the sample size, the rotating sample geometry places tight restrictions on the alignment of the sample surface such that the incident beam does not wander off the sample or out of the analyzer analysis area. Even with careful attention to sample mounting, inherently different parts of the surface are measured for different sample angles. The BZ dimensions of the purple bronzes can be as small as 1.0 Å-1

which translates to only a ≈13° angular width of the BZ at the minimum photon energy available of 70 eV. Hence a 1.4° detector angular acceptance of 1.4° achieves a k-space resolution of ≈10% of the BZ width.

Beam damage to the molybdenum bronzes arises from creation of surface defects via photon-stimulated desorption of O atoms above the 4p→4d absorption threshold [11]. The effect is maximum around hν=50 eV and has the effect of suppressing Mo 4d spectral weight near E_F and creating a new defect emission feature at 2 eV binding energy. A typical molybdenum bronze valence spectra, shown in Fig. 1, consists of strong O 2p bands occupy 3-9 eV binding energy and weaker Mo 4d bands near E_F which are of primary interest. The progression of beam damage can be clearly monitored (dashed spectra in Fig. 1). The onset of spectral changes occurs with only a few minutes of dwell time at a single point on the sample using the intense fluxes from this undulator beamline. To minimize beam damage, an automated beam shutter was used while doing experiments, and the movement of the beam on the sample surface for different angles due to slight misalignments actually has a beneficial effect of reducing the beam exposure during automated angle scans. Measurement of many high resolution spectra, however, was problematic.

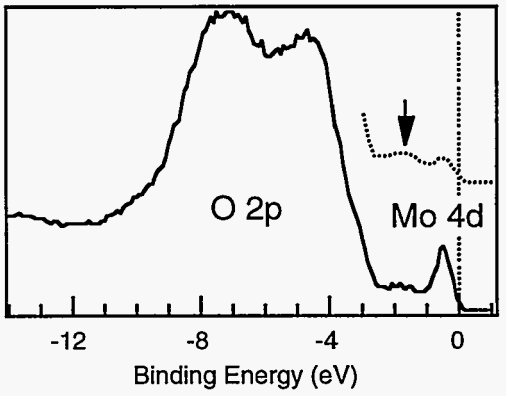

Figure 1. Li purple bronze valence spectra at hν=60 eV. The dashed spectra results after a few minutes of beam exposure.

Despite the severe inconveniences to being able to perform such experiments in this energy range or in this detection geometry, the assets of automation and multi-channel detection still allow some remarkable data to be collected.

$Li_{0.9}Mo_6O_{17}$

Li purple bronze has a large 1D anisoptropy in resistivity with an anomalous upturn in resistivity at 25 K (possibly a spin-density wave) and becomes superconducting at 2 K. Figure 2(a) shows a Fermi-edge angular intensity map at hν=70 eV for $Li_{0.9}Mo_6O_{17}$. The energy window used had a width of 0.4 eV centered at zero binding energy and the image shown is a result of 2-fold symmetrization of a 90° azimuthal sector of data. The symmetry axes of the Fermi-surface image was determined from the larger 360° raw data set. The azimuth alignment of the crystal was also checked *in situ* with Mo 3d x-ray photoelectron diffraction which exhibited a 3-fold symmetry arising from forward-scattering through near-neighbor oxygen atoms in MoO_6 octahedra structures that are linked in planar chains. Overplotted in Fig. 2(a) is the rectangular surface Brilluoin zone. The lack of horizontal crossings in the first BZ is due to surface homogeneity and/or beam damage. Figure 2(b) shows a vertical cut in k-space of the FE intensity obtained by polar scans at a series of photon energies (60-150 eV). The straight vertical lines of intensity verify the conservation of k-parallel at these E_F crossings.

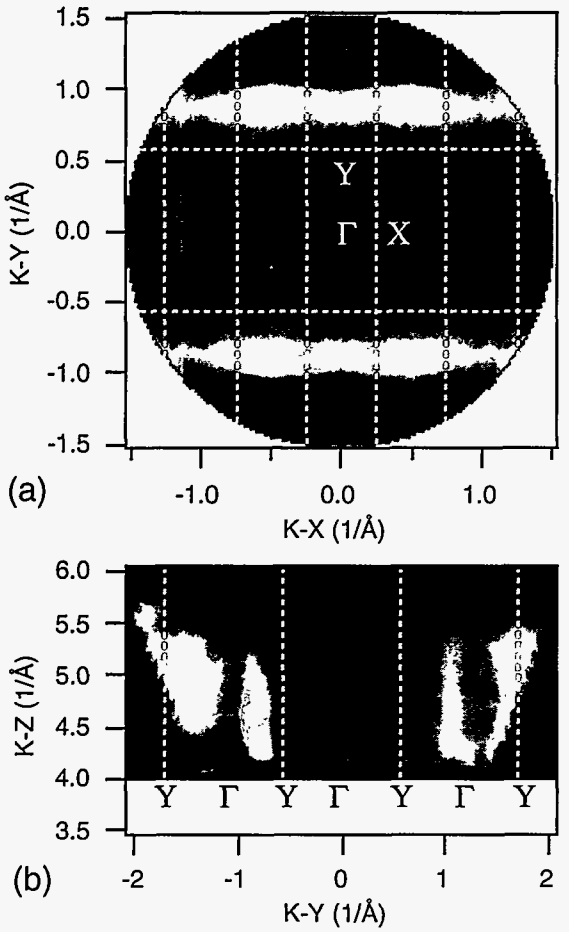

Figure 2. (a) Fermi-edge angular intensity map at hν=70 eV for quasi-1D $Li_{0.9}Mo_6O_{17}$, (b) Polar-photon FE-intensity map (hν=60-150 eV).

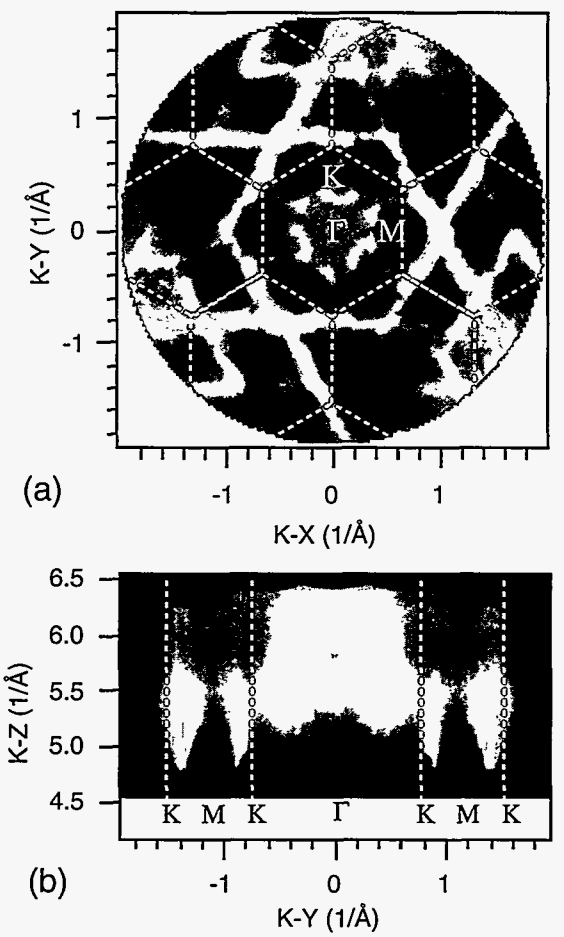

Figure 3. (a) Fermi-edge angular intensity map at hν=70 eV for quasi-2D $NaMo_6O_{17}$, (b) Polar-photon FE-intensity map (hν=70-160 eV).

$NaMo_6O_{17}$

Na purple bronze has a 2D anisotropy in resisitivity, undergoes a metal-metal CDW transition at about 80 K, and also becomes superconducting at 2 K. Similar to Fig. 2, angular and polar-photon E_F intensity maps for $NaMo_6O_{17}$ are shown in Figure 3. In contrast to the quasi-1D Li purple bronze, the k_x-k_y E_F intensity map for Na purple bronze shows a 3-fold pattern of criss-crossing parallel lines that form a 'Star of David' centered in each hexagonal BZ (dashed lines). This simple pattern, observed previously at low photon energy [7,8], arises because the electronic structure consists of weakly interacting quasi-1D chains oriented 120° to one another [12]. Again the intensity of the E_F crossings appear to be weaker in the first BZ and stronger in the second BZs. However, the k_y-k_z E_F map in Fig. 3(b) shows an energy dependence to this behavior with a clear reversal of E_F intensities in the first and second BZ at a higher photon energy of ≈150 eV.

Figure 4 illustrates the use of multi-channel detection to simultaneously measure a range of binding energies while performing an automated angular scan. At each point a snapshot of 16 energy channels is recorded with only ≈1 second dwell time instead of ≈30 sec required to acquire a full spectrum. Using a spectrometer pass energy of 12 eV, the spacing between detector channels is 0.1 eV and the total energy width of the snapshot is 1.6 eV. Figure 4 shows images recorded by 5 different channels corresponding to binding energies from 0.8 eV to 0 eV.

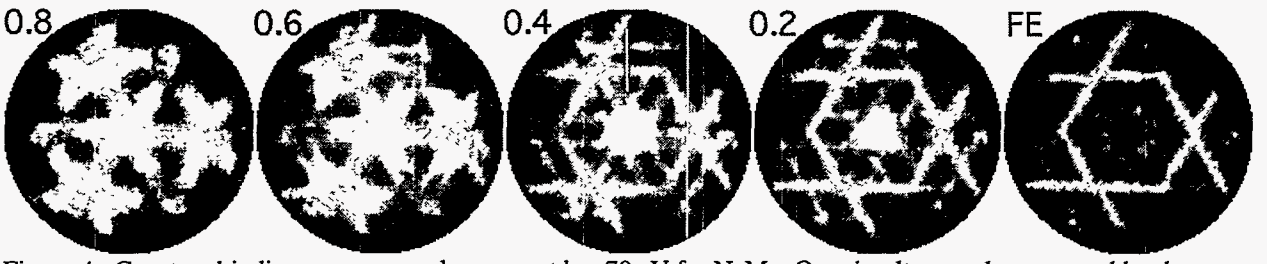

Figure 4. Constant binding-energy angular maps at hv=70 eV for $NaMo_6O_{17}$ simultaneously measured by the spectrometer 16-channel detection. Full 2π maps are obtained from 3-fold symmetrizing a 120° sector. The vertical line represents the polar angle range of Fig. 5.

This sequence of constant binding energy contours illustrates that the Fermi-surface is composed of *pairs* of lines linked by a dispersing band that disperses to ≈0.7 eV binding energy as shown in Fig. 5.

CONCLUSIONS

These results illustrate both the great potential and the great challenge of making such studies with this endstation.

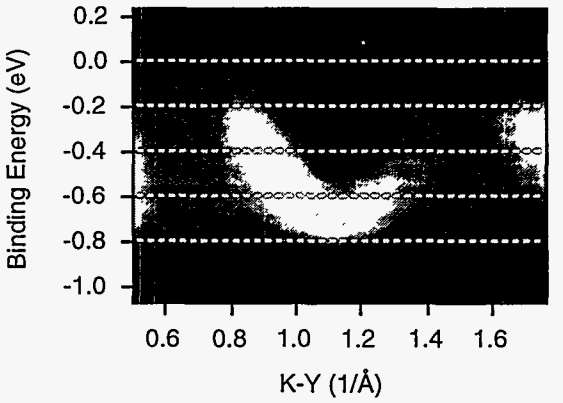

Figure 5. Image of Mo 4d valence spectra taken along K-M-K at hv=70 eV for $NaMo_6O_{17}$. Horizontal dashed lines illustrate the binding energies measured by multi-channel detection in Fig. 4.

REFERENCES

1. *Low Dimensional Electronic Properties of Molybdenum Bronzes and Oxides*, edited by C. Schlenker (Kluwer Academic Publishers, Dordrecht, 1989).
2. B. Dardel *et al*, Phys. Rev. Lett. **67**, 3144 (1991).
3. B. Dardel *et al*, Europhys. Lett. **19**, 525 (1992).
4. K. E. Smith, K. Breuer, M. Greenblatt, W. McCarroll, Phys. Rev. Lett. **70**, 3772 (1993).
5. K. Breuer *et al*, Phys. Rev. Lett. **76**, 3172 (1996).
6. M. Grioni *et al*, Physica Scripta **T66**, 172 (1996).
7. G.-H. Gweon *et al*, J. Phys. Condens. Matter **8**, 9923 (1996).
8. G.-H. Gweon *et al*, Phys. Rev. B **55**, 13353 (1997).
9. J. D. Denlinger *et al*, Rev. Sci. Instrum. **66**, 1342 (1995).
10. E. Rotenberg*et al*, Mater. Res. Soc. Symp. **437**, (1996); E. Rotenberg and S. D. Kevan, Phys. Rev. Lett. **80**, (1997), in press.
11. K. Breuer *et al*, Solid State Comm. **94**, 601 (1995).
12. M.-H. Whangbo, E. Canadell, P. Foury and J.-P. Pouget, Science **252**, 96 (1991).

This work was supported by the U.S. Dept. of Energy (DoE) under contract No. DE-FG02-90ER45416 and by the U.S. NSF under grant No. DMR-94-23741.

Principal Investigator: J. W. Allen, Department of Physics, University of Michigan. Email: jwallen@umich.edu. Telephone: 313-763-1150.

Holography of Acetylene Adsorption on Si(100)-2×1 Surface

S. H. Xu*, Y. Yang, E. Rotenberg[1], T. Yates, Jr.[2], and G. J. Lapeyre
Physics Department, Montana State University, Bozeman, MT 59717
[1]Advanced Light Source, LBNL, Berkeley, CA 94720
[2]Department of Chemistry, University of Pittsburgh, Pittsburgh, PA 15213

INTRODUCTION

An investigation of the adsorption of acetylene on Si(100) surface is important for the formation of silicon carbide, because the adsorption is the first step of whole reaction towards carbide formation. Previous studies[1,2] have proposed a di-σ model. In this model, the acetylene adsorbs on the bridge site across the Si dimer and the carbon-carbon triple bond is rehybridized to a di-σ bond state. However, there are some disagreements on the correct peak assignment in HREELS[1], and the exact nature of the initial bonding geometry of acetylene on the Si(100) surface is still a matter of discussion. In our work, the energy-dependent diffraction is obtained for C 1s core-level emission from the measurement of constant-initial-energy spectra(CIS) for a set of angles which forms a grid over the full-emission hemisphere. Then, we adopt the photoelectron holography to study the adsorption site and 3-D geometry of acetylene on the Si(100)-2×1.

EXPERIMENT

The experimental data is collected at the undulator beam-line 7 station at Advanced Light Source(ALS) in Berkeley. An angle-resolved electron energy analyzer was used to detect the C 1s photoelectrons. N-type Si(100) (4° vicinal cut) samples were prepared by outgassing at 700 K for ~20 hours, and then heated to 1180 K to yield the clean well 2×1 reconstruction. Research grade acetylene (99.9 mol % purity) was dosed when the sample was kept at room temperature(RT). After adsorption of 0.5 monolayer(ML) acetylene, there is no obvious change observed in LEED pattern. A set of 82 CIS was measured for the C 1s where the angles span an irreducible symmetry element, i.e., $0°\leq\theta\leq75°$ and $0°\leq\varphi\leq90°$. The azimuthal angles are referenced to a mirror plane along the Si dimer, $\varphi=0$. Both of azimuthal and polar angles are obtained by rotation of the sample. For each angle, C 1s signal is recorded as a function of the momentum(4.1–10.4 $Å^{-1}$) with a constant momentum $\Delta k=0.15$ $Å^{-1}$. Then we use the small-cone method[3] to get the image of this system.

RESULTS

The holographic image formed from C 1s is complicated, largely because two carbons(labeled as P and Q) in one acetylene molecule occupy inequivalent site. The transfer which converts data to an image put all emitters together at the origin. At the same time, each C atom is a scatterer for another one, then it can be "seen" by another C atom. From the x-y planar cut passing through the C emitters, we find that there are two spots P/Q and Q/P. The distance between them is 2.2 Å. However, the separation between the P/Q and Q/P spots is twice the C-C bond length. So, the C-C bond length is 1.1 Å, which is very close to the free (1.2 Å) and the adsorbed acetylene by calculation[2].

In the x-z planar cut at y=0.0 Å(not show here), there are two spots(A/P, B/Q) of the strongest intensity at $x=\pm1.4$ Å($z=-1.4$ Å). The separation between the spot A/P and B/Q is not the actual separation between Si atom A and B, since these two spots are viewed from the two different C emitter P and Q, respectively. Instead it is the difference between the separation Si atom A and B and the C-C bond length. Then, the actual distance between them is 3.9 Å.

The spots O/Q and O/P at x=±0.55 Å(z=-2.9 Å) come from one Si atom O instead of two Si atoms, since the distance between them is relative small. Then, the distance between spots O/Q and O/P is the C-C bond length. Based on the same reasons, the actual distance between Si atom D and E is 7.5 Å instead of 6.4 Å.

According to these results, we find that the di-σ model is difficult to explain these images. The reasons are discussed in our paper[4]. If we think that acetylene adsorbs on the pedestal site, then it is easy to explain these images. That is to say, all of atomic positions given by the image are well consistent with the pedestal-site model. Some of atomic geometric parameters obtained from our image are compared in Table 1 with those from other sources. We can see that the parameters agree very well with other sources. Thus, we can conclusively think that acetylene adsorbs molecularly on the pedestal site, with no adsorption taking place on the Si dimer. Furthermore, the image provides evidence to show Si dimer is not cleaved.

Table 1. Atomic distance (Å) for Si(100)-2x1–C_2H_2 obtained from the image and other sources.

	this method	others
adsorption height	0.6	0.7[5]
C–C length	1.1	1.2
Si dimer length	2.3*	2.23[6]
Si atom A and B	3.9*	3.84[7]
Si atom D and E	7.5*	7.68[7]
$1^{st}/2^{nd}$ layer Si	0.8	1.0[6]
$2^{nd}/3^{rd}$ layer Si	1.5	1.36[7]

*C–C bond length (1.1 Å) is used. The separation between O/P and O/Q is 1.1 Å.

REFERENCES

[1] M. Nishijima, J. Yoshinobu, H. Tsuda, and M. Onchi, Surf. Sci. **192**, 383(1987).
[2] Ru-Hong Zhou, Pei-Lin Cao, and Lie-Quan Lee, Phys. Rev. B **47**, 10601(1993).
[3] Huasheng Wu and G. J. Lapeyre, Phys. Rev. B **51**, 14549(1995).
[4] S. H. Xu, Y. Yang, E. Rotenberg[1], T. Yates, Jr.[2], and G. J. Lapeyre, to be submitted.
[5] L. Li et al., Phys. Rev. B **56**, 4648(1997).
[6] N. Roberts and R. J. Needs, Surf. Sci. **236**, 112(1990).
[7] Crystal structure of bulk Si.

This work was supported by NSF. ALS of LBNL is supported by the DOE.

*email: shihong@gemini.oscs.montana.edu

Principal investigator: Gerald J. Lapeyre, Physics Department, Montana State University-Bozeman, Bozeman, MT 59717.

How the phenyl rings (benzene) act as building blocks in the π conjugated polymers

J.-H. Guo[1], M. Magnuson[1], C. Såthe[1], J. Nordgren[1], L. Yang[2], Y. Luo[2], H. Ågren[2], K. Xing[2], N. Johansson[2], W.R. Salaneck[2], R. Daik[3], and W.J. Feast[3]

[1]Department of Physics, Uppsala University, Box 530, 751 21 Uppsala, Sweden
[2]Department of Physics and Measurement Technology, Linköping University, 581 83 Linköping, Sweden
[3]IRC in polymer Science and Technology, Durham University South Road, Durham DH1 3LE, United Kingdom

INTRODUCTION

Organic conjugated polymers have the electronic structure of semiconductors and can be doped to become good conductors [1]. Conjugated polymers are now used as active materials in a wide variety of prototype applications such as light emitting diodes [2] and organic transistors [3,4]. Most of the interesting chemistry and physics of conjugated polymers is associated with the details of the electronic structure at the valence and conduction band edges and, in this connection, various electron spectroscopies can be used as tools for diagnosis of the relevant electronic and geometric properties.

The x-ray emission (XE) technique provides a means of extracting chemical information in the form of molecular orbital (MO) population and local density distribution of certain symmetries owing to the dipole character of the radiative decay and the localization of core-hole states. The resonance inelastic x-ray scattering (RIXS) measurements are symmetry selective at high resolution.

X-ray emission occurs due to an interaction of incident x-ray photons with a target consisting of atoms, molecules or a solid. The traget is excited from the ground state $|o\rangle$ to a core excited state $|i\rangle$ by absorption of an incoming x-ray photon (γ) with specific frequency, wave vector and polarization vector. The core excited state is metastable due to vacuum zero vibrations or interelectron Coulomb interaction and can therefore decay to final states $|f\rangle$ in two different ways, by emitting x-ray photons or by emitting high-energy Auger electrons; $M + \gamma \rightarrow M_i \rightarrow M_f + \gamma'$ and $M + \gamma \rightarrow M_i \rightarrow M_f + e^-$ constituting the radiative, respectively, non-radiative decay channels of the x-ray scattering process. When the frequency of the incident x-ray photons is tuned below or closely above the core ionization threshold resonant core excitation takes place. It is natural to refer to this case as to resonant x-ray scattering or x-ray Raman scattering.

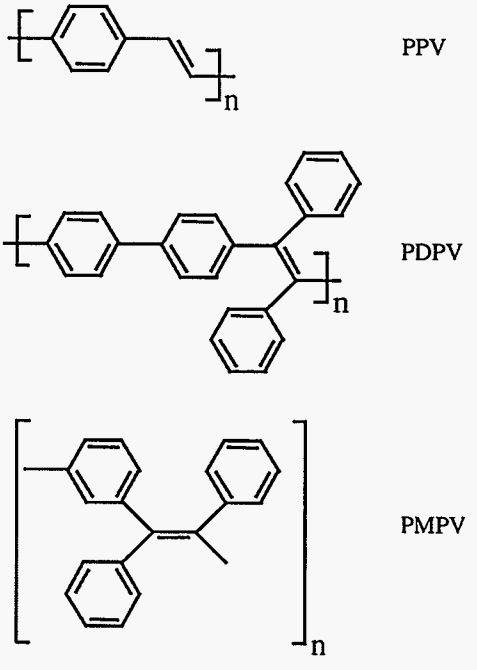

Figure 1. Schematic diagrams of poly(phenylenevinylene)s.

In the present work we probe the electronic structure of a set of poly(phenylenevinylene)s (See in Fig. 1): poly(phenylenevinylene) (PPV), poly(4,4'-diphenylenediphenylvinylene) (PDPV) and,

poly(1,3-phenylenediphenylvinylene) (PMPV), using x-ray absorption and emission spectroscopies which have been shown to be powerful techniques for studying electronic structures in other contexts. These compounds are made up of six membered carbocyclic aromatic rings connected by short hydrocarbon bridges.

EXPERIMENT

The experiments were performed at beamline 7.0 at the Advanced Light Source (ALS), Lawrence Berkeley National Laboratory. The beamline comprises a 99-pole, 5 cm period undulator and a spherical-grating monochromator [5]. Near edge x-ray absorption fine structure (NEXAFS) spectra were obtained by measuring the total electron yield from the sample. The resolution of the monochromator was set to 0.15 eV. The XAS spectra were normalized to the incident photon current using a clean gold mesh to correct for intensity fluctuation in the photon beam. The XE spectra were recorded using a high-resolution grazing-incidence x-ray fluorescence spectrometer [6]. During the XE measurements, the resolution of the beamline was 0.25 eV, and the resolution of the fluorescence spectrometer was set to 0.5 eV for C *K* emission.

The PPV sample was prepared from a soluble THT-leaving group precursor polymer [7]. The precursor was spin-coated onto Si(110) wafers, and converted to PPV at 240°C for 10 hours under a mild vacuum of $5x10^{-6}$ mbar. The PDPV and PMPV samples were prepared by McMurry coupling of 4,4'-dibenzoylbiphenyl and metadibenzoylbenzene respectively, following the method described by Millichamp [8]. The crude products were purified by equilibrium fractionation (chloroform solven/heptane non-solvent @ 20°C) following the technique described previously [9]. The PMPV and PDPV polymers were spin-coated from 2 mg/ml polymer/chloroform solution onto Si(110) substrates. All the samples were sealed in an N_2 atmosphere in glass and has been exposed to air for very short time just before they were introduced into the vacuum system for XE measurement.

RESULTS

The non-resonant XE spectra of the poly(phenylenevinylene)s excited with 310 eV photon-energy aligned together with the NEXAFS spectra are presented in Figure 2 (left). The spectrum of benzene, the main part of which is well understood [10], is also included for comparison. The energy scales of the spectra have been aligned by using the elastic peak in the RIXS spectra presented at the right side in Figure 2. The normal x-ray emission spectra of all systems can be grossly subdivided into 6 bands in the energy range from 265 to 283 eV. The band patterns of the poly(phenylenevinylene)s resemble those of benzene.

Benzene has ground state D_{6h} symmetry with 9 outer valence MO levels with intensity in the XE spectra. The six bands, which are denoted by the italic letters from *A* to *F* from the high energy side, can thus be assigned to x-ray transitions involving the $1e_{1g}$, $3e_{2g}+1a_{2u}$, $3e_{1u}+1b_{2u}+2b_{1u}$, $3a_{1g}$, $2e_{2g}$, $2e_{1u}$ MO's, respectively. The latter two bands are weak because of the 2s character of the corresponding MOs and presumably also because of the breakdown of the molecular orbital picture with accompanying correlation state splittings [11].

The (RIXS) spectra were recorded by tuning the incident x-ray photon beam to the first π^* resonance (284.8 eV) and are presented in Figure 2 (right). Similarly to the nonresonant case, the resonant spectra of poly(phenylenevinylene)s demonstrate a strong similarity with the resonant spectrum of benzene.

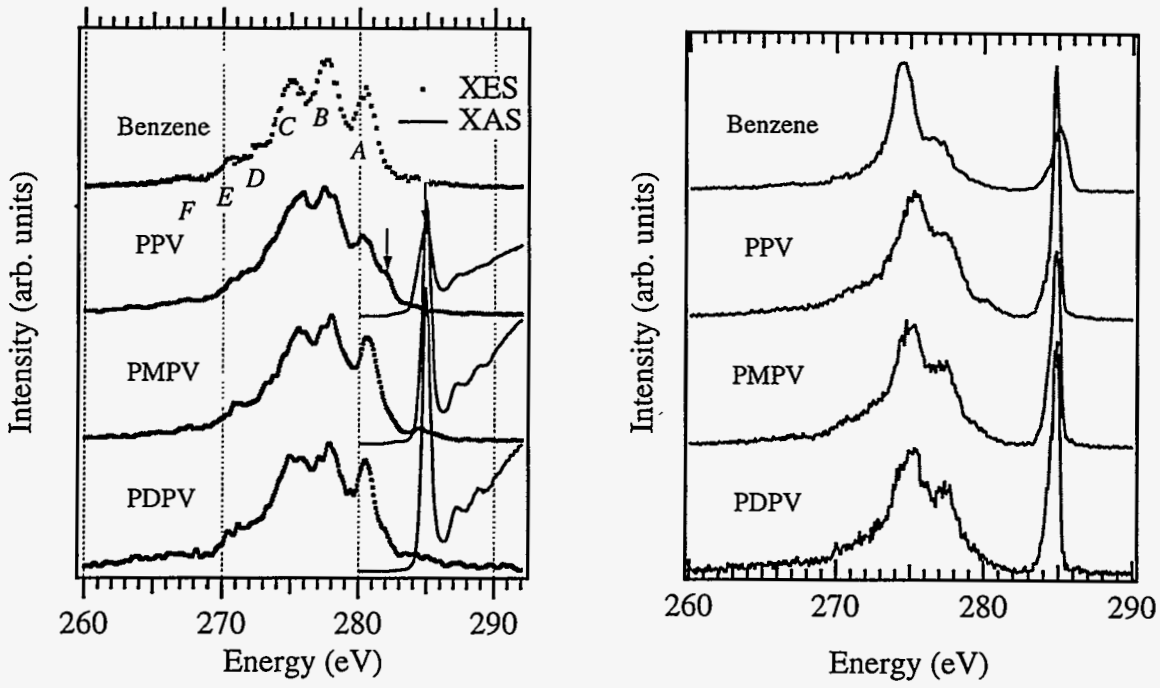

Figure 2. Non-resonant C *K* x-ray emission spectra excited at 284.5 eV together with x-ray absorption spectra of polymers (left) and resonant C *K* x-ray emission spectra excited at 310 eV (right).

DISCUSSION

The lowest unoccupied molecular orbital (LUMO) of C_6H_6 is $1e_{2u}$ (using ground state D_{6h} point group symmetry). When the incident x-ray is tuned to $1e_{2u}$, only electrons occupying the ungerade MO's can fill up the C_{1s} hole according to the parity selection rule for resonant x-ray scattering (gerade - gerade and ungerade-ungerade). This assumes that the core excited state maintains the same symmetry as the ground state D_{6h} . In particular, the HOMO $1e_{1g}$ level, corresponding to emission energy around 280 eV will be symmetry forbidden. This is the reason that the emission band *A* of highest energy in the nonresonant spectrum disappears in the resonant spectrum. The band *B* at 278 eV in the nonresonant spectrum, which originates in transition from the $3e_{2g}$+$1a_{2u}$ levels, should also be depleted in the resonant case due to symmetry selection. Although it does show reduced intensity, there is a significant intensity remaining, which was argued as being due to a final state vibronic coupling effect [10].

For the polymers, there exists no symmetry at all, and one could expect from this point of view that the resonant and nonresonant XE spectra would be similar. On the other hand if the vinylene groups exert only small perturbations on the phenyl ring the local electronic structure of the benzene molecule can remain intact and since the x-ray process is local one can then argue that an "effective" symmetry selection can be restored. The experimental spectra for polymers, indeed show benzene-like features also in the resonant case, with the band *A* intensity considerably reduced. The restoration of the effective symmetry selection (as well as the benzene similarity) must be ascribed to *channel interference*; the x-ray scattering of the different close-lying core-hole states interfere in such a way that the total signal is depleted. To estimate the chemical splitting of the $C_{1s} \rightarrow \pi^*$ transitions from the phenyl ring and vinylene core sites, a static exchange (STEX) calculation has been carried out for PPV. It gives a maximum for the energy splittings of 0.18 eV for the $C_{1s} \rightarrow \pi^*$ excitations corresponding to different core sites (actually also for the C_{1s} ionization potentials).

We note that by combining the resonant and the nonresonant XE spectra, one can obtain the band gap of the polymers. It equals the energy difference between the elastic peak in the RIXS spectrum and the front edge of the non-resonant XE spectrum. They are close to 2.8 eV for all the PPV, PMPV, and PDPV polymers. These quantities seem to fall in between the values obtained from optical absorption spectroscopy [12], 2.45 eV for PPV, and ultraviolet photoelectron spectroscopy 3.1 eV for PPV [13]. The differences might refer to the different broadening mechanisms for the bands and to the actual identification of the adiabatic or vertical transition energies which might come out differently in the different kinds of spectroscopies.

CONCLUSIONS

The conspicuous resemblance with benzene in both resonant and nonresonant x-ray emission spectra indicates no major electronic or geometric structure changes in the phenyl rings connecting with a vinylene group, and indicates also that the phenyl ring works as an excellent building block for these spectra. The benzene-like features in the RIXS spectra of the polymers are interpreted as the result of a strong channel interference. Only by accounting for this interference the π-electron emission derived from the forbidden e_{1g} level in benzene vanishes for the polymers.

The aspect of an alternative way to determine the band gap, as well as the building block character and the particular interference effects here studied, might be worth exploiting for other types of polymers as possible diagnostic tools.

ACKNOWLEDGMENTS

Thanks to T. Warwick and E. Rotenberg for their assistance in the experiment at the beamline.

REFERENCES

1. C.K. Chiang, C.R. Fincher, Y.W. Park, *et al.*, Phys. Rev. Lett. **39**, 1098 (1977).
2. J.H. Burroughes, D.D.C. Bradley, A.R. Brown, *et al.*, Nature **347**, 539 (1990).
3. J.H. Burroughes, C.A. Jones, and R.H. Friend, Nature **335**, 137 (1988).
4. F. Garnier, G. Horowitz, X. Peng, *et al.*, Adv. Mater. **2**, 592 (1990).
5. T. Warwick, P. Heimann, D. Mossessian, *et al.*, Rev. Sci. Instr. **66**, 2037 (1995).
6. J. Nordgren, G. Bray, S. Cramm, *et al.*, Rev. Sci. Instr. **60**, 1690 (1989).
7. P.L. Burn, D.D.C. Bradley, *et al.*, J. Chem. Soc. Perkin Trans. **1**, 3225 (1992).
8. W.J. Feast and I.S. Millichamp, Polym. Commun. **24**, 102 (1983).
9. F. Cacialli, R. Daik, *et al.*, Philos. Trans. R. Soc. London, Ser. A **355**, 707 (1994).
10. P. Skytt, J.-H. Guo, N. Wassdahl, et al., Phys. Rev. A **52**, 3572 (1995).
11. L.S. Cederbaum, W. Domcke, J. Schirmer, et al., J. Chem. Phys. **69**, 1591 (1978).
12. J.L. Bredas, J. Cornil, and A.J. Heeger, Adv. Mater. **00**, 000 (1996).
13. M. Fahlman, M. Lögdlund, S. Stafström, et al., Macromolecules **28**, 1959 (1995).

This work was supported by the Swedish Natural Science Research Council and the G. Gustafsson Foundation for Science and Medicine.

Principal investigator: E. Joseph Nordgren, Department of Physics, Uppsala University. E-mail: joseph@fysik.uu.se. Telephone: +46 18 4713554.

Identification of Green Rust in Environmental Compounds Using XANES of Fe-$L_{II,III}$ Edges

E.M. Kneedler[1], J. Rothe[1], K.W. Weissmahr[2], K. Pecher[3] and B.P. Tonner[1]
[1]Dept. Of Physics, University of Wisconsin-Milwaukee, P.O. Box 413, Milwaukee, WI 53201, USA
[2]Dept. Of Civil & Environmental Engineering, University of California, Berkeley, California 94720, USA
[3]Dept. Of Hydrology, University of Bayreuth, D-95440 Bayreuth, FRG

INTRODUCTION

"Green rust" is the name given to a class of iron oxide compounds that play an important role in soil chemistry, but have not been completely characterized either structurally or for their electronic properties. Green rust has been identified as a crucial intermediate phase in anaerobic bacterial corrosion[1]. To understand the role of green rust in the corrosion process, its presence and charge state in various stages of relevant reactions must be identified.

X-ray adsorption near edge spectroscopy (XANES) is well-suited to identifying different charge states of an element. Because of the rich fine structure in the L-edge transition metal spectrum originating in crystal-field splitting multiplet effects, the distribution of charge states in an inhomogeneous sample can be distinguished in a single spectrum. Two different methods are available for measuring the XANES; a total-electron yield method which detects the composition of the "near-surface" region, and a transmission method which averages over the composition of the bulk of a thin section of material. Both methods lend themselves to spectroscopic imaging, using X-ray photoelectron emission microscopy (XPEEM) for near-surface spectro-microscopy, and scanning transmission x-ray microscopy (STXM) for the bulk measurements. We use the BL-7 Spectro-Microscopy Facility STXM and photoemission apparatus in this work.

To produce our green rust, a reaction was initiated between goethite (α-FeOOH) and a solution of $FeCl_2$. By halting the reaction prematurely, precipitates of green rust could be obtained. After drying, the precipitates, dark in color, were mounted on a sample puck. Powders of two reference compounds were also mounted on the puck, $FeCl_2$ (Fe(II+)) and goethite (Fe(III+)) before insertion into an ultra-high vacuum chamber on BL7.0. To prevent contamination of the green rust sample, which is unstable in an oxygen environment, all stages of preparation and introduction into the analysis equipment were performed anaerobically, using an oxygen-free glove box and sealed transport unit. To obtain XANES spectra for each specimen, the sample current to ground was measured as a function of incident photon energy through the Fe $L_{II,III}$ adsorption edge.

RESULTS

XANES spectra for green rust and two reference compounds are displayed in Figure 1. The distinction between Fe(II+) and Fe(III+) charge states is obvious from a comparison of the two reference compounds $FeCl_2$ and goethite (top and bottom, resp.). The green rust sample (2nd from top) has a distinct signature, which resembles most closely the II+ spectrum, but contains a III+ component; the characteristic peak of the III+ signature is seen as a shoulder to the right of the main L_{III} peak. Thus, the green rust can be regarded to first approximation as a superposition of II+ and III+ character. To establish the effect of oxygen contamination, the green rust was later exposed to air for 50 minutes, and reintroduced for a final XANES spectrum (third from top). While there is still mixed II+/III+ character evident in the spectrum, the III+ component now dominates, indicating a conversion of Fe(II+) charge states to Fe(III+).

CONCLUSION

These XANES measurements show that our green rust can be regarded as predominantly in the Fe(II+) charge state, with a component of Fe(III+). Further experiments are necessary to determine whether this represents the intrinsic signature of the green rust, or if it includes some degree of impurity, such as goethite. It is clear that exposure to oxygen results in a conversion of II+ to III+ states. These data will be used as a basis for detecting green rust in smaller concentrations in natural minerals, such as clays, in an effort to better understand the process of biologically induced corrosion of Fe, and the role of 'green rust' compounds in environmental chemistry. Dry- and wet-sample XANES measurements are currently underway for natural clays. The spectra of powders in vacuum will be compared to those of wet samples in solution (from STXM) to determine if the drying process alters the charge state of the Fe.

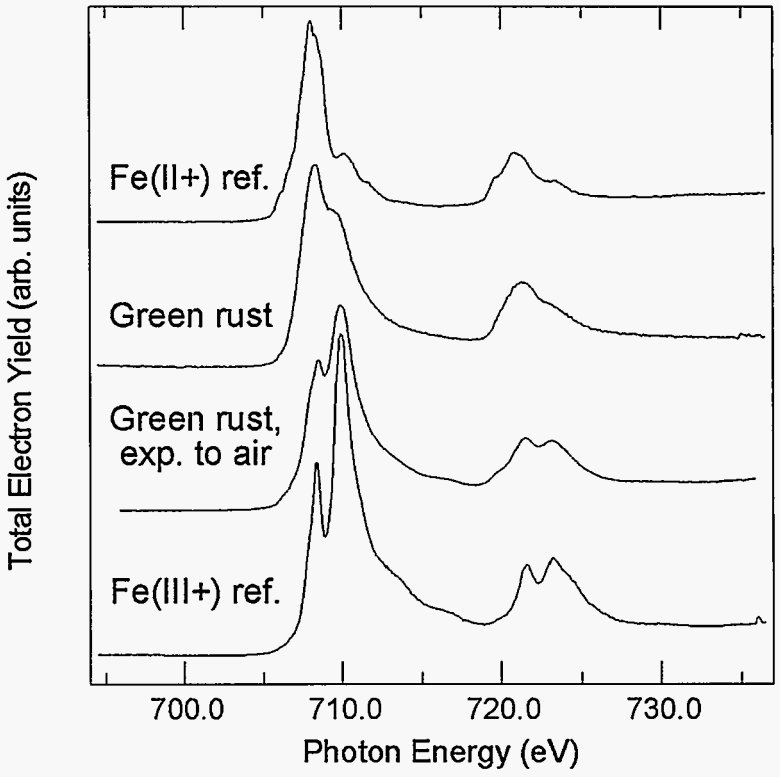

Figure 1. Total electron yield XANES measurements of the Fe-L II,III absorption edges for green rust and reference samples FeCl 2 (II+) and goethite (III+). Spectra are normalized to constant background increase through the edges.

REFERENCES

1. A.A. Olowe, Ph. Bauer, J.M.R. Genin and J. Guezennec, Corrosion NACE 45 (1989) 229-235.

This work was supported by the Department of Energy, OBER, under grant ER-62474.

Principal investigator: Brian Tonner, Department Of Physics, University of Wisconsin-Milwaukee, Email: tonner@csd.uwm.edu. Telephone: 414-229-4626

Resonant and nonresonant x-ray emission spectroscopy of poly(pyridine-2,5-diyl)

M. Magnuson, J.- H. Guo, C. Såthe, A. Agui and J. Nordgren

Department of Physics, Uppsala University, Box 530, S-75121 Uppsala, Sweden

Introduction

Conjugated polymers have been the subject of much interest owing to their unique electronic properties which can be technically exploited e.g., as doping induced electrical conductors and light emitting diodes [1]. Detailed experimental studies of the uppermost π-orbital levels at the valence band edges of these polymers are important to gain an understanding of their properties. Such studies have been carried out by many techniques including photoelectron spectroscopy using photon excitation in both the x-ray and ultraviolet wavelength regimes.

X-ray emission spectroscopy (XES) provides a useful technique for studying conjugated polymers but has yet not been exploited much. XES provides a means of extracting electronic structure information in terms of local contributions to the Bloch or molecular orbitals (MO's), since the x-ray processes can be described by local dipole selection rules. The method is atomic element specific and also angular momentum and symmetry selective at high resolution. However, the relatively low fluorescence yield and instrument efficiencies associated with x-ray emission in the sub keV region places considerable demands. An intense synchrotron radiation (SR) excitation source is therefore required which has earlier limited the experimental activity of studying the behavior for radiative emission spectroscopy of oligomers and polymers.

The nonresonant x-ray emission spectra are obtained when the energy of the incident photons exceed far above the core ionization threshold. In this case the x-ray emission spectral profile is practically independent (besides x-ray satellites) of the excitation energy and has been often described using a two-step model with the emission step decoupled from the excitation step. On the other hand, when the excitation energy is tuned at resonances below or close to the core ionization threshold, the spectral distribution is strongly dependent on the excitation energy. The description in the resonant case must therefore switch from a two-step to a one-step model with the excitation and emission transitions treated as a single scattering event in resonant inelastic x-ray scattering (RIXS).

In a recent work we used a set of poly(*p*-phenylenevinylene)s; PPV, PMPV and PDPV to demonstrate the feasability of studying the electronic structure of conjugated polymers by means of resonant and nonresonant x-ray emission with monochromatic SR excitation [2]. It is of interest to find out how the resonant and non-resonant spectra show up in more complicated hetero-compounds, then also mapping the energy bands by transitions from more than one atomic element. In this present work we present, and analyze for this purpose, the x-ray emission spectra of poly(pyridine-2,5-diyl) (PPy) which is an aza-substituted poly(*p*-phenylene). The analysis based on *ab initio* canonical Hartree-Fock theory indicate isomeric dependence of the carbon x-ray absorption spectra and the resonant x-ray emission spectra [3]. The resonant emission spectra also show that the π electron bands dissappear in the spectra due to symmetry selection and momentum conservation rules.

Experiment

The experiments were carried out at beamline 7.0 at ALS. This undulator beamline includes a spherical-grating monochromator and provides linearly polarized SR of high resolution and high brightness. X-ray absorption (XA) spectra were recorded by measuring the total electron yield from the sample current with 0.25 eV and 0.40 eV resolution of the beamline monochromator for the carbon and nitrogen edges, respectively. The XA spectra were normalized to the incident photon current using a clean gold mesh in front of the sample.

The x-ray emission spectra were recorded using a high-resolution grazing-incidence x-ray fluorescence spectrometer [4]. During the x-ray emission measurements, the resolution of the beamline monochromator was the same as in the XA measurements. The x-ray fluorescence spectrometer had a resolution of 0.30 eV and 0.65 eV, for the carbon and nitrogen measurements, respectively. The energy scale has been calibrated using the elastic peak in the x-ray emission spectra which has the same energy as the incoming photon energy. The sample was oriented so that the incidence angle of the photons was 20 degrees with respect to the surface plane. During the data collection, the samples were scanned (moved every 30 seconds) in the photon beam to avoid the effects from photon-induced decomposition of the polymers. The base pressure in the experimental chamber was 4×10^{-9} Torr during the measurements.

Results

X-ray emission and absorption at the N*1s* threshold

Figure 1 shows resonant (bottom) and non-resonant (top) X-ray emission spectra of PPy excited at 398.8 eV and 408.3 eV photon energy, respectively. In the XA spectrum (dashed lines) an intense peak at about 398.8 eV corresponds to absorption from the core to the π^* lowest unoccupied molecular orbital (LUMO). At higher photon energies, broad shape resonances are observed mainly due to absorption from core to the unoccupied σ^* MO's and multielectron processes. The shape and position of the absorption features are connected to the final core excited state.

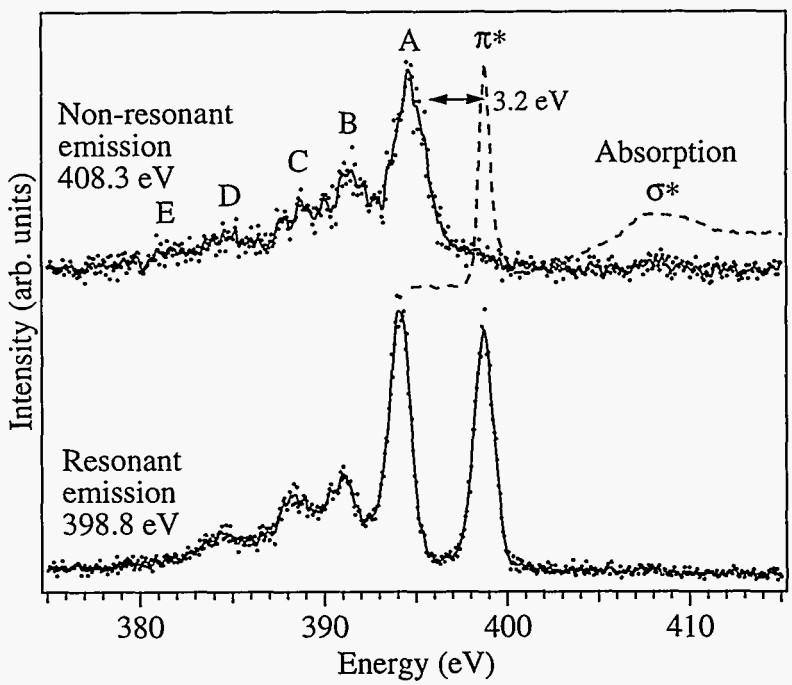

Fig. 1: X-ray emission and absorption spectra of PPy at the N*1s* threshold.

In the resonant emission spectrum a strong elastic (recombination) peak is observed at 398.8 eV. In both the emission spectra, five features (labeled A-E) can be observed. Peak A corresponds to π-electron states at the valence band edge and peak C corresponds to σ electronic states. In the resonant case the band structure is similar to the non-resonant case.

X-ray emission and absorption at the C*1s* threshold

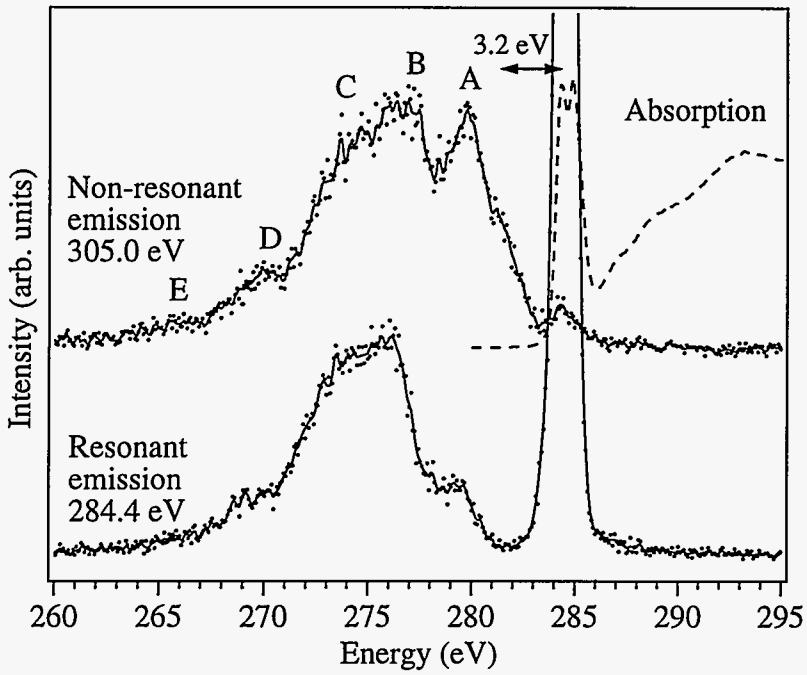

Fig. 2: X-ray emission and absorption spectra of PPy at the C*1s* threshold.

Figure 2 shows resonant (bottom) and non-resonant (top) x-ray emission spectra of PPy excited at 284.4 eV and 305.0 eV, respectively, and an x-ray absorption spectrum (dotted lines) measured at the carbon 1s threshold of PPy. A double peak structure in the absorption spectrum with peaks at 284.4 eV and 285.0 eV, corresponds to the lowest unoccupied molecular C*1s* (LUMO) orbitals which are chemically shifted. At higher energies, similar broad shape resonances as in the nitrogen case are observed in the carbon absorption spectrum.

The x-ray emission spectra of carbon obviously map the same final levels as the nitrogen spectra but with a different energy scale and transition moments owing to the different intermediate states. The non-resonant x-ray emission spectrum is dominated by the 2p -> 1s diagram transitions between the valence and core vacancy states in normal emission. A peak with lower intensity is clearly visible at 284.5 eV due to multielectron satellite transitions.

Discussion

In the C K spectra the MO's of band B have more intensity than in the nitrogen spectra due to a stronger contribution from the carbon atoms as these MO's have a larger dipole overlap with the C*1s* core orbitals than with the N*1s* core orbitals. For the inner MO's, such as band E, the intensities are weaker in both the C and N K spectra due to the larger 2s character of the MO's. Thus, while the carbon spectra show a similar peak structure of the bands, the intensity distribution is different. In both cases the resonant spectra show strong elastic (recombination) peaks. Comparing the resonant and non-resonant C K spectra, the largest difference occurs at about 280 eV photon energy, where band *A* appears only as a weak feature in the resonant spectrum. The vanishing of the A-band has previously been observed for resonant x-ray emission spectra of benzene [5] and is the result of the parity selection rule. In previous studies of aniline [6] and poly(*p*-phenylenevinylene) polymers [2], it was argued that the *multi-channel interference* effects make transitions from π MO's of the *A*-band to the C*1s* core orbitals effectively forbidden. Thus the interference effect, and so the symmetry selectivity, grows progressivly stronger as the chemical disturbance of the benzene rings becomes weaker. Hence, the *A*-band emerges only as a weak feature the spectra. Just as the symmetry selection in the resonant aniline spectrum the momentum conservation for resonant emission in the polymers is an effect of channel interference. For π conjugated polymers this momentum conservation leads to depletion of emission from π-levels, as nicely confirmed in the present work

[3] and in ref. [2] for the PPV compounds. One finds the depletion to be about as strong for PPy as for PPV compounds although one would expect a smaller effect for PPy due to the stronger chemical shifts of the core-excited states. However, we do not observe a corresponding depletion going from the non-resonant to the resonant condition in the nitrogen spectra. This is explained by the fact that the strong high-energy band in these spectra are due to the lone-pair *n* orbitals, localized on the nitrogen sites, which have σ symmetry. The different localization character of the emitting levels are clearly revealed from the anaysis of the resonant spectra. By subtracting the energy of this edge structure in the non-resonant spectrum from that of the elastic peak of the resonant spectrum provides an alternative way of experimentally obtaining the optical band gap as demonstrated in the PPV paper [2]. The band gap obtained for PPy in this way is 3.2 eV which agrees fairly well with the value of 3.05 eV obtained from ultraviolet photoelectron spectroscopy [7] and optical absorption measurements.

References

[1] J. H. Burroughes, D. D. C. Bradley, A. R. Brown, R. N. Marks, K. Mackay, R. H. Friend, P. L. Burns and A. P. Holmes; Nature **347**, 539 (1990).

[2] J.-H. Guo, M. Magnuson, C. Såthe, J. Nordgren, L. Yang, Y. Luo, H.Ågren, K. Z. Xing, N. Johansson, W. R. Salaneck and W. J. Feast, J. Chem. Phys. **108**, in press.

[3] M. Magnuson, L. Yang, J.-H. Guo, C. Såthe, A. Agui, H. Ågren, J. Nordgren, N. Johansson, W. R. Salaneck, L. E. Horsburgh and A. P. Monkman, to be submitted.

[4] J. Nordgren and R. Nyholm, Nucl. Instr. Methods A **246**, 242 (1986); J. Nordgren, G. Bray, S. Cramm, R. Nyholm, J. E. Rubensson and N. Wassdahl, Rev. Sci. Instr. **60**, 1690 (1989).

[5] P. Skytt, J.-H. Guo, N. Wassdahl, J. Nordgren, Y. Luo and H. Ågren; Phys. Rev. A **52**, 3572 (1995).

[6] Y. Luo, H. Ågren, J.-H. Guo, P. Skytt, N. Wassdahl and J. Nordgren; Phys. Rev. A **52**, 3730 (1995).

[7] T. Miyamae, D. Yoshimura, H. Ishii, Y. Ouchi, K. Seki, T. Miyazaki, T. Koike, and T. Yamamoto; J. Chem. Phys. **103**, 2738 (1995).

This work was supported by the Swedish Natural Science Research Council (NFR), the Swedish Research Council for Engineering Sciences (TFR), the Göran Gustavsson Foundation for Research in Natural Sciences and Medicine and the Swedish Institute (SI).

Principal investigator: E. Joseph Nordgren, Physics Department of Uppsala University, Sweden.
E-mail: joseph@fysik.uu.se, Phone +46 18 471 3554.

Resonant, Core Level and Angle Resolved Photoemission Studies of Rare Earth Hexaborides

J.A. Clack[1], J.D. Denlinger[1], J.W. Allen[1],
D. M. Poirier[2], C.G. Olson[2], Z. Fisk[3], D. Young[3] and P.C. Canfield[2]
[1]Randall Laboratory, University of Michigan, Ann Arbor, MI 48109-1120
[2]Ames Laboratory, Iowa State University, Ames, IA 50011
[3]Dept. of Physics and NHFML, Florida State University, Tallahassee, FL

INTRODUCTION

The traditional understanding [1,2,3] of the electronic structure of the cubic compounds AB_6 where A is Sr or a rare earth is that a boron-based valence band is separated by a gap from an A-based conduction band. The boron bonding is such that the valence band lacks two electrons per formula unit of being filled. Whether the material is an insulator or a metal then depends simply on the valence of A, under the reasonable assumption that the partially filled 4f shell of a rare earth element will not lead to conductivity. In this view, SrB_6 with divalent Sr is a normal band insulator, ferromagnetic EuB_6 has divalent Eu and is an insulator, LaB_6 is a metal with trivalent La giving one electron to the La based conduction band, and SmB_6 with Sm mixed valent between divalent and trivalent should also be a metal. With the exception of trivalent metals like LaB_6 [4], this simple view has proved remarkably difficult to establish. Hints of non-insulating behavior in EuB_6 have been ascribed to non-stoichiometry [5] or have caused speculations that EuB_6 is mixed valent [5] or a semi-metal [6]. Various properties of SmB_6 force the view, initially controversial [7] but then established [8], that it has a small single-particle gap, of order 5 to 10 meV, at E_F. However, the situation is further complicated by more recent findings on SmB_6 which imply states within this gap on yet a lower energy scale [9].

Of a group of small-gap mixed valent materials [10-12], SmB_6 was the first to be clearly identified [8]. The earliest picture [13] of the formation of the energy gap was that of a very narrow f-level crossing a broad conduction band just at E_F so that a gap can be opened by f-conduction band hybridization. Such a picture can be explicitly constructed [14] and linked [15] to the Luttinger theorem by interpreting the f-band as the lowest lying fermion excitation of the $f^6 \rightarrow f^5$ type, and by a symmetry analysis showing that, for SmB_6 at least, such a gap can indeed be opened everywhere in the Brillouin zone. A more recent view of these materials, leading to the name "Kondo insulators" replaces the narrow f-level by the effective f-level associated with the Kondo resonance [16,17,18]. Although the Kondo view appears to work well for Ce materials such as $Ce_3Bi_4Pt_3$ [19], which are known to be in the Kondo regime of the Anderson model, it is quite unclear that this view applies to SmB_6, which is strongly mixed valent and displays $f^6 \rightarrow f^5$ transitions just at E_F within experimental resolution.

We have performed complementary photoemission studies at the ALS and the Wisconsin Synchrotron Radiation Center (SRC), in a continuing program directed at the various issues described above. Results to date are described in this abstract.

SrB_6 and EuB_6

Traditionally it has been regarded as important to study the electronic structure of single valent materials such as SrB_6, LaB_6 and EuB_6 as reference materials for the more complex problem of the mixed valence of SmB_6. However, efforts to verify the traditional view of the hexaboride band structure in SrB_6 and EuB_6 have yielded surprises. Band calculations [20,21] show the possibility

that both materials could be intrinsic semimetals due to a small overlap of the valence and conduction bands at the X-point, and recent transport [22,23,24] and Shubnikov-de Haas data [24] require either this semi-metal possibility or off-stoichiometry for SrB_6, or additionally for EuB_6, that it is slightly mixed valent.

Early studies [25] of the Eu 4f spectrum of EuB_6 left open the possibility of slight Eu mixed valence, either intrinsic or due to off-stoichiometry. We have eliminated this possibility by careful resonant photoemission studies at the ALS. Fig. 1 shows the strong enhancement of the Eu^{2+} $4f^7 \rightarrow 4f^6$ emission at binding energy $E_B \approx 1eV$ as the photon energy is varied through the Eu 4d→4f absorption edge. No trace of Eu^{3+} $4f^6 \rightarrow 4f^5$ emission, which would be displaced to higher E_B by the 4f Coulomb repulsion, can be seen.

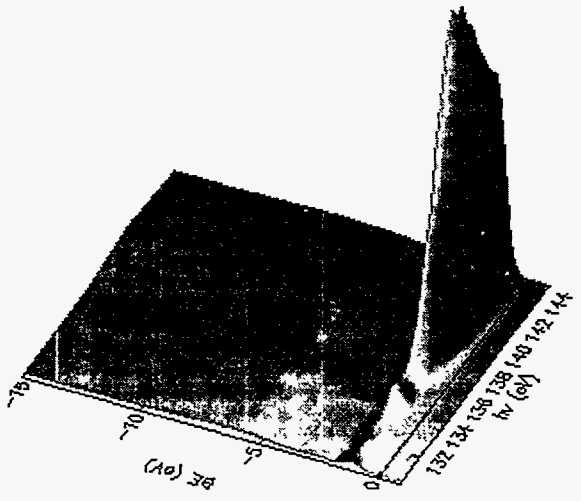

Figure 1. Resonant photoemission of EuB_6 at the Eu 4d→4f absorption edge. Only the Eu $4f^7 \rightarrow 4f^6$ transition corresponding to divalent Eu is resonantly enhanced.

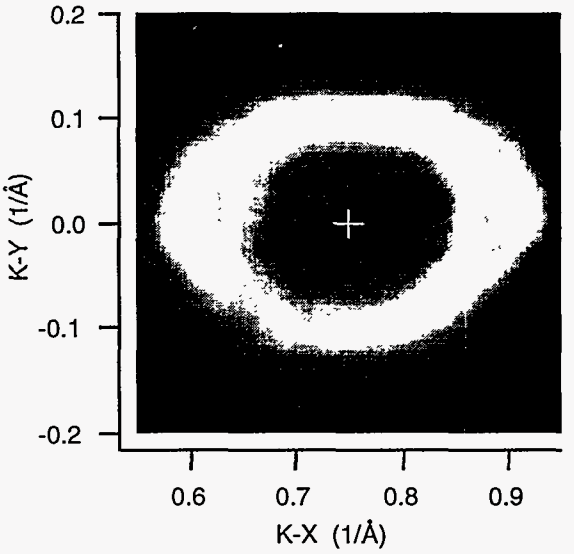

Figure 2. EuB6 Fermi energy intensity map at hn=30 eV centered around the X-point (+). The ring of bright intensity corresponds to a small electron pocket.

Angle resolved photoemission spectroscopy (ARPES) performed with low photon energies at the SRC provides strong evidence that both materials are semi-metals, through the finding of a small piece of Fermi surface (FS) around the X-point. The Fermi energy ARPES intensity map of Fig. 2 provides an image of the EuB_6 FS in the plane of the sample surface. The SrB_6 FS similar but much smaller, consistent with band theory. For EuB_6 the presence of a true FS has important implications [23] for understanding the exchange interactions leading to its ferromagnetism, and for SrB_6 this result provides a concrete framework in which to consider novel low temperature transport properties [22]. We are now analyzing these data and comparing to other evidence [22,23,24] concerning the carrier densities and FS sizes. Important implications for future studies are described below.

SmB_6

Early [26,27] photoemission and resonance photoemission studies of SmB_6 observed bulk Sm^{2+} $4f^6 \rightarrow 4f^5$ emission just at E_F, within the experimental resolution, bulk Sm^{3+} $4f^5 \rightarrow 4f^4$ emission at $E_B \approx 7eV$, and Sm^{2+} $4f^6 \rightarrow 4f^5$ emission surface-shifted by ≈ 0.6 eV. Although our ALS resonant photoemission studies of cleaved single crystals do not have resolution adequate to observe the small gap expected at E_F, they have nonetheless revealed $4f^6 \rightarrow 4f^5$ structure additional to what was seen in early work. Fig. 3 shows the overall resonant structure and Fig. 4 shows the $4f^6 \rightarrow 4f^5$ spectrum at normal emission for a photon energy 135 eV just above the Sm 4d→4f edge.

Expected [28] atomic $4f^5$ final state structure is shown by the line spectrum. The splitting in the peak at $E_B \approx 3$eV was not observed before. The peak nearest E_F shows three pieces of structure where only two are expected. The extra splitting cannot plausibly be ascribed to a surface shift, because the known surface shifted peaks give a replica $4f^5$ spectrum beginning at $E_B \approx 0.6$ eV, and are not even seen in this normal emission spectrum. Further, crystal field splittings of the f^5 multiplets are generally not expected to exceed 10 meV. Detailed and higher resolution studies of the near E_F feature are planned.

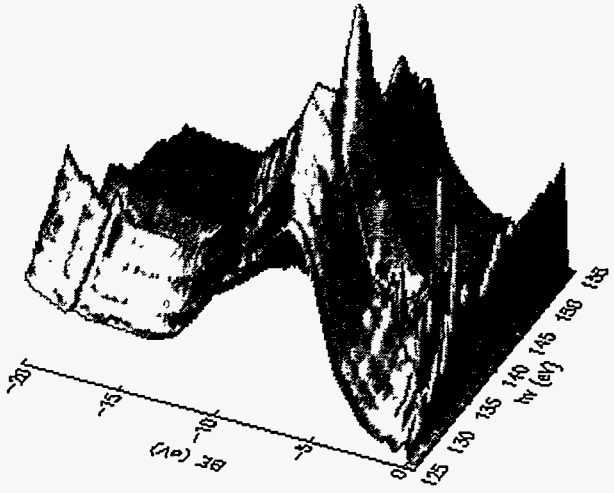

Figure 3. Resonant photoemission of SmB_6 at the Sm 4d→4f absorption edge. Both trivalent and divalent Sm resonant enhancements are present.

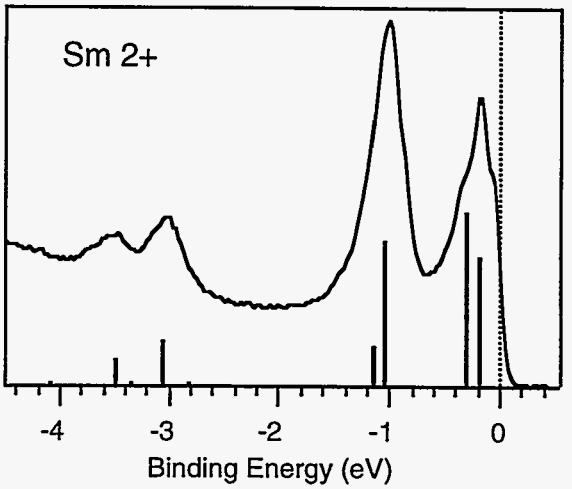

Figure 4. Sm $4f^6 \rightarrow 4f^5$ spectrum at the strongest Sm 2+ resonance (135 eV). Vertical bars are calculated final state multiplets.

The presence of strong 4f emission just at E_F has precluded directly imaging the non-4f FS, but we have observed in ARPES spectra obtained at the SRC a dispersing peak which crosses E_F at essentially the k-value expected from band calculations [29] for LaB_6, assuming the 0.6 conduction electrons/Sm implied by the Sm valence of 2.6.

$Sm_{1-x-y}Sr_xLa_yB_6$ Hexaboride Alloys

Our hexaboride compound results have motivated us to begin studying the alloy system $Sm_{1-x-y}Sr_xLa_yB_6$. The general thrust of these studies is to address the relation between single ion and lattice mixed valence behavior, especially the possibility suggested by Haldane [30,31] that conduction electron screening can promote single-ion mixed valence by pinning the f-level to E_F. In the simplest model, without screening effects, the Sm $f^6 \leftrightarrow f^5$ energy is fixed relative to the conduction band. By varying x and y we can sweep E_F through this energy and so vary from Sm^{3+} in SrB_6 to Sm^{2+} in LaB_6, and we can vary the concentration of Sm from concentrated to dilute while maintaining fixed the number of conduction electrons and hence E_F and hence, perhaps, the intermediate Sm valence. We can determine if the simple scenario actually occurs or if there is a tendency for the f-level to jump to E_F, or cling to E_F,

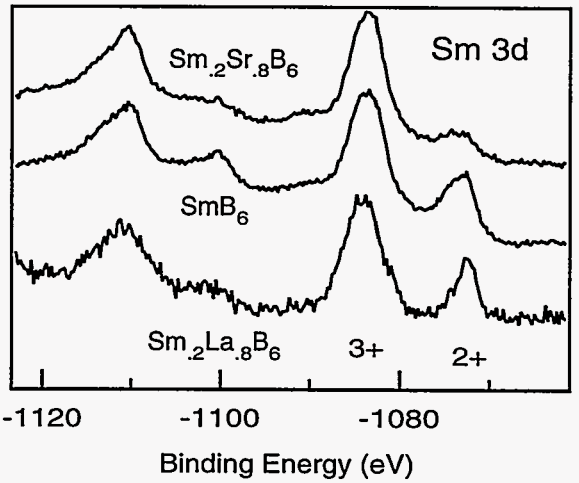

Figure 5. Sm 3d core level spectra using Al Ka x-rays showing varying ratios of Sm 2+ and Sm 3+.

due to screening or to Sm-Sm interaction effects. The spectroscopic results will be correlated with transport studies done by M.C. Aronson. Preliminary studies of Sm core level spectra (see Fig. 5) to determine the valence in several alloy samples indicate departures from the simple scenario.

ACKNOWLEDGMENTS

We gratefully acknowedge stimulation from M.C. Aronson to pursue these studies.

REFERENCES

1. H.C. Longuet-Higgins and M.Roberts, Proc. Royal Society (London) **224**, 336-347 (1954).
2. R.W. Johnson and A. H. Daane, J. Chem. Phys. **38**, 425-432 (1963).
3. J. Etorneau *et al*, J. Solid State Chem. **2**, 332-342 (1970).
4. Y. Ishizawa et al, J. Phys. Soc. Jpn. **42**, 112 (1977).
5. Y. Ishizawa *et al*, Solid State Commun. **22**, 573-576 (1977).
6. Z. Fisk *et al*, J. Appl. Phys. **50**, 1911-1913 (1979).
7. J.W. Allen *et al*, J. Appl. Phys. **49**, 2078-2083 (1978).
8. J.W. Allen *et al*, Phys. Rev. B **20**, 4807-4813 (1979).
9. J.C. Cooley *et al*, Phys. Rev. Lett. **74**, 1629-1632 (1995).
10. T. Takabatake *et al*, Jpn. J. Appl. Phys. **26**, Suppl. 26-3, 547-548 (1987).
11. M. Kasaya *et al*, J. Magn. and Magn. Mat. **47 & 48**, 429-435 (1985).
12. M.F. Hundley *et al*, Physica B **171**, 254-257 (1991).
13. N.F. Mott, Philos. Mag. **30**, 403-416 (1973).
14. J.W. Allen and R.M. Martin, J. Physique **41**, Colloque C5, 171-176 (1980).
15. R.M. Martin and J.W. Allen, in *Valence Fluctuations in Solids*, eds. L.M. Falicov, W. Hanke, and M.B. Maple, (North-Holland, Amsterdam, 1981), p. 85-91.
16. P.S. Riseborough, Phys. Rev. B **45**, 13984-95 (1992).
17. Z. Fisk, Comments Cond. Mat. Phys. **16**, 155-165 (1992).
18. A.J. Millis, in *Physical Phenomena at High Magnetic Fields*, eds. E. Manousakis *et al*, (Addison-Wesley, Menlo Park, 1992), p. 146-155.
19. J.C. Cooley *et al*, Phys. Rev. B **55**, 7533-7538 (1997).
20. A. Hasegawa and A. Yanase, J. Phys. C **12**, 5431-5440 (1979).
21. S. Massida *et al*, Z. Phys. B **102**, 337 (1997).
22. H.R. Ott *et al*, Z. Phys. B **102**, 337-345 (1997).
23. J.C. Cooley, M.C. Aronson, J.S. Serrao and Z. Fisk, preprint.
24. L. Degiorgi, E.Felder, H.R.Ott, J.L. Serrao, and Z. Fisk, Phys. Rev. Lett. **79**, 5134 (1997).
25. Y. Takakuwa *et al,* Jap. J. of Appl. Phys. **17**, 284 (1978).
26. J.-N. Chazalviel *et al,* Phys. Rev. B **14**, 4586 (1976).
27. J.W. Allen *et al,* Phys. Rev. B **21**, 1335 (1980).
28. F. Gerken, J. Phys. F: Met. Phys. **13**, 703 (1983).
29. Y. Kubo and S. Asano, Phys. Rev. B **39**, 8822-8831 (1989).
30. F.D.M. Haldane, in *Valence Instabilities and Related Narrow-Band Phenomena*, edited by R.D. Parks, (Plenum, New York, 1977) p. 191-200.
31. F.D.M. Haldane, Phys. Rev. B **15**, 2477-2484 (1977).

This work was supported by the U.S. Dept. of Energy (DoE) under contract No. DE-FG02-90ER45416 and by the U.S. NSF under grant No. DMR-94-23741. Work at the Ames lab was supported by the DoE under contract No. W-7405-ENG-82. The SRC is supported by the U.S. NSF under grant DMR-95-31009.

Principal investigator: J.W. Allen, Randall Laboratory, University of Michigan, Ann Arbor, MI 48109-1120. Email: jwallen@umich.edu. Telephone: 313-763-1150.

Resonant Inelastic Soft-X-ray-Scattering from DyF_3

S. M. Butorin,[1] J.-H. Guo,[1] D. K. Shuh,[2] and J. Nordgren[1]
[1]Department of Physics, Uppsala University, Box 530, S-751 21 Uppsala, Sweden
[2]Chemical Sciences Division, Lawrence Berkeley National Laboratory, Berkeley, CA 94720

INTRODUCTION

For highly correlated materials, such as rare-earth compounds, studies of low-energy electronic excitations (intra-ionic f-f excitations in this case) can provide a better understanding of ground state properties. In the case of weak hybridization effects, the interlevel coupling and consequently *J*-mixing in the ground state of the system are often disregarded in the interpretation of experimental data by applying a pure atomic approximation (mainly for high-energy spectroscopies) or by using a first order crystal-field theory where the crystal field interaction is assumed to act only within the separate *J* manifolds. This is partly due to complications in extracting information about the ground state *J*-mixing directly from the data. For example, the estimation of the *J*-mixing degree in high-order crystal-field theory by adjusting the crystal-field parameters from the fit of optical absorption or low-energy electron-energy-loss spectra [1,2] may result in a large uncertainty originating from difficulties calculating the intensities of dipole-forbidden transitions. In turn, the possible influence of weak metal-ligand hybridization is difficult to analyze quantitatively in the absence of so-called charge-transfer satellites in high-energy spectroscopic data.

In this situation, the use of alternate spectroscopic means to obtain *J*-mixing information is essential. Recently, Finazzi et al. [4] have shown that the ground-state *J*-mixing can be studied by taking advantage of dichroic properties of rare-earth 3d x-ray absorption. However, the method is restricted to magnetically ordered systems. In this report we discuss the potential of resonant valence-to-core x-ray fluorescence spectroscopy (RXFS) to detect the ground-state *J*-mixing when applied to compounds without distinct long-range magnetic order and significant metal-ligand hybridization.

Similar to optical absorption and electron-energy-loss spectroscopies with respect to probing the low-energy excitations in electron-correlated materials, RXFS at the same time provides the higher level of the transition selectivity due to the element specificity and dipole selection rules. In contrast to systems with the strong metal-ligand hybridization where the charge-transfer process leads to an appearance of additional intense lines in resonant x-ray fluorescence spectra [5] as a result of inter-ionic excitations, *J*-mixing in systems with weak hybridization effects is expected to manifest itself in an intensity gain of some intra-ionic (f-f) transitions which are disallowed for the pure Hund-rule ground state. In other words, transitions with ΔJ other than 0, ± 1, and ± 2 are probed in the resonant excitation-deexcitation process (speaking correctly *J* is not a good quantum number in this case).

EXPERIMENTAL DETAILS

DyF_3 (99.99%) was congruently evaporated from a water-cooled effusion source in a simple preparation chamber utilizing a graphite crucible evaporator. The DyF_3 film (28 Å) was grown on ambient high purity platinum foil substrate at 4×10^{-9} Torr. The evaporation rate was calibrated by a quartz crystal monitor and the film thickness is estimated to be within about 10%. The film was stored under a nitrogen atmosphere and then loaded into the experimental chamber equipped with a

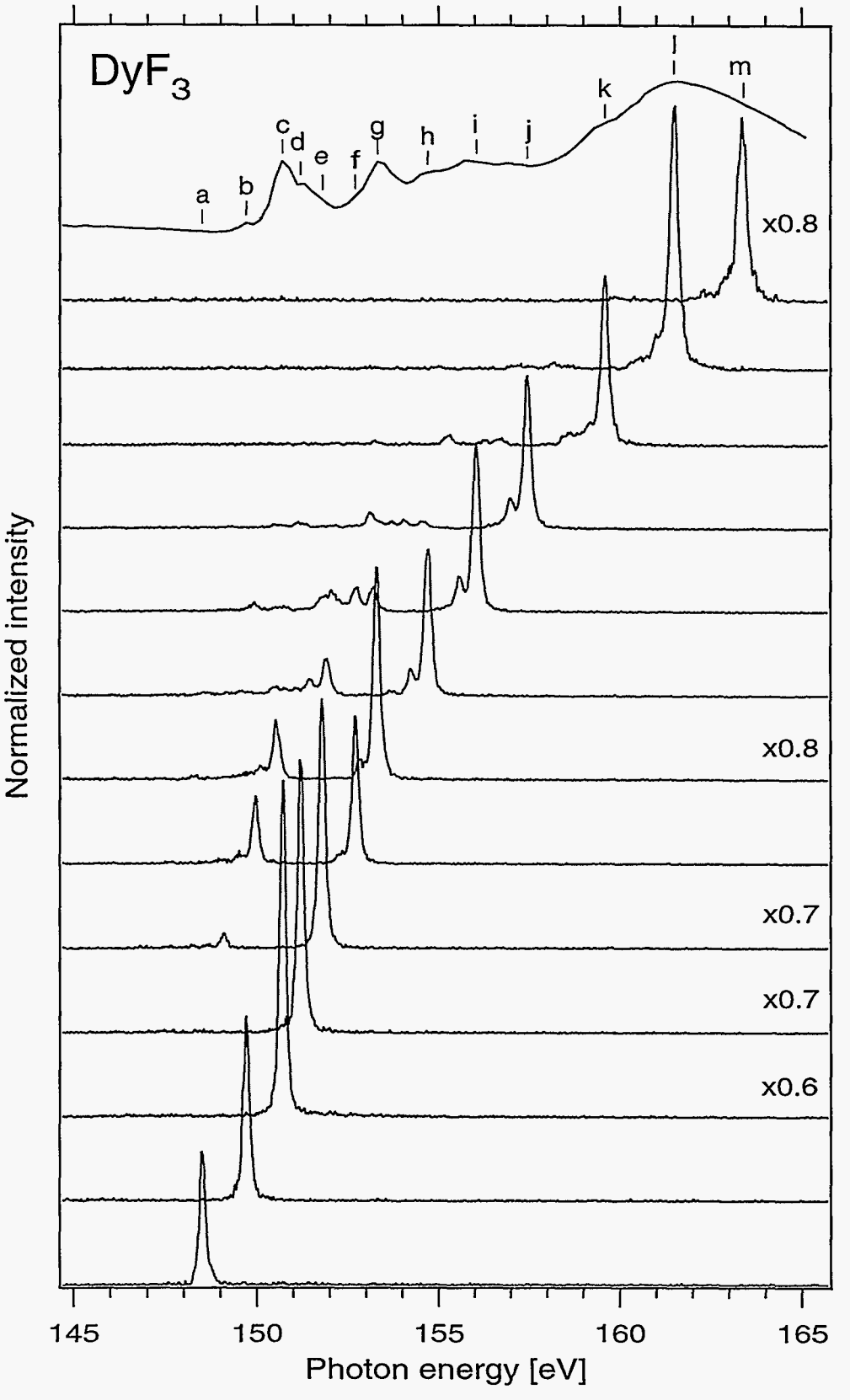

Figure 1. Total electron yield spectrum at the Dy 4d edge and resonant Dy 4f → 4d x-ray fluorescence spectra of DyF_3 normalized to the incoming photon flux. The letters correspond to the excitation energies indicated in the absorption spectrum.

fluorescence spectrometer. The sample was mounted with its surface normal located in the horizontal scattering plane.

The experiment was carried out at beamline 7.0 of the Advanced Light Source, Lawrence Berkeley National Laboratory with a spherical grating monochromator. The Dy 4f → 4d x-ray fluorescence spectra of DyF_3 were recorded using a grazing-incidence grating spectrometer [6] with a two-dimensional detector. The spectrometer resolution was set to 95 meV at 152 eV. The incidence angle of the photon beam was about 2° from the sample surface and the spectrometer was placed in the horizontal plane at an angle of 90° with respect to the incidence beam. To determine the excitation energies, the Dy 4d x-ray absorption spectrum of DyF_3 was obtained by measuring total electron yield at the 90° incidence angle of the incoming radiation. During x-ray absorption and fluorescence measurements, the resolution of the monochromator was set to 76 meV at a photon energy of 152 eV. All of the spectra were recorded at room temperature.

RESULTS AND DISCUSSION

The resonant Dy 4f → 4d x-ray fluorescence spectra of DyF_3 (Fig. 1) show a dispersion-like behavior upon tuning the excitation energy across the Dy 4d absorption edge. The spectra recorded at the excitation energies labeled by *a*, *b*, and *c* appear as a single peak with other low-energy structures being very weak. Further increase in the excitation energy gives rise to an enhancement of these weak structures so that the appreciable spectral weight is observed within the 8.5 eV range below the elastic line, for example, in spectra *i* and *j*. All of the low-energy peaks follow varying excitation energies and therefore can be associated with resonant inelastic x-ray scattering. It is rather unlikely that the spectral weight on the low-energy flank of the elastic line originates from phonon relaxation because this weight consists of distinct structures instead of a continuous structureless band and the structures show different dependence on the excitation energy.

There are two distinct groups of pronounced inelastic-scattering peaks in Fig. 1. The first group is distinguished by small energy losses on the tail of the elastic line, whereas the second is characterized by energy losses more than 2.5 eV. When the excitation energy approaches the main broad maximum of the Dy 4d absorption edge, the first group still possesses significant intensity while the structures of the second group become relatively faint. Regarding the energy scale on which the spectral variations occur, the observed fluorescent transitions can be attributed to intra-ionic f-f excitations. The energy gap between two groups of inelastic x-ray scattering structures reflects the separation between sextuplets and quadruplets of trivalent Dy [7,8] which can be reached due to the excitation-deexcitation process.

The results of preliminary atomic-multiplet calculations for the Dy^{3+} ion show that the dominant elastic peak in all of the Dy 4f → 4d spectra from DyF_3 is to large extent a consequence of strong interference effects in the intermediate state of the coherent second-order optical process. The states constituting the main 4d absorption edge have a lifetime broadening of about 2 eV largely because of the 4d-4f4f Coster-Kronig decay.

A close inspection of experimental 4f → 4d spectra shows that there are some spectral structures which are not revealed in calculations within the pure atomic approximation. Thus, the feature with the energy loss of about 1.15 eV is observed in spectra *h*, *k*, and *l*, presented in detail by Fig. 2. While atomic multiplet theory predicts the non-zero intensities for resonant inelastic x-ray scattering transitions to the $^6H_{13/2}$, $^6H_{11/2}$, and $^6F_{11/2}$ sextuplets of the $4f^9$ configuration, the energy of the extra-feature in experimental spectra *h*, *k*, and *l* (Fig. 2) is close to those of $^6F_{9/2}$ and $^6H_{7/2}$ manifolds of Dy^{3+} in LaF_3 [9]. This is an indication of *J*-mixing and the presence of $J = 13/2$ and

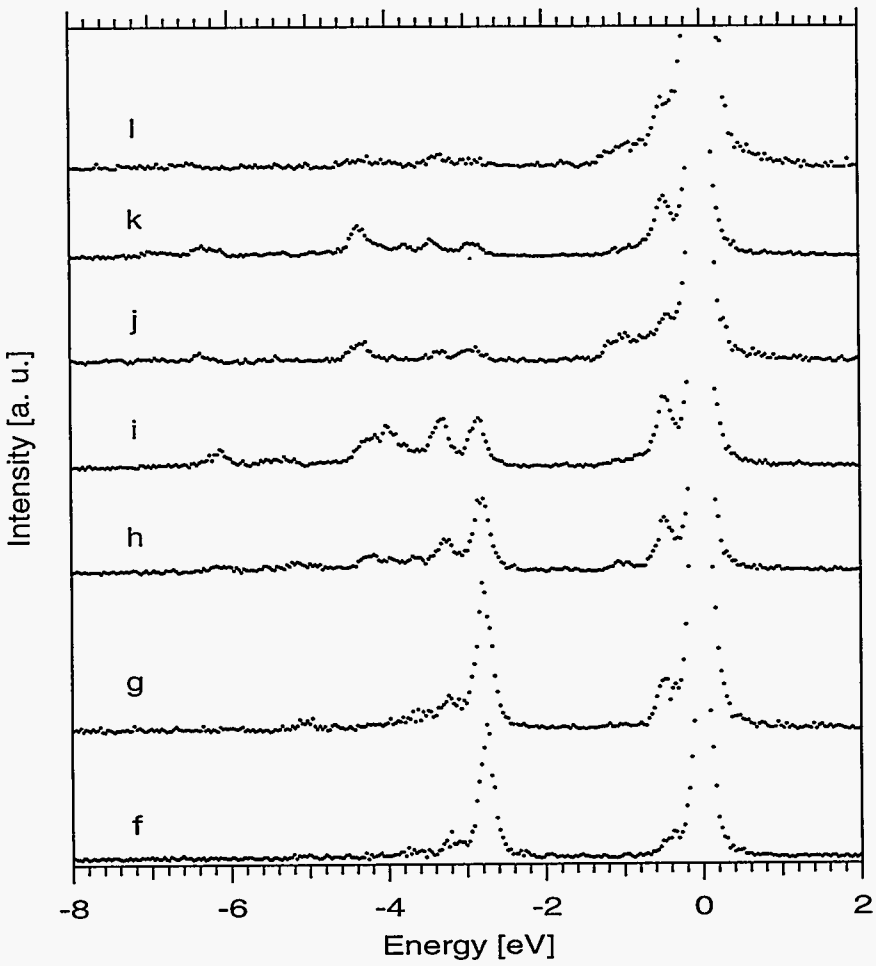

Figure 2. Enlarged inelastic x-ray scattering part of the resonant Dy 4f → 4d spectra from DyF_3.

J =11/2 components in the ground state of DyF_3. Indications of other extra-structures missing from atomic calculations can be seen in the energy range between -2.0 and -1.2 eV, as in spectra *l* and *m*. However, the present level of statistics does not permit identification.

REFERENCES

1. J. D. Axe and G. H. Dieke, J. Chem. Phys. **37**, 2364 (1962).
2. M. D. Seltzer et al., J. Phys. Chem. Solids **57**, 1175 (1996).
3. A. Kotani and H. Ogasawara, J. Electron Spectrosc. **60**, 257 (1992).
4. M. Finazzi et al., Phys. Rev. Lett. **75,** 4654 (1995).
5. S. M. Butorin et al., Phys. Rev. Lett. **77**, 574 (1996).
6. J. Nordgren et al., Rev. Sci. Instrum. **60**, 1690 (1989).
7. D. van der Marel and G. Sawatzky, Phys. Rev. B **31**, 1936 (1985).
8. W. T. Carnall et al., J. Chem. Phys. **49**, 4424 (1968).
9. J. L. Fry et al., J. Chem. Phys. **48**, 2342 (1968).

This work was supported by the Swedish Natural Science Research Council and by the Director, Office of Energy Research, Office of Basic Energy Sciences, Materials Science and Chemical Sciences Division, of the U.S. Department of Energy under Contract No. DE-AC03-76SF00098.

Principal investigator: E. Joseph Nordgren, Physics Department of Uppsala University, Sweden. E-mail: joseph.@fysik.uu.se

Scanned-Energy Mode Photoelectron Diffraction Study of Carbon Adsorption Structures on Ni(100)

R.Terborg[1], J.T.Hoeft[1], R. Lindsay[1], O.Schaff[1], E. Rotenberg[3], J. Denlinger[4], A.M.Bradshaw[1], R.Toomes[2], N.A.Booth[2], D.P.Woodruff[2]

[1] Fritz Haber Institute, Faradayweg 4-6, 14195 Berlin, Germany

[2] Physics Department, University of Warwick, Coventry CV4 7AL, UK

[3] Advanced Light Source, MS2-400, Lawrence Berkeley Natl. Lab., Berkeley, CA 94720, USA

[4] University of Wisconsin-Milwaukee Physics Dept., 1900 E. Kenwood Blvd., Milwaukee, WI 53211, USA

Carbon adsorption is known to induce a (2x2)p4g reconstruction on Ni(100) at a coverage of 0.5 ML. The structural, electronic and vibrational properties of this phase have been studied extensively [1], and it is known that the C atoms occupy four-fold symmetric hollow sites on the surface (in a c(2x2) mesh) but are almost coplanar with the outermost Ni layer, as depicted in Fig. 1. The four nearest-neighbour Ni atoms around each carbon atom are translated parallel to the surface along the <110> directions such that they move away from the carbon atom, enlarging the hollow, and also rotate around it. The nesting of clockwise and counter-clockwise rotations of these Ni atoms around alternate C atoms leads to the larger (2x2) periodicity and the p4g space group symmetry. It is generally believed that this 'clock' reconstruction is a consequence of the penetration of the carbon into the hollow site, forcing the Ni atoms further apart and allowing the adsorbate to interact with the second layer Ni atom below. Surface stress measurements [2] show a build-up of tensile stress with increasing coverage, with a further increase being relieved by the reconstruction. While there are discrepancies between the structural details obtained from LEED, SEXAFS and a prior photoelectron diffraction (PhD) study, especially with regard to the exact amplitude of the surface Ni layer lateral distortion, a key question which remains is the structure of the adsorption phase prior to reconstruction. Although one might assume that the C atoms also occupy hollow sites at low coverage, it is interesting to determine the C-Ni outermost layer spacing and any possible strain associated with the Ni atoms surrounding the site.

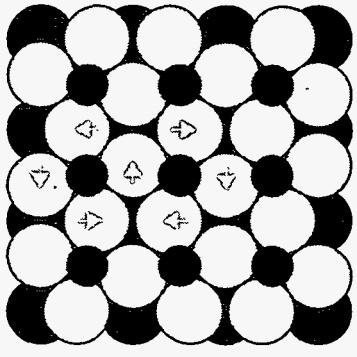

Figure 1. Schematic drawing of the Ni(100)(2x2)p4g-C reconstruction.

To investigate this question, we have conducted a PhD study not only of the (2x2) reconstructed phase, but also of the local structure at the much lower coverage of 0.1 ML. C 1s photoelectron diffraction modulation spectra were obtained using the same methodology we have previously established in many similar studies at the BESSY facility in Berlin [3]. A substantial number of different emission directions were measured over the kinetic energy range 80-440 eV. The high photon flux and high spectral resolution of the ALS were essential to yield the signal-to-background ratio needed to study the low coverage phase. Moreover, it proved possible to measure PhD spectra to much more grazing angles than had been possible in any of our previous studies at BESSY. Particularly significant were the huge amplitude (±70%) modulations in spectra recorded at 80° from the surface normal (10° grazing) in the <100> azimuth discussed briefly below.

Figure 2 shows a selection of the PhD spectra for the two different structural phases. It is clear that while there are similarities in much of the gross structure, there are also very substantial differences in detail. The clear implication is that while the low coverage phase probably also involves a four-fold symmetric hollow site, there are significant differences in the exact structural

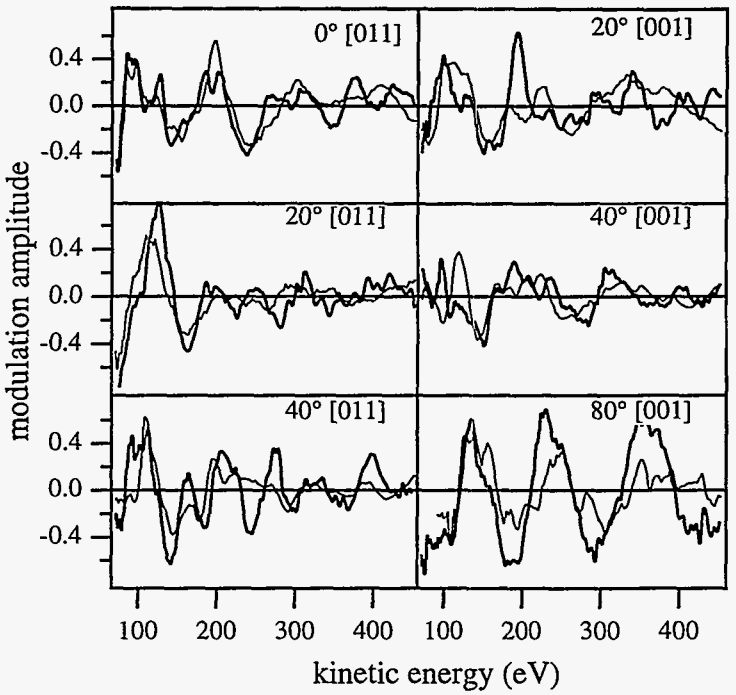

Figure 2. Comparison of the C 1s PhD modulation functions for 0.1 ML C on Ni(100) (bold lines) with the modulation functions for the (2x2)p4g structure. The emission directions are indicated by a polar angle and an azimuthal direction.

parameters. The very strong modulations with a single dominant periodicity seen in both 80° spectra are indicative of the occupation of the hollow site with the C atoms lying low in the surface Ni layer, not only in the reconstructed phase, but also at low coverage. In this geometry the conditions for 180° back-scattering are fulfilled (or nearly fulfilled).

Full analysis of these spectra for both phases using multiple scattering simulations is currently proceeding, but it is already clear that the structural parameters found for the (2x2) clock reconstruction are in excellent agreement with those of previous studies, and that C and Ni atoms in the low coverage phase are almost co-planar. Full details of the optimum structures will be submitted for publication shortly.

ACKNOWLEDGEMENTS

The financial support of the EPSRC (UK) and the BMBF (Germany) in the form of research grants and studentships is gratefully acknowledged.

REFERENCES

1. See e.g. D.P.Woodruff in *The Chemical Physics of Solid Surfaces*, eds. D.A.King and D.P.Woodruff (Elsevier, Amsterdam, 1994) vol 7, p465
2. D.Sander, U.Linke and H.Ibach, Surf.Sci. 272 (1992) 318
3. See e.g. D.P.Woodruff and A.M.Bradshaw, Rep.Prog.Phys. 57 (1994) 1029

Principal investigator: Phil Woodruff, Physics Department, University of Warwick, Coventry CV4 7AL, UK.
Email: Phil.Woodruff@Warwick.ac.uk. Telephone +44-1203-523378

Soft x-ray emission study of chromium hexacarbonyl

J.-H. Guo[1], C. Såthe[1], A. Fölisch[1], J. Nordgren[1], L. Yang[2], and H. Ågren[2]

[1]Department of Physics, Uppsala University, Box 530, 751 21 Uppsala, Sweden
[2]Department of Physics and Measurement Technology, Linköping University, 581 83 Linköping, Sweden

INTRODUCTION

We use a transition metal compound as a bridge between the free and the surface adsorbed species for the interpretation of core electron spectroscopies. Calculations for this purpose are carried out for carbon and oxygen x-ray absorption, x-ray emission and x-ray core electron shake-up spectra for $Cr(CO)_6$. A detailed analysis of spectra are made with some previous assignment being revised [1].

EXPERIMENT

The x-ray emission experiment was carried out at beamline 7.0 of Advanced Light Source, Lawrence Berkeley National Laboratory. This beamline [2] is comprised of a 5 m, 5 cm period undulator and a 10.000 resolving-power spherical grating monochromator. The beamline provides high flux and is capable of focusing the radiation with post-focusing mirrors to a narrow beam at the interaction region.

The soft x-ray emission was recorded using a high resolution-grazing incidence-grating fluorescence spectrometer [3]. The spectrometer provides a choice of three different spherical gratings. It has an entrance slit with adjustable width and uses a two-dimensional detector that can be translated to the focal positions defined by the Rowland circle of the grating in use. In these experiments a slit of 15 μm and 30 μm were selected and gratings with 5m radii and 400 and 1200 lines/mm were used to record the carbon and oxygen *K* emission, respectively. The estimated resolution at full width at half maximum (FWHM) was about 0.3 eV and 0.50 eV, respectively.

The $Cr(CO)_6$ molecule was contained in a gas cell with thin windows transmitting most of the radiation. The synchrotron radiation entered the cell through a 1600 Å thick silicon nitride window and the interaction region was viewed by the spectrometer through a 1600 Å thick polyimide window, supported by a polyimide grid and coated with 150 Å aluminium nitride [4]. The gas pressure was optimized so that most of the fluorescence was absorbed in the view region of the spectrometer. In the spectra presented here the pressure ranged from 0.7 mbar to 1.7 mbar.

RESULTS

The C and O *K* x-ray emission spectra are presented in Figure 1. As one can expect from the one-center picture, the non-resonant x-ray emission spectra (NRXES) are dominated by CO outer valence B band. The CO-localized "4σ" orbital turn up mostly in the oxygen spectrum, while the chromium *3d* band has low intensity in both spectra. One notes that the $8t_{1u}$ (5σ) level is very strong in the carbon spectrum, while the oxygen spectrum is dominated by the 1π derived peaks, which makes the main feature in the oxygen spectrum narrower. Thus much of the signatures of the free CO spectra remain in the spectrum of $Cr(CO)_6$, as actually they do also for the $COCu_N$ clusters [5]. A difference is that the 5σ derived levels (as $8t_{1u}$ and $5e_g$) are mostly of lower energy than the 1π derived levels ($1t_{2u}$, $1t_{2g}$, $7t_{1u}$) while they reverse in order for the $COCu_N$ clusters and for CO/Cu(100).

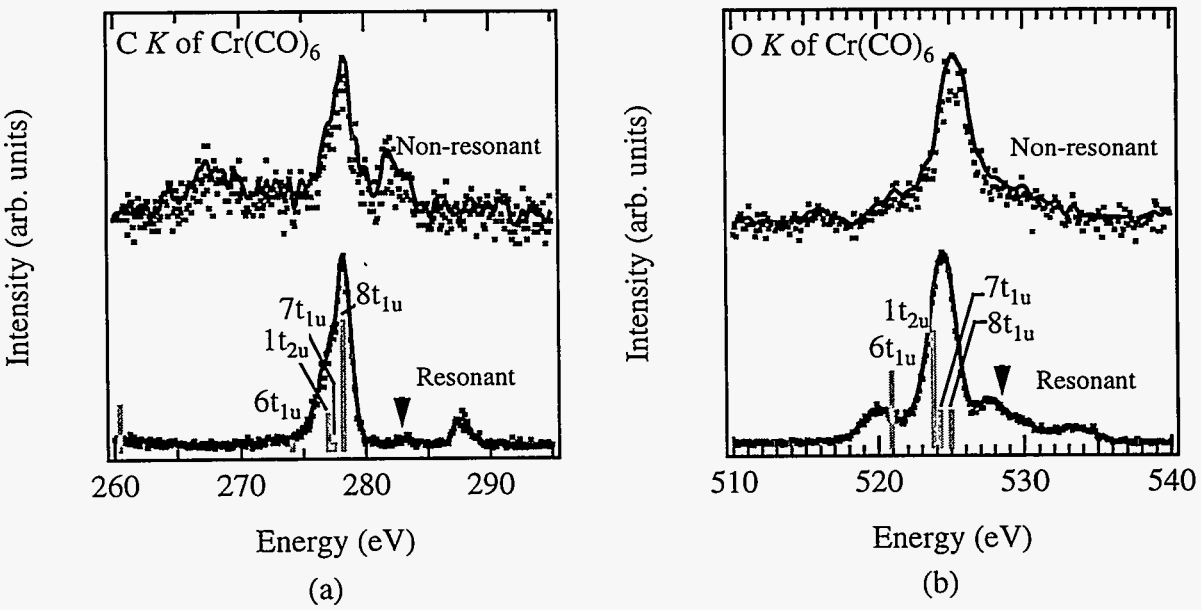

Figure 1. X-ray emission spectra of $Cr(CO)_6$ at C *K*-edge (a) and O *K*-edge (b).

The resonant x-ray emission spectra (RXES) were recorded by tuning the incident x-ray energy to the LUMO $9t_{1u}\pi^*$ MO at hν = 287.5 and 533.9 eV for C *1s*, respectively, O *1s* excitations, which comes out as an elastic peak in the spectra (see the bottom curves). Unlike for non-resonant spectra, symmetry selection operates for RXES, and can in principal be used for symmetry probing of occupied or unoccupied MO levels [6]. $Cr(CO)_6$ belongs to the O_h point group in the ground state, and when the incident x-ray is tuned to $9t_{1u}$, only electrons occupying the ungerade MO's can fill the C *1s* or O *1s* hole orbitals according to dipole selection rule. Thus the RXES spectra are in principle sparser than the NRXES counterparts. There is, of course, still an open question how strong the symmetry-breaking Jahn-Teller effects operating between near-degenerate core excited are, and so if the core excited state really maintains the same symmetry as the ground state or not. The CO_2 molecule was an example when symmetry is indeed broken at the core (O *1s*) excited resonance state [7].

DISCUSSION

The RXES spectra simulated in the frozen orbital approach are presented vertical bars in Figure 1. For a description of such simulations we refer to ref.[8]. Comparing to NRXES, the double peak structure of the two most intensive features in the C *K* emission case, is reduced to one peak ($8t_{1u}(5\sigma)$, with the second feature (due to the $1t_{2u}(1\pi)$ and $7t_{1u}(1\pi)$ levels) forming a weak shoulder at the high energy side. The 4σ ($6t_{1u}$) band remains weak in the C *K* spectrum. For the O *K* spectrum, however, the transitions from the $7t_{1u}(1\pi)$ and $6t_{1u}(4\sigma)$ levels build up the two most intensive features.

It is worth noticing that the *3d* band ($1t_{2g}$) level does not show up in the simulated resonant spectra, due to its gerade character. In the experimental O *K* RXES spectra, however, a very weak feature in the corresponding energy position can be observed (as indicated by an arrow in Figure 1). Because this feature is too far away (more than 3.0 eV) from its closest neighbour MO ($8t_{1u}$), it should represent a separate state. A possible explanation could be the vibronic coupling effects of

the core excited state induce small admixtures of electronic symmetry-forbidden transition (here $1t_{2g}$)in the RXES. It is notable that the similar feature is much weaker in the C *K* case.

CONCLUSIONS

The purpose of this study was to investigate the notion of using a transition metal compound as a bridge between the free and the surface adsorbed species for the interpretation of these core electron spectroscopies. As we found in this investigation this notion forms a good starting point for analyzing the most salient features in all the spectra, while a detailed assignment makes it necessary to account for the particular electronic structure of the compound.

ACKNOWLEDGEMENTS

T. Warwick is thanked for providing us some Si_3N_4 windows which were used in the experiment.

REFERENCES

1. L. Yang, H. Ågren, J.-H. Guo, C. Såthe, A. Fölisch, A. Nilsson, and J. Nordgren, to be published.
2. T. Warwick, P. Heimann, D. Mossessian, W. McKinney and H. Padmore, Rev. Sci. Instr. **66**, 2037 (1995).
3. J. Nordgren, G. Bray, S. Cramm, R. Nyholm, J. E. Rubensson and N. Wassdahl, Rev. Sci. Instr. **60**, 1690 (1989).
4. Custom-made window from Metrorex International Oy, P.O. Box 85, FIN.02201 Espoo, Finland.
5. V. Carravetta, L.G.M. Pettersson, H. Ågren, and O. Vahtras, Surf. Sci. **369**, 146 (1996).
6. P. Skytt, J.-H. Guo, N. Wassdahl, J. Nordgren, Y. Luo, and H. Ågren, Phys. Rev. A **52**, 3572 (1995).
8. Y. Luo, H. Ågren, and F.Kh. Gel'mukhanov, J.Phys B: At. Mol. Phys. **27**, 4169 (1994).

This work was supported by the Swedish Natural Science Research Council and the G. Gustafsson Foundation for Science and Medicine.

Principal investigator: E. Joseph Nordgren, Department of Physics, Uppsala University. E-mail: joseph@fysik.uu.se. Telephone: +46 18 4713554.

Spectromicroscopy of Mn Distributions in Micronodules produced by Bacterial Bio-mineralization

J. Rothe[1], E. M. Kneedler[1], B. P. Tonner[1]
[1]Dept. of Physics, University of Wisconsin-Milwaukee, PO Box 413, Milwaukee, WI 53201, USA
T. Grundl[2], K. H. Nealson[2]
[2]Center for Great Lake Studies, University of Wisconsin-Milwaukee, PO Box 413, Milwaukee, WI 53201, USA

INTRODUCTION

An understanding of the interaction of single cell microorganisms with inorganic substrates is a central issue in both aquatic and soil environmental chemistry. The biochemical pathways of bacterial metabolism based on redox reactions of transition metal compounds involve the processes of microbial attachment to and subsequent modification of inorganic surfaces, as well as the precipitation of inorganic compounds. Bacteria have been discovered which oxidize Mn or Fe into higher valence states, whereas others will reduce the oxides as part of their energy transport cycle [1,2]. Certain basic facts regarding the initial compounds formed by bacteria that metabolize Fe and Mn are still not fully understood. These issues are important to the understanding of bio-corrosion phenomena, to the microbial ecology of oxide precipitates formed by bacteria, and to the future harnessing of bio-mineralization for use in bio-remediation efforts and as a route to novel nanostructures.

This article is a report on the first results obtained for natural Mn nodules (from Green Bay sediment core samples) using high resolution soft x-ray spectromicroscopy at BL7. The first row transition metal L absorption edges, due to 2p→3d core transitions, expose a rich fine structure which allows to differentiate between several valence states of the metal ion. Without spatial resolution, these studies have been seriously limited, because the action of the microorganisms is not spatially homogeneous. This is clearly demonstrated by the comparison of the microspectroscopic measurements to spatially averaging total yield measurements.

EXPERIMENT

One of the major advantages of high resolution soft x-ray absorption spectroscopy at the scanning transmission microscope STXM (ALS *SpectroMicroscopyFacility*) is the possibility to investigate systems in their natural aqueous environments. Measurements on dried samples may not represent the natural state due to chemical or structural changes. For the investigations presented here, by placing the Mn specimens between two Si_3N membranes x-ray transparent wet-cells containing a thin water film have been performed. The adjustment of a thin layer of water by means of capillary forces has been improved by covering the inner surface of the membranes with a surfactant (HTBA). These cells have been shown to keep their liquid contents for at least two days without additional sealing.

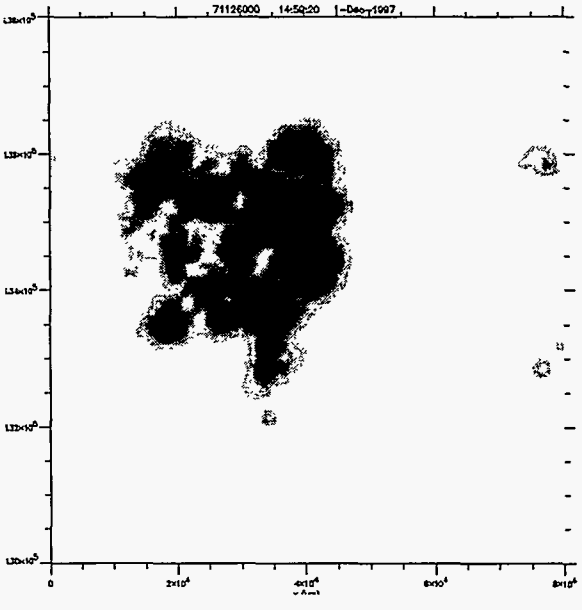

Fig. 1: Scanning X-ray micrograph (20µmx20µm) of Mn micro nodules.

Reference spectra in total electron yield technique have been recorded at the BL7-XPD chamber using dry powders fixed on indium foil.

RESULTS

Fig.1 shows a 20μm×20μm image taken at the BL7-STXM scanning transmission x-ray microscope with a spatial resolution of about 0.25μm. As generally observed for these samples, the micro nodules tend to form larger agglomerates which occur in a wide range of sizes and shapes. In the left part of Fig. 2 the Mn $L_{II,III}$ x-ray absorption spectra recorded at two different positions in such an agglomerate of nodules of sample 'orange' are compared. Additionally, reference spectra taken from aqueous solutions of Mn compounds (0.1M $KMn(VII)O_4$ resp. 0.2M

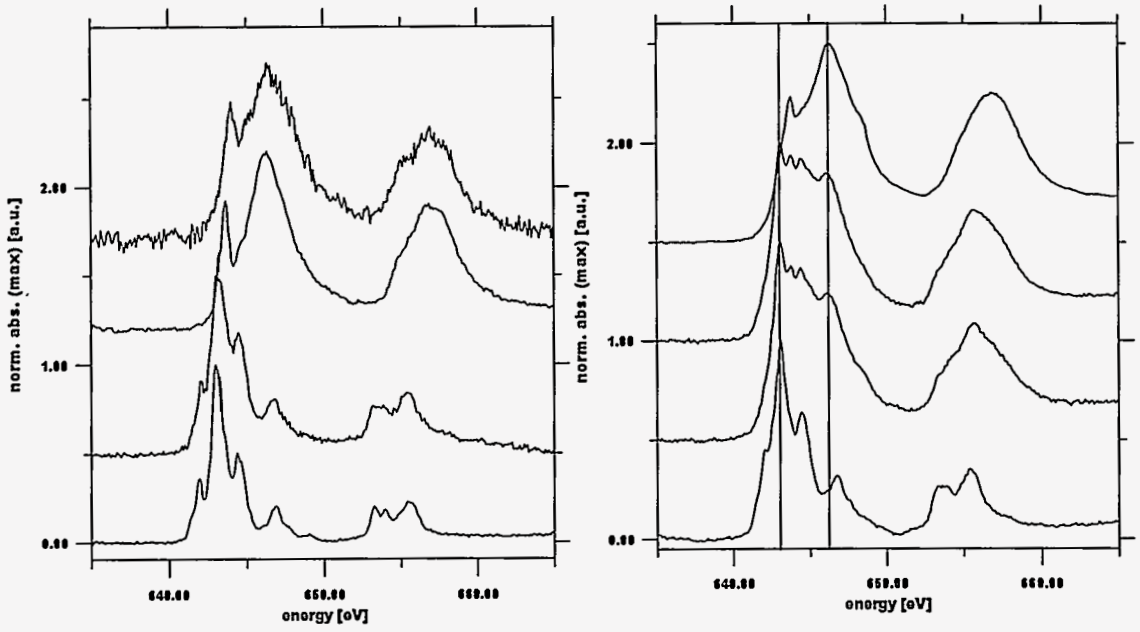

Fig. 2: Mn $L_{II,III}$ x-ray absorption measurements - left (from top to bottom): Mn micro nodules 'orange' (Pos. A), $KMn(VII)O_4$, Mn micro nodules 'orange' (Pos. B), $Mn(II)SO_4$ - right (from top to bottom): $KMn(VII)O_4$, Mn micro nodule 'blue', Mn micro nodules 'orange', $Mn(II)SO_4$ (all spectra have been normalized to their maximum intensity).

$Mn(II)SO_4$ in aq. dest.) are shown. The two lower spectra clearly exhibit the signature of a divalent Mn species, whereas the upper curve, in comparison to the reference compound $KMnO_4$, has to be ascribed to a valence state as high as +7. Considering the transmission measurements at a multitude of different sample spots, the +2 signature was by far the dominant characteristic of both samples—in fact it was the only one observed by STXM measurements for sample 'blue'.

In the right part of Fig. 2 the corresponding Mn $L_{II,III}$ x-ray absorption spectra taken in total electron yield technique are compared. These spatially averaging measurements of the two different samples of Mn nodules turned out to expose a fine structure, which can be immediately explained as the superposition of the +2 and the +7 Mn spectral features. In contrast to the wet-cell transmission measurements, the total yield spectrum of sample 'blue' shows the contribution of the higher valence state. This can be from two causes. One is that the bulk of the particle is a +2 valence, with a 'shell' of higher oxidation state. The other is that sample preparation (drying in air) for the total yield measurement led to some additional oxidation. This ambiguity will be resolved in future experiments.

CONCLUSIONS

Soft x-ray absorption measurements of Mn micro nodules produced by bacterial biomineralization have been performed, both in the naturally hydrated and in the dry state. For the first time it has been shown that the high spatial resolution of the x-ray transmission

microscope STXM allows to differentiate between two species of the transition metal ions which are not homogeneously distributed throughout the agglomerates of micro particles. This can be seen as an important step towards the desired understanding of localized chemical processes induced by single cell microorganisms.

REFERENCES

1. C. Meyers and K. Nealson, 1988. "Bacterial manganese reduction and growth with manganese oxide as the sole electron acceptor." Science 240: 1319-1321
2. D. Lovely and E. Phillips, 1988 "Novel mode of microbial energy metabolism: organic carbon oxidation coupled to dissimilatory reduction of iron or manganese." Appl. Environ. Microbiol. 51: 683-689

This work was supported by the Department of Energy, OBER, NABIR program ER62474.

Principal investigator: Brian Tonner, Department of Physics, and Laboratory for Surface Studies, University of Wisconsin-Milwaukee. Email: tonner@csd.uwm.edu.

Spectroscopic study of CN_x films grown by magnetron sputter deposition

J.-H. Guo[1], W.T. Zheng[2], C. Såthe[1], N. Hellgren[2], A. Agui[1], J.-E. Sundgren[2], and J. Nordgren[1]

[1]Department of Physics, Uppsala University, Box 530, 751 21 Uppsala, Sweden
[2]Department of Physics and Measurement Technology, Linköping University, 581 83 Linköping, Sweden

INTRODUCTION

The determination of the chemistry and microscopic structure of carbon nitride films is of considerable interest because of the scientific and technological importance of such materials [1-4]. CN_x films typically exhibit interesting properties such as füllerene-like or amorphous microstructures, high hardness and extremely elastic properties [2,3], and a good tribological performance [4]. As a consequence of their properties, such films may have found applications as protective coating as well as lubricants.

Several experimental techniques including Fourier transform infrared spectroscopy (FTIR), x-ray photoemission spectroscopy (XPS), and high-resolution electron microscopy (HREM) have been used to investigate the microscopic bonding and structure in CN_x films. Despite all these efforts, the correlation between microstructure and microscopic bonding is far from being understood. Because of their local character the near edge x-ray absorption fine structure (NEXAFS) and x-ray emission spectroscopy (XES) techniques are well suited for structural studies of disordered systems and they have been extensively applied to study materials such as a-C films [5], diamond and graphite [6-9]

EXPERIMENT

Deposition of carbon nitride thin films were carried out in a dc magnetron sputtering with a base pressure of $1x10^{-5}$ pa. The target was a high purity of 99.99% pyrolytic graphite disc, separated by 10 Cm from the resistively heated substrate holder. The target was sputter clean prior to each deposition, with a shutter shielding the substrate from the depositing species. The substrates were Si(001) wafers. They were first cleaned ultrasonically in acetone and alcohol baths consecutively, and heated under vacuum in the deposition system up to 850°C for 10 minutes to remove the surface oxide prior to setting the desired substrate temperature. 99.9999% pure nitrogen was introduced into the sputtering chamber through a mass flow controlling until the required N_2 pressure was obtained. In this experiment we have measured three CN_x samples which were made at different substrate temperatures (T_s).

The experiments were performed at beamline 7.0 at the Advanced Light Source (ALS), Lawrence Berkeley National Laboratory. The beamline comprises a 99-pole, 5 cm period undulator and a spherical-grating monochromator [10]. NEXAFS spectra were obtained by measuring the total electron yield from the sample. The resolution of the monochromator was set to 0.15 and 0.3 eV, respectively, for C and N *1s* absorption edge. The NEXAFS spectra were normalized to the incident photon current using a clean gold mesh to correct for intensity fluctuation of the photon beam. The XES spectra were recorded using a high-resolution grazing-incidence x-ray fluorescence spectrometer [11]. During the XES measurement, the resolution of the beamline was the same as that in XAS measurement, and the resolution of the fluorescence spectrometer was set to 0.45 eV and 0.65 eV, respectively, for C and N *K* emission.

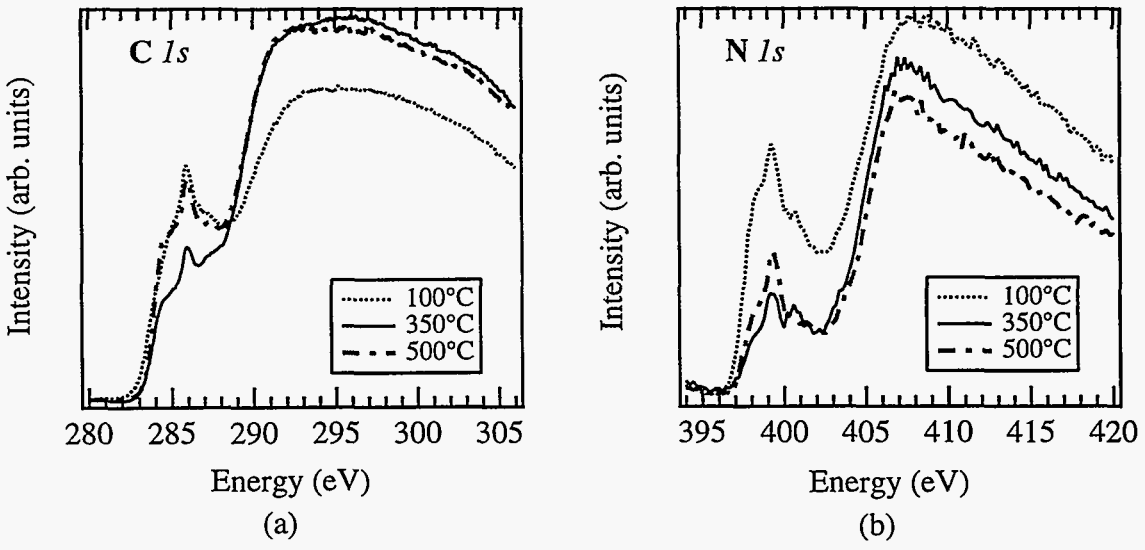

Figure 1. X-ray absorption spectra from CN_x thin films at C 1s threshold (a) and N 1s threshold (b).

RESULTS

The NEXAFS measurement at C *1s* and N *1s* edge from different temperature made CN_x films are presented in Figure 1. The near-edge x-ray absorption occurs when core electrons are excited to unoccupied states. The low energy region (284 - 288 eV) of the C *1s* spectra is composed of a π^* (C = N) transition at 286 eV, with a low-energy shoulder at 285 eV (π^*, C = C). The very broad σ^* resonance centered around 296 eV corresponds to C-C, C-N, C = C, and C = N bonds (sp^2 and sp^3 character) and reveals the disordered nature of the film.

The N *1s* spectra show the π^* (N = C) transition at 398.3 eV. The absorption profile in the π^* resonance region is similar to C *1s* spectra. The σ^* resonance is sharping in N *1s* spectra reflects less bonds to nitrogen sites. There is a shift between the σ^* resonance of different CN_x films, from about 407.7 eV of 100°C sample to 407 eV of 500°C sample.

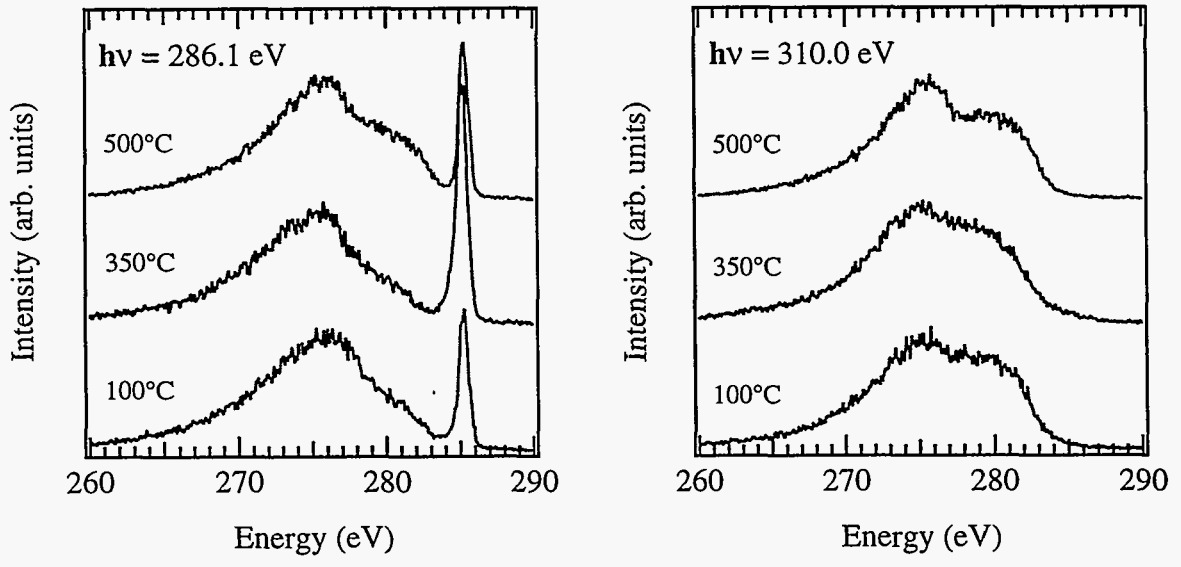

Figure 2. C K x-ray emission spectra with resonant excitation (left) and non-resonant excitation (right).

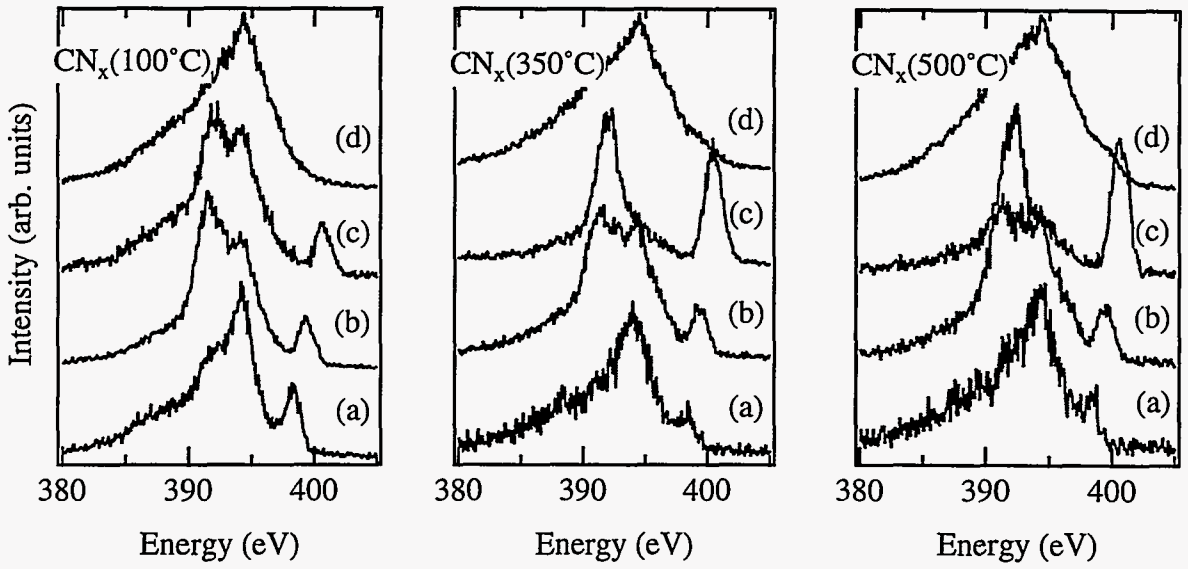

Figure 3. N K x-ray emission spectra with the excitation energy of 398.3 eV (a), 399.3 eV (b), 400.6 eV (c), and 407.9 eV (d).

The C *K* emission spectra of different T_s samples are presented in Figure 2. The C emission bands are centered around 276 eV, no significant difference was observed as a function of T_s.

The N *K* emission spectra of different T_s samples are presented in Figure 3. The spectral profile shows a strong dependence upon the incoming photon energy. For the high photon energy excitation (Top curves), the N emission bands are centered around 394.5 eV, besides the total valence band-width increases with T_s, no significant difference was observed as a function of T_s. The great difference upon T_s is observed at the 400.6-eV-excited resonant x-ray emission spectra.

DISCUSSION

The resonant N *K* emission spectra (curves a, b, and c in Figure 3) can be deconvoluted to two peak structures. The fact that the N resonant x-ray emission spectra show two relatively large peaks at 392 and 394 eV, is due to two different N bonding configurations in the films. Based on the structural analyses, two N configurations are expected, one with N located in the hexagonal C planes and one corresponding to a position in which the bonding configuration is more tetrahedral-like. The latter can be the case if N atoms occupy positions where a basal plane in a basal structure unit terminates. We can assign the N peak at 392 eV to be due to N bonded to sp^3-hybridized C and that at 394 eV to N bonded to sp^2-hybridized C.

REFERENCES

1. A.M. Liu and M.L. Cohen, Science **245**, 841 (1989).
2. H. Sjöström, S. Stafaström, M. Boman, *et al.*, Phys. Rev. Lett. **75**, 1336 (1995).
3. H. Sjöström, L. Hultman, J.-E. Sundgren, *et al.*, J. Vac. Sci. Tech. **A14**, 56 (1996).
4. B. Bhushan, B.K. Gupta, and M.H. Azarian, Wear **181**, 734 (1995).
5. J. Stöhr, NEXAFS Spectroscopy, Spring, New York, 1992.
6. Y. Ma, N. Wassdahl, P. Skytt, *et al.*, Phys. Rev. Lett. 69, 2598 (1992).
7. Y. Ma, P. Skytt, N. Wassdahl, et al., Phys. Rev. Lett. 71, 3725 (1993).
8. P. Skytt, P. Glans, D.C. Mancini, et al., Phys. Rev. B 50, 10457 (1994).
9. J.A. Carlile, E.L. Shirley, E.A. Hudson, et al., Phys. Rev. Lett. 74, 1234 (1995).

10. T. Warwick, P. Heimann, D. Mossessian, *et al.*, Rev. Sci. Instr. **66**, 2037 (1995).
11. J. Nordgren, G. Bray, S. Cramm, *et al.*, Rev. Sci. Instr. **60**, 1690 (1989).

This work was supported by the Swedish Natural Science Research Council and the G. Gustafsson Foundation for Science and Medicine.

Principal investigator: E. Joseph Nordgren, Department of Physics, Uppsala University. E-mail: joseph@fysik.uu.se. Telephone: +46 18 4713554.

Spin-Orbit Split Surface States on Li/W(110)

Eli Rotenberg[1], J-W Chung[2], and S. D. Kevan[3]
[1] Advanced Light Source, Ernest Orlando Lawrence Berkeley National Laboratory,Berkeley CA 94720
[2]Pohang Institute of Science and Technology, Pohang, S. Korea
[3]Department of Physics, University of Oregon, Eugene OR 97403

In a recent study of the surface bands of W(110) in the presence of hydrogen[1], we found a disagreement between the predicted and observed number of surface states on the clean and hydrogen-covered W(110) surfaces. Figure 1 shows bandmapping and fermi contour results from that study, in this case for 1 monolayer of hydrogen on W(110). In fig. 1(a), we see a series of angle-resolved valence band photoemission spectra acquired as a function of polar emission angle θ. By converting θ to k sin θ, we have converted the angle axis directly into electron momentum $k_{||}$ parallel to the surface. Ignoring the emission near the center of Fig. 1(a) (which is due to unimportant bulk transitions), we see two well-defined, parabolic bands of similar intensity.

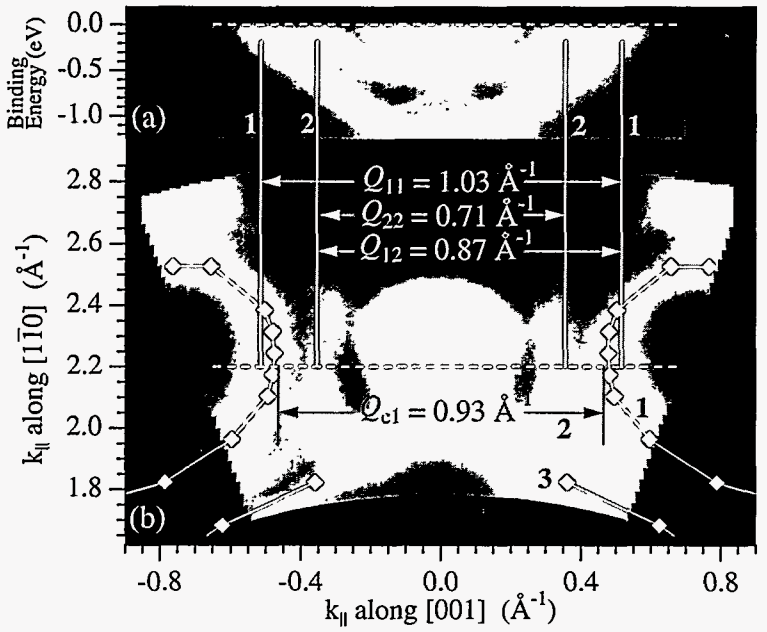

Figure 1. Angle-resolved photoemission results for 1 monolayer of hydrogen on W(110). (a) Valence bandmaps along a line in $k_{||}$-space. (b) Fermi contours over the $k_{||}$-plane. The intensity along the dashed lines in (a) and (b) are along the same line in the two -dimensional $k_{||}$-plane. The vectors Q_{ij} arerelated to electron-phonon coupling, and are discussed in Ref. 1.

To illustrate the momentum-dependence of these states further, consider the photoemission intensity at the Fermi level E_f (zero binding energy). Intensity acquired along the dashed line in Fig. 1(a), which comprises a line in two-dimensional $k_{||}$-space, may be acquired in other directions in the $k_{||}$-plane. Such an intensity map, called a Fermi contour map, is shown in fig. 1(b). For comparison, the dashed line in fig. 1(b) corresponds to the same dashed line in fig. 1(a). In the fermi contour map in fig. 1(b), contours labeled 1 and 2 correspond to the two bands seen in fig. 1(a).

Also shown in fig. 1(b) is a recent calculation by Kohler et al.[2] (diamonds), This calculation finds a similar contour to our contour #1, but misses contour #2. The spin-orbit interaction is a relativistic effect expected to be important for W, and is the only relativistic effect not included in the (scalar relativistic) calculation. To test whether the splitting is due to such relativisitic effects, we have performed a comparison study of H on Mo, as well as the similar systems Li on Mo(110) and Li on W(110). Because of the lighter atomic mass of Mo, relativistic effects should be considerably less important on this surface.

Figure 2 shows Fermi contour maps for Li/W compared to Li on Mo. These maps are over a more extensive region of k-space; for comparison the region in fig. 1(b) corresponds to the

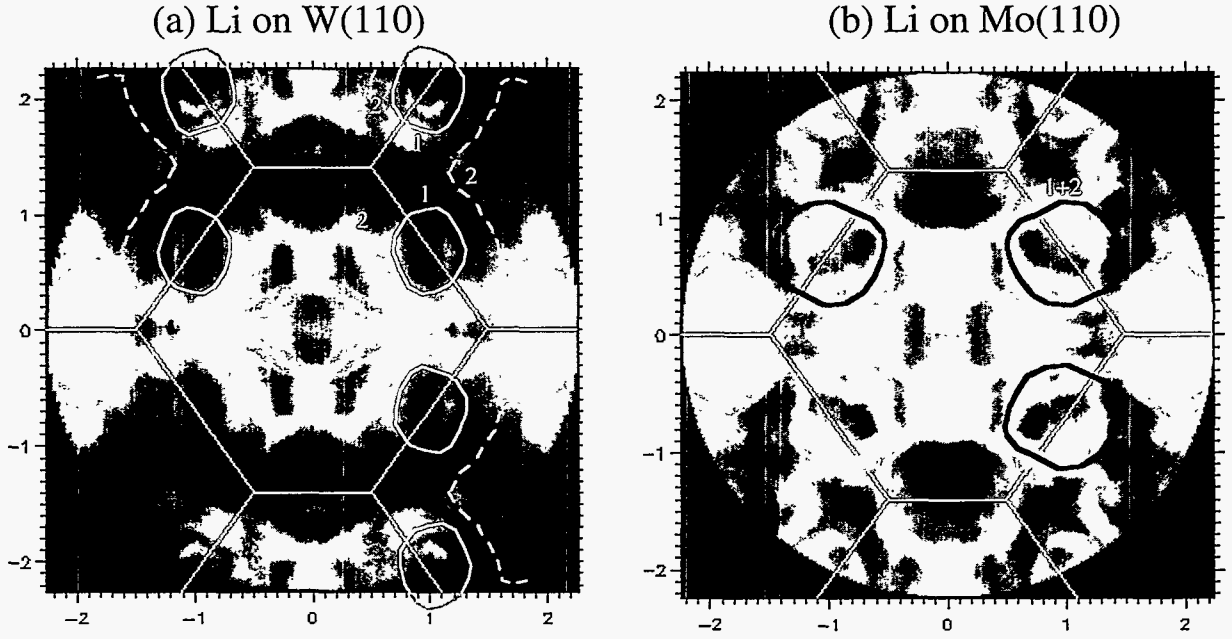

Figure 2. Fermi contour maps for (a) Li on W(110) and (b) Li on Mo(110). The two orbits "1" and "2" in (a) correspond to the single orbit "1+2" in (b),

region at the tops of fig. 2(a-b). Since Li and H have similar outer valence electrons, the results from Li on W are similar to those from H on W: there is a similar pair of Fermi contours, labelled "1" and "2", in fig. 2(a). By changing the substrate from W to Mo, very little should be changed, since W and Mo have the same valence and lattice constants. The most significant difference is the removal of spin-orbit as well as other relativistic interactions. In fig. 2(b), we see the results for Mo. These are very similar to W except that where two orbits "1" and "2" exist for W, we find only a single orbit "1+2" for Mo. Upon more detailed investigation we found that orbit 1+2 for Mo is indeed slightly split at energies below the Fermi level. At the Fermi level, however, the splitting becomes unresolvable.

Recently, a strikingly similar splitting of the surface Fermi contours was observed in the clean Au(111) surface state at zone center,[3] which is not observed either for Ag(111) or Cu(111). In that study, the authors found that a simple model for the spin-orbit interaction could account for the magnitude of the splittings, as well as predict that the spin ordering was in-plane along the tangents of the Fermi contours. In that case, however, the theory was simplified by the near spherical symmetry of the *sp*-derived wavefunctions near zone center. In our case, we have the additional complications that the surface states are far from zone center and are derived from *d* states. Therefore, we cannot apply such a simple theory to determine the spin ordering. The magnitudes of the shifts in energy, however, are consistent with atomic spin-orbit splittings seen in Mo and W in analogy with Ag and Au. It would be interesting to explore this system further theoretically as well as experimentally—perhaps using spin-resolved detection—to more directly confirm that spin-orbit interaction is responsible.

REFERENCES

[1]E. Rotenberg and S. D. Kevan, Phys. Rev. Lett., in press.
[2]B. Kohler, P. Ruggerone, M. Scheffler, Phys. Rev. B. **56**, 13 503 (1997).
[3]S. LaShell, B. A. McDougall, and E. Jensen, Phys. Rev. Lett. **77**, 3419 (1996).

This work was supported by the U.S. Department of Energy under Contract No. DE-FG06-86#$45275.
Principal investigator: Steve Kevan, Department of Physics, University of Oregon. Email: kevan@oregon.uoregon.edu.

Structure Determination of the Si(111)(√3x√3)R30°-B Structure Using Photoelectron Diffraction

J.J. Paggel[1], P. Baumgärtel[1], M. Hasselblatt[1], K. Horn[1], V. Fernandez[1], O. Schaff[1], E. Rotenberg[3], J. Denlinger[4], A.M. Bradshaw[1] and D.P. Woodruff[2]
[1] Fritz Haber Institute, Faradayweg 4-6, 14195 Berlin, Germany
[2] Physics Department, University of Warwick, Coventry CV4 7AL, UK
[3] Advanced Light Source, MS2-400, Lawrence Berkeley Natl. Lab., Berkeley, CA 94720, USA
[4] University of Wisconsin-Milwaukee Physics Dept., 1900 E. Kenwood Blvd., Milwaukee, WI 53211, USA

The influence of dopants on the properties of a semiconductor are of interest both from the scientific and technological points of view. Due to the presence of the solid-vacuum interface one might expect the properties of the near-surface region to be different from those of the underlying bulk semiconductor material. Annealing of a heavily boron-doped Si(111) crystal, for example, gives rise to a (√3x√3)R30° phase in which the concentration of boron is much higher than in the bulk material. Moreover, a surface alloy is formed even though boron and silicon are immiscible in the bulk. The existence of this (√3x√3)R30° phase is well known, but only recently has the rather unusual atomic geometry been quantitatively determined by LEED and surface x-ray diffraction [1,2]. It was found that the boron adopts the substitutional site directly underneath a silicon adatom. All surface (√3x√3)R30° adatoms are therefore Si, in contrast to similar structures formed by other group III elements.

Since both LEED and x-ray diffraction are rather insensitive to the exact local atomic arrangement around the weakly-scattering boron atom, we have conducted a scanned-energy mode photoelectron diffraction (PhD) study of the (√3x√3)R30° structure using the B 1s photoemission signal. The local nature of this probe enables the boron atom position to be determined very accurately. B 1s photoelectron diffraction modulation spectra were obtained using the same methodology we have previously established in many similar studies at the BESSY facility in

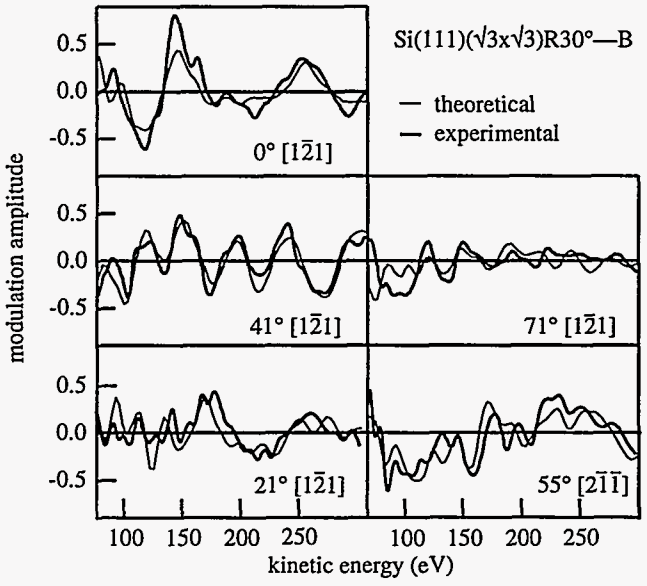

Figure 1. Experimental PhD modulation spectra for the Si(111) (√3x√3)R30°-boron phase (bold lines) together with the simulated spectra for the optimum structure shown in Fig. 2.

Berlin [3]. Spectra were measured at five different emission directions over the kinetic energy range 60-310 eV on beamline 7.0.1. The high photon flux and spectral resolution enabled us to exploit the full energy range, despite the overlap of the B 1s photoemission peak with an intense substrate Auger electron emission peak at a kinetic energy of around 90 eV. A good photon energy resolution is essential to separate the B 1s signal from the Auger background in this energy region.

Fig. 1 shows the experimental PhD modulation spectra measured in five different emission directions. The structure determination was performed by comparing the experimental data (bold curves) with simulated data (faint curves) using a multiple scattering formalism. The model geometry is optimised using an automated search algorithm for the best fit between experiment and theory.

A schematic drawing of the parameters varied and their optimum values is shown in Fig.2. The structural parameters agree with the previous LEED and x-ray diffraction measurements within the precision of the techniques. However, the key parameters, such as the bondlengths to the nearest neighbour atoms of the boron in the different layers, could be determined with much higher precision than hitherto. Full details of the optimum structure will be submitted for publication shortly.

ACKNOWLEDGEMENTS

The financial support of the BMBF (Germany) in the form of research grants and studentships is gratefully acknowledged.

REFERENCES

1. H. Huang, S.Y. Tong, J. Quinn and F. Jona, Phys. Rev. B **41**, 3276 (1990).
2. R.L. Haedrick, I.K. Robinson, E. Vlieg and L.C. Feldman, Phys. Rev. Lett. **63**, 1253 (1989).
3. See, for example: D.P.Woodruff and A.M.Bradshaw, Rep.Prog.Phys. 57 (1994) 1029

Principal investigator: Karsten Horn, Fritz Haber Institute, Faradayweg 4-6, 14195 Berlin, Germany. Email: horn@fhi-berlin.mpg.de. Telephone +49-30-84135640

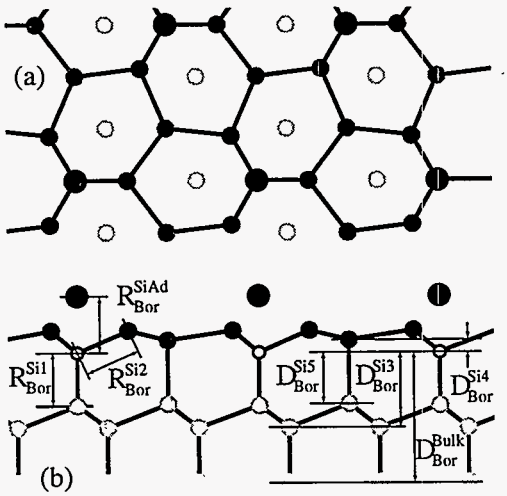

Figure 2. Structural parameters for the Si(111)-($\sqrt{3}$x$\sqrt{3}$)R30° boron phase and their optimised values.

Studies of Sub-Micron Phase Segregation in Polyurethane Polymers by Soft X-Ray Spectromicroscopy

Adam P. Hitchcock[1], Tolek Tyliszczak[1], John Brash[1,2], Rena Cornelious[2], Yew-Meng Heng[2], Stephen G. Urquhart[1,3], Adrian Garcia[3,6], Harald Ade[3], Edward G. Rightor[4,5], Werner Lidy[4], Gary E. Mitchell[5], Rick Steele[6], George Meigs[6] and Tony Warwick[6]

1. BIMR, McMaster University, Hamilton, ON L8S 4M1, Canada
2. Pathology, McMaster University, Hamilton, ON L8S 4M1, Canada
3. Dept. of Physics, North Carolina State University, Raleigh, NC 27895
4. Dow Chemical, B-1470, 2301 N. Brazosport Blvd. Freeport, TX 77541
5. Dow Chemical, 1897 Building, Midland, MI 48667
6. Advanced Light Source, Lawrence Berkeley Lab, Berkeley, CA 94720

INTRODUCTION

The morphology and chemistry of segregated phases determines the physical and chemical properties of many complex polymers, including polyurethanes. Achieving a better understanding of the connections between formulation chemistry, the chemistry and morphology of segregated phases, and the physical properties of the resulting polymer, has the potential to rationalize the development of improved polyurethane-based materials for many applications, ranging from the pedestrian (diapers) to the profound (blood contact polymers). Near edge X-ray absorption spectroscopy (NEXAFS) carried out with sub micron spatial resolution provides imaging and quantitative chemical analysis (speciation) of individual segregated phases.[1,2] We are using the beam line 7.0.1 zone plate microscopes – both the scanning transmission x-ray microscopes (STXM) and the scanning photoemission x-ray microscope (SPEM) - to record images and spectra of model and real polyurethane polymers.

A major thrust over the past year has been to improve the performance of these instruments to take full advantage of the high brightness of the ALS. We are also developing techniques for examining the surfaces (~1 nm) of dry polymers, and for studies of the bulk of fully hydrated polymers (wet cells).[3] Ultimately we hope to develop techniques to examine the *surface* of fully hydrated polymers in contact with blood components (cells, proteins, etc). Here we report on: (i) progress in STXM performance, (ii) application of the UHV SPEM to polymer surfaces, (iii) development of a total electron yield detector for surface studies at atmospheric pressure in STXM, (iv) use of the STXM for quantitative chemical analysis at the C 1s and O 1s edges. Work using a wet cell to study hydrated polymers is described elsewhere.[3]

(i) PERFORMANCE IMPROVEMENTS

In 1997 the standard detector for STXM was changed from gas ionization to a scintillation detector. This has greatly improved the efficiency, dynamic range, and reliability. Identification and elimination of several sources of systematic noise, in conjunction with a major improvement in the scan speed of the fine scale imaging stage, has enabled us to progress from typical dwells of 20 msec/pixel to 0.5 msec/pixel. This has dramatically increased throughput. Working in a different frequency regime has significantly reduced the influence of remaining systematic noise sources on spatial resolution and chemical contrast.

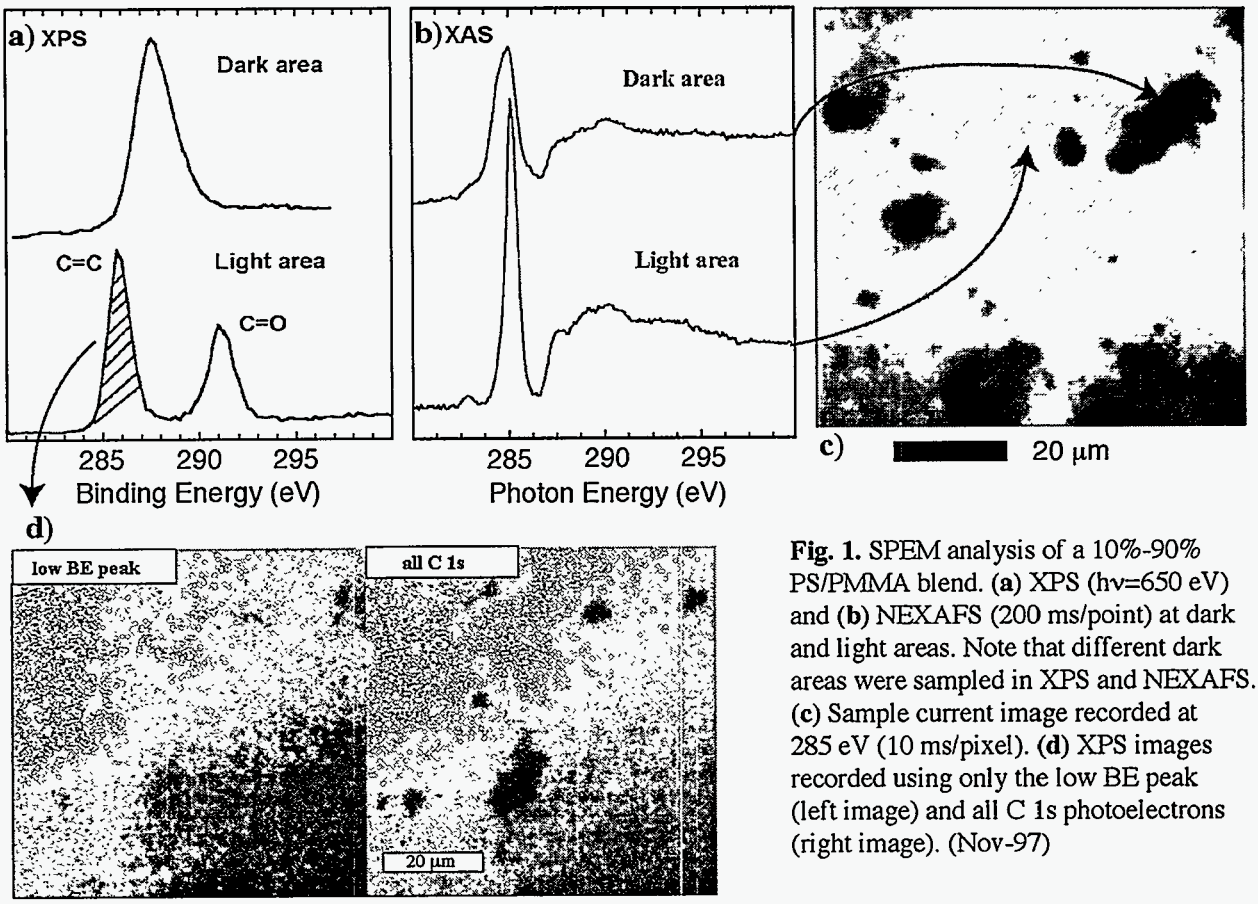

Fig. 1. SPEM analysis of a 10%-90% PS/PMMA blend. **(a)** XPS (hv=650 eV) and **(b)** NEXAFS (200 ms/point) at dark and light areas. Note that different dark areas were sampled in XPS and NEXAFS. **(c)** Sample current image recorded at 285 eV (10 ms/pixel). **(d)** XPS images recorded using only the low BE peak (left image) and all C 1s photoelectrons (right image). (Nov-97)

(ii) SPEM EXPERIMENTS

A 10%polystyrene-90%polymethyl-methacrylate (PS/PMMA) sample was examined by SPEM. C 1s photoemission spectra (nano-XPS) of the PS/PMMA sample clearly distinguished two components (C=C and C=O signals) which were used for selective XPS imaging (**Fig. 1**). Total electron yield (sample current) NEXAFS measurements were also carried out on the PS/PMMA sample. Imaging with 285 eV incident photon energy showed a microstructure similar to that observed in TEM images of samples prepared similarly. The NEXAFS spectrum in the light areas indicates polystyrene is strongly surface segregated, as expected. The XPS and NEXAFS of the dark regions suggest surface contamination rather than PMMA-rich regions. However differential charging effects or radiation damage may also play a role in this image contrast.

(iii) SURFACE IMAGING AT ATMOSPHERIC PRESSURE IN STXM

Fig. 2 presents STXM images and C 1s spectra of a complex model polyurethane (355-PIPA/SAN) in one atmosphere of He, recorded *simultaneously* with transmitted light (I_t) and total electron yield (TEY). The TEY images were recorded using the current to an adjacent electrode ~30 μm away. They exhibit the same microstructure as that seen in the transmission image. In particular they reflect the known chemical composition of the sample - only styrene acrylonitrile (SAN) particles are imaged at 287 eV ($\pi^*_{C/N}$) while both SAN and carbamate (PIPA) particles are imaged at 285 eV ($\pi^*_{C=C}$). This is a clear demonstration that TEY detection in STXM can provide imaging of the near surface region at the limit of STXM spatial resolution. To our knowledge this is the first demonstration of TEY imaging *at atmospheric pressure* at such a low photon energy. Spectra recorded in spot mode with a much longer dwell (~2 s/point) did not exhibit the expected spectral signatures of the SAN and polyurethane matrix. The reason is not yet known, but may be

related either to surface contamination or to charging. We hope to take this detection technology from demonstration to high efficiency and reliability over the next year. If successful, TEY detection will relax sample preparation constraints for 'bulk' investigations (it is difficult to make artifact-free 100 nm thin sections in some materials), and open up the exciting field of surfaces of "real-world" polymers. Simultaneous studies of the surface (~1-5 nm) and bulk (~100-300 nm) of the same material will be extremely valuable for investigations of surface segregation phenomena which are important in many areas, including optimization of biomaterials for blood contact.

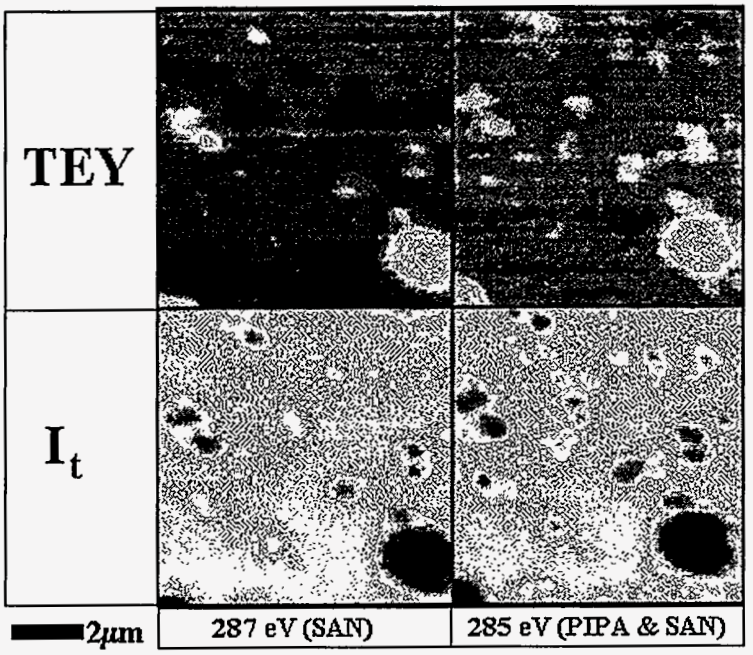

Fig. 2 Images of a polyurethane with two types of filler particles (sample #355) recorded using total electron yield (TEY) and transmitted flux simultaneously in the STXM. The particles seen in both images are SAN whereas those only seen in the right hand images are PIPA. A relatively long dwell (100 ms) and analog filtering were used to obtain adequate quality in the TEY images. The STXM chamber was filled with one atmosphere of He for these measurements.

(iv) QUANTITATIVE ANALYSIS OF POLYURETHANES AT C 1s AND O 1s EDGES

Quantitative chemical analysis can be achieved either by recording images at photon energies corresponding to transitions specific to particular functional groups (*spectro-microscopy*) or by recording core excitation spectra at selected points in the sample (*micro-spectroscopy*). Fig. 2 is an example of the first type. **Fig. 3** is an example of quantitative analysis using spot spectra. The C 1s spectra of two model polyurethanes have been analyzed to determine chemical composition with a few mole % accuracy. In this case normalized spectra, on an oscillator strength per C atom scale, of poly-TDI-urethane (TDI - toluene diisocyanate), poly-TDI-urea, and poly-ether homopolymer models are combined to reproduce the C 1s spectra of the model polyurethanes with different urea/urethane content. The urea/urethane ratio can be determined with reasonable accuracy even when the total (urea + urethane) hard segment component is only 20-30% of the total formula weight.[4]

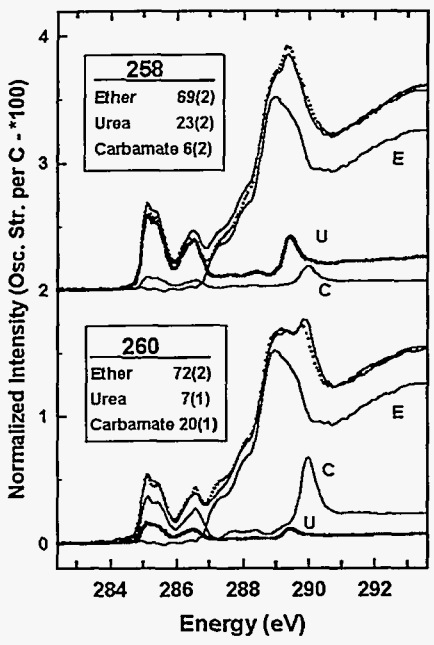

Fig. 3 Compositional analysis of model polyurethanes using sums of C 1s NEXAFS of polymer models. The results agree within 3% of those based on formulation.

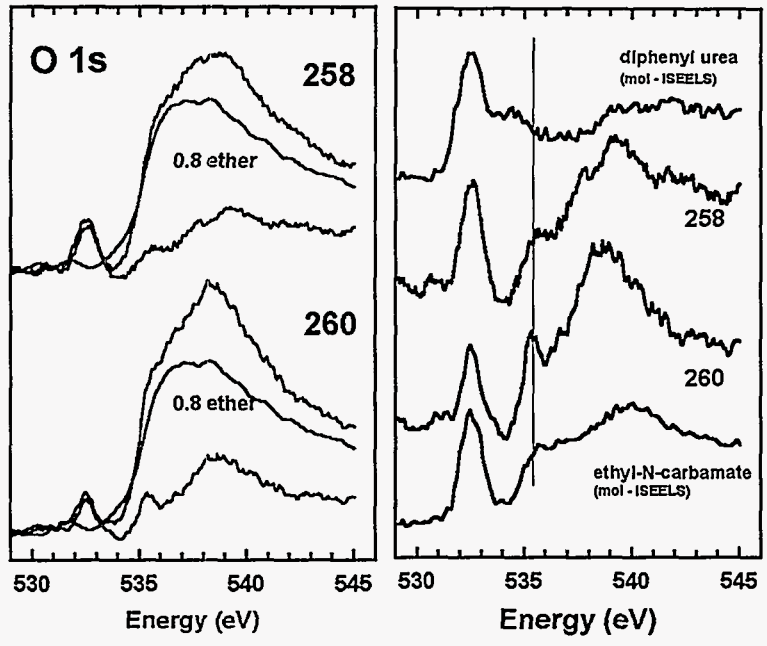

Fig. 4 O 1s spectra of model polyurethanes. *Left*: isolation of aromatic component by subtraction of gaseous ether spectrum. *Right*: comparison of isolated aromatic component with the spectra of gas phase urea and urethane model compounds.

Fig. 4 illustrates the sensitivity to polyurethane chemical composition of O 1s NEXAFS spectra recorded in the STXM. Even though the spectra are dominated by the strong signal from the majority poly-ether component, subtraction of an appropriate model reveals a sensitivity to the aromatic constituents. The changes in the 534-536 eV region indicate one will be able to make a semi-quantitative evaluation of the urea/urethane composition at the O 1s edge. Spectral decomposition procedures like those illustrated in Figs. 3 and 4 are being used to quantify the urea/urethane composition of phase segregated regions in order to study relationships between formulation, processing methodology and properties in a range of polyurethane samples.

ACKNOWLEDGMENTS

We thank Brian Tonner for leadership of the BL 7.0.1 PRT and in the field of spectromicroscopy, and Mario Maronne for help with developing the new detector.

1. H. Ade et al. *Science* **258** (1992) 972; H. Ade et al. *Mat. Res. Soc. Symp. Proc.* **437**, 99 (1996).
2. T. Warwick et al., *Journal of Electron Spectroscopy and Related Phenomena*, **84** (1997) 85
3. G.E. Mitchell et al. *this ALS report (1998).*
4. A.P. Hitchcock et al. *Microscopy and Microanalysis* **3** (1997) 900.

The x-ray microscopes and the Advanced Light Source are supported by the United States Department of Energy, Office of Basic Energy Sciences under contract DE-AC 03-76SF00098. Financial support is also provided by NSERC (Canada).

Principal Investigators: **Edward G. Rightor**, Analytical Sciences, Dow Chemical, 1897 Building, Midland, MI 48667 USA. Email: rightor@dow.com. Tel: (409) 238-3616. **Adam P. Hitchcock**, BIMR, McMaster University, Hamilton, ON L8S 4M1 Canada. Email: aph@mcmaster.ca. Tel: (905) 425-9140 ext. 24749.

Transmission Imaging of Magnetic Domains Using New Circular Polarizing Filter and the STXM

J.B. Kortright,[1] Sang-Koog Kim,[1,2] and T. Warwick[2]
[1]Materials Sciences Division, Lawrence Berkeley National Laboratory,
University of California, Berkeley, California 94720, USA
[2]Advanced Light Source, Lawrence Berkeley National Laboratory,
University of California, Berkeley, California 94720, USA

INTRODUCTION

Imaging magnetic domains with soft x-rays offers several complementary features compared to other techniques. Primary among them is the inherent element-specificity resulting from the core level spectroscopies providing magnetic contrast, thus far utilizing the magnetic circular dichroism (MCD) effect. The first domain images using soft x-rays resulted from imaging emitted secondary photo-electrons [1], and photo-electron emission microscopes (PEEMs) continue to be developed with increasing resolution at the ALS and elsewhere [2]. PEEMs necessarily image surface or near-surface magnetic features, with information depth determined by the escape depth of the secondary electrons (several nm, typically). A second type of magnetic microscope operates in transmission, and thus can study magnetization distributions throughout the bulk of thin films. The first transmission imaging of magnetic domains occurred at BESSY using an imaging zone plate microscope [3] and out-of-plane circular polarization from a bending magnet source to produce MCD contrast on transmission through a sample with perpendicular magnetic anisotropy.

We have produced the first magnetic domain images observed at the ALS using a newly developed circular polarizing filter based on resonant magneto-optical effects in conjunction with the scanning transmission x-ray microscope (STXM) on beamline 7.0. Below is first described the circular polarizing filter, and then early images through demagetized Fe films.

MAGNETO-OPTICAL CIRCULAR POLARIZER USING MCD EFFECT

Our proposal includes two schemes for obtaining magnetic contrast using the linearly polarized undulator illuminating the STXM. One uses a circular polarizer converting linear to circular polarization that then provides MCD contrast in samples having varying magnetization distributions. The other is to sense Faraday rotation through samples using linear polarizers in the transmitted beam [4]. So far only the first approach has been pursued.

Resonant circular polarizing filters using the MCD effect are simple to produce, and operate precisely at those energies required for obtaining MCD contrast in microscopy [5]. Transmission of a linearly polarized beam with wavevector $\boldsymbol{k}$ through a saturated magnetic film with magnetization $\boldsymbol{M}$ results in differential absorption of the + and - helicity components that together make up the incident linear beam, resulting in a transmitted beam with net circular polarization whenever $\boldsymbol{k}\cdot\boldsymbol{M} \neq 0$. This was characterized for a 48 nm thick Fe film with $\boldsymbol{M}$ in-plane by varying the incidence angle θ and measuring the polarization of the transmitted beam using a tunable multilayer linear polarizer. The photon energy was tuned precisely to the peak of the L_3 white line, where MCD is maximum. Figure 1 shows how the measured degree of circular polarization P_C^2 varies with θ, which provides the magnitude of the MCD effect as indicated, based on a simple model of in-plane magnetization. The variation with θ of several other quantities is shown in the figure, including the transmission of + and - helical components (T_+, T_-) relative to their value at 90°, and a figure of merit given by P_C^2T where T is the average

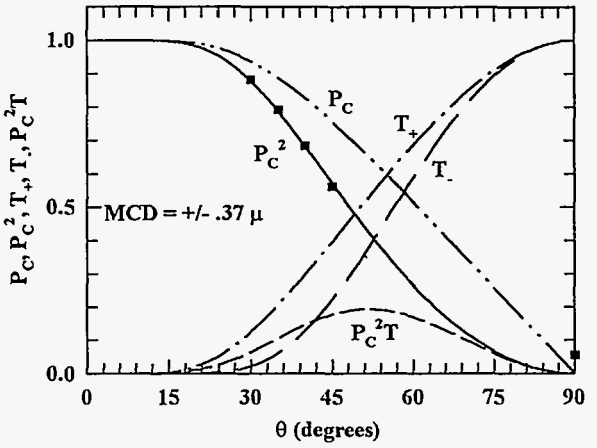

Figure 1. From a linearly polarized incident beam, MCD produces an increasingly circularly polarized transmitted beam as $k \cdot M$ increases (θ decreases). Fits to the the measured degree of circular polarization squared, P_C^2 (squares) yield the magnitude of the MCD effect as +/- .37 of the polarization averaged absorption at the L_3 white line peak. The various lines use this size of the MCD effect together with a simple model to calculate the transmission of + and - helical components relative to their value at normal incidence, and the figure of merit P_C^2T. See ref. 5 for details.

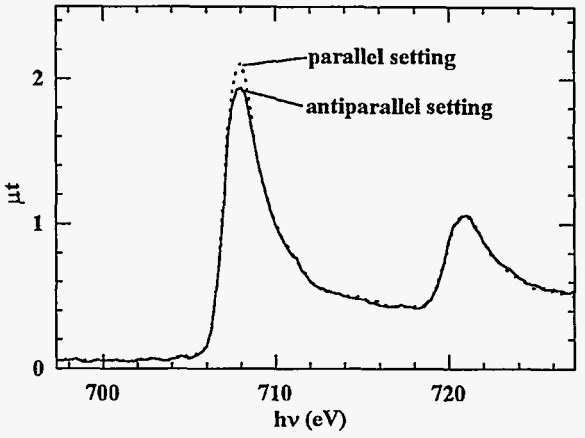

Figure 2. The transmission absorption spectrum from two saturated, 26 nm Fe films, one the circular polarizer and the other the sample, show differences at the L_3 line when M in the two films are nominally parallel and antiparallel to each other. The 15% difference in absorption index in this specific case provides nearly 20% maximum contrast for imaging 180° domains.

of T_+ and T_-. The sense of transmitted helicity can be switched by reversing the sign of M either mechanically or electromagnetically. More details on this new type of circular polarizer, which is the first use of magneto-optical effects as optical elements in the soft x-ray, can be found in ref. 5.

Magnetic contrast in the microscope results from the same MCD effect operative in the circular polarizer. A test of the available contrast was made using two saturated Fe films of equal (26 nm) thickness. The upstream film (in the polarimeter) was set with 45° incidence angle, and the downstream film (in the STXM) with 55° incidence angle. Transmission spectra were measured across the $L_{2,3}$ edges through the two films in different settings, with the magnetizations nominally parallel and antiparallel, by reversing the sign of M in the upstream film. Figure 2 shows the resulting absorption spectrum of both measurements. A significant difference between the two curves is seen at the peak of the L_3 line. When $k \cdot M$ for each film has the same sign, the net absorption is greater than for opposite signs, producing a maximum difference in absorption product μt of about 15 percent between these two settings for this film thickness. The difference in transmitted intensity for these films is nearly 20 percent, setting the maximum contrast for these specific conditions. Somewhat more than 10 percent of the incident flux is transmitted through both polarizer and sample at the L_3 line, and the transmitted flux is of order 10^6 photons per second, providing adequate signal-to-noise at 50-100 msec dwell times to image domains with this contrast.

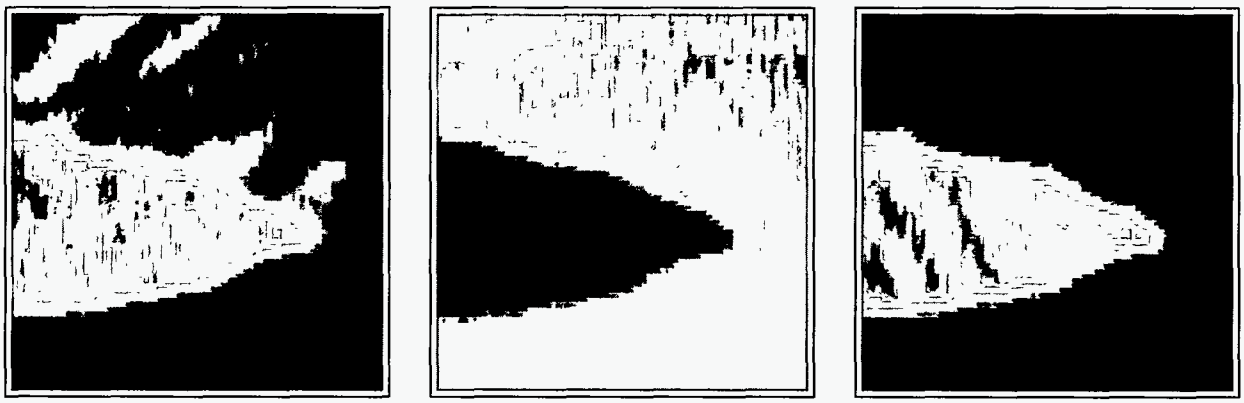

Figure 3. A needle-shaped domain pointing toward the right is surrounded by a larger domain with opposite magnetization in a demagnetized 20 Fe film. All images show the same 40 x 40 μ field. Images at left and center are taken with + and - helicity, respectively, while that at right is the divided image +/-. In addition to the two prominent 180° domains, each domain shows regular fluctuations in magnetization with distinct spatial relationships, presumably associated with the growth of the small domain into the other.

EARLY DOMAIN IMAGES FROM DEMAGNETIZED IRON FILMS

Early magnetic domain images using these techniques were obtained from Fe films and are shown in Figure 3. This 20 nm thick demagnetized film exhibited a needle-shaped domain, with $\boldsymbol{M}$ nominally along needle axis, extending into a large region of film with opposite magnetization. The three images in Fig. 3 all show the same 40 x 40 μ field. The image at left was obtained with + helicity and that at center was obtained with - helicity. At right is the divided image of +/- helicities. In addition to the needle shaped domain pointing to the right, weak features are observed both within the needle domain and above it in the surrounding domain. In each case these weak features are regular fluctuations in magnetization inclined at an angle to predominant direction of $\boldsymbol{M}$ in each domain. In the two different domains these fringes are oriented at nominally 90° to each other in the film plane. These fluctuations in magnetization, even though observed in static images, are presumably related to the dynamics of domain wall motion since the domains result from a demagnetization process. These transmission images are effectively direct maps of $\boldsymbol{k}\cdot\boldsymbol{M}$ projected through the sample, and thus can provide quantitative magnetization maps, especially when aided by multiple angle viewing. Continued analysis and experiments are investigating if these fluctuations are associated with just the interface regions of the films (which seems likely), or if they extend throughout the films.

CONCLUSIONS AND FUTURE DIRECTIONS

Early transmission imaging results in a scanning transmission soft x-ray microscope reveal complementary capabilities to previously demonstrated x-ray techniques for imaging magnetic domains, and point toward future applications and improvements. Working in transmission clearly allows the bulk of thin film structures to be investigated, rather than just near surface features as in electron imaging microscopes. This penetrating ability will allow imaging of magnetization distributions in different magnetic layers of magnetic multilayer structures. Compared to the imaging x-ray microscope [3] which uses only the zone plate to achieve energy resolution, the the grating monochromator associated with the STXM allows high resolution spectroscopy as well as magnetic contrast. This should aid in quantifying observed

magnetization variations, and also allow study of chemical inhomogeneities that might manifest themselves through different spectral (and magnetic) features near absorption edges. Continuing activities combining these features are currently aimed at quantitative imaging of magnetization distrubutions in individual magnetic layers of magnetic multilayers, where the element-specificity of soft x-ray techniques provides unique capabilities to observe domains in a magnetic layer buried underneath other magnetic layers. Such capabilities are of interest both for fundamental studies of magnetic correlations in coupled systems and to characterize technologically relevant structures such as spin valves, where understanding the magnetization behavior in buried layers presents experimental challenges.

Many improvements can be envisioned to make these transmission techniques more sensitive and useful. Spatial resolution of the probe spot in these early images is not better than 150 nm, and should improve perhaps to 50 nm in the future. In situ studies of domain reversal processes will be possible with a coil around the sample. Use of Faraday rotation, just below the L_3 white lines, as a contrast mechanism will allow thicker samples to be studied in transmission. It should be possible to develop a reflecting microscope sensing Kerr rotation with significant depth penetrating ability to allow study of magnetic structures on opaque substrates. The variable polarization of the upcomming elliptically polarizing undulator will enhance the contrast and capabilities of such microscopes considerably.

REFERENCES

1. J. Stohr, Y. Wu, B.D. Hermsmeier, M.G. Samant, G.R. Harp, S. Koranda, D. Dunham, and B.P. Tonner, Science **259**, 658 (1993).
2. Schneider, R. Fromter, C. Ziethen, G. Schonhence, and J. Kirschner, Synch. Rad. News, **10**, 22 (1997).
3. G. Schmahl, P. Guttmann, D. Raasch, P. Fischer, and G. Schutz, Synch. Rad. News, **9**, 35 (1996).
4. J.B. Kortright, M. Rice, and R. Carr, Phys. Rev. B **51**, 10240 (1995).
5. J.B. Kortright, S.-K. Kim, T. Warwick, and N.V. Smith, Appl. Phys. Lett. **71**, 1446 (1997).

This work was supported by the Director, Office of Energy Research, Office of Basic Energy Sciences, Division of Materials Sciences, of the U.S. Department of Energy under Contract No. DE-AC03-76SF00098.

Principal Investigator: Jeffrey Kortright, Materials Sciences Division, Lawrence Berkeley National Laboratory, Email:jbkortright@lbl.gov, Telephone: 510-486-5960.

Vibrationally Resolved O 1s Excitations in CO and NO

R. Püttner[1], I. Dominguez[2], T. Morgan[3], C. Cisneros[4], E. Rotenberg[2], T. Warwick[2], M. Domke[1], G. Kaindl[1], and A.S. Schlachter[2]

[1]Institut für Experimentalphysik, Freie Universität Berlin, Arnimallee 14, D-14195 Berlin, Germany
[2]Lawrence Berkeley National Laboratory, 1 Cyclotron Road, Berkeley, CA 94720, USA
[3]Department of Physics, Wesleyan University, Middeltown, CT 06459, USA
[4]Instituto de Fisica, APDO Postal 139-B, Cuernavaca, 62191, Mexico

INTRODUCTION

Recent improvements in synchrotron light sources and beamlines have made it possible resolving the vibrational fine-structure of numerous core-excited molecules using photon energies up to ≅ 400 eV (e.g. Si $2p^{-1}$, C $1s^{-1}$, N $1s^{-1}$) [see e.g. 1-3]. However, at even higher photon energies, the instrumental resolution of monochromators was not sufficient until very recently to obtain full information on the vibrational fine structure. For example, earlier high-resolution photoabsorption measurements of CO and NO below the O 1s threshold with a resolution ΔE≅120 meV using the SX700/II monochromator at BESSY/Berlin, only partially revealed the vibrational fine structure [1,2].

We report here on new photoabsorption measurements of CO and NO below the O 1s ionization threshold with substantially improved resolution (ΔE ≅ 65 meV), resulting in completely resolved vibrational fine structures. The new spectra allowed Franck-Condon analyses, providing information on the potential-energy surfaces of the core-excited states.

EXPERIMENT

The measurements were performed at BL 7.0.1 at the ALS/Berkeley using the built-in photoionization cell that consists of two parallel plates with an active length of 20 cm for collecting the charged particles. The photoionization cell was separated from the UHV of the monochromator by an 1000-Å thick Al (1% Si) window; it was filled with 10 to 50 μbar of CO and NO. The spectra were measured with 8-μm entrance and exit slits, resulting in a spectral resolution of ΔE ≅ 65 meV.

RESULTS AND DISCUSSION

O 1s excitations in CO

The photoionization spectrum of the O $1s^{-1}\pi^*$ excitation in CO, with completely resolved vibrational fine structure, is shown in Fig. 1. This improved spectrum allowed for the first time to perform a Franck-Condon analysis of this excitation, resulting in an increase of the equilibrium distance from r''=1.1283 Å in the electronic ground state to r'=1.291(3) Å in the core-excited state. In addition, a decrease of the vibrational energy from $\hbar\omega$''=269.025 meV in the ground state to $\hbar\omega$'=166(1) meV in the core-excited state as well as a slight increase of the anharmonicity from $x\hbar\omega$''=1.647 meV to $x\hbar\omega$'=1.8(1) meV were derived. We obtain a decrease of the dissociation energy from D_e''=11.0 eV in the ground state to D_e'=3.9 eV in the core-excited state according to $D_e=(\hbar\omega)^2/4x\hbar\omega$. The resulting parameters of the core-excited state agree fairly well with calculations of Correira et al. [4], with $\hbar\omega$'=176.8 meV, $x\hbar\omega$'=2.3 meV, and r'=1.280 Å. The increase of the equilibrium distance as well as the decrease of the

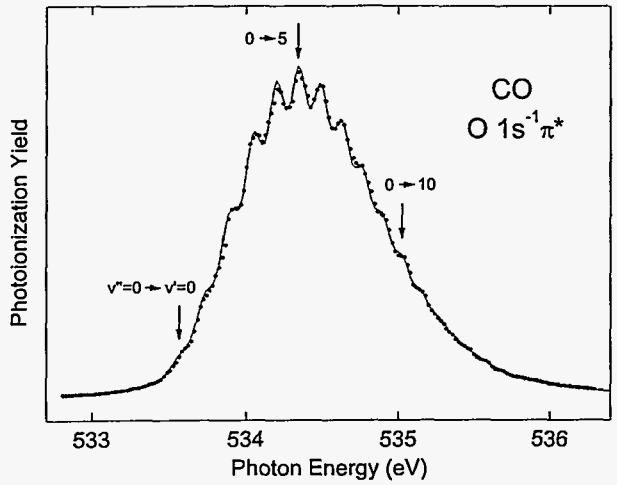

Fig. 1: O $1s^{-1}\pi^*$ excitation in CO. The solid line through the data points represents the results of a Franck-Condon analysis.

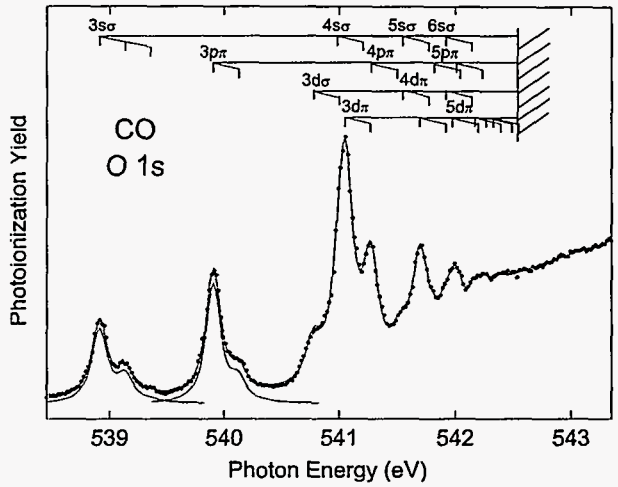

Fig. 2: Rydberg region of CO below the O 1s ionization threshold. The solid line through the data points represents the results of a fit analysis. The subspectra below the spectrum represent the results of a Franck-Condon analysis of the Rydberg states O $1s^{-1}3s\sigma$ and O $1s^{-1}3p\pi$. The assignment is given by the vertical bar diagrams above the spectrum. The first bar for each resonance represents the v"=0 → v'=0 excitation, while the other bars represent higher vibrational substates.

vibrational energy and the dissociation energy upon excitation can readily be understood on the basis of excitation into an antibonding π^* orbital.

The Rydberg region of the O 1s core excitation spectrum of CO is shown in Fig. 2 together with the assignments. For the two lowest Rydberg states at $h\nu \cong 539$ and 540 eV, a Franck-Condon analysis has been performed, resulting in an increase of the equilibrium distance from r"=1.1283 Å in the electronic ground state to r'=1.169(2) Å [r'=1.158(2) Å] as well as a decrease of the vibrational energies from $\hbar\omega$"=269.025 meV to $\hbar\omega$'=223(3) meV [$\hbar\omega$'=223(3) meV] in the O $1s^{-1}3s\sigma$ [O $1s^{-1}3p\pi$] Rydberg state upon excitation. The vibrational-energy splitting and the intensity ratios of vibrational substates of the O $1s^{-1}3p\pi$ Rydberg state is transferred to the higher Rydberg states in order to perform a fit analysis. This analysis results in the assignment given in Fig. 2 with four Rydberg series and quantum defects of δ=1.06 (nsσ series), δ=0.73 (npπ), δ=0.22 (ndσ), and δ= –0.02 (ndπ). These results differ from earlier experiments, where only three Rydberg series (nsσ, npπ, ndσ) with doubtful intensity ratios were observed.

O 1s excitations in NO

NO has one additional electron as compared to CO, which is located in the antibonding π^* orbital. Due to the singly occupied π^* orbital, NO is called an open-shell molecule. Upon core excitation, the single π^* electron can interact with the core hole and the excited electron, leading to new effects as compared to CO, e.g. three substates of the O 1s→π^* excitation and two O $1s^{-1}$ ionization thresholds are observed. A more detailed discussion of this interaction and its influence on the spectral features is given e.g. by Wight and Brion [5].

Fig. 3 shows the O $1s^2\pi^* \rightarrow$O $1s(\pi^*)^2$ excitations in NO, which are represented by three substates ($^2\Sigma^-$, $^2\Delta$, $^2\Sigma^+$) due to the interaction between the core hole and the two π^* electrons.

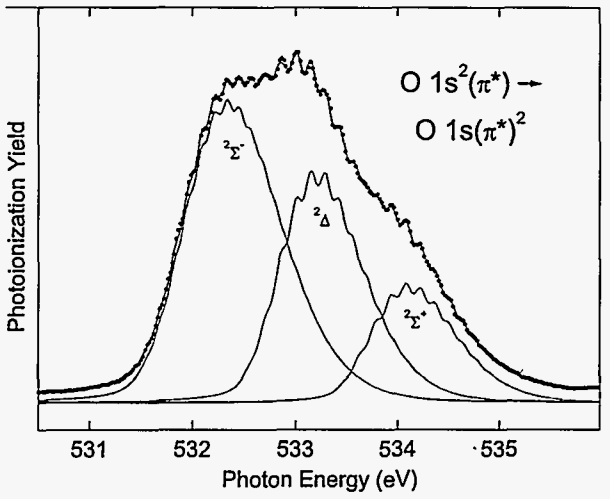

Fig. 3: The O $1s^{-1}\pi^*$ excitation in NO. The solid line through the data points represents the result of a Franck-Condon analysis. The three subspectra describe the three substates.

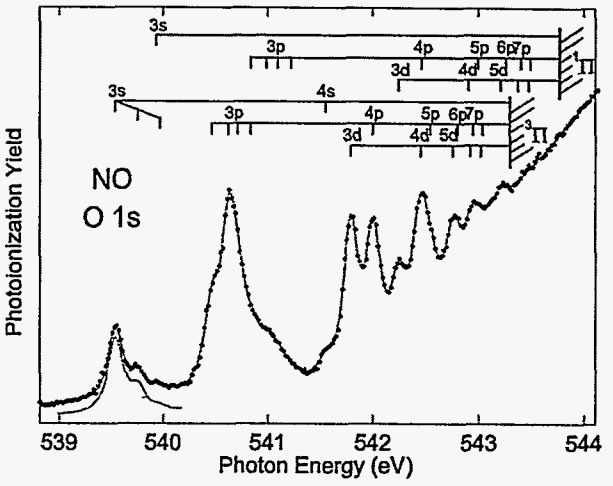

Fig. 4: The Rydberg region of NO below the O 1s ionization threshold. The solid line through the data points represents the result of a fit analysis. The subspectrum below the spectrum describes the result of a Franck-Condon analysis of the O $1s^{-1}3s\sigma$ Rydberg state. The assignments are given by the vertical bar diagrams above the spectrum. The first bar for the 3s resonance represents the v"=0→ v'=0 excitation, while the other bars describe higher vibrational substates.

Contrary to previous high-resolution photoabsorption measurements [2], the vibrational fine structure of the substates are completely resolved and allow a Franck-Condon analysis. The results of this analysis are represented by the solid line through the data points and the three subspectra. The values obtained for the equilibrium distances r' and the vibrational energies $\hbar\omega'$ for the core-excited states are summarized in Table 1. For comparison, the theoretical results obtained by Fink [6] are also given. It can be seen that for all three substates the vibrational energies decrease from $\hbar\omega''$=235.9 meV to $\hbar\omega' \cong 150$ meV and the equilibrium distances increase form r"=1.151 Å to r'≅1.32 Å. Again, this can be understood by excitation into an antibonding orbital. A detailed comparison of the equilibrium distances and the vibrational energies with the values given by Fink reveals good agreement.

The Rydberg region of NO below the O 1s ionization threshold is shown in Fig. 4. The vertical-bar diagrams above the spectrum represent the assignments of the Rydberg states converging towards the O 1s ionization thresholds $^3\Pi$ and $^1\Pi$. This splitting is due to an interaction between the O 1s core hole and the π^* electron. Three Rydberg series with quantum

Table 1: Results of the Franck-Condon analysis of the O $1s^{-1}\pi^*$ excitations in NO. Given are the vibrational energies $\hbar\omega$ and the equilibrium distances r for the electronic ground state (g.s.) the the three core-excited states $^2\Sigma^-$, $^2\Delta$, and $^2\Sigma^+$. For comparison, the theoretical results from Fink [5] are also given.

	$\hbar\omega$ (meV)		r (Å)	
	this work	Fink [6]	this work	Fink [6]
g.s.	235.9		1.151	
$^2\Sigma^-$	137(3)	139	1.348(3)	1.339
$^2\Delta$	154(3)	159	1.311(3)	1.295
$^2\Sigma^+$	157(3)	162	1.306(3)	1.290

defects of δ=1.10 (ns Rydberg series), δ=0.75 (np), and δ=0.00 (nd) are identified.

The vibrational fine structure of the O $1s^{-1}(^3\Pi)3s$ Rydberg state is clearly resolved for the first time and Franck-Condon analysis are performed resulting in a decrease of the vibrational energy from $\hbar\omega''$=235.9 meV to $\hbar\omega'$=218(2) meV and a increase of the equilibrium distances form r''=1.151 Å to r'=1.190(2) Å. The improved spectrum allowed to determine the $^3\Pi$ - $^1\Pi$ splitting of the O 1s ionization threshold to $\Delta I_p = I_p(^3\Pi) - I_p(^1\Pi)$=456(15) meV. This value is more precise and significantly smaller than previous results of 510 meV [2] and 550 meV [7].

CONCLUSIONS

The significantly improved energy resolution of the present work allows resolution of the complete vibrational fine-structure and Franck-Condon analyses, resulting in detailed information on the potential-energy surfaces, i.e. on the vibrational energies and equilibrium distances of molecules after O 1s core excitations.

ACKNOWLEDGEMENT

The authors thank T.X. Carroll and T.D. Thomas for providing the computer code that was used to perform Franck-Condon analyses of the O 1s $\rightarrow \pi^*$ excitations in CO and NO.

REFERENCES

1. M. Domke, C. Xue, A. Puschmann, T. Mandel, E. Hudson, D.A. Shirley, and G. Kaindl, Chem. Phys. Lett. **173**, 122 (1990).
2. G. Remmers, M. Domke, A. Puschmann, T. Mandel, G. Kaindl, E. Hudson, and D.A. Shirley, Chem. Phys. Lett. **214**, 241 (1993).
3. R. Püttner, M. Domke, and G. Kaindl, Phys. Rev. A **57**, 297 (1998).
4. N. Correia, A. Flores-Riveros, H. Ågren, K. Helenelund, L. Asplund, and U. Gelius, J. Chem. Phys. **83**, 2035 (1997).
5. G.R. Wight and C.E. Brion, J. Electron Spectrosc. Relat. Phenom. **4**, 313 (1974).
6. R. Fink, J. Chem. Phys. **106**, 4036 (1997).
7. D.W. Davis, R.L. Martin, B.S. Banna, and D.A. Shirley, J. Chem. Phys. **59**, 4235 (1973).

This work was supported by the Director, Office of Energy Research, Office of Basic Energy Science, Materials Science Division, of the Department of Energy under Contract No. DE-AC03-76SF00098. The work in Berlin was supported by the Bundesminister für Bildung, Wissenschaft, Forschung und Technologie, project No. 05-650-KEA, and the Deutsche Forschungsgemeinschaft, project Do-561/1-1.

Principal investigator: A.S. Schlachter, Lawrence Berkeley National Laboratory, 1 Cyclotron Road, Berkeley, CA 94720, USA. E-mail: Fred_Schlachter@macmail.lbl.gov. Telephone: 510-486-4892. Fax 510-486-6499.

Beamline 7.0.2 Abstracts

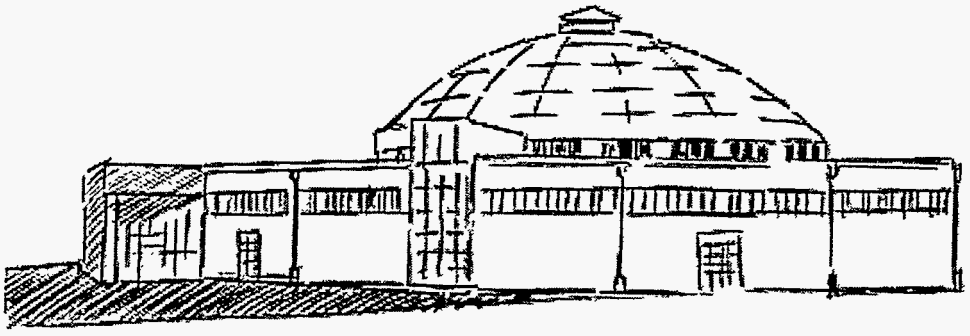

ALS beam line 7.0.2: the pink-beam branch of beam line 7

M. R. Howells
Advanced Light Source, Ernest Orlando Lawrence Berkeley Laboratory, University of California, Berkeley, California 94720, USA.

1. INTRODUCTION

This beam line is a simple but uniquely powerful soft x-ray source. It is designed to provide the highest possible flux, using the natural bandwidth of the undulator, for experiments in coherent optics and coherent scattering. The system consists simply of the beam line 7 undulator source, a flat mirror reflecting at 4 degrees grazing angle and a 0.5 μm beryllium window designed to provide a high-vacuum (10^{-6} torr) sample environment capable of a fast turnaround of samples. The beam line delivers light in the spectral range from 200-650 eV but is most effective in the water-window spectral range from (284-543 eV). The limitation of the flux at the low-energy end of the range is due to the fall off of output in the fundamental at high K. At the high-energy end it is due to the reflectance of the Ni-coated mirror at 4 degrees grazing angle. The performance of the beam line is described below in section 2 while the mirror design is discussed in section 3. General documentation of the beam line is available through the beam-line review committee records [MacDowell 1997] while further technical information is available in the ALS internal reports cited below and listed at the end.

2. BEAM-LINE PERFORMANCE

The performance of the beam line is described below by two figures. The first (Fig. 1) shows the flux per unit solid angle in Watts/mr^2 reflected by the mirror. It shows that peak output is obtained with K=1, corresponding to a fundamental wavelength of 27 Å. This condition produces a power density at the 0.8-mm diameter window of 0.675 W/mm^2. The deposited power is 0.088 W and the transmitted power is 0.25 W. Very little power in orders higher than the third is reflected even at K=4 as indicated by the calculated point on Fig. 1 for all orders at K=4.

Fig 2. shows the useful flux obtained after transmission through the 0.5 μm beryllium window. At the peak this represents about 5×10^{15} photons per second emerging from the window or almost 10^{10} photons per square micron in the *unfocused* beam. The technology of the window is discussed in an internal ALS report [Howells 1997A].

3. THE WATER-COOLED SILICON MIRROR

This flat mirror reflects a portion of the beam down the branch line. It is a silicon and steel structure held together in part by frit bonding. The use of brittle material for the mirror coupled with pressurized water for coolant has required an unusual degree of analysis and testing of the vacuum safety of this system. As of this writing these tests are still going on. The design of the mirror and a theoretical analysis of the consequences of an accident are described in ALS internal reports [Howells 1997B and Howells 1998]. Broadly the safety philosophy is based on the use of generous safety factors in the design to ensure that an accident cannot take place. A further level of protection is provided by the fact that, even if an accident should take place, the rate of exposure of water surface and of evaporation of water from that surface will take place slowly in comparison to the closure speed of the fast valve.

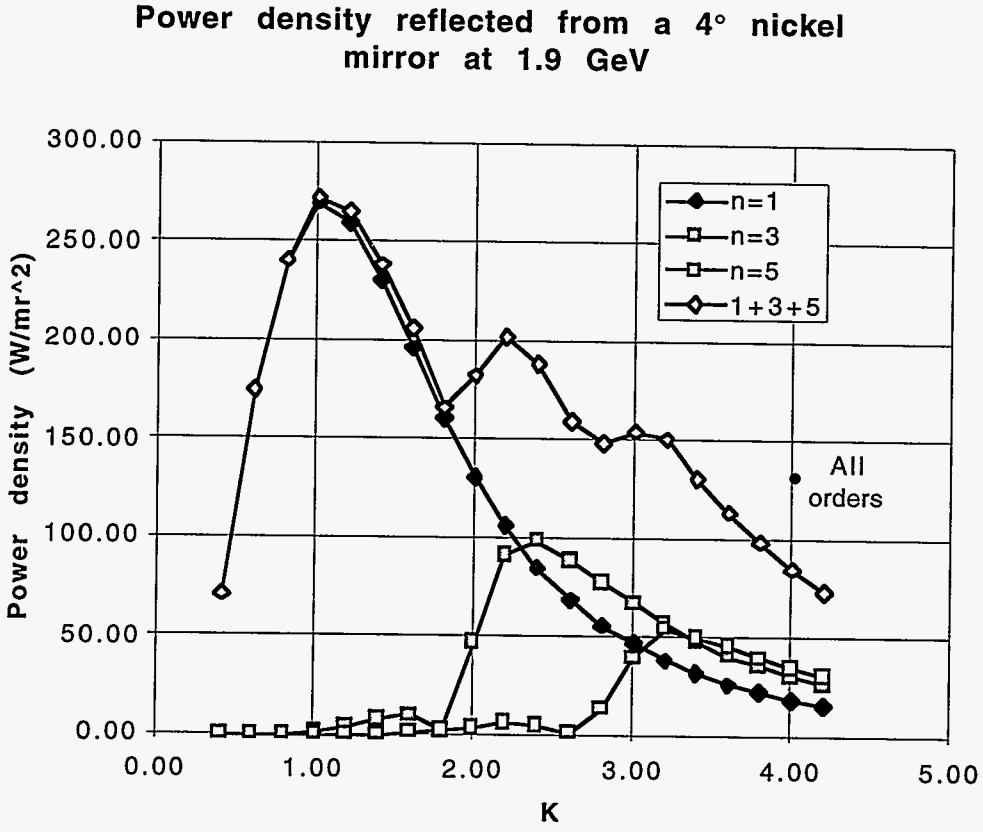

Figure 1.

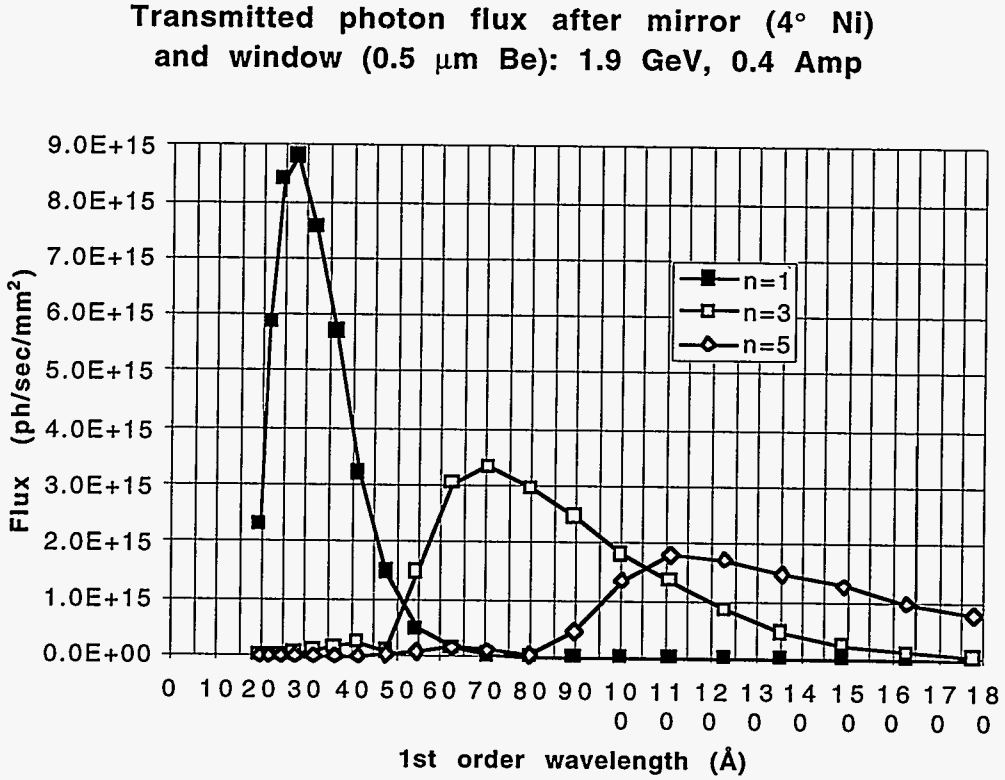

Figure 2.

4. REFERENCES

Howells, M. R. (1997A), "The vacuum barrier on beam line 7.0.2: a beryllium window in a new size regime", LSBL 424.

Howells, M. R. (1997B), "The beam line 7.0.2 silicon mirror", LSBL 425.

Howells, M. R. (1998), "What happens to a mass of water that is suddenly exposed to vacuum?: Analysis of a bursting water-cooled mirror", To be published shortly as an LSBL report.

MacDowell, A (1997), Committee papers submitted to the Beam Line Review Committee for review of beam line 7.0.2 on 12-16-97.

This work was supported by the Director, Office of Energy Research, Office of Basic Energy Sciences, of the U.S. Department of Energy under contract No. DE-AC03-76SF00098.

Principal investigator: Malcolm Howells, Advanced Light Source, Lawrence Berkeley National Laboratory. Email: howells@lbl.gov. Telephone: (510) 486-4949.

Beamline 7.3.1 Abstracts

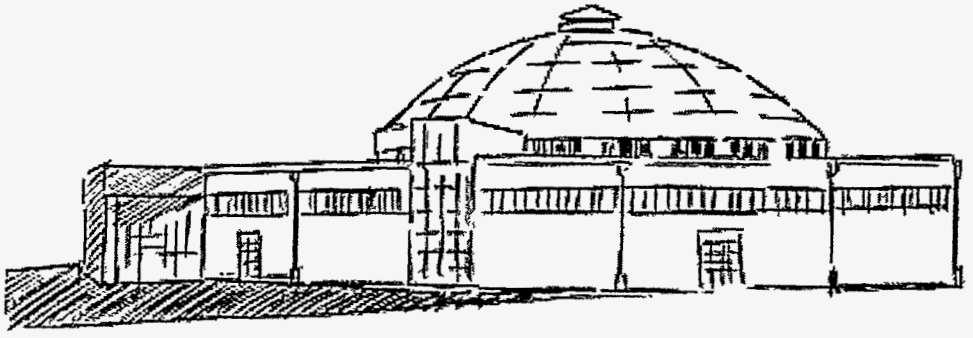

Comparison Between the μXPS Endstation and the PHI Quantum 2000

A. L. Johnson[1,2], G. D. Ackerman[1], M. R. Howells[1], Z. Hussain[1], H. A. Padmore[1], T. R. Renner[1], W. Steele[1], F. Gozzo[2], B. Triplett[2], R. Ynzunza[2], P. D. Kinney[3], R. Odom[4], E. Principe[4]

[1]Lawrence Berkeley National Laboratory, Advanced Light Source, Berkeley, CA
[2]Intel Corporation, Santa Clara CA
[3]MicroTherm LLC, Minneapolis, MN
[4]Charles Evans and Associates, Redwood City, CA

Comparison between analytical instruments allow relative cost/benefit analysis and guides one in optimizing both instruments. We have engaged in comparative studies of the PHI Quantum 2000 (Q2000) and the μXPS endstation at the ALS. Both machines are scanned probe imaging XPS systems (the Q2000 scans the X-ray beam and μXPS scans the sample). Further, the electron analyzer in both facilities are of very similar design.

The design goal of μXPS was to get the greater (resolution)x(intensity) product obtainable using a synchrotron radiation X-ray source. μXPS has higher resolution (1-2μ) at a power level roughly commensurate with the flux delivered by the Quantum 2000 at 100μ resolution (table 1). The synchrotron source allows for variation of the photon energy - making photon energy dependent phenomena (NEXAFS, for example) accessible contrast/analytical tools. The disadvantage of the synchrotron source is the greater difficulty in accessing the facility and variation of the flux with time and energy. μXPS is still being improved (recently the flux was improved 50% from the reported values - design goals are 2-4x more flux and 1μ resolution), but the following results reported here are useful as an interim baseline.

Energy resolution in μXPS is limited by the monochromator and the analyzer - we have similar resolution to the Q2000 at 500eV photon energy. The utility of this resolution for complex systems typical of industrial and environmental samples will be determined by the ability to deal with sample charging and heterogeneity. A small spot makes charge neutralization more difficult but makes it more likely that the sampled volume is homogeneous.

Scattered light determines the signal to noise of spectra of minority species in small regions. The μXPS optics are more demanding than the Q2000, and the scattered light results are worse. This issue may be addressed with improved optics and/or through software.

Instrument productivity (throughput) are influenced by other factors than flux and resolution - the ease of sample introduction, data analysis, and software overheads all play a part. The Q2000 has a highly developed user interface, and is a model to us of user friendliness. The overhead values in the figure are typical results obtained by skilled workers on μXPS and the Q2000 with average samples. This table indicates areas in need of improvement on μXPS: the longer overhead for imaging is being addressed by specialized hardware, the long time necessary to find regions of interest is being addressed by prefiducialization of the samples, and the handling overhead can be minimized by loading multiple sample cassettes at one time.

Stability of the instrument can be broken into issues common to both XPS devices and those specific to μXPS. Samples are positioned in μXPS by a mechanical stage. We installed a laser interferometer and will incorporate it into the control loop to improve scan accuracy. The stability of the μXPS source must be monitored by using reference channels in the data acquisition, and the reference incorporated into the data analysis.

Comparison of μXPS and PHI Quantum 2000

	μXPS	Quantum 2000
Signal Intensity	Sputtered Ag ~33pA @ 1.5μm spot size ~65kc/s 3d 5/2 (850eV hν, 300mA) (80,40)μm slits, 23.5eV pass energy	Sputtered Ag ~50pA @ 100μm spot size 90kc/s 3d 5/2 (1487 hν) 23.5eV pass energy
Spectral Resolution	Sputtered Ag 500eV hν 0.67 eV 870eV hν 1.03 eV 1250eV hν 1.68 eV (80,40)μm slits, 23.5eV pass energy	Sputtered Ag 1486.6eV hν 0.64eV 23.5eV pass energy
Spatial Resolution	1x1.5μm	8μm
Scattered Light	~15%	~10% @ 2 x FWHM ~2% @ 5 x FWHM
Handling Overhead	15-30 minutes (dependent on sample vacuum characteristics)	10-15 minutes (dependent as μXPS)
Localization Overhead	15-30 minutes (dependent on size and visibility of features)	20-30 minutes (dependent as μXPS)
Spectral Overhead	6 minutes for 100x100 image spectra as Q2000	seconds for imaging ~1-2 minutes/spectra
Data Reduction	~10 minutes (conversion and analysis time)	5-10 minutes
Spatial Reproducibility	0.2-1μm with an image 1μm with an experiment <10μm linearity over 40x40mm sample	5-10μm
Spectral Reproducibility	Low (due to varying beam current, damage, etc.) - to be improved	Medium (due to sample damage and source drift)

Table 1

ACKNOWLEDGMENTS

We wish to thank Charles Evans and Associates for their aid in tests of the Q2000 at their facility.

REFERENCES

1. E. Principe, R. W. Odom, Z. Hussain, and, H. Padmore, Proceedings of the 1998 MRS Spring Meeting, San Francisco, CA (submitted).

This work was supported in part by the Director, Office of Energy Research, Office of Basic Energy Sciences, Materials Sciences Division of the U. S. Department of Energy, under Contract No. DE-AC03-76SF00098 and in part by Intel Corp., Santa Clara, CA and Applied Materials Inc., Santa Clara, CA.

Spokesperson for the micro-XPS PRT is Baylor Triplett, Intel Corporation, SC1-3, 3065 Bowers Ave, Santa Clara, CA 95052-8126 Baylor_B_Triplett@ccm.sc.intel.com

High-Resolution X-ray Photoemission Electron Microscopy at the Advanced Light Source

Thomas Stammler[1], Simone Anders[1], Howard A. Padmore[1], Joachim Stöhr[2], Michael Scheinfein[3]

[1] *Lawrence Berkeley National Laboratory, 1 Cyclotron Road, Berkeley, CA 94720*

[2] *IBM Almaden Research Center, 650 Harry Road, San Jose, CA 95120*

[3] *Department of Physics and Astronomy, Arizona State University, Tempe, AZ 85287*

X-ray Photoemission Electron Microscopy (X-PEEM) is a full-field imaging technique where the sample is illuminated by an x-ray beam and the photoemitted electrons are imaged on a screen by means of an electron optics. It therefore combines two well-established materials analysis techniques - photoemission electron microscopy (PEEM) and x-ray spectroscopy such as near edge x-ray absorption fine structure (NEXAFS) spectroscopy. This combination opens a wide field of new applications in materials research and has proven to be a powerful tool to investigate simultaneously topological, elemental, chemical state, and magnetic properties of surfaces, thin films, and multilayers at high spatial resolution. A new X-PEEM installed at the bend magnet beamline 7.3.1.1 at the ALS is designed for a spatial resolution of 20 nm and is currently under commissioning.

INTRODUCTION

Near Edge X-ray Absorption Fine Structure (NEXAFS) spectroscopy is an established technique to study materials properties such as elemental composition, chemical bonding, and molecular orientation [1]. It is based on the availability of X-ray radiation of tunable wavelength produced by a synchrotron. Utilizing the polarization of the synchrotron radiation, one can perform x-ray magnetic dichroism (XMD) spectroscopy to investigate the magnetic structure and atomic magnetic properties of magnetically ordered materials [2]. Third-generation sources of high-brilliance synchrotron radiation make it possible to combine effectively spectroscopic methods like NEXAFS and high spatial resolution microscopy techniques. The latter can be achieved either by scanning techniques or by parallel image acquisition. In scanning x-ray microscopy an x-ray optics focuses the beam and a detector senses photons or electrons as the x-ray spot moves across the sample surface (or as the sample rasters through a fixed x-ray spot). The lateral resolution is therefore determined by the size of the x-ray spot. In contrast, x-ray photoemission electron microscopy (X-PEEM) is a full-field imaging technique where the sample is illuminated by an x-ray spot focused to a size of the largest field of view considered. In this case the resolution is determined by the aberrations of the electron-optical imaging system consisting of two or more electrostatic lenses. In addition, due to a parallel collection of information an imaging technique is inherently fast and allows the study of time dependent processes at video rates. At present, there are several spectromicroscopes in operation at synchrotron radiation facilities. The highest spatial resolution so far reported for such an instrument is 40 nm and has been achieved by the Clausthal group at BESSY I [3]. The new X-PEEM installed at the bend

magnet beamline 7.3.1.1 at the ALS is designed for a spatial resolution of 20 nm and is currently under commissioning. An even more advanced instrument equipped with an electrostatic hyperbolic-field mirror that allows correction of spherical and chromatic aberrations simultaneously is in the design phase. The use of an aberration–correcting mirror has the potential for pushing the spatial-resolution limit of the X-PEEM to a few nm. Another UHV spectromicroscope called SMART with a similar spatial resolution is under construction for a soft x-ray undulator beamline at BESSY II [4].

EXPERIMENTAL SET-UP

Figure 1 shows the schematic layout of the spectromicroscopy beamline 7.3.1.1 at the ALS. The spherical grating monochromator provides soft x-rays in a spectral range from 260 eV to 1500 eV with a resolving power of $E/\Delta E$ = 1800 and $3x10^{12}$ photons/s/0.1%BW at 800 eV. The use of a bend magnet gives the choice of linearly or circularly polarized radiation. The x-ray beam is focused on the sample with a spot size of 30 μm x 30 μm. The objective lens is of conical shape allowing the sample to be illuminated by the x-ray beam at an angle of about 30 degrees (*c.f.,* Fig. 2). The photoemitted electrons are accelerated by the immersion objective lens and form an intermediate image with a magnification of m = 10. In order to reduce spherical and chromatic aberrations the microscope is designed for a rather high accelerating voltage of 30 kV. Three corrector elements are incorporate into the microscope column to accommodate for lens imperfections and misalignment of the individual components. In order to correct for astigmatism an octopole stigmator is located in the back focal plane of the objective lens. Two hexapole deflectors, one located right behind the stigmator, the second one at the back focal plane of the intermediate lens (*cf.*, Fig. 2), correct for beam deflection caused by misalignment of the lens elements. The back focal plane of the objective lens would also be a well-suited place for an angle-limiting aperture which has an electron energy filtering effect and therefore reduces the chromatic aberrations. Since the stigmator/deflector arrangement does not leave enough space, a transfer lens with a magnification of unity is added to form another (conjugate) back focal plane where the aperture can be located. However, the insertion of an aperture reduces the transmittance of the microscope to typically 5% (for an aperture diameter of 12 μm). The intermediate and projective lenses form a magnified image on a phosphorous screen from where the image is transferred to a slow-scan CCD camera using a fiber-optics coupling with a 1:2 taper. The calculated resolution limit is about 20 nm.

OUTLOOK

The new X-PEEM at BL 7.3.1.1 is not only equipped with a surface science preparation chamber and load-lock system for fast sample transfers, it has also incorporated an electron-beam evaporator for *in situ* deposition. The sample manipulator is equipped with an electron-beam heating system for temperatures up to 1500 °C. Therefore the combination of x-ray spectroscopy and high spatial resolution photoemission electron microscopy together with surface science sample preparation capabilities make this X-PEEM a very versatile instrument in the field of materials science. Major future applications will be magnetic domain imaging of magnetic recording materials, elemental and chemical bonding contrast imaging of hard disk coatings and sliders, and the study of dewetting and decomposition phenomena of thin polymer blends and bilayers.

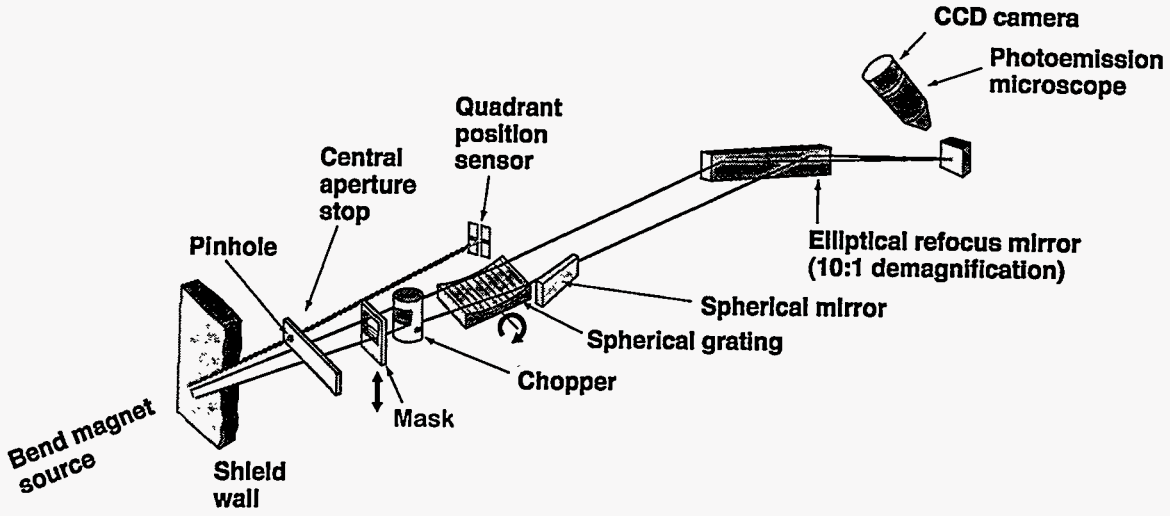

FIGURE 1: Schematic layout of the spectromicroscopy beamline 7.3.1.1 at the ALS.

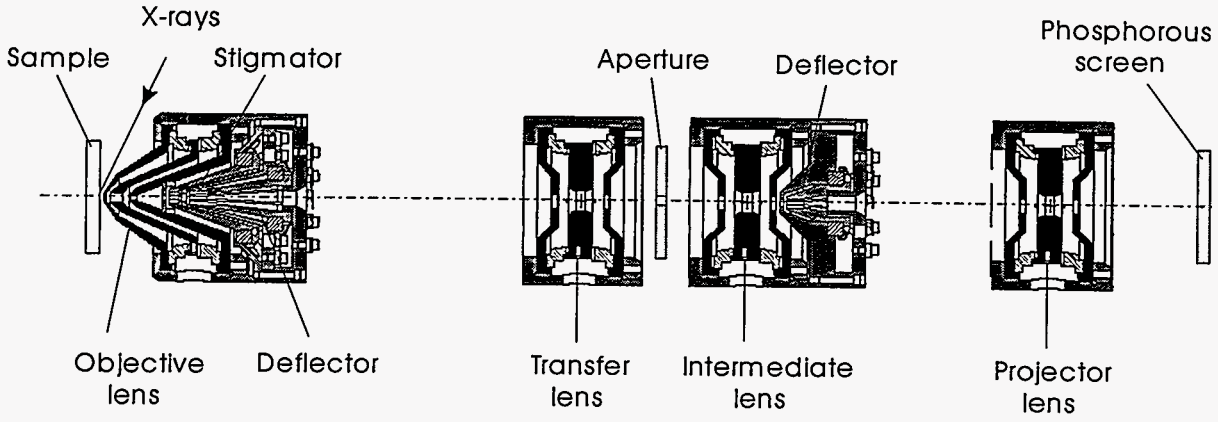

FIGURE 2: Schematic layout of the new X-PEEM electron optics. The lens design was adapted from an existing x-ray transmission microscope [5].

ACKNOWLEDGMENTS

This work was supported by the Director, Office of Energy Research, Office of Basic Energy Science, Materials Science Division, of the U.S. Department of Energy under Contract No. DE-AC03-76SF00098.

REFERENCES

[1] J. Stöhr, *NEXAFS Spectroscopy*, New York: Springer, 1992.

[2] G. Schütz, W. Wagner, W. Wilhelm, P. Kienle, R. Zeller, R. Frahm, and G. Materlik, Phys. Rev. Lett. **58**, 737 (1987)

[3] E. Bauer, T. Franz, C. Koziol, G. Lilienkamp, T. Schmidt, in*: Chemical, Structural and Electronic Analysis of Heterogeneous Surfaces on the Nanometer Scale*, edited by R. Rosei, Kluwer Academic, Dordrecht, in press.

[4] R. Fink, M.R. Weiss, E. Umbach, D. Preikszas, H. Rose, R. Spehr, P. Hartel, W. Engel, R. Degenhardt, R. Wichendahl, H. Kuhlenbeck, W. Erlebach, K. Ihmann, R. Schlögl, H.-J. Freund, A.M. Bradshaw, G. Lilienkamp, Th. Schmidt, E. Bauer, G. Benner, *Journal of Electron Spectroscopy and Related Phenomena* **84** (1997) 231-250.

[5] R.N. Watts, S. Liang, Z.H. Levine, T.B. Lucatorto, F. Polack, and M.R. Scheinfein, Rev. Sci. Instrum. **68** (1997) 3464-3476.

Principal investigator: Simone Anders, Advanced Light Source, Ernest Orlando Lawrence Berkeley National Laboratory. E-mail: sanders@lbl.gov. Telephone: 510-486-5928.

A High Throughput Bending-Magnet Beamline for Soft X-Ray Spectro-Microscopy at the ALS: Design and Performance

G.D. Ackerman[1], R.Duarte[1], K.Franck[1], M.R.Howells[1], Z. Hussain[1], S. Irick[1], A.Johnson[1], G.Morrison[1], H.A.Padmore[1], S.-Y. Rah[1], T.R.Renner[1], B. Sheridan[1], W.Steele[1], C.Ayre[2], H.Fujimoto[2], F.Gozzo[2], B.Triplett[2], R.X.Yunzunza[2], P.D.Kinney[3], Y.S. Uritsky[4]

[1]Lawerence Berkeley National Laboratory, Advanced Light Source, Berkeley, CA
[2]Intel Corperation, Santa Clara, CA, USA
[3]Micro-Therm, Minneapolis, MN, USA
[4]Applied Materials Inc, Santa Clara, CA.

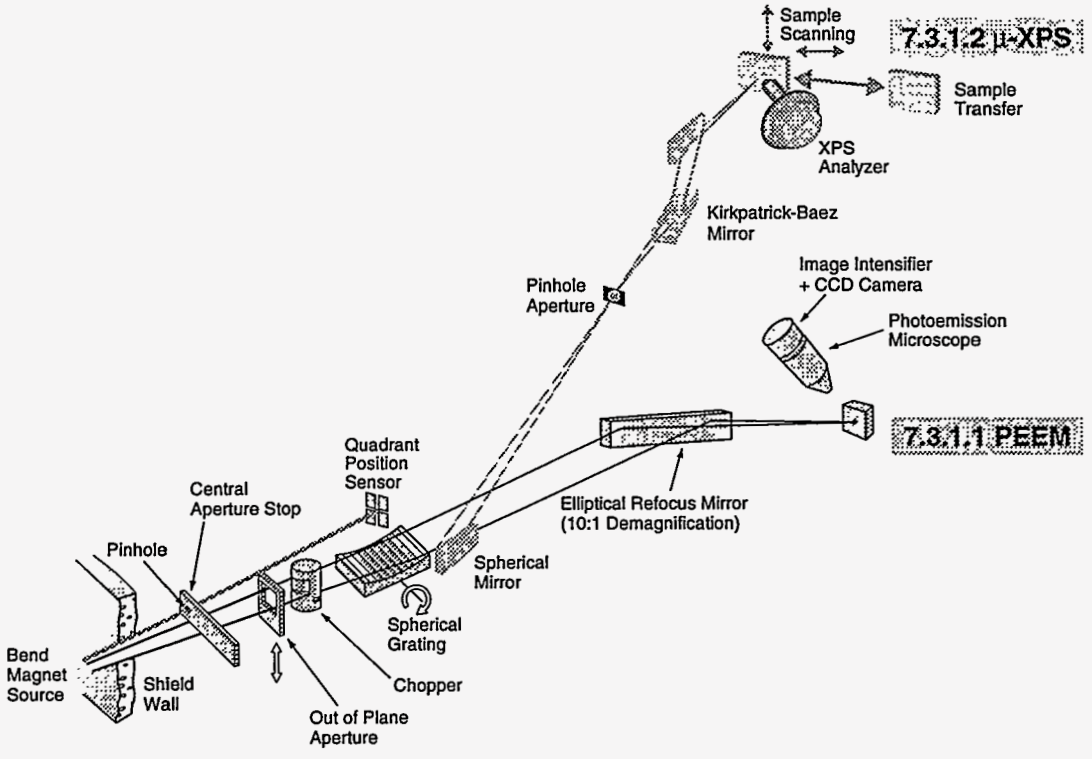

Optical layout of Beamline 7.3.1

Beamline 7.3.1 is a facility for Scanning Micro photoelectron spectroscopy (μXPS) and X-ray photoemission microscopy (PEEM) . The beam line uses an entrance slit-less monochromator of low dispersion with a source-size limited resolving power of 1600 at 800 eV to provide monochromatic soft rays (200 to 1250 eV) from a bending magnet source. The beamline, after the monochromator, diverges into two branch lines: one for scanning, micro-focused x-ray photoelectron spectroscopy (μXPS) that accepts 0.2 milliradians of the bend magnet fan to provide a flux of ≈3 x 10^9 photons / sec at 800 eV, and the second for full field photoelectron emission microscopy (PEEM) which utilizes 2.0 milliradians to provide ≈2 x 10^{12} photon/sec at 800 eV into an illuminated field of < 35 μm.

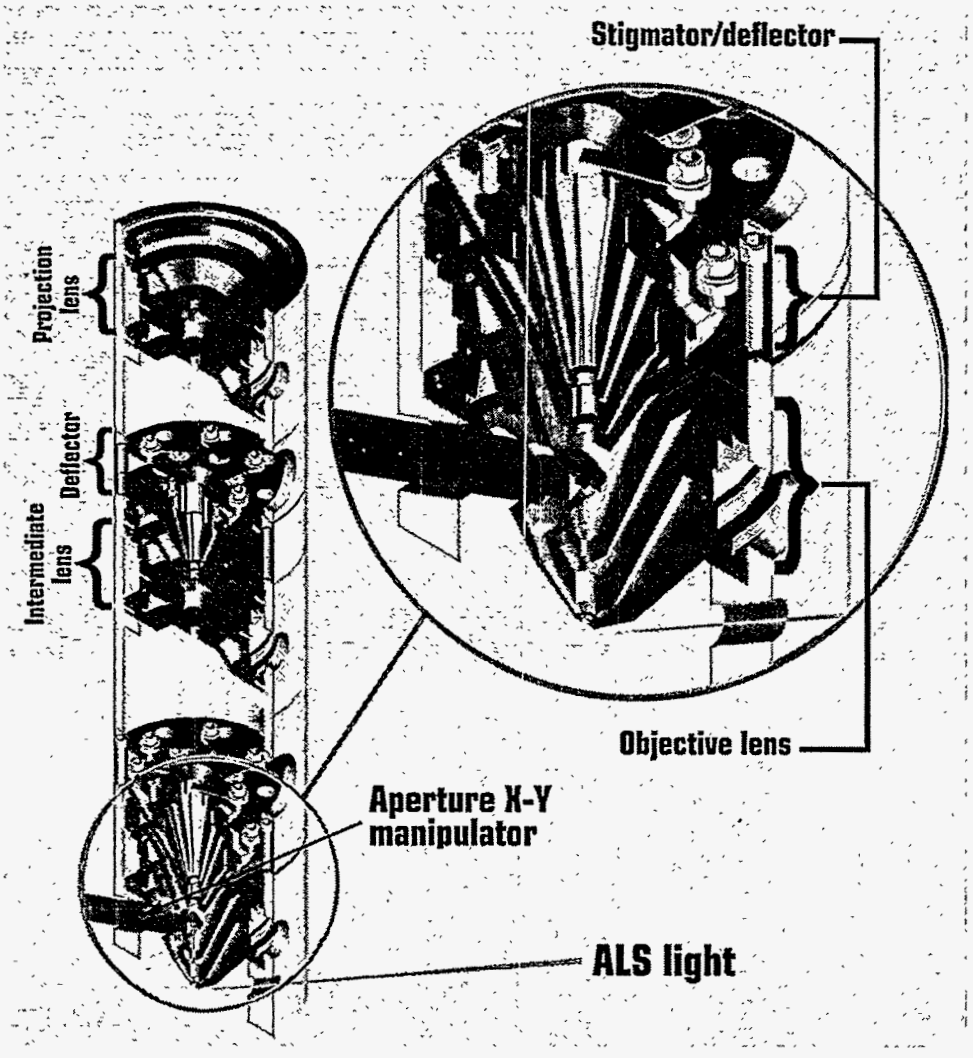

A CAD drawing of PEEM II, Full Field Photo Emission Microscope

Beamline 7.3.1.1, PEEM. The Photoemission Electron Microscope was developed for full field imaging of magnetic materials. These measurements depend on the differential adsorption of circularly polarized light (magnetic circular dichroism, or MCD). A mask and a mechanical chopper are incorporated into the beamline before the monochromater grating to allow switching between the left and right circularly polarized light found above and below the center of the radiation fan. A 1.1 meter elliptical refocusing mirror takes the light after the monochrometer and focuses it on to the sample with a spot size <35 μm.

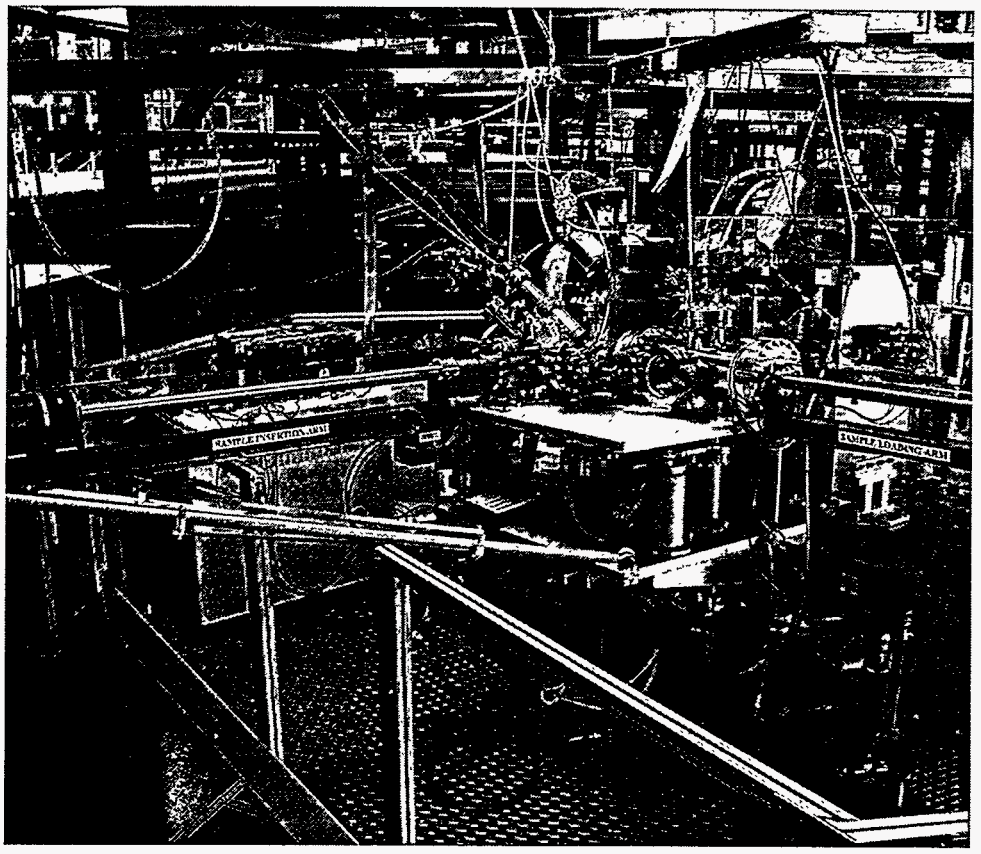

Beamline 7.3.1.2 μXPS endstation

Beamline 7.3.1.2, μXPS. The μXPS branch line was created specifically for analyzing the micro structures in integrated circuits and the silicon wafers from which they are made. A small portion of the light from the monochrometer (≈ .2 milliradians) is focused onto an entrance slit by a bendable refocusing mirror. A pair of elliptically bent mirrors (in a Kirkpatrick-Baez arrangement) in the μXPS chamber focuses the light from the slits to a spot size of <2 by 2 μm on the sample. Photon flux at the sample is ≈3 X 10^9 photons / second and energy resolution is typically <.5 eV at 850 eV photon energy.

Inside the μXPS chamber is a mechanical stage, capable of accepting samples up to 50 by 50 mm, and positioning any portion of the sample under the photon beam to micron accuracy . Samples are introduced into the μXPS chamber by a semi-automatic sample transfer system. Provision has been made for limited sample preparation in a UHV sample preparation chamber, immediately adjacent to the main μXPS chamber. A sample can also be mapped or fiducialized prior to introduction into the system, simplifying navigation. There is also an off-axis, high resolution, optical microscope in the μXPS chamber for direct observation of samples.

Once positioned, the samples can be analyzed either by XPS using a commercial electron analyzer (PHI) or by XANES (using the electron analyzer or sample drain current). The ability to do both XPS and Xanes provides great flexibility in sample analyses. Images based on elemental, chemical or topological contrast can be created by rastering the sample under the photon beam using either XPS or XANES. Data from scans are automatically saved and archived and are accessible for transfer or off line analysis. XPS spectral data may be analyzed using PHI Multi-pac software.

We presently have an Argon sputter gun for surface cleaning and depth profiling and an electron flood gun for sample charge neutralization in place as well as a commercial hard x-ray (Al- and Mg-Ka) source. We are in the process of acquiring a new sample charge neutralizing system which will allow us to perform chemical analyses on insulating samples such as polymers.

To date we have demonstrated the ability to find and perform elemental [1] and chemical [2] analyses on small ($\approx 2 \times 5$ micron) particles . Overall performance and accessibility, including "user friendliness", have been favorably compared with commercial XPS instruments[3]

---

[1]G.D. Ackerman, R. Duarte, K. Franck, M.R. Howells, Z. Hussain, S. Irick, A. Johnson, G. Morrison, H.A. Padmore, S.-Y. Rah, T. Renner, B. Sheridan, W. Steele, C. Ayre, H. Fujimoto, F. Gozzo, B.B. Triplett, R.X. Ynzunza,P.D. Kinney, Y.S. Yuritsky, Presented at the 1998 MRS Spring Meeting, San Francisco CA, 1998

[2] F. Gozzo, B. Triplett, H. Fujimoto, P. Coon, C. Ayre, P.D. Kinney, Y.S. Yuritsky, G.D. Ackerman, A. Johnson,H. Padmore T. Renner, B. Sheridan, W. Steele, Z. Hussain, Presented at the 1998 MRS Spring Meeting, San Francisco CA, 1998

[3] Y.S. Yuritsky, P.D. Kinney, E. L. Principe, I. Mowat and L.Craig, Presented at the 1998 MRS Spring Meeting, San Francisco CA, 1998

This work was supported in part by the Director ,Office of Energy Research, Office of Basic Energy Science Division , of the US Department of Energy under Contract No.DE-AC03-76SF00098 and by Intel Corp., Santa Clara, CA and Applied Materials Inc., Santa Clara, CA.

For further information contact G.D.Ackerman, Advanced Light Source, Earnest Orlando Lawrence Berkeley National Laboratory. Email gdackerman@lbl.gov. Telephone (510) 486 7886

Imaging on μXPS, Beamline 7.3.1.2: Resolution and Contrast

A. L. Johnson[1,2], G. D. Ackerman[1], M. R. Howells[1], Z. Hussain[1], H. A. Padmore[1], T. R. Renner[1], W. Steele[1], F. Gozzo[2], B. Triplett[2], R. Ynzunza[2], P. D. Kinney[3], and R. Odom[4]

[1]Lawrence Berkeley National Laboratory, Advanced Light Source, Berkeley, CA

[2]Intel Corporation, Santa Clara CA

[3]MicroTherm LLC, Minneapolis, MN

[4]Charles Evans and Associates, Redwood City, CA

The maximal resolving power available from any imaging system is a function of the point spread function of the system (the "resolution"), the contrast of the feature being imaged, and the statistics of the image.

For the μXPS endstation, the point spread function is determined by the x-ray spot profile. Knife edge measurements give widths of ~1-2μm (FWHM), and the smallest features measured (Au colloid clusters/carbon) were 1x2μm.

Contrast is determined by imaging mode and the composition and structure of the sample. Secondary electron detection (electrons inelastically scattered to low energies) has the advantage of high signal and a weak dependence on the details of surface charging. Measurement of the core photoelectron intensity is specific to the species of interest and has the advantage of high contrast and specificity but has the disadvantage of strong dependence on surface charging and much lower count rates. We have been focusing on secondary electron detection to utilize high count rates, pending improvements in sample charge compensation.

Image statistics are determined by the detector efficiency and the total x-ray exposure which is limited by sample damage considerations.

To examine the practical implications of these factors, we investigated typical microstructure samples from the electronics industry as well as small particles[1]. Figure 1 shows optical and x-ray images of a region around a transistor connected to a row bus in a memory structure. To give scale to the images, the width of the via (labeled A) is 15 μm, and the lines in the memory array on the right hand side are 3-4 μm wide separated by 4 μm spaces.

Of particular interest are the sources of contrast in the x-ray image. The bright bars are aluminum metallization grounded to the sample mount. Several vias down to lower levels of the metallization are visible, the brightest being feature A. These vias are visible due to topological contrast derived from the details of the x-ray and detector geometry. The angle between the detector and the x-ray beam is 60 degrees and is bisected by the surface normal. What is surprising is the darkness of the aluminum bond pad (feature D) and the visibility of the metallization underneath the oxide layer (feature B). Looking at the XPS spectra of these regions illuminates the mechanism, i.e. the secondary yield is being modulated by charging of the floating metallization of the bond pad and the oxide over the metallization. The oxide not over metallization charges to an even higher voltage.

Finally, feature C, an isolation region etched to the underlying silicon, shows the splitting of the Si2p as expected for native oxide on silicon. This shows that on non-charging regions we have sufficient energy resolution to permit chemical state identification.

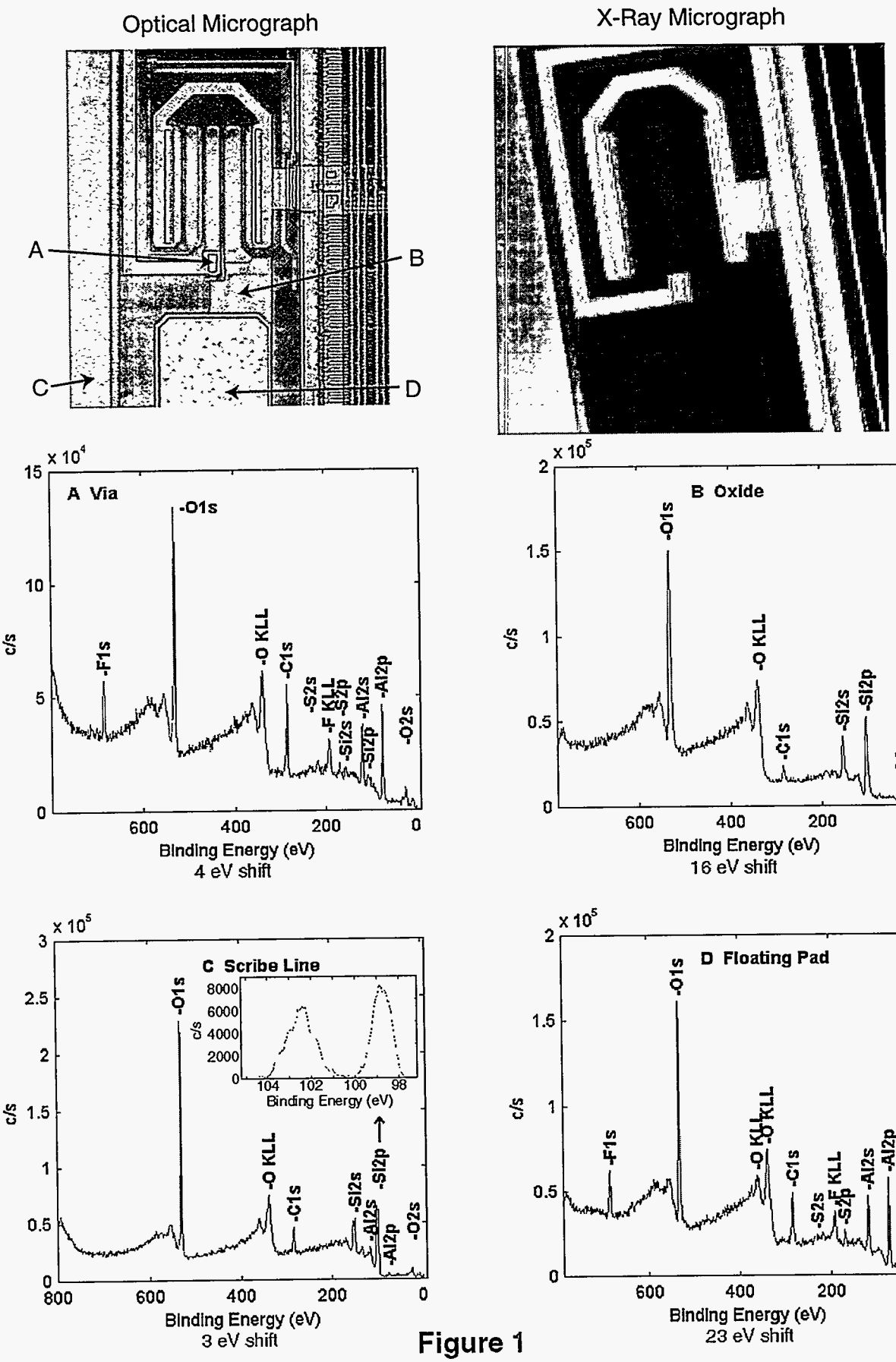
Optical Micrograph
X-Ray Micrograph
A
B
C
D
A Via
-O1s
-F1s
-O KLL
-C1s
-S2s
-F KLL
-S2p
-Si2s
-Al2s
-Si2p
-Al2p
-O2s
x 10^4
c/s
Binding Energy (eV)
4 eV shift
B Oxide
-O1s
-O KLL
-C1s
-Si2s
-Si2p
-O2s
x 10^5
c/s
Binding Energy (eV)
16 eV shift
C Scribe Line
-O1s
-O KLL
-C1s
-Si2s
-Si2p
-Al2s
-Al2p
-O2s
x 10^5
c/s
Binding Energy (eV)
3 eV shift
D Floating Pad
-O1s
-F1s
-O KLL
-C1s
-S2s
-F KLL
-S2p
-Al2s
-Al2p
-O2s
x 10^5
c/s
Binding Energy (eV)
23 eV shift

Figure 1

In summary we demonstrate:

- Resolution of features in the several micron size range.
- Microprobe XPS of those features.
- Imaging of samples of industrial interest, with surprising detail.

ACKNOWLEDGMENTS

We wish to acknowledge Charles Evans and Associates for providing the sample.

REFERENCES

1. F. Gozzo, B. Triplett, R. Ynzunza, P. Coon, C. Ayer, R. D. Kinney, Y. S. Uritsky, G. Ackermann, A. Johnson, H. Padmore, T. Renner, B. Sheridan, W. Steele, and Z. Hussain, Proceedings of the 1998 MRS Spring Meeting, San Francisco, CA (in Press)

This work was supported in part by the Director, Office of Energy Research, Office of Basic Energy Sciences, Materials Sciences Division of the U. S. Department of Energy, under Contract No. DE-AC03-76SF00098 and in part by Intel Corp., Santa Clara, CA and Applied Materials Inc., Santa Clara, CA.

Spokesperson for the micro-XPS PRT is Baylor Triplett, Intel Corporation, SC1-3, 3065 Bowers Ave, Santa Clara, CA 95052-8126 Baylor_B_Triplett@ccm.sc.intel.com

Beamline 8.0.1 Abstracts

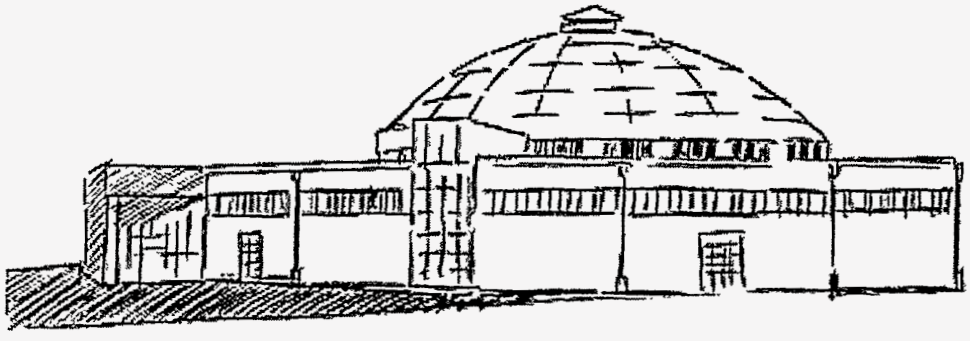

The Adsorption Structure of Glycine Adsorbed on Cu(110); Comparison with Acetate/Cu(110)

J. Hasselström, O. Karis, M. Weinelt, N. Wassdahl, A. Nilsson, M. Nyberg*, L. G. M. Pettersson*, M. G. Samant°, and J. Stöhr°

Department of Physics, Uppsala University, Box 530, S-751 21 Uppsala, Sweden

**FYSIKUM, University of Stockholm, Box 6730, S-113 85 Stockholm, Sweden*

°IBM Research Division, Almaden Research Center, 650 Harry Road, San Jose, CA 95120, USA

The molecular orientation of an ordered monolayer of glycine adsorbed on Cu(110) has been studied using XPS, NEXAFS, X-ray Photoelectron Diffraction, LEED and theoretical calculations. In connection, results from the related molecule acetate adsorbed on Cu(110) will be considered.

The measurements were carried out at beamline 8.0 at the Advanced Light Source (ALS), using a modified spherical grating monochromator. The experimental station, consists of two UHV chambers, one for sample preparation and one for analysis. The analysis chamber is comprised of an electron energy analyzer and an X-ray emission spectrometer, both mounted perpendicular to the incoming photon beam. It also houses a partial yield detector for X-ray absorption measurements. For the NEXAFS measurements a retarding voltage of 200 V, 300 V and 400 V was applied for the carbon, nitrogen and oxygen *K*-edges, respectively. Due to the fact that the substrate has two-fold symmetry, two Cu(110) crystals were mounted on a manipulator, rotated 90° with respect to each other. This enabled us to obtain NEXAFS spectra with the **E**-vector along the close-packed copper rows ([1$\bar{1}$0]-direction), perpendicular to these rows ([001]-direction), and with the **E**-vector normal to the surface ([110]-direction). In order to prepare the acetate overlayer, acetic acid was adsorbed at 450 K, after preadsorbing half of a monolayer of oxygen (ordered (2×1) structure) [1]. Glycine was evaporated from a resistively heated tantalum Knudssen cell. The sample temperature was kept at 400 K during the evaporation. All the measurements were performed at room temperature.

The structure of glycine on Cu(110) was investigated through theoretical calculations at the gradient-corrected DFT level. To determine the structure full geometry optimizations were performed for glycine on a fifteen atom cluster model of the Cu(110) substrate. All degrees of freedom were completely relaxed for the adsorbate, while keeping the internal structure of the cluster model fixed.

LEED for acetic acid adsorbed on a (2×1) oxygen-covered copper surface is known to give a $c(2 \times 2)$ pattern. It is only stable for a few seconds [1]. In contrast, glycine exhibits a sharp (3×2) LEED pattern which is found to be stable for several minute.

Fig. 1 shows the O 1s and C 1s XP spectra obtained for acetate and glycine adsorbed on Cu(110). Only one symmetric O 1s XP line is observed for both adsorbates. This is a consequence of the loss of the acidic hydrogen atom in the adsorption process, which results in two identical C-O bonds. In the carbon region, two peaks are found for both adsorbates. The one at lower binding energy corresponds to the methyl group, whereas the other peak corresponds to the carbon atom of the carboxylic group.

In order to learn about the orientation of the C-C axis in the adsorbates we performed XPD. A photon energy of 1050 eV was used, giving the emitted photoelectrons

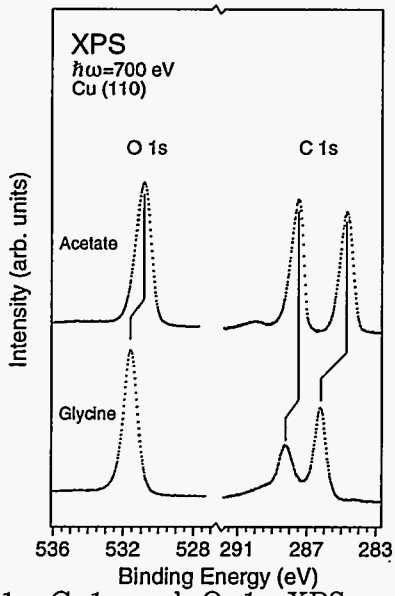

FIG. 1. C 1s and O 1s XPS spectra for glycine (bottom) and acetate (top) adsorbed on Cu(110).

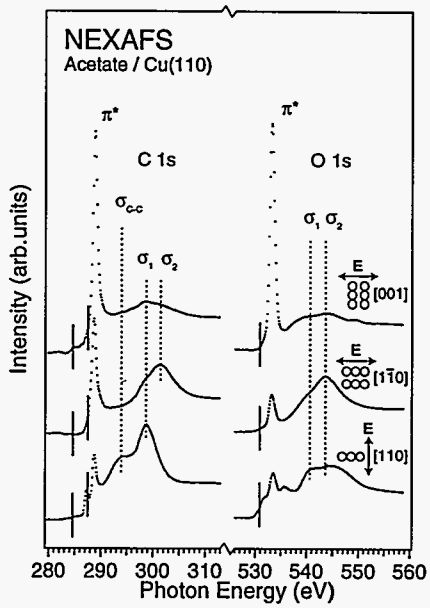

FIG. 2. C 1s and O 1s NEXAFS data obtained for acetate/Cu(110).

a kinetic energy of around 700 eV. The carboxylic-carbon/methyl-carbon C 1s intensity ratios were measured for different polar angles along the [1$\bar{1}$0]- and [001]-directions. For acetate, the XPD-polar scan showed a distinct forward-scattering peak at normal emission, indicating a perpendicular geometry of the C-C axis with the carboxylic group closest to the surface. On the other hand, the glycine XPD spectra showed no pronounced features indicating that the molecular C-C axis is highly tilted.

Turning to the NEXAFS data we will start by considering acetate/Cu(110) shown in Fig. 2. The absorption data gives rise to three clearly different spectra indicating that the adsorbate is azimuthally ordered on the surface. In both the C and O spectra the π-resonance is observed with maximum intensity in the [001]-spectrum. This shows that the molecular plane of the carboxylic group is oriented along the [1$\bar{1}$0]-azimuth.

In the [110]- and [1$\bar{1}$0] C K-edge spectra we observe two shape resonances, σ_1 and σ_2. These resonances are associated to the carboxylic group of the molecule and are also found for formate/Cu(110). At a photon energy of 288 eV we observe a sharp state prior to the π-resonance in the carbon [110]-spectrum. This state is associated with the C-H bonds. Finally, the σ-resonance corresponding to the C-C bond is observed in the [110]-spectrum, at 294 eV.

In the oxygen spectra, a relatively sharp σ-resonance is observed at 543 eV in the [1$\bar{1}$0]-spectrum. In the [110]-spectrum, only a broad distribution of σ states is observed.

Again, this is similar to formate and could thus be assigned to the carboxylic group. In addition, there is a new transition, which we denote σ_1, at 540 eV. This resonance is found to be most intense in the [110]-spectra and arises from a splitting of the σ-system, caused by the interaction of the adjacent C-C and C-O groups [2]. Hence, the C resonance marked σ_{c-c} in Fig. 2 corresponds to the O resonance marked σ_1.

From the above considerations, it is clear that acetate adsorbs in a perpendicular geometry, with the molecular plane oriented along the [1$\bar{1}$0]-azimuth of the substrate, bonding to the surface via the oxygen atoms.

We now turn to the NEXAFS spectra for glycine adsorbed on Cu(110), shown in

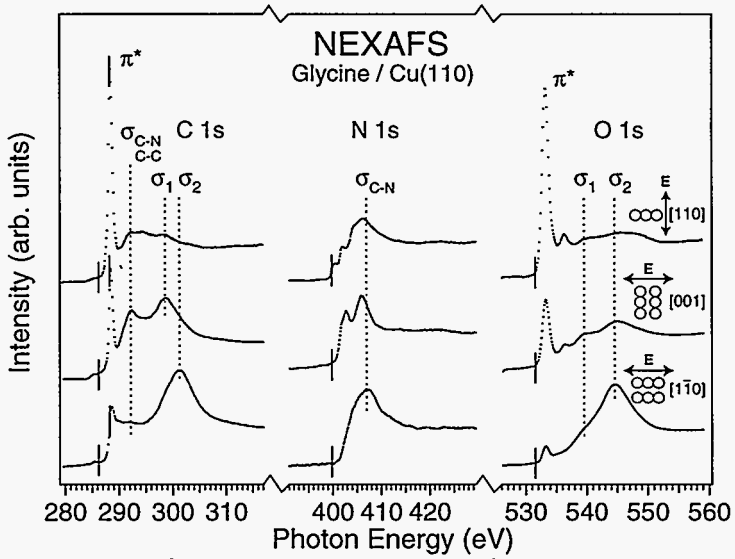

FIG. 3. O 1s, N 1s and C 1s absorption spectra of glycine adsorbed on Cu(110).

Fig. 3. Starting with the oxygen spectra, the π-resonance is observed with maximum intensity in the [110]-spectrum. In accordance with the XPD results, this indicates a highly tilted geometry of the carboxylic group. Shape resonances are found mainly in the [1$\bar{1}$0] spectrum but also in the [001] spectrum. This is expected for an adsorption geometry where the molecular plane is close to parallel to the surface.

The spectral features can be understood in the same manner as discussed for acetate. Hence, the σ_2-resonance corresponds to the shape resonances associated with the carboxylic group, whereas the σ_1-resonance can be viewed as the oxygen contribution to the C-C derived resonance.

In the carbon spectra, two shape resonances associated to the C-C and C-N bonds are in principle expected to appear in the spectra. The interaction between the corresponding σ-orbitals will however result in new hybrid orbitals. Since they are both single bonds, the energies of the bond-prepared "localized" components are expected to be nearly degenerate. The relative weight on the respective hybrid orbitals will be almost equal, making it difficult to distinguish the two resonances from each other.

The contribution from the C-C bond to the σ-resonance arising from interaction between the two adjacent single bonds is expected to appear mainly in the C K [001] absorption spectrum. Inspection of this spectrum reveals that this indeed is the case. As discussed above, it will also contain a strong C-N σ-resonance contribution. We note that there is no enhanced intensity due to this resonance in the [1$\bar{1}$0] spectrum. This indicates that also the C-N axis predominantly is oriented along the [001]-direction.

In order to identify the σ-resonance arising from the C-N bond in the N spectra it is useful to first consider the N-H resonances in more detail. In free ammonia the $2e$ derived transition is known to consist of two degenerated orbitals, e.g., the N $2p_x$ and N $2p_y$ derived orbitals. When going to methylamine the degeneracy will be lifted and one of the orbitals will constitute the antibonding σ-resonance arising due to the formation of the C-N bond. The other orbital will consequently preserve its pure N-H character. For an oriented adsorbate we would expect very little intensity corresponding to the N-H resonance in a geometry where the **E**-vector is close to parallel to the intramolecular axis. Inspection of the N K data re-

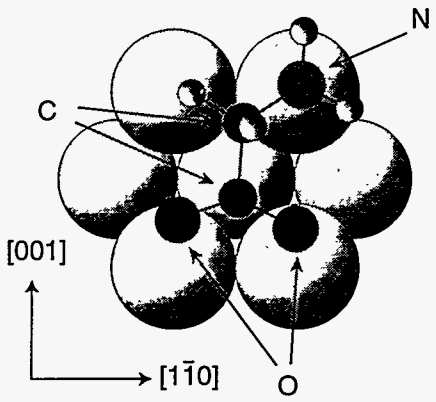

FIG. 4. The optimized adsorption geometry of glycine/Cu(110).

veals that very little intensity corresponding to the N-H resonances in the [1$\bar{1}$0]-spectrum is present. In the other spectra clear evidence of N-H resonances are observed. Based on these considerations we find it plausible that the broad feature at around 406 eV in the [1$\bar{1}$0]-spectrum corresponds to the σ-resonance arising from the C-N single bond. We note that in contradiction to the results derived from the C K spectra, where a linear C-C-N configuration was predicted, the N K results indicate that the C-N bond is likely oriented near parallel to the close packed copper rows, i.e., the [1$\bar{1}$0]-direction.

The starting guess for the geometry optimization was based on qualitative considerations resulting from the experimental data. Thus, the molecule was assumed to span two [1$\bar{1}$0] rows with the oxygens in equivalent near-on-top positions and the amino group binding to the next row; the C-C-N angle was assumed to correspond to sp^3 hybridization with the -CH_2- group over the trough between the rows. A model of the optimized structure is given in Fig. 4.

As discussed above, two different adsorption structures can be deduced from NEXAFS: the carbon spectrum could be interpreted as favoring a linear C-C-N structure, while the N absorption spectra seems to indicate a bent C-C-N configuration, much like the optimized structure shown in Fig. 4. In order to resolve the question of which of the two structures will be favored on the surface we have optimized the structure also starting from the alternative structure that seems to be indicated by the C K data. The result of the optimization is a slow return of the molecule to the bent structure that was the result of the original optimization. No barrier was observed as the oxygens moved from the bridge positions to the favored positions closer to on-top. The energy difference (0.4 eV) between the two proposed structures is not large, but, particularly in combination with the fact that the structure indicated by the carbon absorption data turned out not to be a minimum structure, this is sufficient to allow the conclusion to be drawn that the structure of Fig. 4 should be preferred.

To summarize, it seems that from NEXAFS alone both structures could be supported. Since the structure suggested by the interpretation of the C-C and C-N resonance structures in the C spectra is shown, through the theoretical simulations of the adsorbate structure, not to correspond to a minimum on the energy surface we must exclude this structure. Instead the proposed structure is that of Fig. 4 which was originally obtained through a combination of qualitative results from the experimental data and the theoretical calculations of the adsorbate structure

This work was supported by the Swedish Natural Science Research Council (NFR) and by the Göran Gustafssons foundation for research in natural science and medicine.

[1] S. Haq and F. M. Leibsle, Surf. Sci. Lett. **355**, 345 (1996).

[2] J. Stöhr, *NEXAFS Spectroscopy* (Springer-Verlag, Heidelberg, 1992).

Principle investigator: Anders Nilsson, Uppsala Univesity.

E-mail: anders.nilsson@fysik.uu.se.

Band Widening in Graphite

C. Heske[1], R. Treusch[2], F.J. Himpsel[2], S. Kakar[3], L.J. Terminello[4], and H.J. Weyer[5]

[1]Advanced Light Source, Lawrence Berkeley National Laboratory, Berkeley, California 94720, USA; e-mail: ctheske@lbl.gov

[2]Department of Physics, University of Wisconsin-Madison, Madison, Wisconsin 53706, USA

[3]Department of Applied Science, University of California at Davis/Livermore, Livermore, California 94550, USA

[4]Lawrence Livermore National Laboratory, Livermore, California 94550, USA

[5]Swiss Light Source, Paul-Scherrer Institute, Villigen PSI, Switzerland

INTRODUCTION

Band calculations are at the foundation of understanding the electronic structure of solids. The most common theoretical method for obtaining energy bands and total energies of solids and surfaces is the local density approximation (LDA) [1]. This approach has been very successful for computing band widths, so that it requires very accurate band measurements to detect any systematic difference from the LDA. This paper presents band structure measurements which test LDA and quasiparticle calculations of the graphite band structure. Particular emphasis is placed on the band width, because this is an important quantity characterizing the valence band of a material. So far, a few angle-resolved photoemission measurements have been performed that are accurate enough to detect a few percent difference between measured and theoretical band widths. For a typical simple metal, Na, a band narrowing by 18% has been found relative to the LDA, and quasiparticle calculations suggest varying degrees of self-energy band narrowing [2-4]. For a prototype insulator (LiF) and wide-gap semiconductor (diamond), respectively, a 17% [5] and 7% [6] band widening compared to the LDA has been found in measurements and quasiparticle calculations [7,8].

Earlier experimental results for the valence band width in graphite vary significantly. Results from laboratory-based x-ray photoelectron spectroscopy (XPS) investigations of 24 eV ± 1 eV [9] differ significantly from band widths obtained with angle-resolved photoelectron spectroscopy (ARPES) at synchrotron sources. Bianconi et al. reported a width of 22.5 eV [10], Eberhardt, McGovern, et al. derived 20.6 eV ± 0.3 eV [11], Law et al. found 21 eV and 22.3 eV ± 0.2 eV [12], and Costanzo et al. reported widths of 20.5 eV for polygraphite and 21.0 eV for highly-oriented pyrolytic graphite (HOPG) [13]. In a recent (e,2e) spectroscopy experiment, Vos et al. obtained a width of 21.5 eV to 22.5 eV [14]. Mirroring the large scatter in experimental values, theoretical results vary from 19.2 eV to 21.9 eV, with most of these results being found using the LDA. While early LDA calculations indicated good agreement with some of the above experimental band widths (20.8 eV, 21.5 eV) [15], recent results are generally below 20 eV, and full-potential results appear to be converging to around 19.6 eV [16]. In contrast, our theoretical investigation based on quasiparticle calculations derives a bandwidth of 21.8 eV ± 0.2 eV [17]. Previous quasiparticle calculations by Zhu and Louie [18] indicate a similar value.

EXPERIMENTAL

We have performed an accurate valence band mapping of graphite analogous to a previous work on diamond [6]. It employs an imaging photoelectron spectrometer [19] which allows for a data rate orders of magnitude higher than was obtainable with single-angle spectrometers. The experiments were performed by utilizing the high flux and small spot size of the undulator Beamline 8.0 at the Advanced Light Source. A synthetic single-domain single crystal of graphite was outgassed in vacuum at pressures in the 10^{-10} mbar range, and photoelectron momentum distribution images were taken for a set of 35 different binding energies throughout the valence band. Each of these

images represents an iso-energetic slice through momentum space, i.e. it shows an intensity distribution of emitted photoelectrons for a given initial-state energy, with different locations within an image being directly related to different values of $\mathbf{k}_{\parallel}$, the electron momentum parallel to the sample surface. For all images presented here, the detected electron kinetic energy was kept fixed at 130 eV and the incident photon energy was varied in order to probe electronic states with different binding energies.

RESULTS

Figure 1 shows images for binding energies near prominent points of the graphite valence band structure. Features of high intensity are depicted as dark regions. In order to include the transmission of the analyzer, all images were normalized by an image of the secondary electron distribution at preserved analyzer settings. A symmetrization of the images has been performed according to the threefold symmetry of the three-dimensional graphite crystal. All features in Fig. 1 were clearly visible in the unsymmetrized raw data. In particular, the valence band width reported here could be derived from both symmetrized and unsymmetrized images.

In detail, Fig. 1 (a) shows the distribution pattern near the Fermi energy, for which the central hexagon defines the position of the K points of the first (surface) Brillouin zone, i.e. where the π band intersects the Fermi level, as reported earlier [20] (refer to Ref. 21 for a depiction of the two-dimensional graphite band structure). The K points in higher Brillouin zones are visible towards the edge of the image. Fig. 1 (b) was recorded near the top of the π band (at the M points) of the first Brillouin zone. Note that two of the points of highest intensity in the central ring (the M points) now lie on a vertical line which includes Γ, whereas in Fig. 1 (a) two of the highest intensity points (the K points) were found on a horizontal line. Figure 1 (c) was recorded at a binding energy of 4.5 eV, just below where calculations predict the top of the σ bands at Γ. As evident from the image, no central high-intensity feature was seen, the result of a Brillouin-zone selection effect [21]. Yet σ band emission intensity at Γ is observed in Fig. 1 (c) in higher Brillouin zones (near the edge of the image), consistent with the same selection rule. The central ring feature there is ascribed to the π band, and it continues to decrease in diameter in Fig. 1 (d) until it reaches its bottom at the Γ point at a binding energy close to that of Fig. 1 (e). In Fig. 1 (f), the intensity distribution shows high-intensity features at the K points, showing the uppermost σ band, while Fig. 1 (g) shows high intensity features at both the K

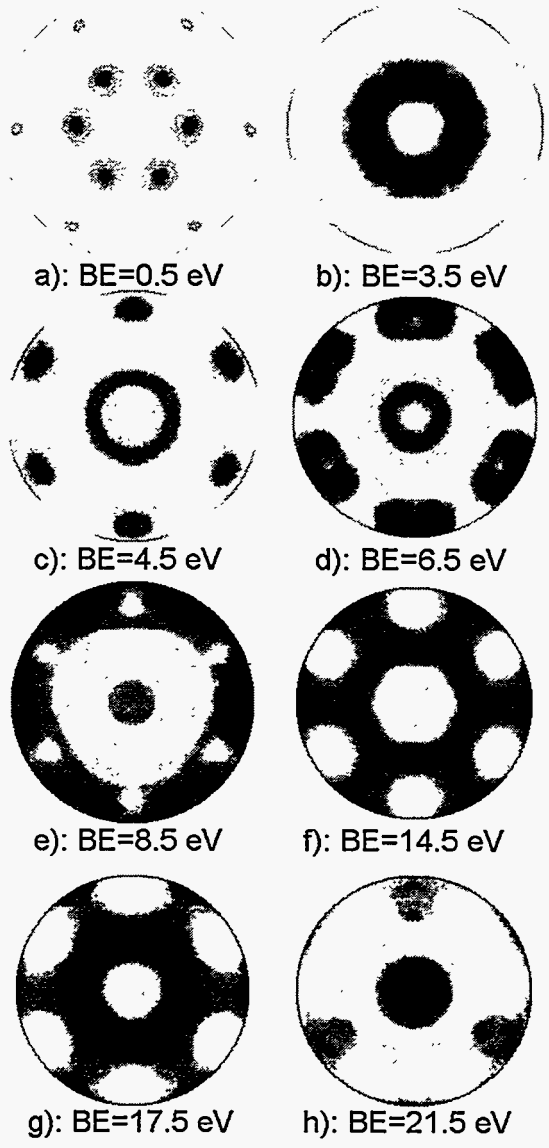

Fig. 1: Photoelectron momentum distribution images for a variety of different binding energies.

and the M points, which stem from the upper and lower σ bands. Finally, Fig. 1 (h) was recorded near the bottom of the lower two σ bands, which are the lowest valence bands.

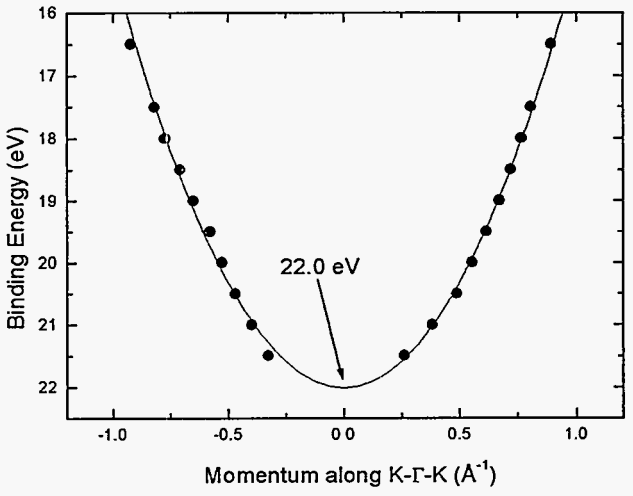

Fig. 2: Parabolic fit to the bottom of the lower σ band, as derived from peak positions of line scans across photoelectron momentum distributions along a K-Γ-K direction.

To obtain accurate information about the overall width of the valence band, we determined the Fermi energy by use of a Ta foil reference in electrical contact with the graphite sample and investigated the closing of the ring structure in the center of our images for binding energies close to the bottom of the valence band, as shown in Fig. 2 for a line scan across the image along a K-Γ-K direction. The peak positions obtained from the line scan were plotted against the binding energy for the associated image and a parabolic fit was applied to determine the binding energy of the bottom of the valence band. The bottom of the band was determined to be close to 22.0 eV. A conservative error analysis led to an error margin of +0.2/-0.4 eV. Our experimental value agrees with our quasiparticle calculations within the error margins and is about 11% larger than the corresponding local density band width of about 19.6 eV.

It is pertinent to motivate discrepancies between the various experimental results. Experimental factors will certainly include differences in resolution and energy calibration. Moreover, the intensity of the relevant features near the Fermi energy and near the bottom of the valence band is very small as compared to the more pronounced valence features of the graphite band structure (note that all images in Fig. 1 are rescaled to optimally utilize the gray scale). While intensity information is not required for our determination of the band width, it strongly affects results obtained using conventional angle-resolved photoemission spectra in the energy-dispersive mode. Furthermore, our determination of the band width is largely independent of the energy resolution of the detector, because a broadening in energy would only lead to a momentum broadening of the image features from which the position of the bottom of the band is derived, in contrast to results from conventional spectra.

In summary, we have presented a high-accuracy determination of the valence band width of graphite. Both the experimental result of 22.0 (+0.2/-0.4) eV and our quasiparticle calculations (21.8 eV ± 0.2 eV) [17] significantly exceed previous experimental results and theoretical predictions based on the local density approximation (LDA) by approximately 11 %.

ACKNOWLEDGMENTS

We gratefully acknowledge a very fruitful collaboration with E.L. Shirley, NIST, and the support and help of the ALS staff, in particular of E. Rotenberg, R. Thatcher, R. DeMarco, D. Robin, G. Portmann, and W. Decking.

REFERENCES

[1] P. Hohenberg and W. Kohn, Phys. Rev. **136**, 864 (1964); W. Kohn and L. J. Sham, Phys. Rev. **140**, 1133 (1965).
[2] J.E. Northrup, M.S. Hybertsen, and S.G. Louie, Phys. Rev. Lett. **59**, 819 (1987); Phys. Rev. B **39**, 8198 (1989).
[3] E.L. Shirley, Phys. Rev. B **54**, 7758 (1996).
[4] E. Jensen and E.W. Plummer, Phys. Rev. Lett. **55**, 1912 (1985); In-Whan Lyo and E.W. Plummer, *ibid.* **60**, 1558 (1988).
[5] F.J. Himpsel, L.J. Terminello, D.A. Lapiano-Smith, E.A. Eklund, and J.J. Barton, Phys. Rev. Lett. **68**, 3611 (1992); E.L. Shirley, L.J. Terminello, J.E. Klepeis, and F.J. Himpsel, Phys. Rev. B **53**, 10296 (1996).
[6] I. Jiménez, L.J. Terminello, D.G.J. Sutherland, J.A. Carlisle, E.L. Shirley, and F.J. Himpsel, Phys. Rev. B **56**, 7215 (1997).
[7] M. Rohlfing, P. Krüger, and J. Pollmann, Phys. Rev. B **48**, 17791 (1993).
[8] M. S. Hybertsen and S. G. Louie, Phys. Rev. Lett. **55**, 1418 (1985); Phys. Rev. B **34**, 5390 (1986).
[9] F.R. McFeely, S.P. Kowalczyk, L. Ley, R.G. Cavell, R.A. Pollak, and D.A. Shirley, Phys. Rev. B **9**, 5268 (1974).
[10] A. Bianconi, S.B.M. Hagström, and R.Z. Bachrach, Phys. Rev. B **16**, 5543 (1977).
[11] W. Eberhardt, I.T. McGovern, E.W. Plummer, and J.E. Fisher, Phys. Rev. Lett. **44**, 200 (1980).
[12] A.R. Law, M.T. Johnson, and H.P. Hughes, Phys. Rev. B **34**, 4289 (1986).
[13] E. Costanzo, G. Faraci, A.R. Pennisi, A. Terrasi, Y. Hwu, and G. Margaritondo, Solid State Commun. **74**, 909 (1990).
[14] M. Vos et al., J. Electron Spectr. Rel. Phen., to be published
[15] N.A. Holzwarth, S.G. Louie, and S. Rabii, Phys. Rev. B **26**, 5382 (1982).
[16] J.C. Boettger, Phys. Rev. B **55**, 11202 (1997) and references therein.
[17] C. Heske, R. Treusch, F.J. Himpsel, S. Kakar, L.J. Terminello, H.J. Weyer, and E.L. Shirley, to be published.
[18] S.G. Louie, in *Topics in Computational Materials Science*, ed. C.Y. Fong (World Scientific, Singapore, 1997), p. 96.
[19] D.E. Eastman, J.J.Donelon, N.C. Hien, and F.J. Himpsel, Nuclear Instruments and Methods **172**, 327 (1980); F.J. Himpsel, Brazilian Journal of Physics, **23**, 31 (1993).
[20] A. Santoni, L.J. Terminello, F.J. Himpsel, and T. Takahashi, Appl. Phys. A **52**, 299 (1991).
[21] E.L. Shirley, L.J. Terminello, A. Santoni, and F.J. Himpsel, Phys. Rev. B **51**, 13614 (1995).

This work was supported by the U.S. Department of Energy, BES-Materials Sciences, under contract W-7405-ENG-48.

Principal investigators: L.J. Terminello, Lawrence Livermore National Lab, Email: terminello1@llnl.gov. Phone: (510) 423-7956. F.J. Himpsel, University of Wisconsin-Madison, Email: himpsel@comb.physics.wisc.edu. Phone: (608) 263-5590.

Beyond the Dipole Approximation: Angular-Distribution Effects in N_2 $1s$ Photoemission

O. Hemmers[1], P. Glans[1], H. Wang[1], R. Wehlitz[2], J.C. Levin[2], I.A. Sellin[2], R.C.C. Perera[3] and D.W. Lindle[1]

[1]Department of Chemistry, University of Nevada, Las Vegas, NV 89154-4003

[2]Department of Physics, University of Tennessee, Knoxville, TN 37996

[3]Lawrence Berkeley National Laboratory, Berkeley, CA 94720

INTRODUCTION

The electric-dipole ($E1$) approximation [1], applied to photoionization, leads to the well-known expression for the differential cross section [2],

$$\frac{d\sigma}{d\Omega} = \frac{\sigma}{4\pi}\left[1+\frac{\beta}{2}\left(3\cos^2\theta-1\right)\right], \tag{1}$$

which describes the angular distribution of photoelectrons from a randomly oriented sample created by 100% linearly polarized light. Here, σ is the partial photoionization cross section, and θ is the angle between the vector of the outgoing electron and the vector of linear polarization. The parameter β completely describes the angular distribution of photoelectrons, within the dipole approximation. In this approximation, all higher-order interactions, such as electric-quadrupole ($E2$) and magnetic-dipole ($M1$), are neglected. This assumption is justified by the argument that the strengths of the $E2$ and $M1$ interactions relative to electric-dipole effects are approximately equal to the ratio of the photoelectron's velocity to the speed of light [3], a ratio which is small except at very high energies.

Over the past two decades, the dipole approximation has facilitated a basic understanding of the photoionization process in atoms and molecules [2], as well as the application of photoelectron spectroscopy to a wide variety of condensed-phase systems.

The first hint of deviations from the dipole approximation was provided by Krause [4] in measurements using unpolarized x-rays [5]. A small deviation from the expected dipolar angular distribution at photon energies between 1 and 2 keV was observed and attributed to the influence of $E2$ and $M1$ interactions. These lowest-order, non-electric-dipole corrections to the dipole approximation lead to so-called *non-dipole* effects in the angular distributions of photoelectrons, described by [6]

$$\frac{d\sigma}{d\Omega} = \frac{\sigma}{4\pi}\left[1+\frac{\beta}{2}\left(3\cos^2\theta-1\right)+\left(\delta+\gamma\cos^2\theta\right)\sin\theta\cos\phi\right] \tag{2}$$

for 100% linearly polarized light. The non-dipole angular-distribution parameters γ and δ are attributable to interference terms between electric-dipole and electric-quadrupole interactions. Fig. 1 describes the geometry and the angles θ and ϕ.

Extensive measurements [7,8], focussing on noble-gas core levels (Ar K and Kr L) and photon energies above 2 keV, have begun to investigate non-dipole effects in photoelectron angular distributions in more detail.

In contrast, the present experiment concentrates on the N_2 $1s$ inner shell at relatively low photon energies ($\leq$1000 eV). Non-dipole effects are observed to be significant in this energy regime and measurable at energies close to threshold, in conflict with a common assumption

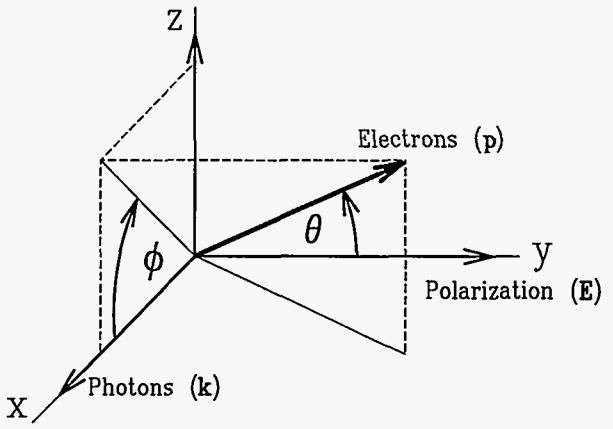

Figure 1: Geometry applicable to photoelectron angular-distribution measurements using polarized light. θ is the polar angle between the photon polarization vector ϵ and the momentum vector p of the photoelectron. ϕ is the azimuthal angle defined by the photon propagation vector k and the projection of p into the x-z plane.

in applications of photoelectron spectroscopy; namely, that the dipole approximation is valid for photon energies below 1 keV. The potential significance of these findings is nicely illustrated by comparison of the present results for the N_2 γ_{1s} parameter with a theory for atomic nitrogen [9], where the influence of non-dipole effects are expected to be much smaller.

EXPERIMENT

The experiments were performed on undulator beamline 8.0, [10], which covers the 100-1500 eV photon-energy range. The monochromator entrance slit was set to 70 μm and the exit slit to 100 μm yielding very high flux, because high photon resolution was not needed. During the measurements the ALS operated at 1.9 GeV in two-bunch mode with a photon pulse every 328 ns. Four time-of-flight (TOF) electron analyzers, equipped with microchannel plates for electron detection, collect spectra simultaneously at different angles. The total electron flight paths are 460 mm, and the analyzers have a full cone acceptance angle of 5°.

The interaction region is formed by an effusive gas jet intersecting the photon beam which has a diameter of about 2 mm. Energy resolution of the TOF analyzers with a focus size of 2 mm is 3% of the electron kinetic energy. Each spectrum was collected for about 600 s. We used either air or a mixture of air and xenon as our target gases. The abundance of Auger lines, especially for kinetic energies below 100 eV, provided for excellent calibration.

RESULTS

Figure 1 shows two superimposed spectra, both taken at the magic angle ($\theta = 54.7°$), but at different ϕ angles. The spectra are scaled to the area of the N_2 KLL Auger lines. The obvious intensity differences between the N_2 $1s$ and satellite peaks in the two spectra are due entirely to non-dipole effects because both spectra are at the magic angle where the β parameter has no influence. For the dipole magic-angle analyzer the differential cross section in Eq. (2) reduces to the partial cross section; $E2$ and $M1$ effects vanish in the $\phi = 90°$ plane even if relativistic effects are included [11]. For the non-dipole analyzer,

$$\frac{d\sigma}{d\Omega} = \frac{\sigma}{4\pi}\left[1 + \sqrt{\frac{2}{27}}(3\delta + \gamma)\right], \tag{3}$$

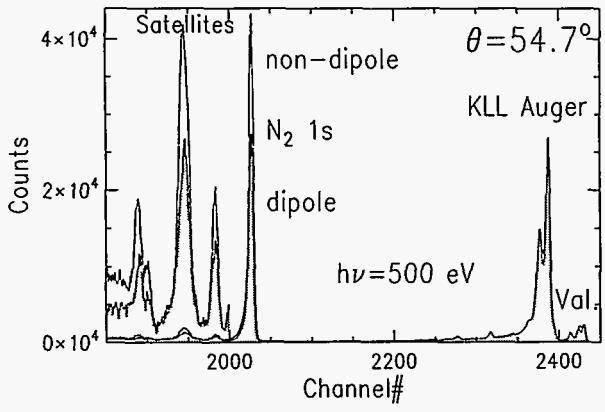

Figure 2: Photoelectron spectra of N_2 measured at a photon energy of 500 eV. The grey spectrum was taken with the dipole magic-angle analyzer and the other spectrum with the non-dipole analyzer. The spectra are normalized to the KLL Auger lines. The intensity differences in the N_2 $1s$ and satellite lines between the two analyzers is due entirely to non-dipole effects.

which simplifies further for s subshells [6,12] in the non-relativistic approach where δ vanishes.

With our experimental geometry, it is possible to measure the γ parameter for s subshells directly if the degree of linear polarization is known by using the two magic angle analyzers. The data points in Fig. 3 show strong non-dipole contributions with a maximum of $\gamma = 1.3$ about 60 eV above the N_2 $1s$ ionization threshold.

These non-dipole contributions originate from dipole integrals in the first-order correction to the dipole approximation. The observed deviations to the theoretical curve for atomic nitrogen are clearly due to molecular potential effects and according to theory [14] it is expected to appear only in molecules with degenerate states, such as N_2, O_2, CO_2 etc. but not CO, N_2O or similar molecules. The lack of correlation between the maximum and width of the absorption curve and the maximum and width of the data-point distribution suggests that it is not a shape-resonance effect. A theoretical interpretation is needed to fully explain the behavior of the γ-parameter. In the photon energy range between 600 eV and 1000 eV there is still a deviation between the theoretical curve for atomic nitrogen and the experimental data for molecular nitrogen. The molecular potential has a very strong

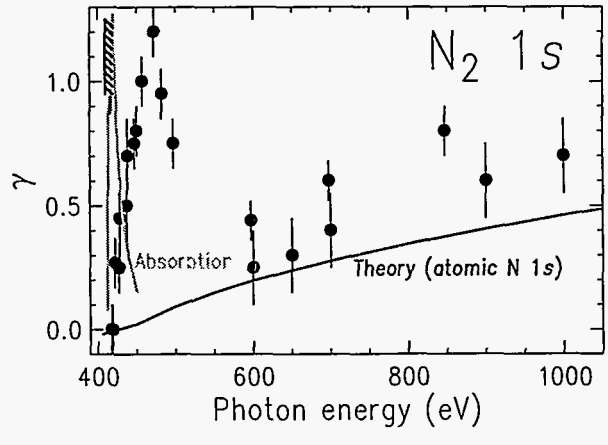

Figure 3: Electron angular anisotropy parameter γ for the N_2 $1s$ photoline from threshold to $h\nu = 1000$ eV. The theoretical curve for atomic nitrogen is from Lajohn and Pratt [9] and the N_2 absorption curve from Kempgens et al. [13].

influence on the non-dipole electron angular distributions far above threshold unlike the shape-resonance that governs the β-parameter just above threshold before it assumes atomic like behavior.
The present results illustrate that any photoemission experiment, whether on gases, solids, or surfaces, can be so influenced at relatively low photon energies, pointing to a general need for caution in interpreting angle-resolved photoemission data.

ACKNOWLEDGMENTS

The authors thank the staff of the ALS for their support, the IBM, LBNL, LLNL, the University of Tennessee, and Tulane University collaboration for beam time at beamline 8.0, and R. H. Pratt for fruitful discussions. This research is funded by the National Science Foundation (NSF, PHY-9303915), the Department of Energy (DOE EPSCOR), Research Corporation, and The Petroleum Research Fund. The ALS is supported by the DOE under Contract No. DE-AC03-76SF00098. O.H. acknowledges financial support by the Deutsche Forschungsgemeinschaft. R.W. is grateful for a Feodor-Lynen-Fellowship.

REFERENCES

1. H.A. Bethe and E.E. Salpeter, *Quantum Mechanics of One- and Two-Electron Atoms* (Springer-Verlag, Berlin, 1957).
2. S.T. Manson and D. Dill, in *Electron Spectroscopy: Theory, Techniques, and Applications*, Vol. 2, ed. by C.R. Brundle and A.D. Baker (Academic, N.Y., 1978).
3. J. Cooper and R.N. Zare, J. Chem. Phys. **48**, 942 (1968).
4. M.O. Krause, Phys. Rev. **177**, 151 (1969).
5. For unpolarized incident light, $\beta/2$ is replaced by $-\beta/4$ in Eq. (1), and θ is measured between the propagation vectors of the photon and the photoelectron. Otherwise, the essential physics is the same.
6. J.W. Cooper, Phys. Rev. A **42**, 6942 (1990); **47**, 1841 (1993).
7. B. Krässig, M. Jung, D.S. Gemmell, E.P. Kanter, T. LeBrun, S.H. Southworth, and L. Young, Phys. Rev. Lett. **75**, 4736 (1995).
8. M. Jung, B. Krässig, D.S. Gemmell, E.P. Kanter, T. LeBrun, S.H. Southworth, and L. Young, Phys. Rev. A **54**, 2127 (1996).
9. L. Lajohn and R.H. Pratt (private communication).
10. R.C.C. Perera, Nucl. Instrum. Methods **A319**, 277 (1992).
11. J.H. Scofield, Phys. Rev. A **40**, 3054 (1989); Phys. Scripta **41**, 59 (1990).
12. M. Ya. Amusia and N.A. Cherepkov, *Case Studies in Atomic Physics*, Vol. 5 (North-Holland, Amsterdam, 1975), p. 47.
13. B. Kempgens, A. Kivimäki, M. Neeb, H.M. Köppe, A.M. Bradshaw, and J. Feldhaus, J. Phys. B **29**, 5389 (1996).
14. P. Langhoff (private communication).

Principal Investigator: Dennis W. Lindle, University of Nevada, Las Vegas. Email: lindle@nevada.edu. Telephone: 702-895-4426.

Breakdown of the Independent Particle Approximation in High-Energy Photoionization

O. Hemmers[1], P. Glans[1], D. L. Hansen[1], H. Wang[1], S. B. Whitfield[1], D. W. Lindle[1], R. Wehlitz[2], J. C. Levin[2], I. A. Sellin[2], R. C. C. Perera[3], E. W. B. Dias[4], H. S. Chakraborty[4], P. C. Deshmukh[4], and Steven T. Manson[5]

[1]Department of Chemistry, University of Nevada, Las Vegas, NV 89154-4003
[2]Department of Physics and Astronomy, University of Tennessee, Knoxville, TN 37996-1200
[3]Advanced Light Source, Lawrence Berkeley Laboratory, Berkeley, CA 94720
[4]Department of Physics, Indian Institute of Technology - Madras, Madras 600036, INDIA
[5]Department of Physics and Astronomy, Georgia State University, Atlanta, Georgia 30303

INTRODUCTION

The response of physical systems to ionizing electromagnetic radiation, photoionization, is a basic process of nature. Because of the weak coupling between incident photons and target electrons, the electromagnetic radiation exerts only a small perturbation on the target, thereby allowing the unambiguous study of target electron properties, e.g., correlation and many-body aspects of electron dynamics. In addition, the photoionization process, along with associated spectroscopies including photoelectron spectroscopy, is of importance in a variety of applications [1] including structural determination in crystalline solids, astrophysical modeling, radiation physics, etc. Owing to its importance, the field has seen a recent upsurge of activity, particularly in the x-ray range, due to the development of third generation synchrotron radiation sources on the experimental side [2], along with the dramatic increase in computer power available, on the theoretical side.
In recent years, a wide variety of studies, both theoretical and experimental, have shown the importance of correlation in the form of interchannel coupling on the photoionization process in the region of the outer shell thresholds [3-10]; in some cases, the single particle viewpoint breaks down completely. An outstanding example is the threshold behavior of Xe *5s*, which is completely dominated by interchannel coupling with the *5p* and *4d* channels [5]. In addition, in the vicinity of inner shell thresholds, dramatic effects are seen in outer shell cross sections due to interchannel coupling. Examples of this phenomenon abound [7], e.g., effects on the outer shell cross sections of atomic Ba in the vicinity of the *4d* threshold [11].

It is generally thought, however, that in the x-ray range (far from the first ionization potential) away from inner shell ionization thresholds, the photoionization process can be well characterized in a single channel [3,7,12,13], or independent particle approximation, theory which omits correlation entirely. If this assertion is not true, then doubt is cast upon the interpretation of a number of studies of atoms, molecules and condensed matter involving x-ray photoabsorption.

Consider the photoionization of an *np* electron, inner or outer, from any atom, molecule or solid. Not far above the *np* ionization threshold will always be an *ns* threshold. Thus, a bit above the *np* threshold, there will always be an *ns* cross section degenerate with the *np* cross section. However, no matter what the relative values of these cross sections are near the thresholds, at energies far above threshold the *ns* cross section will *always* dominate the *np*. This is because, at high energy, the electric dipole photoionization cross section for an *np* subshell falls off with energy as $E^{-(7/2+\ell)}$ [3,7]. Thus,

$$M_{np\to kd(s)}(E) = D_{np\to kd(s)}(E) + \wp\int \frac{\langle \psi_{ns\to k'p} \mid H - H_o \mid \psi_{np\to kd(s)} \rangle}{E-\varepsilon} D_{ns\to k'p}(\varepsilon)d\varepsilon \qquad (1)$$

Because the energies of the photoelectrons from the *np* and *ns* channels are similar, the interaction matrix element falls off only very slowly and remains large with increasing energy, much like the Xe *5s* case. Thus, for both *np* $\rightarrow$ kd and *np* $\rightarrow$ ks, the second term in Eq.(1) becomes a larger and larger contribution to the matrix element, with increasing energy. This is in sharp contradistinction to the notion that the single-particle characteristics of the electric dipole photoionization process dominate at high energy.
As a prototypical example, we consider photoionization of atomic Ne in the 1 keV photon-energy range.

EXPERIMENT

The experiments were performed on undulator beamline 8.0, [17], which covers the 100-1500 eV photon-energy range. The monochromator entrance slit was set to 70 μm and the exit slit to 100 μm yielding very high flux, because high photon resolution was not needed. During the measurements the ALS operated at 1.9 GeV in two-bunch mode with a photon pulse every 328 ns. Four time-of-flight (TOF) electron analyzers, equipped with microchannel plates for electron detection, collect spectra simultaneously at different angles. The total electron flight paths are 460 mm, and the analyzers have a full cone acceptance angle of 5°. The interaction region is formed by an effusive gas jet intersecting the photon beam, which has a diameter of about 2 mm. Energy resolution of the TOF analyzers with a focus size of 2 mm is 3% of the electron kinetic energy. Each spectrum was collected for about 600 s.

RESULTS

New measurements have been made for the ratio of the Ne *2s* to the *2p* cross section which take into account the non-dipole contribution to the photoelectron angular distribution [16], and they are shown in Fig. 1, along with our theoretical results. New calculations also were performed within the framework of the relativistic-random-phase approximation (RRPA) [14,15] for the cross section, σ, and photoelectron angular distribution asymmetry parameter, β, of the *2p* subshell. Four levels of approximation were considered: (i) coupling of all of the relativistic single excitation channels arising from *2p*, *2s* and *1s*; (ii) from *2p* and *2s* only; (iii) from *2p* and *1s* only; (iv) from *2p* alone and *2s* alone. The measurements confirm the accuracy of the calculation by the excellence of the agreement.The most important result demonstrated by Fig. 1 is the divergence between the fully coupled and the uncoupled calculations at the highest energies, and the fact that it is the coupling with *2s* that is important as evidenced by the agreement between the full (*2p* + *2s* + *1s*) calculation and the *2p* + *2s* calculation. In addition, a central-field calculation [3,12,13] was performed using a Hartree-Slater potential [18] and the results (not shown) are virtually identical to the uncoupled *2p* RRPA result of Fig. 1, as expected. Thus, it is clear that the single-particle result does not agree with experiment at higher energies,while the coupled result does, in contrast to the conventional wisdom [3,7,12,13].

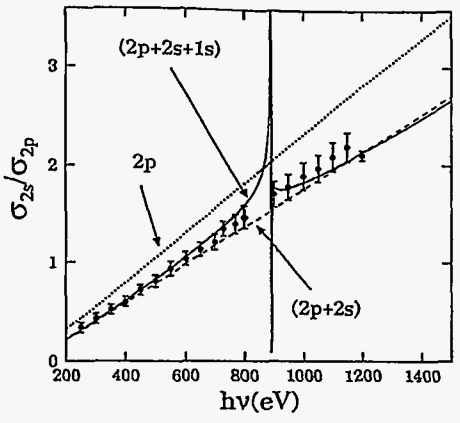

Figure 1. Ratio of the *2s* to *2p* cross section for Ne. The calculations employed the RRPA formalism with the single excitation channels arising from *2p*, *2s* and *1s* coupled (solid curve); *2p* and *2s* coupled (dash curve); and *2p* and *2s uncoupled* to each other (dot curve). The experimental points were measured in the manner discussed in Ref. 16.

Turning to the photoelectron angular distribution parameter, β, the experimental results [16], along with the various levels of calculated results, are shown in Fig. 2; all levels of calculation agree reasonably well at

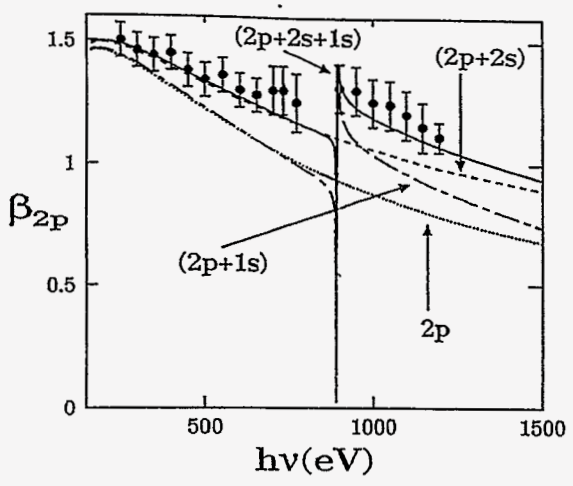

Figure 2. Photoelectron angular distribution asymmetry parameter, β, for Ne *2p* calculated using the RRPA formalism with the single excitation channels arising from *2p*, *2s* and *1s* coupled (solid curve); *2p* and *2s* (dash curve); *2p* and *1s* (dash-dot curve); and *2p* alone (dot curve). The experimental points are from Ref. 16 augmented by some new points reported here using the methodology of Ref. 16.

the lowest energies, but the separation into the same two groups occurs with increasing energy. Agreement of the experimental results with the full RRPA calculation is clear. Our single particle result for β (not shown) also is virtually indistinguishable from the *2p* alone calculation. At the highest energies considered, we see about a 30% shift in β from the single particle calculation, reiterating the point that even out at 1.5 keV, approximately 100 times the threshold energy, interchannel coupling does matter.

This interchannel coupling effect should also be in evidence for *nd* and *nf* subshells as well. In addition, although the detailed example was for an atom, the arguments are exactly the same for molecular and condensed matter targets. One *caveat* should be mentioned, however. At extremely high energies (tens of keV or higher), where relativistic interactions take over [19-21], the photoionization cross sections no longer behave as $E^{-(7/2+\ell)}$ and these arguments no longer apply. But for a very significant energy region below that, they do.

In conclusion, we have shown that the high energy photoionization of all $n\ell$ ($\ell > 0$) subshells will exhibit a breakdown of the independent particle approximation owing to the effect of interchannel coupling with the nearby *ns* channels, and this effect has been demonstrated for Ne *2p* employing both theory and experiment. It is predicted that the same effect applies equally to molecules and condensed matter, as well as atoms.

ACKNOWLEDGMENTS

This work was supported by the National Science Foundation, NASA, the Department of Energy, the Research Corporation and The Petroleum Research Fund. The authors thank the staff of the ALS for their support and the IBM, LBNL, LLNL, University of Tennessee and Tulane University collaboration for beam time at beamline 8.0. R.W. and O.H. thank for financial support by the AvH and DFG, respectively.

REFERENCES

1. H. S. W. Massey, E. W. McDaniel and B. Bederson, eds., *Applied Atomic Collision Physics* (Academic Press, NY, 1983), 5 volumes.
2. A. S. Schlachter and F. J. Wuilleumier, eds., *New Directions in Research with Third Generation Soft X-Ray Sources* (Kluwer, Dordrect, Netherlands, 1992), NATO ASI Series E, Vol. 254.
3. A. F. Starace, in *Handbuch der Physik*, Vol. 31, ed. by W. Mehlhorn (Springer-Verlag, Berlin, 1982), pp. 1-121.
4. J. A. R. Samson, in *Handbuch der Physik*, Vol. 31, ed. by W. Mehlhorn (Springer-Verlag, Berlin, 1982), pp. 123-213.
5. V. Schmidt, Rep. Prog. Phys. **55**, 1483 (1992).

6. B. Sonntag and P. Zimmermann, Rep. Prog. Phys. **55**, 911 (1992).
7. M. Ya. Amusia, *Atomic Photoeffect* (Plenum Press, NY, 1990).
8. T.-N. Chang, ed., *Many-Body Theory of Atomic Structure and Photoionization* (World Scientific, Singapore, 1993).
9. J. Berkowitz, *Photoabsorption, Photoionization, and Photoelectron Spectroscopy* (Academic Press, NY, 1979).
10. H. P. Kelly, in *X-Ray and Inner-Shell Processes*, ed. by T. A. Carlson, M. O. Krause and S. T. Manson (American Institute of Physics, NY, 1990), pp. 292-314.
11. J. M. Bizau, D. Cubaynes, P. Gerard and F. J. Wuilleumier, Phys. Rev. A **40**, 3002 (1989).
12. S. T. Manson and D. Dill, in *Electron Spectroscopy*, ed. by C. R. Brundle and A. D. Baker (Academic Press, NY, 1978), Vol. 2, pp. 157-195.
13. S. T. Manson, Adv. Electronics Electron Phys. **41**, 73 (1976).
14. W. R. Johnson and C. D. Lin, Phys. Rev. A **20**, 964 (1979).
15. W. R. Johnson, C. D. Lin, K. T. Cheng and C. M. Lee, Phys. Scripta **21**, 409 (1980).
16. O. Hemmers, G. Fisher, P. Glans, D. L. Hansen, H. Wang, S. B. Whitfield, D. W. Lindle, R. Wehlitz, J. C. Levin, I. A. Sellin, R. C. C. Perera, E. W. B. Dias, H. S. Chakraborty, P. C. Deshmukh and S. T. Manson, J. Phys. B **30**, L727 (1997).
17. R. C. C. Perera, Nucl. Instrum. Methods **A319**, 277 (1992).
18. F. Herman and S. Skillman, *Atomic Structure Calculations*, (Prentice-Hall, Englewood Cliffs, N.J., 1963).
19. R. H. Pratt, A. Ron and H. K. Tseng, Rev. Mod. Phys. **45**, 273 (1973).
20. I. P. Grant, J. Phys. B **7**, 1458 (1974).
21. A. Ron, I. B. Goldberg, J. Stein, S. T. Manson, R. H. Pratt and R. Y. Yin, Phys. Rev. A **50**, 1312 (1994).

Principal Investigator: Dennis W. Lindle, University of Nevada, Las Vegas. Email: lindle@nevada.edu. Telephone: 702-895-4426.

Characterization of Manganese Oxide Powder Processed by Gas Condensation Method.

Kwang Yong Eun[1], Jong-Koo Park[1], Jeong-Hahn Kim[2], Moo-Young Hur[2], Simone Anders[3] and Thomas Stammler[3]

[1]Materials Science Division, Korea Institute of Science and Technology
P.O. Box 131, Cheongryang, Seoul, 130-650, Korea
[2]Department of Materials Science, College of Engineering, Korea University,
Anam-Dong, Seongbuk-Ku, Seoul, Korea
[3]Advanced Light Source, Ernest Orlando Lawrence Berkeley National Laboratory,
University of California, Berkeley, CA 94720

INTRODUCTION

The manganese oxide powder is considered to be important catode material in the lithium ion secondary battery. The preparation of the finer manganese powder is directly related to the increase of cathode surface area and is consequently able to improve the capacity of static electricity. Manganese powder processing by the gas condensation method was tried to make from several nano meter to decades nano meter sized powder and the near edge x-ray absorption fine structure (NEXAFS) study on the powders was done for the analysis of the oxidation degree depending on the processing condition and the oxidation heat treatment afterwards.

The gas condensation method is one of the unique ultra fine powder making processes and has more advantage than the gas evaporation method since the powder produced by the former method shows finer size and more narrow size distribution[1,2]. There are several other methods for making nano sized ultra fine powders such as mechanical crushing by ball milling, deposition from the salt solution, sprayed thermal decomposition, laser heating and clustering, sol-gel processing etc.[3-6]. However, gas condensation and gas evaporation methods are favorably studied since the powder surfaces are cleaner and less stained by the contamination.

The gas condensation method has two processes, that is, metal powder condensation process and oxidation process. In the metal powder condensation stage, low pressure inert gas is introduced into the vacuum melting chamber and the vaporized metal gas of atomic unit is clustered to each other and condensed to ultra fine size powder by contacting cold gas. In the second step, low pressure oxygen gas is introduced to the chamber and the fine metal powder is oxidized thereafter. Subsequent heat treatment in air atmosphere is done for the further oxidation. First NEXAFS study of the nano sized powder surfaces will be presented and this will define the final oxidation state of the metal powder.

EXPERIMENTAL

Three kinds of nano sized ultra fine manganese powders were produced by melting the pure manganese metal (99.99%) at the temperature of 1150°C in vacuum (1x 10^{-6} Torr), evaporation by introducing low pressure helium gas 1 Torr, 10 Torr and 100 Torr respectively and subsequent holding at a pressure of 300 Torr (firstly filling with helium gas 100 Torr and then filling oxygen gas to 300 Torr) for 3 hours in the cylindrical chamber with 30cm diameter and 55cm height[7]. Melting was done by resistance heating in tungsten boat. The different helium gas pressure during the gas condensation process gave variations in the powder size and oxidation degree.

Three ultra fine manganese powders were heated in air atmosphere to the temperature of 520°C at a heating rate of 10°C per minute since they showed reaction peaks in the range of 200°~300°C and

around 500°C in the DSC curves. On the three raw powders made with different helium pressure and three heat treated powders, NEXAFS analysis has been performed using the photo-emission electron microscope located at beam line 8.0 of ALS. Each powder was put on carbon tape and attached by rubbing the powder repeatedly and spreading as thin as possible. Carbon tape held the powder stictly was fixed on the sample holder. The X-ray diffraction of the same powder samples has been also done and compared to NEXAFS results.

RESULTS and DISCUSSION

Manganese oxide powders made by gas condensation method had ultra fine size and relatively narrow particle size distribution observing the size and morphology by transmission electron microscope. Clustered round particles with similar size showed size increasing trend from about 10 to 40 nm size with increase of helium gas pressure from 1 Torr to 100 Torr during evaporation and condensation process. This indicates that pressure increase retarded evaporation rate and gas convection current in the chamber and accelerated the impingement of helium and metal gas and consequently brought about the growth of the condensed particles.

For the three ultra fine manganese oxide powders, structure analysis by x-ray diffraction was done and β-Mn, MnO and Mn_3O_4 were observed respectively in every powder. β-Mn peak was the strongest intensity in every powder and increased with increase of helium gas pressure. Differential scanning calorimetry from 0 to 900°C at the heating rate of 10°C per minute was applied for three manganese oxide powder and two clear peaks were found, that is, one peak between 200°C and 300°C and the other peak between 500°C and 520°C respectively. These suggest that some kinds of oxidation reaction occurred below 520°C. Therefore, heat treatment to the temperature of 520°C at the heating rate of 10°C was performed for three manganese oxide powders and x-ray diffraction analysis was followed.

X-ray diffraction pattern comparison between the raw and heat treated powders were summarized for the three different manganese oxide powders in Fig.1. The manganese oxide powder processed by 1 Torr helium atmosphere showed higher oxidation to Mn_2O_3 while other two powders processed by 10 Torr and 100 Torr helium atmosphere exhibited less oxidation only to Mn_3O_4. This means that small sized powder oxidized to higher oxidation degree and surface oxidation is retarded by the insufficient oxidation of powder core.

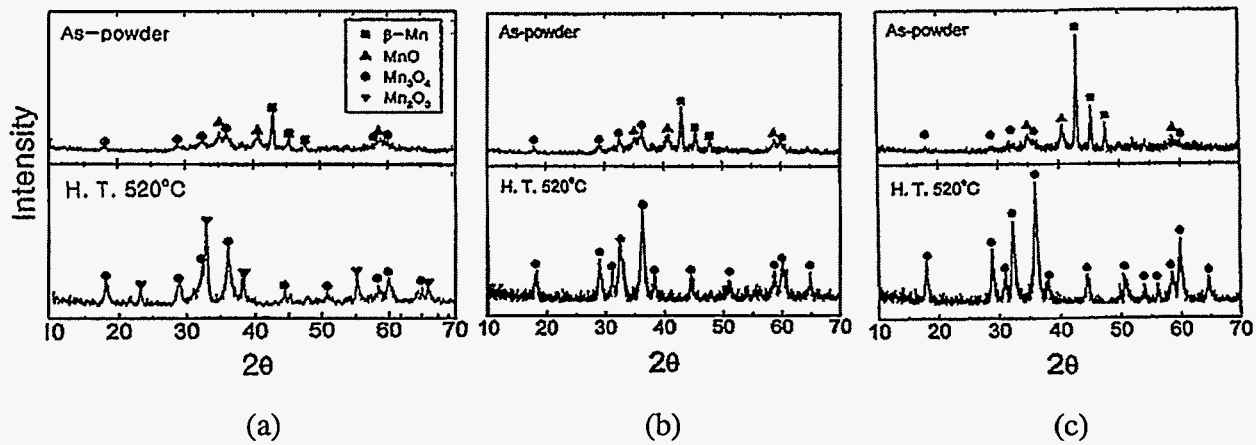

Fig.1. X-ray diffraction pattern comparison of the three different manganese oxide powders before and after heat treatment at 520°C. (a) manganese oxide powders processed by 1 Torr helium gas, (b) those processed by 10 Torr helium gas and (c) those processed by 100 Torr helium gas.

Surface oxide was analyzed by L_3-edge absorption of Manganese NEXAFS spectra for the raw manganese oxide powders and the heat treated ones. In the photo-emission electron microscope of beam-line 8.0.1, powder morphology with different size was observed and the relevant NEXAFS spectra were obtained. In Fig. 2 three sets of Mn L_3 NEXAFS spectra were summarized depending on the helium gas pressure and those of raw powder and heat treated one were compared in each plot.

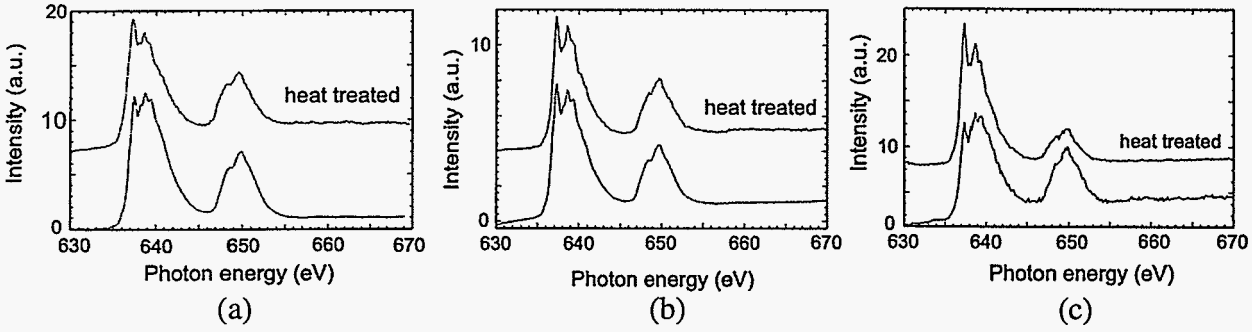

Fig. 2. L_3 NEXAFS spectra of manganese oxide powders synthesized by gas condensation method. (a) powders synthesized by helium gas pressure 1 Torr, (b) powders synthesized by helium gas pressure 10 Torr and (c) powders synthesized by helium gas pressure 100 Torr.

The L_3 NEXAFS spectra showed that oxidation occurred more than MnO in all the powders. In these NEXAFS results, sharp peaks of 637eV and 650eV were clearly and similarly shown in every powder. All the three raw powders had nearly the same peaks and this means that the surface of the powders are covered with Mn_3O_4[8]. Main change occurred in the complicated peaks between 638 eV and 639.5 eV in the shape and height. These change indicates the oxidation of Mn_3O_4 to Mn_2O_3[8]. The powder processed by 1 Torr helium gas showed more pronounced oxidation through heat treatment. This means that the oxidation of the smaller size powder reached early to Mn_2O_3 state while other bigger size powders remained as Mn_3O_4 state. The NEXAFS of Fig.2 and the x-ray diffraction results of Fig.1 show that the oxidation reaction occurred from surface to interior and β-Mn and MnO layers remained in the core of the decades nano particle and also the surface layer of Mn_2O_3 was not thick enough to detect easily by NEXAFS.

CONCLUSION

Gas condensation method was first applied in making ultra fine manganese oxide powder and controlled-size powders from about 10 to 40 nm were obtained by ruling the helium gas pressure from 1 to 100 Torr. These powders were heat treated at the temperature of 520°C and the oxidation degree was analyzed by x-ray diffraction and L_3 edge Mn NEXAFS. Oxidation occurred during gas condensation process but β-Mn and MnO layer remained in the core of the decades nano meter sized powder. More oxidation at the temperature of 520°C made the powder surface Mn_3O_4 and Mn_2O_3. The Mn NEXAFS studies for the nano sized manganese powder revealed surface oxidation results consistent with x-ray diffraction. Further study on the nano sized powder characterization is needed for better understanding of the oxidation reaction and podwer surface properties.

REFERENCES

1. H. Gleiter, Deformation of Polycrystals, Mechanisms and Microstructures, Proc. of 2nd Riso Int. Symp., ed. N. Hansen, A. Horsewell, T. Leffers and H. Lilhot, Roskilde, Denmark,15(1981)
2. R. Birringer, H. Gleiter, H.P. Klein, P. Marquart, Phys. Lett. A,102, 611(1984)

3. J. Karch, R. Birringer, H. Gleiter, Nature, 330, 556(1987)
4. C. Suryanarayana, F. H. Froes, J. Mater. Res., 5, 1880(1990)
5. K. Laihing, R. G. Wheeler, W. L. Wilson, M. A. Duncan, J. Chem. Phys., 87,3401(1987)
6. R. A. Roy, R. Roy, Mater. Bull., 19, 169(1984)
7. Jeong. H. Kim, M. S. Thesis , Dept. of Metal. Eng. Graduate School, Korea Univ.(1997)
8. F. de Groot, Ph.D. Thesis, X-Ray Absorption of Transition Metal Oxides, University of Michigan, (1991)

This research was supported by the Laboratory Technology Research Partnership.Program, Office of Energy Research, U.S. Department of Energy under a CRADA (Cooperative Research and Development Agreement) between Lawrence Berkeley National Laboratory and IBM; and by the Director, Office of Energy Research, Office of Basic Energy Sciences, under U.S. DOE Contract DE-AC03-76SF00098.

Principal investigator: Simone Anders, Berkeley Lab. Email: sanders@lbl.gov. Telephone: 510-486-4928.

Contamination Free O Kα Spectrum Emitted from MgO

M.Uda [1,2], T. Yamamoto [1], A.Kanai [2], H.Kanno[2], H. Wakita [3], K. Taniguchi [4], T.A. Callcott[5], M.M. Grush[5], D.L. Ederer[6] and R.C.C. Perera[7]

[1] Laboratory for Materials Science and Technology, Waseda University, Nishiwaseda, Shinjuku-ku, Tokyo 169, Japan

[2] Department of Materials Science and Engineering, Waseda University, Ohkubo, Shinjuku-ku, Tokyo 169, Japan

[3] Department of Chemistry, Fukuoka University, Nanakuma, Jonan-ku, Fukuoka 814-01, Japan

[4] Osaka Electro Communication University, Hatsucho, Neyagawa, Osaka 572, Japan

[5] Department of Physics, University of Tennessee, Knoxville, TN 37996, USA.

[6] Department of Physics, Tulane University, New Orleans, LA 70118, USA.

[7] Center for X-ray Optics, Lawrence Berkeley National Laboratory, Berkeley, California 94720, USA

INTRODUCTION

Pronounced chemical bonding effects of two types are observed in X-ray emission spectra when an electron fills an inner-shell vacancy localized on a valence band. One is fine structure originating from molecular orbital components on the valence band, and the other is a difference in X-ray satellite intensities caused by emission from multiply ionized states. However, these emission features have almost the same energies and they can not be observed separately without a tunable monochromator. The Advanced Light Source (ALS) is a powerfultool for separating these spectra - by employing excitation energies large enough for single ionization but too small for multiple ionization. X-ray emission spectra from light elements that are free from the satellites caused by multiple ionization are fascinating targets for study because they reflect the electronic structure of the valence band. In the present study, an observed O Kα spectrum emitted from MgO has been compared with a theoretical spectrum derived from the discrete variational (DV) Xα molecular orbital (MO) calculation.

EXPERIMENTAL RESULTS and MO CALCULATIONS

O Kα emission spectra of MgO shown in Fig.1 were measured using a grating spectrometer at B.L.8. Excitation energies are written in the figure (a-g). Spectra noted as a and d are magnified in the left-hand figure. The Raman scattered peaks shift to high energy sides if high excitation energies are employed, and then the Raman peaks are overlapped with MO peaks at ~522eV and ~525eV when photons with less energies than 533eV are used for excitation. On the other hand photons with higher energies than 555eV produce the satellite noted as K^1L^1 on the 580eV excitation spectrum. Here K^1L^1 denotes a satellite emitted from a state with one K- and one L-shell vacancies. This means that the spectrum excited with 539eV photons is free from the Raman and the satellite peaks, and then can simply be explained by a MO scheme. Both

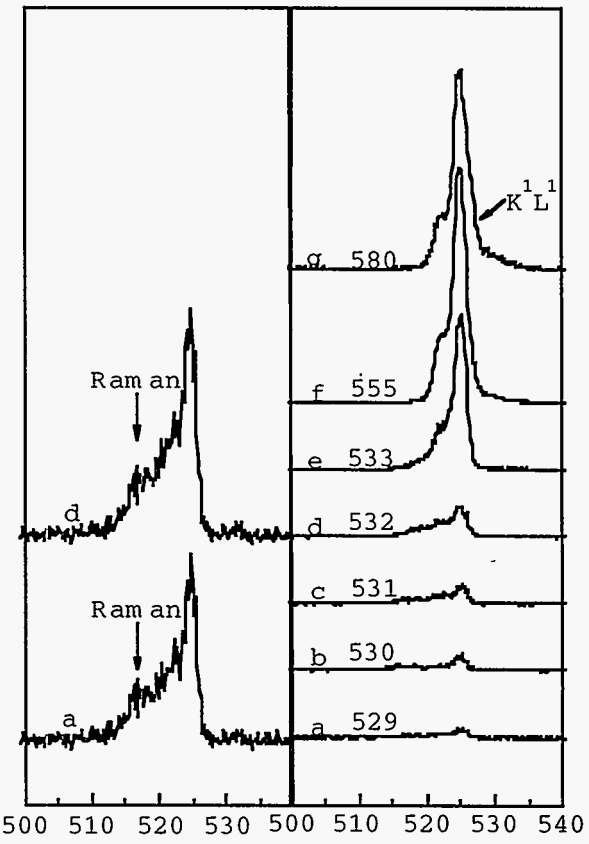

Fig. 1 O Kα emission spectra from MgO

experimental and theoretical spectra are compared with each other, as shown in Fig.2, and their conformity is satisfactory. Here the DV-Xα MO calculations[1),2)] were carried out under the conditions of 1) basis sets for O and Mg: 1s~3p, 2) a well potential: $0.7a_0$ in width and -3.0 Hartree in depth, 3) sample points: 2000. Now a_0 is an interatomic distance between Mg and O.

FURTHER APPLICATION

Similar spectra were taken from CaO and SrO, which were compared with theoretical ones as shown in Fig. 3. Agreement between them is unsatisfactory. On the low energy sides of the observed spectra a weak shoulder or a peak can clearly be seen. To confirm the validity of the theoretical spectra, O Kα emission spectra of CaO and SrO were reexamined by x-ray fluorescence (XRF) spectrometry. If CaO and SrO were exposed to air for a few hours, O Kα spectra with a weak peak at ~522 eV were recorded (unfortunately 7th reflection of Ca Kα is overlapped with the main peak of O Kα for CaO). This means that difference in the shape of O Kα spectra is expected to be seen among MgO, CaO and SrO, if surface of these chemical compounds are clean.

REFERENCES

1) D.E.Ellis, H.Adachi, F.W.Averill, Surf. Sci. 58 (1976) 497
2) H.Adachi, M.Tsukada, C.Satoko, J. Phys. Soc. Jap. 45 (1978) 875

This work was supported by Rigaku, Waseda University, and Hitachi.

Principal Investigator: M. Uda, Laboratory for Materials Science and Technology, Waseda University.

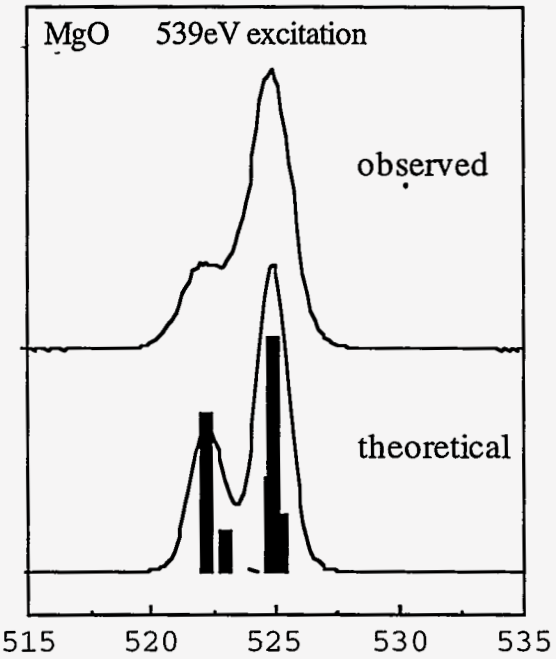

Fig. 2 Comparison between observed O Kα free from Raman and satellite spectra, and theoretical 2p density of states calculated by the DV-Xα method for MgO

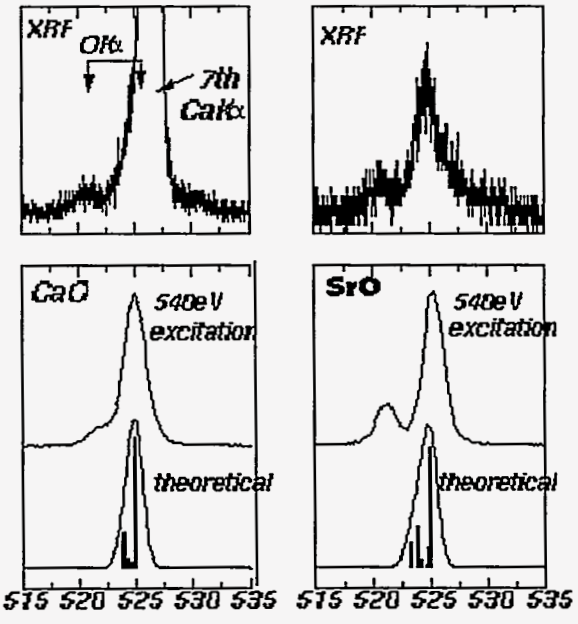

Fig. 3. O Kα XRF spectrum from CaO and SrO (top) which were exposed to air for a few hours. Observed Kα from CaO and SrO at ALS BL 8.0 and theoretical 2p density of states calculated with the DV-Xα method are shown in bottom figures.

Elastic and inelastic scattering of 4d inner shell electrons in $(Y,Gd)_2O_3$ studied by synchrotron radiation excitation.

A.Moewes[1], S.Stadler[2], R.P.Winarski[2], D.L.Ederer[2], M.M.Grush[3], and T.A.Callcott[3]

[1]Center for Advanced Microstructures and Devices, Louisiana State University, Baton Rouge, LA 70803, USA

[2]Department of Physics, Tulane University, New Orleans, LA 70118, USA

[3]University of Tennessee, Knoxville, Tennessee 37996, USA.

ABSTRACT

Excitations within the 4f shell of Gd^{3+} in $(Y,Gd)_2O_3$ are observed by resonant elastic and inelastic soft x-ray scattering with synchrotron radiation[1]. Inelastic scattering takes place when exciting $4d^{10}4f^7 \rightarrow 4d^9 4f^8$ transitions and extends over an energy range of about 10 eV. The features can be assigned to the net transition from the $^8S_{7/2}$ ground state to the sextet multiplets of the $4f^7$ configuration in Gd^{3+} which have the same parity as the ground state. The inelastic scattering is maximal when the excitation energy is tuned to the $4d^9 4f^8$ (^6D) intermediate state[1].

INTRODUCTION

Rare earth elements are characterized by their partially filled 4f-shell. The 4f electrons are highly localized due to the centrifugal term in the potential and have a low binding energy (about 9 eV in Gd). When a 4d electron is promoted to a 4f state ("4d-4f transition"), the strong interaction of the 4d vacancy with the open 4f shell leads to a complex multiplet structure of 37 terms in triply ionized gadolinium. Due to the strong electron correlation, these 4d-4f transitions produce what is called the "giant resonance", which extends over an energy range of up to 20 eV for some of the rare earth elements. In the case of gadolinium, the 4d ionization threshold is at 151 eV and 156 eV just above the "giant resonance", whose absorption maximum is at 149 eV[2].

In $(Y,Gd)_2O_3$, gadolinium exists as the triply ionized atom (Gd^{3+}) due to the ionic binding to the oxygen atom. The configuration of the outer electrons in Gd^{3+} is $4d^{10}5s^25p^64f^7$, and the half filled 4f shell forms an octet ground state level of $^8S_{7/2}$. The ground state $^8S_{7/2}$ has a spherical symmetry which is very stable and therefore much less affected by the crystal field than ions with an f^6 or f^8 electron configuration. We present the first measurements of ground state excitations to even parity localized final state Gd^{3+} 4f orbitals by high-resolution soft x-ray inelastic scattering. The energy loss mechanisms are explained by our calculations of the energy loss spectra. We have also investigated the variation in the cross sections of these transitions with photon excitation energy. In addition to the inelastic scattering we found that the elastic scattering profile is significantly narrower than the absorption spectrum.

EXPERIMENT

Our experiments were performed at the beamline 8.0 of the Advanced Light Source, ALS, Lawrence Berkeley Laboratory. The undulator beamline is equipped with a spherical grating monochromator[3] with a maximum resolving power of $E/\Delta E = 2000$. The fluorescence end station consists of a Rowland circle grating spectrometer that provides a resolving power of about 400. The incident angle of the p-polarized beam was about 10° to the sample normal.

The absorption spectrum of $(Y,Gd)_2O_3$ in the region where a 4d inner shell electron is promoted to a 4f orbit is shown in Fig. 1 (solid line). The main peak is centered at about 149 eV and has a full

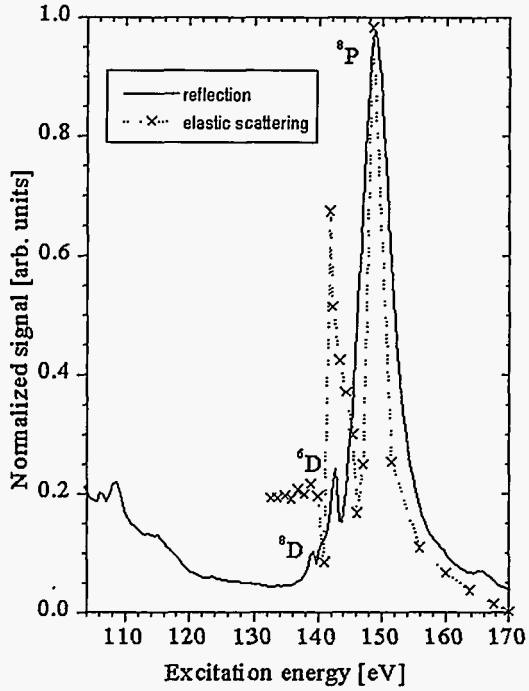

Figure 1: Absorption spectra of $(Y,Gd)_2O_3$ in the photon energy range of the 4d-4f transitions. The terms which characterize the electron configuration of the excited state ($4d^94f^8$) are given in the figure. The spectra are obtained by measuring the radiation reflected (solid line) and elastically scattered (X) by the sample.

width at half maximum of about 5.9 eV. The spectrum represents primarily the transition from the ground state $^8S_{7/2}$ to the ^8P level. At lower photon energies weaker features occur that result from the excitation of the core electron to the ^8D and ^6D levels. Transitions from the octet ground state to the sextet state become partially allowed due to the strong spin-orbit interaction.

Fig. 2 shows the soft x-ray energy loss spectra in $(Y,Gd)_2O_3$ in the vicinity of the 4d-4f resonances (134-168 eV). The energy loss (or in other words the excitation energy of the final state) has been obtained by subtracting the energy of the incoming photons (excitation energy) from the energy of the emitted photons. The spectra are normalized to 300 mA of storage ring current and the number of counts is plotted versus the energy loss of the scattered photons. The counting time for each spectrum has been 30 minutes. Three principal types of photon-in photon-out features can be distinguished in all spectra: The peaks of elastically scattered radiation, of inelastically scattered radiation and of fluorescence radiation. The elastically scattered radiation appears at the energy of the exciting radiation, which corresponds to an energy loss of 0 eV. Due to the magnified scale, the elastic peaks are not fully displayed in Fig. 2. Therefore the maximum count rate in the elastic peak at each excitation energy is represented by an X in Fig. 1. The dotted curve in Fig. 1 is drawn through the experimental points to guide the eye. The energetic position of the main features is the same for the elastic scattering curve (dotted line) and the absorption curve (solid line). The $4d^94f^8 \rightarrow 4d^{10}4f^7$ emission is maximal when the excitation energy is tuned to the ^8P resonance in the absorption curve where the 4d hole is immediately refilled by the excited 4f electron as it scatters the incoming photon. The peak width for the elastic scattering curve is much smaller (3 eV) than the absorption curve (5.9 eV). The autoionization width found by Richter et al.[3] is 5.2 eV. The different peak width is due to the different final states the excited configuration ($4d^94f^8$). It can decay via the main process, autoionization ($4d^94f^8 \rightarrow 4d^{10}4f^6 + e^-$), which produces mostly 4f electrons or via elastic scattering leads to the final state $3d^{10}4f^7$.

Near threshold the decay of a core hole-state can be very different from the decay mechanisms at higher energies. Soft x-ray emission and (radiationless) Auger-electron emission can appear as coherent one-step processes also known as the (resonant) Raman effect.

The intermediate states correspond to $4d^94f^8$ ^8D, ^6D, and ^8P resonance states and the energy loss can be assigned to the difference in energy between the initial and final state often designated as the "net transition". At energies above the threshold, the inelastic scattering evolves into fluorescence, and possible inelastic scattering produced by electron momentum scattering in the Brillouin zone, where soft x-ray inelastic scattering has been used to elucidate band symmetries and probes specific regions of the Brillouin zone.

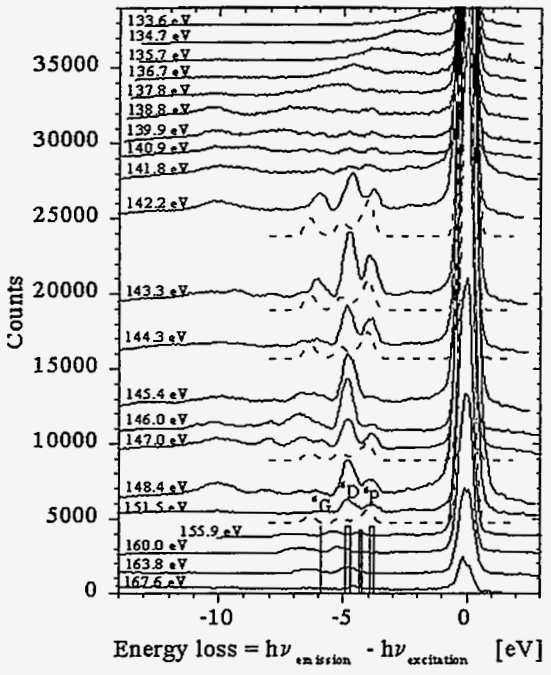

Figure 2: Energy loss spectra on $(Y,Gd)_2O_3$ in the region of the 4d-4f threshold. The excitation energy is given above each spectrum. Calculated energetic positions for the terms that are assigned to the energy losses and represent excitations within the 4f shell are plotted as vertical bars. The dashed lines represent calculated energy loss spectra.

We have calculated the loss spectra[1] using transition probabilities from the ground state to the intermediate states and back to the final metastable states obtained by Cowan's method[4], summing incoherently over all the intermediate states of the $4d^94f^8$ configuration.

An onset of three inelastic excitations at an excitation energy of about 139 eV is observed (Fig. 2). These features remain at a constant difference in energy relative to the elastic peak throughout the energy range of excitation. In Gd the 4f shell is half filled and the absence of valence band-electrons in the vicinity of the Gd ion leads to a term scheme with only a few possible excitations. The next terms above the ground state $^8S_{7/2}$ belong to the sextet multiplet: ^6P_J, ^6I_J, ^6D_J and ^6G_J of the same electron configuration $4f^7$. The energetic positions of these states for Gd^{3+}:LaF_3 as calculated by Carnall et al.[6] are plotted in Fig. 2. Optical and UV absorption spectroscopy data and calculations for Gd doped in various compounds show that the energetic differences in this term scheme for the different materials and their different crystal fields are smaller than 0.02 eV which is small compared to our energy resolution (<0.4 eV). The width of the bars in Fig. 2 represents the energy range over which the various J-levels extend for a given term. Reconfigurations within the 4f-shell ("f-f transitions") by photon excitation are dipole forbidden due to the spin selection rule $\Delta S=0$for L-S-coupling. The inelastic scattering produces energy losses of less than 6 eV and is due to net transitions from the $^8S_{7/2}$ ground state (electron configuration: $4d^{10}4f^7$) to the sextet multiplets ^6P_J, ^6D_J and ^6G_J of the $4d^{10}4f^7$ configuration. The transitions occur through the intermediate states ^8D_J, ^6D_J and ^8P_J ($4d^94f^8$). Population of the ^6I term of $4d^{10}4f^7$ is not observed because of the large change in orbital momentum this transition would require. Different J-levels of the final states are also not resolved. At excitation energies higher than the peak energy of the 4d-4f excitation (149 eV), the inelastic processes become weaker (151.5 eV), shift in energy loss (above 155.9) and finally disappear (167.6 eV). It is worth noticing that the partial cross sections for the three inelastic excitations behave differently. Only the strongest inelastic peak that comes from the excitation to the ^6D state remains intense over an energy range of about 9 eV. At an excitation energy of about 156 eV the inelastic peaks become very weak and the magnitude of the energy loss changes.

While we observe intense inelastic and elastic scattering as the photon energy is tuned to the 4d-4f resonances ($4d^94f^8 \rightarrow 4d^{10}4f^7$), we do not observe fluorescence at excitation energies above the 4d shell ionization threshold due to $4d^94f^7 \rightarrow 4d^{10}4f^6$ transitions. This is expected because the partial cross section to produce a 4d hole is small[2] and the 4d hole is filled by competing Auger processes with high probability. A weak fluorescence feature can be seen at an energy loss of 10 eV in the

spectrum taken at 142.2 eV. With smaller excitation energy this peak shifts towards the elastic peak. We suggest that this weak fluorescence feature belongs to a charge transfer state because Gd^{3+} does not offer transitions at this energy. We conclude that in the region of the giant resonance, autoionization and elastic scattering are the dominant interaction mechanisms. Inelastic scattering compared to elastic scattering is weaker by about two orders of magnitude.

To summarize, we have used high-resolution soft x-ray emission spectroscopy with synchrotron radiation to study inner shell 4f excitations of Gd^{3+} in $(Y,Gd)_2O_3$. The soft x-ray emission spectra have been studied when exciting the 4d electrons selectively and strong inelastic features have been observed. According to our calculations, we interpret the energy losses as excitations within the 4f shell. The incident photons excite electrons from the ground state $^8S_{7/2}$ primarily to the intermediate state ^6D_J and are inelastically scattered to the sextet final states $4d^{10}4f^7$ $(^8S_{7/2})\rightarrow 4d^9 4f^8$ $(^6D_J)\rightarrow$ $4d^{10}4f^7$ (^6P_J, ^6D_J, ^6G_J). The energy losses between 4 and 6 eV are due to net transitions from the octet ground state $^8S_{7/2}$ to the low lying sextet terms of the $4f^7$ configuration ^6P_J, ^6D_J and ^6G_J.

ACKNOWLEDGMENTS

This work was supported by National Science Foundation grant DMR-9017997, the Science Alliance Center for Excellence Grant from the University of Tennessee and a DoE-EPSCor cluster research grant DoE-LEQSF (1993-95)-03. The Advanced Light Source is supported by the office of Basic Energy Sciences, U.S. Department of Energy, under contract no. DE-AC03-76SF00098. The authors are grateful for support from CAMD, where much of the preliminary data were taken.

REFERENCES

1. A. Moewes, T. Eskildsen, D.L. Ederer, Jianyi Wang, Jim McGuire, and T.A. Callcott, Phys. Rev. B, Rapid Communications Vol. 57, No. 13.
2. M. Richter, M. Meyer, M. Pahler, T. Prescher, E.v. Raven, B. Sonntag, and H.-E. Wetzel, Phys. Rev. A 40, 7007 (1989).
3. J.J. Jia, T.A. Calcott, J. Yurkas, A.W. Ellis, F.J. Himpsel, M.G. Samant, G. Stöhr, D.L. Ederer, J.A. Carlisle, E.A. Hudson, L.J. Terminello, D.K. Shuh, and R.C.C. Perera, Rev. Sci. Instrum. 66 (2), 1394 (1995).
4. R.D. Cowan, The theory of atomic structure and spectra, University of California press, Berkeley, 1981.
5. W.T. Carnall, G.L. Goodman, K. Rajnak, and R.S. Rana, Report of Argonne National Laboratory, ANL-88-8 (1988).

Principal investigator: Alexander Moewes, Center for Advanced Microstructures and Devices, Louisiana State University. Email: moewes@lsu.edu. Telephone: (504) 388-0419.

The Electronic Structure of Tungsten Carbide

S. Stadler[1], R. P. Winarski[1], D. L. Ederer[1], J. MacLaren[1], J. van Ek[2], A. Moewes[3], M. M. Grush[4], T. A. Callcott[4], and R. C. C. Perera[5]

[1]Department of Physics, Tulane University, 2001 Percival-Stern Hall, New Orleans, LA 70118.

[2]Seagate Recording Heads, 7801 Computer Ave. S., Bloomington, MN 55435-5489

[3]Center for Advanced Microstructures and Devices, Louisiana State University, Baton Rouge, LA 70803.

[4]University of Tennessee, Knoxville, TN 37996.

[5]Lawrence-Berkeley National Laboratory, Berkeley, CA 94720.

INTRODUCTION

Transition metal carbides have long been used in industry because of their resilient physical properties. Strength at high temperatures, high melting points, and corrosion and wear resistant properties make them obvious candidates for many commercial applications.[1] WC has been shown to be an effective catalyst in some chemical reactions usually catalyzed by noble metals such as Pt.[2,3] Carbides, particularly WC alloyed with other monocarbides, are the basis for "cemented carbide" cutting tools and wear resistant coatings.

The electronic structures of transition metal carbides have been studied experimentally using photoelectron spectroscopy [2,4-6] and photoemission spectroscopy.[7] The purpose of this study was to obtain detailed soft x-ray emission (XES) and absorption (XAS) data to directly observe hybridization of the occupied states and probe the structure of the unoccupied states of these compounds. Since soft x-ray valence emission represents the partial density of states (PDOS) of a specific angular momentum of the valence band, C 1s emission spectra were compared to p-projected PDOS (p-PDOS) from LMTO-ASA and full-potential KKR electronic structure calculations.

EXPERIMENTAL

All fluorescence and TFY data were measured at undulator beamline 8.0 at the Advanced Light Source (ALS) at Lawrence-Berkeley National Laboratory (LBNL), Berkeley, CA. The samples were illuminated with monochromatic synchrotron radiation via a spherical grating monochromator. Fluorescent soft x-ray radiation was analyzed with a Rowland geometry, spherical grating spectrometer under ultrahigh vacuum (UHV) conditions. The spectrometer has a fixed entrance slit, four spherical diffraction gratings, and a position sensitive area detector. All measurements were made with a 50 μm entrance slit. C 1s spectra were obtained with a 1000 lines/mm, 10 meter radius grating. The band pass of the spectrometer was estimated to be less than 0.4 eV at the carbon edge. Pressure in the sample chamber was below 5×10^{-9} torr. Details of this beamline and endstation are described elsewhere.[8]

WC

C 1s XES spectra are shown as a function of incident energy in Fig. 1. The spectra were normalized to the incident intensity and calibrated using published carbon spectra.[10] Spectra excited far above threshold exhibited four peaked features centered at about 278 eV. Photoelectron measurements yield an estimate of the binding energy of the C 1s electron in WC to be 282.6 eV.[2]

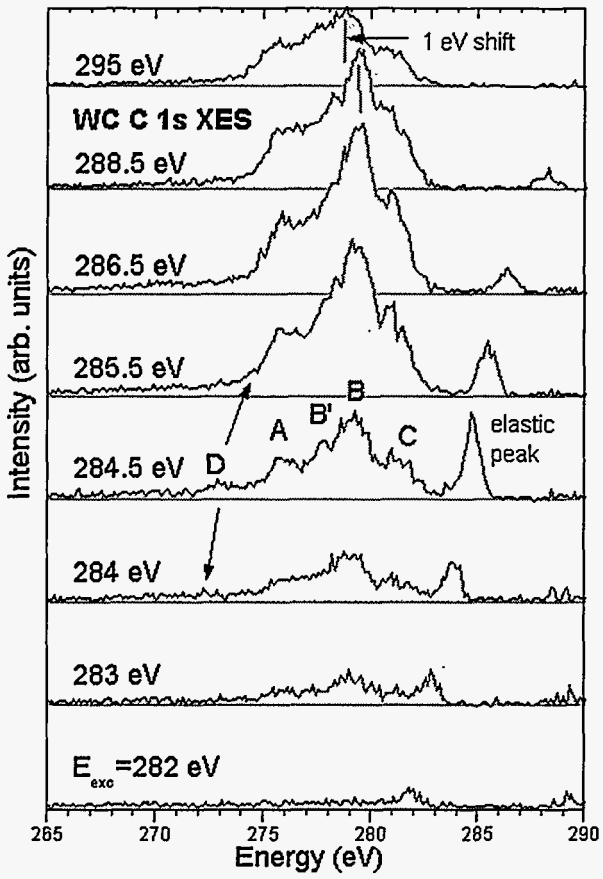

Fig. 1. The C 1s XES of hexagonal WC. Four main features were observed in the spectra: A, B, B', and C. The feature D appearing in the spectrum excited at 284.5 eV was identified as either a Raman effect or a feature of the C p-PDOS. The arrows indicate evidence of tracking of the peak D with excitation energy. The spectrum excited at 295 eV, and all other spectra excited at higher energies, were shifted by about 1 eV relative to the spectra excited at energies lower than 295 eV. The shift is explained as an effect of core hole screening by the C 1s electron excited to a localized level of p-symmetry above the Fermi level.

The elastic peak resonates at about 284.5 eV, which is indicative of a localized unoccupied state of p-symmetry above the Fermi level. The largest feature, B, shifts by about 1 eV to higher energy between E_{exc}= 290.5 and 288.5 eV as the excitation energy is lowered through threshold. This shift of emission spectra to higher energy when the excitation is near threshold (in the elastic resonance) implies that the C 1s electron is excited to a 2p level that is localized at the carbon atom, thereby screening the valence electrons from the core hole. By the same reasoning, the excited electron is no longer localized at the C atom when the excitation energy exceeds 290.5 eV.

CALCULATIONS

Linear muffin-tin orbital (LMTO) calculations were performed within the atomic sphere approximation (ASA).[12] The exchange and correlation effects are treated within the local density approximation (LDA) of density functional theory.[13] Self-consistent solutions to the Kohn-Sham equations were obtained for all electrons in the system by using the exchange-correlation potential as formulated by Hedin and Lundqvist.[14] The core electron states were obtained as solutions of the Dirac equation, and scalar relativistic terms were retained in the LMTO Hamiltonian for band states.

LMTO Calculations for WC

Tungsten carbide (WC) is hexagonal with a unimolecular cell of dimensions a=2.9065 Å and c=2.8366 Å, and has the symmetry of the $D^1_{3h}(P\bar{6}3m)$ space group.[15] The atomic positions in hexagonal coordinates are (0,0,0) and $\left(\frac{2}{3},\frac{1}{3},\frac{1}{2}\right)$ for W and C, respectively. The Wigner-Seitz radii were chosen in ratio of their published ionic radii and to have a total unit cell volume Ω=140.041 a.u.^{3}.[16] The radii computed for W and C were 2.9687 and 1.9370 a.u., respectively. 288 *k*-points were sampled in the irreducible wedge.

The LMTO energy bands are shown in Fig. 2 and agree well with previously published calculations.[17-20] Other electronic structure calculations have been performed on the high-temperature NaCl phase of WC.[20-22] The local C p-PDOS of WC was compared to C 1s emission excited at E_{exc}=320 eV (Fig. 3). C p-PDOS was broadened to account for experimental broadening with ΔE=1.0 eV. The experimental data agree well with these calculations, as well as with previously published ones, verifying conclusions drawn from them regarding bonding

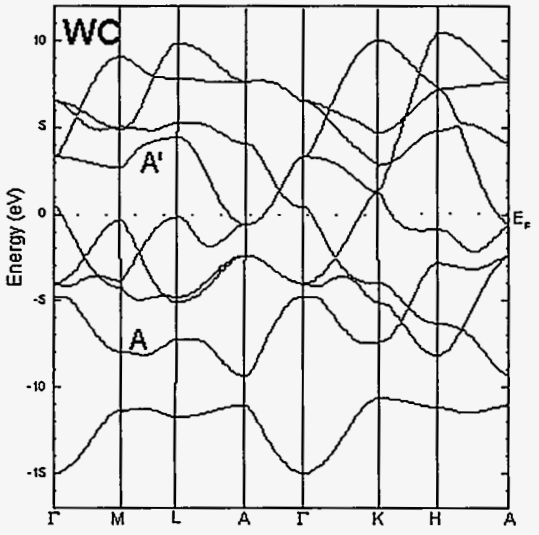

Fig 2. The LMTO energy bands of WC (left) and the corresponding symmetry points of the Brillioun zone. The points A and A' label flat bands that represent an energy loss mechanism, in the form of an interband transition, which may account for the peak D in Fig.1.

mechanisms and electronic structure.[17-20,23] The fact that the LMTO calculations agree well with full potential calculations[24] and the experimental data is important in evaluating the performance of the LMTO method in modeling these systems. One inference drawn from these calculations includes the interpretation of hybridization between C p and W d electrons as a covalent bonding mechanism. Since C p- and W p-PDOS have the same shape and relative intensities in the region between -2.5 and -8.0 eV, it was concluded that hybridization occurs between the C 1s and W 5d states, which is indicative of covalent bonding in WC. In addition to this p-d hybridization, it was noted that the d-band is much larger than the p-band, indicating that some of the W d-states are not involved in the p-d hybridization. The d-states that are not involved in p-d hybridization form a peak at about -2.0 eV. This peak matches another peak in the W d DOS at about +2.5 eV. It was concluded that the d-band is split into bonding-antibonding states implying d-d hybridization acts as a metal-metal, second-nearest-neighbor bonding mechanism in WC. It was also noted that the W p states hybridize with those of C p and W d .

The p-d hybridization and the filling of only the bonding d-d hybrids was deduced as the reason for the high strength of WC.[23] This experiment confirms the p-d hybridization, but valence s and d emission from W was too weak to make any conclusions about the d-d hybridization.

The peak A in Fig. 3 is a subband of the p-PDOS that is the result of hybridization between C 2s and W 5d electrons. Evidence of this s-d hybridization was apparent in the C s-and W d-PDOS. The s-d hybridization may be an alternative explanation (the other one was Raman scattering) of why peak D appears in the XES spectrum of Fig. 1 excited at 284.5 eV.

A localized unoccupied state above the Fermi level is indicated by peak B in the C p-PDOS in Fig. 3. It was concluded that localized p-PDOS is responsible for resonant elastic scattering in WC.

CONCLUSIONS

XES spectra excited near the C 1s threshold of WC were presented and exhibited little or no dispersion. Calculated LMTO DOS were in good agreement with experimental data. A localized state above the Fermi level was revealed by resonant elastic scattering. The effect of this localized electron was realized by a shift of the emission spectra to higher energies. At the elastic resonance a peak appeared in the emission spectrum at about 273 eV. The peak was identified as either an energy loss facilitated by an interband transition or emission from the C s-d hybrid subband.

Agreement of LMTO calculations with experimental data and full potential (LAPW) calculations indicates that the LMTO method is sufficient regarding the calculation of electronic properties of

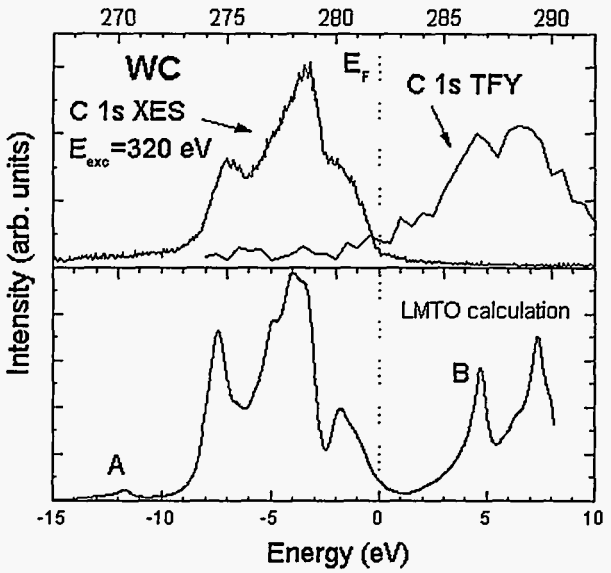

Fig. 3. The C 1s XES excited above threshhold and TFY spectra are compared to the LMTO C p-PDOS. The C p-PDOS were broadened by 1.0 eV. The feature A, a C s -W d hybrid subband, may account for the feature D of the WC C 1s spectrum (Fig. 1.) excited at 284.5 eV. The peak B is a localized unoccupied band of p-symmetry that may be responsible for the observed resonance in elastic scattering.

these systems. Interpretations of previous calculations regarding bonding mechanisms and electronic structure, particularly hybridization, were verified.

ACKNOWLEDGMENTS

This project was funded by NSF grants (No. DMR-9420425) and the DOE EPSCOR and Louisiana Education Quality Fund (Grant No. DOE-LEQSF (1993-95)-03). The work at the Advanced Light Source at Lawrence Berkeley National Laboratory was supported by the U.S. Department of Energy (Contract No. DE-AC03-76SF00098).

REFERENCES

[1] L. E. Toth, *Transition Metal Carbides and Nitrides*, Academic Press, New York (1971).
[2] R. J. Colton, J-T. J. Huang, and J. W. Rabalais, Chem. Phys. Lett. **34**, 337 (1975).
[3] R. B. Levy and M. Boudart, Science **181**, 547 (1973).
[4] H. Ihara, M. Hirabayashi, and H. Nakagawa, Phys. Rev. B **14** (4), 1707 (1976).
[5] V. V. Nemoshkalenno, V. V. Antonov, VL. N. Antonov, W. John, H. Wonn, and P.Ziesche, Phys. Stat. Sol. (b) **111**, 11 (1982).
[6] L. H. Bennett, T. R. Cuthill, A. J. McAlister, N. E. Erickson, and R. E. Watson, Science **184**, 563 (1974).
[7] P. M. Stefan, M. L. Shek, I. Lindau, W. E. Spicer, L. I. Johansson, F. Herman, R. V. Kasowski, and G. Broyen, Phys. Rev. B **29**, 5423 (1984).
[8] J. J. Jia, T. A. Callcott, J. Yurkas, A. W. Ellis, F. J. Himpsel, M. G. Samant, J. Stöhr, D. L. Ederer, R. C. C. Perera, Rev. Sci. Instrum. **66** (2), 1394 (1995).
[9] J. H. Underwood, E. M. Gullikson, M. Koike, and P. J. Bodson, SPIE **3113**, 214 (1997).
[10] J. A. Carlisle, E. L. Shirley, E. A. Hudson, L. J. Terminello, T. A. Callcott, J. J. Jia, D. L. Ederer, R. C. C. Perrera, and F. J. Himpsel, Phys. Rev. Lett. **74** (7), 1234 (1995).
[11] J. J. Jia, T. A. Callcott, E. L. Shirley, J. A. Carlisle, L. J. Terminello, A. Asfaw, D. L. Ederer, F. J. Himpsel, and R. C. C. Perera, Phys. Rev. Lett. **76** (21), 4054 (1996).
[12] O. K. Anderson, Phys. Rev. B **12**, 3060 (1975).
[13] W. Kohn and L. J. Sham, Phys. Rev. **140**, A1133 (1965).
[14] L. Hedin and B. I. Lundqvist, J. Phys. C **4**, 2064 (1971).
[15] R. W. G. Wyckoff, *Crystal Structures*, Interscience, New York (1965).
[16] C. Kittel, *Introduction to Solid State Physics*, Wiley & Sons (1986).

[17] L. F. Mattheiss and D. R. Hamann, Phys. Rev. B **30** (4), 1731 (1984).
[18] F. Herman, R. V. Kasowski, P. M. Stefan, and W. E. Spicer, Bull. Am. Phys. Soc. **27**, 249 (1982).
[19] E. S. Alekseev, R. G. Arkhipov, and S. V. Popova, Phys. Status. Solidi B **110**, k151 (1982).
[20] V. P. Zhukov and V. A. Gubanov, Solid State Comm. **56** (1), 51 (1985).
[21] A. J. Liu and M. L. Cohen, Solid State Comm. **67**, 907 (1988).
[22] M. Rajagopalan, P. Saigeetha, G. Kalpana, ang B. Palanivel, Jpn. J. App. Phys. **33**, 1847 (1994).
[23] A. Cottrell, *Chemical Bonding in Transition Metal Carbides*, The University Press, Cambridge (1995).
[24] D. L. Price and B. R. Cooper, Phys. Rev. B **39** (8), 4945 (1989).
[25] V. A. Gubanov, A. L. Ivanovski, and V. P. Zhukov, *Electronic Structure of Refractory Carbides and Nitrides*, The University Press, Cambridge (1994).

Principal investigator: Shane Stadler, Tulane University. Email: shane@one.camd.lsu.edu.
Telephone: 504-766-1608.

Excitation Energy Dependent Soft X-ray Emission Experiments on Some Complex Oxides, and Sulfides and Irradiated Polymers

E.Z. Kurmaev,[1] S. Stadler,[2] R. Winarski,[2] D.L. Ederer [2] A. Moewes,[3] J. van Ek,[2] S. Shin,[4] M.M. Grush,[5] T.A. Callcott,[5] R.C.C. Perera[6]

[1]Institute of Metal Physics, Russian Academy of Sciences-Ural Division, 620219 Yekaterinburg GSP-170, Russia

[2]Tulane University, New Orleans, LA 70118

[3] Center for Advanced Microstructures and Devices, Baton Rouge, LA 70888

[4]Institute for Solid State Physics, The University of Tokyo, 3-2-1 Modoricho, Tanashi, Tokyo 188, Japan

[5]University of Tennessee, Knoxville , TN 37996

[6] Advanced Light Source, Lawrence Berkeley Laboratory, Berkeley, CA 94720

INTRODUCTION

We are in the midst of a new revolution in materials development, and the ability to measure their electronic properties by a photon probe. Of course the copper oxide perovskites and related compounds have been of intense interest for years because of the superconducting nature of many of these materials. More recently colossal magnetoresistance has been observed [1] in manganese oxides. In addition many of these compounds show very interesting phase changes as a function of temperature near 100K. Furthermore it has been shown that pressure induces a phase change in the perovskite $PrNiO_3$ and V_2O_3, where pressure produces an increase in the overlap of the oxygen-2p orbitals and the cation d-orbitals. [2,3] These effects were measured near the metal-antiferromagnetic insulator transition that occurs at approximately 100 K.[4] A recent use of inelastic x-ray scattering in V_2O_3 has revealed a plasmon like excitation at an energy loss of 12 eV which depends on the photon momentum transfer and another loss at 9.2 eV that is associated with a new type of valence band exciton. Measurements of this type compliment the photoemission measurements the were used to study V_2O_3 and obtain an insulating band gap of about 0.2 eV.[5] The compound V_2O_3 is important because it is an example of a classic Mott-Hubbard system in which an insulating gap forms because of short range interactions between the electrons and the atomic site. The electrical and magnetic properties of these materials are subject to delicate changes in the extent of nd orbitals as demonstrated in these experiments and more recently D.N. Argyriou *et al* [6]demonstrated that the compressibility in the Mn-O bonds of $La_{1.2}Sr_{1.8}Mn_2O_7$ change sign when traversing Tc. A detailed understanding of all these phenomena is still at the frontier of condensed matter physics.

In a broad collaboration with the Institute of Metal Physics in Yekaterinburg, Russia, Tulane University, University of Tennessee, the Center for Advanced Microstructures and Devices at LSU, and Lawrence Berkeley Laboratory, we have obtained X-ray fluorescence spectra and calculated the electronic structure of a number of compounds, including superconductors, magnetic materials, layered compounds having a perovskite structure, and irradiated polymer films in order to elucidate the electronic properties of some of these advanced materials. The excitation energy dependent measurements for a number of sample systems are summarized in the following paragraphs. Several of the materials studied will be highlighted in separate abstracts.

RESULTS:

1. Superconductors

The excitation energy dependence of the O Kα X-ray emission spectra (2p→1s transition) of the copperless oxide superconductor Sr_2RuO_4 has been measured near the O 1s absorption threshold at excitation photon energies between 529.2 and 543.7 eV.[7] Spectral features in the emission spectra are attributed to the excitation of inequivalent O(1) in-plane and O(2) apical oxygens. From these spectra we were able to deduce the distribution of the corresponding O 2p-density of states and compare our results with band structure calculations. We found a marked difference in the electronic structure of Sr_2RuO_4 and superconducting cuprates in that O(1) 2p-states are mixed with d(t_{2g})-states in Sr_2RuO_4 forming p-bonds.

2. Layered compounds having a perovskite structure

The sulfur $L_{2,3}$ X-ray emission spectra (3s→2p transitions) of $BaCo_{1-x}Ni_xS_2$ layered compounds having a perovskite structure were measured[8] near the 2p-threshold of sulfur at photon energies between 163.5 and 173.5 eV. The data are compared with soft x-ray photoemission (XPS) spectra and FLAPW band structure calculations of $BaNiS_2$ and $BaCoS_2$. By using various energies to excite the S $L_{2,3}$ emission, the distribution of S(2) and S(1)+S(2) 3s 3d partial density of states in the valence band of $BaCo_{1-x}Ni_xS_2$ compounds was mapped. Our spectra and calculations yielded evidence that Sulfur 3d-states participate in chemical bonding by hybridizing with Ni 3d-states.

3. Metal sulfides

The sulfur $L_{2,3}$ X-ray emission spectra of the transition metal sulfides, CuS, FeS_2 , and $CuFeS_2$ were excited by tunable synchrotron radiation near the sulfur 2p threshold.[9] An excitation energy dependence of the sulfur $L_{2,3}$ XES is only observed for CuS, and it is attributed to the presence of inequivalent sulfur atoms in CuS. Two thirds of the sulfur atoms form S_2 dimers (as in FeS_2) while the remaining sulfur atoms remain as monomers (as in $CuFeS_2$,) in accordance with XPS measurements and band structure calculations,[9] we have shown that selective excitation of valence band emission spectra can be used to determine the atom-decomposed partial density of states for inequivalent sites in solids, occupied by chemically identical species.

4. Electronic density of states of $Eu_{1-x}Co_xMnO_3$

The results of measurements of XPS, O 1s total fluorescence yield and fluorescence x-ray emission valence band spectra (O K and Mn $L_{2,3}$) near the O 1s and Mn 2p- absorption thresholds in the compound $Eu_{1-x}Co_xMnO_3$ are compared with LSDA and LDA+U band structure calculations.[10] We find that LSDA method is more accurate than the LDA+U approach for describing the spectroscopic properties of the orthorhombic $EuMnO_3$ system.

5. Emission from annealed sulfur compounds

Sulfur $L_{2,3}$ X-ray emission spectra, excited by synchrotron radiation at energies near the sulfur 2p threshold at photon energies between 163-165 eV, have been obtained[11] in samples containing 240 ppm S in Ni, annealed to 400-700 C. We found that S $L_{2,3}$ x-ray emission spectra (XES) of S-impurity atoms in Ni show a fine structure which can be simulated by a superposition of the sulfur $L_{2,3}$ spectrum from nickel sulfide and from pure sulfur. This suggests that the sulfur atoms are present after annealing both in solid solution and in clusters where they form S-S bonds. The variation of temperature and time of annealing (T=400 °C for 1 hr and T=700 °C for 2 hrs) leads to a redistribution of the intensity of the S $L_{2,3}$ x-ray emission valence band spectra,

which can be attributed to changes in the number of S-Ni and S-S bonds in accordance with the limit of sulfur solubility at these temperatures.

6. Carbon Kα emission from PI and PCS films

Fluorescent ultra-soft C Kα x-ray emission spectroscopy has been used[12] for the characterization of bonding configurations of C-atoms in polyamide (PI) films irradiated with N^+ and Ar^+ ions with doses ranging from $1x10^{14}$ to $1x10^{16}$ ions/cm^2, and polycarbosilane (PCS) films after annealing and irradiation with C^+ ions to a concentration of $5x10^{15}$ ions/cm^2. We found that the fine structure of C Kα x-ray emission of PI changes for concentrations greater than $1x10^{14}$ ions/cm^2, which we attribute to the degradation of polyamide films and creation of carbon clusters within the material. The width of the band gap for the heavily irradiated PI films, as determined from high-energy decrease of C Kα x-ray emission, decreases with increasing ion dose. This behavior correlates with an increase of conductivity due to polymer carbonization in these films. We find that the bonding configuration of C-atoms of PCS films after irradiation with C^+ ions at $5x10^{15}$ ions/cm^2 is close to that of a diamond-like films, while films receiving a treatment of annealing in addition to irradiation have an electronic structure more like silicidated graphite. Our observations suggest that annealing a PCS film at a temperature 1000 °C leads to the conversion of the annealed polycarbosilane films to a ceramic with a structure similar to that of amorphous $Si_{0.77}C_{0.23}$:H.

ACKNOWLEDGMENTS

The authors are especially grateful to the staff at the Center of Advanced Microstructures and Devices where the preliminary measurements took place, and to the staff at the Advanced Light source, whose dedicated efforts made these measurements possible.

REFERENCES

1. S. Jin, M. McCormack, R.A. Fastnacht, R. Ramesh, and L.H. Chen, Science **264**, (1994) 413.
2. P.L. Canfield, J.D. Thompson, S.-W. Cheong, and L.W. Rupp, Phys. Rev. B **47** (1993) 12357.
3. X. Obradors, L.M. Paulius, M.B. Maple, J.B. Torrance, A.I. Nazzal, I. Fontcuberta, and X. Granados, Phys. Rev. B **47** (1993) 12353.
4. E.D. Isaacs, P.M. Platzman, P. Metcalf, and J.M. Honig, Phys. Rev. Lettrs. **76**, 4211 (1996).
5. S. Shim, Y. Tezuka, T. Kinoshita, T. Ishii, T. Kashiwakura, and Y. Suda, J. of the Phys. Soc. Japan, **64** (1995) 1230.
6. D.N. Argyriou, J.F. Mitchell, J.B. Goodenough, O. Chmaisse, S. Short, and J.D. Jorgensen, Phys. Rev. Lettrs. **78** (1997) 1568.
7. E.Z.Kurmaev, S.Stadler, D.L.Ederer, Y.Harada, S.Shin, M.M.Grush, T.A.Callcott, R.C.C.Perera, M.Kasai, Y.Tokura, T.Takahashi, Phys. Rev. B **57** (1998) 1558 .
8. E.Z.Kurmaev, S.Stadler, D.L.Ederer, Y.Hase, Yu.M.Yarmoshenko, M.Neumann, D.A.Zatsepin, A.Fujimori, M.Sato, R.C.C.Perera, M.M.Grush, T.A.Callcott, Phys. Lett. A **235** (1997) 191.
9. E.Z.Kurmaev, J. van Ek, D.L.Ederer, L.Zhou, T.A.Callcott, R.C.C.Perera, V.M.Cherkashenko, S.N.Shamin, V.A.Trofimova, S.Bartkowski, M.Neumann, A.Fujimori, and V.P.Moloshag, J. Phys.: Condens. Matter **10** (1998) 1687-1697.
10. E.Z.Kurmaev, V.M.Cherkashenko, M.Neumann, S.Stadler, D.L.Ederer, Y.M.Mukovski, I.V.Solovyev, N.A.Ovechkina, V.R.Galakhov, A.Fujimori, M.M.Grush, T.A,Callcott, and

R.C.C.Perera, J. Electron Spectroscopy and Related Phenomena, 1998 (accepted for publication).
11. E.Z.Kurmaev, S.Stadler, D.L.Ederer, Yu.M.Yarmoshenko, D.A.Zatsepin, M.Neumann, T.A.Callcott, M.M.Grush, R.C.C.Perera, S.E.Danilov, and V.L.Arbuzov, (submitted to Mater. Transactions).
12. R.Winiarski, D.L.Ederer, E.Z.Kurmaev, S.N.Shamin, A.Moewes and J.-C.Pivin (to be published).

This work was supported by the Russian State Program "Atomic and Spatial Structures," Russian Science Foundation for Fundamental Research (Project 96-15-96598), a NATO Linkage Grant (HTECH.LG 971222), INTAS-RFBR (95-0565), National Science Foundation grants DMR-9017997 and DMR-9420425, the Science Alliance Center for Excellence Grant from the University of Tennessee and a DoE-EPSCor cluster research grant DoE-LEQSF (1993-95)-03. The final experiments were conducted at the Lawrence Berkeley National Laboratory Advanced Light Source, which is supported by the office of Basic Energy Sciences, U.S. Department of Energy, under contract no. DE-AC03-76SF00098.

Principal investigators: Institute of Metal Physics, Russian Academy of Sciences-Ural Division, 620219 Yekaterinburg GSP-170, Russia, e-mail: kurmaev@ifmlrs.uran.ru, David L. Ederer, Physics Department, Tulane University, New Orleans, LA 70118. E-mail dlederer@mailhost.tcs.tulane.edu and Thomas A. Callcott, Physics Department, University of Tennessee-Knoxville,TN 37996. E-mail : tcallcott@utk.edu

Experimental and Theoretical Investigation of the Electronic Structure of Transition Metal Sulfides: CuS, FeS_2, and $FeCuS_2$

E.Z.Kurmaev[1], J.van Ek[2], D.L.Ederer[2], L.Zhou[3], T.A.Callcott[3], R.C.C.Perera[4], V.M.Cherkashenko[1],S.N.Shamin[1], V.A.Trofimova[1], S.Bartkowski[5], M.Neumann[5], A.Fujimori[6] and V.P.Moloshag[7]

[1]Institute of Metal Physics, Russian Academy of Sciences-Ural Division, 620219 Yekaterinburg GSP-170, Russia

[2]Department of Physics, Tulane University, New Orleans, LA 70118, USA

[3]Department of Physics, University of Tennessee, Knoxville, TN 37996, USA

[4]Lawrence Berkeley Laboratory, Berkeley, CA 94720, USA

[5]Universität Osnabrück, Fachbereich Physik, D-49069 Osnabrück, Germany

[6]Department of Physics, University of Tokyo, Hongo, Bunkyo-Ku, Tokyo 113, Japan

[7]Institute of Geology and Geochemistry, Russsian Academy of Sciences- Ural Division, 620151 Yekaterinburg, Russia

INTRODUCTION

Recent developments in instrumentation and synchrotron radiation sources give a new impulse to the study of the electronic structure of solids with the aid of soft X-ray emission spectroscopy (XES).[1-2] As a result of the high brightness of third generation synchrotron sources, the intensity of fluorescence X-ray emission in the soft X-ray energy range (where non-radiative decay processes of core vacancy states dominant[3]) has increased. This makes it possible to study the electronic structure of impurity atoms in different materials.[4-5] Use of tunable synchrotron radiation for excitation of XES has several advantages for the study of the electronic structure. First, selective excitation of XES avoids the overlap of satellites and valence spectra that originate from transitions into the spin-orbit split core levels ($L_{2,3}$, $M_{2,3}$, $M_{4,5}$ etc.). This is important for the analysis of the density of states (DOS) in the vicinity of the Fermi level in 3d, 4d and 5d transition metal alloys and compounds.[6] Second, chemically identical atoms at inequivalent sites in the crystal can be subsequently excited as the excitation energy increases. Hence, the local electronic structure of atoms with electrons in states at slightly different binding energies can be determined.[7-9]

The present paper describes how tunable synchrotron radiation was used for selective excitation of inequivalent sulfur atoms in CuS. Thus, for the first time, the sulfur $L_{2,3}$ XES of S_1 atoms that form S_2-dimers is measured separately. The obtained results compare favorably with the density of states determined from density functional band structure calculations. This study is an illustration of the power of combining XES and photoelectron spectroscopy (PES) with band calculations to determine the partial site-specific density of states.

RESULTS

While we made measurements and calculations on FeS_2, $FeCuS_2$, and CuS, we will just present our results for CuS to illustrate the point that combining XES and PES with calculations is a powerful method toward the elucidation of the electronic structure of a great number of materials. The details of the measurements and the calculations can be found in the publication.[10]

Our PES and XES measurements and our calculations were consistant with the assertion that in $FeCuS_2$ the sulfur atoms occupy the sulfur sites as single atoms, while in FeS_2 the sulfur atoms occupy the sulfur sites as dimers.

An excitation energy dependence of the sulfur $L_{2,3}$ x-ray emission spectra led us to make core photoemission measurements and calculations. LMTO calculations were used as an aid along with the measurements on the FeS_2 and $FeCuS_2$ compounds to aid in the interpretation of the energy dependence of the soft x-ray and photoelectron spectra. From these results we were led to the conclusion that two thirds of the sulfur atoms form dimers while the remaining sulfur atoms are single. The results of the calculations and the measurements for the XPS and XES are shown in the accompanying figure. In this figure the two different sulfur sites show up as a broadening of the sulfur L spectra taken at 163.5 eV. One can also see how the sulfur d states hybridize with the copper by comparing the copper L emission spectrum with the sulfur L: spectrum. This figure is an excellent example of how calculation s and site specific spectroscopes can be used to map out a relative density of states of different symmetries. It would be an important contribution to be able to put these spectra on a absolute intensity scale and that serves as a future challenge.

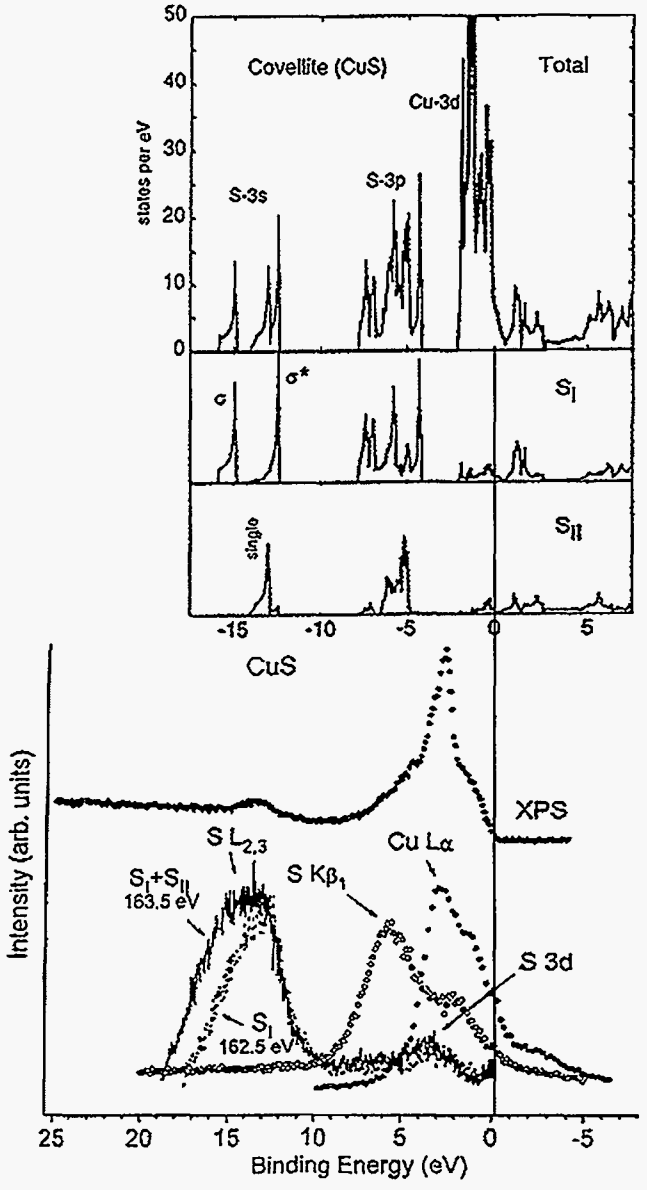

Figure 1. Photoemission and SX emission spectra for the Cu-L_1, S-K, S_I-$L_{2,3}$ and (S_I+S_{II})-$L_{2,3}$ spectra compared with calculated densities of states. The data show good agreement and clearly resolve the contributions of sulfur in two dissimilar sites.

ACKNOWLEDGMENTS

The authors are especially grateful to the staff at the Center of Advanced Microstructures and Devices where the preliminary measurements took place, and to the staff at the Advanced Light source, whose dedicated efforts made these measurements possible.

REFERENCES

1. T.A.Callcott, J.J.Jia, L.Zhou,D.L.Ederer, L.J.Terminello, J.A.Carlise, R.C.C.Perera, M.G.Samant, F.J.Himpsel, and E.T.Arakawa, Mat. Res. Soc. Symp. Proc. **437**, 137 (1996)
3. E.J.Nordgren, J. Electr. Spectr. Relat. Phenom. **78** , 25 (1996)
4. M.O.Krause, At. Nucl. Data Tables, J. Chem. Phys. Ref. Data **8**, 307 (1979)
5. K.Lawniczak-Jablonska, J.J.Jia, L.Lin, M.M.Grush, T.A.Callcott, A.Astaf, J.A.Carlise, L.J.Terminello, F.J.Himpsel, D.L.Ederer, J.H.Underwood, and R.C.C.Perera, Applied Physics A **65**, 173 (1997)
6. E.Z.Kurmaev, S.Stadler, D.L.Ederer, Yu.M.Yarmoshenko, D.A.Zatsepin, M.Neumann, T.Callcott, M.M.Grush, R.Perera, S.E.Danilov and V.L.Arbuzov (submitted to J. Mater. Res.)
7. E.Z.Kurmaev, Yu.M.Yarmoshenko, M.Neumann, S.Stadler, D.L.Ederer, I.Hase, A.Fujimori, M.Sato, R.C.C.Perera, M.M.Grush, T.A.Callcott, D.A.Zatsepin, V.A.Trofimova, and V.Sokolov (to be published)
8. J.-H.Guo, S.M.Butorin, N.Wassdahl, P.Skytt, J.Nordgren, and Y.Ma, Phys. Rev. B **49**, 1376 (1994)
9. S.M.Butorin, J.-H.Guo, N.Wassdahl, P.Skytt, J.Nordgren, Y.Ma, C.Ström, L.-G.Johansson, and M.Qvarford, Phys. Rev. B **51**, 11915 (1995)
10. E.Z.Kurmaev, J. van Ek, D.L.Ederer, L.Zhou, T.A.Callcott, R.C.C.Perera, V.M.Cherkashenko, S.N.Shamin, V.A.Trofimova, S.Bartkowski, M.Neumann, A.Fujimori, and V.P.Moloshag, J. Phys.: Condens. Matter **10** (1998) 1687-1697.

This work was supported by the Russian State Program "Atomic and Spatial Structures," Russian Science Foundation for Fundamental Research (Project 96-15-96598), a NATO Linkage Grant (HTECH.LG 971222), INTAS-RFBR (95-0565), National Science Foundation grants DMR-9017997 and DMR-9420425, the Science Alliance Center for Excellence Grant from the University of Tennessee and a DoE-EPSCor cluster research grant DoE-LEQSF (1993-95)-03. The final experiments were conducted at the Lawrence Berkeley National Laboratory Advanced Light Source, which is supported by the office of Basic Energy Sciences, U.S. Department of Energy, under contract no. DE-AC03-76SF00098.

Principal investigators: **E.Z. Kurmaev**, Institute of Metal Physics, Russian Academy of Sciences-Ural Division, 620219 Yekaterinburg GSP-170, Russia, e-mail: kurmaev@ifmlrs.uran.ru; **David L. Ederer**, Physics Department, Tulane University, New Orleans, LA 70118. E-mail dlederer@mailhost.tcs.tulane.edu; and **Thomas A. Callcott**, Physics Department, University of Tennessee-Knoxville,TN 37996. E-mail : tcallcott@utk.edu

Graphitization of CVD Diamond Thin Film by X-Ray Synchrotron Radiation

Kwang Yong Eun[1], Young-Joon Baik[1], Clemens Heske[2], Simone Anders[2]

[1]Thin Film Research Center, Korea Institute of Science and Technology,
P. O. Box 131, Cheongryang, Seoul, 130-650, Korea

[2]Advanced Light Source, Ernest Orlando Lawrence Berkeley National Laboratory, Berkeley, CA 94720, USA

INTRODUCTION

CVD diamond films are attracting widespread interest due to their potential applications ranging from wear resistant coatings and thermal spreaders to optical and micro-electronic parts. The quality of the diamond films has recently been improved significantly by increasing the plasma density of the CVD deposition region, and nearly flat, polycrystalline diamond films with well aligned (100) surfaces can be obtained by bias-enhanced nucleation treatment and a controlled growth process [1-4]. It is, however, still very difficult to define the diamond quality quantitatively and to understand the various impurity distributions in the polycrystalline CVD diamond precisely. Raman spectroscopy has been the most popular analysis method to know the impurity of graphite and amorphous carbon relatively to diamond but it has some limitations to determine the quantitative amount clearly. Polycrystalline CVD diamond films have many defects like twins, vacancies, inclusions, grain boundaries, and surface imperfections, and in these defect areas some structural defects of graphite and/or amorphous carbon can easily be included. The near edge x-ray absorption fine structure (NEXAFS) analysis of the C K-edge is a very useful method to differentiate the carbon bonds (sp^1, sp^2, and sp^3) more exactly. For the understanding of CVD diamond films, several NEXAFS studies were performed and the basic differece from graphite and amorphous carbon were determined[5-8], but quantitative analysis of the graphite component in diamond has not seen yet.

During the NEXAFS study of various grades of CVD diamond films, we observed the change of peak shape and height. This change showed clearly the graphitization of the diamond films by x-ray synchrotron radiation damage. To study this phenomena more clearly, we increased radiation time and radiation intensity and observed the structure variation.

EXPERIMENTAL

Diamond films were synthesized on a silicon wafer by microwave plasma CVD process. During the deposition, 4000W power was applied and the substrate temperature was kept at 950°C. Gas pressure and composition was 110 Torr and 6% methane and 94% hydrogen, respectively. Deposition was performed for 15 minutes and the diamond film thickness was 0.67μm.

NEXAFS measurements were done at the photo-emission electron microscope situated at the undulator beamline 8.0 of the ALS. Exposure time was accumulated by repeated NEXAFS measurement. After five repeated measurement, the entrance and exit slit of the beamline were completely opened and maximum radiation was applied for 10 minutes before the sixth and seventh measurement, respectively. The mean photon number per second was calculated by averaging the integration of the I_0 current data, and the total photon number was calculated by accumulating the applied radiation time.

RESULTS and DISCUSSION

The diamond film synthesized in the microwave plasma CVD process showed gray color but the very good quality of diamond was obtained, as shown in the Raman spectrum in Fig.1, even though the high methane gas composition was applied. The sharp peak at a wave number of 1332cm^{-1} has very narrow full width at half maximum, which means that the diamond quality is very good. Also, a broad and very low peak around the wave number of 1550 cm^{-1} exhibits that a very small amount of graphite and/or amorphous carbon exists in the diamond film.

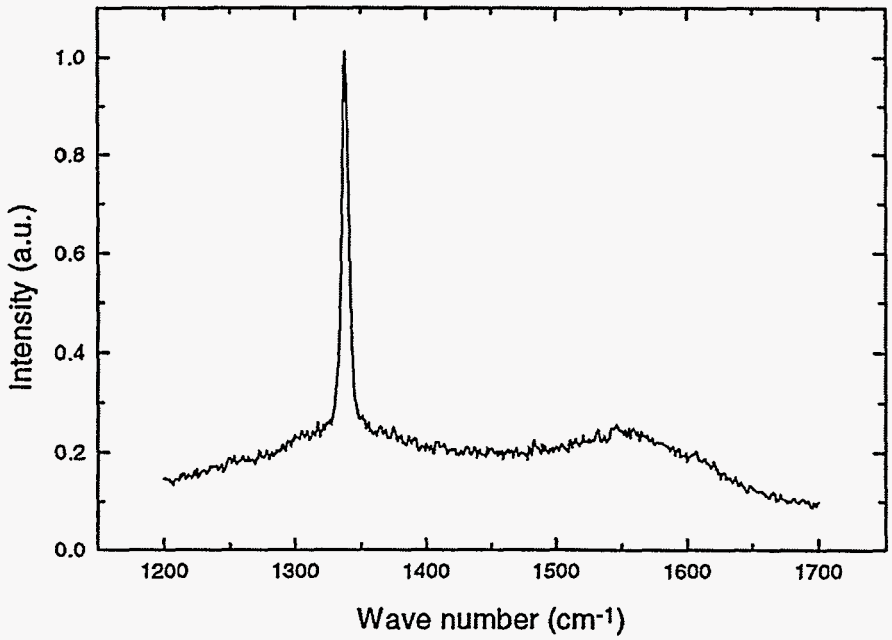

Fig.1. Raman spectrum of CVD diamond film synthesized at 950°C and with 6% methane gas composition at a pressure of 110 Torr.

NEXAFS measurements were performed by repeated energy scans. The measured NEXAFS plots are summarized in Fig.2. The number written on each curve indicates the total number of accumulated photons radiated on the film sample. All carbon K-edge spectra showed similar peaks in the range between 285 eV to 315 eV but the peak height varied. The first spectrum of original film showed a typical diamond spectrum except for a small amount of sp^2 component. This is consistent with the Raman spectra of Fig.1. As the radiation on the film increased, the sp^2 peak at 285 eV increased and the typical diamond peak between 289 eV and 310 eV decreased gradually. Even after the severe radiation of 18×10^{17} photon, the typical diamond peaks including the exciton peak at 289 eV remained visible. When the radiated surface was investigated by optical microscope after NEXAFS measurements, a circle with about 200 μm diameter with a black core circle of 10 μm diameter was seen. The outer circle is consistent with the beam size and the inner circle seemed to be the area where the transformation from diamond to graphite occurred on the film surface. More analysis is needed to identify the radiated and graphitized surface but the surface of the diamond film in the irradiated center part clearly showed a transformation from diamond to graphite.

It is clear here that the diamond surface is very sensitive to radiation damage and that the structure analysis should be performed below a certain threshold number of photons. Graphitization of roughened diamond is reported to be possible at temperatures of more than 1500°C [9].

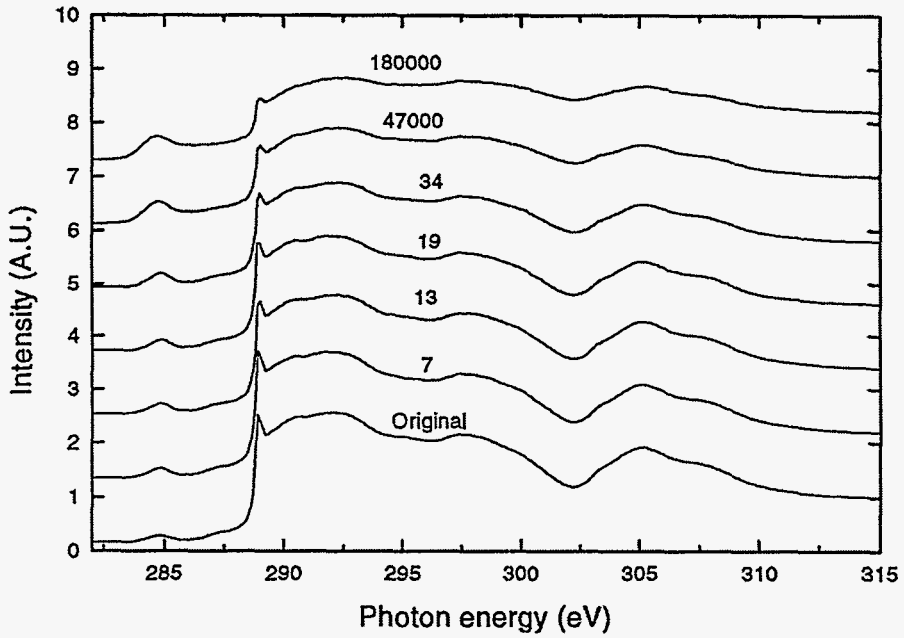

Fig.2. Carbon K-edge NEXAFS spectra for the diamond film which received x-ray synchrotron radiation repeatedly. The number on the curve is the accumulated number of irradiated photons which should be multiplied by 10^{13}.

CONCLUSION

Diamond thin films were synthesized by microwave plasma CVD and carbon K-edge NEXAFS measurement were performed. During NEXAFS measurements, radiation damage was observed and a graphitization of the diamond film surface was detected. For quality analysis of diamond films by measuring the sp^2 component, x-ray synchrotron radiation exposure should be limited by a threshold number of photons, which should be determined for each individual case.

REFERENCES

1. B. R. Stoner, G. H. Ma, S. D. Wolter, J. T. Glass, Phys. Rev. B **45**, 11067 (1992).
2. S. Yugo, K. Semoto, K. Hoshina, T. Kimur, H. Nakai, Diamond Relat. Mater. **4**, 903 (1995).
3. J. Gerber, J. Robertson, S. Sattel, H. Ehrhardt, Diamon Relat. Mater. **5**, 261 (1996).
4. C. Wild, R. Kohl, N. Herres, W. Muller-Sebert, P. Koidl, Diamond Relat. Mater. **3**, 373 (1994).
5. G. Comelli, J. Stohr, C. J. Robinson, W. Jark, Phys. Rev. B **38**, 7511 (1988).
6. M. Jaouen, G. Tourillon, J. Delafond, N. Junqua, G. Hug, Diamond Relat. Mater. **4**, 200 (1995).
7. D. M. Gruen, A. R. Kraus, C.D. Zuiker, R. Csencsits, L. J. Terminello, J. A. Carlisle, I. Jimenez, D. G. J. Sutherland, D. K. Shuh, W. Tong, F. J. Himpsel, Appl. Phys. Lett. **68**, 1640 (1996).
8. F. L. Coffman, R. Cao, P. A. Pianetta, S. Kapoor, M. Kelly, L. J. Terminello, Appl. Phys. Lett. **69**, 568 (1996).
9. B. N. Davidson, W. E. Pickett, Phys. Rev. B **49**, 14770 (1994).

This research was supported by the Laboratory Technology Research Partnership.Program, Office of Energy Research, U.S. Department of Energy under a CRADA (Cooperative Research and Development Agreement) between Lawrence Berkeley National Laboratory and IBM; and by the Director, Office of Energy Research, Office of Basic Energy Sciences, under U.S. DOE Contract DE-AC03-76SF00098.

Principal investigator: Simone Anders, Berkeley Lab. Email: sanders@lbl.gov. Telephone: 510-486-5928.

PEEM and NEXAFS studies of hard disks and sliders

Simone Anders[1], Thomas Stammler[1], C. Singh Bhatia[2], Joachim Stöhr[3], Walton Fong[4], Chao-Yuan Chen[4], David B. Bogy[4], and C. Heske[1]

[1]Advanced Light Source, Ernest Orlando Lawrence Berkeley National Laboratory, University of California, Berkeley, California 94720, USA

[2]SSD/IBM, 5600 Cottle Road, San Jose, CA 95193

[3]IBM Almaden Research Center, 650 Harry Road, San Jose, CA 95120

[4]Computer Mechanics Laboratory, Department of Mechanical Engineering, University of California, Berkeley, CA 94720

INTRODUCTION

X-ray Photo Emission Electron Microscopy (X-PEEM) and Near Edge X-ray Absorption Fine Structure (NEXAFS) spectroscopy are two modern analysis methods based on the availability of tunable X-ray radiation produced by a synchrotron. X-PEEM combines high spatial resolution with the ability to obtain local NEXAFS spectra. NEXAFS yields information about the elemental composition and bonding structure of the elements in the sample, and orientation of molecules (if a preferred orientation is present). All this information is obtained in a PEEM with submicron resolution, in addition to topological contrast which is present in a PEEM also.

Both methods have been applied to study the tribological behavior of the head/disk interface of magnetic storage devices. For storage devices with smaller and smaller spacing between slider and disk approaching pseudo-contact and contact-recording, the tribochemical properties of the system consisting of the carbon overcoat of the disk, the lubricant, and the slider surface (carbon coated or uncoated) become more and more important.

EXPERIMENTAL

Experiments have been performed at the undulator beamline 8.0 of the ALS. The monochromatized X-rays were focused by a Kirkpatrick-Baez pair of mirrors into a 200 μm diameter spot on the sample. The PEEM working principle is based on the electron emission caused by the X-ray illumination of the sample which is proportional to the X-ray absorption. The absorption is a function of the elemental and chemical state of the sample and the X-ray wavelength. An electron optical column forms an image of the emitted electrons. By tuning the X-rays through the absorption edge of the element of interest and taking images at incrementally increased photon energy it is possible to obtain locally resolved NEXAFS spectra with a resolution given by the resolution of the electron optics which is is about 200 nm for the microscope we used for the experiments described in this paper. The microscope is a two-lens system operating at a nominal voltage of 10 kV, and it is described in detail elsewhere [1].

RESULTS AND DISCUSSION

Studies of hard disks exposed to thermal desorption experiments

Samples from disks which were coated with 7.5 nm sputter deposited, nitrogenated amorphous hard carbon (CN_x) and lubricated with 0.85 nm perfluoropolyether (Z-dol) were exposed to a thermal desorption experiment. They were heated in UHV (base pressure $<10^{-6}$ Pa) up to 425°C for a duration of 10min. The desorbed gaseous products can be measured using a quadrupole mass spectrometer to determine the processes leading to the degradation of the lubricant due to thermal effects. We have studied the disks before and after the thermal desorption experiments using (not spatially resolved) NEXAFS spectroscopy in the total yield mode. Figure 1 shows the

carbon K edge (1a), fluorine K edge (1b), and nitrogen K edge (1c) spectra before and after heating of the disks.

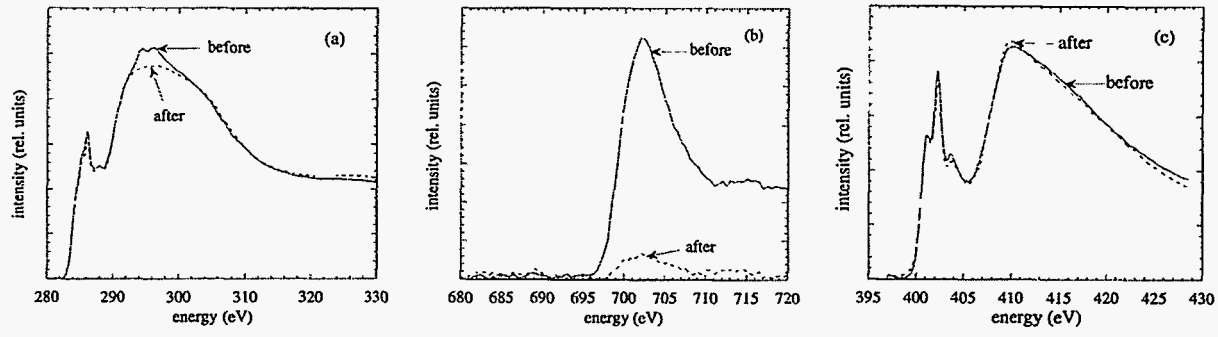

Figure 1: K edge NEXAFS spectra of (a) carbon, (b) fluorine, and (c) nitrogen, of a hard disks before (solid line) and after (dashed line) thermal desorption experiments.

The spectra were normalized to the X-ray beam current so that their relative intensity reflects the relative amount of the corresponding element on the surface of the disk. It can be seen in Figure 1a that the peaks which are characteristic for C=C π^* bonds at 285eV and σ bonds (broad peak around 300 eV) as well as the C=N peak around 286.2eV [3] and the C=O peak around 288.1eV [2] are not influenced by the heat treatment. The peaks at 294.5 and 296.3eV, respectively, which are due to C-F bonds [4, 5], practically disappear after the heating. The nitrogen spectra (Fig. 1c) show no modification within the accuracy of the measurements, but the fluorine signal (Fig. 1b) is reduced to 10% of its original value by the heating. The data indicate that the CN_x film is not modified in structure and composition by the heating, but 90% of the fluorine from the lubricant has been removed. This is in good agreement to FTIR measurements performed before and after the heating to determine the thickness of the lubricant which showed a thickness of 0.85 nm before and 0.08 nm after heating.

Study of wear tracks on disks

Supersmooth disks were coated with 5 nm cathodic arc deposited amorphous hard carbon and lubricated with 0.85 nm perfluoropolyether (Z-dol). They were used in a tribochamber wear test. The tribochamber is equipped with a spindle in UHV (base pressure < 10^{-6} Pa) and a quadrupole mass spectrometer to measure the erosion products during the wear test. The disks were worn in a continuous drag test with Advanced Air Bearing design sliders at a speed of 0.2 m/s and a load of 30 mN. Two kinds of sliders were used: uncoated sliders (Al_2O_3/TiC) and sliders coated with sputter deposited CH_x. After the wear test the disks were studied using the PEEM microscope.

Fig. 2a shows a PEEM image of the edge of the wear track. The scratch is caused by one of the rails of the slider. The image was taken at a photon energy of 280 eV which is below the carbon K edge, therefore the image contrast is mainly topological. Local NEXAFS spectra were taken in the undamaged area of the disk, at the edge of the wear track caused by the rail, and in the area between the rails. Fig. 2b shows the carbon K edge spectra and Fig. 2c the fluorine K edge spectra.

The spectra show that the carbon overcoat/lubricant are identical in the undamaged area and between the rails. At the edge of the wear track in the scratch caused by one of the rails the

fluorine is almost completely removed and the carbon spectrum shows a new peak at 288.5eV which can be attributed to the formation of carboxylic bonds [2].

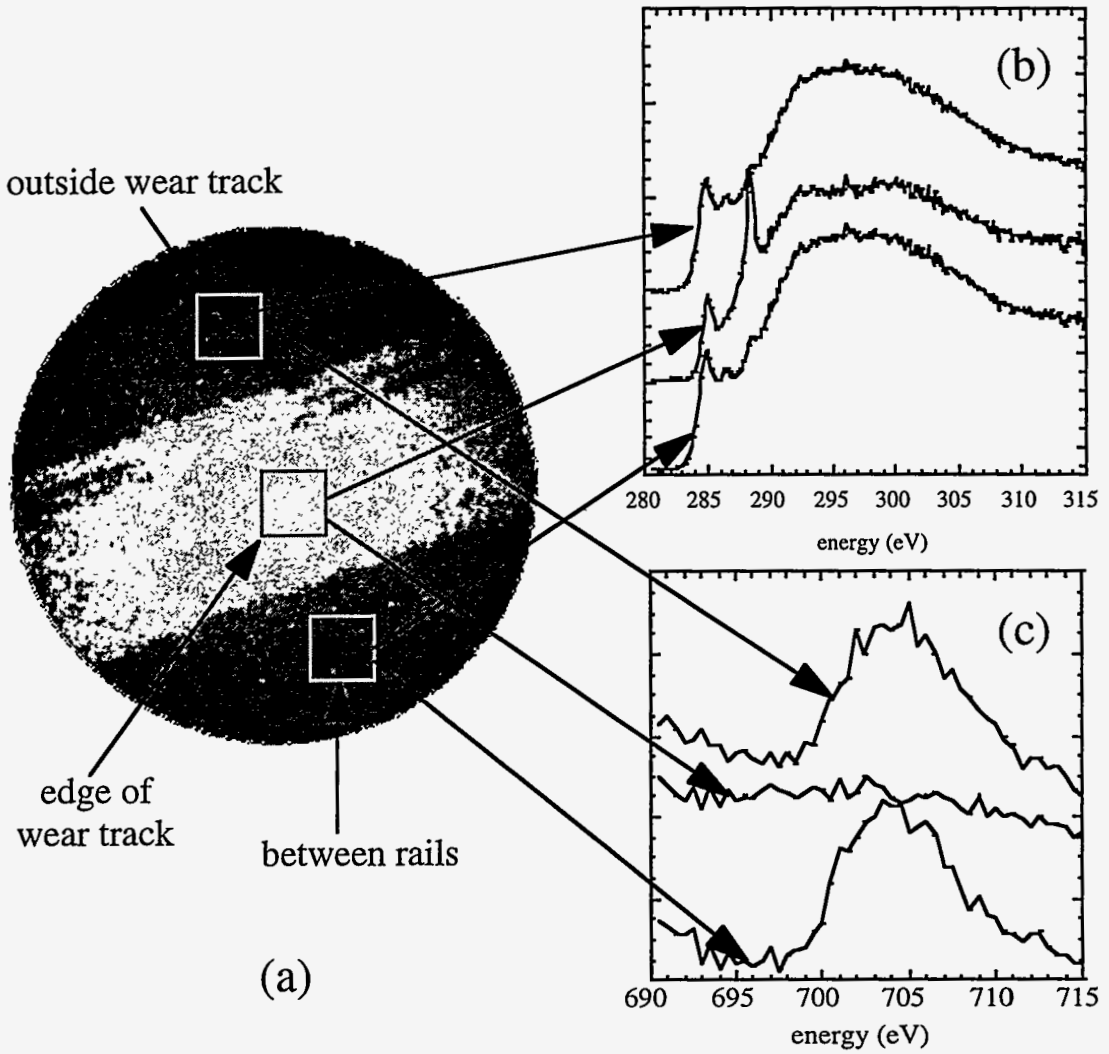

Figure 2: (a) PEEM image of the edge of a wear track taken at a photon energy of 280 eV. The field of view is 150µm. (b) Local carbon K edge NEXAFS spectra of indicated areas. (c) Local fluorine K edge NEXAFS spectra of indicated areas.

Study of slider surfaces

The sliders which were used to wear the disks in the tribochamber for the experiments described above were also investigated using the PEEM microscope. We observed a number of scratches at the slider surface of both, the coated and uncoated slider. Figure 3 shows the NEXAFS spectra at the carbon K edge, the oxygen K edge, and the titanium $L_{2,3}$ edge taken in one scratch and outside the scratch of an uncoated slider.

The carbon spectra show basically no carbon on the undisturbed slider surface but a strong signal in the scratch. The spectrum is very similar to the one observed at the edge of the wear track on the disk (Fig. 2b). The oxygen spectrum outside the scratch shows one peak probably connected to the Al_2O_3 of the slider material, but a strong, sharp additional peak around 539 eV appears inside the scratch that can be correlated to the presence of carboxyl bonds [2]. The titanium signal is much weaker in the scratch indicating that some material has been deposited on the surface. All

these data led us to conclude that material has been transferred from the disk to the slider, and this material is the same as the material at the edge of the wear track. It is probably some form of degraded lubricant which is formed during the wear.

On the coated slider we found undamaged CH_x in most of the areas, and observed the same kind of carbon K edge spectrum in scratches with the additional peak around 288.5eV as we found in scratches of uncoated sliders and at the edge of the wear tracks of the disks.

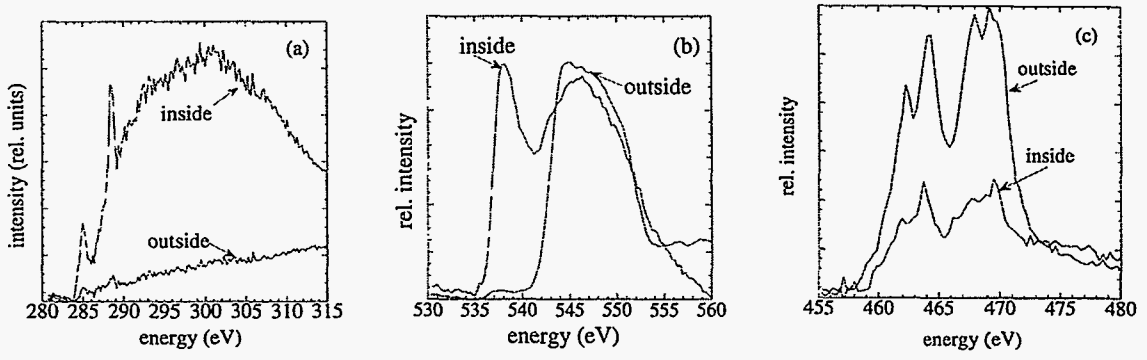

Figure 3: Local NEXAFS spectra at (a) carbon K edge, (b) oxygen K edge, and (c) Ti $L_{2,3}$ edge, taken inside and outside a scratch on a slider surface after wear.

CONCLUSIONS

The experiment which are presented here demonstrate that NEXAFS and PEEM are useful tools to study the problems of the head/disk tribology. It was found that the heating of disks lubricated with perfluoropolyether (Z-dol) up to 425°C for 10min. does not change the CN_x structure and elemental composition of the hard carbon overcoat of the disk, but 90% of the lubricant is removed during this process. Wear of disks lubricated with perfluoropolyether (Z-dol) leads to a strong reduction of the fluorine content in the worn areas and to the formation of new carboxyl bonds. Degraded lubricant showing the carboxyl peak in the carbon K edge spectrum was found also in scratches of coated and uncoated sliders.

REFERENCES

[1] B. P. Tonner, D. Dunham, T. Droubay, and M. Pauli, J. Electron Spectrosc. Relat. Phenom. **84** (1997) 211.

[2] J. Stöhr, NEXAFS Spectroscopy, Springer Verlag, New York, 1992.

[3] B. Holloway, Thesis, 1997

[4] Ch. Ziegler, Th. Schedel-Niedrig, G. Beamson, D. T. Clark, W. R. Salaneck, H. Sotobayashi, and A. M. Bradshaw, Langmuir **10** (1994) 4399.

[5] T. Ohta, K. Seki, T. Yokoyama, I. Morisada, and K. Edamatsu, Physica Scripta **41** (1990) 150.

This work was supported by the Director, Office of Energy Research, Office of Basic Energy Sciences, Materials Science Division, of the U.S. Department of Energy under Contract No. DE-AC03-76SF00098. It was also supported by the Computer Mechanics Laboratory, Mechanical Engineering Department, U.C. Berkeley, and by the National Storage Industry Consortium (NSIC).

Principal investigator: Simone Anders, Advanced Light Source, Ernest Orlando Lawrence Berkeley National Laboratory. Email: SAnders@lbl.gov. Telephone: 510-486-5928.

PEEM studies of thin film bilayers and blends of polystyrene and brominated polystyrene

Simone Anders[1], Thomas Stammler[1], Harald Ade[2], Dan Slep[3], Jonothan Sokolov[4], Miriam Rafailovich[4], Clemens Heske[1], and Joachim Stöhr[5]
[1]Advanced Light Source, Ernest Orlando Lawrence Berkeley National Laboratory, University of California, Berkeley, California 94720, USA
[2]Department of Physics, North Carolina State University, Raleigh, NC 27695-8202
[3]Advanced Development and Research, Hilord Chemical Corp., Hauppauge, NY11788
[4]Materials Science and Engineering, SUNY@Stony Brook, Stony Brook, NY11794
[5]IBM Almaden Research Center, 650 Harry Road, San Jose, CA 95120

INTRODUCTION

Thin films of polymers have considerable technological importance and are used in numerous applications such as multi-color photographic printing, adhesives, indexed matched optical coatings, and low dielectric electronic packaging. Dewetting and decomposition phenomena of blends and bilayers are crucial for the use of these polymers in, for example, colloidal paint systems where wetting controls the dispersion of color pigments. Compared to bulk properties, relatively little is known about the properties of polymer thin films and surfaces. A detailed understanding of thin film properties, such as composition and morphology, is highly desirable and numerous studies on blends [1-7] and bilayers [8, 9] have recently been undertaken. Most of these studies rely on Atomic Force Microscopy or other methods that do not provide quantitative compositional maps. Hence, blends and bilayers of polystyrene (PS) and brominated polystyrene (PBrS) have recently been studied using the scanning transmission X-ray microscope (STXM) at the National Synchrotron Light Source. STXM provides quantitative composition maps integrated along the direction of the surface normal. These studied [10] reveal the morphology formed as the PS and PBrS phase separates, as well as the morphology that forms as the PBrS dewetts the PS substrate layer during annealing at elevated temperature. For example, as the PBrS dewetts, round holes form first and subsequently grow in size until they impinge on each other and a network of spines is formed. Upon further annealing, the spines break up and coalesce into drops of PBrS. A thin layer of PS remains present throughout the sample which is much thinner than the original PS layer thickness. STXM data shows that PS wetts the spines of PBrS and forms rather thick and tall walls around PBrS spines. STXM data even indicates that the PS is actually encapsulating the PBrS at this point of the dewetting, even though the PBrS started out on top. However, STXM could not conclusively show that encapsulation ocurs, as it can not distinguish the surface from the subsurface polymer. We have thus utilized Photoemission Electron Microscopy (PEEM) at the Advanced Light Source to determine the composition of the surface of various PS/PBrS thin films. PEEM combined with tunable X-ray illumination provides the ability to obtain local Near Edge X-ray Absorption Fine Structure (NEXAFS) spectra in the total yield mode with 200 nm spatial resolution. For polymers, this provides information about the composition and bonding on the sample surface with a probing depth of about 10 nm.

EXPERIMENTAL

Experiments have been performed at beamline 8.0 of the ALS. A Kirkpatrick-Baez pair of mirrors was used to focus the monochromatized X-rays into a 200 μm diameter spot on the sample. The electron optical column of the microscope is used to form an image of the emitted electrons. The microscope is a two-lens system operating at a nominal voltage of 10 kV, and it is described in detail elsewhere [11]. The electron emission caused by the X-rays is proportional to the X-ray absorption. The absorption is a function of the elemental and chemical state of the sample and the

X-ray wavelength. By tuning the X-rays through the absorption edge of the element of interest and taking images at incrementally increased photon energy it is possible to obtain locally resolved NEXAFS spectra with a resolution given by the resolution of the electron optics (200 nm).

Blends and bilayers of PS and PBrS on silicon substrates were used for these studies. The blends contained 50% PS and 50% PBrS and had a total thickness of 43 nm, the bilayers consisted of a 30 nm thick PBrS layer on top of a 30 nm thick PS layer produced by spin casting. For the bilayers, the PS and PBrS were prepared separately, and then the PBrS layer was floated on top of the PS layer. The samples were annealed for different durations at 180°C in a vacuum oven. After annealing the samples were investigated in the PEEM microscope.

RESULTS AND DISCUSSION

Figure 1 shows the (not spatially resolved) NEXAFS spectra at the carbon K edge of the blend and the bilayer before annealing. The first peak at 285eV can be identified as the PS π* resonance [10], and it is the dominant feature in both spectra. The peak which is characteristic for the PBrS π* resonance at 286.3eV is only present in the spectrum of the bilayer which has the PBrS layer on the surface. The blend of 50% Ps and 50% PBrS does not show this resonance. The process of blending and spin casting these two polymers from a toluene solution already initiates the decomposition and the formation of a PS top layer.

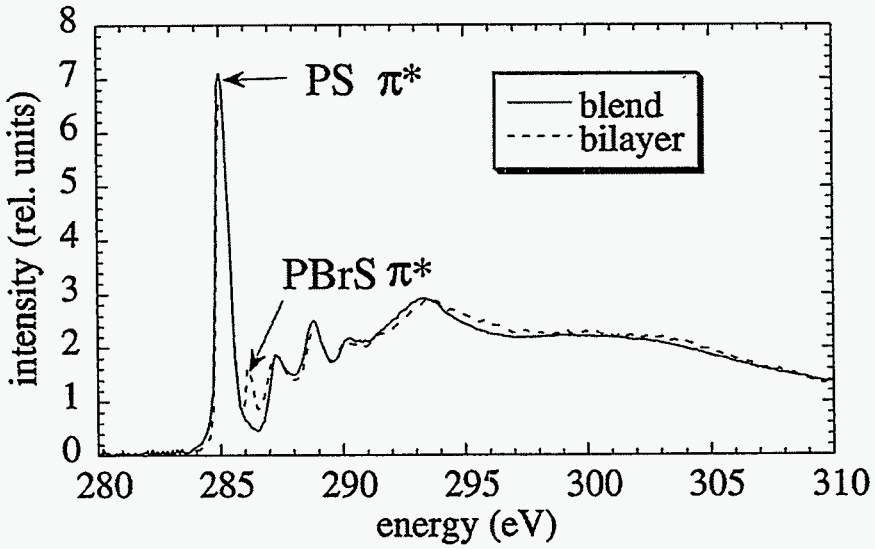

Figure 1: NEXAFS carbon K edge spectra (integrated over a 200 μm spot) of PS/PBrS blend and bilayer before annealing.

Figure 2 shows the NEXAFS carbon K edge spectra of the bilayer after annealing of various duration. The PBrS π* resonance is still visible after 1 hour of annealing, slightly weaker after 2 days of annealing, and not present anymore after 11 days of annealing.

PEEM microscopy of the 2 days annealed sample confirms that the dewetting process starts locally in small areas. Figure 3a shows a PEEM image of the 2 days annealed sample where we observed a contrast variation in a small spot when the area was imaged at the PS π* resonance and the PBrS π* resonance wavelength. The spot appeared in the same brightness as the surrounding at the PS π* resonance, and dark at the PBrS π* resonance. The image in Figure 3a is acquired at

286.3eV (PBrS π* resonance, spot dark). Local NEXAFS spectra were acquired in the spot (Figure 3b, graph 1) and in two adjacent areas outside the spot (Figure 3b, graphs 2 and 3) for reference. The spectra show that in the spot the underlaying PS layer is exposed as the PBrS dewetts, whereas outside the spot the PBrS is still at the surface.

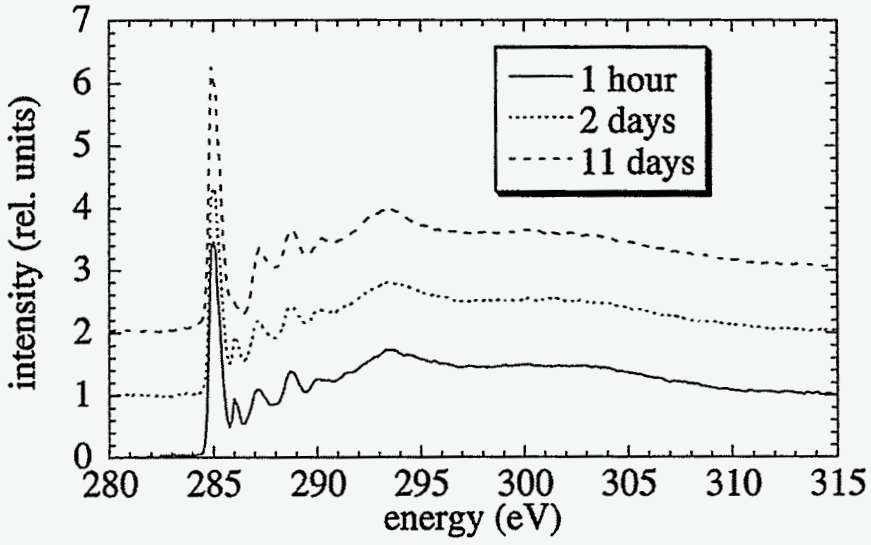

Figure 2: NEXAFS carbon K edge spectra (integrated over a 200 μm spot) of PS/PBrS bilayer after annealing at 180°C of various duration. Spectra are offset for better clarity.

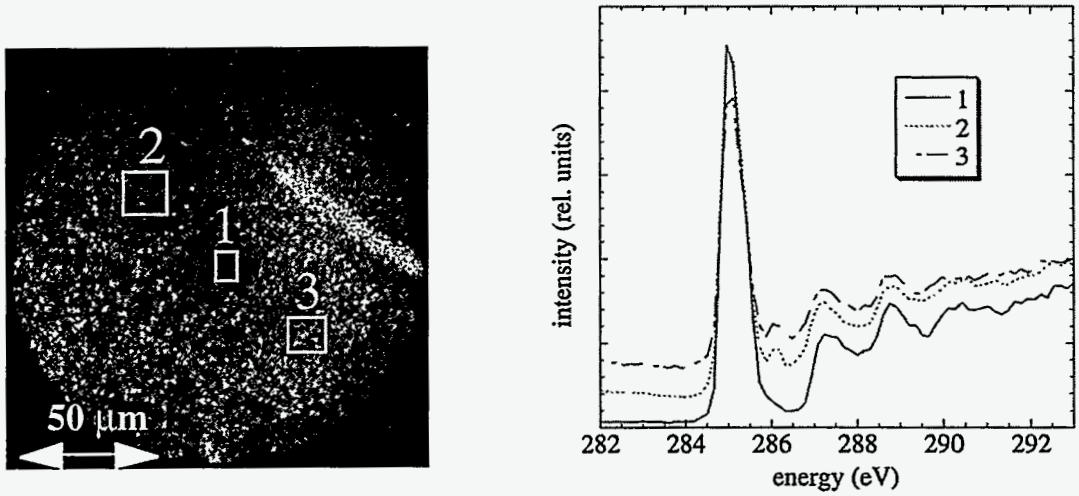

(a) (b)

Figure 3: (a) PEEM image of a 2 days annealed PS/PBrS bilayer taken at 286.3eV. The image indicates the 3 areas where the local NEXAFS spectra were taken. (b) Local carbon K edge NEXAFS spectra of the areas in (a). Spectra offset for clarity.

Images acquired of bilayers annealed for longer duration (Figure 4a) show the same network of spines as observed with STXM. Contrast is based soly on topography, and no chemical contrast was observed. In all areas at the surface only PS was found (Figure 4b).

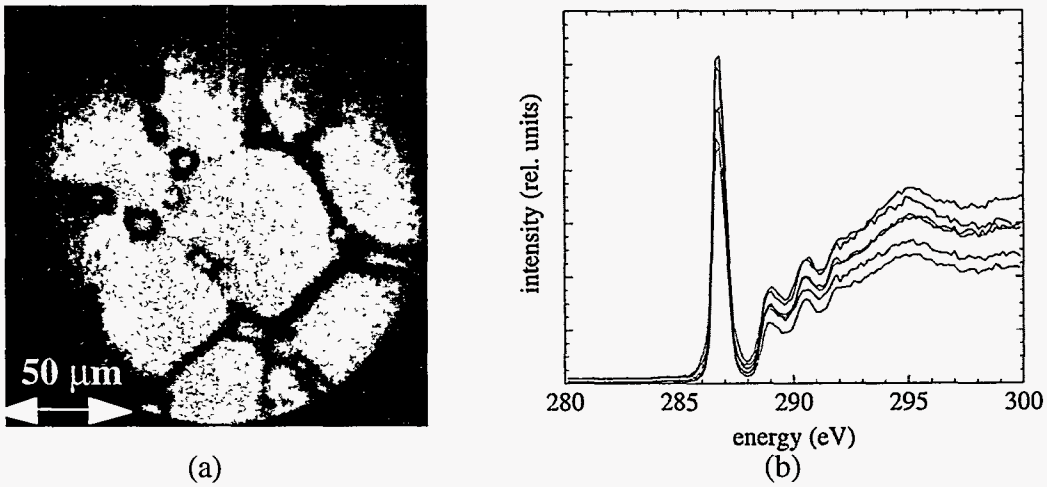

Figure 4: (a) PEEM image of a 4 days annealed PS/PBrS bilayer taken at 286.3eV. (b) Local carbon K edge NEXAFS spectra taken at 6 different areas of (a). None of the spectra shows the PBrS π^* resonance at 286.3eV.

CONCLUSIONS

The PEEM results showed that the dewetting of the PBrS polymer from the PS sublayer initially exposes a pure PS surface in small areas, while in most areas PBrS is still present at the surface. The formation of spines as the dewetting progresses was observed with both methods. STXM could identify that the spines are composed of PBrS, but only PEEM observation could show that these PBrS spines are covered by a thin PS layer. The combination of these two methods allows the study of complex polymer systems, and both methods yield complementary imnformation which, if combined, give a complete understanding of the processes taking place during dewetting of the polymer systems.

REFERENCES

[1] J. Genzer, E. J. Kramer, Phys. Rev. Lett. 78, 4946-4949 (1997).
[2] S. Affrossman, G. Henn, S. A. O'Neill, R. A. Pethrick, M. Stamm, Macromol 29, 5010-5016 (1996).
[3] E. Kumacheva, L. Li, M. A. Winnik, D. M. Shinozaki, P. C. Cheng, Langmuir 13, 2483-2489 (1997).
[4] G. Krausch, E. J. Kramer, M. H. Rafailovich, J. Sokolov, Appl. Phys. Lett. 64, 2655-2657 (1994).
[5] W. Straub, et al., Europhysics Letters 29, 353-358 (1995).
[6] K. Tanaka, A. Takahara, T. Kajiyama, Macromol 29, 3232-3239 (1996).
[7] S. Wahlheim, M. Boltau, J. Mlynek, G. Krausch, U. Steiner, Macromol 30, 4995-5003 (1997).
[8] P. Lamboony, K. C. Phelan, O. Haugg, G. Krausch, Phys. Rev. Lett. 76, 1110 (1996).
[9] S. Qu, et al., Macromolecules 30, 3640-3645 (1997).
[10] D. A. Winesett, H. Ade, A. P. Smith, M. Rafailovich, S. Sokolov, and D. Slep, Microscopy and Microanalysis, to be published (1998).
[11] B. P. Tonner, D. Dunham, T. Droubay, and M. Pauli, J. Electron Spectrosc. Relat. Phenom. **84** (1997) 211.

This work was supported by the Director, Office of Energy Research, Office of Basic Energy Sciences, Materials Science Division, of the U.S. Department of Energy under Contract No. DE-AC03-76SF00098. HA is supported by an NSF Young Investigator Award (DMR-9458060).

Principal investigator: Simone Anders, Advanced Light Source, Ernest Orlando Lawrence Berkeley National Laboratory. Email: SAnders@lbl.gov. Telephone: 510-486-5928.

Photon energy dependence of the vibrational fine structure in the C1s line of c(2x2)CO/Ni(100) in the threshold region

A. Föhlisch, J. Hasselström, O. Karis, N. Wassdahl, D. Menzel†, N. Mårtensson and A. Nilsson

Department of Physics, Uppsala University, Box 530, S-751 21 Uppsala, Sweden

†Physik Department E20, Technische Universität München, 85747 Garching, Germany

Core-level ionization in molecules leads to an electronic redistribution which modifies the molecular potentials, thus leading to vibrational excitation [1]. The vibrational progressions found in free molecules exhibit a strong photon energy dependence. At the shape resonance this energy dependence is due to the temporary trapping of the photoelectron in the effective molecular potential. The shape resonance is known to be sensitive to both the overall bond length and also to detailed modifications of the molecular potential [2,3]. The photon energy dependence of the vibrational progression in the photoelectron C1s line has been studied in the free CO molecules where strong variations are observed [4]. For the study of adsorbates the occurance of the shape resonance has been a valuable tool to determine i.e. molecular order and orientation in x-ray absorption spectroscopy [3]. Recently we have resolved vibrational fine structure in the C1s and O1s core level lines on CO chemisorbed on Ni(100) with x-ray photoemission (XP) spectroscopy. This opens up the possibility to study the photon energy dependence of the vibrational progression on a chemisorbed molecule.

The XP measurements were performed at the Advanced Light Source, Lawrence Berkeley National Laboratory, by combining highly monochromatic soft x-rays from beamline 8.0 with a Scienta SES 200 electron analyzer [5]. The overall resolution $\frac{\lambda}{\Delta\lambda}$ was approx. 12000 between 300 eV and 450 eV photon energy. All spectra were recorded at 80 K in normal emission in such a way that the electric field vector of the synchrotron radiation was normal to the crystal surface. We prepared the CO/Ni(100) phase as described elsewhere [6]. CO adsorbes on Ni(100) in a c(2x2) superstructure, where the molecule occupies in an upright position top sites with the carbon end down [7,8]. A XPS spectrum of the clean Ni(100) surface was measured for each excitation energy and subtracted from the adsorbate covered one. For the least squares fits we employed Doniach-Sunjic line profiles [9] convoluted with Gaussian functions. For each vibrational progression the same line profile was used for all components.

In Figure 1 we show the vibrationally resolved C1s line of c(2x2)CO/Ni(100) as a function of photon energy. We clearly observe different vibrational progressions for different photon energies. The higher vibrational components are enhanced between 310 eV and 320 eV photon energy, slightly above the known shape resonance position. At photon energies just above threshold (i.e. 299.2 eV) the higher vibrational components are very weak and the C1s line is dominated completely by the adiabatic transition.

We have quantified this description with a numerical fit. The vibrational progression is summarized in Table I and is found to follow to be evenly spaced. In Figure 2 the relative intensities $\nu_i / \sum \nu_i$ of each vibrational component ν_i and the branching ratio $\frac{\nu_i}{\nu_0}$is shown as a function of photon energy.

The observed behaviour is not explainable within the Franck-Condon picture [10], where

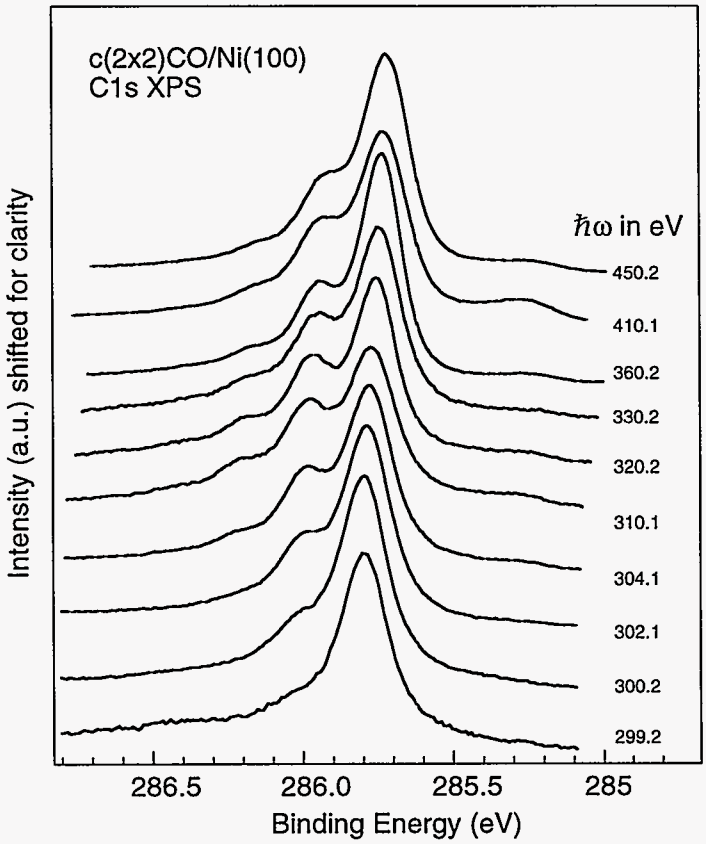

FIG. 1. Vibrational fine structure in the C1s line of c(2x2)CO/Ni(100) as a function of photon energy. Normal emission geometry.

the electronic transition moments are independent of the nuclear coordinates. We observe modifications of the Franck-Condon intensities with photon energy at the shape resonance. The shape resonance is known to depend on the nuclear coordinates [3]. So does the electronic wave-function of the system. If the Franck-Condon approximation does not hold, depend the electronic transition elements on the nuclear coordinates. Since different vibrational final states sample different internuclear geometries in the real space, will each vibrational state be associated with a different electronic transition element, leading to a modification of the Franck-Condon intensities. As a matter of fact is the excited and trapped electron part of the electronic wave function describing the molecular potentials. Changing

TABLE I. Vibrational Progression: Splitting between adiabatic transition and vibrationally higher excited states.

Vibrational transition $\nu \rightarrow \nu'$	Splitting to adiabatic peak (meV)
0→1	217.7±2.2
0→2	440.3±3.1
0→2	655.1±8.9

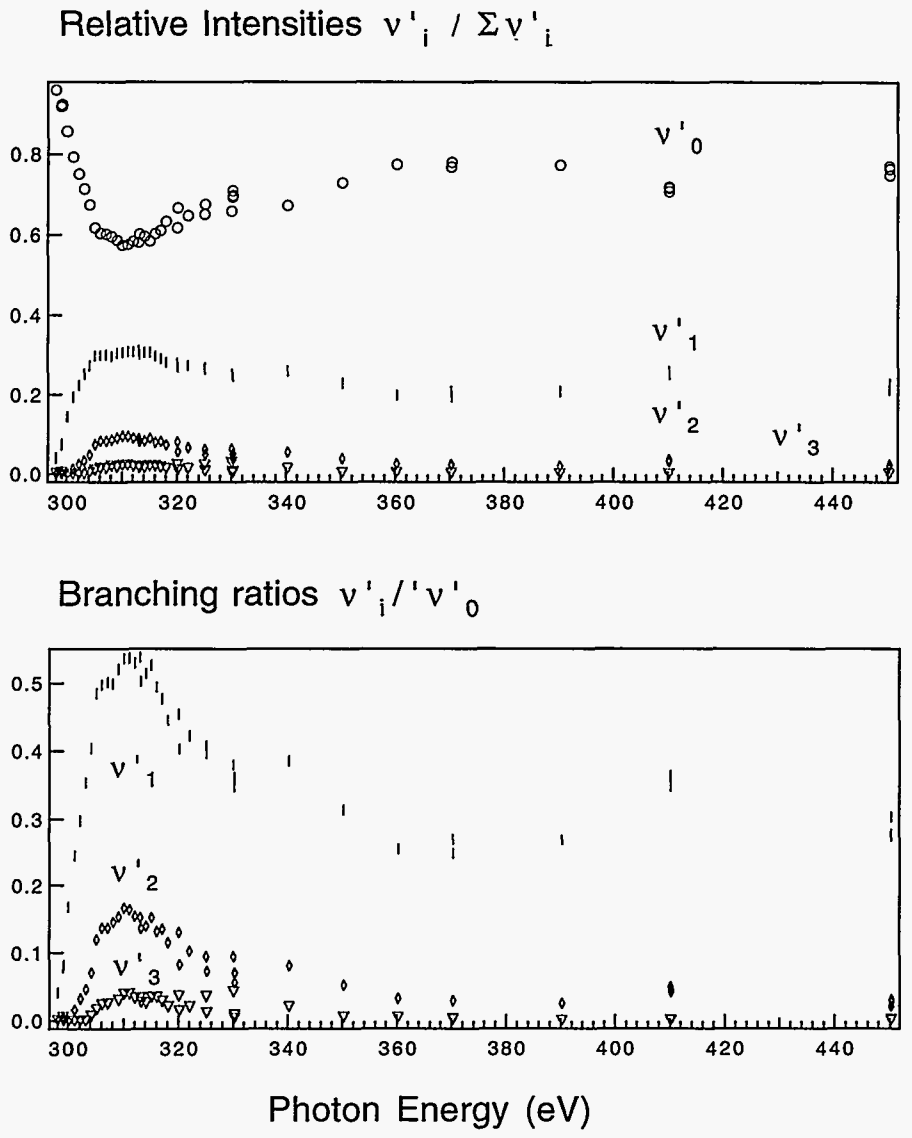

FIG. 2. Relative Intensities and Branching ratio of the vibrational components in the C1s lines of c(2x2)CO/Ni(100) as a function of photon energy, from Fig. 1.

the photon energy alters the excitation and trapping process. Consequently are the molecular potentials influenced by the photon energy and a photon energy dependence of the vibrational progression is found around an electronic resonance.

Viewing the shape resonance as a temporary trapping of the photoelectron implies, that the width of the shape-resonance is related to the trapping time according to the Heisenberg principle of uncertainty. We see from Figure 2 that the shape-resonance spanns at least 5 eV to 6 eV associated with a trapping time shorter than 0.1 fs. The time-scale of trapping is rather short in comparison to the nuclear motion. This indicates that the observed vibrational fine structure is mostly due to vertical transitions, where the nuclear coordinates are unchanged on the time-scale of the photoemission process. The energy dependent modifications in the vibrational progression are within this reasoning due to the dependence of the electronic transition element on nuclear coordinates, as discussed above. However, the idea

of vertical transitions is based on the validity of the Born-Oppenheimer approximation. It is not certain, as a matter of fact, that this approximation is still valid in our case.

So far discussed effects were concerned with the molecular nature of CO adsorbed on Ni(100). In the case of adsorbed molecules one also has to consider substrate-dependent contributions. It has been established previously, that charge transfer screening plays an important role in photoemission on adsorbates. On a qualitative level it is clear that the extend of charge transfer should depend on the distance between the CO molecule and the substrate. This CO-substrate distance is then again related to the intermolecular distance. Consequently could the selection of different vibrational final states with different internuclear distances also modify the screening probability through charge transfer from the metallic substrate. An other substrate-dependent contribution could be effects related to the spatial order of the adsorbate system. Photo-electron diffraction in the back-scattering regime are energy dependent phenomena and can also be seen as a temporary trapping of the out-going photoelectron. Some deviations between the behaviour in the free molecule and the adsorbed molecule could be asscribed to this additional process.

This work was supported by the Swedish Natural Science Research Council (NFR), the Göran Gustavsson Foundation for Research in Natural Sciences and Medicine. ALS is supproted by the U.S. Department of Energy.

---

[1] U. Gelius *et al.*, Chem. Phys. Lett. **28**, 1 (1974).
[2] J. L. Dehmer and D. Dill, Phys. Rev. Lett. **35**, 213 (1975).
[3] J. Stöhr, *NEXAFS Spectroscopy*, Vol. 25 of *Springer Series in Surface Sciences* (Springer, Berlin, 1992).
[4] K. J. Randall *et al.*, Phys. Rev. Lett. **71**, 1156 (1993).
[5] N. Mårtensson *et al.*, J. El. Spec. Rel. Phenom. **70**, 117 (1994).
[6] H. Tillborg, A. Nilsson, and N. Mårtensson, Surf. Sci. **273**, 47 (1992).
[7] S. Andersson and J. B. Pendry, Phys. Rev. Lett. **43**, 363 (1979).
[8] P. Uvdal *et al.*, Surf. Sci. **202**, 167 (1988).
[9] S. Doniach and M. Sunjic, J. Phys. C **3**, 285 (1970).
[10] G. Herzberg and J. W. T. Spinks, *Molecular spectra and molecular structure* (Prentice-Hall, New York, 1966), Vol. 1.

Principal investigator: Anders Nilsson, Department of Physics, Uppsala University, Box 530, S-751 21 Uppsala, Sweden. anders.nilsson@fysik.uu.se

Soft X-ray emission spectroscopy of early-transition-metal compounds

S. Shin,[1] M.Fujisawa,[1] H.Ishii,[1] Y.Harada,[1] M.Watanabe,[2] M.M.Grush,[3] T.A.Callcott,[3] R.C.C.Perera,[4] E. Z. Kurmaev,[5] A.Moewes,[6] R.Winarski,[7] S.Stadler,[7] and D.L.Ederer[7]

[1]Institute for Solid State Physics, University of Tokyo, 3-2-1 midoricho, Tanashi, Tokyo 188, Japan
[2]PF, KEK, 1-1 Oho, Tsukuba, Ibaraki 305, Japan
[3]University of Tennessee, Knoxville, Tennessee 37996, USA
[4]ALS, LBNL, 1 Cyclotron Road, Berkeley, CA 94720, USA
[5]Institute of Metal Physics, 620219 Yekaterinburg GSP-170, S.Kovalevskaya str.18, Russia
[6]CAMD, Baton Rouge, LA 70803, USA
[7]Physics Department, Tulane University, New Orleans, LA 70118, USA

INTRODUCTION

It is well known that transition metal compounds are very useful materials for applications. Here, the problem is how we could know the information of the electronic structure of early transition metal compounds by measuring the soft x ray Raman scattering. It is known that the transition metal compounds have narrow band dispersions. Instead of the band dispersion curve, we might know the charge transfer energy Δ and the d-d Coulomb interaction energy U, and the other important parameters that decide the electronic structure of transition metal compounds.

It is known that the heavy transition metal compounds belong to the charge transfer insulators, because charge transfer energy is smaller than the Coulomb energy. On the other hand, early transition metal compounds belong to the Mott-Hubbard insulators, because the Coulomb energy is smaller than the charge transfer energy. In the case of late transition metal compounds, the elementary excitation has been already known to be d-d transition within 3d states. It is a problem what is it in the early transition metal compounds.

EXPERIMENTAL

Soft x-ray emission measurements were carried out at BL19B in Photon Factory(PF) at KEK and at BL8 in Advanced Light Source(ALS) at LBNL. The Sc and Ti compounds were measured at PF. The Cr and V compounds were mainly measured at ALS.

RESULTS AND DISCUSSION

Figure 1 shows the comparison between the photoemission[1] and several soft x-ray emission spectra[2] of vanadium dioxide VO_2.

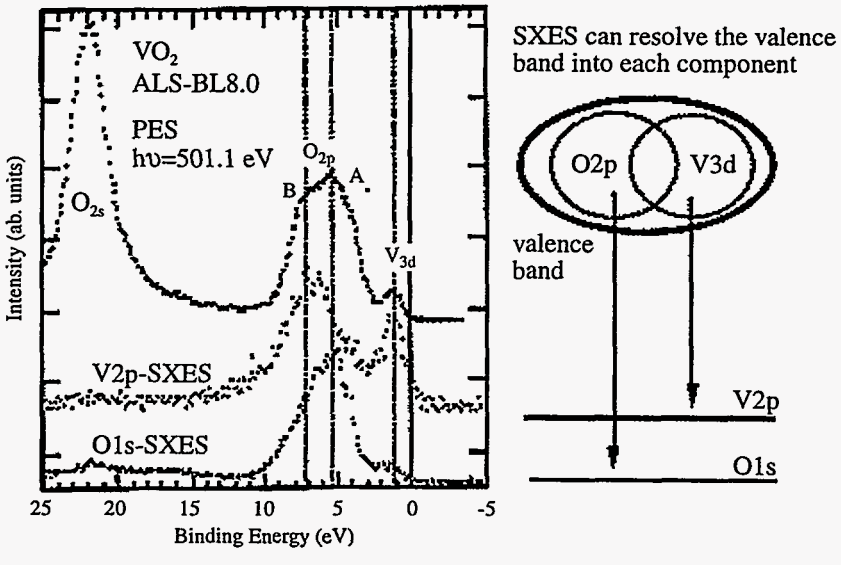

Fig. 1. Comparison of the photoemission spectrum and V L3-, V L2-, and O K-SXE spectra of VO2

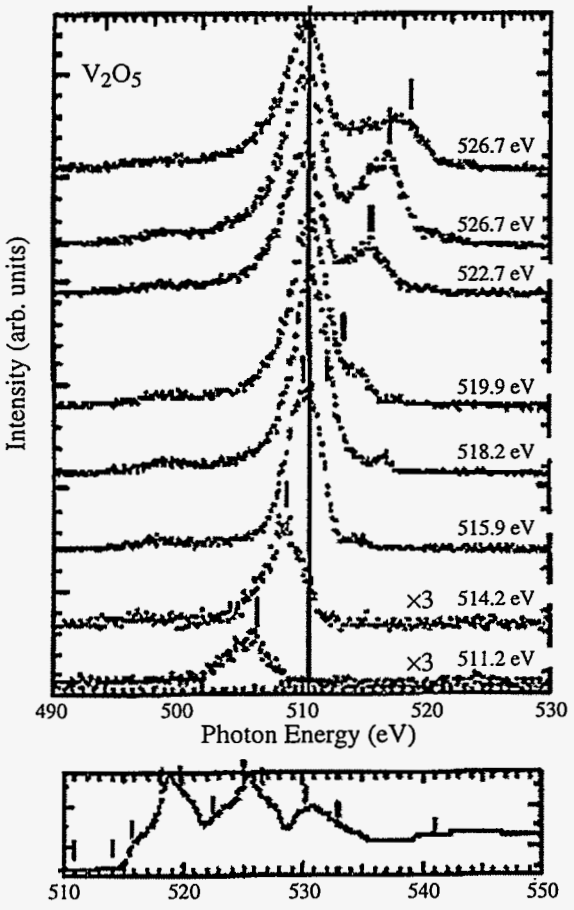

Fig. 2. Upper panel shows the V $L_{2,3}$ -SXE spectra of V_2O_5 measured by various photon energies. The lower panel shows the total electron yield spectrum of V_2O_5. The vertical bars in the lower panel correspond to the photon energies where the SXE spectra were measured.

band at lower binding energy band and that of the V2p emission spectra coincides with that of the O2p band at the higher binding energy as well as the V3d band at Fermi level. The band B has a strong 3d component in the O2p band. On the other hand, it is also found that there is an intensity of O2p component in the 3d band at Fermi level. These facts show both components are strongly hybridized with each other.

In the case of the nominally d^0 system, there is no d-d transition. Figure 2 shows soft x-ray emission spectra[3] of V_2O_5. One Raman scattering band is found at around 6.2 eV, as indicated by vertical bars. This band is thought to correspond to the transition from the O2p valence band to the V3d conduction band.

The dots in the middle are the V2p emission spectrum and the lowest is the O1s emission spectrum. It is known that the valence band of VO_2 mainly consists of O2p and V3d components. Vanadium 2p emission reflects V3d partial density of state and O1s emission reflects O2p partial density of state. The sum of the two soft x-ray emission spectra roughly equal to the photoemission spectrum, if we consider the cross section of each component. The valence band can be resolved into the V3d and O2p components by soft x-ray emission spectra. It is known that the photoemission spectra have two main bands; the O2p component is dominant at higher binding energy and the V3d component is located just below Fermi level. Furthermore, the O2p bands have two structures. It is found that the energy position of O1s soft x-ray emission spectroscopy coincides with that of the O2p

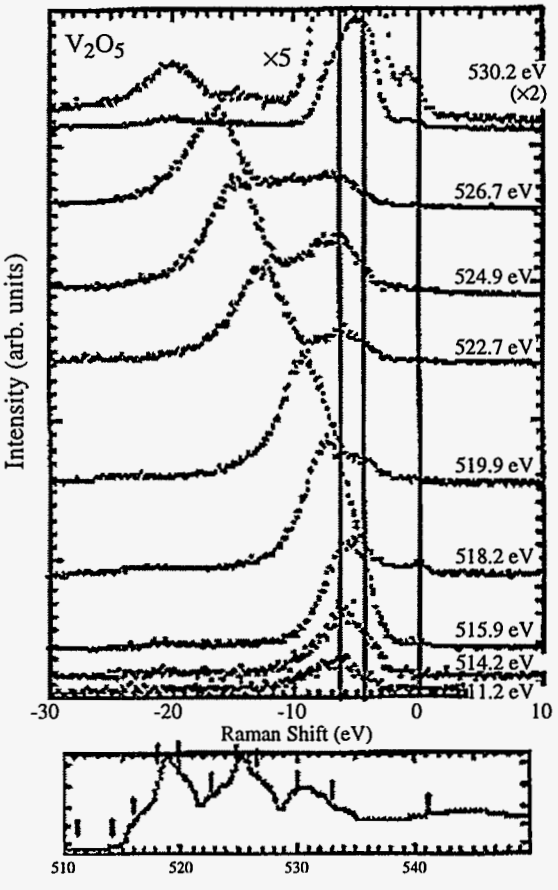

Fig. 3. Soft x-ray Raman spectra of V2O5 measured by various photon energies. The vertical bars correspond to the Raman scattering

Figure 4 shows the photoelectron spectrum and O1s absorption spectrum. Oxygen 1s absorption spectrum is used instead of the inverse photoemission spectrum, in order to know the conduction band. The 6.2 eV of the Raman band corresponds to the transition from the valence band to the conduction band peaks, as shown by the arrow in Fig.4. Such a similar assignment has been carried out in the SXES of TiO2.[4]

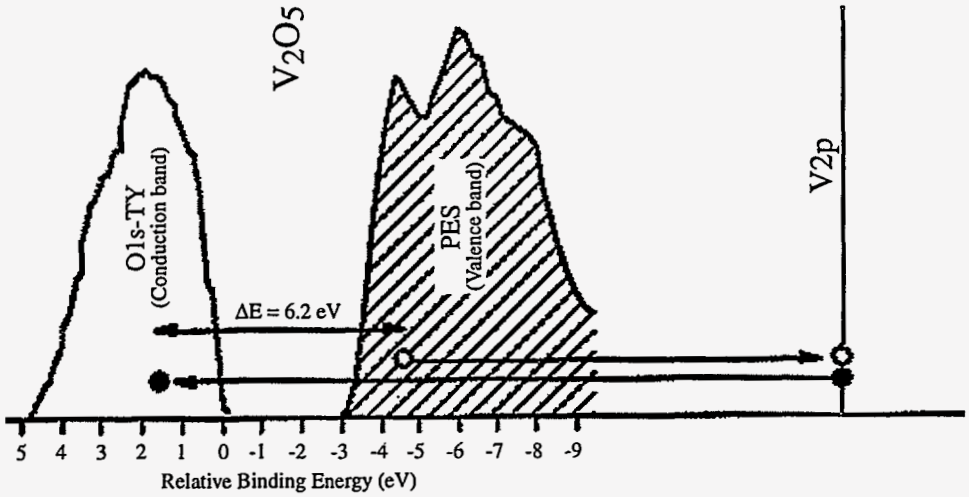

Fig. 4. Schematic diagram of soft x-ray Raman scattering of V_2O_5 by O1s total yield and photoemission spectra.

Another assignment of this Raman band might be the charge transfer transition when one consider the localized electron picture. Figure 5 shows the photoemission spectra of Sc, Ti, and V compounds in the valence band energy region.[5] They have no 3d electrons nominally. These are the main valence bands which mainly consist of the ligand 2p components hybridized by 3d components. The features located below the main bands are the charge transfer satellite structures.

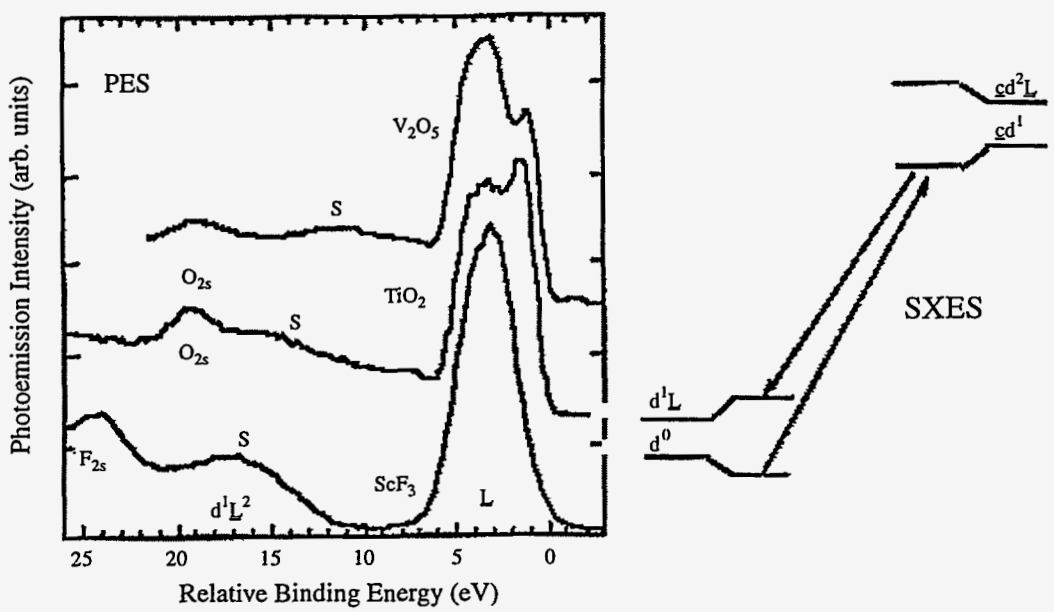

Fig. 5. Photoemission spectra of nominally d^0 system, V_2O_5, TiO_2, and ScF_3. Right panel shows the schematic diagram of soft x-ray Raman scattering of nominally d^0 system by cluster picture.

The energy separation is mainly determined by the hybridization energy and the charge transfer energy. Clearly the intensity and the binding energy decrease from Sc to V compounds. This fact reflects the decreasing charge transfer energy. The right panel of the Fig.5 shows the schematic diagram of the Raman scattering, when it is considered by the localized electron picture of the cluster. In this case, the Raman scattering is assigned to be the transition to the charge transfer state $d^1\underline{L}$.

In the case of scandium compounds, it is better to consider the charge transfer transition, instead of the transition from valence band to conduction band. In the case of ScF_3, there are two satellite structures of photoemission spectra.[6] The satellite at about 13 eV is called as the bonding state and that at about 10 eV is called as nonbonding state. The photon energy dependence of the Sc2p soft x-ray emission spectra of ScF_3 shows that there are two groups in the Raman scattering. This Raman scattering does not change much by the excitation energy. These two Raman scattering well correspond to the two satellite structures which are seen in the photoemission spectra. When one considers the localized electron picture of the nominally d^0 system, the ground state is made by the hybridization between d^0 and the charge transfer state $d^1\underline{L}$. The hybridized states make three states including nonbonding state. Thus, we can see one Rayleigh scattering and two Raman scattering.

REFERENCES

1. S.Shin, S.Suga, M.Taniguchi, M.Fujisawa, H.Kanzaki, A.Fujimori, H.Daimon, Y.Ueda, K.Kosuge, and S.Kachi, Phys. Rev.B41, 4993(1990).
2. S.Shin, A.Agui, M.Watanabe, M.Fujisawa, Y.Tezuka, and T.Ishii, Electron Spec. and Related Phenomena 79, 125 (1996).
3. S.Shin, M.Fujisawa, H.Ishii, Y.Harada, M.Watanabe, M.M.Grush, T.A.Callcott, R.C.C.Perera, E.Z.Kurmaev, A.Moewes, R.Winarski, S.Stadler, D.L.Ederer, Electron Spec. and Related Phenomena, in press.
4. Y.Tezuka, S.Shin, A.Agui, M.Fujisawa, and T.Ishii, Phys. Soc. Jpn. 65 (1996); Raman emission by x-ray scattering, World Scientific, Edited by D.L.Ederer and J.H.McGuire, 1996.
5. S.Shin, Y.Tezuka, T.Ishii, and Y.Ueda, Solid State Commun. 87, 1051(1993).
6. M.Umeda, Y.Tezuka, S.Shin and A.Yagishita, Phys.Rev. B53, 1783 (1996).

This work was supported by Tulane University, NSF grant DMR-9017997, the University of Tennessee Science Alliance, and a DOE-EPSCOR cluster grant DOE-LEQSF (1993-95)-03.

Principal investigator: Shik Shin, Institute for Solid State Physics, Tokyo University. Email: shin@issp.u-tokyo.ac.jp. Telephone: +81-424-69-2140 (office, direct). Fax: +81-424-61-5401.

SOFT X-RAY EMISSION STUDIES OF THE ELECTRONIC STRUCTURE IN SILICON NANOCLUSTERS

T. van Buuren, L.N. Dinh[1], L.L. Chase[1], L.J. Terminello[1], M. Grush[2], T.A. Callcott[2], D.L. Ederer[3], J.A. Carlisle[4]

1 Chemistry and Materials Science Department, Lawrence Livermore National Laboratory, Livermore, CA , 94556

2 Department of Physics, University of Tennessee, Knoxville, TN 37996

3 Department of Physics, Tulane University, New Orleans, La 70118

4 Department of Physics, Virginia Commonwealth University, Richmond, VA 23284-2000

INTRODUCTION

The discovery of visible photoluminescence in ultra fine Si particles has lead to tremendous interest in their electronic and optical properties [1]. It is generally agreed that quantum confinement caused by the restricted size of the nanometer scale silicon particles is essential for the light-emitting properties[2]. A prediction of the quantum confinement model is that the energies of the valence band (VB) and conduction band (CB) edges are shifted relative to the bands of bulk silicon. Silicon nanocrystals were synthesized by thermal vaporization of Si in an Argon buffer gas follow by exposure to atomic hydrogen to passivate the surface. Synthesis techniques have been reported in detail earlier [3,4]. The electronic structure of the Si cluster is then investigated in-situ using x-ray absorption (XAS) and soft x-ray fluorescence (SXF) spectroscopies. SXF and XAS measurements were performed on beamline 8.0 at the Advanced Light Sources. Characterization of the size and morphology of the Si clusters was done ex-situ using atomic force microscopy.

RESULTS

Two Si cluster samples were grown by evaporation of Si at 1700•C in an argon buffer gas of 40 and 80 mTorr and deposited on a Ge substrate. AFM measurements after spectroscopic characterization show that the average diameter of the clusters is 1.6 nm in the 40 mTorr sample and 2.0 nm in the 80 mTorr sample. In Fig.1 we show the x-ray absorption spectra of the $L_{2,3}$ edge absorption for bulk silicon and the two silicon nanocluster samples. The $L_{2,3}$ -edge of the cluster samples is shifted to higher energy relative to the bulk silicon by 0.14 eV for the 2.0 nm clusters and 0.22 eV for the 1.6 nm clusters, in agreement with quantum confinement which raises the energy of the bottom of the conduction band as the nanocluster particle size is decreased. In addition the well defined double threshold behavior associated with the 0.6 eV splitting of the Si 2p core level is less pronounced in the L-edge of the nanoclusters. We also note that the onset of the absorption edge in the clusters is not as sharp as that in the bulk silicon. We attribute these features to a distribution of quantum shifts caused by the variation of particle size within the sample.

Changes in the electronic structure of the VB were monitored by SXF spectroscopy on the same samples that there previously investigated by x-ray absorption. In the SXF process a valence electron fills the core vacancy previously generated by the absorption of a photon. The generated fluorescence photon was analyzed in a spherical grating Rowland spectrometer. In all spectra presented the excitation energy was chosen to be below the Si L_2 absorption edge as determined from the absorption spectra. Therefore, the fluorescence spectrum is generated by transitions from the valence band to the silicon $2p_{3/2}$ core hole. The SXF technique has an advantage over photoemission because it is insensitive to sample

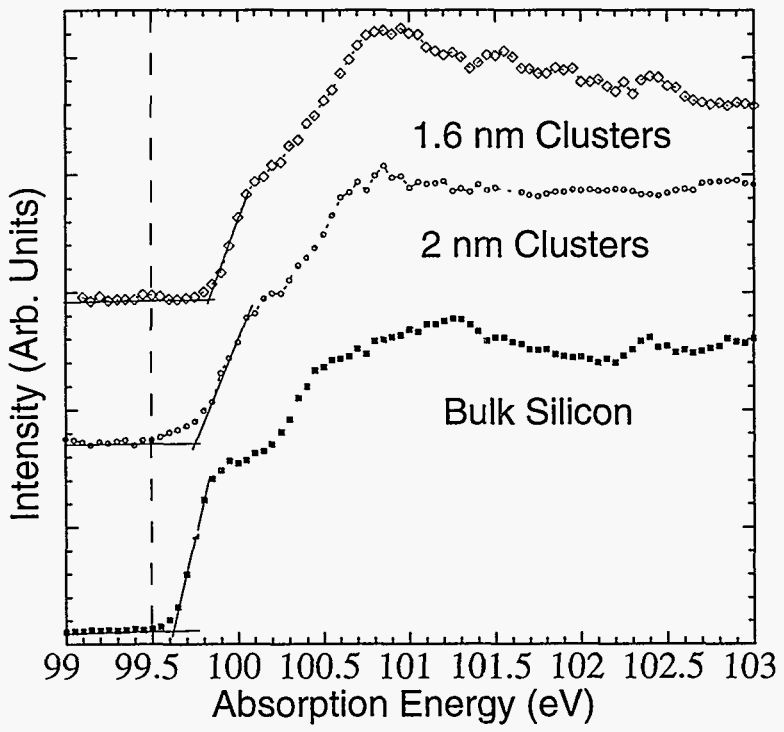

Fig. 1. Fluorescence yield x-ray absorption spectra at the silicon $L_{2,3}$ edges in bulk silicon, of silicon nanoclusters with an average size of 2.0 nm and 1.6 nm. The solid line indicates the extrapolation of the L_3 edge to baseline in order to determine the CB edge position.

charging and is a bulk probe due to the large photon mean free path (~0.1 micron). By tuning the excitation energy below the Si L-edge absorption threshold of SiO_x we selectively investigate the electronic structure of the Si nanocluster not any surface oxide or substrate feature.

In Fig. 2 we show the SXF spectra for bulk silicon and the same two cluster samples as shown in Fig. 1. The SXF spectra were excited at 100 eV for the bulk silicon and the 1.6 nm clusters and 100.2 eV for the 2nm clusters. The bulk silicon SXF spectrum exhibits the three characteristic peaks, one at 89 eV associated with low-lying 3s states, another due to a density of states (DOS) maximum at 91.5 eV with strong s-p hybridization and a high DOS at 96 eV which is dominated by p-type states [5]. The intense peak at approximately 100 eV is due to reflected light from the undulator beamline into the spectrometer. The corresponding peak in the bulk Si spectrum is very weak as the reflectivity of the polished Si wafer is low in the non-specular position. Using these reflection peaks we reference the emission energy to the excitation energy and the x-ray absorption spectra.

The overall appearance of the nanocluster spectra is different than that of the bulk silicon. In the nanocluster spectra the valence band is shifted to lower emission energy by 0.30 eV and 0.51 eV for the 2.0 nm and 1.6 nm clusters respectively. The VB edge is much sharper in the cluster samples than in the bulk Si opposite to what is observed in the x-ray absorption edge. Also the shape of the spectra is flattened from a peak like feature in the bulk Si to a plateau in the silicon nanoclusters. This effect has been observed in the SXF spectra of porous silicon and has been attributed to changes in the DOS at the VB edge due to confinement effects in the Si crystallites which alter the bulk electronic band structure [5].

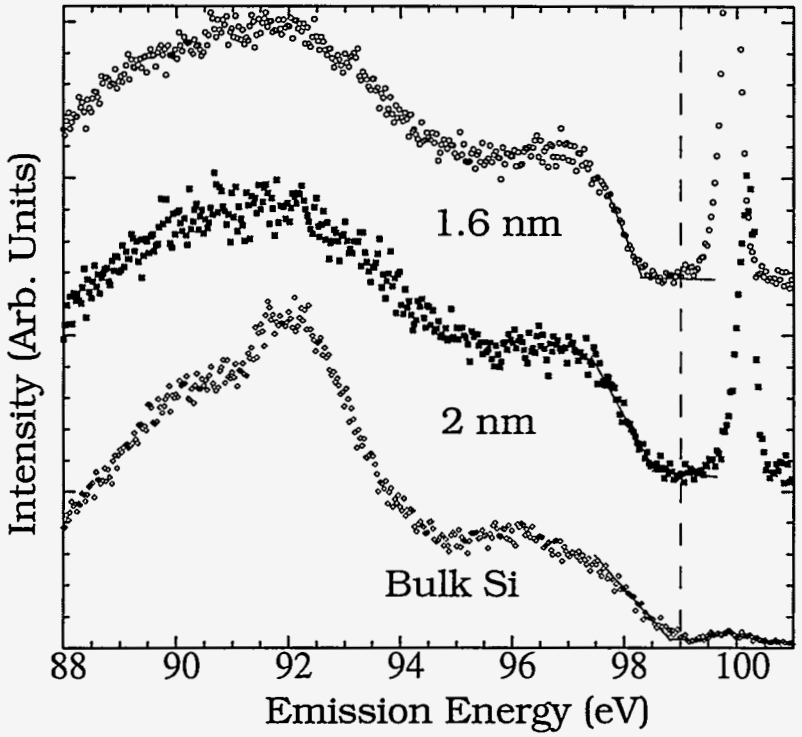

Fig. 2. The L_3 emission spectrum of bulk silicon and the 2.0 and 1.6 nm diameter cluster samples. The excitation energy is 100 eV for the bulk silicon and for the 1.6 nm clusters and 100.2 eV for the 2nm clusters. This corresponds to the L_3 edge measured in the absorption spectra so the L_2 edge is suppressed. The solid lines indicate the extrapolation of the high energy cut-off to the baseline in order to determine the VB edge position.

The pronounced peak at 91.5 eV is not observed in the SXF spectra for the silicon nanoclusters. In fact the spectra looks more like what is observed for amorphous silicon [6]. Yet x-ray diffraction and TEM studies of these clusters have shown they are crystalline in nature [4]. It is interesting to note that the peak at 91.5 is observed in the SXF spectra of hydrogenated porous silicon [5].

It can be seen that the smaller silicon nanoclusters exhibit a larger VB shift as well as a larger conduction band shift. The VB shifts are larger than the shifts in the CB in accordance with theory and are similar to recent photoemission data on silicon clusters although the ratio of the conduction band shift to valence band shift is slightly larger than that found in the photoemission study [7].

In conclusion, we were able to investigate the unoccupied and occupied electronic states in silicon nanoclusters combining total fluorescence yield x-ray absorption and selectively excited SXF spectroscopy. We observe shifts in the both the CB and VB edges indicating quantum size effects in the band structure of the nanoclusters. The onset of the absorption edge progressively broadens with increased confinement due to a distribution in cluster size. A steeper VB edge is observed in the nanoclusters as compared to bulk Si due to a change in the DOS at the VB edge.

ACKNOWLEDGMENTS

This work was supported by the Division of Material Science, Office of Basic Energy Sciences, and performed under the auspices of the Department of Energy by LLNL under Contract No. W-7405-ENG-48, this work was done at the ALS, which is supported by the Department of Energy under Contract No. DE-AC02-76CH0016.

REFERENCES

1. H. Takagi, H. Ogawa, Y. Yamazaki, A. Ishizaki, and T. Nakagiri, Appl. Phys. Lett. **56**, 379 (1990).
2. T. Canham, Appl. Phys. Lett. **57**, 1046 (1990).
3. T. van Buuren, L.N. Dinh, I. Jimenez. L.J. Terminello, M. Grush, T.A. Callcott and J.A. Carlisle, Mater. Res. Soc. Symp. Proc. **452**, (1996).
4. L.N. Dinh, L.L Chase, M.Balooch, W.J. Siekhaus, F. Wooten, Phys. Rev. B **54**, 5029 (1996).
5. S. Eisibitt, S.N. Patitsas, T. Tiedje, T. van Buuren, J. Luning, J.-E. Rubensson and W. Eberhardt , Europhysics Letters, **37** , 133 (1997).
6. K.E. Miyano, D.L. Ederer, T.A. Callcott, W.L. O'Brien, J.J. Jia, L.Zhou, Q.-Y. Dong, Y.Ma, J.C. Woicik and D.R. Mueller, Phys. Rev B **48**,1918 (1993).
7. T. van Buuren, L. N. Dinh, L. L. Chase, W. J. Siekhaus, L.J. Terminello accepted to be published Phys. Rev. Lett.

Principle Investigator: Tony van Buuren, Chemistry and Materials Science Department, Lawrence Livermore National Laboratory, Livermore Ca.
Email: tvb@oasis.llnl.gov
Telephone (925) 423-5639

Soft X-Ray Fluorescence Measurements of Irradiated Polymer Films

R.P. Winarski[1], S. Stadler[1], D.L. Ederer[1], E.Z. Kurmaev[2],
T.A. Callcott[3], M.M. Grush[3], A. Moewes[4], and R.C.C. Perera[5]
[1]Department of Physics, Tulane University, New Orleans, Louisiana 70118, USA
[2]Institute of Metal Physics, Russian Academy of Sciences-Ural Division, 620219 Yekaterinburg GSP-170, Russia
[3]Department of Physics, University of Tennessee, Knoxville, Tennessee 37996, USA
[4]Center for Advanced Microstructures and Devices/Louisiana State University,
Baton Rouge, Louisiana 70803, USA
[5]Advanced Light Source, Ernest Orlando Lawrence Berkeley National Laboratory,
Berkeley, California 94720, USA

INTRODUCTION

Polyimide films that are heavily irradiated by ions exhibit a significant increase in electrical conductivity nearing that of inorganic semiconductors [1-4]. It has been shown that ion irradiation induces marked changes in the chemical structure of the polyimide films and increased conductivity due to polymer carbonization [5-7]. Conversion of polycarbosilane films to ceramics by ion implantation leads to increased hardness and oxidation resistance [8]. It is thought that some of the carbon in the PCS film segregates during the irradiation and annealing processes, leading to different local structures and hybridization states.

EXPERIMENTAL RESULTS

Fluorescent soft x-ray carbon Kα emission(XES) and carbon 1s total fluorescent yield(TFY) spectra have been used to characterize the bonding of carbon atoms in polyimide(PI) and polycarbosilane(PCS) films. The PI films have been irradiated by nitrogen and argon ions with concentrations ranging from $1x10^{14}$ to $1x10^{16}$ ions/cm^2. The PCS films have been annealed to 1000° C and/or irradiated with 200 keV carbon ions to a concentration of $5x10^{15}$ ions/cm^2. We find that the fine structure of the carbon XES of the PI films changes with implanted ion concentrations above $1x10^{14}$ ions/cm^2 which we believe is due to bond degradation and the creation of carbon clusters in the films. The electrons in the atoms of these clusters fill unoccupied states in the valence and conduction bands and lead to a narrowing of the band gap. We find that the bonding of carbon atoms in the PCS films after carbon ion irradiation is similar to the bonding in diamond films, and the bonding after irradiation and subsequent annealing appears more like the bonding found in graphite-like silicon films. The non-irradiated PCS film that was annealed at 1000° C converts to a ceramic with the composition of amorphous $Si_{0.77}C_{0.23}$:H.

IRRADIATED POLYIMIDE FILMS

Soft x-ray emission spectroscopy is governed by the dipole selection rules, and because the excitation is site specific, the x-ray fluorescence can be used to gain information about the local bonding environment of a sample. XES probes the valence band states and can be compared with partial density of states calculations. The x-ray transitions are limited to the first coordination sphere of the emitting atom, and XES is therefore sensitive to short-range order. In this way, the technique can be used to examine changes in the local environment and chemical bonding of the emitting atom due to various thermal and physical treatments.

The results of measurements of the carbon Kα XES of irradiated PI films are presented in Figure 1. The peak structure labeled by A, B, and C is only observed for implanted ion concentrations below $1x10^{14}$ ions/cm^2. The structure can be attributed to the occupied molecular orbitals(MO) of the polyimide chains, particularly the occupied states of the carbon 2p atomic orbitals which are probed by the 2p→1s transitions of the carbon Kα XES.

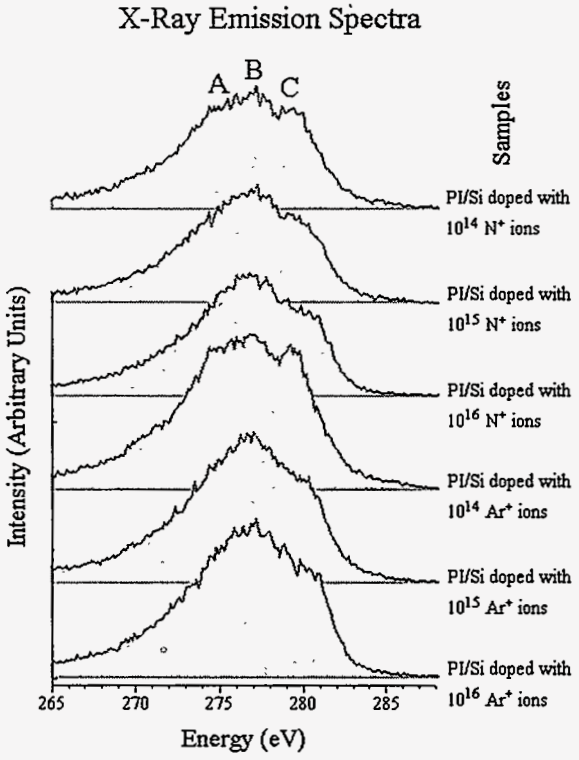

The relative intensities of peaks A and C progressively decrease(with respect to peak B) for ion concentrations above $1x10^{14}$ ions/cm^2. Interestingly the changes in these features are the same for both ion types, indicating that the structural changes to the carbon atoms in these samples is not related to the ion-carbon bonding. We also noted a narrowing of the gap as determined from XES and TFY measurements as implanted ion concentrations increased. The XES for the $1x10^{16}$ ions/cm^2 samples resembled those of amorphous carbon films, suggesting the formation of carbon clusters in these prepared PI films [8].

Figure 1. C Kα XES for irradiated polyimide films. Note the change in shape of the spectra as the ion concentration increases.

IRRADIATED POLYCARBOSILANE FILMS

Measurements of the carbon Kα XES of the PCS films are presented in Figure 2. The spectra exhibit distinct changes between deposited polymer films, annealed films(One hour at 1000° C), irradiated films($5x10^{15}$ ions/cm^2 concentration of 200 keV carbon ions), and combined treatment films(irradiation followed by annealing). According to infrared Raman measurements of these films, irradiation causes a segregation of some of the carbon atoms in the polymer resulting in a chemical state similar to that of a diamond-like film [9]. After a combined treatment, XES spectra of these films more closely resemble the features of a graphite-like spectrum. To investigate these conclusions we compared the carbon Kα XES of the various PCS films with spectra from known samples of HOPG, silicidated graphite and diamond-like films[8].

Our carbon Kα XES measurements confirm the results of the Raman spectra, in that the chemical states of the carbon atoms in irradiated PCS films resemble those of diamond-like films, and in combined treatment films they resemble graphite-like silicon systems. The spectra from our annealed PCS films show a conversion to an amorphous ceramic with the composition of $Si_{0.77}C_{0.23}$:H [8].

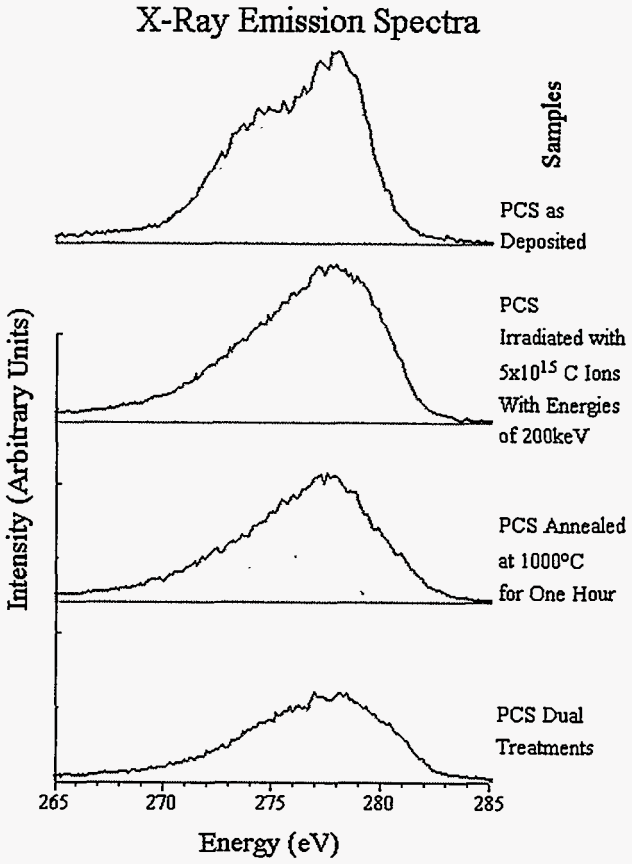

Figure 2. C Kα XES for PCS films. Note the change in shape of the spectra for different treatments (annealing and irradiation).

REFERENCES

1. J. Davenas and X.L. Xu, Nucl. Inst. Methods B 71 (1992) 33
2. V. Svorcik, V. Rubka, V. Hnatowicz, and J. Kvitek, Mat. Lett. 19 (1994) 329
3. T. Trigaud, J.P. Moliton, C. Jussiaux, and B. Maziere, Nucl. Inst. Methods B 107 (1996) 323
4. I.H. Loh, R.W. Oliver, and P. Sioshansi, Nucl. Inst. Methods B 34 (1988) 337
5. V. Svorcik, R. Endrst, V. Rybka, E. Arenholz, V. Hnatowicz, and F. Cerny, Eur. Polym. J. 31 (1995) 189
6. D. Xu, X.L. Xu, G.D. Du, R. Wang, S.C. Zou, and X.H. Liu, Nucl. Inst. Methods B 80/81 (1993) 1063
7. M. Iwaki, K. Yabe, A. Fukuda, H. Watanabe, A. Itoh, and M. Takeda, Nucl. Inst. Methods B 80/81 (1993) 1080
8. R.P. Winarski, D.L. Ederer, E.Z. Kurmaev, S.N. Shamin, T.A. Callcott, A. Moewes, J.-C. Pivin, and R.C.C. Perera (to be published).
9. J.-C. Pivin and P. Colombo, J. Am. Ceram. Soc. (In Press)

This work was supported by the Russian State Program "Atomic and Spatial Structures," Russian Science Foundation for Fundamental Research (Project 96-15-96598), a NATO Linkage Grant (HTECH.LG 971222), INTAS-RFBR (95-0565), NSF Grants (DMR-9017997 and DMR-9420425) and the DOE-EPSCOR and Louisiana Education Quality Special Fund (DOE-LEQSF (1993-95-03). The experiments were conducted at Lawrence Berkeley National Laboratory's Advanced Light Source which is supported by the United States Department of Energy under contract (DE-AC03-76SF00098).

Principal investigator: Robert P. Winarski, Department of Physics, Tulane University. Email: rwinarsk@mailhost.tcs.tulane.edu. Telephone: 504-865-5520.

Structure Analysis of Diamond-like Carbon Films by NEXAFS

Kwang Yong Eun[1], Kwang-Ryeol Lee[1],Simone Anders[2] and Thomas Stammler[2]

[1]Thin Film Technology Research Center, Korea Institute of Science and Technology,
P.O. Box 131, Cheongryang, Seoul, 130-650, Korea

[2]Advanced Light Source, Ernest Orlando Lawrence Berkeley National Laboratory,
University of California, Berkeley, CA, 94720, USA

INTRODUCTION

The economical and technological properties of diamond-like carbon (DLC) films have attracted the interest of many researchers [1-5]. DLC films exhibit excellent properties regarding hardness, electrical insulation, chemical inertness, optical transparency, surface smoothness, resistance to wear, and electron emission.

For the deposition of hydrogenated DLC films, the r.f. plasma CVD process is one of the well established methods and the properties of the films can vary depending on the process parameters such as bias voltage, precursor gas, gas pressure, and so on [1-5]. Among these variables, the bias voltage shows the most significant effect on the mechanical, optical, and electrical properties. This means that bias voltage change results in a structure variation of DLC films during deposition.

The bias voltage is strongly related to the mean ion energy during CVD deposition. It is very important to measure the sp^2 and sp^3 composition in the DLC films since the properties are clearly dependent upon the sp^2/sp^3 ratio. In order to evaluate the ratio of sp^2 and sp^3 in the Raman spectra of DLC films, the graphic separation of individual peaks is needed for the complicated broad peak between 1300 and 1600 cm^{-1}, and this allows only qualitative analysis. On the other hand, the π^* resonance peak at 285 eV in the K-edge carbon NEXAFS spectra is very sharp and is very sensitive to the sp^2 fraction [6-8]. For the basic study of the structure of the hydrogenated DLC films, different samples were prepared by varying bias voltage, and NEXAFS analysis was performed for the quantitative analysis of the sp^2 and sp^3 ratio, and consequently for the better understanding of the properties of the films.

EXPERIMENTAL

DLC films were synthesized on silicon (001) wafers by r.f. plasma CVD at a pressure of 10 mTorr . Precursor gas was benzene and bias voltage was varied from -100 to -700 volt. Details of experimental set-up was described elsewhere [9]. The deposited thickness of all DLC films was 1μm. The NEXAFS measurements were performed at the photo-emission electron microscope situated at the undulator beam-line 8.0 of the ALS. Beam intensity was carefully controlled at a low level.

RESULTS and DISCUSSION

The properties of deposited DLC films showed monotoneous increasing or decreasing trend with increase of bias voltage applied. Hydrogen content decreased from 30% to 22%, and the hardness and residual stress of the films increased from 1500 to 1800 kg mm^{-2} and from 0.5 to 1.8 GPa respectively with increase of the bias voltage. This property variation is known to be dependent on the ion energy which is proportional to $Vb/\sqrt{P}$ where Vb is bias voltage and P is gas pressure [5]. The properties should be dependent upon the bias voltage since the pressure was kept constant.

The NEXAFS plots of the DLC films showed clear decreasing trend of graphite peak height in 285 eV with increase of bias voltage as shown in Fig. 1.

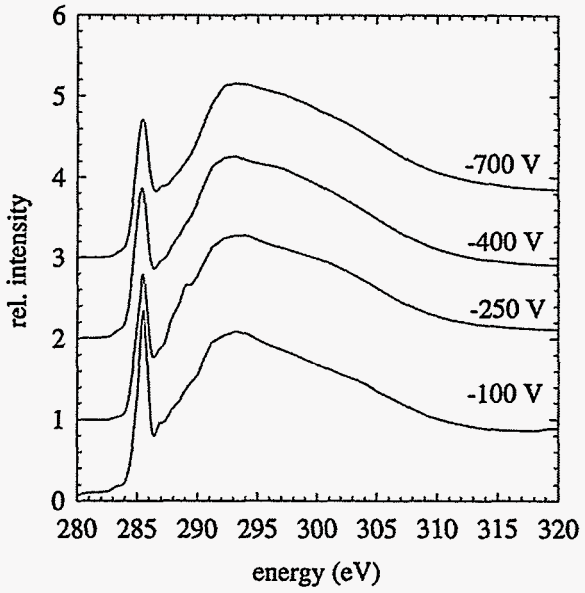

Fig.1. Carbon K-edge NEXAFS spectra of DLC films deposited with different bias voltage from -100 volt to -700 volt .

There are very small peaks between 286.5eV and 290 eV. The small peak at around 287 eV shows decreasing trend with increase of bias voltage. This is consistent to the decreasing trend of the hydrogen content in the films. This hydrogen peak height is so low that the amount of C-H bond seems to be not so high comparing the sp^2 and sp^3 bond. The curves at energies higher than 320 eV were very flat as in Fig.1 and this constant value is known to be proportional to the total carbon amount in the films [10]. The film deposited at -250 bias voltage shows a particular peak at 289eV and a higher value in the flat curve for energies higher than the 315 eV. The reason for this is not clear yet.

The sp^3 component can be calculated by the equation 1-{(sp2-Tc)/Tc} where sp2 is the peak height of the π^* resonance at 285 eV and Tc is the height of the flat part above 320 eV, neglecting the hydrogen component[10]. Fig.2 shows the calculated sp^3 fraction plot depending on the bias voltage variation.

The sp^3 component in the DLC films increased significantly with increase of the bias voltage as shown in Fig.2, and this increasing trend of the diamond bond component is consistent to the same increasing trend of the hardness and the residual stress in the films. The radiation damage of the x-ray synchrotron might give some errors in the sp^2 peak height. The confirmation of the sp^2 and sp^3 composition in the DLC films by EELS analysis is required to evaluate the error ranges. Further study is needed for the composition variety of DLC films and the standardization of the quantitative analysis results.

CONCLUSION

The hydrogenated DLC films with different composition were obtained by the bias voltage variation from -100 to -700 volt during the r.f. plasma CVD synthesis. The sp^2 peak showed a

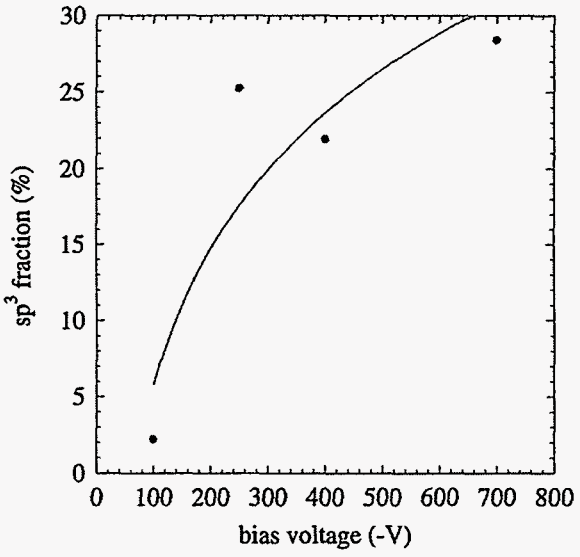

Fig.2. Calculated sp^3 fraction variation in the hydrogenated DLC films depending on the applied bias voltage during the r.f. plasma CVD synthesis

clear decreasing trend with the increase of the applied bias voltage. The sp^3 composition of each film was derived from the calculation of the sp^2 composition by the normalization and fractionalizing the total carbon content measured from the flat value above the 320 eV . The increasing trend of the calculated sp^3 composition in the DLC films with increase of the biasvoltage was consistent with the increasing trend of the hardness and residual stress depending on the same variation.

REFERENCES

1. C. Wild, J. Wagner, P. Koidl, J. Vac. Sci. Technol. A, 5, 2227 (1987)
2. X. Jiang, J. W. Zou, K. Reichelt, P. Grunberg, J. Appl. Phys., 66, 4729 (1989)
3. J. Robertson, Surf. Coat. Techno., 50, 185 (1992)
4. A. Grill, V. Patel, Diamond Relat. Mater., 2, 1519 (1993)
5. K.-R. Lee, Y.-J. Baik, K. Y. Eun, Diamond Relat. Mater., 3, 1230 (1994)
6. G. Comelli, J. Stor, C. J. Robinson, W. Jark, Phys. Rev. B 38, 7511 (1988)
7. A. Gutierrez, J. Diaz, M. F. Lopez, Appl. Phys. A, 61, 111 (1995)
8. M. Jaouen, G. Tourillon, J. Delafond, N. Junqua, G. Hug, Diamond Relat. Mater., 4, 200 (1995)
9. K.-R. Lee, Y.-J. Baik, K. Y. Eun, Diamond Relat. Mater., 2, 218 (1993)
10. S. Anders, Unpublished Data on the sp^2 and sp^3 ratio of a-C

This research was supported by the Laboratory Technology Research Partnership.Program, Office of Energy Research, U.S. Department of Energy under a CRADA (Cooperative Research and Development Agreement) between Lawrence Berkeley National Laboratory and IBM; and by the Director, Office of Energy Research, Office of Basic Energy Sciences, under U.S. DOE Contract DE-AC03-76SF00098.

Principal investigator: Simone Anders, Berkeley Lab. Email: sanders@lbl.gov. Telephone: 510-486-5928.

Symmetry of bonding states determined by resonant inelastic x-ray scattering: Ethylene/Cu(110)

P. Väterlein[1], L. Triguero[2], M. Weinelt[1], A. Föhlisch[1], J. Hasselström[1], N. Wassdahl[1], O. Karis[1], L.G.M. Petterson[2], H. Ågren[3], J. Stöhr[4], and A. Nilsson[1]

[1] Department of Physics, Uppsala University, Box 530, S-751 21 Uppsala Sweden.

[2] FYSIKUM, University of Stockholm, Box 6730, S-113 85 Stockholm, Sweden.

[3] Institute of Physics and Measurement Technology, Linköping University, S-581 83 Linköping, Sweden.

[4] IBM Research Division, Almaden Research Center, 650 Harry Road, San Jose, CA 95120-6099, USA.

INTRODUCTION

During the last years *X-ray emission (XE)* spectroscopy has become a powerful tool in the study of the bonding of molecules on solid surfaces [1]. It combines the element and (atomic) site specificity of a core level spectroscopy with a sensitivity towards the chemical environment similar to valence photoelectron spectroscopy. In a XES experiment the fluorescence photons from the sample are analyzed following a core excitation. If the primary excitation is resonant, i.e. corresponds to a NEXAFS resonance, excitation and decay have to be treated as one single inelastic scattering process [2]. In comparison with "ordinary" XE spectra *resonant inelastic x-ray scattering (RIXS)* spectra of well-defined adsorbate systems contain additional information about the symmetry of the participating electronic states since primary excitation and radiative decay are governed by dipole selection rules [3]. These can be exploited by studying the dependence of the RIXS spectra on the polarization of the incoming light and the angle dependence of the emitted radiation.

For strongly coupled adsorbates, however, the difference between RIXS and XE spectra should (almost) vanish since the core excited electron is delocalized rapidly, which leads to a less well defined core excited intermediate state. Such observations have been reported for resonantly excited Auger spectra of chemisorbed molecules [4].

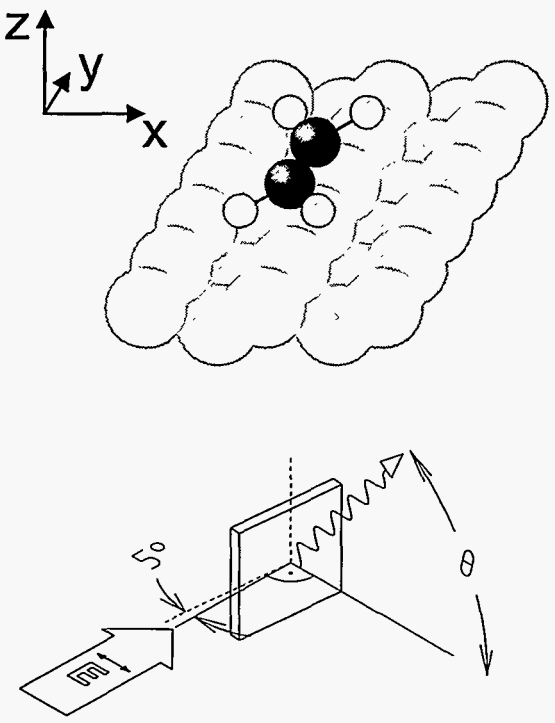

Figure 1: Top: adsorption geometry of ethylene on Cu(110). Bottom: schematic view of the experimental geometry used in the present work. In this geometry the π^*-resonance of the ethylene molecule could be excited with maximum efficiency.

In the present abstract we report RIXS measurments of ethylene adsorbed on the Cu(110) surface, where significant changes in the decay spectrum in dependence of the primary excitation are observed. To interpret these changes and to elucidate the coupling mechanism between the ethylene molecules and the Cu-surface, model calculations have been performed whithin the framework of *Density Functional Theory (DFT)*.

EXPERIMENTAL SETUP AND DATA EVALUATION

The experiments have been performed at Beamline 8.0. The endstation consists of two UHV chambers for sample preparation and analysis. The base pressure in the system was $1 \cdot 10^{-10}$ mbar. The analysis chamber is rotatable around an axis parallel to the incoming beam and houses an electron energy analyzer (Scienta SES 200) [5], an x-ray emission spectrometer [6](both mounted perpendicular to the beam and a multichannel plate de-

tector for x-xay absorption (XA) measurements. Two Cu(110) single crystals were mounted on a manipulator at an angle of about 5° between the surface and the direction of the incoming light (cf. Fig.1) with their [1-10] directions parallel and perpendicular, respectively, to the plane of incidence. The crystals could be rotated about the axis of the incoming beam thus enabling independent variation of the polarization of the incoming light (by rotation of the sample) and the direction of detection of the emitted light (by rotation of the spectrometers). Saturated monolayers were prepared by dosing ethylene on the Cu surface at a temperature of 80K.

RIXS spectra were measured in normal ($\theta = 0°$) and grazing ($\theta = 80°$) emission geometries on both crystals. From these raw spectra the background signal from the substrate and the elastically scattered peak were removed. Due to the only twofold symmetry of the Cu(110) surface and to the „di-σ" adsorption geometry of the ethylene molecules with their C-C bond parallel to the [1-10] direction of the surface (cf. Fig. 1), spectra for all three polarization directions of the emitted light could be extracted from the measured spectra assuming equal population of the C $2p_x$-, p_y-, and p_z-orbitals contributing to the different molecular orbitals and of dipolar distribution of the emitted fluorescence photons.

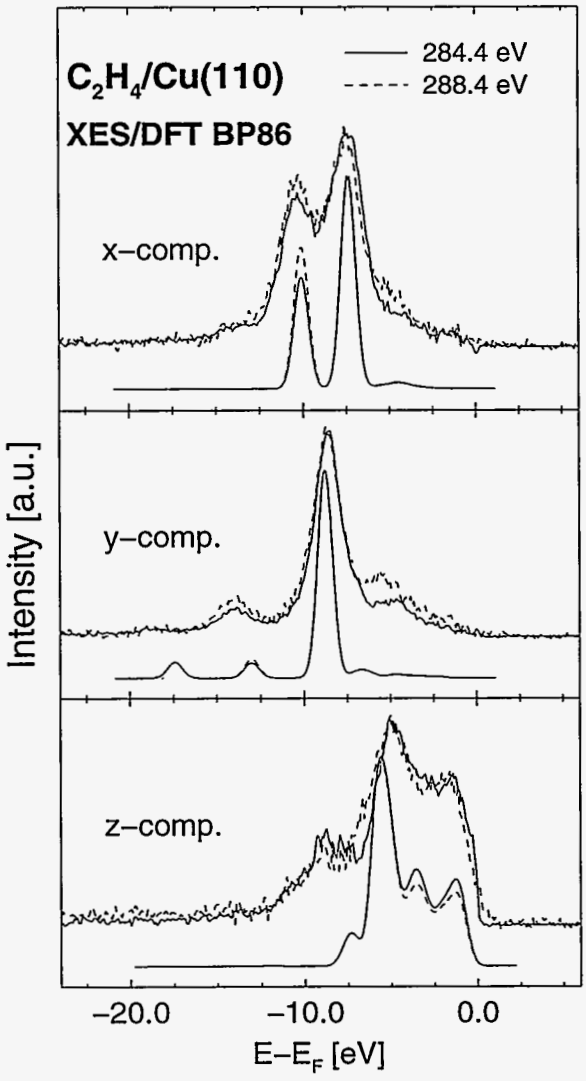

Figure 2: Experimental and calculated RIXS spectra of ethylene/Cu(110) for three different polarizations of the emitted radiation after excitation at two different photon energies.

THEORETICAL BACKGROUND

For the model calculations the „deMon" program package [7] was used which allows self consistent calculation of the electronic structure of molecules and clusters using the Kohn-Sham formalism. For the exchange and correlation interactions the gradient corrected functionals described by Becke [8] and Perdew and Wang [9], respectively, have been used. The substrate was simulated by a cluster consisting of 86 Cu atoms. For a central cluster of 14 atoms all electrons were treated explicitly while for the rest of the Cu atoms only the 4s electrons were included explicitly into the calculation. The geometry of the adsorbate was optimized during the calculations while the geometry of the cluster was fixed to the experimental bulk values. The dipole matrix elements for the primary excitation and the radiative decay were calculated using ground state wave functions (frozen orbital approximation) and the Kramers-Heisenberg equation [10] was employed to calculate the RIXS intensities. To facilitate comparison with the experimental data, the spectra have been broadened by a gaussian of 0.8 eV width (FWHM).

RESULTS AND DISCUSSION

Figure 2 shows the RIXS spectra for three different polarizations of the emitted light after excitation at two different photon energies. Below the experimental spectra the corresponding calculated spectra are plotted. All spectra have been normalized to maximum intensity. The lower excitation energy (284.8 eV) corresponds to an exci-

tation into the π* resonance of ethylene while the higher energy (288.4 eV) corresponds to an excitation into the rydberg manifold. The *x*- and *y-components* comprise those states derived from "σ-orbitals" of the ethylene molecule, while the z-component contains the "π-orbitals". The energy scale of the plot is with respect to the Fermilevel which corresponds to an emission energy of 284.3 eV as was determined by photoelectron spectroscopy (PES). In the experimental spectra for all three polarizations subtle but significant differences between the two excitation energies can be observed which are well reproduced in the calculations.

For the free ethylene molecule strict symmetry selection rules apply following resonant excitation: the π*-resonance is due to excitation of a C 1s electron into an orbital of *gerade* parity ($1b_{3g}$). Thus only orbitals with *gerade* parity contribute to the resonant decay spectrum. For the chemisorbed molecule the inversion symmetry is lifted. The selection rules are now those of the C_{2v} point group. Nevertheless a stronger variation between resonant and off-resonant emission spectra is to be expected. The reason for the experimentally observed weak variations is revealed by the calculations: across the Fermi level a mixing of states derived from the *highest occupied molecular orbital (HOMO)* of the ethylene molecule ($1b_{2u}$) and of states derived from the *lowest unoccupied molecular orbital (LUMO)* ($1b_{3g}$) occurs. Therefore the resonant excitation does not only comprise excitations in π–states of former gerade parity, which now belong to the b_1-representation but also into in π–„ungerade" states (now a_1) derived from the HOMO. The same is true for the off-resonant excitation but with different weights of the LUMO- and HOMO-like states which is the reason for the observed excitation energy dependence. This mixing of states can be observed directly in the z-component spectra: in the gasphase the XE spectrum of ethylene contains only one peak with π-symmetry ($1b_{2u}$). The *z-component* spectra in Fig. 2, however, show a broad structure which extends from -12 eV up to the Fermi level. According to the DFT calculations this structure also contains intensity from decay of both HOMO- and LUMO-like states. In contrast the σ-orbitals of the ethylene molecule remain essentially unchanged as can be concluded from the *x*- and *y-component* spectra which are very similar to the corresponding components of the gas phase XE spectrum [11]. The observed small differences are basically due to a weak distortion of the molecules upon adsorption. This is also corroborated by the DFT calculations.

Based on these findings a significant contribution of the σ-orbitals to the chemical bond between the ethylene molecule and the Cu(110) surface can be excluded. The bonding is due to a π-donation π*-backdonation mechanism. The DFT calculations furthermore show a predominant contribution of Cu 3d states to the bonding orbitals

CONCLUSIONS

In conclusion we used the *resonant inelastic x-ray scattering (RIXS)* technique to investigate the chemical bond of ethylene molecules on the Cu(110) surface. Our spectra show a subtle but significant dependency on the exciting photon energy which proves a mixing of states with the symmetries of the HOMO and LUMO of ethylene, respectively, above the Fermi level. A similar mixing can be observed directly as broadening of emission lines in the z-component of the XE spectrum. These experimental findings are supported by model calculations carried out whithin the framework of *density functional theory (DFT)*. A significant contribution of the σ-orbitals of ethylene to the adsorbate-substrate bond could not be found. Therefore our experimental and quantum-chemical results lead unambigously to a description of the chemical bond between the ethylene molecule and the Cu(110) surface by a π-donation π*-backdonation mechanism.

ACKNOWLEDGEMENTS

The authors would like to acknowledge valuable and stimulating discussions with Joseph Nordgren and Nils Mårtensson.

REFERENCES

[1] A. Nilsson, M. Weinelt, T. Wiell, P. Bennich, O. Karis, N. Wassdahl, J. Stöhr, M.G. Samant, Phys. Rev. Lett. **78**(14) 2874 (1997).

[2] T. Åberg, Physica Scripta **21**, 495 (1990).

[3] P. Glans, K. Gunnelin, P. Skytt, J.-H. Guo, N. Wassdahl, J. Nordgren, H. Ågren, F. Kh. Gel'mukhanov, T. Warwick, E. Rotenberg, Phys. Rev. Lett. **76**(14) 2448 (1996).

[4] W. Wurth, C. Schneider, R. Treichler, D. Menzel, and E. Umbach, Phys. Rev. B **37**, 8725 (1988); A. Sandell, O. Björneholm, A. Nilsson, J.N. Andersen, and N. Mårtensson, Phys. Rev. B **49**(15) 10136 (1994).

[5] N. Mårtensson, P. Baltzer, P. Brühweiler, J.O. Forsell, A. Nilsson, A. Stenborg, and B. Wannberg, J. Electron Spetrosc. Relat. Phenom. **70**, 117 (1994).

[6] J. Nordgren, G. Bray, S. Cramm, R. Nyholm, J.-E. Rubensson, and N. Wassdahl, Rev. Sci. Instrum. **60**, 1690 (1989).

[7] D.R. Salahub, R. Fournier, P. Mlynarski, I. Papai, A. St-Amant, and J. Ushio in *Density Functional Methods in Chemistry*, J. Labanowski and J. Andzelm eds., Springer, New York (1991) p. 77; A. St-Amant, PhD thesis, Université de Montréal, 1992. The present version of the program has been substantially modified by L.G.M. Petterson.

[8] A.D. Becke, Phys. Rev. A **38**, 3098 (1988).

[9] J.P. Perdew and Y. Wang, Phys. Rev. B **33**, 8822 (1986).

[10] H.A. Kramers and W. Heisenberg, Z. Phys. **31**, 681 (1925); J.J. Sakurai, *Advanced Quantum Mechanics*, Addison Wesley (1967).

[11] J. Nordgren, private communication.

This work was supported by the Director, Office of Energy Research, Office of Basic Energy Sciences, Materials Science Division, of the U.S. Department of Energy under Contract No. DE-AC03-76SF00098, by the Swedish Natural Science Research Council (NFR), the Swedish Institute (SI), and the Göran Gustafsson Foundation for Research in Natural Science and Medicine. One of us (P.V.) gratefully acknowledges a stipend from the Deutsche Forschungsgemeinschaft .

Principal investigator: Anders Nilsson, Dept. of Physics, Uppsala University, Box 530, S-751 21 Uppsala, Sweden. Email: anders.nilsson@fysik.uu.se. Telephone: +46-(0)18-471-3609. Fax: +46-(0)18-471-3611.

X-Ray Emission Spectroscopy of NO Molecules Adsorbed and Coadsorbed with Oxygen on Ru(001)

M. Stichler[1], C. Keller[1], A. Föhlisch[2], A. Nilsson[2], C. Heske[3], W. Wurth[1] and D.Menzel[1]
[1]Physik Department E20, Technische Universität München, 85747 Garching, Germany
[2]Department of Physics, Uppsala University, Box 530, S-75121 Uppsala, Sweden
[3]Advanced Light Source, Ernest Orlando Lawrence Berkeley National Laboratory, University of California, Berkeley, California 94720, USA

INTRODUCTION

X-ray emission spectroscopy (XES) has recently proven to be a very promising tool for the investigation of trends in the chemical bond of adsorbates to surfaces [1]. For low Z-elements the final states reached after fluorescence decay of the core hole state are energetically equivalent to valence electronic states reached in photoemission. Due to the localisation of the core hole excited in the primary step of the emission process this technique is highly atom specific. The transition matrix element involved is the dipole matrix element so that angle dependent measurements on oriented adsorbates allow the use of symmetry selection rules to assign the spectral features. On the basis of comparisons with model calculations it has been suggested that the observed intensities can be interpreted in terms of the symmetry restricted local valence electronic density of the adsorbates in the ground state i.e relaxation effects in the initial core hole state appear to play a minor role.

The goal of our joint study was to test the applicability of the technique and the appropriate interpretation for more complicated coadsorption systems of NO and oxygen on a Ru(001) surface. The adsorption of NO on the bare Ru(001) surface is particularly interesting because two very distinctly different NO adsorption states (v_1- NO and v_2-NO) are populated simultanously in this case. The two states can be distinguished for example using vibrational spectroscopy or high resolution x-ray photoelectron spectroscopy (XPS). Coadsorption of NO with oxygen on the Ru(001) surface leads, depending on the preparation, to a situation where either v_1-NO or v_2-NO is present on the surface. Both NO adsorption states have been characterised very thoroughly in our lab using different techniques like vibrational spectroscopy, work function measurements, XPS and geometric structure determination with LEED [2]. On the basis of these results it has been suggested that the two states are very different in terms of electronic structure (v_1-NO being electronegative and v_2-NO being electropositive). Due to energetic differences in the positions of the respective x-ray absorption resonances the two species can even be excited separately in the case where both are present simultaneously on the surface. Hence XES with resonant excitation should be ideally suited to gain more insight on the atom specific electronic structure of these two adsorption states.

EXPERIMENTAL

The experiments have been performed at the Swedish endstation at beamline 8.0. The x-ray spectrometer, which can be rotated around an axis parallel to the incoming beam, is based on three interchangeable grazing incidence gratings in combination with a moveable multichannel detector [3]. The resolution of the spectrometer for our experiments was about 0.5 eV. The preparation of the different layers was controlled by high-resolution XPS using a SCIENTA electron analyzer which can also be rotated around the incoming beam.

RESULTS AND DISCUSSION

Figure 1 shows results for the v_1-NO species in the presence of oxygen. The top part of the figure shows the states with σ-symmetry while in the bottom part the π-states are depicted. For both symmetries the results for N-K-emission (full symbols) and O-K-emission (open symbols) are

plotted on a common binding energy scale. Before we start with the discussion it should be noted that the intensity of the features seen in the emission spectra is governed by the local 2p-character of the respective orbitals because of the dipole transitions to the 1s-core orbitals. The relative intensities of the features seen in the O and N K-emission spectra, respectively, are normalized in such a way that the areas of the two sets of spectra are equal.

First we will discuss the states with σ-symmetry. From the spectra it is quite clear that the 2p-contribution to the 4σ-orbital is localized on the nitrogen end of the molecule while the 2p-contribution of the 5σ-orbital seems to be more evenly distributed. The contribution of σ-type orbitals (marked by a horizontal line) in the region of the metal d-bands closer to the Fermi level is fairly small.

This is quite different in the case of the π-type states. Here the states close to the Fermi level (again marked by a horizontal line), are much more pronounced. For the oxygen end of the molecule the 2p-derived contributions are higher than for the nitrogen end. It is also obvious that the maxima are significantly shifted in energy. Pronounced differences between the oxygen and nitrogen ends of the molecule are also observed for the 1π-orbital. Here the 2p-character is more pronounced on the nitrogen end of the molecule. Particularly interesting is the observed splitting of the 1π-orbital (see inset). We attribute this splitting to the fact that the v_1-NO-species are adsorbed in rows of threefold hollow sites on the surface parallel to adjacent oxygen rows in a (2x1)-configuration. In this configuration the symmetry of the NO-molecule is reduced and the 1π-orbitals along the rows and perpendicular to the rows are no longer degenerate.

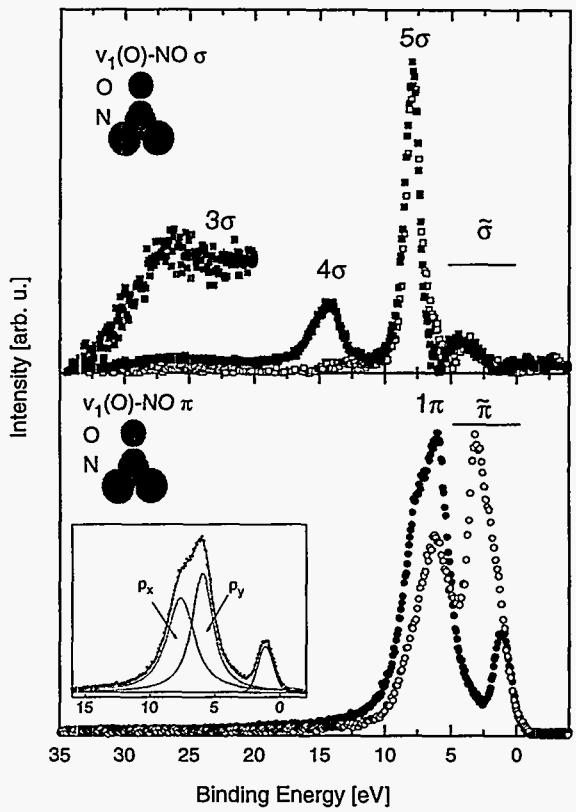

Figure 1: Symmetry resolved XE spectra for oxygen and nitrogen of v_1-NO +O /Ru(001)

In the following we will compare the results for the v_1-NO species with those obtained for the on-top v_2-NO species, again in the presence of coadsorbed oxygen. Figure 2 shows the resulting XE-spectra for the v_2-NO species in the presence of oxygen. The top part of the figure shows again the states with σ-symmetry while in the bottom part the π-states are depicted. As before we plot the results for N-K-emission (full symbols) and O-K-emission (open symbols) for both symmetries on a common binding energy scale.

Comparison of the states with σ-symmetry reveals that in the case of the v_2-species the 2p-character of the 4σ-orbital is more evenly distributed across the molecule. The states with σ-symmetry in the range of the metal d-band are even less visible than before.

While the differences between the two species are not so striking in the σ-type orbitals, they are much more pronounced in the π-system. Again there are strong π-symmetric states close to the Fermi level in the range of the metal d-band. As in the case of v_1-NO, the 2p-character of these states is more localized on the oxygen end of the molecule. In comparison to the v_1-species the intensity of these features is now significantly reduced. Even more striking is the complete

absence of a splitting of the 1π-derived states. This can be understood on the basis of the known geometry of the v_2-NO species. As mentioned above this species is adsorbed in an on-top position surrounded by oxygen atoms in a hexagonal configuration. Therefore the molecule is still in a high symmetry configuration and the 1π-orbital is degenerate.

Currently we are in the process of comparing our experimental results with density-functional cluster calculations for the two different NO-species [4]. It appears as if the ground-state calculations of the local 2p-character of the valence electronic distribution already explain most of the trends observed quite satisfactorially. Most of the features observed can be explained qualitatively in a three-center bond picture between NO and Ru. The differences in electronic structure between the two species correlate well with the expectations from the known changes in the structural parameters [2]. However, particularly in the d-band regime the differences are much less than expected from the previously assumed differences in electronegativity which may be due to influences of core hole screening.

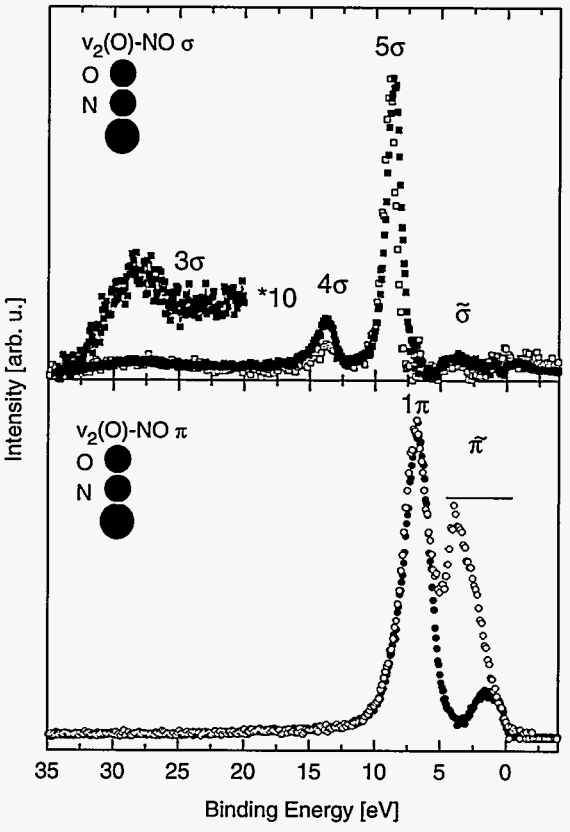

Figure 2: Symmetry resolved XE spectra for oxygen and nitrogen of v_2-NO +O /Ru(001)

In summary, even though the local charge distribution can only be derived in a symmetry restricted sense from the XES data, the information obtained is nevertheless unique and provides a very important experimental measure for the quality of theoretical descriptions of adsorbate chemical bonds.

REFERENCES

[1] A.Nilsson, M. Weinelt, T. Wiell, P. Bennich, O. Karis, J. Stöhr, M.G. Samant, Phys. Rev. Lett. **78**, 2847 (1997); N. Wassdahl, A. Nilsson, T. Wiell, H. Tillborg, L.C. Duda, J.H. Guo, N. Mårtensson, J. Nordgren, J.N. Andersen, R. Nyholm, Phys. Rev. Lett. **69**, 812 (1992)

[2] M.Stichler, R. Weimar, D. Menzel, Surf. Sci. **384**, 179 (1997), P. Jakob, M. Stichler, D. Menzel, Surf. Sci. **370**, L185 (1997).

[3] J. Nordgren, G. Bray, S. Cramm, R. Nyholm, J.E. Rubensson, N. Wassdahl, Rev. Sci. Instrum. **60**, 1690 (1989).

[4] M. Stichler, C. Keller, A. Föhlisch, A. Nilsson, C. Heske, L.G.M. Pettersson, M. Stauffer, U. Birkenheuer, N. Rösch, W. Wurth, D. Menzel, to be published.

This work was supported by the Deutsche Forschungsgemeinschaft under project Me266/22-1

Principal investigator: Dietrich Menzel, Physik Department E20, Technische Universität München, 85747 Garching, Germany. Email: menzel@e20.physik.tu-muenchen.de Telephone: +49-89-289-12609.

X-ray Photoemission and Photoabsorption of Organic Electroluminescent Materials

R. Treusch[1], S. Kakar[2,3], C. Heske[4], T. van Buuren[3], L. J. Terminello[2,3], F. J. Himpsel[1], V. V. Dinh[2], H. W. Lee[3], K. Pakbaz[3], G. Fox[3], and I. Jiménez[3,5]

[1]Dept. of Physics, University of Wisconsin-Madison, Madison, WI 53706-1390

[2]Dept. of Applied Science, University of California-Davis, Livermore, CA 94550

[3]Lawrence Livermore National Laboratory, Livermore, CA 94551

[4]Advanced Light Source, Lawrence Berkeley National Laboratory, Berkeley, CA 94720

[5]Present address: Dept. Intercaras y Crecimiento, ICCM-CSIC, Campus de Cantoblanco, E-28049 Madrid, Spain

Core level and valence band photoemission as well as core level photoabsorption of thin films of Tris-(8, hydroxyquinoline) aluminum (Alq_3) and N,N'-diphenyl-N,N'-bis (3-methylphenyl)- 1,1'-biphenyl-4,4'-diamine (TPD) were studied using synchrotron radiation. Thin films of Alq_3 and TPD were sublimed from purified powders onto Si wafers in ultra high vacuum. Photoemission data were obtained with the ellipsoidal mirror analyzer (EMA) at beamline 8.0 at the Advanced Light Source while the absorption data were taken at beamline 8.2 at the Stanford Synchrotron Radiation Laboratory. Both spectroscopies were used to elucidate the element-specific electronic structure of Alq_3 and TPD. These molecules are materials of choice for organic light emitting devices (OLEDs) used in future applications such as flat panel displays [1]. For Alq_3, the experimental data were compared to calculations based on density functional theory (fig. 1). Since the calculations for the occupied density of states reproduce the measured valence band photoemission data quite well, we were able to assign all features to specific atoms/bonds in the molecule [2]. Determining the positions of the highest occupied and lowest unoccupied molecular orbitals we estimated the potential barriers at the Alq_3/TPD interface to get a better understanding of the charge transport properties of the OLED [3].

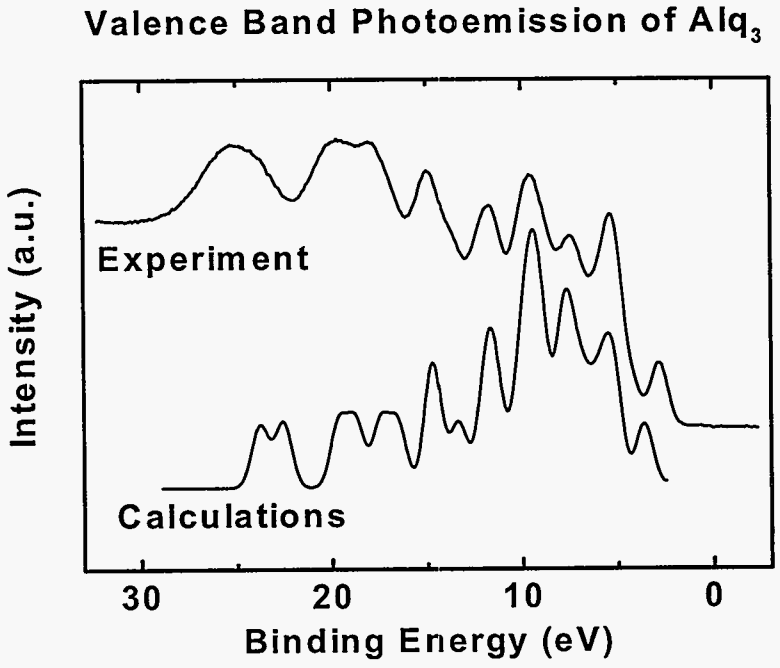

Figure 1. Comparison of the valence band photoemission of Alq_3 ($h\nu$ = 240 eV) with calculations based on density functional theory [2]. The calculations were broadened with a Gaussian function of 1.2 eV (FWHM) to account for solid state effects and experimental resolution. The good agreement between experiment and theory makes it possible to assign all features to specific atoms/bonds in the molecule [2].

A comparison of freshly evaporated films of Alq_3 and TPD with films that have been exposed to intense radiation or oxidative conditions shed light on possible damage mechanisms of the molecules [3]. This knowledge is crucial to understand and overcome present lifetime limitations of the OLEDs where oxidation and other effects lead to a significant degradation of the brightness within several 100 to a few 1000 hours. The experimental results in combination with the theoretical understanding open the way to analyze and improve the device performance, and, in particular, to tailor molecules for specific needs.

REFERENCES

1. J. R. Sheats, H. Antoniadis, M. Hueschen, W. Leonard, J. Miller, R. Moon, D. Roitman, and A. Stocking, Science **273**, 884 (1996)

2. A.Curioni, W. Andreoni, R. Treusch, F. J. Himpsel, E. Haskal, P. Seidler, C. Heske, S. Kakar, T. van Buuren, and L. J. Terminello, accepted for Appl. Phys. Lett. (1998)

3. R. Treusch, S. Kakar, C. Heske, T. van Buuren, L. J. Terminello, F. J. Himpsel, V. V. Dinh, H. W. Lee, K. Pakbaz, G. Fox, and I. Jiménez, in preparation (1998)

This work was supported by the Director, Office of Energy Research, Office of Basic Energy Sciences, at the LLNL under Contract No. W-7405-ENG-48, by the NSF under Award Nos. DMR-9632527 and DMR-9531009, and by the Spanish Ministerio de Educación y Ciencia.

Principal investigators: Louis J. Terminello, Lawrence Livermore National Laboratory
E-mail: terminello1@llnl.gov. Phone: (510) 423-7956
Franz J. Himpsel, University of Wisconsin-Madison
E-mail: himpsel@comb.physics.wisc.edu. Phone: (608) 263-5590

Beamline 9.0.1 Abstracts

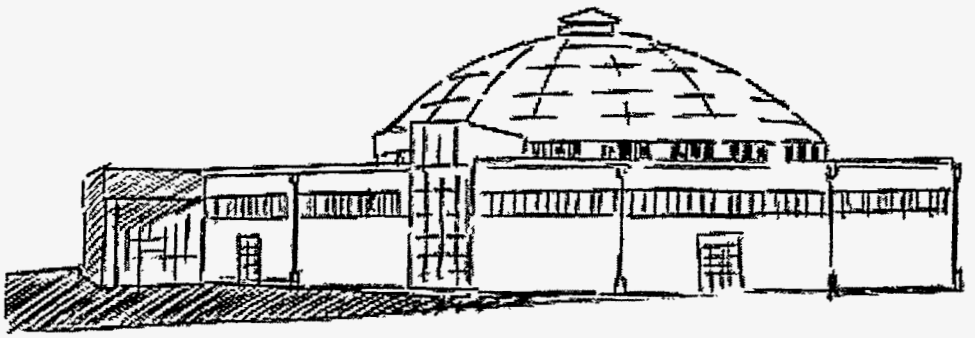

Angle-Resolved Study of Ar $2p_{1/2,3/2}^{-1}$ ns,d Resonant Auger Decay

A. Farhat[1], M. Humphrey[1], B. Langer[1], N. Berrah [1], J. D. Bozek[2] and D. Cubaynes[3]

[1]Physics Department, Western Michigan University, Kalamazoo, MI 49008
[2]Lawrence Berkeley National Laboratory, Advanced Light Source,
Mail Stop 2-400, Berkeley, CA 94720
[3]LSAI, URA 775, CNRS, Université Paris Sud, Orsay France

INTRODUCTION

After the excitation of an inner shell electron, an atom can relax nonradiatively through one of the following mechanisms, summarized here for the Ar $2p^{-1}4s$ resonance:

$2p^5 4s \rightarrow 2p^6 3s^2 3p^4 4s + e^-$	*Spectator Auger decay*	*(a)*
$2p^5 4s \rightarrow 2p^6 3s^2 3p^5 + e^-$	*Participator Auger decay - shake down*	*(b)*
$2p^5 4s \rightarrow 2p^6 3s^2 3p^4 4p + e^-$	*Participator Auger decay - shake up*	*(c)*
$2p^5 4s \rightarrow 2p^6 3s^2 3p^4 + 2e^-$	*Participator Auger decay - shake off.*	*(d)*

In previous non-angular-resolved studies of intensity distributions, it has been reported that the decay of the Ar $2p^{-1}4s$ states can be described well by the spectator model, while the decay of the Ar $2p^{-1}3d$ and $2p^{-1}4d$ states is dominated by shake up processes [1]. In its purest form, the strict spectator model assumes no interaction between the spectator electron, which was resonantly excited from an inner shell, and the core. Previous angular-resolved measurements of Auger decays, observed at the Ar $2p^{-1}4s$ resonance, have suffered from poor resolution in the photoelectron spectra [2], and such measurements of the $2p^{-1}3d$ and $2p^{-1}4d$ resonances have been unobtainable due to insufficient photon resolution.

RESULTS

We have reported angle-resolved measurements of the Ar $2p_{1/2,3/2}^{-1}4s$, 3d, and 4d resonant Auger decays which can be found in Farhat et al. [3]. These measurements were achieved using time-of-flight electron spectroscopy along with high flux synchrotron radiation from the Advanced Light Source. The intensity distributions and angular distribution anisotropy parameters (β) have been reported for nearly all of the $3p^4nl$ final ionic states, and a comparison of these measurements with previous results demonstrates good agreement. We have shown that a large majority of the β parameters are either small positive or negative, due to parity unfavored transitions. Also, as predicted by the spectator model, we found that the averaged β is isotropic in the case of the $2p_{1/2}^{-1}4s$ resonance. This result corroborates the work by Cooper [4] using the angular momentum transfer theory. In addition, our higher resolution measurements allowed the determination of individual large β values which appear much weaker in previously unresolved measurements due to a strong cancellation effect by neighboring lines.

It has also been demonstrated that while the intensity distributions between different resonances originating from different 2p spin states (i.e. $2p_{1/2}$ vs. $2p_{3/2}$) are not always similar, the extracted β parameters for the two resonances agree in many cases. Our results for the intensity distributions further support the prediction of the spectator model for the $2p_{1/2,3/2}^{-1}4s$ resonances, but demonstrate the breakdown of this model for the $2p_{1/2,3/2}^{-1}3d$ and $2p_{1/2,3/2}^{-1}4d$ resonances. While our results

our results agree with much of the theoretical work for the $2p_{1/2,3/2}^{-1}4s$ resonances, we hope that this report, which is the first in the case of the β parameters for the $2p_{1/2,3/2}^{-1}3d$, the $2p_{3/2}^{-1}4d$ resonances, and for the intensity and β parameter for the $2p_{1/2}^{-1}4d$ resonance, will stimulate further experimental and theoretical work.

ACKNOWLEDGMENT

This work was supported under contract No. DE-FG02-95ER 14299 by the US Department of Energy, Office of Basic Energy Science, Division of Chemical Sciences. B.L. is indebted to the Alexander von Humboldt Foundation for partial financial support under the Feodor Lynen program. We would like to thank Ant Wills and Uwe Becker for useful discussions and comments.

REFERENCES

1. U. Becker, D. Szostak, M. Kupsch, H. G. Kerkhoff, B. Langer, and R. Wehlitz, J. Phys. B: At. Mol. Opt. Phys. **22**, 749 (1989).
2. T. A. Carlson, D. R. Mullins, C. E. Beall, B. W. Yates, J. W. Taylor, D. W. Lindle, and F. Grimm, Phys. Rev. A **39**, 1170 (1989).
3. A. Farhat, M. Humphrey, B. Langer, N. Berrah , J. D. Bozek and D. Cubaynes, Phys. Rev. A **56,** 501 , 1997.
4. J. W. Cooper, Phys. Rev. A **39**, 3714 (1989).

Principal investigator: Nora Berrah, Western Michigan University. Email: berrah@wmich.edu.
Telephone: (616) 387-4955.

Angle-Resolved Two-Dimensional Mapping of Electron Emission Following Cl 2p Excitations in the HCl Molecule

E. Kukk,[1,2] A. A. Wills,[1] B. Langer,[3] J. D. Bozek,[2] O. Nayandin,[1] M. Alshehri,[1] A. Farhat,[1] D. Cubaynes[4] and N. Berrah[1]

[1]Physics Department, Western Michigan University, Kalamazoo, MI 49004
[2]Lawrence Berkeley National Laboratory, Advanced Light Source, University of California, Berkeley, CA 97420.
[3]Fritz-Haber-Institut der Max-Planck-Gesellschaft, Faradayweg 4-6, D-14195, Berlin, Germany.
[4]Laboratoire de Spectroscopy Atomique et Ionique, URA 775, CNRS, Université Paris Sud, 91405 Orsay, France.

INTRODUCTION

Inner-shell processes in small molecules have been studied with growing interest during recent years. Rapid improvements in experimental techniques have revealed new details in Auger and photoelectron spectra such as anisotropy of electron emission [1-3], molecular field splitting [4] and post-collision interaction [5]. However, these studies have been performed at only a few selected photon energies.

RESULTS AND DISCUSSIONS

We have measured a complete angle-resolved two-dimensional experimental picture of electron emission from a diatomic molecule over the pre-edge structure and into the continuum of a core ionization threshold. The extensive set of data demonstrates many phenomena associated with core excitation and ionization. They are described in Kukk et al. [6] along with the experimental method. Briefly, we have measured Auger and valence photoelectron spectra of HCl over 14 eV wide photon energy range across the Cl 2p ionization thresholds as shown in Fig.1. Auger decay spectra of dissociative core-excited states were observed to change with photon energy, reflecting a change in the rate of dissociation. Auger electron spectra at the first Rydberg states were analyzed and the evolution of the resonant Auger to the normal Auger decay, distorted by post-collision interaction, was examined. Valence photoionization channels were shown to resonante strongly at the photon energies of the core-to-Rydberg excitations. We derived the angular distributions of the photo-and Auger electron lines and observed strong fluctuations of the asymmetry parameter β values of the 2π photoline at some Rydberg resonances. However, the anisotropy of the Auger decay at the σ^* and that of Rydberg excitations was found to be different, with the latter showing uniformly negative β values.

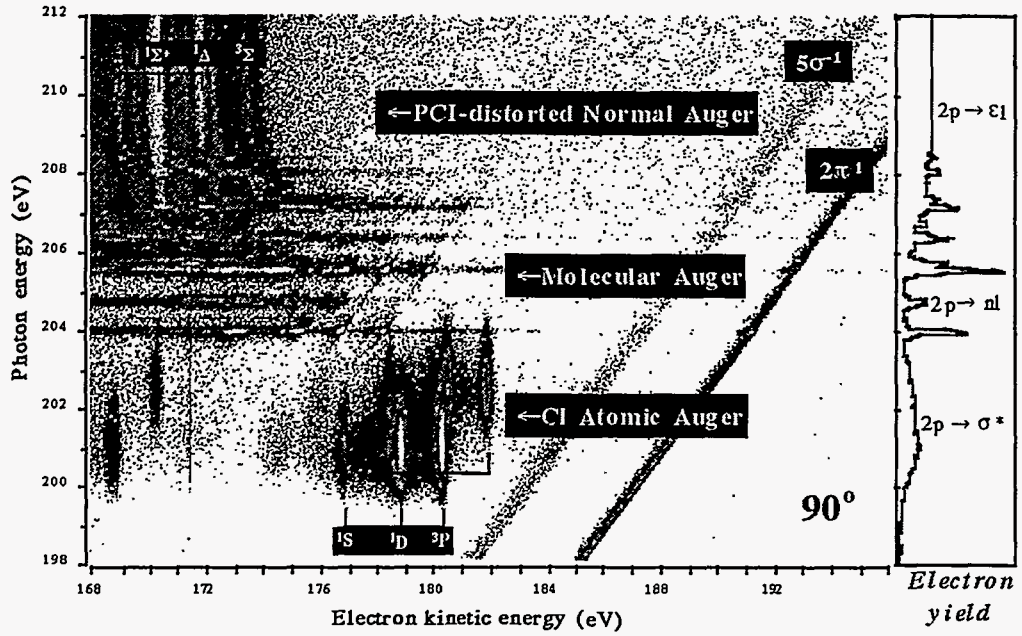

Fig.1. Two-dimensional (2D) map of electron emission from the HCl molecule across the Cl 2p ionization threshold, taken at 90° relative to the polarization plane. The total electron and partial 2π photoelectron yields are shown on the right.

ACKNOWLEDGMENTS

This work was supported by the US Department of Energy, Office of Basic Energy Science, Division of Chemical Science under contract No. DE-FG02-95ER14299.

REFERENCES

1. U. Becker, R. Holzel, H. G. Kerkhoff, B. Langer, D. Szostak, and R. Wehlitz, Phys. Rev. Lett. **56**, 1455 (1986)
2. O. Hemmers, F. Heiser, J. Eiben, R. Wehlitz, and U. Becker, Phys. Rev. lett. 71, 987 (1993).
3. U. Hergerhahn and U. Becker, J. Electron Spectrosc. **72**, 243 (1995).
4. H. Aksela, E. Kukk, S. Aksela, O. P. Sairanen, A. Kivimaki, E. Nommiste, A. Ausmees, S. J. Osborne, and S. Svensson, J. Phys. B. **28**, 4259 (1995).
5. M. Neeb, M. Biermann and W. Eberhardt, J. Electron Spectrosc. **69**, 239 (1994).
6. E. Kukk, A. A. Wills, N. Berrah, B. Langer, J. D. Bozek, O. Nayandin, M. Alsherhi, A. Farhat, and D. Cubaynes, Phys. Rev. A **57** R1485 (1998).

Principal investigator: Nora Berrah, Western Michigan University. Email: berrah@wmich.edu.
Telephone: (616) 387-4955.

Angular Distributions of Resonant and Non-Resonant Auger Electrons as a Test Case for the Validity of the Spectator Model: The Argon L_2MM Case

B. Langer[1,2], N. Berrah[1], A. Farhat[1], M. Humphrey[1], D. Cubaynes[3], A. Menzel[2] and U. Becker[2]

[1]Department of Physics, Western Michigan University, Kalamazoo, Michigan 49008-5151, USA
[2]Fritz-Haber-Institut der Max-Planck-Gesellschaft, Faradayweg 4-6, D-14195 Berlin, Germany
[3]LSAI, Université Paris-Sud, F-91405 Orsay Cedex, France

INTRODUCTION

Ever since the first measurements of resonant Auger spectra, following excitation of inner-shell resonances, have been measured they have been compared with normal Auger spectra following above threshold ionisation. A strong similarity was anticipated because the excited electron could be considered as a spectator of the decay process, shielding the core hole and thereby shifting the whole electron spectrum to higher kinetic energies [1]. This simple picture was true for many cases but pronounced deviations from the model were found soon after the study of these processes was tremendously promoted by the use of monochromatic synchrotron radiation.

RESULTS

We have measured the Ar $2p \rightarrow ns,d$ selective excitation with high resolution and a complete analysis can be found in Langer et al. [2]. Here we will only describe the case of the $2p_{1/2} \rightarrow nd$ resonances.

$2p_{1/2} \rightarrow nd$ Resonances.

The complete $2p_{1/2} \rightarrow 3d$ resonant Auger spectrum is shown in Figure 1. Contrary to the $2p \rightarrow 4s$, this resonant transition does not obey the predicted behavior of the spectator model in its most simple form, i.e. the observed spectra are much different from the normal Auger spectra. Instead, the spectra are dominated by shake-up processes. A possible reason for this has been discussed by Aksela and Mursu [3], who have demonstrated the importance of the shake-up process arising from the different degree of collapse of the 3d wave function in the initially excited $2p \rightarrow 3d$ state. This is due to a larger repulsive exchange interaction between the 3p and 3d electrons in the $^1P_1$ state, as compared to the final ionic state. Another explanation has been provided by [4], who has described in some detail the spatial properties of the wave function which leads to a high shake-up probability.

No theoretically predicted β values are available, therefore no comparison is possible at present. However, a comparison with the spectator model can be made if we restrict it to the so-called "gross spectator model" (GSM) and to the $2p_{1/2} \rightarrow 3d$ resonance. In the light of the argumentation at the beginning of this paragraph this seems to be unjustified because of the difference in the structures of the resonant and non-resonant spectrum. But, as mentioned earlier, the validity of the spectator model may be discussed in the context of two different situations: the presence of a strong shake-up probability, and the existence of strong configuration interaction and singlet-triplet mixing. It is the second situation that really causes a breakdown of the spectator model [5]. The shake-modified spectator model would predict the same β values for the diagram and shake-up transitions because shake-up probability is basically an overlap factor that does not affect the rest of the Coulomb matrix elements. Thus,

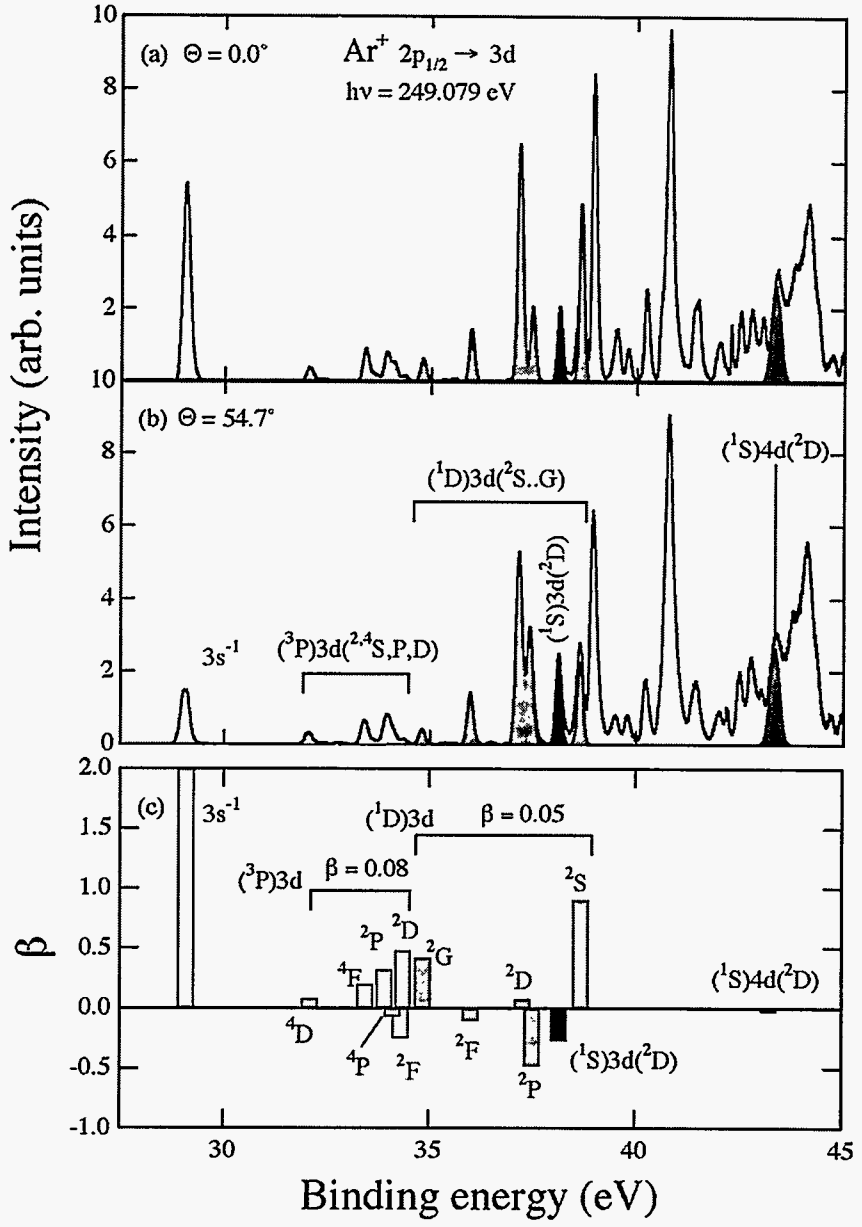

Fig. 1. High resolution resonant Auger spectrum taken on the Ar $2p_{1/2} \rightarrow 3d$ resonance. The light-grey shaded lines correspond to the ^3P core, the dark-grey shaded lines to the ^1D core, and the black lines to the ^1S core. The β values in part (c) are shown by bars shaded correspondingly. The average β of all lines with the same core parent term are shown above or underneath by their numbers

the spectrum may look quite different but the angular distribution is similar. How could this be proved without numerical calculations? The test case are the $2p_{1/2} \rightarrow nd$ excitations because they converge to the same ionisation limit as the ns excitations with a spherical $2p_{1/2}$ final ionic state. Therefore, all the arguments for the ns excitations apply also to the nd excitations. Since we have no β values for the different multiplets we can compare our data only with the sum of the doublet and quartet states. This sum of β has to be zero according to the spectator model which in this particular restricted version is known as gross spectator model. A comparison with the ^1S, ^1D and ^3P states shows β values of -0.27, 0.05, and 0.08, respectively, corresponding quite well - except for the ^1S state - with the prediction of the spectator model.

The deviation of the ^1S core state is most pronounced for the 3d ^2D state with its $\beta = -0.27$. The even stronger shake-up state 4d ^2D, however, shows already a β value close to zero in accordance with the gross spectator model. The collapsed 3d wavefunction may cause mixing between different parent states but also between the $2p_{1/2}$ and $2p_{3/2}$ core hole states. Both interactions would cause a measurable deviation from the GSM predictions. These deviations, however, seem to disappear already for n=4 suggesting to consider the 3d behavior as a collapse induced anomaly rather than a common deviation in resonant Auger decay. In order to prove if this statement holds also for higher n, the spectrum of the $2p \rightarrow 4d$ resonance was examined. Concentrating on the ^1S, ^1D and ^3P parent states with 4d spectator electron the sum of the β parameters are the following: 0.06, 0.11, and -0.04. Obviously, the correspondence with the gross spectator model prediction is much more favorable than in the case of the $2p_{1/2} \rightarrow 3d$ excitation. All three parent states of the 4d spectator electron still agree quite well. In contrast, the 3d shake-down state deviates significantly from the predicted vanishing Auger anisotropy. The observed β value is somewhat more negative than the value observed for the 3d excitation, but still relative similar.

In summary, we have reported [2] on new measurements of the resonant Auger spectra following selective excitation of the Ar $2p \rightarrow ns,d$ resonances by angle-resolved electron spectroscopy. The results are interpreted in terms of testing the validity of the spectator model in its different forms such as gross and strict spectator model, in particular in the case of the $2p_{1/2}$ excitations which are specifically suited for testing the spectator model due to alignment considerations. The comparison proves the validity of both spectator models for the Ar $2p \rightarrow 4s$ but shows the breakdown of the strict but also a partial breakdown of the gross spectator model for the Ar $2p \rightarrow nd$ excitations for n=3. Mixing of the core and maybe hole states due to the 3d wave function collapse is considered the most probable reason for this breakdown. The recovery of the gross spectator model, however, starts unexpectedly early with n=4, a trend being experimentally confirmed via shake-up states up to n=6. Specific measurements are suggested to prove this statement for even higher n up to threshold.

ACKNOWLEDGMENTS

B.L. is grateful for a Feodor-Lynen Fellowship from the Alexander von Humboldt Foundation. This work was supported by the US Department of Energy, Office of Basic Energy Science, Division of Chemical Science, under Contract No. DE-FG02-95ER14299.

REFERENCES

1. M. O. Krause, T. A. Carlson, and W. E. Moddemann , J. Phys. (Paris) **32** C4-139 (1971).
2. B. Langer, N. Berrah, A. Farhat, M. Humphrey, D. Cubaynes, A. Menzel and U. Becker, J. Phys. B **30**, 4255 (1997).
3. H. Aksela and J. Mursu, Phys. Rev. A **54** 2882 (1996).
4. M. Meyer, E. v. Raven, B. Sonntag, and J.E. Hansen, Phys. Rev. A **43** 177-188 (1991).
5. U. Hergenhahn, S.B. Whitfield, J. Tulkki, F. Heiser, N.M. Kabachnik, B. Langer, and U. Becker, Phys. Rev. A **55** 2050-2066 (1996).

Principal investigator: Nora Berrah, Western Michigan University. Email: berrah@wmich.edu. Telephone: (616) 387-4955.

Breakdown of LS Coupling for a Parity Unfavored Transition in Neon: Angle Resolved 2D Imaging of Two Electrons Processes

A.A. Wills[1], T.W. Gorczyca[1], B. Langer[2], E. Kukk[1,4], Z. Felfi[3], M. Alshehri[1], O. Nayandin[1], J.D. Bozek[4], and N. Berrah[1]

[1]Physics Department, Western Michigan University, Kalamazoo, MI 49004

[2]Fritz-Haber-Institut der Max-Planck-Gesellschaft, Faradayweg 4-6, D-14195, Berlin, Germany

[3]Center for Theoretical Studies of Physical Systems, Clark Atlanta University, Atlanta GA 30314

[4]Lawrence Berkeley National Laboratory, Advanced Light Source, University of California, Berkeley CA 94720.

INTRODUCTION

The mechanism by which two electrons can be simultaneously excited by a single photon has been subjected to significant experimental and theoretical investigations over many years. Since this process only occurs via inter-electron correlations, the many body dynamics of an atom can be probed. These studies have, for the most part, focused on helium [1], as it represents the simplest system for which two-electron processes can be investigated. Systems in which the ground state electrons occupy higher angular momentum orbitals provide the opportunity to observe more complex effects since there are many more optically allowed transitions. Until the recent availability of third generation sources, the study of doubly excited states in heavier atoms was limited by the achievable resolving power [2,4]. The first photoabsorption measurements in neon [5] indicated that all of the structure due to two electrons excitation, with only one exception, could be well described by LS-coupling. However, a recent very high resolution photoionization experiment, below 53 eV [6], exhibited rich resonance structure which could not be explained in a simple LS coupling picture. This corroborates the general importance of LS coupling breakdown in neon pointed out by Samson et al. [3]. In the present study, we have concentrated on achieving a complete picture of the excitation and decay processes of doubly excited states in neon,

$$h\nu + Ne\ (2s^2 2p^6\ {}^1S_0) \rightarrow Ne^{**}\ (2s^2 2p^4\ nln'l')$$
$$\rightarrow Ne^{+*}\ (2s^2 2p^4\ n''l'') + e^-$$

by measuring the ejected electrons' energies as a function of exciting photon energy while simultaneously determining their angular distributions.

EXPERIMENTAL TECHNIQUE

We used a technique that combines for the first time, angle-resolved time-of-flight (TOF) spectrometry with two-dimensional (2D) imaging. Specifically, this method uses two highly efficient TOF energy analyzers [7] to produce angle-resolved, two-dimensional images of electron emission processes. The TOF spectrometers are set at 0° and 54° with respect to the electric field vector of the incident radiation from the High Resolution Atomic, Molecular and Optical (HRAMO) undulator beamline (9.0.1) at the Advanced Light Source at Lawrence Berkeley National Laboratory.

RESULTS AND INTERPRETATION

A part of the overall data collected is shown in Fig. 1. It shows the population of three ionic states, (a) $2s^2p^6$ (^{2}S), (b) $2s^22p^4$ (^{3}P), and (c) $2s^22p^4$ (^{3}P)3s(^{2}P), appearing along lines of constant binding energy parallel to the photon energy axis. Resonant enhancement is clearly seen at a number of well defined photon energies, as indicated by localized changes in the shade levels. More conventional one dimensional spectra showing the population of a given ionic state as a function of photon energy can easily be extracted from the data of Fig. 1 for more quantitative analysis.

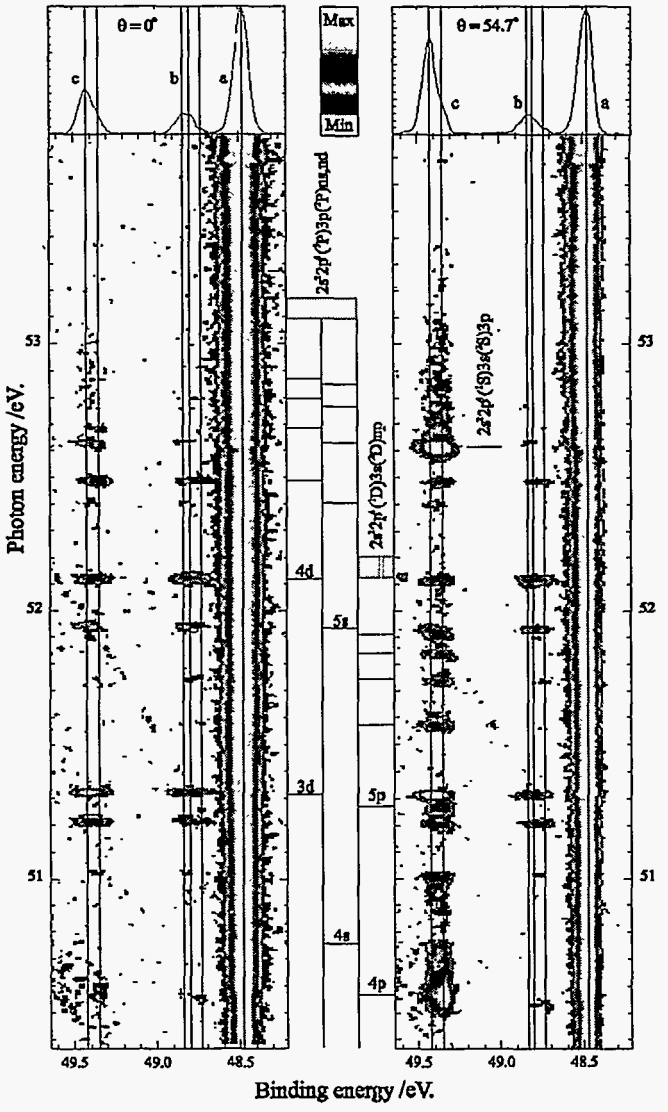

Figure 1. 2D images of electron emission processes taken at 0° and 54.7°. The images represent the electron yield as functions of the electron binding energy and the photon energy. The positions of three doubly excited Rydberg series are indicated in between the two images.

Such spectra are presented in Fig. 2 along with the derived asymmetry parameter β values. In this figure, three Rydberg series are observed which clearly have different behavior at the two different angles giving rise to mostly negative β values. The collected data, when viewed with the 2D representations at both angles (as seen in Fig. 1), allows the easy identification of certain unexpected features. For example, the angular distribution of electrons corresponding to the $2s^2 2p^4(^3P)3s(^2P)$ continuum is such that it is absent in the $\Theta = 0°$ spectrum throughout the range 50.5–60 eV, with the general exception of the decay of members of two Rydberg series, $2s^2 2p^4(^3P)3p(^2P)$ ns,nd as shown in Fig. 1 and Fig. 2. From angular momentum transfer consideration [8] this ionic state is produced by a parity-unfavored transition with only one outgoing wave (εp) in LS-coupling. These class of transitions are characterized by angular distributions in which the electrons are predominantly ejected in a direction orthogonal to the electric field, with angular asymmetry parameter β=-1. This means that the appearance of any signal at Θ=0° as can be seen from Fig. 1 and 2, is an immediate indication of the breakdown of LS coupling for these resonances. Preliminary R-matrix calculations for this process had difficulty

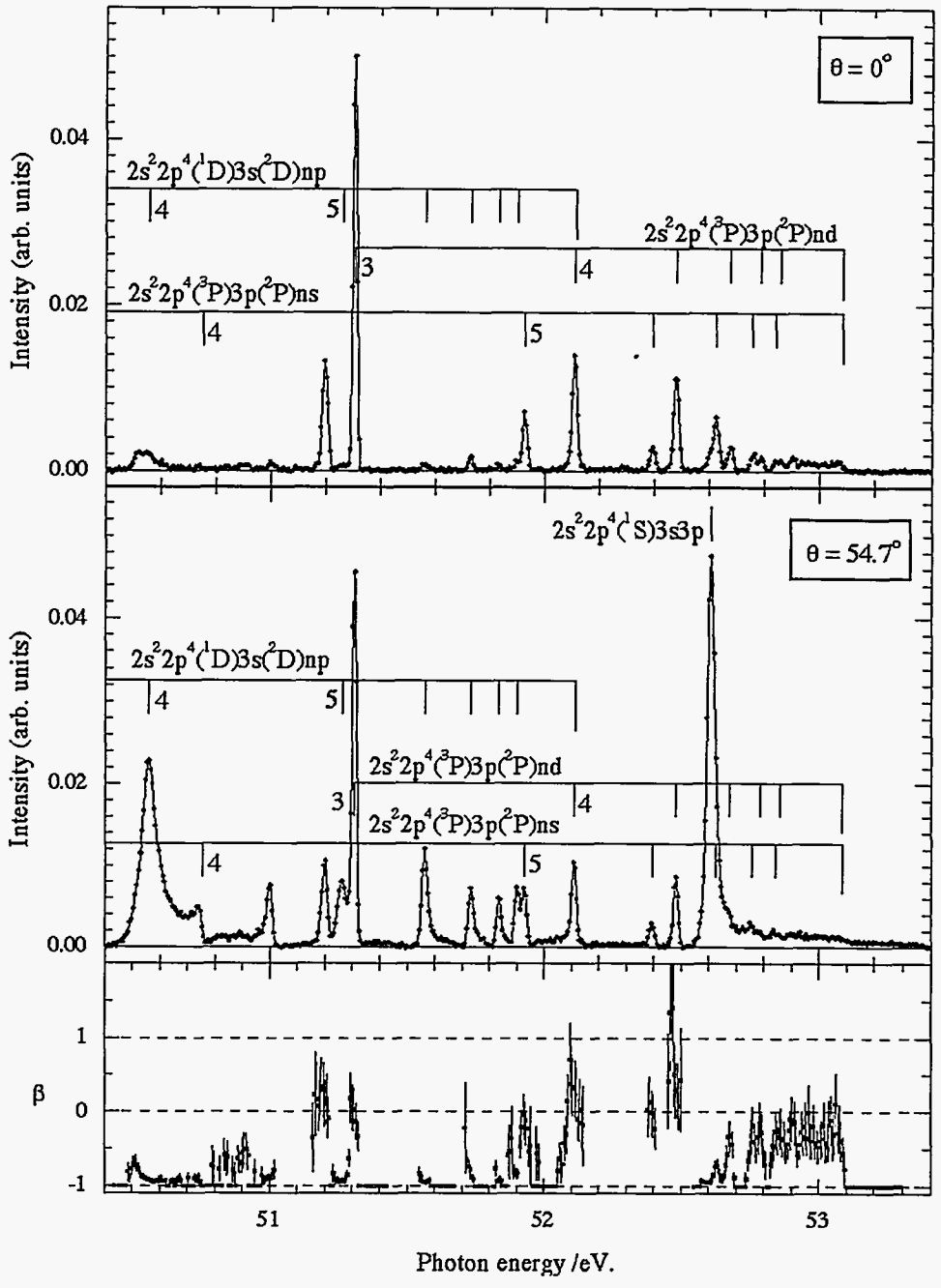

Figure 2. Spectra showing the $2s^2 2p^4(^3P)3s(^2P)$ ionic state as a function of photon energy at 0° and 54.7° along with the derived β values.

giving accurate predictions for the above deviation from LS coupling since extensive configuration interaction and spin-orbit effects are both required. We have also measured (using data from Fig. 1) a non-constant ratio of fine structure levels, unexpected in such a light atom, but observed previously in higher-Z [9] atoms since spin-orbit effects are expected to play a significant role.

Important implications of our findings [10] are twofold. First, viewing 2D photoionization images at various angles permits the easy identification of any unexpected behavior, such as the LS-forbidden, that might be overlooked using less-detailed probing techniques. Second, detection of prominent spin-orbit effects means that it is not safe in general to assume the validity of LS

coupling, even for a system as light as neon, when performing detailed theoretical calculations, spectroscopic assignments, or experimental calibrations.

ACKNOWLEDGMENTS

This work was supported by the US Department of Energy, Office of Basic Energy Science, Division of Chemical Science under contract No. DE-FG02-95ER14299. We would like to thank S. T. Manson and A. F. Starace for several useful discussions.

REFERENCES

1. K. Schulz et al., Phys. Rev. Lett. **77** , 3086 (1996) and references therein.
2. U. Becker et al., Phys. Rev. Lett. **56**, 1120 (1986.
3. J. A. R. Samson, Y. Chung and E. M. Lee, Phys. Rev. A **45**, 259 (1992).
4. A. A. Wills et al., J. Phys. B **23**, 2013 (1990).
5. K. Codling, R. P. Madden and D. Ederer, Phys. Rev. **155**, 26 (1967).
6. K. Schultz et al., Phys. Rev. A **54**, 3095 (1996).
7. N. Berrah et al., J. Phys. B **29**, 5351 (1996); B. Langer et al., in proceedings of the *Atomic Physics with Hard X-rays from High Brilliance Synchrotron Light Sources Workshop*, ANL/APS/TM-16, 245, (1996).
8. See for instance, S. T. Manson and A. F. Starace, Rev. Mod. Phys. **54**, 389 (1982) and references therein.
9. M. G. Flemming et al. Phys. Rev. A **44**, 1733 (1991).
10. A. Wills, T. W. Gorczyca, B. Langer, E. Kukk, Z. Felfi, M. Alshehri, O. Nayandin, and J. D. Bozek (submitted to Phys. Rev. Lett.)

Principal investigator: Nora Berrah, Western Michigan University. Email: berrah@wmich.edu.
Telephone: (616) 387-4955.

Experimental Quantification of Many-Body Interactions through the Alignment Measurements of Satellite States

K.W. McLaughlin, O. Yenen, and D.H. Jaecks
Department of Physics and Astronomy, University of Nebraska-Lincoln, Lincoln NE 68588-0111, USA

Excited ionic states produced during photoionization are referred to as satellite states due to their inherent weaker transition rate compared to the main photoline where the residual ion is unexcited. The observation of the fluorescence from these ionic states provides a sensitive method in the study of many-body interactions since measurements can be obtained at threshold with high resolution and efficiency [1]. Polarization analysis of this fluorescence allows one to determine magnetic-substate partial cross sections and the relative strength of the radial matrix elements for production of photoelectron partial waves [2]. We will further show that a measure of many-body interactions can be directly quantified from such a polarization analysis.

The satellite states of argon display a widely varying angular momentum content, the total angular momentum quantum number varying from $J = 1/2$ to as high as 9/2 [3]. Since the ionizing photon brings only one unit of angular momentum, this implies that there is a significant interaction between the residual atomic electrons and the continuum photoelectron in order to redistribute such an angular momentum content. With no hyperfine-structure, and its fine-structure resolvable by fluorescence, argon provides a convenient atomic system to explore and quantify the partitioning in such a redistribution. A quantitative measure of this angular momentum sharing can be gleaned from the determination of the total alignment of the excited ionic state since this atomic parameter, obtainable from a measurement of the linear polarization of the fluorescent radiation, is one measure of the distribution of the magnetic-substate population [2].

In the measurements reported here, an atomic beam of argon has been photoionized in the energy range from 35.4 to 36.6 *eV* with a resolution of 2 to 3 *meV*. This high resolution without a prohibitive loss of flux was achieved with the spherical-grating monochromator on the 10 *cm* undulator of ALS beam-line 9.0.1. The linearly polarized radiation [4] was made to intersect an effusive beam of argon with the linear polarization axis aligned along the atomic beam propagation axis. Fluorescence was observed orthogonal to this collision plane as well as along two collection axes within this plane: at 45° and 60° off axis from the quantization axis set by the polarization of the ionizing radiation. Each fluorescence collection system consisted of a photomultiplier coupled to the interaction region by a $f/1.9$ lens along with a linear polarizer and 0.3 *nm* bandwidth interference filter. By alternating the alignment of the linear polarizer, the fluorescent intensity parallel ($I_{\parallel}$) and perpendicular ($I_{\perp}$) to the linear polarization axis of the synchrotron radiation were measured at a fixed ionizing photon energy. Each individual intensity was normalized to the ionizing photon flux monitored by the displacement current from a biased aluminum surface intercepting the synchrotron beam as it exited the interaction region. Repeating the measurement upon incrementing the ionizing photon energy allowed the total intensity $I_t = I_{\parallel} + I_{\perp}$ and linear polarization $P = (I_{\parallel} - I_{\perp})/I_t$ of a fine-structure resolved, satellite state fluorescence to be determined as a function of the ionizing photon energy.

Fig. 1 gives the total intensity spectra for four Ar^+ $4p \rightarrow 4s$ fluorescent transitions. The spectra shown is in the immediate vicinity of the threshold for the excitation of these $4p$ satellite states. As evidenced in Fig. 1, the onsets for these fine-structure resolved thresholds were abrupt with only the dark counts for the photomultiplier tubes registered prior to threshold. The ionizing

photon energy was calibrated using the photoelectron yield for the Ar $3s \rightarrow np$ window resonances [5] along with six thresholds for similar satellite state fluorescence [2].

Overlain in the figures are predictions for Rydberg series which account for most of the structure of the spectra. Parity and angular momentum conservation restrict the orbital angular momentum of the Rydberg electron to only these values for the indicated excited ionic cores. The series predictions are based on previously accepted [3,5,6] quantum defects for argon along with the well-established [7] energy levels for the excited ionic cores.

Directly proportional to the expectation value of the zero component of the electric quadrupole tensor, the total alignment parameter $A_0(J)$, which is defined [8] as

$$A_0(J) \equiv \frac{\langle 3J_z^2 - J^2 \rangle}{J(J+1)} = \frac{\sum_{M_J} \sigma(J, M_J)\left[3M_J^2 - J(J+1)\right]}{J(J+1)\sum_{M_J} \sigma(J, M_J)} \tag{1}$$

can be obtained from the measured linear polarization of each satellite state fluorescence [2]. The derived alignment spectra are shown in Fig. 2. Even though we determine the total alignment parameter from our polarization measurement of the $3p^4 4p$ satellite state fluorescence, we can *further quantify the alignment of both the* $4p$ *valence electron as well as that of the* $3p^4$ *subshell.* Decoupling the ionic total angular momentum into its orbital L and spin S components provides the relationship between the partial cross-sections for the orbital and total components:

$$\sigma(L, M_L) = \sum_{M_J} \left\langle L M_L S M_S \middle| J M_J \right\rangle^2 \sigma(J, M_J)\,. \tag{2}$$

Substituting (2) into an expression comparable to (1) for the alignment of the orbital angular momentum yields a relationship between the alignment parameter for the orbital and total angular momentum of the satellite state. This decomposition can be carried one step further by decoupling the total orbital angular momentum of the ion L into its constituent $4p$ electron orbital angular momentum ℓ and orbital angular momentum L_c for the $3p^4$ [^{3}P] subshell. This decoupling allows the alignment parameter $A_0(L_c)$ for the orbital motion of the $3p^4$ subshell of each excited ionic state, as well as that for the $4p$ valence electron $A_0(\ell)$, to be written in terms of the measured alignment parameters $A_0(J)$ presented in Fig. 2. For example, for the $^2D_{3/2}$ satellite state:

$$A_0(L_c) = A_0(\ell) = \tfrac{1}{2} A_0(L) = \tfrac{7}{16} A_0(J)\Big|_{[^3P]4p\,^2D_{3/2}} \tag{3}$$

Thus, for the autoionizing resonances in which the ionic core is isotropic, such as the following

$$\left\{\begin{matrix} 3p^4[^3P]4p\ ^2S\ ns,n'd \\ 3p^4[^1S]4s\ ^2S\ np \end{matrix}\right\} \xrightarrow{\text{autoionization}} 3p^4[^3P]4p \left\{\begin{matrix} ^2D_{3/2,5/2} \\ ^2P_{3/2} \end{matrix}\right\} + \varepsilon s,d$$

our alignment measurements of the $3p^4$ [^{3}P] $4p$ $^2D_{3/2,5/2}$ and $^2P_{3/2}$ satellite states provide an *experimentally accessible, direct quantitative measure of the many-body interaction* between the autoionizing $n\ell$ Rydberg electron with the $3p^4$ subshell and the $4p$ valence electron.

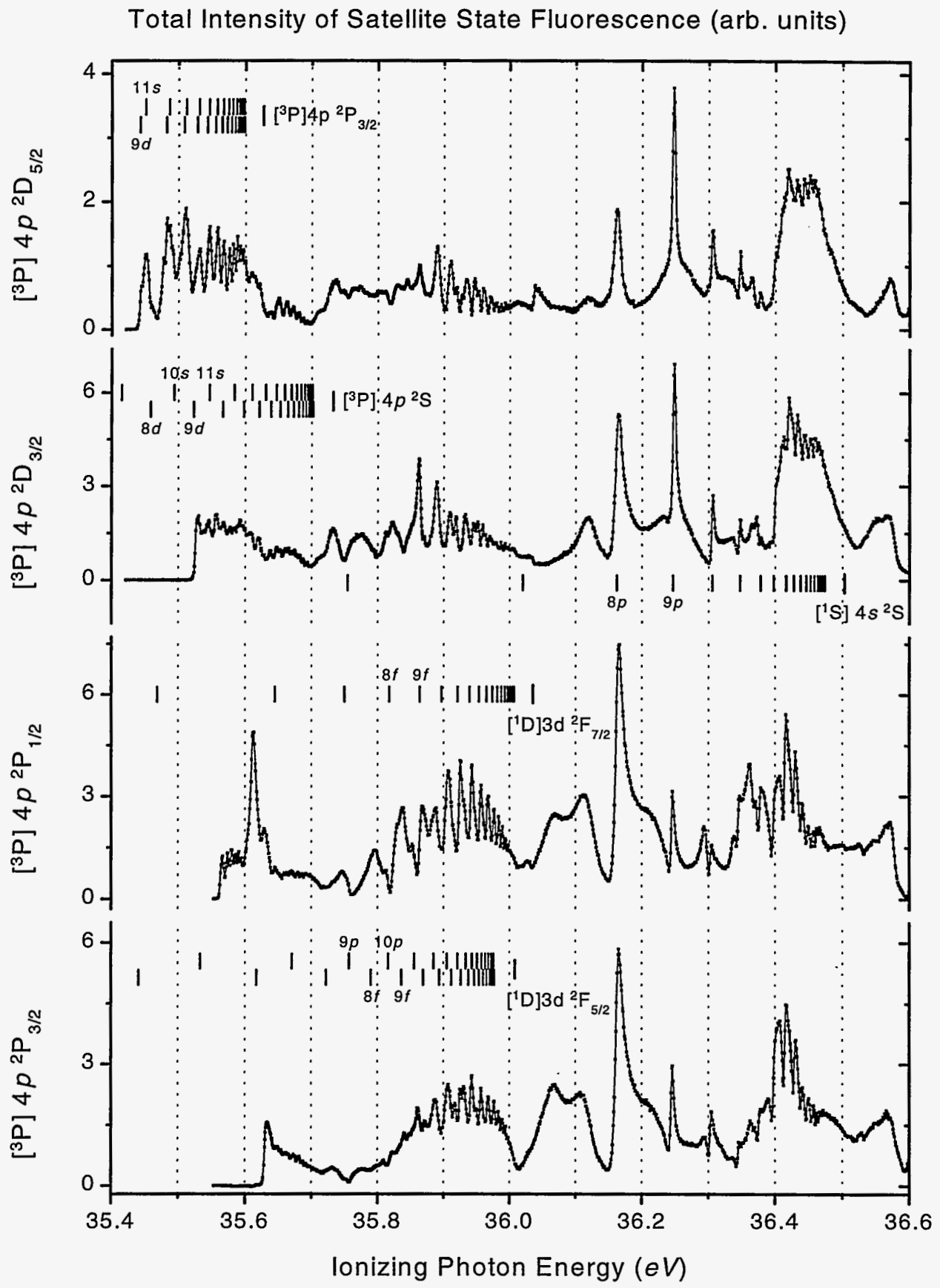

Figure 1. Total intensity of Ar^+ $3p^4$ [^{3}P] 4p ^{2}P and ^{2}D fine-structured resolved satellite state fluorescence in the near-threshold region.

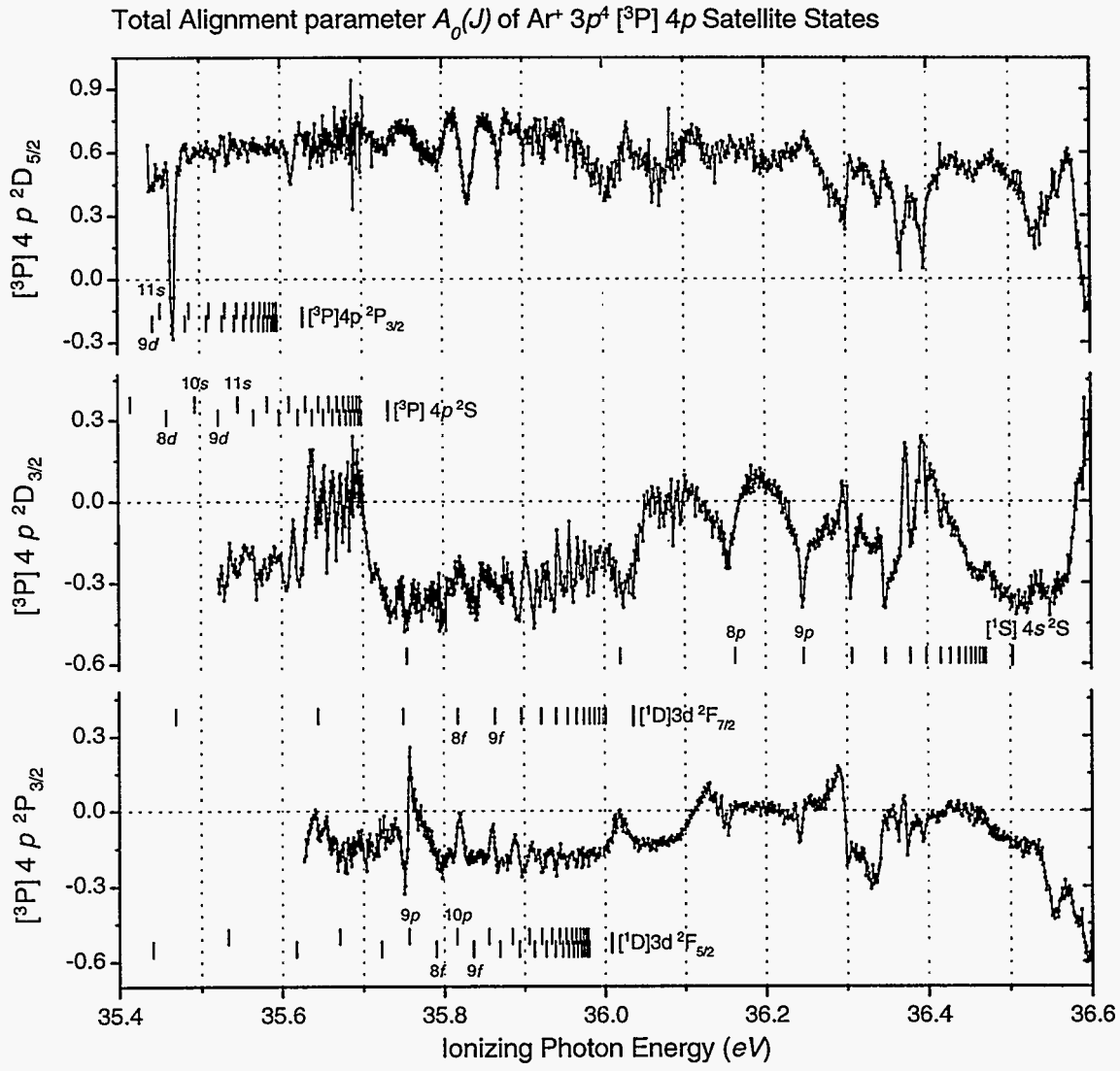

Figure 2. Alignment of the Ar^+ $3p^4$ [^{3}P] $4p$ $^2P_{3/2}$ and $^2D_{3/2, 5/2}$ satellite states in the near-threshold region.

REFERENCES

1. J.A.R. Samson, E.-M. Lee, and Y. Chung, J. Electron Spect. & Rel. Phenom. **66**, 75 (1993).
2. O. Yenen, K.W. McLaughlin, and D.H. Jaecks, Phys. Rev. Lett. **79**, 5222 (1997).
3. A.A. Wills, A.A. Cafolla, F.J. Currell, J. Comer, A. Svensson, and M.A. MacDonald, J. Phys. B **22**, 3217 (1989).
4. N. Berrah, B. Langer, J. Bozek, T.W. Gorczyca, O. Hemmers, D.W. Lindle, and O. Toader, J. Phys. B **29**, 5351 (1996).
5. R.P. Madden, D.L. Ederer, and K. Codling, Phys. Rev. **177**, 136 (1969).
6. J.A.R. Samson, E.-M. Lee, and Y. Chung, Physica Scripta. **41**, 850 (1990).
7. C.E. Moore, *Atomic Energy Levels*, (U.S. Govt. Printing Office, Washington, 1971), Vol. I, pp. 211-218; L. Minnhagen, Ark. Fys. **25**, 203 (1963); J. Opt. Soc. Am. **61**, 1257 (1971).
8. U. Fano and J.H. Macek, Rev. Mod. Phys. **45**, 553 (1973).

This work is supported by the National Science Foundation under Grant PHY-9419505

Principal investigator: Prof. Duane H. Jaecks, Dept. of Physics & Astronomy, University of Nebraska-Lincoln, Lincoln NE 68588-0111, USA. Email: djaecks@unlinfo.unl.edu. Telephone: 402-472-3274.

High-Resolution Carbon 1s Photoelectron Spectrum of Small Molecules

J. Bozek[1], T. X. Carroll[2], G. Gard[3], J. Hahne[4], L. J. Sæthre[5], J. True[4], and T. D. Thomas[4]
[1]Advanced Light Source, Lawrence Berkeley National Laboratory, University of California, Berkeley, CA 94720
[2]Keuka College, Keuka Park, NY 14478
[3]Department of Chemistry, Portland State University, Portland, OR 97207
[4]Oregon State University, Corvallis, OR 97331-4003
[5]Department of Chemistry, University of Bergen, N-5007 Bergen, Norway.

A challenge for inner-shell photoelectron spectroscopy has been the study of organic molecules in which the carbon atoms have similar ionization energies even though they are quite distinct chemically. A typical example is propene, $CH_3CH=CH_2$, whose three carbons have very different chemical reactivity, but core-ionization energies that differ by only 0.56 eV [1]. Only recently has it been possible to resolve the contributions from these carbons in the carbon 1s photoelectron spectrum of this molecule and to correlate the ionization energies with the reactivity.[1] The very high resolution capabilities of the Advanced Light Source present a long-awaited opportunity to examine inner-shell photoelectron spectra of such molecules and to gain chemical insights that were previously inaccessible.

The complete analysis of such a spectrum requires an understanding of a number of factors: the vibrational excitation that occurs during ionization, the line broadening that results from the finite lifetime of the core-ionized state, and the distortion of the line shape that results from interaction of the outgoing photoelectron with the Auger electron (emitted in the deexcitation of the core hole). In addition it is necessary to understand the instrumental features that affect the spectrum. These include the calibration of the energy scales of the monochromator and electron-energy analyzer, the resolution of the photon beam, the resolution of the electron-energy analyzer, and the variation of the analyzer transmission with electron energy.

Our program during 1997 aimed at providing the basis for this understanding with measurements of a number of simple carbon containing molecules: CH_4, CO, CO_2, CF_4, and $H_2C=CH_2$. In addition it included studies of the carbon 1s photoelectron spectra of several novel molecules for which lower resolution studies showed that we would benefit from the high-resolution available at the Advanced Light Source. These included $SF_5CH_2CH_3$, SF_5CHCH_2, and SF_5CCH, molecules, which illustrate the interaction of the highly electronegative SF_5 group with singly, doubly, and triply bonded systems.

For most of these measurements, the analysis is still in progress. However, the work on ethene ($H_2C=CH_2$) has been published and illustrates many of the features of these spectra. [2]

The carbon 1s photoelectron spectrum of ethene

When core-ionization takes place in a molecule, there is typically vibrational excitation of the resulting ion, leading to vibrational structure in the photoelectron spectrum. This structure can be regarded as an opportunity for elucidating the changes in bond lengths and angles that accompany photoionization, or it can be regarded as a challenge to be dealt with in achieving understanding of other features of the spectrum, such as the resolution of contributions from inequivalent carbon atoms with similar ionization energies. In understanding this vibrational structure it is helpful to have guidance from ab initio theory.

In other studies [3] we have shown that a relatively simple level of ab initio theory gives reasonably accurate predictions of the carbon 1s photoelectron spectra of a number of simple hydrocarbons. The measurements on ethene provided us with an opportunity to test this approach with data collected at higher resolution than had been possible previously. The ethene spectrum collected on beam line 9.0.1, with an experimental resolution of 55 meV is shown in Fig. 1 as the points. Here it is compared with our theoretical predictions of the spectrum, shown as the solid line. The shape of the curve has been predicted entirely from ab initio theory, and the only adjustable parameters are the overall height and position and a constant background. The theory is relatively simple and, considering its simplicity, the agreement between experiment and theory is quite satisfactory.

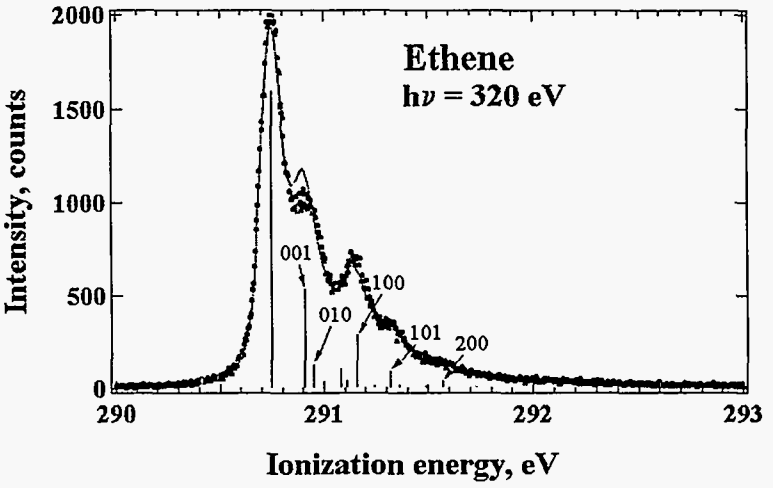

Figure 1. Experimental and calculated photoelectron spectra for carbon 1s photoionization in ethene. The points show the experimental data. The vertical lines show the positions and intensities of 14 of the predicted vibrational transitions. Several of these are labeled with the appropriate vibrational quantum numbers. The solid line represents the predicted vibrational structure dispersed so as to show the combined effects of experimental resolution, lifetime, and post-collision interaction. The overall intensity and position of this line as well as a constant background have been fit to the experimental data by least squares.

REFERENCES

1. L. J. Sæthre, O. Sværen, S. Svensson, S. Osborne, T. D. Thomas, J. Jauhiainen, and S. Akslea, Phys. Rev. A 55, 2748 (1997).
2. J. Bozek, T. X. Carroll, J. Hahne, L. J. Sæthre, J. True, and T. D. Thomas, Phys. Rev. A 57, 157 (1998).
3. T. D. Thomas, L. J. Sæthre, S. L. Sorensen, and S. Svensson, submitted to J. Chem. Phys.

This work was supported by the Office of Basic Energy Sciences of the U.S. Department of Energy; the National Science Foundation (Grant No. CHE-94083868); and the Research Council of Norway.

Principal investigator: T. Darrah Thomas, Oregon State University. Email: thomast@chem.orst.edu. Telephone: 541-737-6711.

New Interseries Interferences in Doubly-Excited Helium

R. Püttner[1], M. Domke[1], M. Martins[1], A.S. Schlachter[2], and G. Kaindl[1]

[1]Institut für Experimentalphysik, Freie Universität Berlin, Arnimallee 14, D-14195 Berlin, Germany
[2]Lawrence Berkeley National Laboratory, 1 Cyclotron Road, Berkeley, CA 94720, USA

INTRODUCTION

Doubly-excited helium has been a prototypical system for the study of electron-electron correlation since the pioneering work of Madden and Codling [1] and its interpretation by Cooper et al. [2] in 1963. In the early 1990's, the progress in synchrotron-radiation facilities and monochromator design led to a spectral resolution of ΔE=4.0 meV at the SX700/II monochromator at BESSY/Berlin [3,4], resulting in more detailed insight into the doubly-excited states of helium by resolving new Rydberg series as well as the first interseries interferences. Up to now the observation of 6 interseries interferences has been reported [5].

The resolution in the soft x-ray region was very recently improved to ΔE=1.0 meV at beamline 9.0.1 of the ALS/Berkeley. [6]. At the beginning, this improved resolution was used to reexamine the double excitations below the N=2 and N=3 ionization thresholds (N=quantum number of the inner electron). Here, we report on the observation of three hitherto unobserved interseries interferences below the N=4, 6, and 8 ionization thresholds.

EXPERIMENT

The experiments were performed at BL 9.0.1 of the ALS, using a 925-lines/mm spherical grating. The photoionization measurements were done with a gas cell containing two parallel charge-collecting plates of 10-cm active length, filled with He at pressures from 100 to 500 μbar, and separated from the monochromator vacuum by a 1200-Å thick carbon window. All spectra were normalized to the incident photon flux monitored with a gold grid in front of the gas cell. The spectra presented were recorded at a resolution of $\Delta E \cong 1.7$ meV.

RESULTS AND DISCUSSION

The optically excited $^1P^o$ double-excitation states of helium can be assigned by N,K_n, with N (n) denoting the quantum number of the inner (outer) electron and K the angular-correlation quantum number [7]. The 2N+1 Rydberg series converging towards the $He^+(N)$ ionization threshold can be distinguished by K=N-1, N-2, ..., -(N-1). Below most ionization thresholds, $He^+(N)$, only the most intense Rydberg series with K=N-2 (principal series) and the second most intense series (secondary series) are observed. Starting with N=5, the lowest Rydberg state is below the N-1 ionization threshold and can influence the N-1 Rydberg series as a perturber, leading to an interference. An interference is expected if N-K is equal for the two series, the Rydberg series and the perturber state [8]. We report on the three previously unresolved interferences of the principal series $4,2_n$ with the perturber state $5,3_5$ ($4,2_n/5,3_5$), the series $6,4_n$ with the perturber state $7,5_8$ ($6,4_n/7,5_8$), and $8,6_n$ with the perturber state $9,7_{11}$ ($8,6_n/9,7_{11}$).

Fig. 1. shows the interference of the Rydberg series $6,4_n$ with the perturber $7,5_8$. The solid line through the data points represents the fit results, with the solid (dotted) subspectrum describing the principal (secondary) series. The calculated energy position and natural linewidth of the perturber $7,5_8$ is also indicated [9]. The assignments of the Rydberg states are given by the bar diagrams on top of the spectrum. The spectrum in Fig. 1 show all characteristic features of an interference: due to the perturber, the intensities and the linewidths of the $6,4_n$ resonances exhibit a Fano-like behavior [5] decreasing from n=13-18 and subsequently increasing from

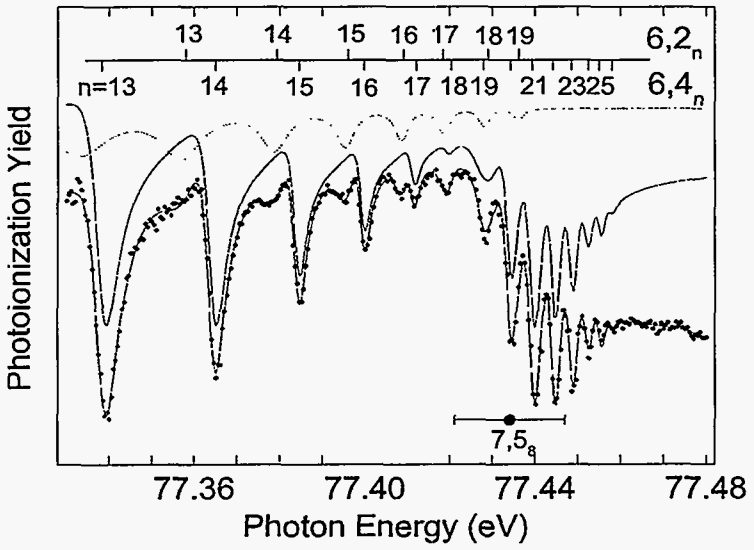

Fig. 1: The $6,4_n$ Rydberg series with the perturber $7,5_8$. The solid line through the data points represents the fit result. The solid (dotted) line represents the principal series $6,4_n$ (secondary series $6,2_n$). The theoretical position and natural linewidth of the perturber are also indicated. The assignment of the resonances is given in the vertical-bar diagram above the spectrum.

n=19-22. The reduced linewidth, defined as $\Gamma^*=\Gamma_n \times (n-\delta)^3$ (with Γ_n= natural linewidth and δ: quantum defect), is constant for an unperturbed Rydberg series, but it is influenced by the perturber leading to a Fano-like variation of Γ^* (q>1) [5]. Since one cannot distinguish between the perturber and the Rydberg series, the perturber is counted to the series, resulting in an increase of the quantum defect δ by 1 for the series. This can also be seen in the spectrum: between the $6,2_{17}$ and $6,2_{18}$ resonances of the unperturbed secondary series with constant quantum defect δ, two states of the principal series are observed, namely $6,4_{18}$ and $6,4_{19}$ resonances, which clearly demonstrates the described increase of the quantum defect by 1.

The principal series $4,2_n$ interacting with the perturber $5,3_5$ is shown in Fig. 2. The principal series $4,2_n$ is resolved up to n=23 and the secondary series $4,0_n$ up to n=17. The behaviors of the principal and secondary series are analogous to those of the series $6,4_n$ and $6,2_n$. However, this spectrum reveals a peculiarity: the perturber $5,3_5$ is calculated to be quite broad with Γ=59.2 meV and extends beyond the N=4 ionization threshold. Only the lower part of the interference is resolved, causing an increase of the quantum defect δ by less than one (see below).

Fig. 3 shows the $8,6_n$ principal series up to n=26 with the interferences with the $9,7_{10}$ and $9,7_{11}$ perturbers resolved. The interference $8,6_n/9,7_{10}$ has been studied previously [10], while the interference $8,6_n/9,7_{11}$ is observed in the present work for the first time.

The quantum defects δ derived from the energy positions of the $4,2_n$, $6,4_n$, and $8,6_n$ resonances are displayed in Fig. 4. The gray-colored area shows the energy region of the newly resolved interferences due to improved energy resolution. The quantum defects, calculated on the basis of quantum defect theory by using the theoretical energy positions and the natural widths of the perturber states [9], are indicated by the three solid lines. A good agreement between the observed and calculated quantum defects is clearly seen: As expected, the quantum defect increases by one in the energy regions of the interferences $6,4_n/7,5_8$ and $8,6_n/9,7_{11}$. In the energy region of the interference $4,2_n/5,3_5$, on the other hand, the quantum defect increases by only $\cong$0.5, due to the fact that the perturber is very broad and has also an effect above threshold.

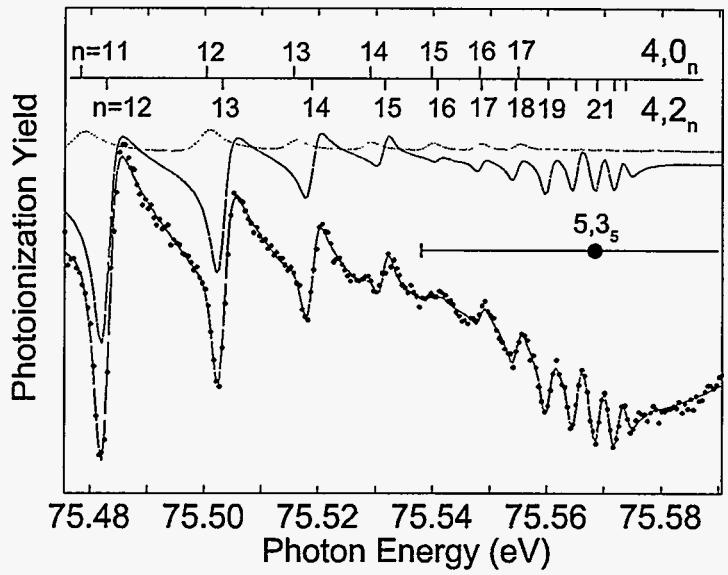

Fig. 2: The $4,2_n$ Rydberg series with the perturber $5,3_5$. The solid line through the data points represents the fit result. The solid (dotted) line represents the principal series $4,2_n$ (secondary series $4,0_n$). The theoretical position and natural linewidth of the perturber are also indicated. The assignment of the resonances is given in the vertical-bar diagram above the spectrum.

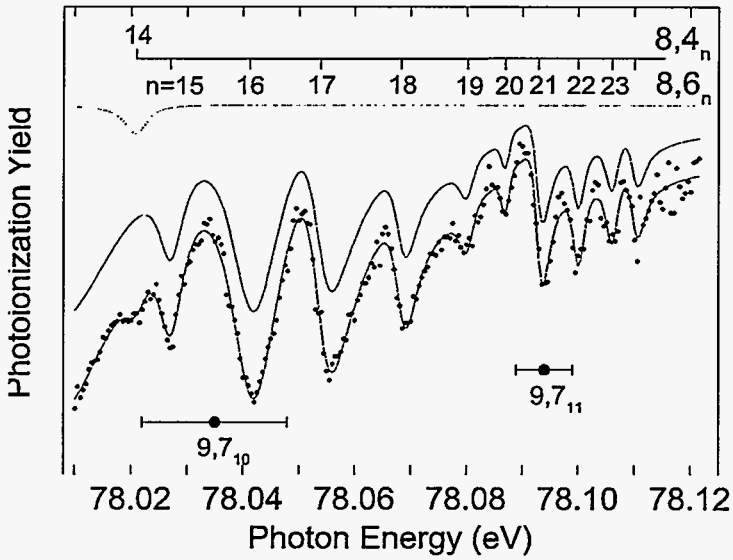

Fig. 3: The $8,6_n$ Rydberg series with the perturbers $9,7_{10}$ and $9,7_{11}$. The solid line through the data points represents the fit result. The solid (dotted) line represents the principal series $8,6_n$ (secondary series $8,4_n$). The theoretical positions and natural linewidths of the perturber are also indicated. The assignment of the resonances is given in the vertical-bar diagram above the spectrum.

As a consequence, the increase of the quantum defect is not limited to the energy range below threshold.

CONCLUSIONS

We studied three previously unresolved interseries interferences in helium. The derived quantum defects of the resonances behave as expected on the basis of quantum-defect theory.

ACKNOWLEDGEMENT

The authors appreciate valuable experimental assistance at BL 9.0.1 by J.D. Bozek.

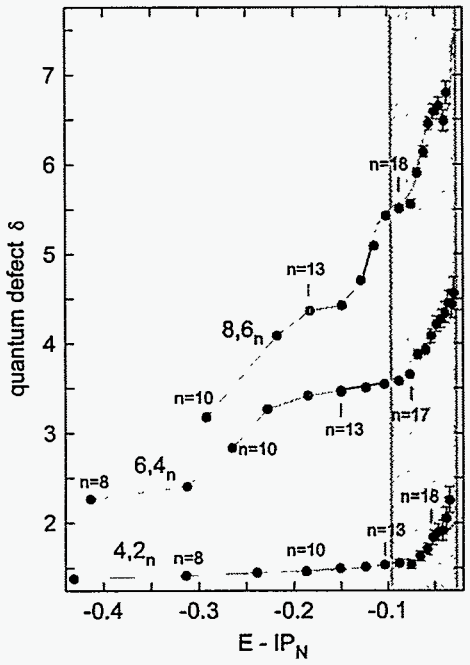

Fig. 4: Quantum defects δ of the resonances of the principal series $4,2_n$, $6,4_n$, and $8,6_n$ plotted as a function of the term energy, i.e. the energy difference to the relevant ionization threshold $He^+(N)$. The solid lines represent the calculated values of the quantum defect (see text).

REFERENCES

1. R.P. Madden and K. Codling, Phys. Rev. Lett. **10**, 516 (1963).
2. J.W. Cooper, U. Fano, and F. Prats, Phys. Rev. Lett. **10**, 518 (1963).
3. M. Domke, C. Xue, A. Puschmann, T. Mandel, E. Hudson, D.A. Shirley, G. Kaindl, C.H. Greene, H.R. Sadeghpour, and H. Petersen, Phys. Rev. Lett. **66**, 1306 (1991).
4. M. Domke, T. Mandel, A. Puschmann, C. Xue, D.A. Shirley, G. Kaindl, H. Petersen, and P. Kuske, Rev. Sci. Instrum. **63**, 80 (1992).
5. M. Domke, K. Schulz, G. Remmers, G. Kaindl, and D. Wintgen, Phys. Rev. A **53**, 1424 (1996).
6. G. Kaindl, K. Schulz, P.A. Heimann, J.D. Bozek, and A.S. Schlachter, Synchrotron Radiation News **8**, 29 (1995).
7. K. Schulz, G. Kaindl, M. Domke, J.D. Bozek, P.A. Heimann, A.S. Schlachter, and J.M. Rost, Phys. Rev. Lett. **77**, 3086 (1996).
8. A. Bürgers and D. Wintgen, J. Phys. B **27**, L131 (1994).
9. J. M. Rost, K. Schulz, M. Domke, and G. Kaindl, J. Phys B **30**, 4663 (1997).
10. M. Domke, K. Schulz, G. Remmers, A. Gutiérrez, G. Kaindl, and D. Wintgen, Phys. Rev. A **53**, R4309 (1995).

This work was supported by the Director, Office of Energy Research, Office of Basic Energy Science, Materials Science Division, of the Department of Energy under Contract No. DE-AC03-76SF00098. The work in Berlin was supported by the Bundesminister für Bildung, Wissenschaft, Forschung und Technologie, project No. 05-650-KEA, and the Deutsche Forschungsgemeinschaft, project Do-561/1-1.

Principal investigator: G. Kaindl, Institut für Experimentalphysik, Freie Universität Berlin, Arnimallee 14, D-14195 Berlin-Dahlem , Germany. E-mail: kaindl@physik.fu-berlin.de. Telephone: ++49-30-838-2977. Fax ++49-30-838-6560.

Photo Double Ionization of Spatially Aligned D_2

H.Bräuning[1,3], R.Dörner[2], J.M.Feagin[4], C.L.Cocke[1], T.Osipov[1], M.Achler[2], A.Bräuning-Demian[2], O.Jagutzki[2], V.Mergel[2], M.H.Prior[3], J.Bozek [3], N.Berrah [5], J.Ullrich[6], R.Moshammer[6], H.Schmidt-Böcking[2]

[1]Dept. of Physics, Kansas State University, Manhattan, Kansas 66506

[2]Institut für Kernphysik, Universität Frankfurt, August- Euler Str.6, 60486 Frankfurt, Germany

[3]Lawrence Berkeley National Laboratory, Berkeley, California 94720

[4]Dept. of Physics, California State University - Fullerton, Fullerton, California 92634

[5]Western Michigan University, Kalamazoo, Michigan

[6]Universität Freiburg, 79104 Freiburg, Germany

INTRODUCTION

Double ionization by a single photon is one of the simplest and most fundamental many-electron processes. As the ejection of two electrons following the absorption of one photon is prohibited in an independent particle approximation, the study of this process provides an efficient probe of electron-electron correlations. Using the technique of Cold Target Recoil Ion Momentum Spectroscopy (COLTRIMS) [1] we have already extensively studied the most basic atomic two electron system: helium [2-4]. We have now extended our experiments towards the molecular equivalent, namely D_2, which provides a link between atomic and molecular photoionization studies.

EXPERIMENTAL SETUP

We have used COLTRIMS to achieve a simultaneous imaging of the ion and electron momenta. The experiments were performed at BL 9.0.1 during double bunch mode. A precooled supersonic jet of D_2 is intersected by a focused beam of linearly polarized light resulting in an interaction volume of $2 \times 1 \times 1$ mm^3 with a gas pressure of about 10^{-5} mbar. Both ions of the fragmented D_2 are collected by a weak electric field of 1V/cm onto a position sensitive channel plate detector with 4π solid angle detection efficiency. Using a delayline anode for position encoding and a LeCroy 3377 multi-hit TDC both fragments can be detected on the same detector provided their arrival times differ by at least 15 nsec. From their position on the detector and the time-of-flight the three dimensional momentum vector of the ions can be calculated. Because there is no intermediate molecular state after double ionization these momentum vectors provide a direct image of the spatial alignment of the molecule at the instant of the photon's absorption. In addition, selecting only events where both fragments have been detected yields an unambigous signature of a double ionization process. The electrons are detected on a second position sensitive channel plate detector in single hit mode. This means only one of the two electrons will be detected. A 10 G magnetic field was used to achieve 4π solid angle detection efficiency for electrons up to 10 eV in energy. Again, from the position on the detector and the time-of-flight the momentum vector of the ejected electron can be calculated.

RESULTS

We will present here our first results, showing differential cross sections for photo double ionization at 58.8 eV photon energy. In addition we have taken data at 64 eV and various other higher energies to measure the ratio of single to double ionization. These data are not yet analysed.

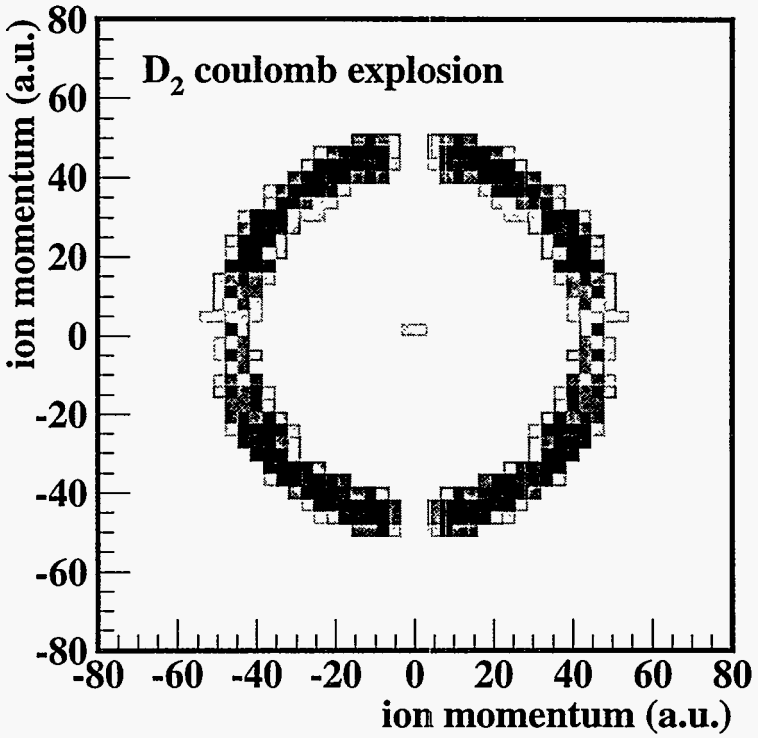

Figure 1. Momentum distribution of the D^+ fragments from photo double ionization of D_2 by 58.8 eV linearly polarized light. The polarization vector is along the x axis. The gap in the data is due to deadtime of our setup.

Figure 1 shows the momentum of the ionic fragments in the plane defined by the polarization vector (x axis) and the propagation of the light (y axis). The gap in the data around x = 0 is due to both ions hitting the detector at the same time, which can therefore not be detected. Still it can be seen that the molecule breaks apart slightly more probable perpendicular to the polarization axis. More information can be extracted from the electron distribution with respect to the molecular axis and the polarization axis. Figure 2 shows the angular distribution of the detected electron for selected geometries in D_2 and He for comparison. The data are necessarily integrated over all emission angles of the undetected electron. For helium the emission of electrons in the plane defined by the polarization axis and the propagation of light is independent of the emission angle (Fig. 2a). In the case of D_2 we show the two extreme cases: one with the molecule aligned along the polarization axis (Fig. 2b) and one with the molecule aligned perpendicular to it (Fig. 2d). In both cases the distribution deviates from the isotropic case of helium with an enhanced emission along the polarization axis. Furthermore a difference in response to the electric field vector between the two orientations of the molecule with respect to the polarization axis can be seen. Fig. 2c shows the angular electron distribution in the plane perpendicular to the polarization axis for the case of the molecule being aligned perpendicular to the polarization axis and along the x axis of the plot. No orientation of electron emission with respect to the molecular axis is found. Thus the orientation of the initial state influences the beta parameter of electron emission in the lab frame, but does not lead to any preferred direction of emission in the molecular frame. A detailed discussion of these data and comparison with 4th order Wannier theory will be part of a forthcoming paper [5].

ACKNOWLEDGEMENTS

H.Bräuning gratefully acknowledges support from the Feodor-Lynen program of the Alexander v. Humboldt-Stiftung. R.Dörner gratefully acknowledges support from the Habilitanden Programm der DFG.

REFERENCES

1. J. Ullrich et al., Comments At. Mol. Phys. **30**, 285 (1994).
2. R. Dörner et al., Phys. Rev. Lett. **76**, 2654 (1996).
3. R. Dörner et al., Phys. Rev. Lett. **77**, 1024 (1996).
4. H. Bräuning et al., J. Phys. B: At. Mol. Opt. Phys, **30**, L649 (1997).
5. R. Dörner et al., to be published.

This work was supported by the Division of Chemical Sciences, Office of Basic Energy Sciences, Office of Energy Research, U. S. Dept. of Energy, BMBF, DFG, DAAD, the Max-Planck Preis der Alexander von Humboldt-Stiftung and GSI.

Principal investigator: R. Dörner, Institut für Kernphysik der J.W.G.-Universität Frankfurt, August-Euler-Str. 6, 60486 Frankfurt, Germany. Email: doerner@ikf007.ikf.physik.uni-frankfurt.de

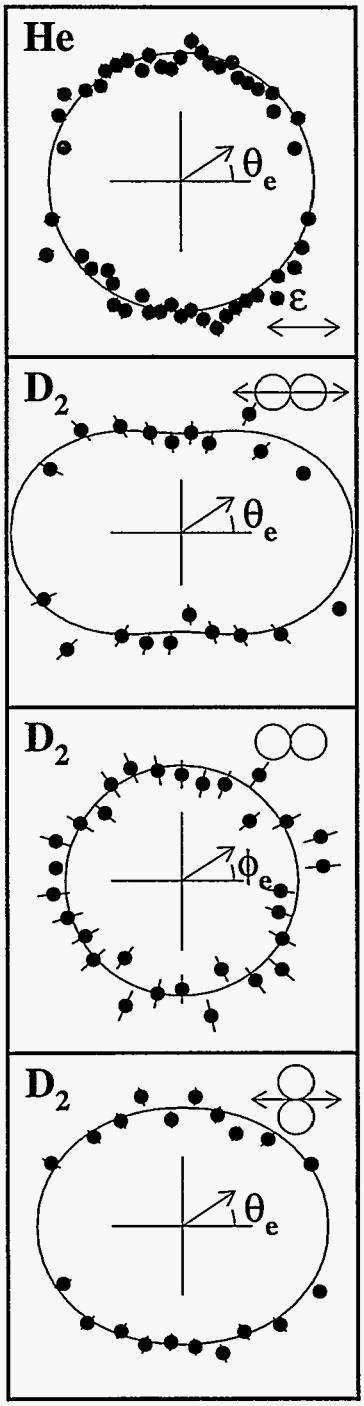

Figure 2. Angular distributions of the detected photoelectron. (a) For He at 7 eV excess energy in the plane defined by the polarization axis (x) and the propagation of light (y). (b) for D_2 in the same plane with the molecule oriented along the polarization axis. (c) for D_2 in the plane perpendicular to the polarization axis with the molecule aligned perpendicular to it along the x axis of the plot. (d) for D_2 in the same plane as (b) but with the molecule aligned perpendicular to the polarization axis.

Photoexcitation and Decay of Hollow Lithium States by Electron Spectroscopy

F. J. Wuilleumier,[1] S. Diehl,[1] D. Cubaynes,[1] J.-M. Bizau,[1] C. Blancard,[2] N. Berrah,[3] E. T. Kennedy,[4] T. J. Morgan,[5] J. Bozek,[6] A. S. Schlachter.[6]

1. LSAI, Université Paris Sud, B. 350, 91405-ORSAY Cedex, France
2. CEA, DRIF, Limeil-Valenton, France
3. Western Michigan University, Kalamazoo, MI, USA
4. Dublin City University, Glasnevin, Dublin 9, Ireland
5. Wesleyan University, Middletown, CT 06457, USA
6. Ernest Orlando Lawrence Berkeley Laboratory, ALS, Berkeley, CA 94720, USA

A hollow atomic system is an atom or an ion in which at least one inner-shell is empty. Lithium, with one additional electron outside the $1s^2$ core, is the simplest open-shell many electron system. Simultaneous excitation of all three electrons can create hollow atoms of the type nln'l'n"l", with $n \geq 2$. Because all the electrons have $n > 2$ outside an empty K-shell, the role of electron correlations is expected to be very important and so hollow Li constitutes an ideal test case for many-body theory. The decay mechanisms for hollow atomic states are of fundamental interest and also because they may provide insight into physical processes relevant to interaction of hollow atoms with surfaces in ion-surface collisions.

The exploration in *photoabsorption* of the lowest $2s^22p\ ^2P^o$ resonance at 142.3 eV energy was first achieved.[1] Soon after, two studies[2,3] using the total photoion yield technique revealed the existence of numerous high lying resonances decaying into Li^+ and Li^{++} final states, in agreement with the predictions of a R-Matrix calculation by L. VoKy.[4] However, neither photoabsorption nor ion yield measurements can discriminate against transitions into various continua of the Li^+ ion, and so cannot test the many-body calculations in detail.

Photoelectron spectroscopy is the only experimental method allowing to determine partial photoionization cross sections to leave the singly charged ion in its different final states. When lithium atoms are photoionized in the 1s shell, according to $1s^22s\ ^2S_{1/2} + h\nu \rightarrow 1snl\ ^{1,3}L + el'$, the residual Li^+ ion can be left in any of the following ionic states: $1s2s\ ^3S$ and ^1S (main lines in a photoelectron spectrum, corresponding to single photoionization); $1s2p\ ^3P$ and ^1P, $1s3l\ ^{1,3}L$, and $1snl\ ^{1,3}L$, with $n > 3$ (corresponding to various types of correlation satellites).

In our first measurements at the Super ACO storage ring in Orsay,[4,5] the resolution was modest (0.5 eV and 0.23 eV on the bending magnet and undulator beam lines, respectively.) During the summer of 1995 and 1996, we had access to the 9.0.1 undulator beam line of the Advanced Light Source (A total of 2x20 shifts were used).

We have first made a comparison of the actual photon flux and resolution we obtained with our electron spectrometer (we transferred all our experimental set up from Orsay to Berkeley), i. e., using exactly the same apparatus on all beam lines.[5] Compared to the resolution we had in Orsay, we measured at ALS an improvement in the spectral resolution effectively used to be able to do the experiments of at least a factor 10. We have been able to run the experiment, i.e., to get effectively data within the allocated periods of beam time, with a 40 meV resolution (a factor 6 better than on the undulator at Super ACO), and, in some special cases, with 20 meV. We would have liked to work always with this 20 meV resolution, but the time was too short to do so. At the same time, the photon flux (with 40 meV resolution and also with a resolution on

the electron spectrometer improved by a factor of 2) was higher than in Orsay (with a 230 meV resolution) by a factor of 2 to 3. To conclude with this experimental aspect, ALS has provided:

- A much higher spectral resolution
- The capability to use a better resolution of the electron spectrometer
- A higher flux (by a factor 2) even with these improved spectral and experimental resolutions, allowing to have a greater sensitivity in the detection of the electrons.

We briefly summarize the data that we have obtained in 1995 and 1996 which have been published in 1996 and in 1997, or are going to be published:[5-11]

1) We have measured partial photoionization cross sections over the energy range from 142 eV to 164 eV with unprecedented resolution.[5,6] Our measurements are compared with the R-matrix calculations of L. VoKy. There is an amazing agreement between tthe results of our calculations using the R-matrix theory and our experiment, on a relative basis, which confirm the quality of the experimental data and the advance in theory made possible by VoKy. Thanks to the high brightness of ALS, it is the first time that a many-body calculation is tested up to the finest details.

2) We have measured in detail the autoionization of a very weak resonance, the $2p^3$ hollow state at 148.75 eV. Although the cross section is very small, it is a particularly interesting resonance, because the three excited electrons are in the same orbitals (same principal and orbital quantum numbers). This state allows a severe test of the treatment of electron correlations.[7]

3) We have observed a number of Auger lines corresponding to two-step autoionization into the continuum of Li^+ 1s ion. Since many highly excited states of Li^+, such as $2s^2\ ^1S$, $2s2p\ ^3P$, $2p^2$, ...,.are lying very near some hollow atomic states, these states of neutral lithium are sometimes a few tenths of an electron-volt above the highly excited states of Li^+., in such a way that the propability to first decay by autoionization to these Li^+ states is very high. The corresponding electrons have a very low kinetic energy and we do not observe them. But the nln'l' states of Li^+ further decay, in a second step, into the continuum of Li^+, producing Auger electrons with characteristic energies. We observed several of them, some of them for the first time, some others remain still unidentified.[8]

4) We have measured with the highest resolution the autoionization of the $2s^22p\ ^2P$ state at 142.31 eV into the $1s2p\ ^1P$ final ionic state. R-matrix calculations predicted this resonance to be quite narrow and the resonant enhancement to be quite large. Our experimental results are in good agreement with the calculations. They also allow us to measure an acurrate value for the natural width of this state. The value we obtained, < 0.12 eV, is lower than all previous experimental determinations. It is an important parameter for the description of these hollow states.[5,6]

5) We have succeded to excite hollow states from the laser-excited $1s^22p$ lithium atoms.[9] The two main resonances predicted by R-matrix calculations to be near 143 eV ($2s2p^2\ ^2S$) and 145 eV ($2s2p^2\ ^2D$) have been measured at these energies and partial cross sections have been measured for photoionization into the ($1s2p\ ^1P$ + and ^3P + el channels. We have also measured higher-lying resonances decaying strongly in the 1s3l ionic states. Excitation from excited atomic states allow us to access autoionizing states of opposite parity from those achievable

from the ground state. Also, starting from excited atoms allows us to sample larger regions of space in the atom than for atoms in the ground state, providing a severe test of many-body calculations.

6) We have discovered the existence of several Rydberg series among the many hollow states. Using the multi-quantum defect theory, we have determined the quantum defect for three of them, again in excellent agreement with R-matrix calculations.[10]

7) We have succeeded to observe the first doubly hollow state, i. e., the lowest energy triply excited state with empty K- and L-shells. In the one electron notation, this state has a $3s^2 3p\ ^2P$ configuration. We measured the energy and the width of this state, in good agreement with the results of the Saddle-point and R-matrix calculations.[11]

8) One very important feature is also the angular dependence of autoionization which can reveal the symmetry of the hollow excited states. This is important to determine the identification and the mixing of the hollow atomic states. We have measured the first angle-resolved photoelectron data for two hollow states, namely the $2s^2 2p\ ^2P$ and $2p^3\ ^2P$ triply excited states in the one-electron notation.[7]

9) Above 160 eV photon energy and up to the triple ionization limit at 210 eV, we have made some exploratory experiments, which revealed many interesting new features that have never been seen before and are worthwhile to be investigated in more details.

1. L. M. Kiernan, E. T. Kennedy, J.-P. Mosnier, J. T. Costello, and B. F. Sonntag, *Phys. Rev. Lett* **72**, 2359 (1994)
2. L. M. Kiernan, M-K Lee, B. F. Sonntag, P. Sladeczek, P. Zimmermann, E. T. Kennedy, J.-P. Mosnier, and J. T. Costello, *J. Phys. B* **28**, L161 (1995).
3. Y. Azuma, S. Hasegawa, F. Koike, G. Kutluk, T. Nagata, E. Shigemasa, A. Yagishita, and I. Sellin, *Phys. Rev. Lett.* **74**, 3768 (1995).
4. L. Journel, D. Cubaynes et al. *Phys. Rev. Lett.* 30, 30 (1996).
5. F. J. Wuilleumier, S. Diehl, D. Cubaynes and J.-M. Bizau, in "X-ray and Inner-Shell Processes, AIP Proc. n°389, eds. R. Johnson, H. Schmidt-Böcking, and B. F. Sonntage (Am. INst. Phys., New York, 1997) p. 625-645.
6. S. Diehl, D. Cubaynes et al. *Phys. Rev. Lett.* 30, 3915 (1996).
7. S. Diehl, D. Cubaynes, et al., to be submitted (1997).
8. S. Diehl, D. Cubaynes, et al., J. Phys. B, 30, L595 (1997).
9. D. Cubaynes, S. Diehl, et al. *Phys. Rev. Lett.* 77, 2974 (1996).
10. S. Diehl, D. Cubaynes, F. J. Wuilleumier et al., *Phys. Rev. Lett.* **79**, 1241 (1997).
11. S. Diehl, D. Cubaynes, K. T. Chung et al. *Phys. Rev. A*, Rapid Communications, **56**, 1171R (1997).

This work was supported by a contract with DAM-CEA, by CNRS, and by the Université Paris-Sud.

Principal investigator: François Wuilleumier, Université Paris-Sud. Email: francois.wuilleumier@lsai.u-psud.fr.

Sharing of the Angular Momentum between Electronic Subshells of Multielectron Ions Formed in Photoionization

O. Yenen, K. W. McLaughlin, and D.H. Jaecks
Department of Physics & Astronomy, University of Nebraska-Lincoln, Lincoln NE 68588-0111, USA

For physical processes involving more than two particles, conserved quantities such as energy, momentum, angular momentum can be shared in principle in an infinite number of ways. However, it is desirable, from a scientific point of view, to formulate broad organizing principles describing tendencies in sharing these conserved quantities among the constituents of a few-particle system. Atomic photoionization studies are ideal for gaining insight in these matters for that there is a large accumulated knowledge about atomic properties. As a convenient and accessible system, we have already successfully used high resolution polarization analysis of fluorescent radiation from $(Ar^+)^*$ to show that certain doubly excited states of Ar have a tendency to conserve their spherically symmetric cores during autoionization.[1]

In this abstract we will show that from the measurement of the polarization of the 476.5 nm fluorescence radiation produced by $3p^4\,[^3P]\,4p\ ^2P_{3/2}$ to $3p^4\,[^3P]\,4s\ ^2P_{1/2}$ transition in Ar^+, we obtain quantitative measures of how the different constituents of the residual excited atom share the single unit of angular momentum brought into the system by the ionizing photon. The quantitative measures in question are the total alignment coefficient $A_0^c(j)$ of the total angular momentum j of the excited ionic state, $A_0^c(L)$ of the total orbital angular momentum L of the excited ion, $A_0^c(L_c)$ of the orbital angular momentum L_c and $A_0^c(S_c)$ of the spin S_c of the optically inactive $3p^4\,[^3P]$ core electrons, and, $A_0^c(\ell)$ of the angular momentum ℓ of the optically active 4p valence electron.[2]

In the experiment described here, an effusive atomic beam of Ar intersects the ionizing photon beam of the 9.0.1 beam line of ALS at right angles. The linear polarization axis of the synchrotron radiation is aligned along the atomic beam direction. The photoionization reaction can be represented as

$$h\nu_0 + Ar \rightarrow (Ar)^{**} \rightarrow Ar^+(3p^4\,[^3P]\,4p\ ^2P^o_{3/2}) + e^-$$
$$\hookrightarrow Ar^+(3p^4\,[^3P]\,4s\ ^2P^o_{1/2}) + 476.5\ \text{nm}.$$

We scan the energy of the ionizing photons from 35.6 to 38.3 eV with a resolution of $E/\Delta E \approx 12{,}700$. The intensities of the fluorescent light at 476.5 nm, polarized parallel ($I_\parallel$) and perpendicular ($I_\perp$) with respect to the polarization axis of the incident synchrotron radiation are measured perpendicular to the collision plane determined by the momenta of the Ar atoms and the incident photons. From these measurements we determine the intensity $I(90) = I_\parallel + I_\perp$ and the polarization $P(90) = (I_\parallel - I_\perp)/(I_\parallel + I_\perp)$ of the satellite line. The total alignment coefficient $A_0^c(j)$ which is a measure of the distribution of different $|m_j|$ sublevels is obtained from the measured polarization P(90) using [3, 4]

$$A_0^c(j) = \frac{\langle 3j_z^2 - j^2 \rangle}{j(j+1)} = \frac{\sum_{m_j} \sigma(j,m_j)[3m_j^2 - j(j+1)]}{j(j+1)\sum_{m_j}\sigma(j,m_j)} = \frac{4\,P(90)}{h^{(2)}[3 - P(90)]} \qquad (1)$$

where $h^{(2)}$ is a constant depending on the total angular momenta of the initial and final states.

To determine the alignments of different angular momenta of the constituents of the excited residual ion we use the angular momentum decoupling rules. We denote by $|\alpha, j\rangle$ the excited $3p^4\ [^3P]4p\ ^2P^o_{3/2}$ states of Ar^+, where j is the total angular momentum and α all other quantum numbers to completely characterize the state. $|\alpha, j\rangle$ can be expanded in terms of its magnetic substates

$$|\alpha, j\rangle = \sum_{m_j} a_{m_j} |\alpha, j m_j\rangle \tag{2}$$

The coefficients a_{m_j} contain the dynamical information of the double photo-excitation and the following autoionization to form the satellite states. For our case where j=3/2, $|a_{m_j}|$ can be calculated from the measurements and their squared magnitudes give the magnetic sublevel cross sections normalized to their sum.

The excited $3p^4\ [^3P]4p\ ^2P^o_{3/2}$ states of Ar^+ are best described by a LS-coupling scheme [4] and $\mathbf{j} = \mathbf{L}+\mathbf{S}$. Therefore, one can decouple the $|\alpha, j m_j\rangle$ into total orbital **L** and total spin **S** angular momenta eigenstates. Omitting α, the expansion is

$$|j m_j\rangle = \sum_{M_L M_S} \langle LM_L SM_S | j m_j\rangle |LM_L\rangle |SM_S\rangle \tag{3}$$

where $\langle LM_L\ SM_S | j m_j\rangle$ are Clebsch-Gordon coefficients. The probability of forming a satellite state with given total orbital angular momentum quantum number L and magnetic quantum number M_L is

$$\left|\langle LM_L | \alpha, j\rangle\right|^2 = \frac{\sigma(LM_L)}{\sigma_{total}} \tag{4}$$

where $\sigma(LM_L)/\sigma_{total}$ is the relative cross section for forming a satellite state with total orbital angular momentum L and magnetic quantum number M_L. Using equations (2) and (3) one can express these cross sections in terms of the dynamical parameters a_{m_j}. We can also express the alignment $A_0^c(L)$ due to the orbital motion of the electrons, in a manner similar to eq. (1)

$$A_0^c(L) = \frac{\langle 3L_z^2 - L^2\rangle}{L(L+1)} = \frac{\sum_{M_L} \sigma(L, M_L)[3m_L^2 - L(L+1)]}{L(L+1)\sum_{M_L} \sigma(L, M_L)} \tag{5}$$

Substituting the $\sigma(LM_L)/\sigma_{total}$ cross sections in terms of the dynamical parameters a_{m_j} in equation (5), we obtain

$$A_0^c(L) = \frac{1}{2}[|a_{3/2}|^2 - |a_{1/2}|^2 - |a_{-1/2}|^2 + |a_{-3/2}|^2] \tag{6}$$

Since the initial ionizing photon is linearly polarized, there is no circulation of electronic charge, which means the orientation parameter is zero, and the probability amplitudes for m_j and $-m_j$ are the same i.e., $a_{m_j} = a_{-m_j}$. Since $|a_{m_j}| = \sigma(jm_j)/\sum_{m_j}\sigma(jm_j)$ we find

$$A_0^c(L) = \frac{5}{8} A_0^c(j) \tag{7}$$

The total orbital angular momentum L can also be decoupled into the orbital angular momentum L_c of the $3p^4\ [^3P]$ core electrons and the orbital angular momentum ℓ of the 4p valence electron. Similarly, the total spin S=1/2 of the satellite state can be decoupled

into the spin S_c of the $3p^4$ [^{3}P] core and the spin s=1/2 of the 4p valence electron and their alignments can also be calculated. Following a procedure similar to the one described above, and using equation (7) we find

$$A_0^c(L_c) = -\frac{5}{16} A_0^c(j) = -\frac{1}{2} A_0^c(L) = A_0^c(\ell) \qquad (8)$$

We have performed the **j=L+S** and $\mathbf{L} = \mathbf{L_c} + \ell$ decouplings for a variety of Ar^+ satellite states and in each case we found proportionality relations similar to eq. (8). The sign and the value of the proportionality constants depend on the satellite state.

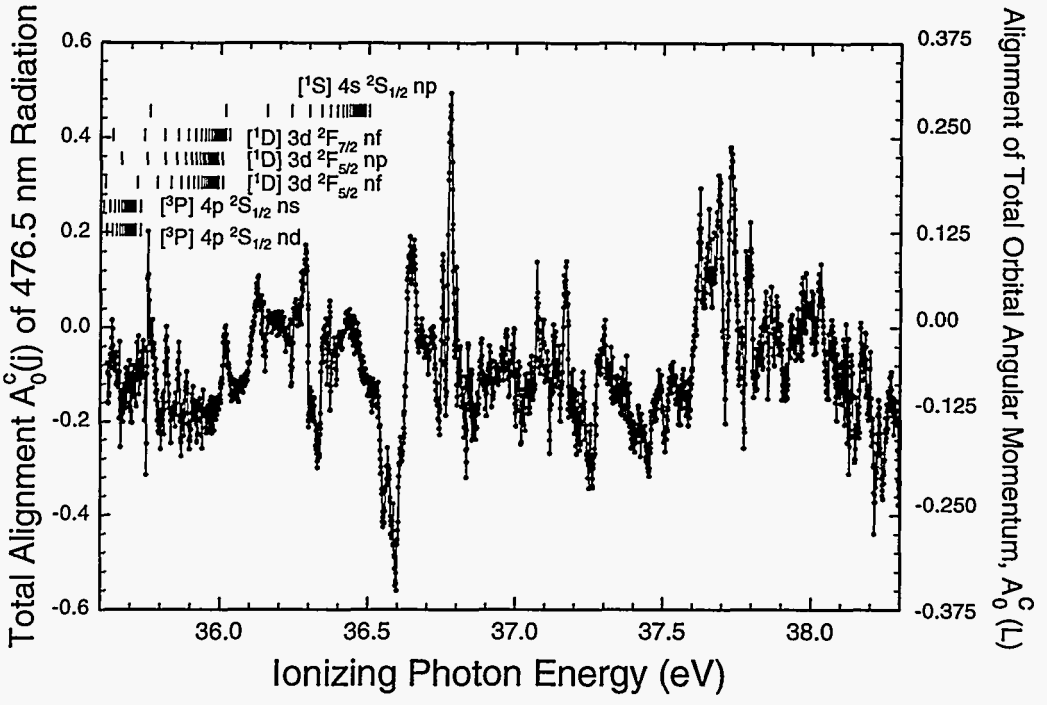

Figure 1: The alignment $A_0^c(L)$ of the total orbital angular momentum L is proportional to the alignment $A_0^c(J)$ of the total angular momentum j of the excited ionic state. Vertical lines denote the assigned doubly excited Rydberg series of Ar. Identification of doubly excited states above 36.6 eV is in progress.

Fig. 1 shows the alignment $A_0^c(j)$ of the total angular momentum and the alignment $A_0^c(L)$ of the total orbital angular momentum of the excited ionic state calculated from the measured polarization. Also shown on Fig. 1 are the positions of the doubly excited Rydberg series of Ar. Since the identification of the doubly excited states of Ar above 36.6 eV is still in progress, we did not show them on Fig. 1. One should note here that the extreme allowed values of $A_0^c(j)$ are ± 0.8.

Fig. 2 shows the alignment $A_0^c(L_c)$ of the orbital angular momentum of the $3p^4$ [^{3}P] core and the alignment $A_0^c(\ell)$ of the 4p valence electron of the excited ionic state calculated using equations (8).

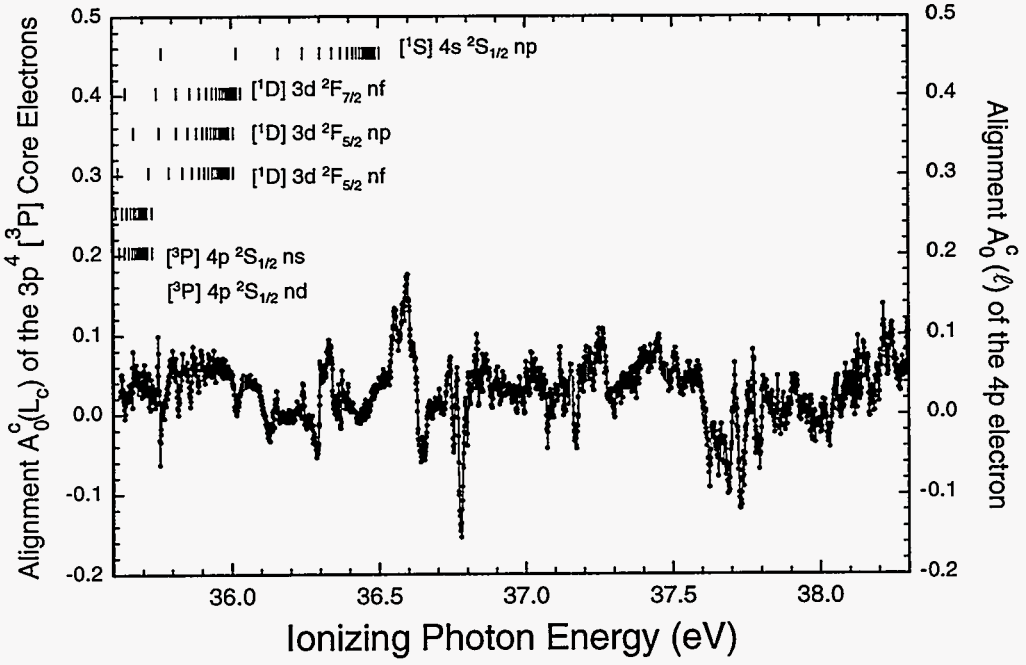

Figure 2: Alignment $A_0^c(L_c)$ of the orbital angular momentum of the $3p^4$ [^{3}P] core and the alignment $A_0^c(\ell)$ of the 4p valence electron of the excited ionic state.

In this abstract, we have shown that the combination of the characteristics of high resolution ionizing radiation from a third generation synchrotron source with the added information of polarization of fluorescent light leads to quantitative information about angular momentum sharing that cannot be obtained in any other way.

REFERENCES

1. O. Yenen, K.W. McLaughlin, and D.H. Jaecks, Phys. Rev. Lett. **79**, 5222 (1997).
2. The alignments of the spin of the 4p valence electron and the total spin S of the excited ion are trivially zero.
3. B.W. Moudry, O. Yenen, D.H. Jaecks, and, J.H. Macek, Phys. Rev. A **54**,4119(1996).
4. U. Fano and J. Macek, Rev. Mod. Phys. **45**, 553 (1973)

This work is supported by the National Science Foundation under Grant No. PHY-941905

Principal investigator: Duane H. Jaecks, Department of Physics, University of Nebraska-Lincoln.
Email: djaecks@unlinfo.unl.edu. Telephone: (402) 472-3274

Beamline 9.0.2 Abstracts

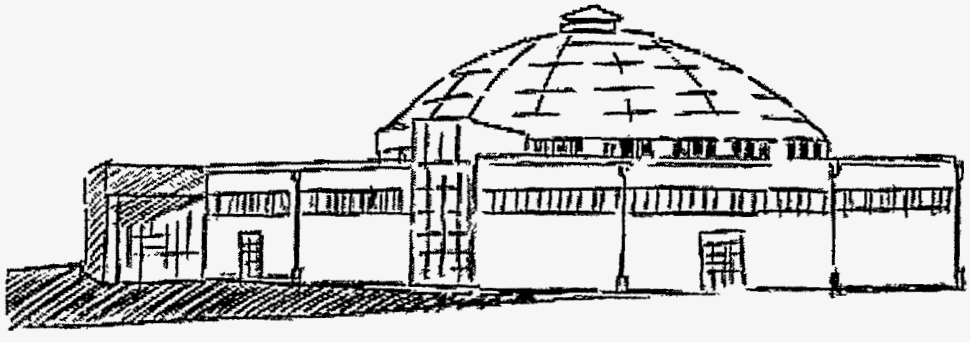

Crossed beam reaction of atomic chlorine with n-pentane: primary vs. secondary H atom abstraction dynamics

Naoki Hemmi and Arthur G. Suits
Lawrence Berkeley National Laboratory, University of California, Berkeley, CA 94720, USA

We present a study of the dynamics of the reaction $Cl + C_5H_{12} \rightarrow HCl + C_5H_{11}$, probed using undulator radiation to effect soft ionization of the pentyl radical product. The study of chemical reactions in crossed molecular beams allows one to investigate chemistry under well-defined conditions:[1] the use of crossed supersonic molecular beams provides reagents in very low rotational states and yields a precisely defined collision energy rather than a Boltzmann average. Moreover, these studies are performed under single collision conditions, ensuring that the measured product velocity distributions directly reflect the energy released in the reaction. In addition, since the approach direction of the molecular beams is well-defined, the product scattering angles with respect to this direction can be used to reveal important dynamical information.

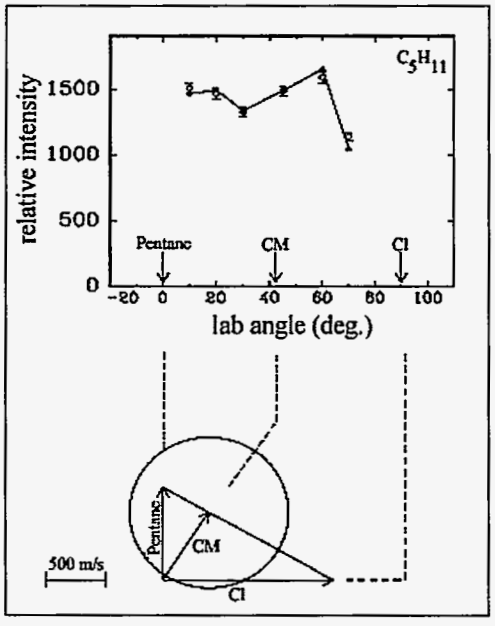

Figure 1. Laboratory angular distribution (top) and Newton diagram (bottom) for reaction of Cl + n-pentane at a collision energy of 16.4 kcal/mol. The circles with error bars are experimental points, the squares with connecting lines are the result of the simulation described in the text. The circle superimposed on the Newton diagram represents the maximum energetically allowed for formation of the 1-pentyl radical.

Free radical abstraction of hydrogen atoms in saturated hydrocarbons are reactions of great importance in combustion, and the differing propensities for reaction of terminal, or *primary*, H atoms vs. *secondary* H atoms, as well as the different dynamics underlying these two processes, are important to a detailed understanding of combustion chemistry. We have used reaction of Cl atoms with saturated hydrocarbons as a first step toward a detailed investigation of these abstraction reactions. Our initial studies focused on the slightly exoergic reactions of Cl with propane (C_3H_8)[2,3], with probe of the C_3H_7 product using tunable undulator radiation. These studies showed differing dynamics for the forward and backward scattered products. The former were ascribed to facile abstraction of the secondary H atoms, while the latter were believed to result from more strongly coupled collisions involving the terminal H atoms. Here we extend these studies to reaction of Cl with n-pentane, where the different energetics are used to explore these underlying trends in the reaction dynamics.

In these studies, conducted on Endstation 1 of the Chemical Dynamics Beamline 9.02, a beam of chlorine atoms seeded in helium gas is crossed at 90 degrees by a beam of n-pentane, and the reactively scattered C_5H_{11} is probed using photoionization by tunable undulator radiation, with the resulting ions mass-selected by means of a quadrupole mass filter. The yield of pentyl radicals is recorded as a function of the neutral time-of-flight (by means of a pseudo-random chopper) and the angle between the molecular beams and the detector. Fig. 1 shows the laboratory angular distribution for the reaction along with the result of a forward convolution simulation from which we infer the

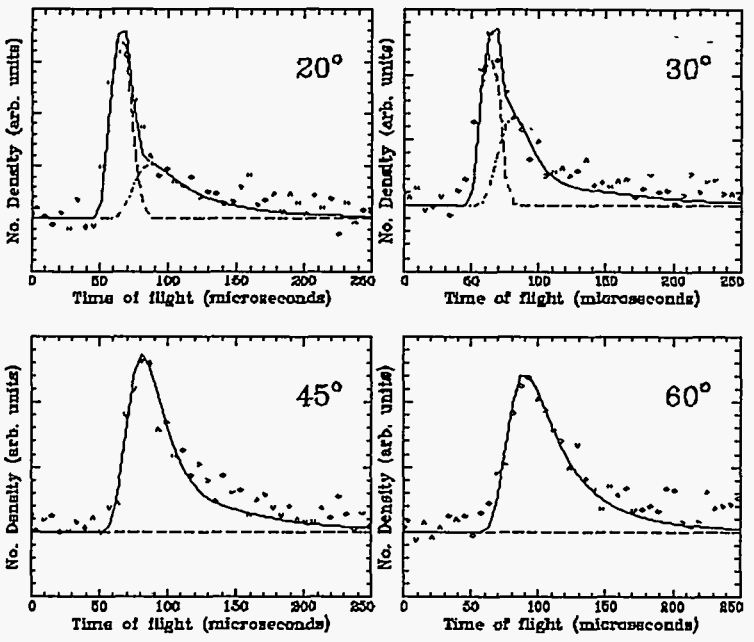

Figure 2. Time-of-flight spectra for m/e=71, pentyl, recorded with 10 eV probe photon energy at the indicated laboratory angle. The points represent experimental data, the solid line is the result of the simulation.

Also shown in Fig. 3B are energy thresholds corresponding to the formation of the 1-pentyl and 2-pentyl radicals. The translational energy release in the forward direction (channel one) extends beyond the energetic limit for abstraction of one of the primary H atoms, thereby excluding the possibility of formation of the 2-pentyl radical for this channel.

It is also interesting to note that the translational energy release for this channel extends very nearly to the energetic limit, implying formation of 1-pentyl radicals and HCl with no internal energy.

Although these trends are similar in Cl-pentane and Cl-propane, both showing forward scattered distributions near the thermodynamic limit along with slower backscattered distributions, the magnitude of the difference in translational energy release for the two components in the pentane case is quite striking. In both cases, it is likely that the backscattered distribution arises from abstraction of the primary rather than secondary H atoms, which involves an entrance barrier and the need for low-impact parameter, near-collinear center-of-mass translational energy and angular distributions (the double differential cross sections) for the reaction. Fig. 2 shows typical time-of-flight which are important to an accurate determination of the translational energy distributions. The center-of-mass distributions obtained from fitting the experimental data in Figs. 1 and 2 are shown in Fig. 3. The scattering distributions have been decomposed into two components: channel 1 is the forward scattered component (Fig. 3A), also associated with a much larger translational energy release (Fig. 3B) while channel 2 is the backward scattered component, found to have a much lower translational energy release.

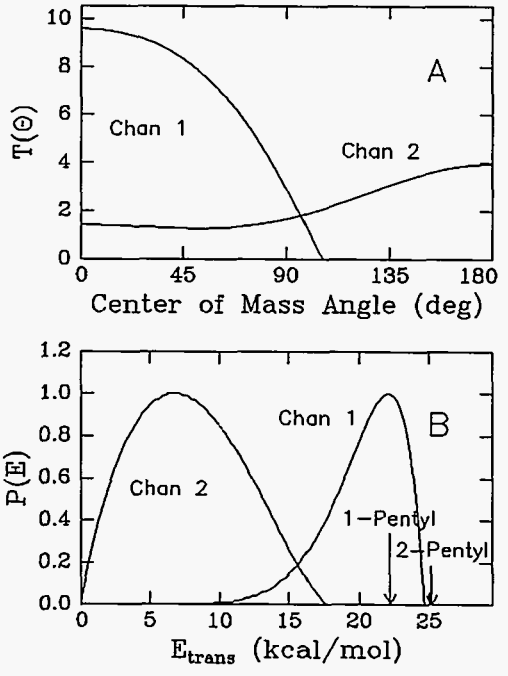

Figure 3. A. Center-of-mass angular distributions derived from the experimental data. B. Center of mass translational energy distributions inferred from the data.

Cl-H-C geometries to overcome this barrier. However, the energetics are not so distinct for these two systems, so the differences must be solely owing to the different dynamics arising from the momentum transfer to the extended carbon skeleton in the low impact parameter collisions.

REFERENCES

1. Y. T. Lee, Science **236**, 793 (1987).
2. D. A. Blank, N. Hemmi, A. G. Suits and Y. T. Lee, Chem. Phys. (in press).
3. D. A. Blank, Ph.D. Thesis, University of California, Berkeley, 1997.

This work was supported by the Director, Office of Energy Research, Office of Basic Energy Sciences, Chemical Sciences Division of the U. S. Department of Energy under contract No. DE-ACO3-76SF00098.

Principal investigator: Arthur G. Suits, MS 10-110, Chemical Sciences Division, Lawrence Berkeley Laboratory, Berkeley CA 94720. Email agsuits@lbl.gov.

A crossed molecular beam investigation of the reaction Cl + propane → HCl + C_3H_7 using VUV synchrotron radiation as a product probe.

David A. Blank[1], Naoki Hemmi[1], Arthur G. Suits[1] and Yuan T. Lee[2]

[1]Lawrence Berkeley National Laboratory, University of California, Berkeley, CA 94720, USA

[2]Office of the President, Academica Sinica, Nanking, Taipei 11529, Taiwan

Radical abstraction of primary or secondary H atoms in hydrocarbons represents a crucial aspect of the dynamics of these reactions, important for developing a predictive understanding of combustion systems. We have used the crossed molecular beam technique to study the hydrogen atom abstraction from propane by atomic chlorine over a wide range of collision energies. The experiments were carried out using endstation 1 on the Chemical Dynamics Beamline at the ALS. The use of soft ionization via tunable undulator radiation has allowed for direct measurements of the radical fragment in these reactions for the first time. We have measured laboratory TOF spectra and angular distributions for Ecoll = 8.0, 11.5, and 31.6 kcal/mol. Center-of-mass flux maps were generated from the measured laboratory distributions.

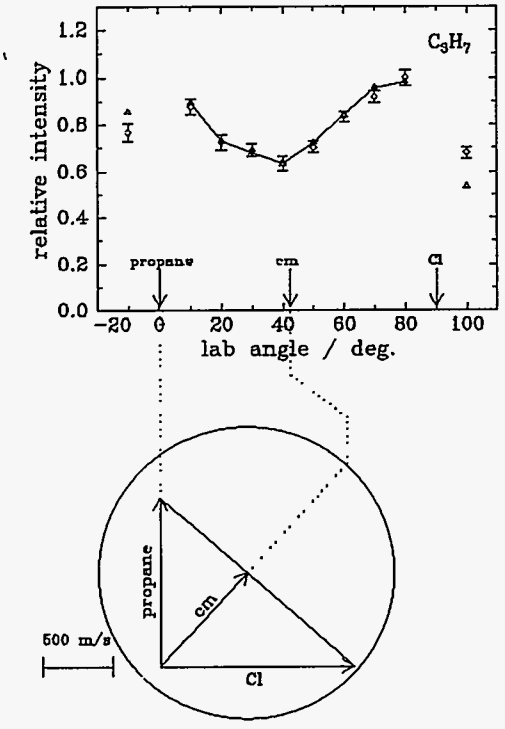

Figure 1. Laboratory angular distribution and Newton diagram for propyl radical product from the crossed beam reaction of Cl+propane at a collision energy of 8.0 kcal/mol.

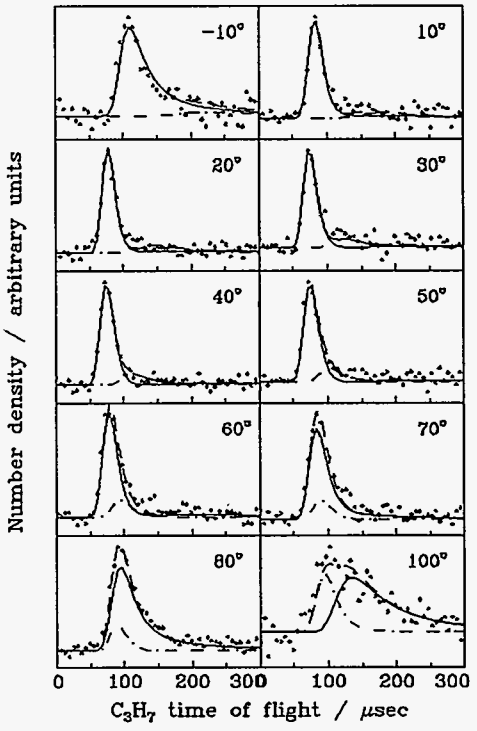

Figure 2. Time-of-flight data at the indicated lab scattering angle for propyl radical product from crossed-beam reaction of Cl+propane at 8 kcal/mol collision energy.

The experimental angular distribution (Fig. 1) and time-of-flight spectra (Fig 2) for this reaction at a collision energy of 8.0 kcal/mol are shown in Figs. 1 and 2. From the distributions in Figs. 1 and 2, we derive the center-of-mass translat onal energy distributions shown in Fig. 3. The results demonstrate two distinct reaction mechanisms that depend on the impact parameter of the reactive collision. Large impact parameter collisions proceed via a stripping mechanism resulting in forward scattered products with very little momentum change in going from reactant to product.

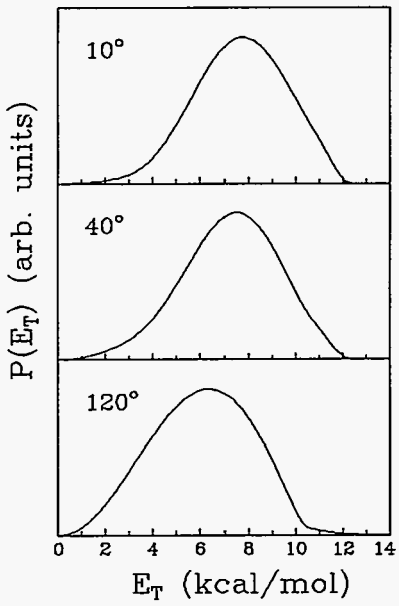

Figure 3. Translational energy distributions inferred from the simulations for the indicated center of mass scattering angles. The results show near stripping behavior for the forward scattered product, implying long-range collisions with little momentum transfer. The backscattered product shows lower translational energy release, implying a 'close collision' and greater momentum transfer.

The stripping reactions are most likely dominated by abstraction of secondary hydrogen atoms. Smaller impact parameter collisions lead to direct reactions with an impulsive recoil and are consistent with a preference for collinear transition state geometry, -C-H-Cl. Direct collision via this collinear configuration is necessary to overcome the entrance barrier for abstraction of primary H atoms. At higher collision energy, the effect of this barrier becomes less important, leaving the ratio of primary to secondary hydrogen abstraction to be dictated by simple statistics. These experiments reveal distinct dynamics and internal energy distributions for the two different radical products resulting from secondary or primary H atom abstraction from propane.

REFERENCES

1. D. A. Blank, N. Hemmi, A. G. Suits and Y. T. Lee, "A crossed molecular beam investigation of the reaction Cl + propane→ HCl + C_3H_7 using VUV synchrotron radiation as a product probe," Chem. Phys. (in press). LBNL-40947
2. D.A. Blank, PHD thesis, University of California, Berkeley (1997).
3. M. Ahmed, D. Blunt, D. Chen, and A.G. Suits, "UV photodissociation of oxalyl chloride yields four fragments from one photon absorption," J. Chem. Phys., 106, 7617 (1997). LBNL-39681
4. N. Hemmi and A. G. Suits, "Photodissociation of oxalyl chloride at 193nm probed via synchrotron radiation," J. Phys. Chem. A, 101, 6633 (1997). LBNL-40055

This work was supported by the Director, Office of Energy Research, Office of Basic Energy Sciences, Chemical Sciences Division, of the U.S. Department of Energy.

Principal investigators: **Y.T. Lee**, Academica Sinica; and **Arthur Suits**, Lawrence Berkeley National Laboratory, Email agsuits@lbl.gov, Telephone 510-486-4754.

Direct identification of photofragment isomers: the photodissociation of propyne at 193nm.

Weizhong Sun, Keiichi Yokoyama, Jason C. Robinson, Arthur G. Suits and Daniel M. Neumark
Department of Chemistry, University of California
and
Chemical Sciences Division, Lawrence Berkeley National Laboratory,
Berkeley, CA 94720

The C_3H_3 radical, an important molecule in hydrocarbon combustion,[1-5] has been proposed as the critical intermediate leading to the first aromatic ring in soot formation during combustion.[3,6] It is also an important radical in interstellar chemistry.[7-8] Astronomers have found C3 formation in comets, as well as cyclopropenylidiene, which is currently thought to be the most abundant hydrcarbon in interstellar space.[9-12] However, the particular structure of the C_3H_3 radical produced from dissociation of precursors having the form C_mH_nX (X=Cl, Br, CN..., H) is still an open question. In 1966, Ramsay and Thistlethwaite[13] found that the flash photolysis of allene, propyne and XCH_2CCH (X=Cl, Br, CH_3...) gave the same spectrum as the CH_2CCH radical molecule. These results suggested that either the other C_3H_3 isomers have a lifetime shorter than 25 ìs or all the precursors produced the C_3H_3 as the lowest energy form, the propargyl radical (H_2CCCH). These suggestions appeared reasonable, since the acetylenic C-H bond energy is 130 kcal/mol, much higher than the C(1)-H bond energy of 89 kcal/mol.[14] However, in 1991, two studies were performed which indicated that photodissociation of propyne (H_3CCH) breaks the much stronger acetylenic C-H bond. The evidence was indirect, however, and the product isomer was not directly identified, so that rearrangement of the initially formed radical to the lowest energy form could not be ruled out.[14,15] Also in 1991, Y. T. Lee's group studied allene photolysis at 193 nm. The results suggested that the product C_3H_3 in that case is the internally excited propargyl radical.[16]

We have used the technique of photofragment translational spectroscopy on Endstation 1 of the Chemical Dynamics Beamline 9.02, to complement laboratory studies of the dissociation dynamics of propyne following absorption at 193 nm. The technique uses a supersonic molecular beam of reactant seeded in neon, which is crossed at 90 degrees with the output of an excimer laser operating on the ArF transition (193.3 nm). The photoproducts that recoil out of the molecular beam are ionized by tunable undulator radiation, then mass selected by means of a quadrupole mass filter. Finally, the angle-resolved time-of-flight mass spectra are recorded. The use of tunable VUV undulator radiation is critical to an unambiguous identification of the chemical structure of the products as shown below.

We have directly observed follow dissociation channels:

$$CH_3CCH \rightarrow H + CH_3CC \text{ (or } CH_2CCH) \quad (1)$$
$$CH_3CCH \rightarrow H_2 + CH_2CC \quad (2)$$

The secondary photodissociation channels have also been observed:

$$CH_3CC \rightarrow C_3H_2 + H \quad (3)$$
$$\rightarrow C_3H + H_2 \quad (4)$$
$$C_3H_2 \rightarrow C_3H + H \quad (5)$$
$$\rightarrow C_3 + H_2 \quad (6)$$

We did not get distinguishable signal for the following channel, which was found by others[12,14]:

$$C_3H_3 \rightarrow CH + C_2H_2 \qquad (7)$$

This indicated that channel (7) in our experiments should be less than 0.06% of all channels, which is determined by limitations of the detector used in these experiments.

Time-of-flight spectra were obtained on a laboratory instrument using photofragment translational spectroscopy with electron bombardment ionization. Product translational energy distributions for mass 39 (C_3H_3) and 38 (C_3H_2) were obtained from these distributions. However, identification of the product C_3H_3 structure is very important to understanding basic isomerization processes of hydrocarbon reactions. The use of soft ionization by tunable undulator radiation on the Chemical Dynamics Beamline at the Advanced Light Source (ALS) allows for direct determination of the product structure. Figure 1a shows the photoionization efficiency (PIE) spectra for the C_3H_3 product from propyne photolysis, and figure 1b shows the C_3H_3 product from allene photolysis, both at 193nm. The ionization of C_3H_3 from the photolysis of the two different precursor molecules shows very different probe photon energy dependence. The ionization onset from the PIE spectrum of C_3H_3 from propyne photolysis is higher than 10 eV; in fact very close to the calculated CH_3CC IP of 11 eV. Meanwhile, the PIE spectrum of C_3H_3 from allene photolysis indicated an onset consistent with formation of propargyl radical (8.67 eV). These experimental results strongly suggest that the photodissociation of propyne at 193 nm breaks the acetylenic C-H bond, clearly forming the propynyl radical. The available energy of this channel should be less than 20 kcal/mol. The very weak lower photon energy curve in Fig 1a may come from allene impurity in the propyne sample (about 2.4% allene impurity in propyne) or possibly from a very small amount of propargyl radical produced directly from photolysis. This

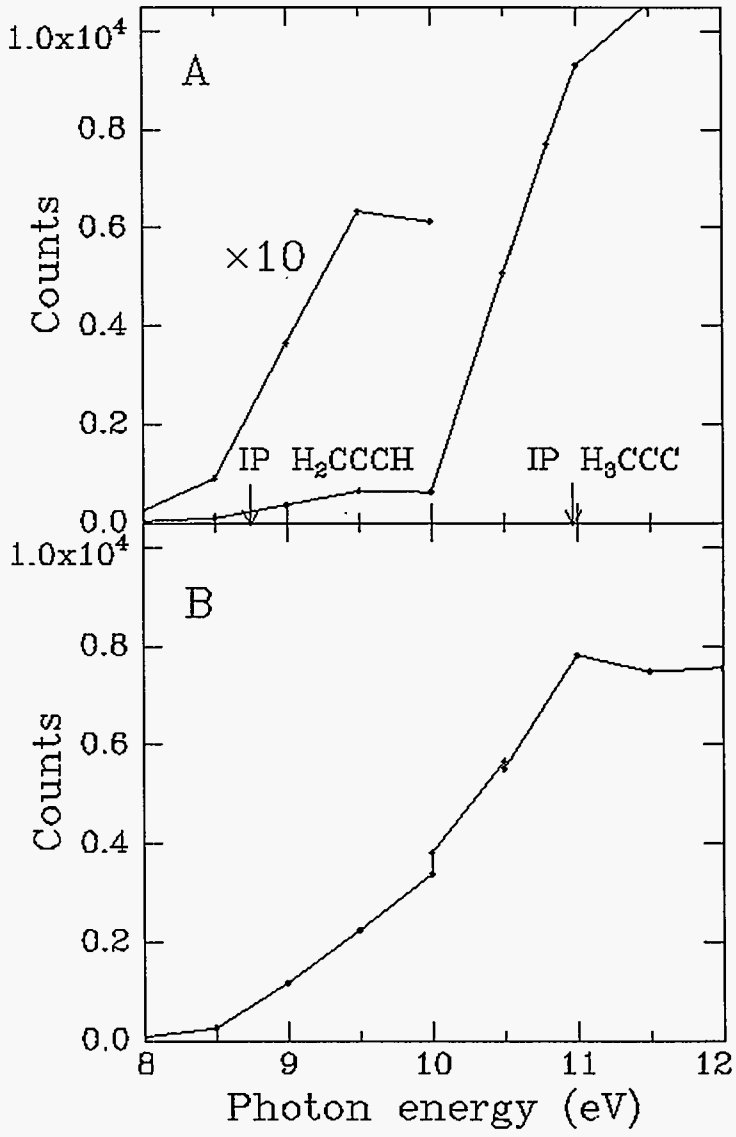

Figure 1. Photoionization efficiency spectra for mass 39 product from photolysis of propyne (A) and allene (B) at 193nm.

explains why Ramsay and Thistlethwaite did not observe an isotopic shift in the flash photolysis of CH_3CCH and CH_3CCD, since both precursors will give the same propynyl radical product.

These results demonstrate the unique capabilities of the combination of tunable VUV probe with photofragment translational spectroscopy to reveal otherwise inaccessible features of hydrocarbon dissociation dynamics. Further, the results show clear bond selective chemistry operating in the photolysis of propyne, where the much stronger acetylenic C-H bond is broken. This is likely owing to the localization of the electronic transition on the pi-bond system of the molecule, which then couples directly to the adjacent C-H bonds rather than to the remote C-H bonds in the methyl group.

REFERENCES

1. Kern, K. Xie, and H. Chen, Combust. Sci. and Tech. 85, 77(1992).
2. Collin, H. Deslauriers, G. R. De Mare, and R. A. Poirier, J. Phys. Chem. 94, 134(1990).
3. Westmoreland, A. M. Dean, J. B. Howard, and J. P. Longwell, J.Phys. Chem. 93, 8171(1989), and references therein.
4. Rotzell, Int. J. Chem. Kinetics 17, 637(1985).
5. Smith, Combust. Flame 35, 179(1979).
6. Alkemade and K. H. Homann, Z. Phys. Chem. 91, 4455 (1987).
7. Herbst, H. H. Lee, D. A. Howe, and T. J. Millar, Mon. Not. Royal Astrnomical Society 268, 335(1994).
8. Symposium on Titan (ESA-SP 338, ESTEC, Noordwijk, 1992).
9. Slagle and D. Gutman, 21st International Symposium on Combustion (the Combustion Institute, Pittsburgh, PA, 1986), P.875.
10. Thaddeus, J. M. Vrtilek, and C. A. Gottlieb, Astrophys. J. 299, L63(1985).
11. Marsden, Annu. Rev. Astron. Astrophys. 12, 1(1974).
12. Jackson, Laboratory studies of photochemical and spectroscopic phenomena related to comets, edited by L.L. Wilkening (University of Arizona, AZ, 1982), p. 480.
13. Ramsay and P. Thistlethwaite, Can. J. Phys. 44, 1381 (1966).
14. Seki and H. Okebe, J. Phys. Chem. 96, 3345 (1992).
15. Jackson, D. Anex, R. E. Continetti, B. A. Balko and Y. T. Lee, J. Chem. Phys. 95, 7327 (1991).
16. Miller and C. F. Melius, Combustion and Flame 91, 21 (1992).

This work was supported by the Director, Office of Energy Research, Basic Energy Sciences, Chemical Sciences Division, of the U.S. Department of Energy.

Principal investigators: **D.M. Neumark**, University of California Berkeley and Lawrence Berkeley National Laboratory, Email neumark@cchem.berkeley.edu; and **A.G. Suits**, Lawrence Berkeley National Laboratory, Email agsuits@lbl.gov.

High Resolution Pulsed Field Ionization Photoelectron Study of O_2: Predissociation Lifetimes and High-n Rydberg Lifetimes Converging to $O_2^+(B^2\Sigma_g^-, v^+=0 \text{ and } 5)$

C.-W. Hsu[1], M. Evans[2], S. Stimson[2], and C. Y. Ng[2]

[1]Chemical Science Division, Ernest Orlando Lawrence Berkeley National Laboratory, University of California, Berkeley, CA 94720, USA

[2]Ames Laboratory, USDOE and Department of Chemistry, Iowa State University, Ames, IA 50011, USA

INTRODUCTION

The rotationally resolved photoelectron bands for $O_2^+(B^2\Sigma_g^-, v^+=0 \text{ and } 5)$ in the energy range of 20.27-20.95 eV have been measured using synchrotron based pulsed field ionization photoelectron techniques at an instrumental resolution of 5 cm^{-1} (full-width-at-half-maximum). In addition to the determination of accurate ionization energies and rotational constants, we have also obtained the predissociative lifetimes of 0.9 ± 0.3 ps for $O_2^+(B^2\Sigma_g^-, v^+=0)$ and 0.50 ± 0.06 ps for $O_2^+(B^2\Sigma_g^-, v^+=5)$. The (nominal) effective lifetimes for high-n Rydberg states converging to $O_2^+(B^2\Sigma_g^-, v^+=0$ and 5) are measured to be ≈0.4 μs, which are significantly shorter than those of ≈1.9 μs observed for $O_2^+(b^4\Sigma_g^-, v^+=0\text{-}5)$. The shorter (nominal) effective lifetimes for high-n Rydberg states converging to $O_2^+(B^2\Sigma_g^-, v^+=0$ and 5) are attributed to the higher kinetic energy releases (or velocities) of O^+ fragments resulting from predissociation of the $O_2^+(B^2\Sigma_g^-, v^+=0$ and 5) ion cores.

EXPERIMENT

In the supersonic beam experiment, a continuous O_2 beam was produced by supersonic expansion of pure O_2 through a stainless steel nozzle (diameter=0.127 mm, T=298 K) at a stagnation pressure of 760 Torr. As shown below, the simulation of PFI-PE spectra obtained using a supersonically cooled O_2 sample indicates that the rotational temperature of O_2 achieved is ≈35 K. The O_2 sample intersects the monochromatic VUV light beam 7 cm downstream in the photoionization/ photoexcitation (PI/PEX) region. We have also performed PFI-PE measurements using an O_2 effusive beam, which was introduced into the PI/PEX region by a metal orifice (diameter= 0.5 mm) at room temperature and a distance of 0.5 cm from the PI/PEX region.

In the present experiment,[1] the nominal dc electrostatic field at the PI/PEX region was zero by setting the repeller plates at the same potential before the application of the Stark electric field pulse. A pulsed electric field (height=1.1V/cm, width=40 ns, delayed by 20 ns with respect to the beginning of the 60 ns synchrotron dark gap) was applied to the repeller at the PI/PEX region every one (or two, or three) ring period. The pulsed electric field was used to ionize the high-n Rydberg states and extract the PFI-PEs toward the detector. As demonstrated in the $Ne^+(^2P_{3/2})$ PFI-PE band shown in Fig. 1, the PFI-PE resolution achieved here was 0.63±0.05 meV or 5.0±0.4 cm^{-1} (FWHM) at 21.5648 eV.

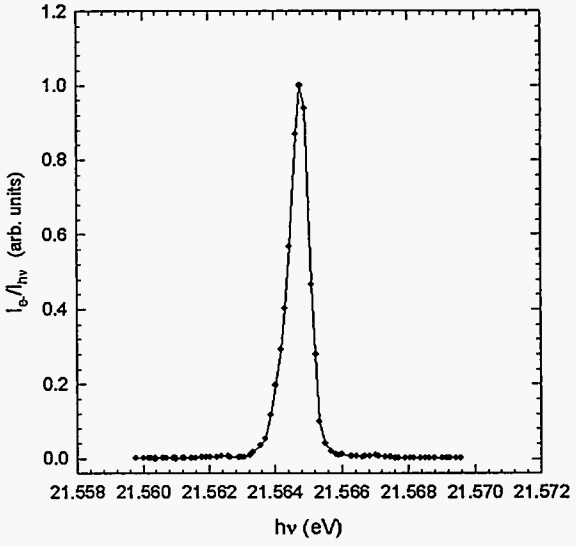

Figure 1. PFI-PE spectra of $Ne^+(^2P_{3/2})$ obtained using monochromator entrance/exit slits of 50/50 μm. The PFI-PE resolution achieved was 0.63±0.05 meV.

RESULTS

Figures 2(a) and 2(b) show the PFI-PE bands for $O_2^+(B^2\Sigma_g^-, v^+=0)$ (upper curves, open circles) in the photon energy range of 20.670-20.710 eV obtained using a supersonic O_2 beam and an effusive O_2 sample, respectively. The PFI-PE band for $O_2^+(B^2\Sigma_g^-, v^+=5)$ in the energy range of 20.905-20.945 eV observed using an effusive O_2 sample is depicted in Fig. 3 (upper curve, open circles). We note that the rotational features resolved for the $v^+=0$ band are narrower than those for the $v^+=5$ band.

The relative rotational intensities in individual vibrational bands have been simulated using the Buckingham-Orr-Sichel (BOS) model,[2] which was derived to predict rotational line strengths observed in one photon ionization of diatomic molecules. Due to nuclear spin statistics, the even levels of N" in $O_2(X^3\Pi_g)$ and N^+ in $O_2^+(B^2\Sigma_g^-)$ do not exist. Thus, only the rotational branches with ΔN (= N^+-N") = even are possible. The observed rotational branches ΔN = -2, 0, and +2 (O, Q, and S) branches, are marked in Figs 2(a), 2(b), and 3. For a g ↔ g transition, the photoelectron angular momentum *l* must be odd. Thus, the partial waves for the ejected electron are restricted to the *l*=1 and 3 continuum states.

The simulation of the PFI-PE bands for v+=0 and 5 yields ionization energies (IEs) of $20.2982_5 \pm 0.0005$ and $20.9348_8 \pm 0.0005$ eV for the formation of $O_2^+(B^2\Sigma_g^-, v^+=0, N^+=1)$ and $O_2^+(B^2\Sigma_g^-, v^+=5, N^+=1)$ from $O_2(X^3\Sigma_g^-, v"=0, N"=1)$. The IEs are higher than the literature values by 2.3 and 8 meV, respectively. The simulation also yields rotational constants of 1.243±0.002 cm-1 for the v+=0 state and 1.122 ±0.002 cm-1 for the v+=5 state. These values allow the calculation of the equilibrium bond distances of re = 1.302±0.001 and 1.370±0.001 Å for the v+=0 and 5 states of O2+(B2Σg-), respectively. The latter values are greater than the r_e value of 1.2074 Å for $O_2(X^3\Sigma_g^-, v"=0)$. This observation is consistent with the fact that the formation of the $O_2^+(B^2\Sigma_g^-)$ state involves the ejection of a bonding electron from the $3\sigma_g$ orbital.

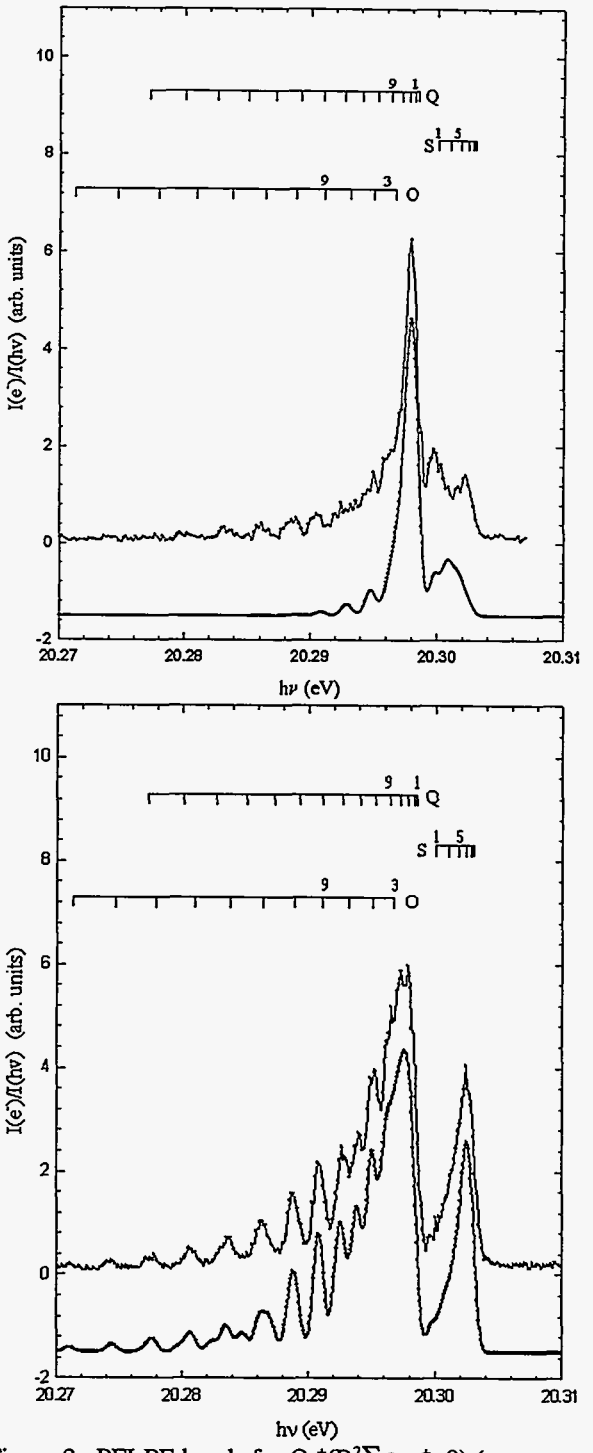

Figure 2. PFI-PE bands for $O_2^+(B^2\Sigma_g^-, v^+=0)$ (upper curves, open circles) obtained using (a) a supersonically cooled O2 sample and (b) an effusive O2 sample. The simulated spectra (lower curves, solid circles) were obtained using rotational temperatures of (a) 35 K and (b) 298 K.

The $O_2^+(B^2\Sigma_g^-)$ state lies significantly above the first dissociation limit of $[O^+(^4S) + O(^3P)]$ at 18.73 eV and is known to be strongly predissociative. This, together with the fact that the energy of $O_2^+(B^2\Sigma_g^-)$ is more than 8 eV higher than that of the ground $O_2^+(X^2\Pi_g)$ state, makes spectroscopic and dynamical studies of $O_2^+(B^2\Sigma_g^-, v^+)$ difficult by employing the ion emission and common laser spectroscopic techniques. Although the $O_2^+(B^2\Sigma_g^-) \rightarrow O_2^+(A^2\Pi_u)$ transition is optically allowed, the emission from $O_2^+(B^2\Sigma_g^-)$ has not been observed. This suggests that the predissociative lifetimes (τ_d's) are significantly shorter than the radiative lifetimes for $O_2^+(B^2\Sigma_g^-, v^+)$. The predissociation dynamics of $O_2^+(B^2\Sigma_g^-, v^+)$ have been investigated extensively using photoelectron photoion coincidence (PEPICO) time-of-flight (TOF) techniques.[3] In these experiments, the measurement of the fragment ion TOF spectrum is triggered by the detection of a threshold photoelectron (TPE). Since the TOF of a TPE to the electron detector usually ranges from 10–100 ns, the traditional PEPICO-TOF technique is not applicable for the measurement of dissociative lifetimes shorter than 10 ns.

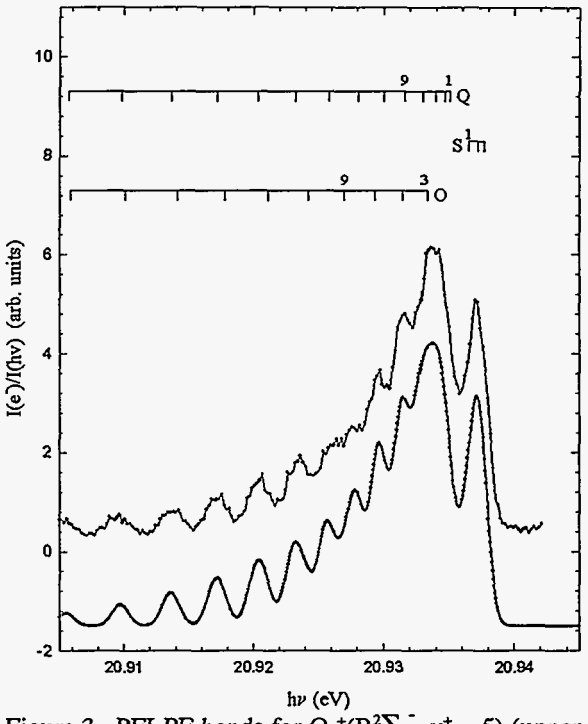

Figure 3. PFI-PE bands for $O_2^+(B^2\Sigma_g^-, v^+ = 5)$ (upper curves, open circles) obtained using an effusive O_2 sample. The simulated spectrum (lower curves, solid circles) was obtained using a rotational temperature of 298 K.

From the Gaussian linewidths used in the BOS simulation, we calculated the natural rotational linewidths for the respective v+=0 and 5 states to be 6.2±1.8 cm^{-1} and 10.9±1.3 cm^{-1}. Since the τ_d's are expected to be significantly shorter than the radiative lifetimes for $O_2^+(B^2\Sigma_g^-, v^+)$, the broadening of the rotational transitions is contributed predominantly to predissociation. Using these natural rotational linewidths we calculate the τ_d values of $(0.9\pm0.3)\times10^{-12}$ s for $O_2^+(B^2\Sigma_g^-, v^+=0)$ and $(0.50\pm0.06)\times10^{-12}$ s for $O_2^+(B^2\Sigma_g^-, v^+=5)$.

The τ values for high-n Rydberg states converging to O_2+$(B^2\Sigma_u^-, v^+=0$ and 5) are measured to be ≈0.4 μs. In a similar study,4 we found that the τ values are ≈1.9 μs for high-n Rydberg states converging to the $O_2^+(b^4\Sigma_g^-, v^+=0\text{-}5)$ states, and are nearly independent of v^+. Since the $O_2^+(b^4\Sigma_g^-, v^+=4$ and 5) states are known to be predissociative with τ_d values in the range of 0.01-4 ns, it is surprising that the τ values for high-n Rydberg states converging to these unstable ion cores are found to be nearly the same as those converging to the stable $O_2^+(b^4\Sigma_g^-, v^+=0\text{-}3)$ ion cores. For an electron in a sufficiently high-n and high-*l* Rydberg state with a near circular orbital, the Rydberg electron may not respond rapidly even when the core is dissociating. This would result in a substantially longer (autoionization) lifetime for the high-n Rydberg state compared to the τd value of the ion core. The latter conclusion should be valid if the kinetic energy for the departing $O^+ + O$ is sufficiently small. Thus, the (autoionization) lifetime of a high-n Rydberg state is effectively decoupled from the dissociative lifetime of the ion core.

Assuming that the autoionization and fluorescence lifetimes for a high-n Rydberg O_2 state, $O_2(n)$, are longer than the τ_d value of the O_2^+ ion core, a plausible decay mechanism for $O_2(n)$ is shown in reactions (1a) and (1b).

$$O_2(n) \rightarrow O(n') + O, \quad (1a)$$
$$\rightarrow O^+ + e^- + O \quad (1b)$$

If the relative velocity for the departing $O^+ + O$ fragment pair resulting from the predissociation of the O_2^+ ion core is not too high, the high-n Rydberg electron originally associated with O_2^+ in $O_2(n)$ may be guided by the Coulombic field to orbit around the departing O^+ ion forming a high-n' Rydberg O atom, O(n'). The relative velocities for the departing $O^+(^4S) + O(^3P)$ fragments from $O_2^+(B^2\Sigma_u^-, v^+=0)$ and $O_2^+(B^2\Sigma_u^-, v^+=5)$ are calculated to be 0.62×10^6 and 0.72×10^6 cm/s, respectively. The corresponding times required for O(n') fragments to move a distance of 0.15 cm, which defines the detection zone of the electron spectrometer, are 0.48 and 0.42 μs. Since these values are comparable to the τ values of ≈0.4 μs observed for high-n Rydberg states converging to $O_2^+(B^2\Sigma_u^-, v^+=0$ and 5), we conclude that the higher velocities (or kinetic energies) for O(n') formed in the dissociation reaction (1a) contribute to the short τ values for high-n Rydberg states converging to $O_2^+(B^2\Sigma_g^-, v^+=0$ and 5). The τ values presented here must be considered as nominal values.

SUMMARY

We have obtained accurate spectroscopic constants and reliable τ_d values for $O_2^+(B^2\Sigma_g^-, v^+=0$ and 5) using high resolution synchrotron based PFI-PE techniques. This method is directly applicable for τ_d measurements of other predissociative states of O_2^+ and predissociative states of other diatomic molecular ions in the inner-valence region. The results for τ measurements of $O_2^+(b^4\Sigma_g^-, B^2\Sigma_g^-)$ show that a high-n Rydberg molecular state with a predissociative molecular ion core is well defined only prior to the dissociation of the molecular ion core. Similar experiments have been performed on the $O_2^+(c^4\Sigma_u^-, v^+=0, 1)$ states and the results are soon to be published.

ACKNOWLEDGMENTS

C.Y.N. acknowledges helpful discussion with Prof. Tomas Baer.

REFERENCES

1. C.-W. Hsu, M. Evans. P. A. Heimann, and C. Y. Ng, Rev. Sci. Instrum., **68**, 1694 (1997).
2. A. D. Buckingham, B. J. Orr, J. M. Sichel, Phil. Trans. Roy. Soc. Lond. A **268**, 147 (1970).
3. T. Akahori, Y. Morioka, M. Watanabe, T. Hayaishi, K. Ito, and M. Nakamura, J. Phys. B **18**, 2219 (1985).
4. C.-W. Hsu, M. Evans, S. Stimson, C. Y. Ng, and P. Heimann, Chem. Phys., accepted.

This work was supported by the Director, Office of Energy Research, Office of Basic Energy Sciences, Chemical Sciences Division of the U.S. Department of Energy under Contract No. DE-AC03-76SF00098 for the Lawrence Berkeley National Laboratory and Contract No. W-7405-Eng-82 for the Ames Laboratory.

Principal investigator: Prof. C.Y. Ng, Ames Laboratory, USDOE and Department of Chemistry, Iowa State University, Ames, IA 50011, USA. Email: cyng@ameslab.gov. Telephone: 515-294-4225

A High Resolution Study of Low Lying Correlation Satellites in Xenon

R.C. Shiell[1], M. Evans[2], S. Stimson[2], C-W. Hsu[3], C.Y. Ng[2] and J.W. Hepburn[1]
[1]Chemistry Department, University of Waterloo, Waterloo, Ontario N2L 3G1 Canada
[2]Ames Laboratory, USDOE and Department of Chemistry,
Iowa State University, Ames, IA 50011, USA
[3]Chemical Science Division, Ernest Orlando Lawrence Berkeley National Laboratory,
University of California, Berkeley, CA 94720, USA

ABSTRACT
The technique of pulsed field ionization - zero kinetic energy photoelectron spectroscopy, typically applied to the investigation of ionic states in atoms and molecules resulting from single electron excitation, has been used to probe the correlation satellite states of xenon between 23.6-24.7 eV. The resulting spectra show the formation of clearly resolved satellite states with intensities of similar magnitude to that of the $5s5p^6\ ^2S_{1/2}$ ionic state. This technique can be extended to other atomic and molecular species to obtain the positions and cross-sections for formation of such states.

INTRODUCTION
As the energy of light incident upon an atom or molecule is increased above that of the lowest ionization energy a variety of neutral and ionic electronic states can be formed. The former include singly excited states converging onto an ion state with one hole in an inner orbital and doubly excited states converging onto an ionic (satellite) state with two electrons excited from the neutral configuration. These neutral resonances may decay to lower lying ionic states through the process of autoionization. The ionic states include single hole and satellite ionic states formed directly in conjunction with a free electron. Probing the formation and characteristics of these ionic states is a primary aim of photoelectron spectroscopy. In traditional photoelectron spectroscopy the photon energy is scanned and all electrons formed with a specific kinetic energy and angular distribution are detected. Threshold photoelectron spectroscopy uses static electric fields to allow the selective detection of electrons with near-zero kinetic energy formed in conjunction with a cationic state. Satellite states can be difficult to probe using this technique; in general such states are formed at high photon energies, they produce low signal intensities, and they contribute to a highly congested spectrum. The introduction of pulsed-field ionization zero kinetic energy (PFI-ZEKE) photoelectron spectroscopy in recent years[1] has largely overcome this problem and enabled a high-resolution spectroscopic probe of ionic states formed by excitation and subsequent field ionization.

The formation of singly-excited neutral or ionic states may be understood by invoking the single particle model whilst formation of neutral doubly excited or satellite states is forbidden within this approximation and is solely the result of the correlated motions of electrons within the species. It has been useful in the past to separate the correlation effects that result in the formation of satellite states into 'intrinsic' and 'dynamic' in regard to their threshold behavior[2] and deducing from this behavior the dominant correlations contributing to the intensity of a given satellite.

Calculations beyond the single-particle approximation in xenon that predict satellite positions and intensities are particularly challenging due to large relativistic effects and strong mixing between configurations. The Xe satellite spectrum has previously been measured over a wide incident photon energy range from the near-threshold[3] to the x-ray[4] regions using traditional photoelectron spectroscopy and the partial strengths of various ionic states have been obtained. Formation of an

ionic state with one hole in its core results in a 'main line' peak at specific energy in the photoelectron spectrum, whilst formation of a satellite state results in a peak on the low kinetic energy side of a main line peak. The resolution with which low lying satellite states have been observed is typically 50 meV at photon energies of 40.8 eV,[5] 130 meV at energies less than 100 eV,[6] and 300 meV at 1.487 keV.[4] In the region containing the lowest-lying satellite states of xenon 8 ionic states are known to exist from 23.6-24.7 eV, with some separated by an energy as small as 5 meV.[7] Obtaining the partial strengths of each ionic state at any photon energy is therefore often complicated by the fact that there are many unresolved satellite states belonging to different symmetry manifolds within the spectra. A high resolution light source and detection technique is required to unambiguously determine partial strengths for each ionic state formation at a particular photon energy. We report the use of a high resolution spectrometer at the Chemical Dynamics Beamline[8] at the Advanced Light Source (ALS) to detect and obtain the relative intensities of formation of the 5s main line peak and 7 satellite states of xenon.

EXPERIMENTAL

The spectrometer has been discussed in detail elsewhere[8] and so only an outline will be given here. The atomic beam was formed by a supersonic expansion of 99.999 % (research grade) xenon at a stagnation pressure of 500 Torr through a metal nozzle of 0.127 mm diameter at 298 K. The ALS was operated in multi-bunch mode, with 304 light bunches within 608 ns followed by a dark gap of 48 ns, forming one ring period. As the photon energy was scanned across high-lying states that converge to an ionic state, Rydberg states of xenon containing one highly-excited electron were formed. Below the threshold for the $5s^{-1}$ state at 23.397 eV these Rydberg states were singly excited and below each threshold for satellite formation (e.g. the $5s^25p^4(^3P)6s\ ^4P_{5/2}$ ion state at 23.669 eV) they were doubly-excited states containing one high-lying electron. During every alternate dark gap a 40 ns pulsed electric field of 0.67 V/cm was applied to the interaction region, field ionizing those states formed within 4 cm^{-1} of an ionic limit[9], and accelerating the resulting near-threshold electrons towards a tandem steradiancy-hemispherical analyzer for selective detection. By calibrating the photon energy scale using the ionization onsets of neon and helium, the positions of the lines were found to be at their expected positions within experimental uncertainty (0.5 meV) and more exact energy calibration was done by comparison with the known optical data[7].

RESULTS

Figure 1 shows a split energy scale spectrum of the observed ionic states formed due to PFI in xenon. Within the energy range sampled the 5s main line peak (the $5s5p^6\ ^2S_{1/2}$ state) and seven of the eight known satellite peaks were observed. We did not observe the $5s^25p^45d\ ^4F_{9/2}$ state and conclude its intensity is less than that of the observed $5s^25p^45d\ ^4D_J$ states.

An expanded view of the observed $5s^25p^45d\ ^4D_J$ states is given in Figure 2, which show a full width at half maximum (FWHM) of 0.9 meV. The intensities of all peaks have been calculated by computing the areas under the peaks after correcting for the background and are displayed (relative to the $5s5p^6\ ^2S$ main line peak with magnitude 100) in Table 1. The experimental error in each satellite intensity, due to variations in conditions and statistical fluctuations, is estimated to be from 20% to 30%, with the higher values for the less intense peaks. For comparison the reported relative peak heights of these satellite states formed from unpolarized He II light at 40.8 eV [5] and polarized synchrotron light at 63.5 eV [10] are shown in Table 1. It should be noted that the former is not taken at the magic angle with respect to the beam (see ref. 6 for details) and thus could show a maximum difference by a factor of four from the true relative cross-sections of some states. Also

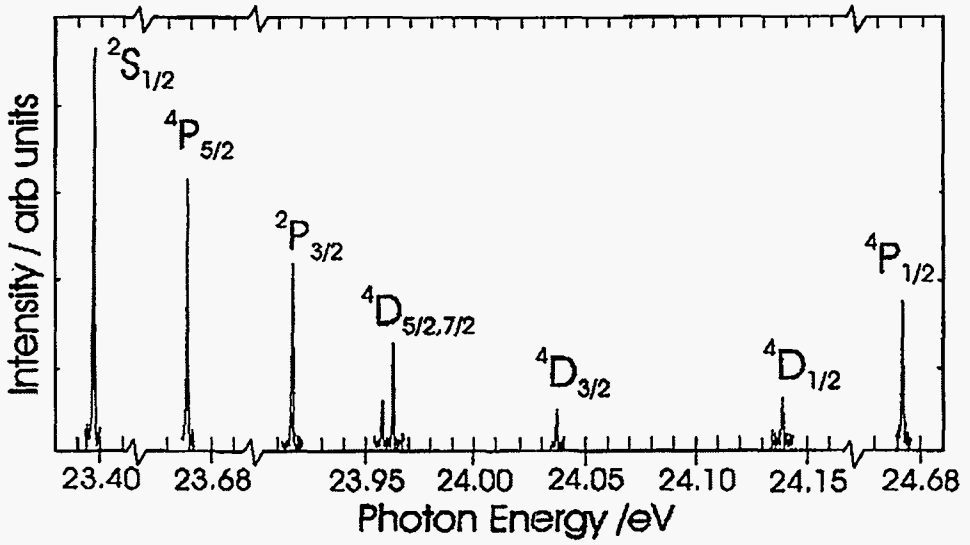

Figure 1. A split-energy spectrum with consistent energy scale, normalised by photon flux, of the ionic states in xenon observed through PFI-ZEKE photoelectron spectroscopy. The main line state at 23.397 eV is shown and seven correlation satellites. The position of each peak is calibrated from the analysis by Hansen and Persson [7] and labeled with LS notation, see text.

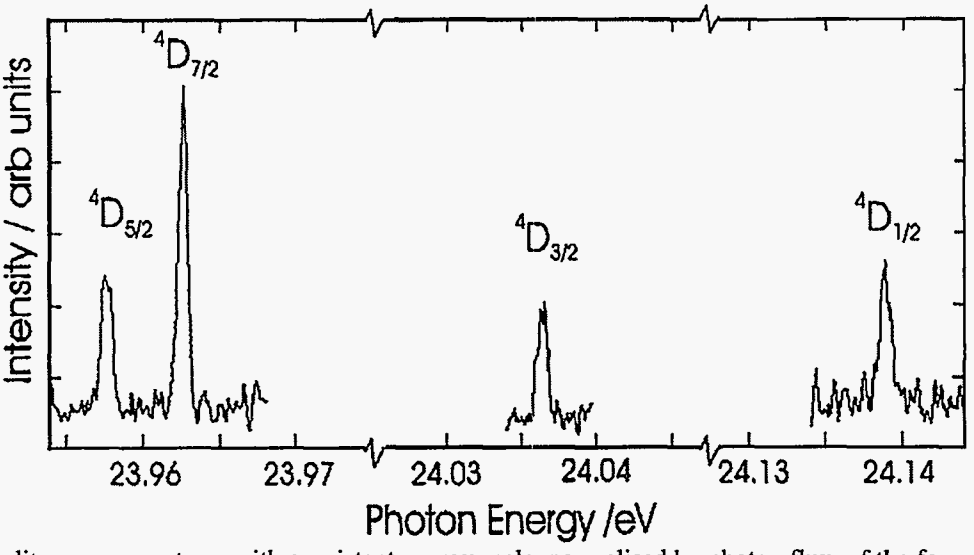

Figure 2. A split-energy spectrum with consistent energy scale, normalised by photon flux, of the four satellite states belonging to the $5s^25p^45d\ ^4D_J$ manifold, showing the width of each peak to be 0.9 meV.

shown are the absolute partial ionization cross-sections of the satellites, calculated from our intensity data. These were obtained by scaling the 5s photoionization cross-section data of Samson and Gardner[11], which was recorded at photon energies down to 23.6 eV and shows a leveling off towards threshold.

The process which has been observed is one of single or double excitation to a Rydberg state and subsequent removal of the Rydberg electron by the pulsed electric field. At threshold it is apparent that satellite states with high and low J values are formed with equal preference. All such states have intensities not dissimilar to that of the main line peak with those containing the same ionic core having similar intensities. The first two characteristics are noticeable in the lower resolution threshold spectrum of Hall *et al.*[3], but more detailed comparisons with their work are complicated

TABLE 1. Intensities and cross-sections of nine of the ionic states of xenon with binding energies in the range of 23.3-24.7 eV observed at the thresholds, at 40.8 eV and 63.5 eV.

Ion state[a]	Energy[b] / eV	Relative Intensities[c]			Cross-section at threshold[e] / Mb
		at threshold (this work)	at 40.8 eV[d] (ref 5)	at 63.5 eV (ref 10)	
$5s5p^6(^2S_{1/2})$	23.3967	100	100	100	0.50
$(^3P)6s(^4P_{5/2})$	23.6689	54	0.21	-	0.27
$(^3P)6s(^2P_{3/2})$	23.9164	55	0.76	0.2	0.28
$(^3P)5d(^4D_{5/2})$	23.9576	15	0.52	-	0.08
$(^3P)5d(^4D_{7/2})$	23.9627	24	0.09	-	0.12
$(^3P)5d(^4D_{3/2})$	24.0366	9.2	0.58	-	0.05
$(^3P)5d(^4D_{1/2})$	24.1388	12	0.23	-	0.06
$(^3P)5d(^4F_{9/2})$	24.4546	-	0.74	0.2	-
$(^3P)6s(^4P_{1/2})$	24.6719	47	2.4	4.8	0.24

a) States given in LS notation. The parental configuration of the satellite states is $5s^25p^4(^3P)$.
b) ref 7.
c) The intensity for the $5s^{-1}$ main line is arbitrarily normalized to 100.
d) Data not taken at the magic angle, see text.
e) Scaled from the data for threshold formation of the $5s^{-1}$ state from Samson and Gardner, ref 11.

by both the number of unresolved states within and possible resonant enhancements contributing to their spectrum.

The trend from low to high photon energies, with the dominant correlations expected to change, can be clearly seen in Table 1. The results at 40.8 eV and 63.5 eV are expected to be intermediate between the two extremes, where most states have not reached their high energy limits and others have already subsided in intensity from their threshold values. Indeed, by 72 eV, data presented by Lagutin *et al.*[6] show the majority of states observed with binding energy from 23-34 eV correspond to J=1/2 and 2, indicating a strong contribution from the $5s^{-1}$ main line. This becomes more extreme at still higher photon energies, and in the x-ray region states with J=1/2 are exclusively observed[6].

SUMMARY

In summary, we have verified the positions and made the first determination of the relative intensities of the seven observed xenon correlation satellites formed at threshold between 23.6-24.7 eV. The high resolution obtained has allowed determination of the absolute partial cross sections and provides a stringent test for the comparison of theoretical predictions. We expect such studies to be extended to the investigation of a variety of atomic and molecular systems, and to higher-lying satellite states, in the near future.

REFERENCES

1. K. Muller-Dethlefs and E. W. Schlag, Annu. Rev. Phys. Chem. **42,** 109 (1991).
2. U. Becker and D.A. Shirley, Phys. Scr. **T31,** 56 (1990).
3. R. I. Hall *et al.*, J. Phys. B: At. Mol. Opt. Phys. **23,** 4469 (1990).
4. S. Svensson *et al.*, J. Elec. Spec. and Rel. Phen. **47,** 327 (1988).
5. M. Carlsson-Göthe, P. Baltzer and B. Wannberg, J. Phys. B: At. Mol. Opt. Phys. **24,** 2477 (1991).
6. B. M. Lagutin *et al.*, J. Phys. B: At. Mol. Opt. Phys. **29,** 937 (1996).
7. J. E. Hansen and W. Persson, Phys. Scr. **36,** 602 (1987).
8. C.-W. Hsu *et al.*, Rev. Sci. Instrum. **68,** 1694 (1997). C.-W. Hsu *et al.*, J. Chem. Phys. **106,** 8931 (1997).
9. Rydberg states of Atoms and Molecules, edited by R. F. Stebbings and F. B. Dunning, (Cambridge University Press, Cambridge, 1983).
10. A. Kikas *et al.*, J. Elec. Spec. And Rel. Phen. **77,** 241 (1996).
11. J. A. R. Samson and J. L. Gardner, Phys. Rev. Lett. **33,** 671 (1974)

This work was supported by the Natural Sciences and Engineering Research Council of Canada (NSERC), by the donors of the Petroleum Research Fund administered by the American Chemical Society and by the Director, Office of Energy Research, Office of Basic Energy Sciences, Chemical Science Division of the U.S. Department of Energy.

Principal investigator: J.W. Hepburn, Chemistry Department, University of Waterloo, Waterloo, Ontario N2L 3G1 Canada. Email: hepburn@uwaterloo.ca. Telephone: (519) 888-4065.

High Resolution Vacuum Ultraviolet Pulsed Field Ionization Photoelectron Band for $OCS^+(X^2\Pi)$: An Experimental and Theoretical Study

S. Stimson[1], M. Evans[1], C. Y. Ng[1], C.-W. Hsu[2] and P. Heimann[2],
C. Destandau,[3] G. Chambaud,[3] and P. Rosmus[3]
[1]Ames Laboratory, USDOE and Department of Chemistry,
Iowa State University, Ames, Iowa 50011
[2]Chemical Sciences Division and Advanced Light Source Accelerator and Fusion Research Division
Lawrence Berkeley National Laboratory Berkeley, CA 94720
[3]Theoretical Chemistry Group, Université de Marne-la-Vallée, F-93166 Noisy le Grand, France

INTRODUCTION

The vacuum ultraviolet pulsed field ionization photoelectron (PFI-PE) band for $OCS^+(X^2\Pi)$ in the energy region of 11.09-11.87 eV has been measured using high-resolution monochromatic synchrotron radiation. The ionization energies (IEs) for the formation of the (0,0,0) $X^2\Pi_{3/2}$ and (0,0,0) $^2\Pi_{1/2}$ states of OCS^+ are determined to be 11.1831±0.0005 eV and 11.2286±0.0005 eV, respectively, yielding a value of 367±1.2 cm^{-1} for the spin-orbit splitting. Using the internally contracted multi-reference configuration interaction approach, three-dimensional potential energy functions (PEFs) for the $OCS^+(X^2\Pi)$ state have been generated and used in the variational Renner-Teller calculations of the vibronic states. The energies of all vibronic states (J=P) for J = 1/2, 3/2, 5/2, and 7/2 have been computed in the energy range of ≈4000 cm^{-1} above the IE [$OCS^+(X^2\Pi_{3/2})$] for the assignment of the experimental spectrum. By a minor modification of the *ab initio* PEFs, good correlation is found between the experimental and theoretical Renner-Teller structures. Similar to the PFI-PE bands for CO_2^+ ($X^2\Pi_g$) and $CS_2^+(X^2\Pi_g)$, weak transitions have been detected in the PFI-PE band for $OCS^+(X^2\Pi)$, which are forbidden in the Franck-Condon approximation. The non-vanishing single-photon ionization cross sections involving the excitation of the bending vibrational modes of OCS^+, CO_2^+, and CS_2^+ in their ground electronic states are attributed to the symmetries of the geometry dependent electronic transition dipole operator components.

EXPERIMENT

The design and combined performance of the high-resolution monochromatic VUV synchrotron source and the photoion-photoelectron apparatus has been described previously.[1-5] The high resolution VUV synchrotron source essentially consists of an undulator with a 10 cm period (U10), a gas harmonic filter, and a 6.65m off-plane Eagle mounted monochromator. The photon energy corresponding to the U10 undulator fundamental peak can be tuned easily to cover the energy range of 8-25 eV. Using Ne (pressure ≈ 30 Torr) as the filter gas in the present experiment, VUV radiation due to higher undulator harmonics with photon energy above the ionization energy (IE) of Ne (21.56 eV) was greatly suppressed (suppression factor = 10^{-4}) before entering the monochromator. Thus, the present experiment was essentially free from interference by photoionization and photoexcitation effects caused by higher order undulator radiation. The grating employed was an Os coated 4800 l/mm grating (Hyperfine Inc.) with a dispersion of 0.32 Å/mm. The monochromator entrance/exit slits used vary in the range of 75-400 μm, which correspond to wavelength resolutions of 0.024-0.128 Å (FWHM).

A continuous molecular beam of pure OCS was produced by supersonic expansion from a room temperature nozzle (diameter = 0.127 mm) at a stagnation pressure of ≈760 Torr. The molecular beam was skimmed by a home made conical skimmer (diameter = 1 mm) before intersecting the

dispersed VUV photon beam 7 cm downstream in the photoionization region. The experimental scheme designed for PFI-PE measurements using multibunch synchrotron radiation has been described in detail.[2,4,6] The key to the success of this method is the use of a high resolution [0.8 meV (FWHM)] zero kinetic energy photoelectron (ZEKE-PE) spectrometer for filtering prompt background electrons. The ZEKE-PE spectrometer used here consists of a steradiancy analyzer (drift length = 12.8 cm, entrance and exit apertures = 3 mm) and a hemispherical energy analyzer arranged in tandem. When the electron spectrometer is tuned to maximize the transmission of PFI-PEs, prompt electrons slightly dispersed in space are greatly discriminated. Our analysis shows that for a stray field of 0.1 V/cm, it only requires a delay of ≈8 ns for prompt electrons to escape from the detection of the ZEKE-PE spectrometer. This in essence overcomes the requirement for a delay in the μs range as in laser PFI-PE studies.

RESULTS

Figures 1(a) and 1(b) show the PFI-PE spectrum for OCS in the energy region of 11.09-11.87 eV obtained using monochromator slits of 200 and 400 μm. As mentioned above, the observed width of 2.5-2.8 meV (FWHM) for the PFI-PE peaks are believed to be limited by the rotational temperature (≈100 K) of the OCS gas sample. A section of this spectrum in the energy region of 11.155-11.292 eV measured using a colder OCS sample (rotational temperature ≈50 K) and monochromator slits of 75 μm is plotted in Fig. 2. The PFI-PE peak widths observed in this spectrum are 2.2 meV (FWHM). However, the structures resolved in the spectra of Figs. 1(a) and 2 are essentially identical.

The strong features observed in these figures[7-9] are similar to those reported in previous TPE and HeI photoelectron spectroscopic studies. However, the fine structures between the strong peaks in the PFI-PE spectra were not observed in these previous experiments. Since rotational transitions are not resolved in this experiment, the observed PFI-PE peak contours are mainly the result of overlapping

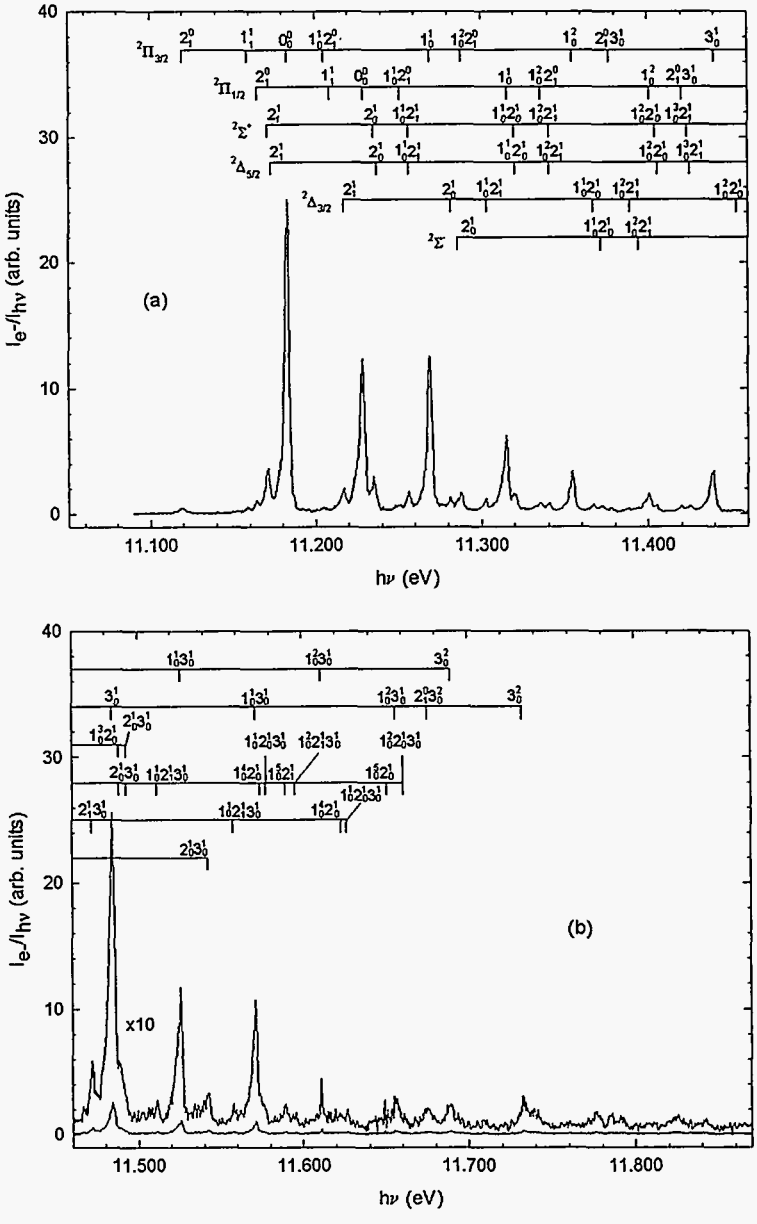

Figures 1a (top) and 1b (bottom). OCS^+ ($X^2\Pi$), Rotational Temperature ~100K

rotational branches in the photoionization transition. The rotational profiles appear to shade toward the red, consistent with the fact that the C-S bond distance in $OCS^+(X^2\Pi)$ is longer than that in OCS ($X^1\Sigma^+$).

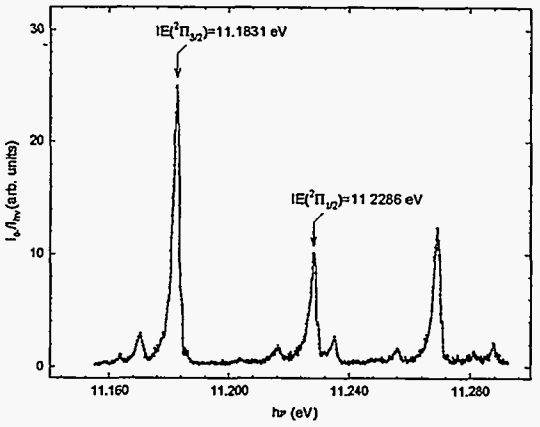

Figure 2. OCS^+ ($X^2\Pi$), Rotational Temperature ~50 K

For a linear molecule, such as $OCS^+(X^2\Pi)$, with v_2^+ bending quanta, the vibrational angular momenta along the molecular axis can have values l_vh, where $l_v = v_2^+, v_2^+-2, 1,$ or 0. Since the electronic orbital angular momentum has a nonzero projection of Λ_h along the molecular axis, the Renner-Teller coupling between Λ and l_v forms a new quantum number, $K = |\Lambda \pm l_v|$. Including coupling of the projection of the spin angular momentum on the molecular axis (Σ), the projected angular momentum is $P = \Lambda + l_v + \Sigma$. In Table III, the calculated vibronic levels for the electronic ground state of OCS^+ are given for energies up to $\approx$4000 cm^{-1} above the (0,0,0) $X^2\Pi_{3/2}$ ground state. In the present work, we have performed calculations for J = 1/2, 3/2, 5/2, and 7/2, i.e., K could take values 0, 1, 2, and 3 (Σ, Π, Δ, and Φ vibronic states), and only the J=P levels (each having its own rotational stack) are given. The μ levels can be approximately associated with the lower potential component (A') and the κ levels with the higher one (A"). The energies [$\Delta\nu$(theo) in cm^{-1}] in Table III for the vibronic levels, (v_1^+, v_2^+, v_3^+) $^2\Sigma_{1/2}^+$ ($^2\Sigma_{1/2}^-$, $^2\Pi_{3/2,1/2}$, $^2\Delta_{5/2,5/2}$, and $^2\Phi_{5/2,7/2}$), of the $OCS^+(X^2\Pi)$ state are given with respect to the energy of the (0,0,0) $^2\Pi_{3/2}$ level.

Due to the Renner-Teller coupling and the strong anharmonic resonances, the assignments of the calculated vibronic levels of $OCS^+(X^2\Pi)$ to (v_1^+, v_2^+, v_3^+) harmonic vibrational states are not straightforward except for the levels lying within $\approx$1700 cm^{-1} above the (0,0,0) $X^2\Pi_{3/2}$ state of OCS^+. The harmonic vibrational quantum numbers were attributed to particular states by inspection of the contour plots for both vibrational parts and the weights of the basis functions in the vibronic wavefunctions. In the $^2\Sigma$ states, we could assign all levels to Fermi polyads, even though in some cases the $^2\Sigma^+$ members of a polyad were found to interact with different $^2\Sigma^-$ members of another polyad. The same situation is found in the $^2\Pi$ and $^2\Delta$ states, where in some cases strong interactions between different polyads in the μ and κ states exist. In the $^2\Phi_{5/2}$ states the distinction between the μ and κ states is hardly possible and, therefore, has not been included in the assignment of the PFI-PE peaks of the OCS spectrum shown in Figs. 1(a) and 1(b). We find also in many cases K-coupling (i.e., the $^2\Pi$ states mix with the $^2\Delta$ states etc.). A reliable analysis of this effect requires more accurate PEFs than those of the present work. Referring to Table III, the levels with the corresponding unique level designations are marked by asterisks. A, b, c, etc designate Fermi polyad members. The numerical value, such as 05, designates $v_3^+ = 0$, and $2v_1^+ + v_2^+ = 5$ (i.e., polyad five) etc. The prime in, e.g., 07' designates the upper Renner-Teller polyad. The equal sign means that the level belongs to two polyads. Generally, for all higher energy levels the assignments with harmonic quantum numbers are only tentative.

CONCLUSIONS

We have obtained a high resolution PFI-PE spectrum for OCS in the energy range of 11.09-11.87 eV. In addition to strong photoelectron bands assignable to $(v_1^+, 0, v_3^+)\ ^2\Pi_{3/2}$ and $(v_1^+, 0, v_3^+)\ ^2\Pi_{1/2}$ for $OCS^+(X^2\Pi)$, weaker Renner-Teller structures are observed for the first time. Accurate theoretical predictions for the Renner-Teller levels for the $OCS^+(X^2\Pi)$ state have also been obtained. The observed transitions in the PFI-PE spectrum are assigned satisfactorily by using the calculated energy positions of the vibronic levels.

ACKNOWLEDGMENTS

The electronic structure calculations were made on CRAY computers at the computer center of IDRIS and UMLV. M.E. acknowledges the GAANN Fellowship for 1994-1997 and Dow Chemical Fellowship for 1997, and S.S. acknowledges the GAANN Fellowship for 1994-1997.

REFERENCES

1. P. Heimann, M. Koike, C.-W. Hsu, M. Evans, K. T. Lu, C. Y. Ng, A. Suits, and Y. T. Lee, *Rev. Sci. Instrum.* **68**, 1945 (1997).
2. C.-W. Hsu, M. Evans, C. Y. Ng, P. Heimann, *Rev. Sci. Instrum.* **68**, 1694 (1997).
3. C.-W. Hsu, M. Evans, P. Heimann, K. T. Lu, and C. Y. Ng, *J. Chem. Phys.* **105**, 3950 (1996).
4. C.-W. Hsu, M. Evans, S. Stimson, C. Y. Ng, and P. Heimann, *J. Chem. Phys.* **106**, 8931 (1997).
5. M. Evans, C. Y. Ng, C.-W. Hsu, and P. Heimann, *J. Chem. Phys.***106**, 978 (1997).
6. C.-W. Hsu, P. Heimann, M. Evans, S. Stimson, and C. Y. Ng, *Chem. Phys.*, submitted.
7. J. Delwiche, M. J. Hubin-Franskin, G. Caprace, P. Natalis, and D. Roy, *J. Electron Spectrosc. Relat. Phenom.* **21**, 205 (1980).
8. L.-S. Wang, J. E. Reutt, Y. T. Lee, and D. A. Shirley, *J. Electron Spectrosc. Relat. Phenom.* **47**, 167 (1988).
9. R. Frey, B. Gotchev, W. B. Peatman, H. Pollak, and E. W. Schlag, *Int. J. Mass Spectrom. Ion Phys.* **26**, 137 (1978).

This work was supported by the Director, Office of Energy Research, Office of Basic Energy Sciences, Chemical Science Division of the U.S. Department of Energy under Contract No. W-7405-Eng-82 for the Ames Laboratory, Contract No. DE-AC03-76SF00098 for the Lawrence Berkeley National Laboratory and the EC Grant ERFMRXCT960088.

Principal Investigator: Prof. C.Y. Ng, Ames Laboratory, USDOE and Department of Chemistry, Iowa State University, Ames, IA 50011, USA. Email: cyng@ameslab.gov. Telephone: 515-294-4225.

Rotationally Resolved Photoelectron Study of O_2: Identification of the Vibrational Progressions for $O_2^+(2^2\Pi_u, {}^2\Sigma_u^-)$ at 19.6-21.0 eV

C.-W. Hsu[1], M. Evans[2], S. Stimson[2], and C. Y. Ng[2]
[1]Chemical Science Division, Lawrence Berkeley National Laboratory Berkeley, CA 94720, USA
[2]Ames Laboratory, USDOE and Department of Chemistry, Iowa State University Ames, IA 50011, USA

INTRODUCTION

In this abstract, we present the results of a rotationally resolved pulsed field ionization photoelectron (PFI-PE) study of the vibrational bands observed at 19.63 and 20.35 eV. These bands have been firmly established by experiments previously (e.g. [1,2]), but definitive assignment of these progressions remains to be made. The rotational structures observed for these bands make possible the unambiguous assignment of the progressions beginning at 19.63 and 20.35 eV to transitions associated with the $O_2^+(2^2\Pi_u)$ and $O_2^+({}^2\Sigma_u^-)$ states, respectively.

EXPERIMENT

The experimental arrangement has been described in detail previously [3]. The O_2 sample was introduced as an effusive O_2 beam ($\approx 10^{-3}$ Torr in the photoionization/photoexcitation region) through a metal orifice (diameter = 0.5 mm) at room temperature and a distance of 0.5 cm from the photoionization/photoexcitation region. The rotational temperature of the O_2 sample is expected to be ≈298 K. This, together with other improvements of the electron lenses and magnetic shielding of the hemispherical energy analyzer, has made possible a nearly 100 fold increase in the PFI-PE intensity as compared to that observed previously using a neat O_2 supersonic beam [3]. The PFI-PE resolution achieved is 0.6 meV or 5 cm^{-1} (FWHM) as measured by the PFI-PE band for $Ne^+(^2P_{3/2})$.

RESULTS

Figure 1 depicts the PFI-PE spectrum for O_2 (upper curve) in the region of 19.590-19.650 eV, which corresponds to the first vibrational bands observed initially by Merkt and Guyon [2]. The relative intensities for rotational transitions resolved here were simulated using the Buckingham-Orr-Sichel (BOS) model [4]. This model was derived to predict rotational line strengths observed in one photon ionization of diatomic molecules.

A successful simulation of the experimental PFI-PE band at 19.63 eV is obtained assuming $O_2^+(^2\Pi_u, v^+, N^+) \leftarrow O_2(X^3\Sigma_g^-, v \leq 0, N'')$ ionization transitions. The angular momentum coupling constants were calculated using the formula for a Hund's case (b) to (a) transition. The known spectroscopic constants for the $O_2(X^3\Sigma_g^-)$ state were used [5]. Due to the nuclear spin statistics, the even N'' rotational levels in $O_2(X^3\Pi_g)$ do not exist. The spin-rotation splittings for $O_2(X^3\Sigma_g^-)$ are in the range of 0.1-0.2 meV for each

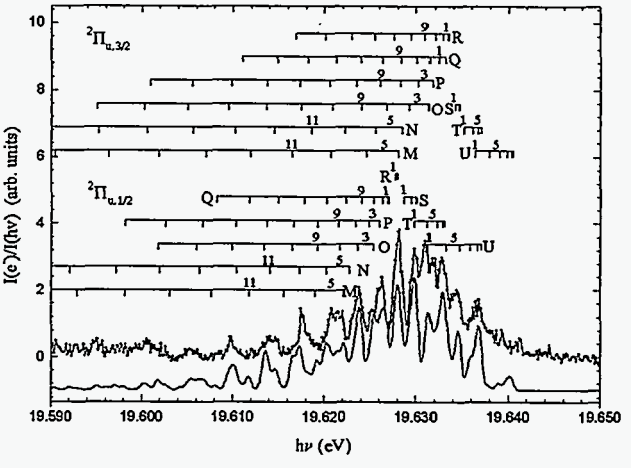

Figure 1. Comparison of the simulated (lower curve, solid circles) and experimental (upper curve, open circles) PFI-PE spectrum of O_2 in the energy range of 19.590–19.650 eV obtained using a neat effusive O_2 beam at 298 K.

rotational state and result in a broadening of the rotational lines by ≈0.1 meV in the simulated spectra. The best fit to the experimental spectrum (lower curve of Fig. 1) was obtained using $C_\lambda = 0.25$ (The BOS coefficients) for λ=1-4 for both the spin-orbit components and a temperature of 300 K for O_2. The rotational branches ΔN (= N^+-N'') = -4, -3, -2, -1, 0, 1, 2, 3, and 4, which are designated correspondingly as the M, N, O P, Q, R, S, T, and U branches, are marked in Fig. 1. For a g ↔ u transition, the photoelectron angular momentum l must be even. Thus, the partial waves for the ejected electron are restricted to l = 0, 2, and 4.

The simulation of the PFI-PE band shown in Fig. 1 yields IE[$O_2^+(2^2\Pi_{u1/2})$] = 19.62684±0.00050 eV and IE[$O_2^+(2^2\Pi_{u3/2})$] = 19.63287±0.00050 eV. Considering the fact that the origin of 19.6299±0.0005 eV found is consistent with the predicted IE[$O_2^+(2^2\Pi_u)$] of 19.69 eV, we conclude that the weak PFI-PE vibrational band at 19.63 eV is the origin, i.e., the $v^+ = 0$ level, of the vibrational progression. We note that the observed ω_e values [2] of 0.110-0.100 eV for this progression are also in accord with the theoretical ω_e of 0.106 eV [1]. The spin-orbit splitting and rotational constant (B_0) for the $O_2^+(2^2\Pi_u, v^+=0)$ level are determined to be 54±3 and 1.08±0.02 cm^{-1}, respectively. Using the latter value, we calculated a value of 1.397±0.012 Å for the equilibrium bond distance (r_e) of $O_2^+(2^2\Pi_u)$, which agrees well with the theoretical r_e of 1.403 Å. We note that the $O_2^+(2^2\Pi_u)$ state correlates to the third dissociation limit [$O(^3P)$ + $O^+(^2D)$] at 22.06 eV[2], and thus has a bond dissociation energy of 2.43 eV [1].

The rotationally resolved PFI-PE spectrum for O_2 (upper curve) in the energy region of 20.320–20.365 eV is plotted in Fig. 2. Based on the $^{18}O_2$ TPE study of Merkt and Guyon[2], we assume that this band is the origin, i.e., the v^+=0 level, of the vibrational progression. The rotational structure of this band indicates that it is associated with an excited O_2^+ state of the Σ symmetry. Since the PFI-PE resolution is not sufficient for resolving the spin-rotation splittings, the PFI-PE spectrum of Fig. 2 cannot distinguish between the $^4\Sigma$ and $^2\Sigma$ states. However, on the basis of the fitting and photoionization selection rules [6], we can exclude the $^{2,4}\Sigma_g^-$, $^{2,4}\Sigma_u^+$, and $^{2,4}\Sigma_g^+$ states are possible candidates. Considering the IE and ω_e values for excited O_2^+ states predicted by Beebe *et al.* in the energy region of 19.5-21.5 eV [7], the most likely candidate is the $O_2^+(^2\Sigma_u^-)$ state. Although the predicted ω_e (825 cm^{-1}) [7] value for this state is close to the experimental [1,2] value of 810 cm^{-1}, the predicted IE (≈21.2 eV) [7] for this state is more than 0.8 eV greater than the experimental IE of 20.35 eV. Assuming that the ionization transitions correspond to $O_2^+(^2\Sigma_u^-, v^+=0, N^+) \leftarrow O_2(X^3\Sigma_g^-, v''=0, N'')$ and that the rotational temperature of O_2 is 300 K, we obtained an excellent fit (lower curve of Fig. 2) to the experimental spectrum. The angular momentum coupling constants were calculated using the formula for a Hund's case (b) to (b) transition. The

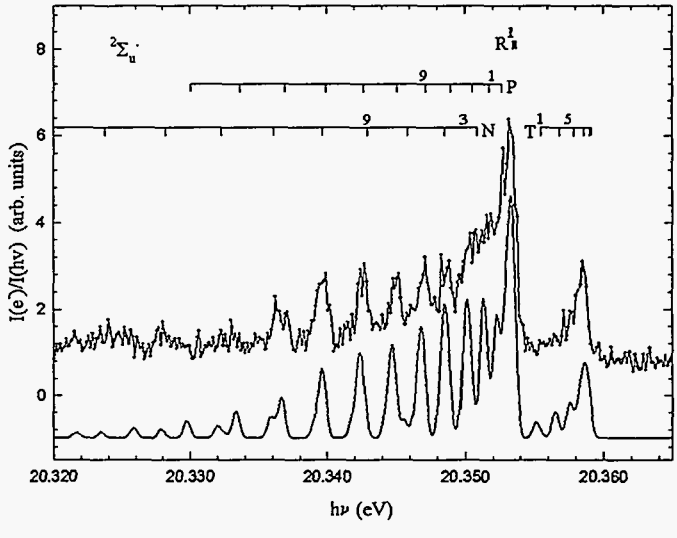

Figure 2. Comparison of the simulated (lower curve, solid circles) and experimental (upper curve, open circles) PFI-PE spectrum of O_2 in the energy range of 20.320–20.365 eV obtained using an effusive O_2 beam at 298 K.

simulation yields an IE value of 20.3526±0.0005 eV and a B_0 value of 1.14±0.02 cm^{-1}. The latter value corresponds to r_e = 1.360±0.012 Å, which is larger than r_e =1.30 Å for the $O_2^+(B^2\Sigma_g^-)$ state, but significantly smaller than the theoretical prediction [7] of r_e=1.522 Å for the $O_2^+(^2\Sigma_u^-)$ state. Both experiment [1,2] and theory [1,7] show that the $O_2^+(B^2\Sigma_g^-)$ and $O_2^+(^2\Sigma_u^-)$ states correlate to the dissociation limit of $O(^3P) + O^+(^2D)$. Thus, the dissociation energy for $O_2^+(^2\Sigma_u^-)$ determined here is 1.707 eV. The BOS coefficients obtained from the stimulation are C_1=0.7 and C_3=0.3, indicating that the *l* values for the out going electron are restricted to 0, 2, and 4. The rotational transitions for the N, P, R and T branches are marked in Fig. 2.

CONCLUSION

In summary, we have demonstrated that rotationally resolved photoelectron spectroscopy, together with high level theoretical *ab initio* calculations, can provide unambiguous assignments of weak photoelectron bands observed in the inner-valence region.

REFERENCES

1. P. Baltzer, B. Wannberg, L. Karlsson, M. Carlsson Gothe, and M. Larsson, *Phys. Rev. A* **45**, 4374 (1992).
2. F. Merkt, P.M. Guyon, and J. Hepburn, *Chem Phys.* **173**, 479 (1993); F. Merkt and P.M. Guyon, *J. Phys. Chem.* **99**, 15775 (1995).
3. C.-W. Hsu, M. Evans. P. A. Heimann, and C. Y. Ng, *Rev. Sci. Instrum.*, **68**, 1694 (1997).
4. A. D. Buckingham, B. J. Orr, J. M. Sichel, *Phil. Trans. Roy. Soc. Lond. A* **268**, 147 (1970).
5. K. P. Huber and G. Herzberg, "Molecular Spectra and Molecular Structure, Vol. IV, Constants of Diatomic Molecules" (Van Nostrand, New York, 1979); G. Herzberg, "Molecular Spectra and Molecular Structure, Vol. I, Spectra of Diatomic Molecules" (Van Nostrand, Princeton, 1950).
6. J. Xie and R. N. Zare, *J. Chem. Phys.* **93**, 3033 (1990).
7. N. H. F. Beebe, E. W. Thulstrup, and A. Anderson, *J. Chem. Phys.* **64**, 2080 (1976).

This work was supported by the Director, Office of Energy Research, Office of Basic Energy Sciences, Chemical Science Division of the U.S. Department of Energy under Contract No. DE-AC03-76SF00098 for the Lawrence Berkeley National Laboratory.

Principal investigator: Cheuk-Yiu Ng, Ames Laboratory, USDOE and Department of Chemistry, Iowa State University. Email: cyng@ameslab.gov. Telephone: 515-294-4225.

Rotational-Resolved Pulsed Field Ionization Photoelectron Bands for $H_2^+(X^2\Sigma_g^+, v^+=0, 2, 9$ and $11)$

S. Stimson[1], Y.- J. Chen[1], M. Evans[1], C.-L. Liao[1], C. Y. Ng[1], C.-W. Hsu[2] and P. Heimann[2]

[1]Ames Laboratory, USDOE and Department of Chemistry, Iowa State University Ames, Iowa 50011

[2]Chemical Sciences Division and Advanced Light Source Accelerator and Fusion Research Division, Lawrence Berkeley National Laboratory Berkeley, CA 94720

INTRODUCTION

We have obtained the rotational-resolved pulsed field ionization photoelectron (PFI-PE) spectrum for H_2 at a resolution of 7 cm^{-1} (full-width-at-half-maximum) in the photon energy range of 15.30-18.10 eV. We present here the assignment and simulation of rotational transitions for the $H_2^+(X^2\Sigma_g^+, v^+= 0, 2, 9,$ and 11) vibronic bands using the Buckingham-Orr-Sichel (BOS) model.[1] The BOS simulation shows that perturbation of PFI-PE rotational line intensities due to near-resonance autoionization decreases as v^+ increases. Experimental rotational constants for $H_2^+(X^2\Sigma_g^+, v^+= 0, 2, 9,$ and 11) are determined with higher accuracy than those obtained in previous HeI and NeI photoelectron studies. In agreement with previous experimental and theoretical investigations, only the $\Delta N = 0$ and ± 2 rotational branches are observed in the PFI-PE spectrum for H_2.

EXPERIMENT

The design and performance of the Chemical Dynamics Beamline at the ALS has been described previously.[2-5] Briefly, the major components for the high-resolution photoionization facility at this beamline include a 10 cm period undulator, a gas harmonic filter; a 6.65m off plane Eagle mounted monochromator, and a photoion-photoelectron apparatus. The fundamental light from the undulator is then directed into the 6.65 m monochromator and dispersed by an Os coated 4800 l/mm grating (dispersion = 0.32 Å/mm) before entering the experimental apparatus. A continuous molecular beam of pure H_2 was produced by supersonic expansion through a stainless steel nozzle (diameter = 0.127 mm) at a stagnation pressure of 330 Torr and a nozzle temperature of 298 K. The molecular beam was then skimmed by a circular skimmer (diameter = 1 mm) before intersecting the monochromatic VUV light beam 7 cm downstream in the photoionization region. The present experiment is performed in the multibunch mode with 304 bunches in the synchrotron orbit, corresponding to a repetition rate of 464 MHz. A pulsed electric field (height = 0.67 V/cm, width = 40 ns) was applied to the repeller at the photoionization/photoexcitation region to field ionize high-n Rydberg states and extract photoelectrons toward the detector, and was applied every 2 (1.31 μs) ring periods. The monochromator entrance/exit slits used are 150/150 μm, corresponding to a wavelength resolution of 0.048 Å (or 0.9 meV at 800 Å) (FWHM).

RESULTS

The rotational-resolved PFI-PE bands for $H_2^+(X^2\Sigma_g^+, v^+=0, 2, 9, \text{and } 11)$ areshown in Figs. 1-4, respectively. The assignment of the rovibonic lines are based on the theoretical calculations of Hunter, Yau, and Prichard (HYP). Photoelectron peaks in Figs. 1-4, which are not assigned to (N^+, J'') ionization thresholds, can be partly attributed to prompt electron background features from autoionizing Rydberg levels of H_2. The contamination by prompt electron peaks is expected to be less serious at higher v^+ states because strong autoionizing Rydberg states are mostly concentrated in the energy range (≈15.3-16.5 eV) covering the lower v^+ (<5) states. This expectation is confirmed by the PFI-PE spectra of Figs. 1-4. The $v^+= 0$ and 2 PFI-PE bands exhibit many strong near-resonance autoionization peaks unassignable to rotational transitions, whereas the PFI-PE bands for $v^+= 9$ and 11 are nearly free from such autoionization features.

In accordance with the selection rule due to nuclear spin statistics, only the $\Delta N = N^+ - J''=$ even, i.e., 0, ±2, ±4..., transitions are allowed. As shown in Figs. 1-4, the dominant rotational transitions for $v^+=0$, 2, 9, and 11 are $\Delta N = 0$, i.e., (0, 0), (1, 1), (2, 2), and (3, 3). In general, the PFI-PE intensity for (1, 1) is higher than that for (0, 0) within a given vibrational band. This observation and the low PFI-PE intensities for transitions involving $J'' \geq 4$ are in general accord with the thermal distribution of J'' for H_2. Weak transitions attributable to $\Delta N = \pm 2$, i.e., (2, 0), (3, 1), (0, 2), (4, 2), (1, 3), and (5, 3) are also observed. The dominance of the rotational transitions with $\Delta N = 0$ over that with $\Delta N = \pm 2$ is consistent with the results of previous experiments and theoretical predictions. Here, we present the simulation of the relative rotational intensities observed in the PFI-PE bands for $H_2^+(X^2\Sigma_g^+$, $v^+=0, 2, 9, \text{and } 11)$ using the BOS model. This model was derived to predict rotational line strengths observed in one photon ionization of diatomic molecules. Basically, the rotational line strength is separated into two factors. The factor C_λ is associated with the electronic transition

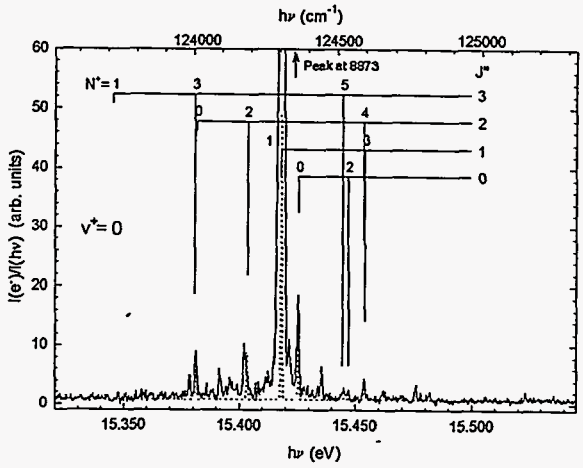

Figure 1. $H_2^+ X^2\Sigma_g^+$, $v^+=0$

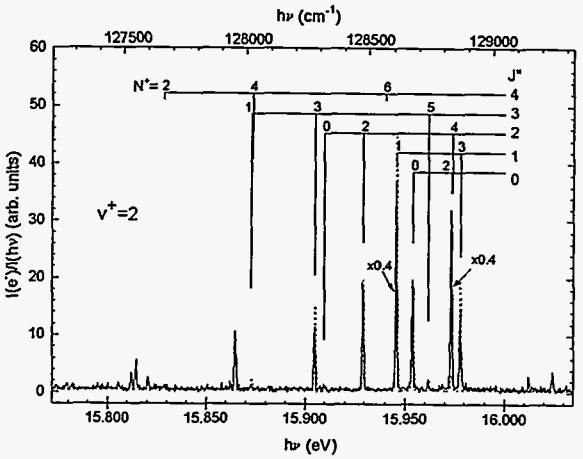

Figure 2. $H_2^+ X^2\Sigma_g^+$, $v^+=2$

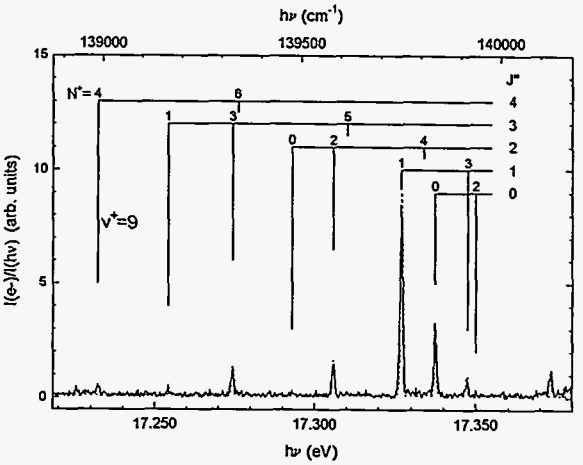

Figure 3. $H_2^+ X^2\Sigma_g^+$, $v^+=9$

moments, which is the linear combination of electron transition amplitudes for the possible angular momenta ℓ of the ejected electron. The general interpretation of λ is that of the angular momentum transfer in the photoionization process. The other factor is determined by the standard angular momentum coupling constants (Clebsch Gordon Coefficients), which were calculated using the formula for a Hund's case (b) to (b) transition in the present study. The known spectroscopic constants for the $H_2(X^1\Sigma_g^+$, $v''=0$) were used. The best fits for the PFI-PE bands for $H_2^+(X^2\Sigma_g^+$, $v^+=0$, 2, 9, and 11) are depicted as dashed curves in Figs. 1-4. The fact that only the $\Delta N = -2$, 0, and +2 rotational branches are observed implies that only the BOS coefficients C_0 and C_2 are nonzero. The C_0 and C_2 values for the simulated spectra shown in Figs. 1-4 are listed in Table I. The dominance of the $\Delta N = 0$ or Q-branch observed in the experimental spectra is consistent with the significantly higher C_0 values than the corresponding C_2 values. As expected, the BOS simulation, which has not taken into account the effect of near-resonance autoionization, cannot account for the overwhelming intensity for the (1, 1) transition observed in the $v^+=0$ PFI-PE band. Surprisingly, general agreement is found between the experimental spectra and the BOS simulation of the PFI-PE bands for $v^+ \geq 1$ states. In general, the agreement becomes better for higher v^+. Disregarding the C_0 and C_2 values for the $v^+=0$ band, we find that the C_0 value generally increases compared to the C_2 value as v^+ is increased. Such a trend is consistent with the observation that the $\Delta N = \pm 2$ rotational branch diminishes as v^+ is increased.

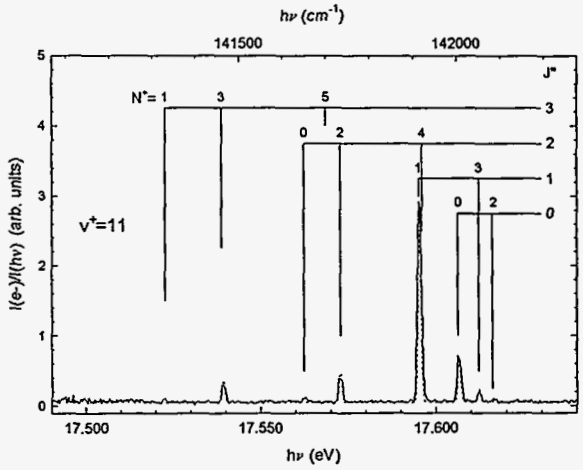

Figure 4. H_2^+ $X^2\Sigma_g^+$, $v^+=11$

Table I.

v^+	BOS Coefficients	
	C_0	C_2
0	90	10
2	75	25
9	85	15
11	90	10

In addition, we have obtained the rotational constants B_{v+} and D_{v+} for $H_2^+(X^2\Sigma_g^+$, $v^+=0$, 2, 9, and 11) by fitting the rotational structures resolved in Figs. 1-4. These values are compared with those reported in the previous HeI photoelectron study of Pollard *et al.*[6] and theoretical predictions.[7] The B_{v+} and D_{v+} values obtained in the present experiment are more accurate than previous results of Pollard *et al.* As expected, the results of the present experiment and the theoretical predictions are in excellent agreement.

CONCLUSIONS

We present here rotationally resolved PFI-PE data for the formation of $H_2^+(X^2\Sigma_g^+$, $v^+=0$, 2, 9, and 11). The analysis of these data has provided rotational constants B_{v+} and D_{v+} for these states with higher accuracy compared to those reported in previous experimental studies. The simulated photoelectron bands based on the BOS model are in good agreement with PFI-PE bands of higher v^+ states, indicating that the strong perturbation of the relative intensities for rotational transitions occurs mostly at lower v^+ (≤ 5) states.

ACKNOWLEDGMENTS

M.E. and S.S. acknowledge the GAANN Fellowship support for 1994-1995 and 1996-1997. Y.J.C acknowledges the 1997 research Award from Iowa State University. M.E. is a recipient of the Dow Fellowship for 1997-1998.

REFERENCES

1. S. Stimson, Y.- J. Chen, M. Evans, C.-L. Liao, C.-W. Hsu, P. Heimann, and C. Y. Ng, Chem. Phys. Lett., accepted.
2. C.-W. Hsu, M. Evans, P. Heimann, K. T. Lu, and C. Y. Ng, *J. Chem. Phys.* **105**, 3950 (1996).
3. M. Evans, C. Y. Ng, C.-W. Hsu, and P. Heimann, *J. Chem. Phys.***106**, 978 (1997).
4. C.-W. Hsu, M. Evans. P. A. Heimann, and C. Y. Ng, *Rev. Sci. Instrum.*, **68**, 1694 (1997).
5. P. Heimann, M. Koike, C.-W. Hsu, M. Evans, K. T. Lu, C. Y. Ng, A. Suits, and Y. T Lee, *Rev. Sci. Instrum.***68**, 1945 (1997).
6. J. E. Pollard, D. J. Trevor, J. E. Reutt, Y. T. Lee, and D. A. Shirley, *J. Chem. Phys.* **77**, 34 (1982).
7. F. Merkt, H. Xu, and R. N. Zare, *J. Chem. Phys.* **104**, 950 (1996).

This work was supported by the Director, Office of Energy Research, Office of Basic Energy Sciences, Chemical Science Division of the U.S. Department of Energy under Contract No. W-7405-Eng-82 for the Ames Laboratory and Contract No. DE-AC03-76SF00098 for the Lawrence Berkeley National Laboratory.

Principal Investigator: Prof. C.Y. Ng, Ames Laboratory, USDOE and Department of Chemistry, Iowa State University, Ames, IA 50011, USA. Email: cyng@ameslab.gov. Telephone: 515-294-4225.

UV Photodissociation Dynamics of Furan

J. J. Wang, Naoki Hemmi and Arthur G. Suits
Lawrence Berkeley National Laboratory, University of California, Berkeley, CA 94720, USA

We have studied the photodissociation of furan, C_4H_4O, at 193nm (Fig. 1) on endstation 1 of the Chemical Dynamics Beamline using tunable undulator radiation as a probe of the neutral photofragments. Furan is one of the simplest oxygen-containing aromatic molecules, and its dissociation exhibits both molecular and radical decay channels that can provide insight into the dynamics of ring-opening and H-migration pathways in these systems. In these studies, a continuous supersonic molecular beam of furan in helium is crossed by the output of a pulsed excimer laser at 193nm. Neutral fragments travel 15cm into the triply differentially pumped detector region where they are ionized by broadband (2.2% bandwidth) undulator radiation, with the resulting ions mass selected using a quadrupole mass filter, then counted as a function of time and scattering angle.[1]

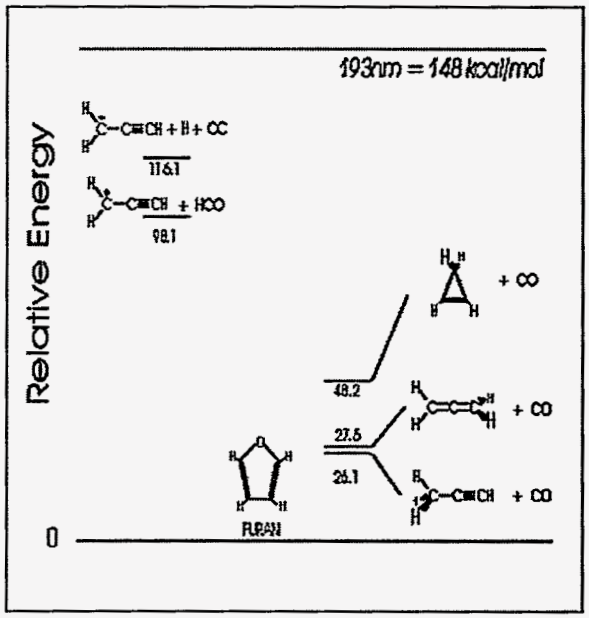

Figure 1. Energetics for possible pathways in decomposition of furan following excitation at 193nm.

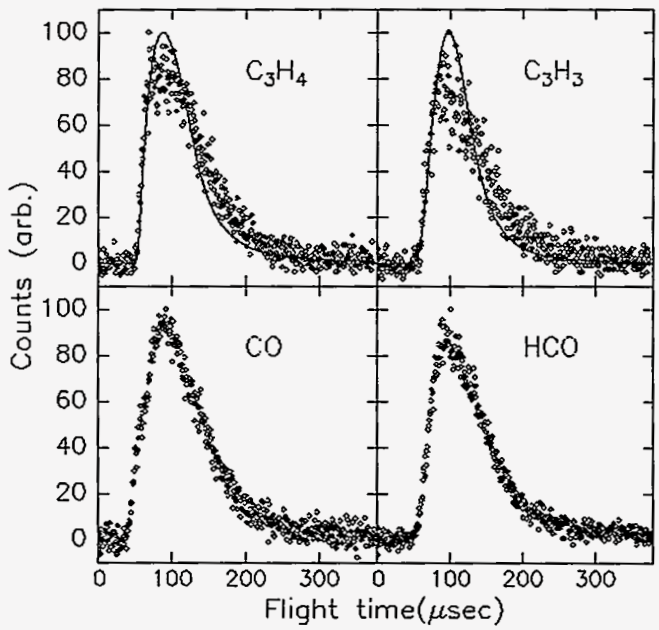

Figure 2. Time-of-flight spectra for four observed fragments of furan photodissociation at 193nm recorded at a laboratory scattering angle of 10 degrees. Fragment identity and probe photoionization energy are indicated in each spectrum.

We observe only two channels in this dissociation process: a molecular channel yielding C_3H_4+CO, and a radical channel giving C_3H_3 +HCO. These latter species are both key radicals in hydrocarbon combustion chemistry. Fig. 2 shows time-of-flight spectra for these four fragments at a laboratory angle of 10 degrees, along with simulations that are used to generate the translational energy distributions. Both channels show relatively little of the available energy appearing in translation, but the distributions peak away from zero energy, indicating a likely exit barrier. It is interesting that we observe no H or H_2 elimination in this system, in striking contrast to the dissociation of pyrrole, C_4H_4NH, the analogous N-containing system.[2] It is clear from the fact that we observe only these two dissociation channels that opening of the ring is the

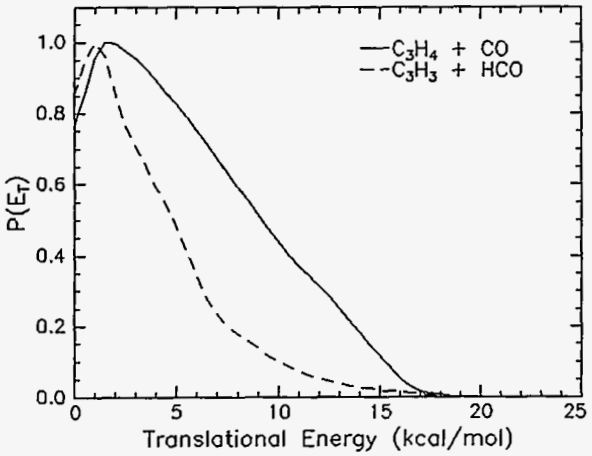

Figure 3. Total center-of-mass translational energy distributions for the two primary channels indicated.

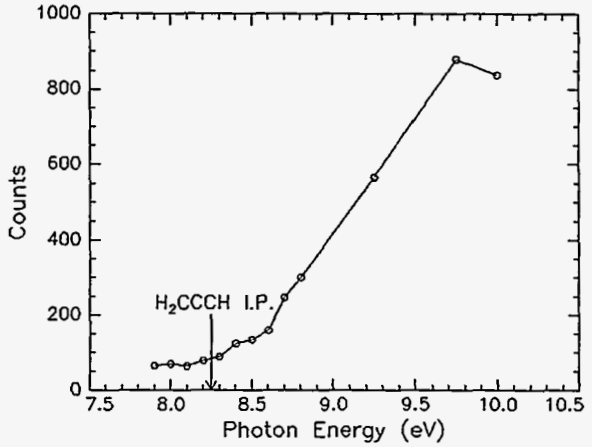

Figure 4. Photoionization efficiency spectrum of C_3H_3 photofragment.

initial step. The radical channel can then result immediately from C-C bond fission, although H migration is then necessary in the C_3H_3 fragment in order to yield the lowest energy H_2CCCH isomer. Using the tunable undulator radiation, we can probe the photionization efficiency of this radical product; this is shown in Fig. 4 along with the threshold indicated for the C_3H_3 isomers.

For the molecular channel, three product isomers are possible for C_3H_4: these are propyne, H_3CCH, allene, H_2CCH_2 and cyclopropene, c-C_3H_4. On the basis of the photoionization dependence of that molecule we can likely eliminate the formation of cyclopropene as an important component. The differences in the ionization potentials of allene and propyne are too small, however, to allow us to distinguish them on this basis. In addition to the primary contributions to the CO and HCO products, we observe some CO arising from secondary decomposition of the HCO. With further analysis, we hope to use this process to quantify the branching between these two channels.

REFERENCES

1. X. Yang, D.A. Blank, J. Lin, A.G. Suits and Y.T. Lee and A.M. Wodtke, *Rev. Sci. Instrum.*, **68**, 3317 (1997).
2. D. A. Blank, S. North and Y. T. Lee, *Chem. Phys.*, (1996).

This work was supported by the Director, Office of Energy Research, Office of Basic Energy Sciences, Chemical Sciences Division of the U. S. Department of Energy under contract No. DE-ACO3-76SF00098.

Principal investigator: Arthur G. Suits, MS 10-110, Chemical Sciences Division, Lawrence Berkeley Laboratory, Berkeley CA 94720. Email agsuits@lbl.gov.

Beamline 9.3.1 Abstracts

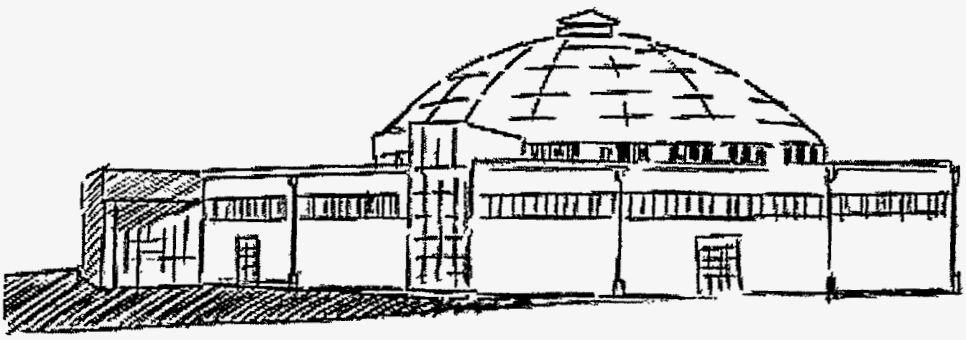

Neutral Dissociation of Hydrogen Following Photoexcitation of HCl at the Chlorine K-Edge

D. L. Hansen, M. E. Arrasate, J. Cotter,[1] G. R. Fisher,[2] K. T. Leung,[3] J. C. Levin,[4] R. Martin, P. Neill,[1] R. C. C. Perera,[2] I. A. Sellin,[4] M. Simon,[5,6] Y. Uehara,[7] B. Vanderford, S. B. Whitfield,[8] and D. W. Lindle

Department of Chemistry, University of Nevada, Las Vegas, NV 89154-4003

[1] *Department of Physics, University of Nevada, Reno, NV 89557-0058*

[2] *Lawrence Berkeley National Laboratory, Berkeley, CA 94720*

[3] *Department of Chemistry, University of Waterloo, Waterloo, Ontario, N2L 3G1, Canada*

[4] *Department of Physics, University of Tennessee, Knoxville, TN 37996*

[5] *LURE, Bâtiment 209D, Université Paris-Sud, 91405 Orsay Cedex, France*

[6] *CEA/DRECAM/SPAM, Bâtiment 522,CEN Saclay, 91191 Gif/Yvette Cedex, France*

[7] *Mitsubishi Electric Corporation, Amagasaki, Hyogo, 661 Japan*

[8] *Department of Physics and Astronomy, University of Wisconsin, Eau Claire, WI 54702*

Time-of-flight mass spectroscopy was used to study the relaxation dynamics of HCl following photoexcitation in the vicinity of the Cl K-edge (~2.8 keV) using monochromatic synchrotron radiation from B.L. 9.3.1. At the lowest resonant excitation to the $6\sigma^*$ antibonding orbital, almost half of the excited molecules decay by emission of a neutral H atom, mostly in coincidence with a highly charged Cl^{n+} ion. The present work demonstrates that neutral-atom emission can be a significant decay channel for excited states with very-short lifetimes (1 fs).

As a simple diatomic with deep-core electrons, HCl was chosen for the present experiment because the core-level spectroscopy is well understood and because of the relatively few ion fragments possible, facilitating interpretation of the subsequent mass spectra. Also, electron-spectroscopy measurements for the shallow-core Cl 2p level of HCl as well as ion-spectroscopy measurements of the K-shell of Ar, which is iso-electronic with HCl, are available for comparison. Fig. 1 shows the ratio of the yield of H^+ to the sum of the yields for all Cl charge states. On the $6\sigma^*$ resonance Fig. 1 shows a drop in the H^+/Cl^{n+} ratio of about 40%. The magnitude of this effect is particularly surprising considering the short lifetime of a Cl K-shell hole (1.1 fs), and that there is enough energy in the system to form highly charged chlorine ions (up to Cl^{6+}).

Corresponding to the decrease in the H^+ yield is an increase in the relative yields of Cl^{3+} and Cl^{4+}, suggesting an association with formation of neutral hydrogen on resonance. These results suggest one or some combination of the following types of decay paths following resonant excitation of HCl:

$$HCl^*(1\sigma^{-1}6\sigma^*) \longrightarrow H^0 + Cl^*(1s^{-1}3p^6) \quad (Fragmentation) \tag{1}$$

$$Cl^*(1s^{-1}3p^6) \longrightarrow Cl^{+*}(2p^{-2}3p^6) + e^- \quad (Atomic\ KLL\ Auger) \tag{2}$$

or

$$HCl^*(1\sigma^{-1}6\sigma^*) \longrightarrow HCl^{+*}(1\pi^{-2}6\sigma^*) + e^- \quad (Molecular\ KLL\ Auger) \tag{3}$$

$$HCl^{+*}(1\pi^{-2}6\sigma^*) \longrightarrow H^0 + Cl^{+*}(2p^{-2}3p^6) \quad (Fragmentation). \tag{4}$$

Auger decay of the two L-shell holes leads to the formation of a Cl^{3+} ion. Dissociation prior to or after the relaxation of the K-shell hole is the key point of comparison in these mechanisms.

From the present experiments, it is impossible to determine which of these paths is more probable. The higher electron density around the H atom in the excited σ^* orbital, coupled with the fact that the H atom has very little time to move during the lifetime of the core hole, opens up the possibility that the excited electron in the σ^* orbital remains as a spectator electron, localized around the H atom. The spectator electron which is not ejected in the subsequent Auger decay, thus allows the H atom to fragment as a neutral. Electron spectroscopy of the KLL-Auger electrons would reveal if the Auger decay takes place from an atomic or molecular species, and in the case of molecular decay, if the electron in the σ^* orbital is a spectator or participator in the Auger decay, thus determining if the dissociation of the molecule occurs on the same time scale as the Auger decay. Studies done at the Cl L-edge of HCl indicate that at the Cl 2p$\longrightarrow$ 6σ^* resonance, dissociation followed by Auger decay of the atomic Cl fragment is the dominant decay path. However, the fact that a Cl K-shell hole has a shorter lifetime than an L-shell hole by a factor of about 6 [a K-shell hole has a lifetime = 1.1fs (0.6 eV); for an L-shell hole the lifetime is 6.6 fs (0.1 eV)] may allow Auger decay to compete more favorably as the first step in the decay process.

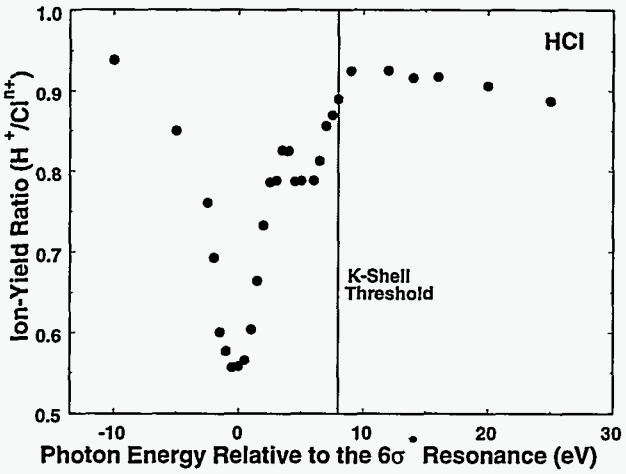

FIG. 1. Ratio of hydrogen ions detected to the sum of all chlorine ions detected in singles mode.

The authors thank the staff of the ALS for their excellent support. Support from NSF, Nevada DOE EPSCoR, Research Corporation, The Petroleum Research Fund, and the UNLV University Research Grants and Fellowships Committee is gratefully acknowledged. This work was performed at the Advanced Light Source DOE (DE-AC03-76SF00098), and at the National Synchrotron Light Source DOE (DE-AC020-76CH00016).

Team Leader Dennis Lindle, E-mail: lindle@nevada.edu, Fax: 1 702 895 4072

Photofragmentation of Small Molecules Following Excitation at Deep-Core Levels

D. L. Hansen, M. E. Arrasate, J. Cotter,[1] G. R. Fisher,[2] K. T. Leung,[3] J. C. Levin,[4]
R. Martin, P. Neill,[1] R. C. C. Perera,[2] I. A. Sellin,[4] M. Simon,[5,6]
Y. Uehara,[7] B. Vanderford, S. B. Whitfield,[8] and D. W. Lindle
Department of Chemistry, University of Nevada, Las Vegas, NV 89154-4003
[1] *Department of Physics, University of Nevada, Reno, NV 89557-0058*
[2] *Lawrence Berkeley National Laboratory, Berkeley, CA 94720*
[3] *Department of Chemistry, University of Waterloo, Waterloo, Ontario, N2L 3G1, Canada*
[4] *Department of Physics, University of Tennessee, Knoxville, TN 37996*
[5] *LURE, Bâtiment 209D, Université Paris-Sud, 91405 Orsay Cedex, France*
[6] *CEA/DRECAM/SPAM, Bâtiment 522, CEN Saclay, 91191 Gif/Yvette Cedex, France*
[7] *Mitsubishi Electric Corporation, Amagasaki, Hyogo, 661 Japan*
[8] *Department of Physics, and Astronomy, University of Wisconsin, Eau Claire, WI 54702*

The relaxation dynamics of HCl, DCl, H_2S, and D_2S following photoexcitation in the vicinity of the Cl and S K-shell thresholds (~2.8 keV for Cl, ~2.5 keV for S) were studied by means of ion time-flight mass spectroscopy using light from B.L. 9.3.1. In all cases, a significant amount of neutral dissociation of hydrogen was found to occur on resonance, as well as the onset of pre-edge core-shell photoexcitation.

The data presented here were collected in two different modes. In the "singles" mode, time-of-flight spectra are collected with only one or two electron bunches circulating in the storage ring. The start pulse for the timing circuit is provided by the detection of an individual ion, while the ring timing pulse, produced by the periodic pulsing of the SR (328 ns for ALS 2-bunch), provides the stop signal. In the PIPICO mode of operation, two ions from the same molecule provide the start and stop signals for the timing circuit (in this case, H^+ provides the start, and Cl^{n+} or S^{n+} provide the stop). Thus the difference in flight time between the two ions is measured, and the operation mode of the storage ring is irrelevant. These measurements inherently discriminate against decay processes where the molecule does not dissociate, or where the molecule dissociates but one of the fragments is neutral. Fig. 1 shows spectra taken on resonance for HCl, and H_2S. The most notable feature of these spectra is the high degree of ionization of the atoms (+6 for Cl, +5 for S), and the fact that fragmentation of the molecule happens following the majority of interactions, with less than 1% of the yield being the result of molecular ions. The data analysis procedure is essentially the same for both PIPICO and singles spectra. Spectra were taken at a number of photon energies in the Cl K-shell region. Peaks in these spectra were integrated in order to calculate fractional yields as a function of energy.

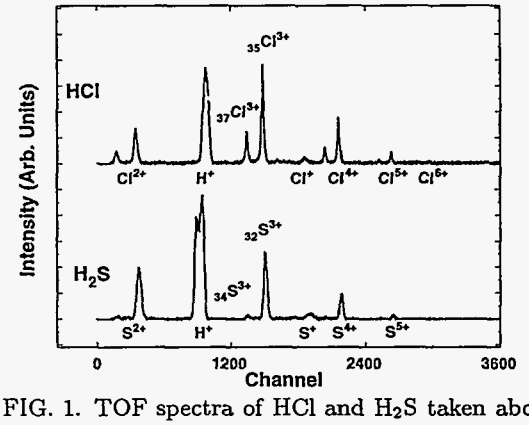

FIG. 1. TOF spectra of HCl and H_2S taken above the first resonance Two isotopes of chlorine and sulfur are visible.

In the photon energy regime below the $1s \rightarrow 6\sigma^*$ resonance gradual changes in the relative abundances of the different ionic states are visible in the average charge state for both the singles and PIPICO spectra (Fig. 2). We attribute this effect to pre-edge inner-shell ion-

ization, where the photoelectron is excited to the Lorentzian profile of a continuum state. Previous studies have observed the onset of this effect at tens of eV below the 1s→4s resonance for Ar and for more than 10 eV below the first sulfur K-edge resonance in OCS and CS_2. While in this study, the data does not allow for an accurate determination of the onset of pre-edge ionization, it can be safely said that it occurs at energies more than 5 eV below the 1s→ $6\sigma^*$ resonance.

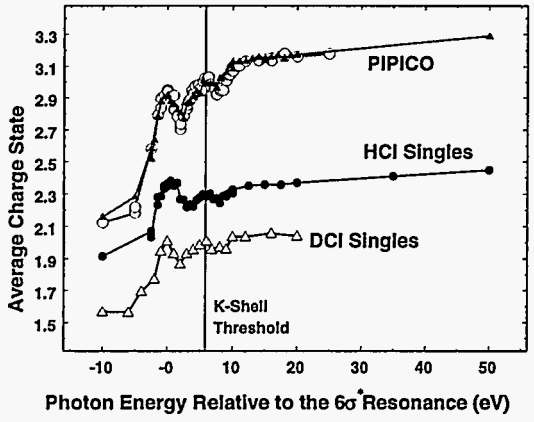

FIG. 2. Average charge state for HCl and DCl singles and PIPICO spectra. Circles represent the HCl data, triangles represent the DCl data.

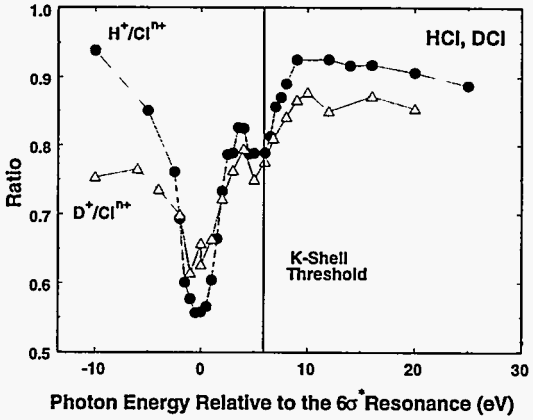

FIG. 3. Ratio of hydrogen or deuterium ions detected to the sum of all chlorine ions detected in singles mode.

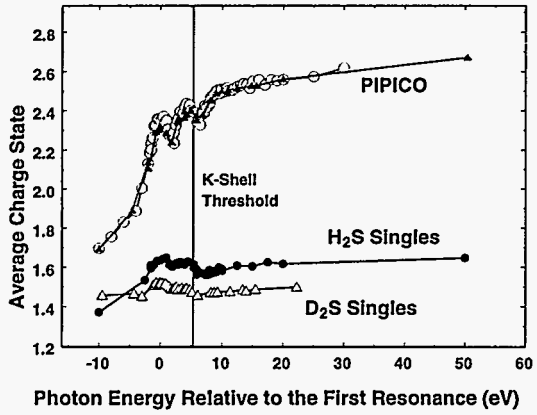

FIG. 4. Average charge state for H_2S and D_2S singles and PIPICO spectra. Circles represent the H_2S data, triangles represent the D_2S data.

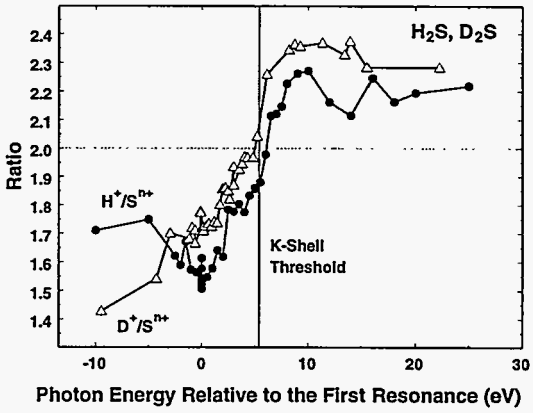

FIG. 5. Ratio of hydrogen or deuterium ions detected to the sum of all sulfur ions detected in singles mode.

Fig. 3 shows the ratio of the H^+ yield to the sum of the yields for all Cl charge states. The most notable feature in this data is the drop in the hydrogen to chlorine ratio of as much as 40% for HCl, and 20% for DCl on resonance. Although the DCl molecule undergoes the same decay transitions as the HCl molecule, the amount of neutral hydrogen produced is less by almost a factor of two. This is easily explained by the fact that the heavier deuterium does not escape the attractive potential of the Cl^{+n} ion as quickly as the hydrogen atom, and it is thus more difficult for the deuterium atom to carry away an electron in the presence of the more electronegative chlorine ion.

Discussion of the results for H_2S and D_2S can, for the most part, parallel the discussion for HCl and DCl. Trends in the the average charge state of the S^{n+} ion (Fig. 4) indicate

the onset of pre-edge inner-shell ionization, and, again there is a dip in the ratio of H^+/S^{n+} on resonance. Both of these effects are analogous to those observed in HCl. However in the energy regime below resonance, the ratio of D^+/S^{n+} is significantly lower than on resonance values. This can be attributed to a higher production of the molecular ion below resonance. Because the ratio is lower than that for H_2S, it seems likely that the trends are a result of a kinematic effect where the heavier deuterium is not able to escape the sulfur ion as easily as the hydrogen.

The authors thank the staff of the ALS for their excellent support. Support from NSF, Nevada DOE EPSCoR, Research Corporation, The Petroleum Research Fund, and the UNLV University Research Grants and Fellowships Committee is gratefully acknowledged. This work was performed at the Advanced Light Source DOE (DE-AC03-76SF00098), and at the National Synchrotron Light Source DOE (DE-AC020-76CH00016).

Team Leader: Dennis Lindle, E-mail: lindle@nevada.edu, Fax: 1 702 895 4072

Post-Collision-Interaction Effects in HCl Following Photofragmentation Near the Chlorine K-Edge

D. L. Hansen, G. B. Armen,[1] M. E. Arrasate, J. Cotter,[2] G. R. Fisher,[3] K. T. Leung,[4]
J. C. Levin,[1] R. Martin, P. Neill,[2] R. C. C. Perera,[3] I. A. Sellin,[1]
M. Simon,[5,6] Y. Uehara,[7] B. Vanderford, S. B. Whitfield,[8] and D. W. Lindle
Department of Chemistry, University of Nevada, Las Vegas, NV 89154-4003
[1] *Department of Physics, University of Tennessee, Knoxville, TN 37996*
[2] *Department of Physics, University of Nevada, Reno, NV 89557-0058*
[3] *Lawrence Berkeley National Laboratory, Berkeley, CA 94720*
[4] *Department of Chemistry, University of Waterloo, Canada, N2L 3G1*
[5] *LURE, Bâtiment 209D, Université Paris-Sud, 91405 Orsay Cedex, France*
[6] *CEA/DRECAM/SPAM, Bâtiment 522, CEN Saclay, 91191 Gif/Yvette Cedex, France*
[7] *Mitsubishi Electric Corporation, Amagasaki, Hyogo, 661 Japan*
[8] *Department of Physics and Astronomy, University of Wisconsin, Eau Claire, WI 54702*

Ion time-of-flight mass spectroscopy was used to study the relaxation dynamics of HCl following photoexcitation in the vicinity of the Cl K threshold (≈2.8 keV) using light from B.L. 9.3.1 at the ALS. We present the first detailed quantitative analysis describing PCI-moderated dissociation of molecules. We find that recapture effects observed in the ion yields of Cl^{n+} following photodissociation of HCl are related to K-shell-Auger emission, and that these effects in molecules can be described with a hydrogenic PCI model. In addition, we also find that the H^+ yield increases in the first few eV immediately above threshold, suggesting that this fragment sometimes captures the Cl 1s photoelectron, an effect which cannot be described using conventional atomic-PCI models.

In the region just above the K-shell threshold at 2829.8 eV, each Cl^{n+} PIY is affected by two PCI-induced electron-recapture effects; a decrease resulting from the loss of Cl^{n+} ions to the $Cl^{(n-1)+}$ charge state, and an increase arising from $Cl^{(n+1)+}$ ions recapturing electrons to become Cl^{n+}. For example, the yield of Cl^{4+} will be reduced by Cl^{4+} ions which recapture electrons and become Cl^{3+}, but will be augmented by Cl^{5+} ions which recapture and become Cl^{4+}. In order to isolate the recapture effect on each charge state, we first assume that because the Cl^{6+} yield is negligible, PCI trends in the Cl^{5+} PIY (Fig. 1(a)) reflect only the loss of Cl^{5+} ions through electron recapture. Thus, an estimate of the Cl^{5+} relative recapture cross section at energies just above threshold is obtained from the Cl^{5+} PIY by subtracting the near-threshold PIY values from the asymptotic Cl^{5+} yield. The asymptotic yield was taken as the average of the data points around 7 eV, above the energy regime where PCI effects are most prevalent, while below the energy where double-ionization effects begin. This recapture cross section for Cl^{5+} is then subtracted from the Cl^{4+} PIY to give an adjusted PIY curve with the contribution of Cl^{5+} recapture removed (Fig. 1(b) circles). The procedure is then repeated using each adjusted PIY curve, in turn, to isolate the recapture effect on each Cl^{n+} charge state.

In order to interpret the results in Fig. 1, we have attempted to reproduce the modified PIY curves using electron escape probabilities calculated with a hydrogenic model using a core-hole width of 0.6 eV. The hydrogenic model is based on the assumption that once a K-shell hole localized around the Cl atom is created, the intermediate states are localized far from the molecule (i.e. $\langle r \rangle \geq 50$ a.u.). Thus the structure of the core is unimportant, and the electron in the excited state sees an HCl^+ ion. The escape probabilities plotted in Fig. 1 were normalized to the PIY curves above threshold. Within the experimental uncertainties for Cl^{3+}, Cl^{4+}, and Cl^{5+} charge states, the data agree with the K-shell PCI curves indicating that PCI recapture occurs in conjunction with K-shell Auger decay, and that the process of PCI recapture for the Cl^{n+} ions in HCl is similar to that observed in ions formed following

relaxation of excited atomic species. The disagreement between the model and the data for the first two eV above threshold is at least partially explained by the excitation of the Cl K electron to Rydberg orbitals, and the photon and natural line widths.

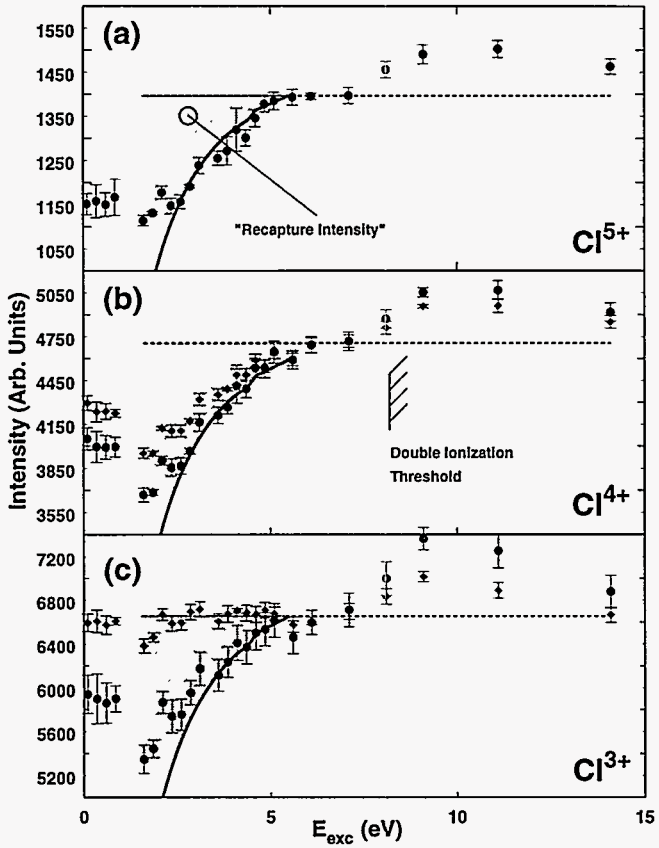

FIG. 1. (a) Partial ion yield (circles) for Cl^{5+}. (b) Partial ion yield (diamonds), and partial ion yield modified for PCI recapture (circles) for Cl^{4+}. (c) Partial ion yield (diamonds), and partial ion yield modified for PCI recapture (circles) for Cl^{3+}. The solid line represents the hydrogenic model for PCI following K-shell Auger electron ejection. No modifications were made to the Cl^{5+} yield because the Cl^{6+} yield was negligible. The dashed line represents the asymptotic limit for single electron ionization. The shaded region represents the loss in intensity as a result of PCI recapture.

Fig. 2 shows the PIY for H^+ (circles) following K-shell photoexcitation, and the TIY (diamonds) normalized to the H^+ PIY. The yield for H^+ increases with energy just above threshold similar to, but smaller than, those observed for the Cl^{n+} ($n \geq 3$) charge states. Comparison to the TIY for HCl indicates that this is not merely a result of a change in cross-section for K-shell excitation of the HCl molecule. Because of the atomic-like PCI behavior for the Cl^{n+} ions it seems that a likely explanation for the data is recapture of the photoelectron by H^+ following dissociation of the molecule, suggesting that the H^+ fragment also is involved in PCI, occasionally recapturing the Cl 1s photoelectron. This marks the first observation of PCI-mediated fragmentation, where the photoelectron is recaptured by an ion around which the initially excited orbital is not localized.

Comparison of the H^+ yield to the hydrogenic model, as well as to a semi-classical model for PCI shows a clear deviation of the data from PCI theory. This is hardly surprising because the empirical formula is based on the assumption that the electrons are receeding in a spherical Coulombic potential. This is not the situation at the time of Auger decay due to

perturbations in the potential well resulting from the close proximity of the H^+ ion, and the fact that recapture by H^+ is a molecular effect, and is not included in the current models; an entirely new physical effect is being observed.

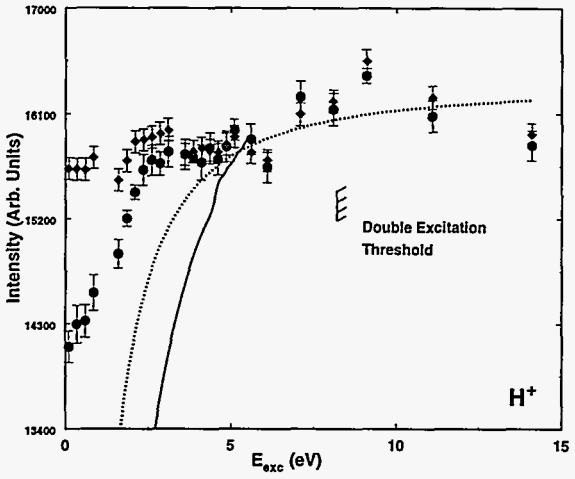

FIG. 2. Partial ion yield for hydrogen (circles), and total ion yield for HCl (diamonds). The TIY has been normalized to the H^+ PIY in order to facilitate comparison. The solid line represents the hydrogenic model for PCI following K-shell Auger electron ejection, the dotted line represents the semi-classical model.

The possibility that the photoelectron is recaptured while the hydrogen atom is still part of the molecule is worthy of mention. The H^+ PIY shows the greatest deviation from the TIY in the first 2.5 eV above resonance. We previously noted that the PIYs for the Cl^{n+} ions did not follow the PCI curves in this energy regime and attributed it to excitations to Rydberg orbitals, coupled with photon and natural line widths. In most cases, if the photoelectron is recaptured in a molecular orbital, the molecule will still dissociate, and because of its higher electronegativity, the Cl^{n+} ion would most likely retain the electron instead of the hydrogen. This process produces an identical result to the case where recapture by $Cl^{(n+1)+}$ follows fragmentation. An exception to this may arise if the electron is recaptured in an anti-bonding orbital, leading sometimes to neutral dissociation, as observed previously following resonant excitation to the $6\sigma^*$ orbital. In addition, in cases where the photoelectron is ejected in the direction of the H^+ ion, it is possible for recapture by H^+ to occur whether or not an Auger electron is emitted. Regardless of the explanation(s) for the PCI effect on the H^+ PIY, it is clear that a novel physical effect, unexplainable by conventional models of PCI, has been observed.

The authors thank the staff of the ALS for their excellent support. Support from NSF, Nevada DOE EPSCoR, Research Corporation, The Petroleum Research Fund, and the UNLV University Research Grants and Fellowships Committee is gratefully acknowledged. This work was performed at the National Synchrotron Light Source, which is supported by DOE (DE-AC020-76CH00016) and at the Advanced Light Source, also supported by DOE (DE-AC03-76SF00098).

Team Leader: Dennis Lindle, E-mail: lindle@nevada.edu, Fax: 1 702 895 4072

Thermal stability of cathodic-arc amorphous hard carbon films studied by NEXAFS, Raman spectroscopy, and nanoindentation

Simone Anders[1], Javier Díaz[1#], Joel W. Ager[2] III, Roger Yu Lo[3] and David B. Bogy[3]

[1]Advanced Light Source, Ernest Orlando Lawrence Berkeley National Laboratory, University of California, Berkeley, California 94720, USA

[2]Materials Science Division, Ernest Orlando Lawrence Berkeley National Laboratory, University of California, Berkeley, California 94720, USA

[3]Computer Mechanics Laboratory, Department of Mechanical Engineering, University of California, Berkeley, CA 94720

[#]Present address: Departamento de Fisica. Facultad de Ciencias, Universidad de Oviedo, Avda calvo Sotelo s/n Oviedo, 33007, Spain

INTRODUCTION

Amorphous hard carbon films have properties which are of great interest and importance for a number of tribological and protective applications. They are very hard, chemically inert, have a low coefficient of friction, and are very smooth. They consist of a random structure of sp^2 and sp^3 bonded carbon atoms. It has been that a carbon ion energy of about 100 eV is the optimum condition to produce films with the highest sp^3 fraction. The sp^3 fraction can reach up to 85% [1], the mass density up to 3.0 g/cm^3 [2], and the hardness up to 95 GPa [3]. If a magnetic macroparticle filter is used, the films are very smooth and free of macroparticles, the surface roughness can be as low as <0.1 nm rms and a few tens of a nanometer peak-to-valley [4].

Many properties of cathodic arc deposited films have been studied in great detail, but little is known about the thermal stability of these films. It was found that elevated temperature of the films during deposition leads to a more graphitic character of the films, whereas cooling of the substrate during deposition leads to films with a higher sp^3 content [3]. McKenzie et al. [2] investigated cathodic arc deposited films with and without nitrogen doping during annealing in vacuum for 1 hour up to 700°C. They observed very little change in the plasmon energy of about 29.5 for films during the heat treatment from which they concluded a stabile thermal behavior.

We found in earlier measurements that -100V substrate bias leads to the highest sp^3 fraction (85%) of the deposited films [1]. In a study of the thermal stability of cathodic arc deposited films in air using Raman spectroscopy and nanoindentation [5] we found that films deposited at no bias or at a bias of -500V or higher are stable up to 200°C. For higher temperatures the films graphitize as indicated by the Raman spectra, and above 400°C a considerable loss of film thickness occurs due to oxidation. Films deposited at -100V showed a constant Raman spectrum for temperatures up to 500°C, but they start to oxidize for temperatures above 450°C. Due to complete loss of the films at 550°C (the initial film thickness was 450 nm) we could not observe their thermal behavior at higher temperatures in air, whereas the present study with annealing in vacuum allows it.

EXPERIMENTAL

The samples were deposited on silicon substrates at -100V bias (for maximum sp^3 content) using a cathodic-arc plasma source combined with a 90 degrees bent magnetic macroparticle filter. The source and filter are described in detail elsewhere [6]. The film thickness was 70 nm. Samples were annealed in vacuum (base pressure $p=5\times10^{-8}$ Pa, up to 5×10^{-6} Pa during annealing) at temperatures from 300-850 °C; the annealing time was 15 minutes.

NEXAFS spectroscopy at the carbon K edge was performed at beamline 9.3.1. of the ALS. The energy resolution of this beamline at the carbon K edge is about 0.15 eV. The samples were mounted at an angle of 54.7° to the incident X-rays; this is the "magic angle" which eliminates the dependence of the p and s states on the polarization of the X-ray source [7]. Figure 1 shows the carbon K edge NEXAFS spectra in the total electron yield mode for the cathodic arc deposited carbon sample heated to different temperatures. For comparison there is also shown a spectrum of highly oriented pyrolytic graphite. The spectra of the deposited carbon are typical diamond-like spectra, with the π^* antibonding state resonance located at 284.9 eV and the broad σ^* shape resonance around 300 eV [8-10]. The spectra remain essentially unchanged up to a temperature of 700°C. For 800 and 850°C heating temperature the spectra change and the graphite exciton peak appears at 292 eV.

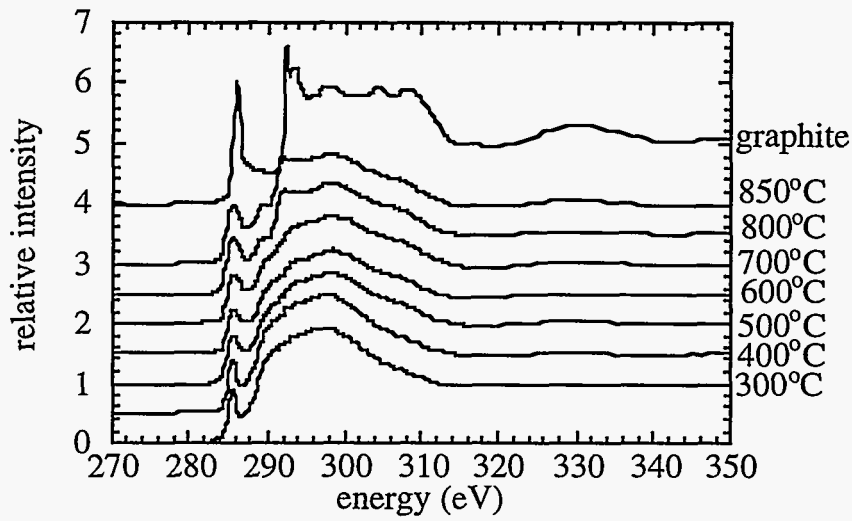

Fig. 1: NEXAFS carbon K egde spectra of cathodic arc deposited amorphous hard carbon film heated at different temperatures in UHV. A weak graphitic exciton peak appears at 292 eV at annealing temperatures of 800 and 850 °C.

Raman spectroscopy was performed on the same sample before and after heating to 850°C in vacuum. Raman spectra were obtained using 10 mW of 476 nm laser light. The spot size was ca. 20 microns and the integration time was 3 minutes. The Raman spectrum of cathodic-arc deposited films is a single, broad, asymmetric feature centered at ca. 1550 cm^{-1} (G-band). The peak center of this feature was determined by the zero-crossing of the differentiated spectrum. The precision of this procedure, as determined by repeat measurements on the same film, is ± 2 cm^{-1}. The Raman spectrum is only slightly changed after the heat treatment; a very small shoulder around 1350 cm^{-1} indicates the appearance of the graphitic D-band.

Nanoindentation was performed using a Hysitron nanoindenter. The hardness and elastic modulus of the cathodic arc film were determined before and after annealing to 850°C. It was found that the hardness as well as the elastic modulus are very high (about 90 GPa and 400 GPa, respectively) and are not changed by the heat treatment.

DISCUSSION

The NEXAFS results show a stable film structure up to 700°C and a modification (graphitization) of the film above 700°C whereas the Raman spectra are changed only very slightly, and

nanoindentation measurements show constant film properties up to 850°C. This discrepancy can be explained by the surface sensitivity of NEXAFS whereas Raman spectroscopy and nanoindentation integrate over the whole film thickness (70 nm). The sensitivity of NEXAFS is given by the electron escape depth which is typically about 5 nm [11] whereas the Raman spectrum collects the scattered light from a depth of about 200 nm given by the absorption coefficient of the film. Nanoindentation measures the hardness and elastic modulus as a function of the contact depth, and can further be influenced by the substrate.

CONCLUSIONS

The study has shown that amorphous hard carbon films formed by cathodic arc deposition using a pulsed substrate bias of - 100V are thermally very stable. Heating in vacuum up to 850°C modifies (graphitizes) only the surface layer whereas bulk properties such as hardness and elastic modulus remain stable. Up to 700°C heating in vacuum no change in the film properties was observed.

ACKNOWLEDGMENTS

The authors would like to thank Eddy Moler, Xin Zhou, and Zahid Hussain for their help in performing the NEXAFS measurements.

REFERENCES

[1] G. M. Pharr, D. L. Callahan, S. D. McAdams, T. Y. Tsui, S. Anders, A. Anders, J. W. Ager III, I. G. Brown, C. S. Bhatia, S. R. P. Silva, and J. Robertson, Appl. Phys. Lett. **68**, 779 (1996).

[2] D. P. McKenzie, Y. Yin, N. A. Marks, C. A. Davis, E. Kravchinskaia, B. A. Pailthorpe, and G. A. J. Amaratunga, J. Non-Cryst. Solids 164-166 (1993) 1101.

[3] R. Lossy, D. L. Pappas, R. A. Roy, J. J. Cuomo, and V. M. Sura, Appl. Phys. Lett. **61**, 171 (1992).

[4] M.C. Salvadori, G.Galvao, O.R. Monteiro and I.G. Brown, Thin Solid Films, to be published

[5] S. Anders, J. W. Ager III, G. M. Pharr, T. Y. Tsui, and I. G. Brown, Thin Solid Films, to be published

[6] A. Anders, S. Anders, and I. G. Brown, Plasma Sources Sci. Technol. **4**, 1 (1995).

[7] J Stöhr and R. Jaeger, Phys. Rev. B **26**, 4111 (1982).

[8] F. L. Coffman, R. Cao, P. A. Pianetta, S. Kapoor, M. Kelly, and L. J. Terminello, Appl. Phys. Lett. **69**, 568 (1996).

[9] M. Jaouen, G. Tourillon, J. Delafond, N. Junqua, and G. Hug, Diamond Relat. Mater. **4**, 200 (1995)

[10] A. Gutiérrez, J. Díaz, and M. F. Lopez, Appl. Phys. A **61**, 111 (1995)

[11] J. Stöhr, *NEXAFS Spectroscopy* (Springer, Berlin 1996), p. 123

This work was supported by the Director, Office of Energy Research, Office of Basic Energy Sciences, Materials Science Division, of the U.S. Department of Energy under Contract No. DE-AC03-76SF00098. It was also supported by the Computer Mechanics Laboratory in the Mechanical Engineering Department at U.C. Berkeley.

Principal investigator: Simone Anders, Advanced Light Source, Ernest Orlando Lawrence Berkeley National Laboratory. Email: SAnders@lbl.gov. Telephone: 510-486-5928.

Beamline 9.3.2 Abstracts

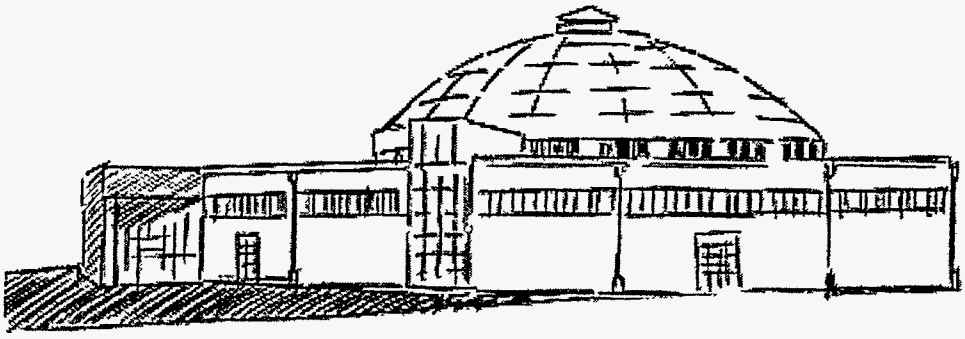

An Angle-Resolved Photoemission Extended Fine Structure Study of Clean Ni(111) Surface Structure

X. Zhou[1,2], E.J. Moler[1], Z. Hussain[1], Y.-F. Chen[3] and D.A. Shirley[1]
[1]Advanced Light Source, Ernest Orlando Lawrence Berkeley National Laboratory, University of California, Berkeley, California 94720, USA
[2]Department of Physics, Pennsylvania State University, University Park, Pennsylvania 16802, USA
[3]Materials Sciences Division, Ernest Orlando Lawrence Berkeley National Laboratory, University of California, Berkeley, California 94720, USA

INTRODUCTION

Angle-Resolved Photoemission Extended Fine Structure[1,2] (ARPEFS) has been successfully applied to various adsorbate systems since its inception twenty years ago. It generally yields very precise bond length and inter-layer distance information in the neighborhood of 0.02Å to 0.05Å. When applying Fourier Transform to ARPEFS data, strong peaks emerge at photoelectron Path Length Differences (PLD) which can be derived from geometrical settings of experimental apparatus. Most of these peaks can be understood in light of single backscattering and the cluster model.

However, when we measure photoemission from adatoms, which are usually sparsely placed on surface, the scattering between the emitter atoms themselves is weak, and there is no forward focusing/defocusing phenomenon involved. When we turn to a clean metal surface, like Ni(111), we have a unique opportunity to look at the photoelectron diffraction process inside the top layer itself, as well as the complication of many layers of emitter atoms in one experiment[3]. We report here the complete ARPEFS of Ni3p and Ni3s photoelectrons and their respective fittings through a new version of a multiple-scattering calculation program based on Rehr-Albers separable propagator.

EXPERIMENT

The experiment was performed in an Ultra-high vacuum chamber (base pressure of 4×10^{-11}torr), equipped with a PHI hemispherical electron energy analyzer and a liquid-Nitrogen-cooled 5-degrees-of-freedom sample manipulator, on beamline 9.3.2 at the Advanced Light Source of Lawrence Berkeley National Laboratory. The Ni(111) crystal was cleaned by the standard procedure of ion sputtering and annealing cycles. The surface order and cleanliness were periodically monitored with synchrotron XPS and LEED. The sample surface temperature was kept at 120K throughout the data collection. The photon polarization vector was oriented 30° from electron analyzer lens axis. Every ARPEFS curve is reduced from a series of photoemission spectra, with each spectrum looking at the constant initial state with particular photon energy to provide equal $0.05Å^{-1}$ steps in terms of photoelectron wavevector. The data reduction process is described in detail elsewhere[4].

RESULTS AND DISCUSSION

A comparison between experiment and calculation (Fig.1) reaffirms the validity of the cluster model in describing photoelectron diffraction process in a system much more complicated than the prototypical S/Ni(100) case. The R-factor of the fit in this case is as good as that of the benchmark S/Ni(100). The determined surface structure is a bulk-terminated surface with little or no relaxation.

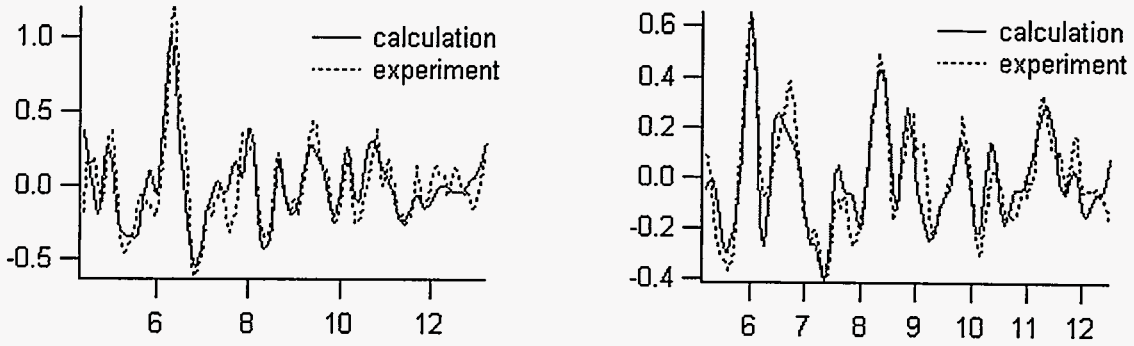

Figure 1. Normal emission ARPEFS. Left panel is Ni3s, right panel is Ni3p. The x-axis is the photoelectron wavevector in $Å^{-1}$.

More analysis is underway for off-normal emission data and the 6eV and 12eV satellites of the Ni3p core-level.

ACKNOWLEDGMENTS

We thank G.Andronaco, N.Hartman, M.Z. Hasan, S.A.Kellar, K.Kellogg, J.K.Lee, X.-J. Zhou, G.-R.Zhuang, for their help in the experiment.

REFERENCES

1. S.D. Kevan *et al*, Phys. Rev. Lett. **41**, 1565 (1978).
2. J.J. Barton *et al*, Phys. Rev. Lett. **51**, 272 (1983).
3. W.R.A. Huff *et al*, J. Elec. Spec. Rela. Phen. **80**, 41 (1996).
4. L.-Q. Wang *et al*, Phys. Rev. B **44**, 13711 (1991).

This work was supported by the Director, Office of Energy Research, Office of Basic Energy Sciences, Materials Science Division, of the U.S. Department of Energy under Contract No. DE-AC03-76SF00098.

Principal investigator: David A. Shirley, Advanced Light Source, Ernest Orlando Lawrence Berkeley National Laboratory. Email: dshirley@lbl.gov. Telephone: 510-486-5926.

An Angle-Resolved Photoemission Extended Fine Structure Study of Ni Valence Band and the 6-eV satellite

X. Zhou[1,2], E.J. Moler[1], Z. Hussain[1] and D.A. Shirley[1]
[1]Advanced Light Source, Ernest Orlando Lawrence Berkeley National Laboratory, University of California, Berkeley, California 94720, USA
[2]Department of Physics, Pennsylvania State University, University Park, Pennsylvania 16802, USA

INTRODUCTION

Angle-Resolved Photoemission Extended Fine Structure[1,2] (ARPEFS) has been successfully applied to various adsorbate systems to study their surface structures and obtain very precise geometrical parameters. Recently this experimental technique has also been applied to clean metals[3] and various satellite structures[4] in core-electron photoemission. When we carefully look at the behavior of the spectra in a wide photon energy range (100eV – 800eV), and the behavior of their Fourier Transforms, a lot can be learned about the origin of the satellites. A Ni(111) single crystal is studied in this experiment as Ni is a strongly correlated system with narrow bands and interesting satellite structures. The experimental setup[5] and the data reduction process are described in detail elsewhere.

RESULTS AND DISCUSSION

The most striking feature in the ARPEFS (Fig.1) is that the satellite photoemission intensity oscillates much more than the main peak intensity, which implies that the satellite is much more localized than the main peak. People have attributed the 6-eV satellite to a two-hole bound state, $3d^8 4s^2$ in atomic notation, and the valence band main peak to $3d^9 4s$, with strongest evidence so far coming from resonance photoemission experiments[6]. Our study supports this assignment in a totally new way. More analysis is underway for modeling the ARPEFS curves with multiple-scattering calculations based on Rehr-Albers separable propagator.

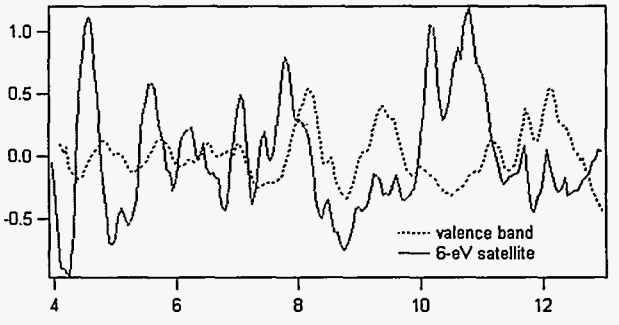

Figure 1. Ni(111) normal emission ARPEFS. The x-axis is the photoelectron wavevector in $Å^{-1}$.

REFERENCES

1. S.D. Kevan *et al*, Phys. Rev. Lett. **41**, 1565 (1978).
2. J.J. Barton *et al*, Phys. Rev. Lett. **51**, 272 (1983).
3. W.R.A. Huff *et al*, Phys. Rev. B **56**, 1540 (1997).
4. E.J. Moler *et al*, Phys. Rev. B **56**, 16016 (1997).
5. X. Zhou *et al*, ALS Compendium, 1998.
6. S. Hüfner, *Photoelectron Spectroscopy*, 2nd ed. (Springer, Berlin, 1994), p. 90.

This work was supported by the Director, Office of Energy Research, Office of Basic Energy Sciences, Materials Science Division, of the U.S. Department of Energy under Contract No. DE-AC03-76SF00098.

Principal investigator: David A. Shirley, Advanced Light Source, Ernest Orlando Lawrence Berkeley National Laboratory. Email: dshirley@lbl.gov. Telephone: 510-486-5926.

An Applied Materials Chamber for Surface Science and Materials Science Studies

X. Zhou[1,2] , S.A. Kellar[3], E.J. Moler[1], G.L. Gantner[1], G.-R. Zhuang[4], N. Hartman[1], G. Andronaco[1], N.L. Kellogg[1], Z. Hussain[1] and D.A. Shirley[1]

[1]Advanced Light Source, Lawrence Berkeley National Laboratory, Berkeley, CA 94720, USA
[2]Department of Physics, Pennsylvania State University, University Park, PA 16802, USA
[3]Department of Applied Physics, Stanford University, Stanford, CA 94305, USA
[4]Chemical Sciences Division, Lawrence Berkeley National Laboratory, Berkeley, CA 94720, USA

INTRODUCTION

On the bending magnet beamline 9.3.2 [1] at the ALS is installed an Ultrahigh Vacuum Applied Materials Chamber (AMC) designed for Angle-Resolved X-ray Photoemission Spectroscopy and X-ray Absorption Spectroscopy, coupled with the circularly polarized light capability of the beamline. Since its commissioning, many outside users [2,3,4] and Berkeley Lab scientists [5] have come to utilize this system's unique versatility to achieve their diverse scientific goals.

SYSTEM CAPABILITIES

The AMC (Fig. 1) is equipped with a Physical Electronics, Inc. (PHI) Spherical Capacitor Electron Energy Analyzer with an angle-resolving Omni V lens system, variable apertures, a high-speed 16-element multi-channel detector and a high-resolution power supply. The 5-degrees-of-freedom (X, Y, Z, continuous θ and continuous ϕ) sample movements are facilitated by a state-of-the-art manipulator, which is able to cool the sample surface to 110K by liquid Nitrogen and easily heat it up to well over 2000K by electron bombardment. The chamber also has a PHI dual-anode X-ray tube for off-line XPS work, a reverse-view linear-travel LEED system for sample characterization, a PHI ion gun for sample cleaning, an Omicron Evaporator and Quartz Crystal micro Balance (QCB) for sample preparation. For absorption type experiments, we have an angle-integrated electron Partial Yield Detector (PYD) and a shielded-wire sample current collector. Recently, we have installed a differentially pumped sample transfer stage that can move samples from atmosphere into UHV on a short notice. Users routinely reconfigure some ports on the chamber to suit their different needs, e.g. add cleavers or scrapers for studies of high-Tc samples.

FURTHER IMPROVEMENTS

The analyzer power supplies are currently under a major upgrading effort. We plan to use four 18-bit Digital/Analog Converters to build a high-stability, high-resolution, fast-response power supply for the analyzer retard, lens and pass energies. A combination of this next-generation power supply and a new fast 96-element multi-channel detector (under development) will help to improve the energy resolution of the analyzer up to about 20meV.

ACKNOWLEDGMENTS

Thanks to ALS technical staff for their excellent support, especially in leak-checking the chamber.

REFERENCES

1. Z. Hussain, W.R.A. Huff, S.A. Kellar, E.J. Moler, P.A. Heimann, W. McKinney, H.A. Padmore, C.S. Fadley, and D.A. Shirley, J. Elec. Spec. and Rel. Phen. 80, 401 (1996).
2. F. Gozzo, A. Cossy-Favre, B. Triplett, H. Fujimoto, and H.A. Padmore, ALS Compendium 1993-1996, 107, (1997).
3. T. Saitoh, P.M.Villella, D.S. Dessau, Y. Moritomo, Y. Tokura, X. Zhou, E.J. Moler, and Z. Hussain, ALS Compendium 1993-1996, 406 (1997).
4. M.A. Brewer, H.L. Ju, K.M. Krishnan, A.T. Young, V. Martynov, E.J. Moler, X. Zhou, S.A. Kellar, and Z. Hussain, ALS Compendium 1993-1996, 409 (1997).
5. X. Zhou, E.J. Moler, Y.-F. Chen, Z. Hussain, and D.A. Shirley, ALS Compendium 1997, this volume (1998).

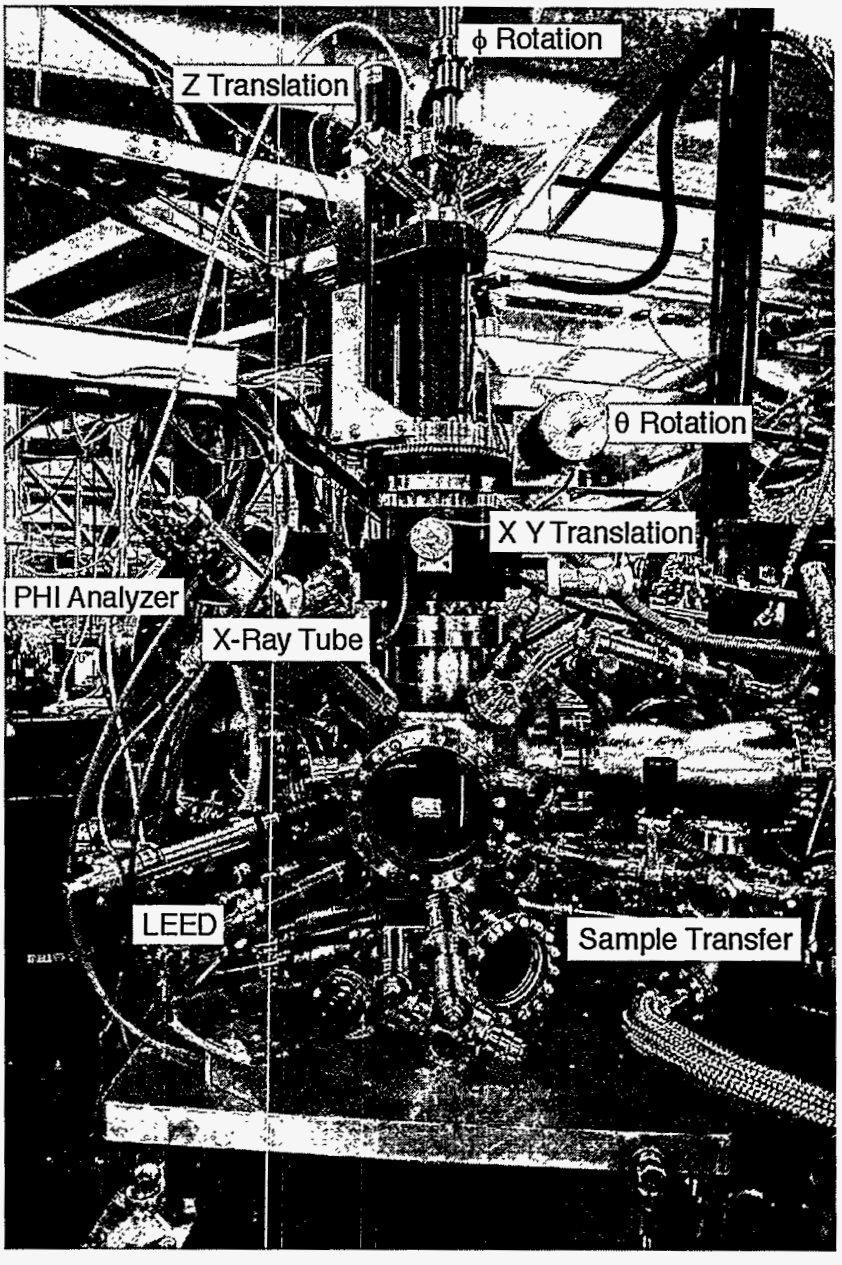

Figure 1. Photograph of the AMC.

This work was supported by the Director, Office of Energy Research, Office of Basic Energy Sciences, Materials Science Division, of the U.S. Department of Energy under Contract No. DE-AC03-76SF00098.

Principal investigator: Zahid Hussain, Scientific Support Group, Advanced Light Source, Ernest Orlando Lawrence Berkeley National Laboratory. Email: ZHussain@lbl.gov. Telephone: 510-486-7591.

This system is available for use to independent investigators with arrangement.

Modern Spectral Analysis of Angle-Resolved Photoemission Extended Fine Structure

X. Zhou[1,2], Z. Hussain[1] and D.A. Shirley[1]
[1]Advanced Light Source, Ernest Orlando Lawrence Berkeley National Laboratory, University of California, Berkeley, California 94720, USA
[2]Department of Physics, Pennsylvania State University, University Park, Pennsylvania 16802, USA

INTRODUCTION

Modern spectral analysis methods have been widely used in areas involving limited-length evenly-spaced data sequences in place of the traditional direct Fourier Transforms to enhance spectral resolution and signal detectability. We introduce some of these contemporary spectral analysis techniques into Angle-Resolved Photoemission Extended Fine Structure (ARPEFS), and show that they can be a powerful tool in understanding surface structures.

REVIEW OF IMPLEMENTED METHODS

Currently we have written computer programs for four different modern spectral analysis methods (Fig.1): AutoRegression-Linear Prediction (ARLP), AutoCorrelation-AutoRegression (ACAR), AutoCorrelation-Eigenvector analysis (ACE), and Maximum Entropy Minimum Variance (MEMV). Each method has its own idiosyncrasies that we have to be careful about when applying them to analyze real world data. In our experience, we found that autocorrelation is a very good first step to enhance signal, reduce noise and stabilize the final result[1,2].

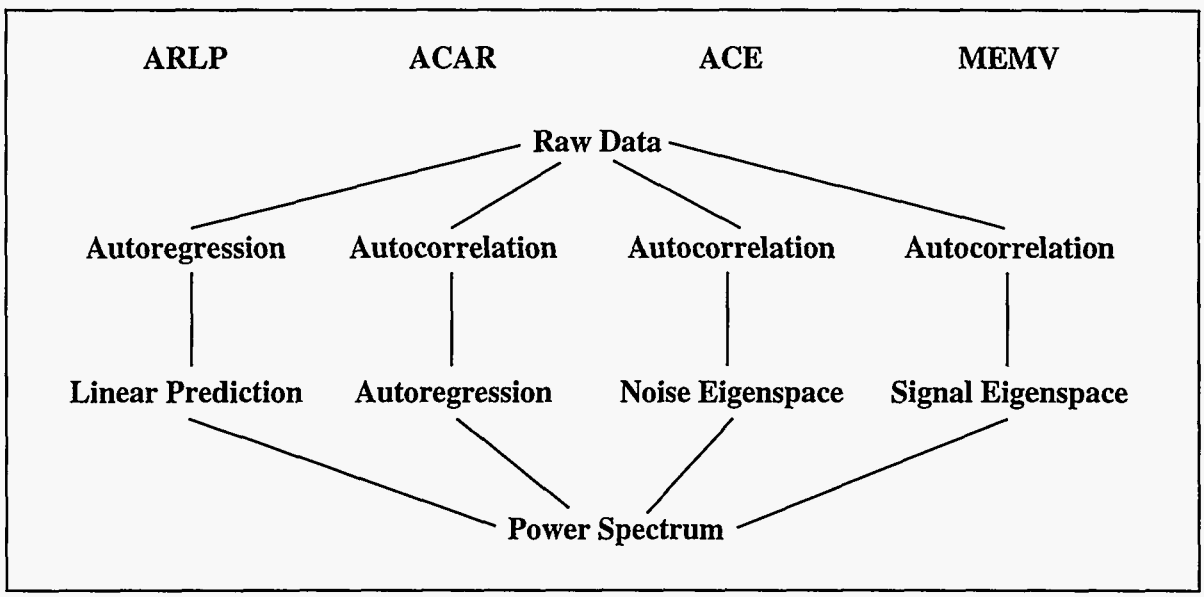

Figure 1. Flow chart comparing four modern spectral analysis methods.

APPLICATIONS

Since it was discovered that Fourier Transform of energy-scan photoelectron diffraction data yields meaningful peaks[3], people have tried to devise alternative ways to the taper-and-transform approach in the hope of finding better-looking spectra[4]. For example, in the case of ACE, we first construct an autocorrelation matrix from the raw data, then calculate the eigenvalues and their corresponding eigenvectors of this matrix. Assuming that the signals give much bigger

eigenvalues than the noises, we can single out the noise subspace that is perpendicular to the signal subspace. When we put the inner product of a harmonic with the noises in the denominator, we see a peak if the harmonic had the same frequency as one of the signals. Let's compare the performances between direct FT and ACE in the prototypical case of S/Ni(100). The picture (Fig.2) declares a clear winner.

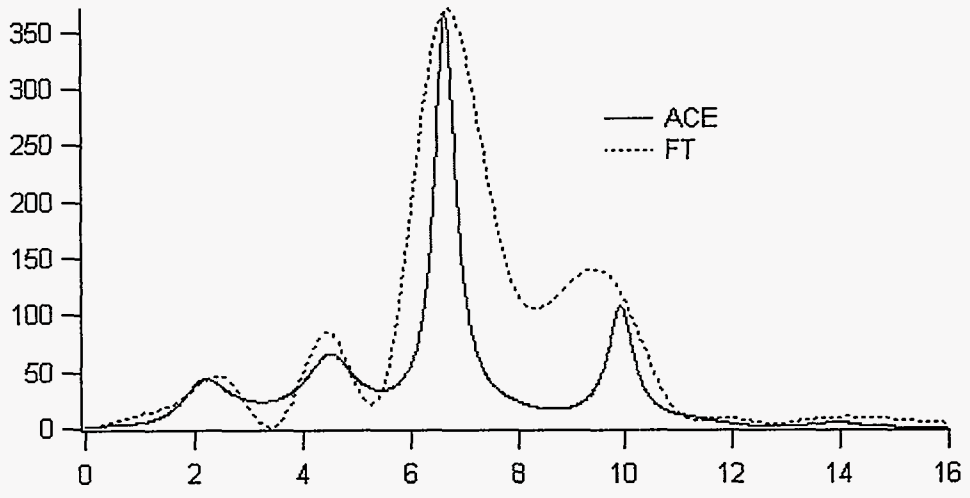

Figure 2. Power spectral density functions of normal emission S1s ARPEFS from a S/Ni(100) sample. The FT curve is obtained through a Hanning window to eliminate side-lobes and has been scaled to the same maximum height as the ACE curve. The x-axis is Path Length Difference (PLD) in Å.

ACKNOWLEDGMENTS

Thanks to W.R.A. Huff, S.A. Kellar, E.J. Moler, Y. Zheng for their helps in using the original ARLP program on a VAXstation 3100 machine.

REFERENCES

1. E. Matthias and D.A. Shirley, Nucl. Instr. **45**, 309(1966).
2. S. Koicki, T.A. Koster, R. Pollak, D. Quitmann, and D.A. Shirley, Phys. Lett. **32**B, 351(1970).
3. Z. Hussain, D.A. Shirley, C.H. Li, and S.Y. Tong, Proc. Natl. Acad. Sci. USA **78,** 5293 (1981).
4. J. Barton and D.A. Shirley, Lawrence Berkeley National Laboratory Report No. LBL-14758 (1985).

This work was supported by the Director, Office of Energy Research, Office of Basic Energy Sciences, Materials Science Division, of the U.S. Department of Energy under Contract No. DE-AC03-76SF00098.

Principal investigator: David A. Shirley, Advanced Light Source, Ernest Orlando Lawrence Berkeley National Laboratory. Email: dshirley@lbl.gov. Telephone: 510-486-5926.

Photoelectron Diffraction of Free CO Molecules

O. Geßner[1], F. Heiser[1], E. J. Moler[2], Z. Hussain[2], D. A. Shirley[2], and U.Becker[1]
[1]Fritz-Haber-Institut der Max-Planck-Gesellschaft, 14195 Berlin, GERMANY
[2]Advanced Light Source, Ernest Orlando Lawrence Berkeley National Laboratory,
University of California, Berkeley, California 94720, USA

INTRODUCTION

Core-level photoelectron diffraction techniques have been applied to surface structure studies on an atomic scale for more than 20 years [1]. The basic physical process responsible for the production of a photoelectron diffraction pattern is the elastic scattering of the emitted photoelectron wave. In core level photoemission, a photon illuminates an atom surrounded by other atoms and an electron from an atomic core level is ejected and detected at a distance from the emitter atom. The emitted electron wave may either be detected directly or scattered by neighbouring atoms before detection occures. The interference (diffraction) between the different pathways depends sensitively on the relative atomic positions and the wavelength of the outgoing photoelectron wave. Thus the yield of this process, when measured as a function of photon energy and/or emission angles, contains information about the atomic structure in the vicinity of the emitter.

In the gas phase these effects are only visible if measurements on spatially oriented molecules are performed otherwise the intensity modulations in the electron yield are strongly reduced. So far as we are aware no experiment on this subject has been performed due to difficulties in preparing or determining the spatial orientation of the molecule. In this report we describe an attempt to adapt an experimental setup, already successful in the measurement of the photoelectron angular distribution of spatially oriented molecules [2,3], to photoelectron diffraction studies. The experiment was performed at the beamline 9.3.2 at the Advanced Light Source.

EXPERIMENT

The key element of this experiment is a time-of-flight ion spectrometer with a position sensitive anode optimized for short dead-time [4]. This ion-detector makes it possible to trace the momentum direction of ionic molecular fragments and thus the molecular orientation at the moment of photoionization assuming that the dissociation time is small compared to the timescale of molecular rotation, a condition also known as axial recoil condition. Figure 1 shows a scheme of the experimental setup used for this angular correlation experiment between ionic fragments and photoelectrons.

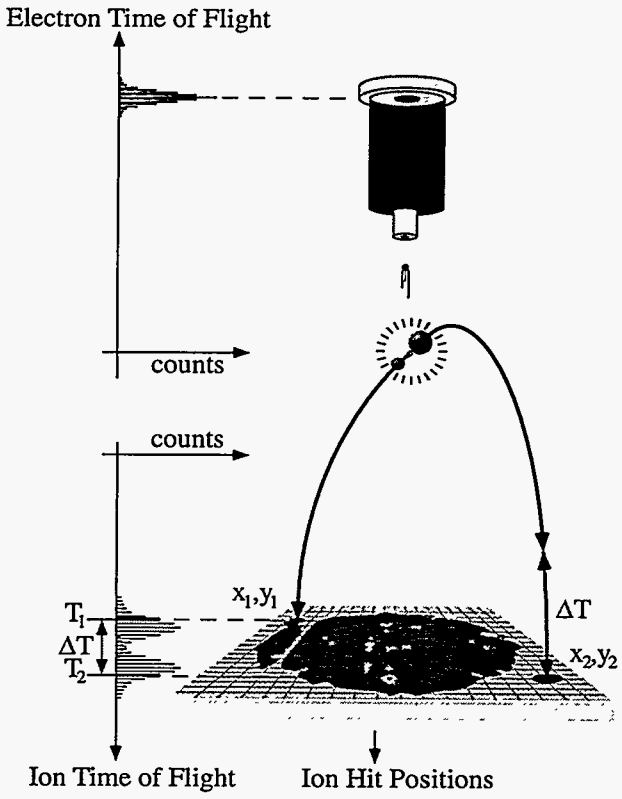

Figure 1. Schematic illustrating the experimental setup with an electron time-of-flight spectrometer (upper part) and an ion time-of-flight spectrometer with a position sensitive anode (lower part).

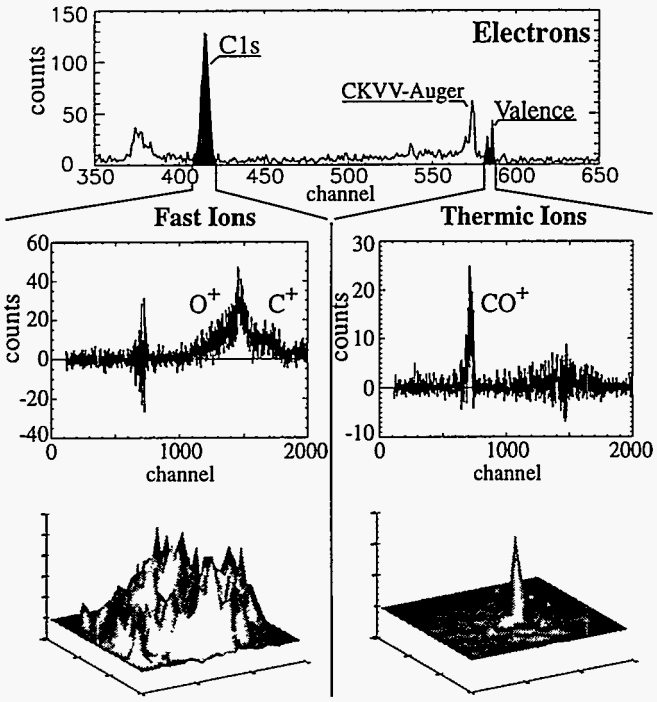

Figure 2. Coincident electron time-of-flight spectrum (upper diagram), ion time-of-flight spectra (middle diagrams) and ion anode hit position distributions (lower diagrams).

The detection of an electron serves as the trigger for an extraction pulse for the ions. Electron time-of-flight, ion time-of-flight, and the ion impact positions on the anode were recorded in coincidence. The resulting experimental coincidence spectra were corrected afterwards for both, uncorrelated and random coincidences by subtraction of normalized spectra obtained by applying pulses from a pulse generator instead of electron signals as a trigger for the ion extraction pulse.

Figure 2 shows some electron and ion time-of-flight spectra of CO at a photon energy of 340.5 eV and the corresponding distributions of hit positions on the ion anode. The upper spectrum is a coincident electron spectrum, while in the middle diagrams ion spectra are shown which correspond to selected kinetic energy ranges of the coincident electrons. The right spectrum shows all ions in coincidence with valence electrons. These processes lead mainly to stable nonfragmenting CO^+ ions characterized by a sharp peak in the corresponding pattern on the anode. This is clearly visible in a three-dimensional plot of the anode positions below the ion spectrum. Ionic fragmentation following K-shell ionization, into C^+ and O^+ ions in coincidence with the detection of a C(1s) photoelectron (left ion spectrum) yields a two dimensional intensity pattern on the anode (left bottom) which reflects the angular distribution of the fragments. All ion spectra are corrected for uncorrelated and random coincidences.

RESULTS

The ejection angles of the fragment ions were calculated offline using the time-of-flight and the anode hit position information of each electron-ion coincidence event in the experiment. Figure 3 shows the preliminary results of the experiment done in August 1997 during two weeks of double bunch mode of the storage ring. This diagram shows the yield of C(1s) electrons from spatially oriented CO molecules with molecular axes lying within a cone of ±25° around the electric vector of light. The electrons were detected along the electric vector of light within

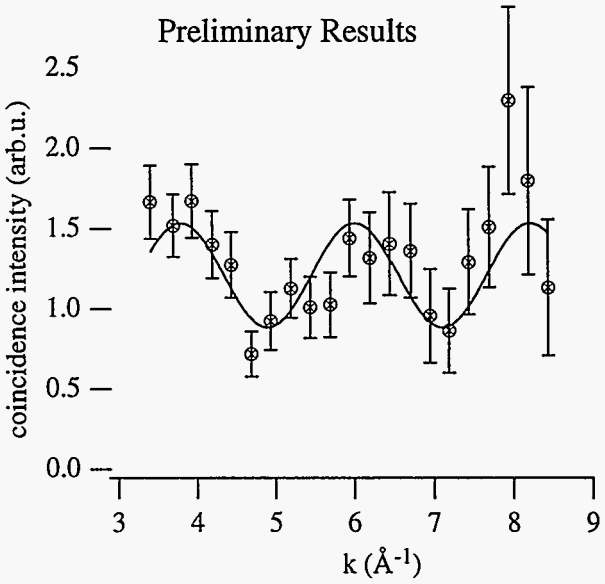

Figure 3. The variation of the C(1s) electron yield detected along the electric vector of light. The emitting CO molecules are orientated in a ±25° cone around the electric vector of light, with the C atom pointing in the direction of the electron detector. The solid line is a simple sin function to guide the eye.

an cone of ±2.6°. The C^+ ion was pointing towards the electron detector. Figure 3 clearly shows the variation of intensity along the k-value of the outgoing photoelectron resulting from the interference between the direct and scattered photoelectron waves.

In summary, we have shown for the first time quantum interference effects following K-shell photoionization of free CO molecules using a time-of-flight electron spectrometer and a position resolving ion time-of-flight spectrometer. Further analysis of the observed intensity variations is needed in order to reveal the geometrical information which is inherently contained in these data. In future experiments, diffraction patterns of larger molecules may be investigated with respect to electron density distributions which are so far not accessible.

REFERENCES

1. S.D. Kevan, D.H. Rosenblatt, D. Denley, B.-C. Lu, and D.A. Shirley, Phys. Rev Lett. **41**, 1565 (1978).
2. F. Heiser, O. Geßner, U. Hergenhahn, J. Viefhaus, K. Wieliczek, N. Saito, and U. Becker, J. Electron Spectrosc. Relat. Phenom. **79**, 415 (1996).
3. F. Heiser, O. Geßner, J. Viefhaus, K. Wieliczek, R. Hentges, and U. Becker, Phys. Rev. Lett. **79**, 2435 (1997).
4. N. Saito, F. Heiser, O. Hemmers, K. Wieliczek, J. Viefhaus, and U. Becker, Phys. Rev. A **54**, 2004 (1996).

This work has been supported by the Deutsche Forschungsgemeinschaft under contract no. BE 860/14-2.

Principal investigator:
E. J. Moler
Advanced Light Source
Ernest Orlando Lawrence Berkeley National Laboratory
University of California
Berkeley, CA
94720
USA
E-mail: ejmoler@lbl.gov
Phone: +1-510-486-7637

Progress in Soft-X-Ray Fourier Transform Spectrometry

S. C. Locklin, E. J. Moler, J. Spring, Z. Hussain, M. R. Howells*

March 31, 1998

***Advanced Light Source, LBNL, 1 Cyclotron Rd., Berkeley, CA 94720**

Introduction

The Soft X-Ray Fourier Transform Spectrometer (FTSX) on bend magnet beamline 9.3.2 is a modified Mach-Zender interferometer spectrometer designed for ultra-high resolution spectrometry in the 10-20nm (120-60eV) range. The theoretical resolving power ($\frac{E}{\Delta E}$) of this instrument, as with all spectrometers, is proportional to the number of waves of incident light in the maximum path length difference introduced by the instrument to the beam. The FTSX has a design travel of 1 centimeter, giving a theoretical resolving power of the order of a million. The instrument is designed for high resolution exploration of the autoionizing states of helium.

Instrument Design

The mechanical layout of the modified Mach-Zender interferometer system is outlined in figure 1 below. It consists of a sixteen point cartwheel flexure rectilinear motion stage which was EDM machined from a single block of Vascomax 300 maraging steel. The rectilinear motion is achieved by external hydraulic ram, and the position is monitored by means of a commercial HP laser interferometer. Beam splitters are mounted to the stationary part of the stage. The four mirrors are optically contacted to a rhombus prism which is attached to the moving stage.[1]

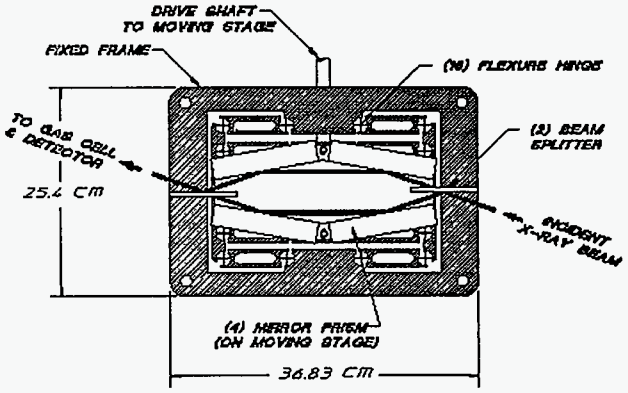

Figure 1 FTSX Schematic

Accomplishments to Date

The construction and assembly of the FTSX has required the design and manufacture of a number of components to new levels of precision. The translation stage itself was a considerable engineering feat. The total allowed pitch error over the full motion of the flexure hinge stage was calculated to be on the order of 0.5 μrad.[2] The stage, as delivered, was substantially out of specification; extra slots had to be machined, and taper pins added and adjusted to correct the tilt errors. After corrections, the stage tilt errors were measured to be 0.38 μrad over the full travel of the mirrors[3].

The beamsplitters are the first of their kind. They were manufactured by RocketDyne from a single crystal of silicon. A set of 50 μm wide, 15mm long slots were photolithographically etched into the surface with a 100 μmperiod, then coated with molybdenum to make a

wavefront dividing, soft X-ray beamsplitter. The surface roughness of these beamsplitters was measured with the ALS Optical Metrology Lab (OML) Wyco Micromap phase-shifting interferometer, and found to have an RMS roughness of less than 5 angstroms. The surface figure of the beamsplitters as measured by the OML Long Trace Profiler was found to be flat to below 0.5 μrad. The four mirrors, manufactured by Photon Sciences and coated with molybdenum, are also of exceptional quality; showing a flat surface figure to within 0.6 μrad and a surface roughness of only 2 angstroms RMS. The alignment tolerance was ascertained to be 1.5 microradians of error between the relative tilts of the wavefront[2], hence a total of 1.5 microradians of error in the alignment of all of the optical surfaces. The mirrors were aligned to each other by optical contacting to a prism base. This was measured by Photon Sciences using Hadinger fringes to be aligned to less than 0.6μrad of error, leaving a beamsplitter to mirror alignment tolerance of about a microradian[1].

Previous Results

In the original conception of the workings of the instrument the beamsplitters themselves were held in place and aligned via a system of 6-32 screws held in place by set screws pressing against 0.5 to 1.5 ft.-lb. spring loaded pins; gross adjustments were to be performed outside of the vacuum chamber by using the LBNL Coordinate Measuring Machine (CMM) facilities.. Two leaf spring flexures with picomotor adjustments were added for *in-situ* fine adjustment of downstream beamsplitter "roll" and "yaw" when aligning at the XUV. It was hoped that this mounting would be sufficiently stable to hold at least a rough alignment. Unfortunately, the laboratory CMM machine was located on the opposite side of the campus, so the instrument was subjected to various unpredictable forces on its trip back from CMM alignment to its ALS vacuum chamber on beamline 9.3.2.

More problematic, if more predictable; there were problems with screw backlash, walking of the screws upon application of their set screws, and the overall crudeness of adjustment using this rough grade screw, which made any adjustments of these settings largely irreproducible. The operator made the adjustment by counting Hadinger fringes as the screws were nudged in one or another direction, and noting their relative quality. Worse, the set screws were not sufficient to hold the alignment screws in place. This was not clear until the instrument was aligned well enough to obtain an interferogram of visible partially coherent neon light (see figure 1 below). The alignment which produced this interferogram was lost as the instrument sat static overnight.

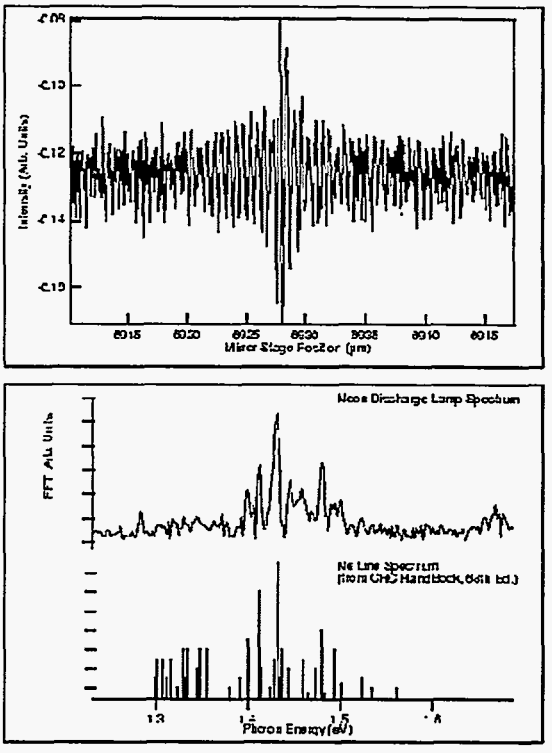

Figure 2 Interferogram from neon discharge lamp and associated spectra

Modifications to Beamsplitter Mounts

The beamsplitter mounts were modified to use New Focus picomotors with 1/4-80 threaded screws. According to the sales literature[4] these are able to move a step as small as 40 nanometers via a 2 mrad rotation, and also grasp

the screw itself when the piezo actuator is in the relaxed position. Unfortunately, these devices do not function like stepper motors; i.e. sending a pulse to a picomotor does not move the motor by a reproducible step; it may not move at all on a given pulse!

As such, some kind of position monitor was needed to close the loop of the beamsplitter position adjustment subsystem. We chose to use Linear Variable Differential Transformers (LVDT) from Macrosensors as our position monitor. The use of LVDT in combination with picomotors had already been pioneered by Paul Denham et. al. on CXRO metrology beamline 12. These devices had a number of advantages over rotary encoders; among them, low cost, a relatively simple wiring scheme, small size (as small as 0.75" long by 3/8" diameter), excellent stability, good vacuum qualities and good, direct linear position resolution. Some simple aluminum mounts were fabricated, set pins were attached to the LVDT cores, the beamsplitter mount was fitted for the LVDT mountings, and the same spring loaded pins were used to keep the set pin/LVDT core pressed against the beamsplitter at final assembly. A modified version of the CXRO controller box, which was essentially a shielded box and power supply for several Analog Devices AD698 LVDT Signal Conditioner IC chips, was used. This chip generates a waveform which can be selected for amplitude, frequency and scaling factors to match the individual LVDT, then converts the return signal into a DC voltage. In its present form, the LVDT controller box output is read by a simple 12 bit A/D converter in the VME Crate which gives an overall resolution of about 2.5mV. The LVDT controller box output seems to be about a factor of 10 more sensitive, so more resolution is available should we decide to use this controller with a GPIB voltmeter rather than the simple ADC.

In tests with micrometers, the LVDTs were found to have a sensitivity of about 300nm per millivolt. When calibrating the LVDT output to the actual angular change using the OML Autocollimator, the rough adjustments of the beamsplitter mounts were found to have a resolution of about 14 μrad on the yaw axis, and $40\mu rad$ on the roll axis. The downstream beamsplitter leaf-spring flexure reduction axes have a resolution of about 0.21 μrad on the yaw axis and 0.27 μrad on the roll axis. These resolutions should be sufficient to align the beamsplitters to their $1\mu rad$ tolerance. As implied before, these resolutions can be improved upon using a more sensitive voltage measuring device such as a GPIB voltmeter, and taking some steps to reduce the system noise.

Should it be deemed useful at some point to return to the old CMM alignment methodology, the LVDTs will certainly prove useful in not only retaining the best possible CMM alignment, but also forming something of a non-indexing CMM, once the LVDTs are locked down and calibrated with respect to the position measurements of the CMM itself.

Modifications to Software

The computer control for this instrument consists of several levels of hardware. At the heart of the system is the VME crate and the Motorola 68040 CPU MVME167 controller card running the VxWorks realtime operating system. This card controls various other cards on the VME Bus, including several I/O cards, the H.P. laser position monitor controller card and a dual DSP subsystem for realtime signal processing. A Sun IPX workstation running SunOS release 4.1.4 was used as a development platform for the VxWorks code, as well as providing a Labview user interface.

In the prior software configuration, a TCP socket interface was used to communicate between the Labview and VxWorks code across a standard ethernet connection. This code had a number of bugs which occasionally caused the system to hang during datataking. The nature of this socket level code also made it difficult to develop new data or control channels as the controller code and the instrument itself increased in complexity. With the recent addition of computer control for the hydraulics, the picomotors and the LVDT sensors, it was decided to use the higher level Sun "Remote Procedure Call" (RPC)[5] in order to facilitate quicker network software development cycles, as well as providing a cleaner "client/server" software model for multithreading of the main VxWorks control program. The data streaming from VxWorks to Labview is also presently being changed from a streaming "ring buffered" model to an interrupt driven, block buffered model to increase reliability, data transfer speed

and overall VxWorks code efficiency. Rather than relying on the speed and reliability of the Labview software in accepting the data on the IPX end, the new code also uses operating system level, hence faster and more reliable, SunOS RPC Network File Server (NFS) calls to write the interferogram data to the IPX workstation.

Conclusions and Expectations of Performance

At present, there are no mechanical restraints or software problems which will prevent the successful alignment of the interferometer. All mechanical specifications of the individual components have been met. Several proven methodologies for *in-situ* and out of chamber CMM alignment of the beamsplitters with respect to the mirror planes exist. The addition of picomotor actuators as well as LVDT position measuring sensors for the beamsplitters will provide a reliable mechanism for finding and keeping beamsplitter alignment with respect to the mirror plane, even while the spectrometer is under vacuum. This was the last major remaining engineering hurdle to the commissioning of the FTSX on ALS beamline 9.3.2.

Acknowledgements

The authors would like to thank Steve Irick for use of OML equipment, Paul Denham for LVDT technical assistance and the CXRO for use of the LVDT controller hardware.

References

1) E. J. Moler, Ph. D. Thesis dissertation *"Design and Characterization of High Resolution Fourier Transform Soft X-Ray spectrometer for Synchrotron Radiation"* (Lawrence Berkeley Laboratory, University of California, Berkeley 1995; LBNL-38901; UC-401)

2) M. R. Howells *"Manufacturing Tolerances for the ALS Soft X-Ray Interferometer,"* Lawrence Berkeley Laboratory, LSBL-186

3) R. Duarte, M. R. Howells, Z. Hussain, T. Lauritzen, R. McGill, E. Moler, J. Spring *"A Linear Motion Machine for Soft X-Ray Interferometry"* Lawrence Berkeley Laboratory LSBL-400, Proceedings of the SPIE 1997 Conference, San Diego, CA (Note that there are several values in their error budget table of this article which disagree with reference 1; ref. 1 should be considered the authoritative source).

4) New Focus Picomotor manual and data sheet (document number 880113 Rev C)

5) J. Bloomer, *"Power Programming with RPC"* O' Reilly & Associates (1992)

Principal Investigator: David A. Shirley

Corresponding Author: Scott Locklin MS2-400,

1 Cyclotron Road, Berkeley CA 94720 (+1 510 486 4647)

<locklin@gabor.lbl.gov>

This work was funded by the U.S. Department of Energy under Contract No. DE-AC03-76SF00098.

The Surface Structure of α-Fe_2O_3(0001) by Low Energy X-Ray Photoelectron Diffraction

S. Thevuthasan, Y.J. Kim, and S.A. Chambers
Environmental Molecular Sciences Laboratory, Pacific Northwest National Laboratory, Richland, WA 99352

P. Liu, T. Kendelewicz, G.E. Brown, Jr.
Department of Environmental and Geological Sciences, Stanford University, Stanford, CA 94305

J. Morais[1], R. Denecke[2], and C.S. Fadley[3]
Lawrence Berkeley National Laboratory. Berkeley, CA 94720

INTRODUCTION

The structure and composition of oxide surfaces strongly influence their chemical properties. As such, there is a growing interest in determining the surface termination, reconstruction and relaxation of these surfaces. There is a growing interest in iron oxide surfaces because of their importance in surface geochemistry, heterogeneous catalysis, magnetic recording and integrated microwave devices [1-4]. In a recent study [5] of the selective epitaxial growth of magnetite (Fe_3O_4) and hematite (α-Fe_2O_3), it was shown that the surface of (001) magnetite exhibits a ($\sqrt{2}$x $\sqrt{2}$)R45° reconstruction. The relaxation or contraction of first few layers hasn't been addressed in ref. 5 or any other studies in the literature. Recent theoretical work by Wasserman et. al [6] have shown that (0001) hematite has a single Fe layer termination with relaxations in the first four layers of -48%, -2%, -35%, and 21%, respectively. We recently performed low-energy x-ray photoelectron diffraction measurements at Advanced Light Source on a clean, epitaxially grown hematite(0001) surface. Low-energy photoelectron diffraction data, which are briefly described below, were used to determine the relaxation of the first four layers.

EXPERIMENT

Low-energy photoelectron diffraction experiments were carried out on beam line 9.3.2 at the ALS. The end station at this beam line is equipped with a Scienta SES 200 hemispherical analyzer for collection of photoelectron spectra, along with a five-axis sample manipulator and in situ sample cleaning capabilities. An epitaxially grown α-Fe_2O_3 film grown on a Al_2O_3(0001) substrate at PNNL was cleaned and ordered by annealing in oxygen at a pressure of $1x10^{-6}$ torr and a temperature of 900 K. A photon energy of 400 eV was used to collect several Fe 3p azimuthal scans at different take off angles. The Fe 3p kinetic energy was 344 eV. Although sample charging was neutralized by electrons from a hot filament which was housed close to the sample, it was impossible to get reliable low kinetic energy data for photon energies below 350 eV. The sample was cleaned and ordered at the start of each azimuthal scan and the cleanliness of the surface was checked before and after every scan. Approximately ≤ 0.15 monolayer of hydroxyl, adsorbed during the tranfer from PNNL to ALS, was always seen on the surface and the clean 1x1 LEED pattern indicates that there is no specific ordering of hydroxyl on the surface. Theoretical simulations were carried out using spherical wave single scattering cluster theory for select trial geometries [7] with the partial wave phase shifts being computed using the program FEFF [8]. The cluster size was about 950 atoms for the single scattering calculations.

RESULTS

Our ALS experimental results are summarized in Figs. 1 and 2. Fig. 1 shows the experimental and

theoretical azimuthal scans for take off angles of θ = 10°, 15° and 20°. The experimental and theoretical azimuthal scans for take off angles of θ = 26° and 32° are presented in Fig. 2. The theoretical scans are the photoelectron diffraction intensities simulated from an optimized single Fe

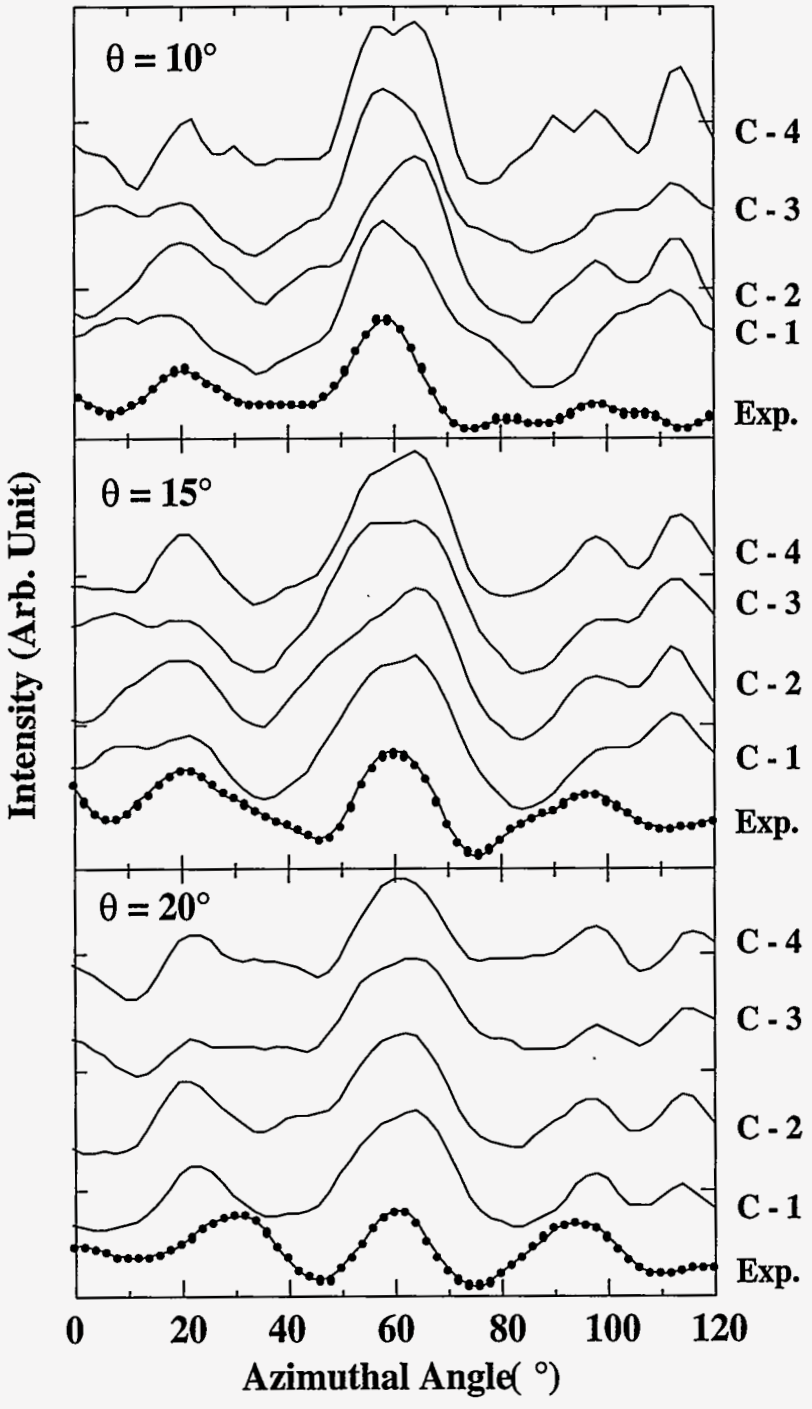

Fig. 1: Experimental and theoretical photoelectron diffraction intensities as a function of azimuthal angle for the take off angles, θ = 10°, 15°, and 20°; C-1 = optimized Fe-terminated cluster, C-2 = optimized O-terminated cluster, C-3 = cluster derived from the relaxations proposed by Wasserman et al.[6], and C-4 = C-3 with one monolayer of OH [6].

layer terminated surface (C-1), an optimized O layer terminated cluster (C-2), a relaxed single Fe layer terminated cluster(C-3), proposed by Wasserman et al. [6] and a relaxed single Fe terminated cluster with one monolayer of hydroxyl attached a top all the cation sites (C-4), proposed by Wasserman et al. [6]. Layer spacings were systematically varied between ±0.600 Å with 0.10 Å steps for these calculations and a detailed R-factor analysis was carried out. From the low take off angles data, especially for $\theta = 10°$, and 15° which are more surface sensitive, the misfit between the experimental intensities and the intensities calculated from the optimized O-terminated cluster (C-2) and Fe terminated cluster with one monolayer of hydroxyl (C-4) could be clearly seen. The main peak around the azimuthal angle range of 58°-60° appeared to be shifted by about 6-8° for C-2 and about 3-4° for C-4 respectively for the take off angles of 10° and 15°. These results confirm that the hematite surface is terminated by a single Fe layer. The R-factors for the five angles are summed and the average R-factor, R_1 (the other four R-Factors, R_2-R_5 vary as R_1) for optimized C-1 and C-2, proposed clusters C-3, and C-4 along with the layer spacings are given in Table I. The results from the R-Factor analysis also suggest that the surface is Fe-terminated. The differences of R-factors between the clusters are small since the kinetic energy of 344 eV is not completely surface sensitive. However, since the anisotropies of these scans vary between 30-40%, the change in R-Factors reflect the change in the geometry of the cluster.

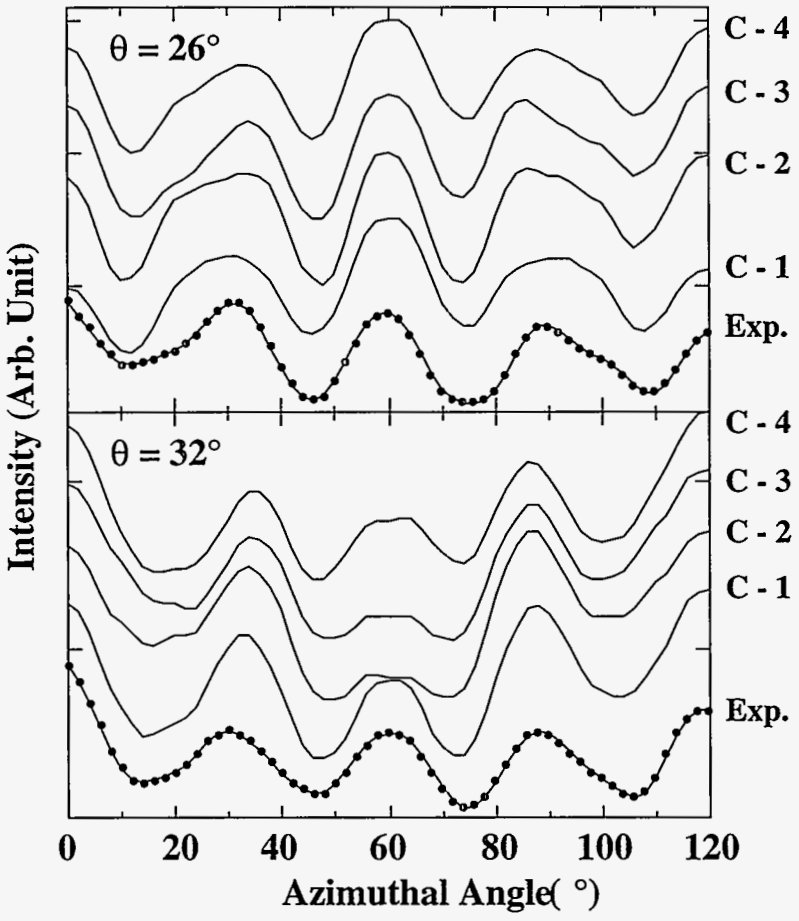

Fig. 2: Experimental and theoretical photoelectron diffraction intensities as a function of azimuthal angle for the take off angles, $\theta = 26°$, and 32°; C-1 = optimized Fe-terminated cluster, C-2 = optimized O-terminated cluster, C-3 = cluster derived from the relaxations proposed by Wasserman et al.[6], and C-4 = C-3 with one monolayer of OH [6].

TABLE I: The optimized layer spacings, and the average R_1 for four different clusters

Cluster	Layer 1 Fe-B=0.845Å O-B=0.845 Å	Layer 2 Fe-B=0.845Å O-B=0.605 Å	Layer 3 Fe-B=0.605Å O-B=0.845 Å	Layer 4 Fe-B=0.845Å O-B=0.845 Å	Average R_1
C-1 Fe-terminated	0.500 Å -41%	0.995 Å 18%	0.555 Å 8%	1.245 Å 47%	0.07625
C-2 O-terminated	1.195 Å 41%	0.605 Å 0%	0.745 Å -12%	0.795 Å -6%	0.07853
C-3 Fe-terminated Ref. 7	0.436 Å -48%	0.825 Å -2%	0.394 Å -35%	1.021 Å 21%	0.08519
C-4 Fe-term./OH Ref. 7	0.819 Å -3%	0.853 Å 1%	0.425 Å -30%	0.980 Å 16%	0.07738

CONCLUSIONS

In conclusion, we have used photoelectron diffraction to determine the surface structure of hematite (0001) surface. The surface appears to be Fe-terminated and the first four layer spacings are -41%, +18%, -8%, and 47% of the associated bulk values, respectively.

ACKNOWLEDGEMENTS

The authors gratefully acknowledge partial support from US Department of Energy Environmental Management Science Program and the Office of Basic Energy Sciences, Materials Science Division under Contract No. DE-AC03-76SF00098 (LBNL & UC Davis). The authors gratefully acknowledge Dr. G.S. Herman at EMSL, PNNL for helpful suggestions and Alex Kay at UC Davis for assisting the experiments.

REFERENCES

[1] Present address: UNICAMP-IFGW-DGA, Caixa Postal: 6165, Campinas, SP 13083-970, Brazil.
[2] Present address: MAX-Lab., University of Lund, P.O. Box 118, S-22100 Lund, Sweden.
[3] Also at University of California at Davis, Davis, CA 95616.

1. D.M. Lind, S.D. Berry, G. Chern, H. Mathias, and L.A. Testardi, Phys. Rev. B 45, (1992) 1838.
2. J.W. Geus, Appl. Catal. 25, (1986) 313.
3. T.D. Waite, Rev. Mineral. 23, (1990) 559.
4. Y. Gao, Y.J. Kim, S.A. Chambers, and G. Bai, J. Vac. Sci. Technol. A 15 (1997) 332.
5. Y.J. Kim, Y. Gao, and S.A. Chambers, Surf. Sci. 371 (1997) 358.
6. E. Wasserman, J.R. Rustad, A.R. Felmy, B.P. Hay, and J.W. Halley Surf. Sci. 383 (1997).
7. D.J. Friedman, and C.S. Fadley, J. Electron Spectrosc. Relat. Phenom. 51 (1990) 701; A. P. Kaduwela, D.J. Friedman, and C.S. Fadley, J. Electron Spectrosc. Relat. Phenom. 57 (1991) 223.
8. J. Mustre de Leon, J.J. Rehr, S.I. Zabinsky, and R.C. Albers, Phys. Rev. B44 (1991) 4146.

Principal investigator: Scott A. Chambers, Environmental Molecular Sciences Laboratory, Pacific Northwest National Laboratory. Email: sa.chambers@pnl.gov Telephone: (509)376-1766.

Surface Structure via Photoelectron Diffraction of Surface Core Level States

M.Stichler[1], W. Wurth[1], D. Menzel[1], R. Denecke[2,3] and C.S. Fadley[2,3]
[1]Physik-Department E20, Technische Universität München,
Garching 85747, Germany
[2]Materials Science Division, Ernest Orlando Lawrence Berkeley National Laboratory,
University of California, Berkeley, California 94720, USA
[3]Department of Physics, University of California at Davis,
Davis CA 95616, USA

INTRODUCTION

At the ALS bending magnet beamline 9.3.2 and using its Advanced Photoelectron Spectrometer/Diffractometer experimental endstation [1], we have measured high-resolution photoemission spectra of the Ru-$3d_{5/2}$ core level for the clean Ru(001) surface, as well as covered by several adsorbates. The surface core level shift (SCLS) of the clean surface and the adsorbate-induced SCLS's due to H, O, CO, NO, and coadsorption layers were distinct, and the latter proved to be adsorbate-specific. In the next step, we measured the same spectra as functions of the electron emission angle and of the photon energy for the clean and the O covered Ru(001) surface with the aim of attaining a structure determination via photoelectron diffraction.

SURFACE CORE LEVEL STATES

Fig.1 depicts high resolution (E/ΔE>5000) $3d_{5/2}$ core level spectra for the clean and adsorbate-covered surfaces. It is evident that each spectrum is composed of at least two components. Focusing on the core level spectra of the clean surface (see the spectrum at the bottom) the deconvolution indicates three states - B, S1 and S2 - separated in binding energy by 363 and 135 meV, respectively. For the identification of the surface and bulk states the simplest way is the comparison with the adsorbate covered surfaces. B is the only state whose binding energy does not change upon adsorption and thus can be assigned to the bulk state. S1 and S2, whose binding energies vary with the different adsorbates must belong to layers close to the surface. Without restriction of generality it can be assumed that the distortion of the topmost surface layer is more pronounced than in sublayers. Consequently S1 can be related to the top layer and S2 to a transition state between the surface and the bulk, most likely the second layer. In agreement with a model of Spanjaard et al. [2] S1 shifts energetically to lower binding energies for transition metals with more than half filled valence bands because of conservation of quasi-neutrality.

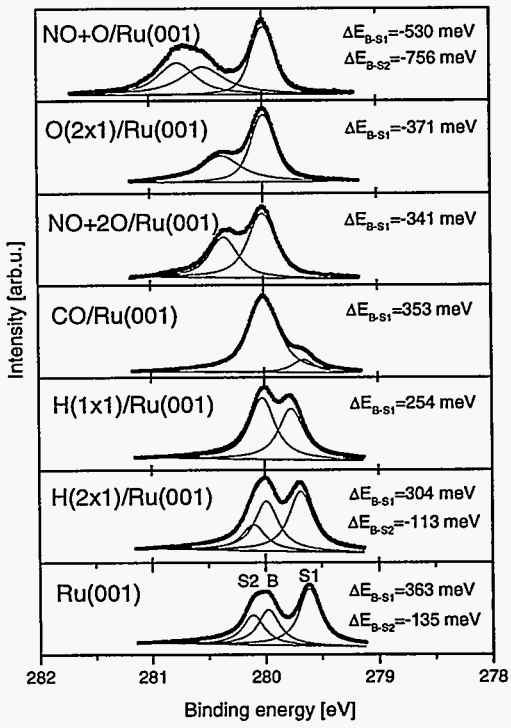

Figure 1: Surface core level shift: high resolution Ru-$3d_{5/2}$-XPS spectra measured at grazing incidence for the clean and several adsorbate covered (ordered overlayers) Ru(001) surfaces.

In the case of the adsorbate covered surfaces, which are all characterized by ordered superstructures, the most striking feature is the change in the position of the surface state with respect to the bulk state. The first class of adsorbates, which includes H and CO, shows an intermediate surface state between S1 and B of the clean surface, while the second class, comprising O and NO, induces a shift to higher binding energies of the surface state with respect to the bulk state. It is obvious that the surface core level spectra are sensitive and adsorbate specific for different adsorbate covered surfaces.

SURFACE STRUCTURE VIA PHOTOELECTRON DIFFRACTION

In the next step we measured angle and energy dependent photoelectron diffraction patterns for the clean and oxygen covered surfaces, aiming at direct structural determinations via the surface state S1 as well as via the bulk state B. For the O-covered layer we also measured the diffraction patterns of the O1s level for comparison with the Ru-$3d_{5/2}$ results. In the case of the angle dependent measurements, the angle between the linearly polarized incident radiation and the electron emission direction was fixed at 70 degrees, with the sample being rotated around two perpendicular axes to obtain the full diffraction pattern. The photon energies used were 400 and 700 eV for the Ru-$3d_{5/2}$ core level and 650 eV for O1s. In the case of the energy dependent measurements, we varied the excitation energy from 300 to 800 eV. We are presently working at the extraction of structural parameters from these diffraction patterns by comparing the experimental with theoretical results of multiple scattering calculations for scattered photoelectrons, via an R-factor analysis. The final results will be compared with LEED-IV results for the clean and the p(2x1)-O covered Ru(001) surfaces [3,4].

REFERENCES

1. Z. Hussain et al., J. Elec. Spec. and Rel. Phen. 80, 401 (1996)
   C.S. Fadley et al., J. Elec. Spec. and Rel. Phen. 75, 273 (1995)
2. D. Spanjaard et al., Surf. Sci. Rep. 5, 1 (1985)
3. H. Pfnür et al., Surf. Sci. 220, 43 (1989)
4. M. Lindroos et al., Surf. Sci. 222, 451 (1989)

This work has been supported by the Deutsche Forschungsgemeinschaft through project Me 266/22-1 and by DOE, OER, BES, Mat. Sci. Div. (Contract DE-AC03-76SF00098), ONR (Contract N00014-94-1-0162). R.D gratefully acknowledges a postdoctoral fellowship granted by the Deutsche Forschungsgemeinschaft.

Principal investigator: Dietrich Menzel, Physik-Department E20, Technische Universität München, Garching 85747, Germany. E-mail: menzel@e20.physik.tu-muenchen.de.

Beamline 10.3.1 Abstracts

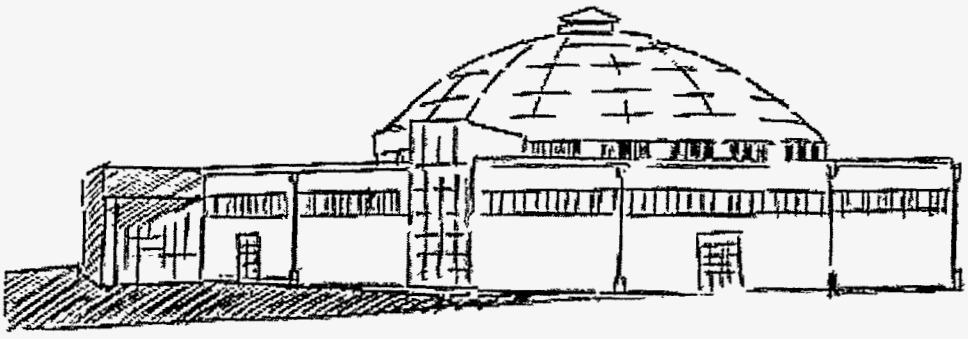

Direct Correlation of Transition Metal Impurities and Minority Carrier Recombination in Multicrystalline Silicon

Scott A. McHugo and A.C. Thompson
Lawrence Berkeley National Laboratory, Berkeley, CA 94720, USA

I. Périchaud and S. Martinuzzi
Laboratoire de Photoélectricité des Semi-Conducteurs, Case 231, University of Marseille, 13397 Marseille Cedex 20, FRANCE

Impurity and minority carrier lifetime distributions were studied in as-grown multicrystalline silicon used for terrestrial-based solar cells. Synchrotron-based x-ray fluorescence and the Light Beam Induced Current technique were used to measure impurity and lifetime distributions, respectively. The purpose of this work was to determine the spatial relation between transition metal impurities and minority carrier recombination in multicrystalline silicon solar cells. Our results reveal a direct correlation between agglomerations of chromium, iron and nickel impurities with regions of high minority carrier recombination. These results provide the first direct evidence that transition metal agglomerates play a significant role in solar cell performance.

Multicrystalline silicon can be used to fabricate solar cells with moderate solar conversion efficiency and low fabrication costs. These cells are presently manufactured for terrestrial-based applications; however, an improvement in the efficiency of these cells would greatly increase their commercial viability, see [1-3]. The primary cause for lowered efficiencies is localized regions of high minority carrier recombination. These regions possess high concentrations of dislocations [4-6]. It is known that minority carrier recombination at dislocations themselves is relatively weak but greatly increases by decoration or precipitation of transition metal impurities [7-10]. This suggests that dislocations in high recombination regions of mc-silicon are decorated with transition metals, however, past research has not presented direct evidence showing the source for carrier recombination at these dislocations. Past work has revealed that metal impurity agglomerations are present at dislocations in mc-silicon [11], however, no correlation was established to carrier recombination. This research seeks to determine whether a correlation between metal impurity distributions and regions of high minority carrier recombination exists in mc-silicon solar cells.

The polycrystalline wafers were formed by an electromagnetic casting method [12], followed by sawing and chemical etching to remove saw damage. Minority carrier recombination was mapped across the as-grown material with the light beam induced current (LBIC) method. The frontside of the samples were analyzed using synchrotron-based XRF mapping in order to determine metal impurity content and distribution. The XRF equipment is located at the Center for X-ray Optics microprobe beamline in the Advanced Light Source Center. It uses 12.5keV monochromatic radiation to excite elements in the sample with a spatial resolution of $1\mu m^2$ and a Si-Li detector to measure fluorescence x-rays from the sample, all in atmospheric conditions. Etch features on the sample surface, caused by slight preferential etching of grain boundaries during the silicon etch prior to Al contact formation, were used as reference points to locate regions of interest.

LBIC mapping of minority carrier recombination across the mc-silicon sample revealed localized regions of high carrier recombination. A typical LBIC map in a portion of the material is shown in Figure 1 where dark regions indicate areas of high carrier recombination. Of particular interest is the band of high carrier recombination located approximately in the center of the scan area.

Figure 1. Light Beam Induced Current of carrier recombination across multicrystalline silicon. Dark regions indicate high carrier recombination. The black box denotes the area analyzed with x-ray fluorescence.

X-ray Fluorescence (XRF) spectra were taken at 1µm^2 points in the region of Figure 1 as denoted by the black box. Typical spectra are shown in Figure 2. No x-ray fluorescent radiation associated with impurities was measured in regions of the mc-silicon with low minority carrier recombination. However, x-ray fluorescent radiation associated with the 3d transition metals was found in regions of the material with high carrier recombination. As seen in Figure 2, the Fe Kα and Fe Kβ fluorescence radiation are clearly discernable above background noise. The ratio of these spectral peak heights is approximately 4:1 for Kα to Kβ. This ratio is in accordance with the expected intensity ratio of Kα to Kβ radiation defined by the electron transition probability. The presence of both Fe Kα and Fe Kβ radiation, with the expected intensity ratios, acts as fingerprint for the presence of Fe and provides direct evidence that Fe is present in this region of the material. Fluorescent radiation at 5.4 keV and 7.47 keV is also clearly distinguished above background noise while small spectral peaks at 5.95 keV and 8.26 keV are only slightly above background. The intense peaks at 5.4 and 7.47 keV concur with the energies of Cr Kα and Ni Kα fluorescent radiation, respectively, while the presence of weaker peaks at 5.95 and 8.26 keV correspond with Cr Kβ and Ni Kβ fluorescent radiation, respectively. Considering the expected intensity ratio of Kα to Kβ for both Cr and Ni is 4:1, and the peak intensity of the presumed Cr Kα and Ni Kα spectral peaks at 5.4 keV and 7.47 keV is only 10 counts, the expected peak intensity of Cr Kβ and Ni Kβ coincides with the approximate intensity of the weaker peaks. This provides strong evidence that Cr and Ni impurities are present in this region of the material.

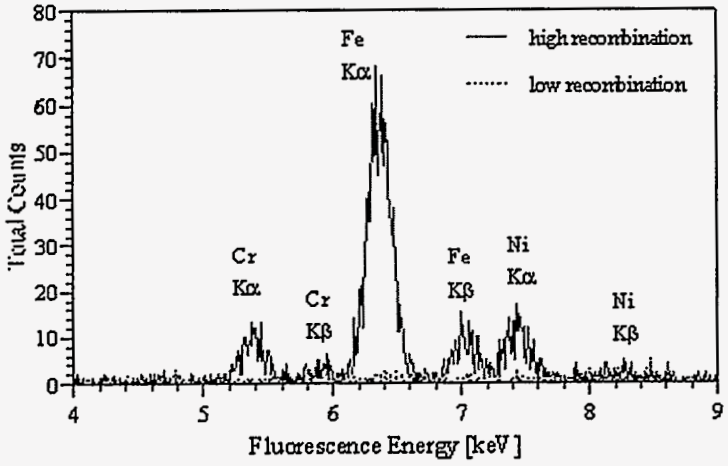

Figure 2. X-ray fluorescence spectra taken in high and low minority carrier recombination regions of multicrystalline silicon. Data was taken at points in the region denoted by the black box of Figure 1. Note the fluorescent signal of Cr, Fe, and Ni in the high-recombination region.

Concentrations of impurities at each 1µm^2 spot were calculated by analysis of the collected spectra in comparison to standard samples with known concentrations of impurities. Impurity maps were produced in the region denoted by the black box in Figure 1. Figures 3a,b and c are impurity maps of Cr, Fe and Ni in this region. Clearly there is a correlation between metal impurity distributions and minority carrier recombination. This is the first direct proof that metal impurity agglomerates play a significant role in mc-silicon solar cell performance.

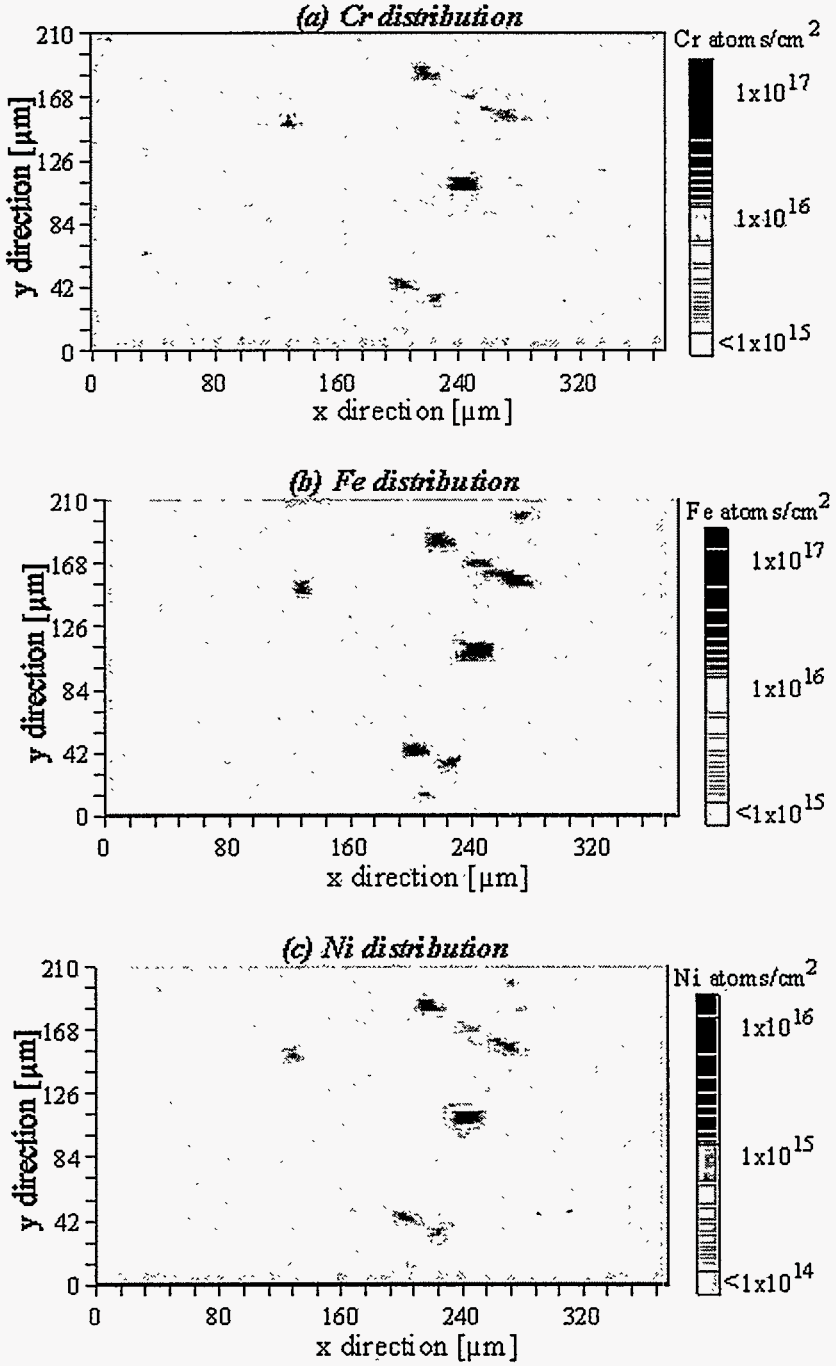

Figure 3. a) Cr, b) Fe and c) Ni distributions in multicrystalline silicon. The mapped area directly corresponds to the area in the black box of Figure 1. Note the correlation between metal impurity distributions and carrier recombination.

In conclusion, Cr, Fe and Ni metal impurities were found in electromagnetically cast multicrystalline silicon used for solar cells. The distribution of impurities correlated directly with regions of high minority carrier recombination. The work presented here is the first direct proof that metal impurity agglomerates significantly affect the performance of multicrystalline silicon solar cells.

ACKNOWLEDGMENTS

Discussions with H.A. Padmore and E.R. Weber are greatly appreciated. This work was supported by the Director, Office of Energy Research, Office of Basic Energy Sciences, Materials Sciences Division, of the U.S. Department of Energy, under Contract No. DE-AC03-76SF00098.

REFERENCES

1. J. M. Gee, R. R. King and K. W. Mitchell, *Proceeding of the 25th IEEE Photovoltaic Specialists Conference,* Washington D.C., pg. 409, (1996)
2. J. Zhao, A. Wang, P. Altermatt and M. A. Green, *Appl. Phys. Lett.* **66**, pg. 3636, (1995)
3. A. Rohatgi and S. Narasimha, *Solar Energy Materials and Solar Cells,* **48**, pg. 187, (1997)
4. S. Pizzini, A. Sandrinelli, M. Beghi, D. Narducci, F. Allegretti, S. Torchio, G. Fabbri, G. P. Ottaviani, F. Demartin and A. Fusi, *J. Electrochem. Soc.* **135**, pg. 155, (1988)
5. B. L. Sopori, L. Jastrzebski, T. Tan and S. Narayanan, *Proceedings of the 12th European Photovoltaic Solar Energy Conference*, Netherlands, pg. 1003, (1994)
6. S. A. McHugo, H. Hieslmair and E. R. Weber, *Appl. Phys. A.* **64**, pg. 127, (1997)
7. C. Cabanel and J. Y. Laval, *J. Appl. Phys.* **67**, pg. 1425, (1990)
8. T. S. Fell, P. R. Wilshaw and M. D. d. Coteau, *Phys. Stat. Sol. (a),* **138**, pg. 695, (1993)
9. V. Higgs and M. Kittler, *Appl. Phys. Lett.* **63**, pg. 2085, (1993)
10. M. Kittler, W. Seifert and V. Higgs, *Phys. Stat. Sol. (a),* **137**, pg. 327, (1993)
11. S. A. McHugo, *Appl. Phys. Lett.* **71**, pg. 1984, (1997)
12. I. Périchaud, G. Dour, B. Pillin, F. Durand, D. Sarti and S. Martinuzzi, *Sol. State Phen.* **51-52**, pg. 473, (1996)

Principal investigator: Scott McHugo, Lawrence Berkeley National Laboratory. Email: samchugo@lbl.gov. Telephone: (510) 486-4874.

Beamline 10.3.2 Abstracts

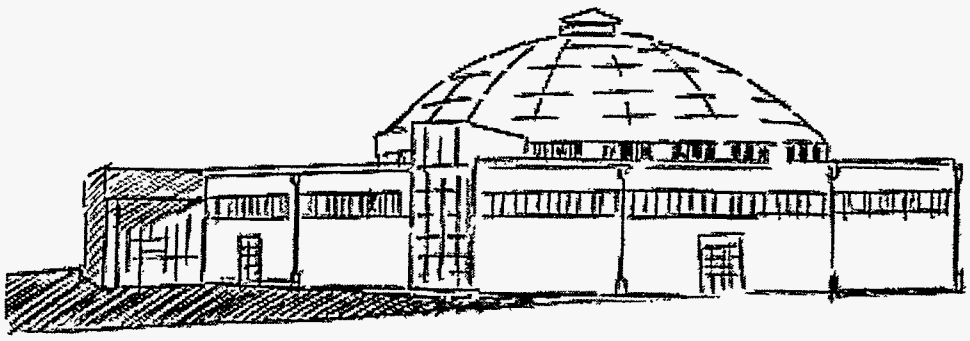

Grain Orientation Mapping of Passivated Aluminum Interconnect Lines with X-ray Micro-Diffraction.

C.H. Chang[1,2], A.A. MacDowell[1], H.A. Padmore[1], J.R. Patel[1,2], A.C.Thompson[3]

[1]Advanced Light Source, Lawrence Berkeley National Laboratory, Berkeley, CA 94720
[2]SSRL/SLAC, Stanford University, Stanford, CA 94309
[3]Center X-Ray Optics, Lawrence Berkeley National Laboratory, Berkeley, CA 94720

A micro x-ray diffraction facility is under development at the Advanced Light Source. Spot sizes are typically about 1-μm size generated by means of grazing incidence Kirkpatrick-Baez focusing mirrors. Photon energy is either white of energy range 6-14 keV or monochromatic generated from a pair of channel cut crystals. Laue diffraction pattern from a single grain in a passivated 2-μm wide bamboo structured Aluminum interconnect line has been recorded. Acquisition times are of the order of seconds. The Laue pattern has allowed the determination of the crystallographic orientation of individual grains along the line length. The experimental and analysis procedure used is described, as is the latest grain orientation result. The impact of x-ray micro-diffraction and its possible future direction are discussed in the context of other developments in the area of electromigration, and other technological problems.

INTRODUCTION

Electromigration is the physical movement of atoms in metallic interconnect lines passing current at high electron density (typically in the range of 10^5 amp/cm^2). Significant material movement results in voids that consequently leads to breakage and circuit failure in the metal lines. This problem gets more severe as the line dimensions continue to shrink on integrated circuits. In spite of much effort in this field (1,2), electromigration is not understood in any depth or detail, but is strongly associated with the physical material properties (stress and strain) within the interconnect material. Throughout this century x-rays have been a powerful tool to measure such material properties, but the ability to make such measurements on the micron scale required by the semiconductor industry has only come into realization with the advent of the latest generation of high brightness synchrotron sources. In this paper we describe the beginnings of a program to carry out various x-ray diffraction measurements on the micron scale. It is presumed that the electromigration properties of a metal line will be dependent to some extent on the grain orientation of adjacent grains in the line. This paper describes the experimental and analysis techniques that allow the grain orientation and indexing of individual micron sized grains along the length of aluminum interconnect line.

X-rays are quite well suited to such measurements as they are able to penetrate several microns into matter. In general, interconnect lines are encased in the insulator silicon dioxide (passivation). X-rays are able to penetrate and study such buried samples.

EXPERIMENTAL

Figure 1 shows the experimental setup. The synchrotron source of size typically 300 × 30 μm FWHM (horizontal and vertical) is imaged with demagnifications of 300 and 60 respectively by a set of grazing incidence platinum-coated elliptically bent Kirkpatrick-Baez (K-B) focusing mirrors (3). Imaged spot sizes on the sample are about a micron in size. Photon energy is either white of energy range 6-14 keV or monochromatic generated by inserting a pair of Si(111) channel-cut monochromator crystals into the beam path. A property of the four crystal monochromator is its ability to direct the monochromatic primary beam along the same direction as the white radiation. Thus, the sample can be irradiated with either white or monochromatic radiation. White radiation is chosen for Laue experiments for the orientation determination and monochromatic radiation for d-spacing measurements in stress/strain determination of single grains in the metal line.

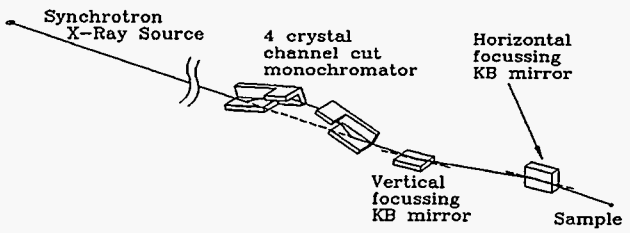

Figure 1. Schematic layout of the K-B mirrors and four crystal channel-cut monochromator.

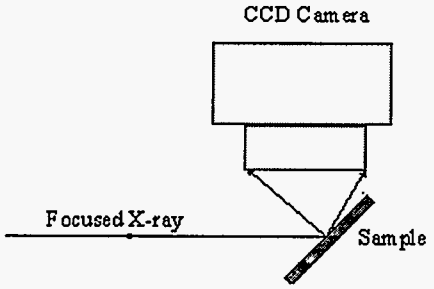

Figure 2. Schematic diagram of experimental arrangement.

The sample was an aluminum line deposited to 0.5-μm thickness and 2-μm width on an oxidized silicon substrate. The line was passivated with a plasma-enhanced chemical vapor deposition (PECVD) nitride at 300°C to 0.3-μm thickness. Laue patterns were collected using white radiation and an x-ray CCD camera. The exposure time was 0.5 sec and sample-to-CCD distance was 16.4 mm. Fig. 2 shows the arrangement of the sample and CCD detector.

RESULTS

Figure 3 shows the Laue pattern from the silicon substrate. Figure 4 shows the Laue patterns from the silicon substrate and the somewhat fainter diffraction spots from a single grain in the aluminum line. Fig. 5a shows the aluminum Laue pattern obtained following digital subtraction of the silicon pattern (Fig. 3) from the silicon and aluminum pattern (Fig. 4).

The origin on the CCD detector array was determined by moving the CCD camera radially from the sample and recording the silicon Laue patterns at various distances from the sample. The origin was determined at the CCD where the lines drawn through the succession of the same Laue spots intersected. All aluminum spot positions were coordinated to the origin and indexed using an indexing software package - LaueX (4). Fig. 5b shows the simulated pattern with reflections indexed. For conformation of the indexation the 4 crystal monochromator was inserted into the beam and scanned in energy to determine the d-spacing of the Al (111) spot.

The aluminum grain orientation can be referenced to the silicon substrate based on the orientation matrix $\mathbf{R}_{Si}$ and $\mathbf{R}_{Al}$ in the silicon substrate and aluminum grain, respectively. The matrix $\mathbf{R}$ relates the crystal system S with axes parallel to the basic crystallographic axes in the crystal to the reference system S^R related to the primary beam direction:

$$S^R = \mathbf{R}S.$$

The aluminum grain orientation measured is then referenced to the silicon substrate as the following orientation matrix:

$$\mathbf{M} = \mathbf{R}_{Si}^{-1}\mathbf{R}_{Al}$$
$$= \begin{pmatrix} 0.707 & 0.475 & -0.524 \\ 0.003 & 0.737 & 0.676 \\ 0.707 & -0.481 & 0.518 \end{pmatrix}^{-1} \begin{pmatrix} 0.916 & 0.039 & 0.399 \\ 0.308 & 0.571 & -0.761 \\ -0.257 & 0.822 & 0.509 \end{pmatrix}$$
$$= \begin{pmatrix} 0.468 & 0.612 & 0.637 \\ 0.787 & 0.045 & -0.615 \\ -0.404 & 0.792 & -0.458 \end{pmatrix}.$$

The experimental accuracy in the determination of the orientation matrix **M** depends mainly on the angular resolution of the Laue camera system, because the Laue diffraction pattern of the aluminum grains always accompanies that of the silicon substrate that is the reference of the aluminum orientation. In the present case with the CCD of 23.5-μm pixel size and sample-to-CCD distance of 16.4 mm, the magnitude of the misorientation angle is determined within a precision of several minutes of arc.

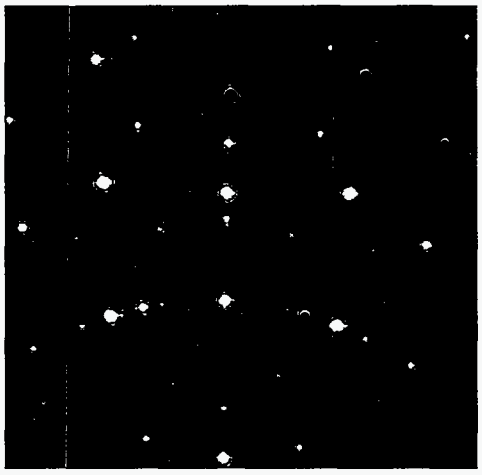

Figure 3. Laue pattern of silicon substrate.

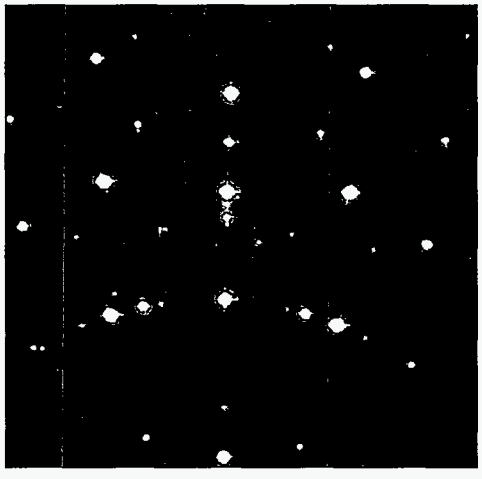

Figure 4. Laue pattern of a single grain in aluminum line as well as the silicon substrate.

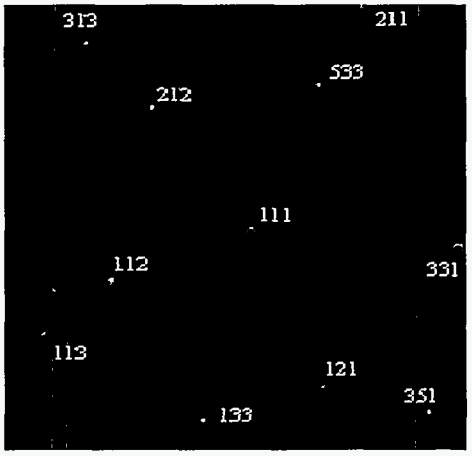

a

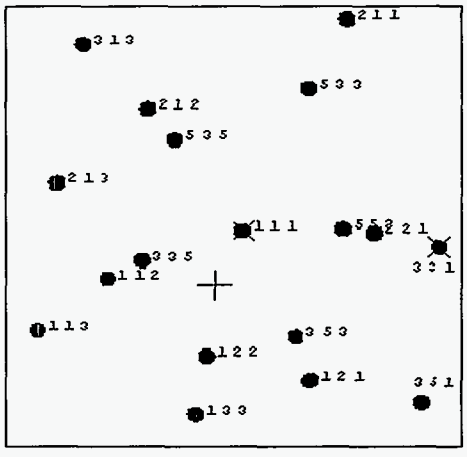

b

Figure 5. (a) Spot pattern of aluminum grain obtained by subtracting the silicon pattern (Fig. 3) from the aluminum pattern (Fig. 4). (b) Simulated pattern with the aluminum spot pattern indexed.

CONCLUSION AND FUTURE DEVELOPMENT

We have demonstrated that the x-ray micro-diffraction is capable of determining the crystallographic orientation of individual grains in passivated interconnect lines. The orientation mapping can be done by collecting the Laue patterns from individual grains along the length of the lines. A computerized indexing code to automate this is under development. Beyond this the requirement is to measure the d-spacing of various aluminum planes to determine the stress and strain state of individual grains along the length of the aluminum interconnect line.

ACKNOWLEDGMENTS

This work was supported by the Director, Office of Basic Energy Sciences, Materials Sciences Division of the US Department of Energy, under Contract no. DE-AC03-76SF00098. Samples from T. Marieb and equipment support from Intel Corporation, Santa Clara, CA.

REFERENCES

1. Marieb T., Flinn P., Bravman J.C., Gardner D., and et al. *J. App Phys.* **78**, 1026-1032 (1995).
2. Wang P.C., Cargill G.S., and Noyan I.C., *MRS Proceedings* **375**, 247-252 (1995).
3. MacDowell A.A., Celestre R., Chang C.H., Franck K., Howells M.R., Locklin S., Padmore H.A., Patel J.R., and Sandler R., *SPIE Proceedings* **3152**, 126-135 (1998).
4. Soyer A., *J. App. Cryst.* **29**, 509 (1996); http://www.lmcp.jussieu.fr/sincris/logiciel/laueX/en/laueX_en.html.

Principal Investigator: Alastair MacDowell, Advanced Light Source, MS 2-400, Lawrence Berkeley National Lab., Berkeley, Ca 74720, Email AAMacDowell@lbl.gov. Tel .510 486 4276

Micro-X-Ray Absorption Near Edge Structure: The Application to the Study of Rock Weathering: Observation of Lichen-induced Oxidation of Fe in Hawaiian Basalt

Geraldine Lamble[1], Mark Conrad[1], Ardyth Simmons[1], William Stringfellow[2], Jennie Hunter-Cevera[2], Stanley Goldman[2], Alastair MacDowell[3], Richard Celestre[3], Howard Padmore[3]

[1]Earth Sciences Division; [2]Center for Environmental Biotechnology; [3]Advanced Light Source, Lawrence Berkeley National Laboratory, Berkeley, CA 94720

INTRODUCTION

Lichens, along with other microorganisms, are known to contribute significantly to the weathering or degradation of rocks and minerals[1]. One such manifestation is the deterioration of buildings etc. It is known that Lichens produce substances that can assist in the chemical breakdown of minerals, such as organic acids etc., though knowledge of the precise mechanisms involved is lacking. We have carried out the preliminary experiments using the micro X-Ray Absorption facility under development at the ALS to study this weathering phenomenon.

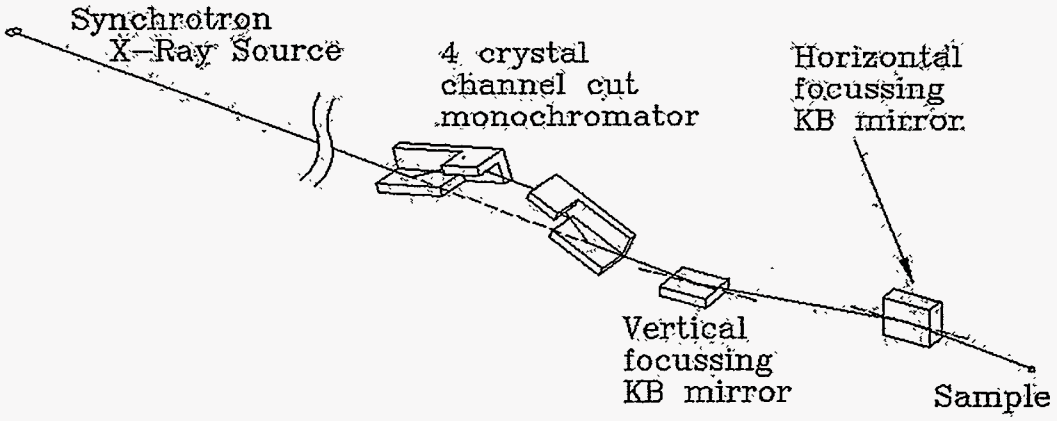

Figure 1. Schematic layout of the K-B mirrors and four crystal channel-cut monochromator.

EXPERIMENTAL

The schematic of the experimental setup is shown in Fig.1. It consists of a Si(111) four crystal monochromator in the (+--+) crystal configuration followed by a Kirkpatrick Baez grazing incidence mirror pair to focus the bending magnet source down to a spot size of around 1 micron (1). The 4 crystal monochromator naturally produces a fixed exit monochromatic beam position which allows the monochromator to be energy scanned whilst maintaining positional stability on the sample to better than 0.5 micron. The sample is mounted on a XY scanning stage and the fluorescent x-rays are detected by a solid state detector.

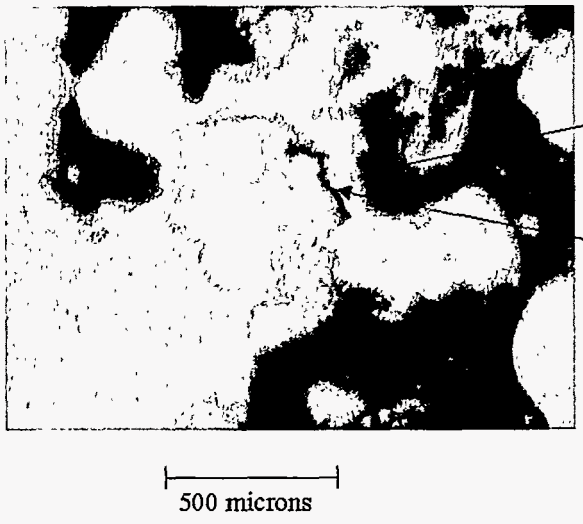

Figure 2. Optical micrograph

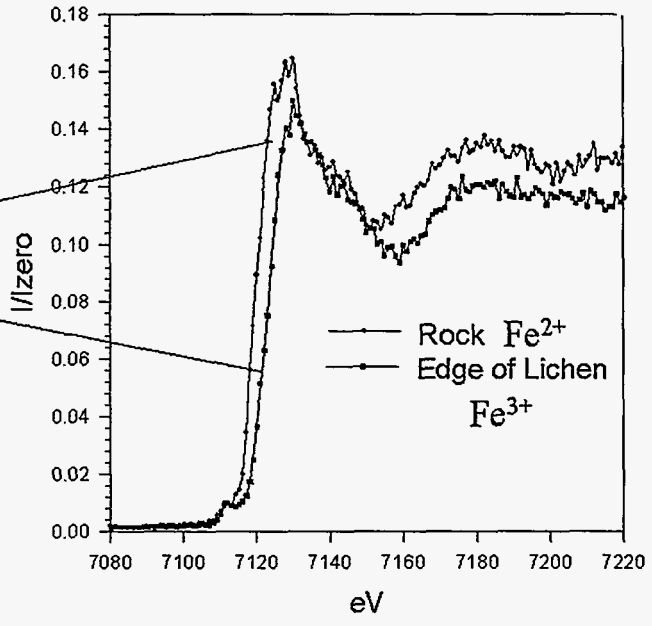

Figure 3. Fe K Near Edge X-ray Fluorecence Spectra

The optical micrograph of fig. 2 shows part of a thin section of basalt rock (dark areas) and part of a resident lichen (white/yellow area in the center). The XAS measurements of fig.3 were made by placing the monochromatic beam (1-2 microns in size) at the points of interest (on the surface of the lichen and in the body of the rock, respectively) then scanning through the characteristic K absorption edge for iron. The absorption edge shift is indicative of the oxidation state change from Fe^{2+} (in the rock) to Fe^{3+} (on the lichen).
The observation demonstrates that the lichen biochemically facilitates this oxidation state change by production of some breakdown compound (eg. organic acid) in order to absorb nutrients to sustain itself. In doing so, it contributes to the overall weathering process.

This demonstration experiment illustrates the importance of this capability to determine oxidation states with spatial resolution on the micron scale. In addition, though this particular sample had been sectioned, it is possible to envisage that the μXAFS tool could be applied to observe microorganism behavior with minimum alteration to the natural setting.

REFERENCES

1. R.M. Easton, Lichens and Rocks: a review, Geoscience Canada **81** p59 (1994)
2. A.A.MacDowell, R.Celestre, C-H.Chang, K.Franck, M.R.Howells, S.Locklin, H.A.Padmore, J.R.Patel and R.Sandler, " Progress towards sub-micron x-ray imaging using Elliptically bent mirrors", *Proc. SPIE,* **3152**, pp.126-135, 1997.

ACKNOWLEDGEMENTS

This work was supported by the Director, Office of Energy Research, Office of Basic Energy Sciences, Materials Sciences Division of the U.S. Department of Energy, under Contract no. DE-AC03-76SF00098.

Principle Investigator: Geraldine Lamble, Earth and Space Science Division, Lawrence Berkeley National Lab., Berkeley Ca 74720. Email: GMLamble@lbl.gov. Tel:510 495 2442

Progress towards Sub-micron X-ray Imaging (4-12keV) using Elliptically Bent Mirrors

A.A.MacDowell, R.Celestre, C-H.Chang, K.Franck, M.R.Howells, S.Locklin, H.A.Padmore, J.R.Patel and R.Sandler
Advanced Light Source, Lawrence Berkeley National Laboratory, Berkeley, CA 94720, USA

INTRODUCTION

The advent of third generation synchrotron sources has required the continued development of x-ray focussing optics in order to utilize the available new source brightness. We describe here progress this year made with grazing incidence optics operating in the 4-12keV range, in particular using the Kirkpatrick-Baez (KB) focussing geometry[1] with a single metal film as the reflector. Our aim is to achieve x-ray spot sizes on the spatial scale of 1:m which are considered useful for various material science problems. The desired elliptical shape of the mirror is produced by the controlled bending of a flat mirror. Such optics offer broad bandpass and can be inexpensive. The origin of this technique and its development to date has been described earlier [2,3].

KIRKPATRICK BAEZ FOCUSSING MIRRORS

In the optical system used the synchrotron source is imaged. The mirror dimensions are defined by the source size, operating wavelength, demagnification and the beamline length. The source size at the ALS is around 30 μm x 300 μm (vertical x horizontal FWHM) and the experiment location (beamline 10.3.2) defines the source to mirror distance to be 30m. With a platinum coating, adequate reflectivity is achieved for up to 12 KeV photons with a mirror grazing angle of 5.8 mrad (0.33°). The maximum convergence of the light onto the sample is limited by this critical angle of reflection of the highest energy required. If a higher convergence angle is used it means that at one end of the mirror light will be traveling almost parallel to the surface and at the other it will be exceeding the critical angle and will not be reflected.

In the vertical plane a demagnification of 60 should achieve a 0.5 μm focus with a mirror to focus distance = 500 mm.. For 12 KeV photons the critical energy reflected from a platinum mirror is about 6 mrad. As this is a prototype mirror we opted for a conservative small convergence angle onto the sample of only 1.9 mrad. Mirror length was thus defined as 163mm and angular acceptance = 31 μrads.

Similar arguments apply to the horizontally focussing mirror. The horizontal beam size is approximately 300 μm and thus a demagnification of 300 will result in a 1 micron sized image with a mirror to focus distance of 100 mm, this being considered a reasonable working distance between this mirror and sample. With this a conservative convergence angle onto the sample of 2.3mrad, a mirror length of 40 mm is defined with a horizontal acceptance of 7.6 μrads.

The ideal mirror shape required for imaging the synchrotron source is that of the surface of an off axis plane ellipse. Such a surface is able to perform true point to point imaging. The desired elliptical surface is produced by the controlled bending of a flat mirror produced by holding the ends of the mirror and applying opposite couples of different magnitude. The width of the mirror is also varied along its length which changes the cross sectional moment. In this way the exact ellipse can in principle be obtained. In practice variations in the initial mirror shape and anticlastic bending all conspire to degrade mirror performance.

The mirror flats used in the benders were flat to sub-micro radian slope errors as measured with a long trace profiler and had around 0.2 nm roughness as measured with a micromap optical profiler. The bending was monitored in the ALS optical metrology laboratory, primarily using a long trace profiler [4] to measure slope as a function of position. Typical rms slope errors from the required ellipse over the middle 140 mm of the vertical focussing mirror are around 1.5 μrad. For the shorter horizontal focussing mirror we measured an rms slope error from the required ellipse over the central 32 mm of 0.6 μrad.

X-RAY PERFORMANCE

We have performed knife edge tests on the KB focus with white light radiation. The knife edge used was a 50-μm Gold coated Tungsten wire. By reducing the mirror acceptance aperture to about 50%, the best horizontal and vertical foci achieved were 1.2 μm and 0.8 μm FWHM respectively.Fig.1 shows the vertical focussed differentiated knife edge scan, showing significant tails to the peak profile. This is consistent with x-ray scattering which is generally considered[5] to arise due to mid spatial frequency errors in the mirror (1mm – 1 μm spatial range) that the Long Trace Profiler is unable to resolve. The next iteration of the micro focus mirrors will require special attention to this mirror specification.

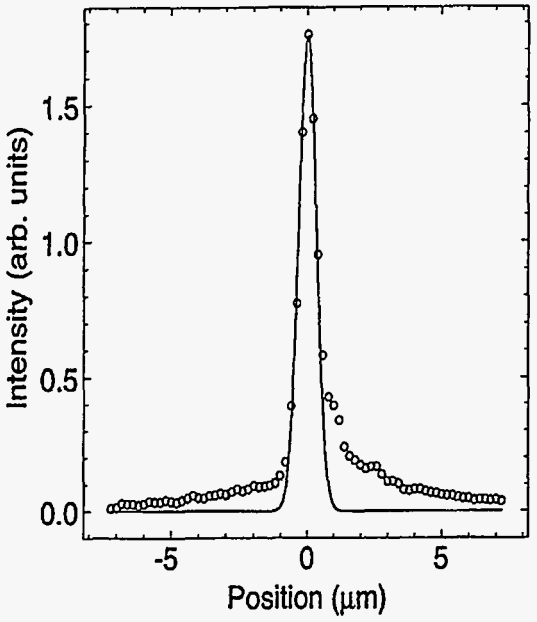

Fig.1. Differentiated knife edge scan in the vertical plane showing the beam profile. FWHM = 0.8 μm, with tails considered to be due to scatter.

ACKNOWLEDGMENTS

This work was supported by the Director, Office of Energy Research, Office of Basic Energy Sciences, Materials Sciences Division of the U.S. Department of Energy, under Contract no. DE-AC03-76SF00098.

REFERENCES

1. P. Kirkpatrick, A.V. Baez, "Formation of optical images by x-rays," *J.Opt.Soc.Am.*, **38**, pp. 766-774, 1948.
2. H. A. Padmore, M. R. Howells, S. Irick, T. Renner, R. Sandler, and Y-M Koo, "Some new schemes for achieving high-accuracy elliptical x-ray mirrors by elastic bending," *Proc. SPIE,* **2856**, pp.145-156, 1996.
3. A.A. MacDowell, R. Celestre, C-H. Chang, K. Franck, M.R. Howells, S. Locklin, H.A. Padmore, J.R. Patel and R. Sandler, "Progress towards sub-micron x-ray imaging using Elliptically bent mirrors," *Proc. SPIE,* **3152**, pp.126-135, 1997.
4. S. Irick, "Improved measurement accuracy in a long trace profiler", *Nucl. Inst. Meth.*, **A347**, 226-30 (1994).
5. J.E. Harvey, K.L. Lewotsky, A. Kotha, "Effects of surface scatter on the optical performance of x-ray synchrotron beamline mirrors," *App.Opt.* **34**, pp. 3024-3032, 1995

Principal Investigator: Alastair MacDowell, Advanced Light Source, MS 2-400, Lawrence Berkeley National Lab., Berkeley, CA 74720, Email: AAMacDowell@lbl.gov. Tel:510 486 4276

Spatial Characterization of Zinc in the 32-Cell Zebrafish (*Danio rerio*) Embryo Using X-ray Fluorescence Microprobe Imaging

K. Peariso[1], F. Su[2], J. Kuwada[2], and J.E. Penner-Hahn[1]
Departments of Chemistry[1] and Biology[2], University of Michigan, Ann Arbor, Michigan 48109, USA

INTRODUCTION

Over the past 50 years, the importance of zinc to biological systems has gained an increasing amount of attention. Zinc has been shown to be essential for the function of a variety of enzymes from transcription factors to proteases [1]. Although zinc has also been demonstrated to be essential to the development, growth, and differentiation of all species, the role of zinc in embryogenesis is largely unknown.

Embryos from species which develop outside of the mature female presumably contain, at fertilization, all of the nutrients needed to develop into a viable organism. Recently, Vallee and colleagues working with *Xenopus laevis* (African Clawed Toad) oocytes [2] and Berg and colleagues working with *Danio rerio* (Zebrafish) embryos [3] have reported that a large amount of zinc (~1mM) is stored within the embryos at the time of fertilization. Subsequent studies using ^{65}Zn were performed on the *Xenopus* embryos to follow the distribution of zinc during embryonic development [4]. The results of these experiments showed that the zinc remained associated with the lipovitellin protein in yolk platelets until the organism reached the tadpole stage of development (~48 hours after fertilization). The interpretation of these results was that zinc did not play a role in the early stages of development but was stored in the lipoproteins until a much later stage of development, at which time it was distributed to other zinc metalloproteins as needed.

Due to the large concentration of zinc in the *Xenopus* and Zebrafish embryo, XANES measurements could be performed on intact single embryos to observe changes in the bulk zinc environment during development. The advantage of these measurements is that they give insight into zinc speciation without the necessity of chemical manipulation. Differences in the normalized XANES spectra clearly suggest that the bulk zinc environment *is* changing, even in the earliest stages of development [5]. The limitation of these results is that they address only the average zinc environment. X-ray fluorescence microprobe measurements provide the opportunity to gain more detailed information on the location of the zinc as well as insight into how the zinc environment is changes during the early stages of development.

RESULTS

Using a filtered white-beam of 2 μm x 2 μm area and 10 μm steps in both x- and y-directions, an image was made of the zinc fluorescence from a 32-cell Zebrafish embryo (Figure 1). The region of highest intensity zinc fluorescence corresponds to the yolk sac, the nutrient storage area of the embryo. More intriguing is the gradient of zinc fluorescence that appears at the boundary between the yolk sac and the animal cells and continues up into the animal cells. This gradient suggests that the zinc is migrating from the yolk sac into the animal cells which are actively dividing in ~15 minute intervals at the earliest stages of development. Images of the zinc fluorescence in embryos need to be made on a variety of embryos during the stages of meroblastic (incomplete) cleavage in order to establish an actual migration trend toward the animal cells.

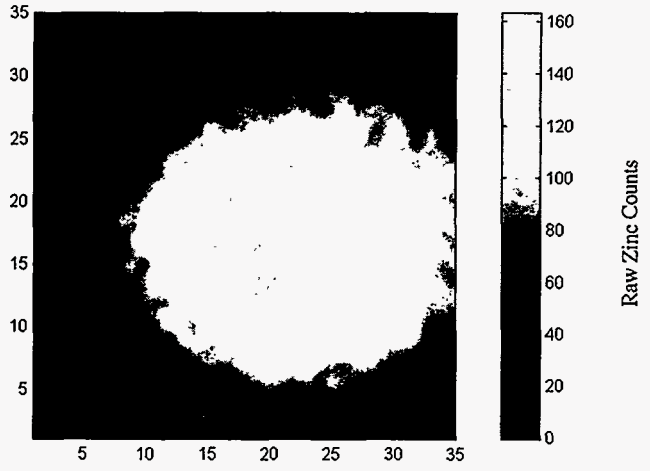

Figure 1. A gray-scale map of the zinc localization in the 32-cell Zebrafish embryo. The zinc is highly localized within the yolk sac. However, the substantial amount of zinc fluorescence in the region of the embryo where cytoplasmic bridges connect the animal cells and the yolk sac suggests there may be migration of zinc from the yolk sac to the rapidly dividing animal cells.

Although the zinc is largely localized in the yolk sac, the image demonstrates a significant concentration in the animal cells. This raises the question of why the zinc is present in the animal cells this early (1.75 hours after fertilization), if it is not utilized until much later in embryogenesis? Since the x-ray microprobe offers very small spatial resolution, the beam could be positioned in relatively intense areas of zinc fluorescence in both the animal and yolk regions of the embryo for microXANES measurements. The preliminary XANES spectra (Figure 2) show distinct differences, but they are difficult to characterize due to the noise level of the data. However, due to the sensitivity of XANES to changes in geometry as well as ligation, the fact that changes are observed in these XANES spectra implies that the zinc does not just exist as a stored nutrient for use in the latter stages of development but may play an integral role at even the earliest cleavage stages. Future efforts will be placed on improving the signal to noise ratio of the XANES measurements so that the changes may be characterized through comparisons with zinc model complexes and the purified embryo proteins. In determining the location as well as the coordination environment of the various zinc species present in the embryo, we can gain insight into the role(s) of zinc in embryogenesis.

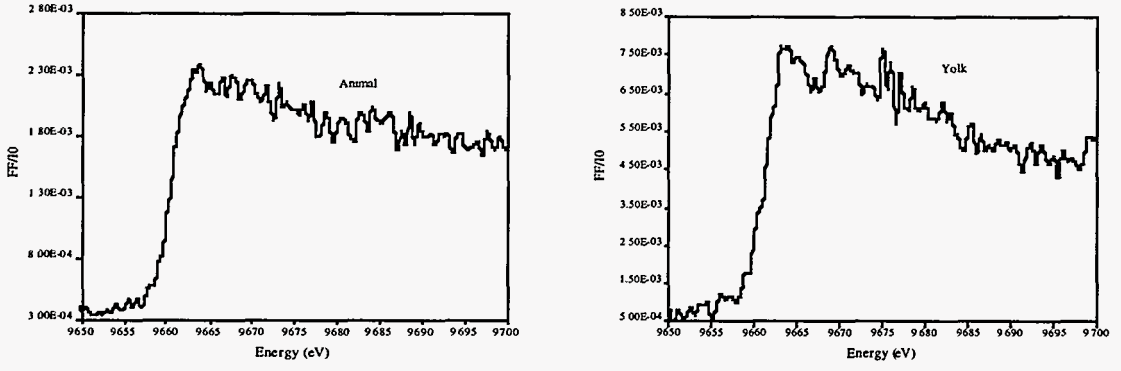

Figure 2. Preliminary microXANES measurements from the animal and yolk regions in the 32-cell Zebrafish embryo show significant position-dependent changes.

REFERENCES

1. Vallee, B.L. Zinc Enzymes; Bertini, I., Luchinat, C., Maret, W., Zeppenzauer, M. eds.; Birkhauser: Boston, 1986, pp. 1-15.
2. Montorzi, M., Falchuck, K.H., and Vallee, B.L. *Biochem* **34**: 10851-58, 1995.
3. Berg, J.M (private communication).
4. Falchuck, K.H., Montorzi, M., and Vallee, B.L. *Biochem* **34**: 16524-31, 1995.
5. Tierney, D.L., McPhate, L.S., Berg, J.M., and Penner-Hahn, J.E., unpublished results.

This work was supported in part by the NIH Grant GM-38047.

Principal investigator: J.E. Penner-Hahn, Department of Chemistry, University of Michigan. Email: JEPH@umich.edu. Telephone: 734-764-7324.

Speciation of Contaminants in Soil at the micron level

G.M.Lamble[1], R.J.Reeder[2], A.A.MacDowell[3], R.S.Celestre[3], H.A.Padmore[3]
1. Earth Sciences Division, Lawrence Berkeley National Lab., Berkeley Ca 74720
2. SUNY Stony Brook, NY 11973
3. Advanced Light Source, Lawrence Berkeley National Lab., Berkeley Ca 74720

INTRODUCTION

The complex heterogeneity of soils has precluded any direct measurements of contaminant speciation. The most reliable of speciation measurements to date have been made indirectly, for instance by chemical extraction methods (ie. by applying a series of chemical reagents to infer how the contaminant is bound within the many mineral and organic components within the soil). These indirect methods generally cause alterations to the true soil-contaminant system in the process of trying to make the measurements and are thus notoriously inaccurate.

EXPERIMENTAL

The newly developed micro X-ray absorption spectroscopy (micro-XAS) facility at the ALS provides a direct spectroscopic probe for contaminants in soils in their natural state. Here we apply a combination of two techniques: μX-ray Fluorescence and μXAFS. The μX-ray Fluorescence measurements determine elemental distribution by irradiating the sample with a micron sized beam of white light or light of a fixed energy, then rastering the sample position to obtain an elemental distribution map over a chosen area. The μXAFS measurements involves energy scanning of a monochromatic micro-beam on a chosen location, to determine the elemental speciation. The critical factors which make this possible are the high brightness of the ALS and advanced X-ray optics which provide small beams with sufficient intensity for making meaningful spectroscopic measurements on the same scale as the so-called "reactive-fraction" of soil minerals (i.e., < 2 microns).

Figure 1 shows a demonstration of these two types of measurement. The optical micrograph shows the area of interest within a sample of Long Island soil particles contaminated by Cr and Pb. The area sampled is 80 X 60 microns. Three elemental maps of Fe, Cr and Pb are shown as determined by X-ray fluorescence. Fe was measured to get an indication of any correlations in the metal distributions as Fe and Mn oxides are often considered influential in the binding of heavy metals. As can be seen from the elemental maps, the contaminants are highly localized (in regions of a few microns in size). The micro-XAS measurements were made by placing the monochromatic micro-beam in these localized regions of greatest contaminant concentration and then scanning over a characteristic absorption edge. Significantly, in the case of Cr we can observe a pre-edge feature which is characteristic of some presence of Cr(VI), which is the oxidation state of greatest concern in terms of its mobility and toxicity.

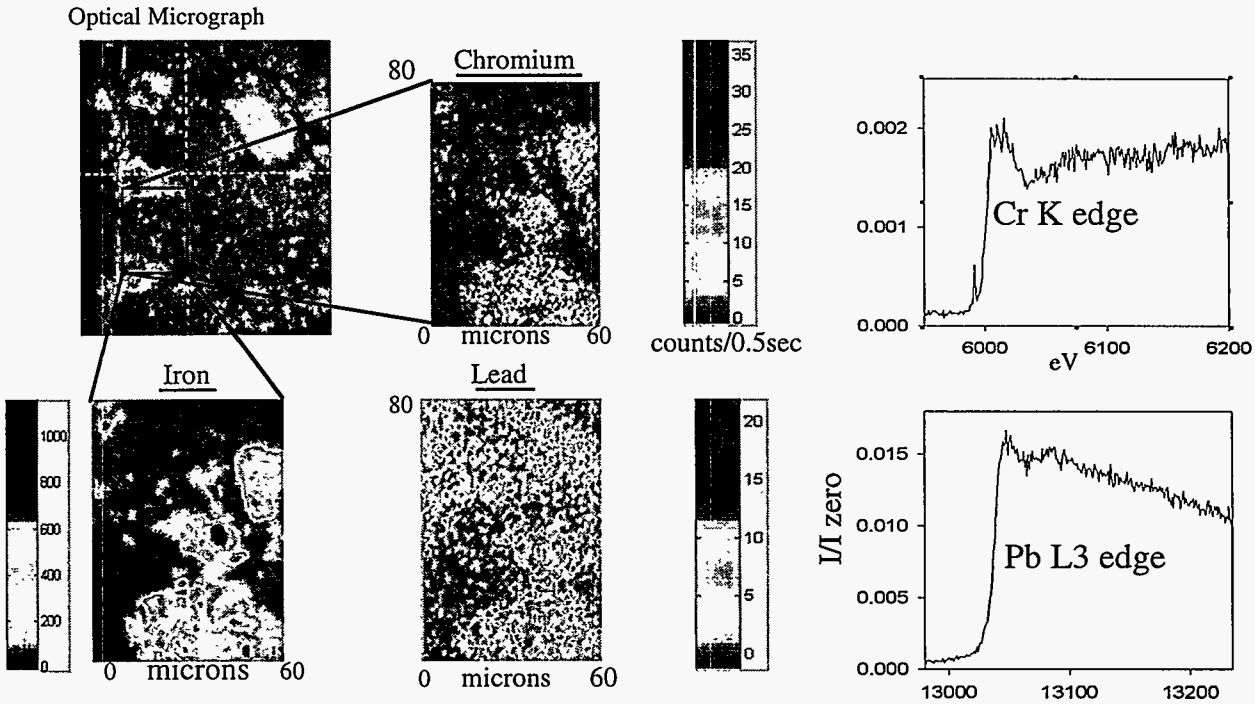

Figure 1. Optical micrograph (top left) of contaminated soil particles and associated elemental maps of Cr, Fe and Pb. The Cr and Pb near edge XAS are also included.

Speciation using unaltered samples of contaminants in such heterogeneous environments as soil represents one of the most important challenges for environmental analysis. When provided in combination with μX-ray Fluorescence for elemental analysis we can additionally monitor the elemental associations of species with particular minerals. Along with knowledge of the species, this determination of the mineral association is also of central importance for devising effective remediation strategies.

REFERENCES

1. A.A.MacDowell, R.Celestre, C-H.Chang, K.Franck, M.R.Howells, S.Locklin, H.A.Padmore, J.R.Patel and R.Sandler, " Progress towards sub-micron x-ray imaging using Elliptically bent mirrors", *Proc. SPIE,* **3152**, pp.126-135, 1997.

This work was supported by the Director, Office of Energy Research, Office of Basic Energy Sciences, Materials Sciences Division of the U.S. Department of Energy, under Contract no. DE-AC03-76SF00098.

Principle Investigator: Geraldine Lamble, Earth and Space Science Division, Lawrence Berkeley National Lab., Berkeley Ca 74720. Email: GMLamble@lbl.gov. Tel:510 495 2442

Time-resolved x-ray diffraction from laser-irradiated crystals

J. Larsson,[1] P.A. Heimann,[2] A. Lindenberg,[1] P.J. Schuck,[1] P.H. Bucksbaum,[3] R.W. Lee[4], H. A. Padmore,[2] J.S. Wark,[5] and R.W. Falcone[1,6]

[1]Physics Department, University of California at Berkeley, Berkeley, CA 94720

[2]Advanced Light Source, Accelerator and Fusion Research Division, Lawrence Berkeley National Laboratory, Berkeley, CA 94720

[3]Center for Ultrafast Optical Science, University of Michigan, Ann Arbor, MI 48109

[4]Lawrence Livermore National Laboratory, Livermore, CA 94551

[5]Department of Physics, Clarendon Laboratory, University of Oxford, Oxford OX1 3PU, U.K.

[6]Center for Beam Physics, Accelerator and Fusion Research Division, Lawrence Berkeley National Laboratory, Berkeley, CA 94720

INTRODUCTION

The properties of semiconductors following irradiation with ultrashort pulse lasers has been studied extensively with optical probes.[1-2] One motivation for this work has been the determination of the mechanism of ultrafast disordering (melting). By probing laser-irradiated material using ultrafast time-resolved x-ray diffraction, it should be possible to directly determine the mechanism for the transition from order to disorder on ultrafast timescales.

In our experiment we studied the disordering of laser-illuminated InSb. The experimental setup utilizes ALS beamline 10.3.2 and is described in more detail in Ref. 3. X-rays are monochromatized and focused to a line using a bent silicon wafer cut in the (111) plane. The Bragg angle is chosen to be 22.5 degrees which gives a photon energy of 4.8 keV for Si (111). A Ti:Al_2O_3-based laser system produced pulses with a duration of about 100 fs at a repetition rate of 1 kHz; it has been synchronized to the electron storage ring with jitter less than 10 ps. The laser beam is focused on a InSb (111) sample at a fluence of about 30 mJ/cm^2, about a factor of two below the threshold for rapid and visible damage. Diffracted x-rays are detected by a x-ray sensitive avalanche photodiode (APD).

In InSb photoabsorption limits the x-ray penetration depth. We note that the linear absorption coefficient at the 800 nm laser wavelength corresponds to a attenuation length of about 100 nm. The x-ray probe depth (at 5 KeV) is about 200 nm.

RESULTS AND DISCUSSION

Using a pump-probe technique, the diffracted x-ray intensity is observed as a function of scanned delay between the laser heating pulse and the x-ray probe. A 30 % drop in the diffraction intensity is seen with a time-resolution limited by the ALS-pulse duration, which is on the order of 70 ps for the operating conditions used. Then, the diffraction efficiency recovers over a 100 ns timescale.

In Fig. 1, we show theoretical and experimental rocking curves with different delays between the laser heating and x-ray probe. The calculation numerically solves the dynamical diffraction equations. We set the initial temperature distribution to be an exponential with a decay depth equal to the laser absorption depth, where the top diffracting layers are at the melting temperature. In comparing experiment and theory we can explain the shape of the rocking curve quite well.

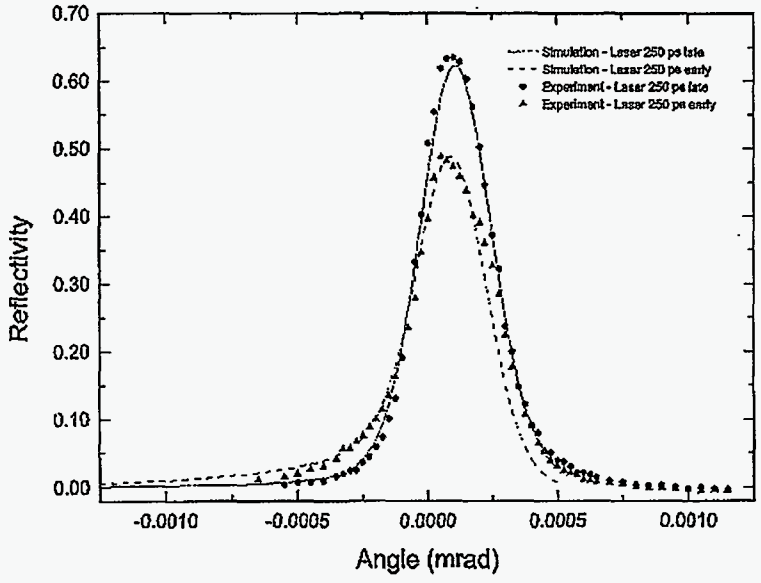

Figure 1. Experimental and theoretical rocking curves for the (111) reflection of InSb.

A change in the diffraction efficiency can be related to several possible effects including: lattice expansion, melting with regrowth, or a phase transition to a different structure. We interpret the data as follows. As the laser interacts with the surface, the top layer (40 nm thick) melts causing a drop in the diffracted intensity. The underlying layers are heated resulting in a strained lattice with increased crystal spacing. Then, the lattice regrows.

In order to access a time resolution beyond the ALS pulse duration, a cross-correlation technique was developed requiring two laser-irradiated crystals. A time derivative of the cross-correlation data shows a change in the x-ray diffraction efficiency of InSb on a timescale of < 2 ps. In conclusion, we show evidence of a laser-induced phase transition in InSb through the study of time resolved x-ray scattering from a laser illuminated crystal.

REFERENCES

1. C.V. Shank, R. Yen and C. Hirlimann, Phys. Rev. Lett. **50**, 454 (1983)
2. I. L. Schumay and U. Höfer, Phys. Rev. **B 53**, 15878 (1996)
3. J. Larsson, Z. Chang, E. Judd, R.W. Falcone, P.A. Heimann, H.A. Padmore, P.H. Bucksbaum, M. Murnane, H. Kapteyn, R.W. Lee and J.S. Wark, Optics Letters **22**, 1012 (1997).

This work was supported by an Academic Research Instrumentation grant from the National Science Foundation, and by the Department of Energy through both Lawrence Livermore National Laboratory and the Lawrence Berkeley National Laboratory.

Principal investigator: Roger Falcone, University of California, Berkeley. Email: rwf@physics.berkeley.edu.

Zinc Speciation in Fungus from Contaminated Forest Soils

G.M.Lamble[1], D.Nicholson[2], A. Moen[2], B. Berthelsen[2],
A.A.MacDowell[3], R.S.Celestre[3], H.A.Padmore[3]

[1]Earth and Space Science Division, Lawrence Berkeley National Lab., Berkeley Ca 94720
[2]Norwegian University of Science & Technology, Trondeim
[3]Advanced Light Source, Lawrence Berkeley National Lab., Berkeley Ca 94720

INTRODUCTION

Much of the forest land in Southern Norway is heavily contaminated with various metals, including Zn, Cu, Pb, Cd. The source of contamination is from metal refining industries, mostly having occurred over the past twenty years. Today, environmental regulations are much more rigid and so this contamination is mostly residual. Large quantities of the contaminant metals are taken up by soil fungi in the top organic layer of the forest surface soils. These species are called ectomycorrhizal fungi and they are known to form symbiotic relationships with the trees via the root network. The fungi obtain carbohydrate from the tree roots in return for mineral supplies from the fungi. We have begun to study these ectomycorrhizal fungi using X-ray Fluorescence Microscopy and micro-XAFS to examine the extent and speciation of metals which are taken up. Whilst it is known that the fungi take up great quantities of the heavy metals, little is known of the precise forms in which they are retained nor of the mechanisms of uptake and conversion. Using the new micro X-ray absorption facility (micro-XAS) at the ALS (1) we have initiated a preliminary study of this problem.

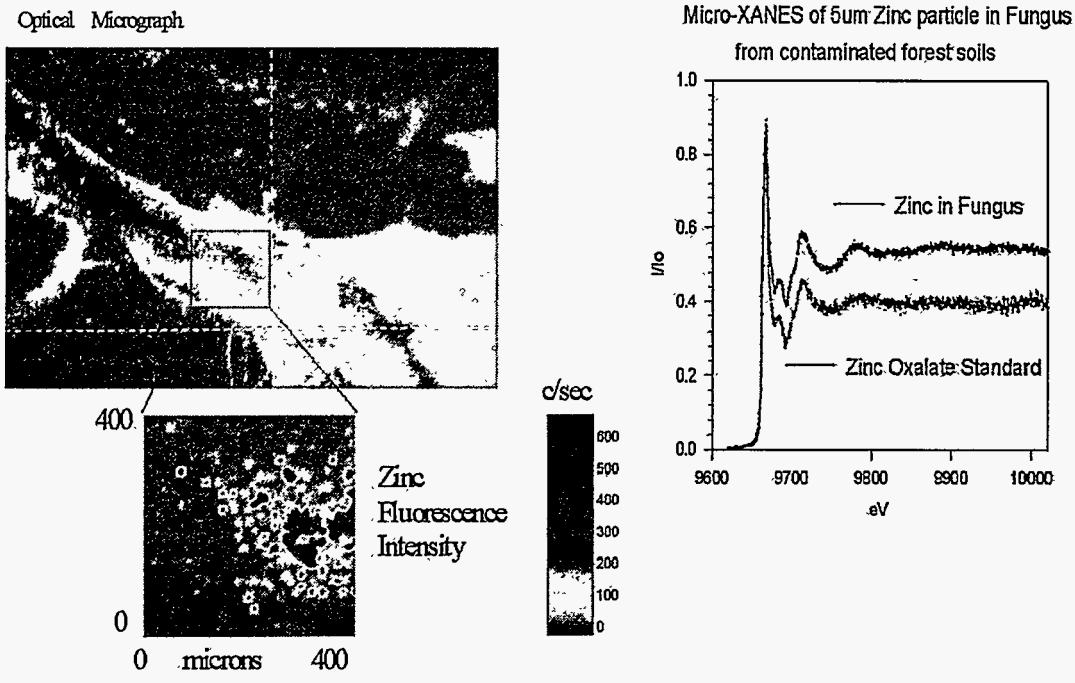

Figure 1. Optical micrograph of fungi in its natural state (top left) with Zinc elemental fluorescence map (lower left). Also included are the near edge zinc XAS spectra of the high concentration zinc particles and a zinc oxalate statndard.

EXPERIMENTAL

The micro-graph shows an area on a sample of the live fungus. A 400 x 400 micron area of interest is marked on the image. The elemental distribution of Zn within that area is indicated by the X-ray fluorescence intensity map shown below the micro-graph. This map shows that the Zn is localized in very small regions of dimensions of only a few microns.

On the right hand side we see the micro-XAFS scans taken by placing the monochromatic micro-beam on the area of greatest concentration and scanning over the Zn K edge at 9659 eV. The signal/noise is sufficiently good to scan some way into the Extended XAFS region, which indicates the potential for extracting structural parameters for this system. In this case a preliminary analysis of the short extended region is consistent with the observation by simple comparison with the very distinctive XAFS from the zinc oxalate standard, that there is a high likelihood that this species is Zinc oxalate. In addition, our conclusion supports that of recent work by Sarret et al. (2), which showed using conventional XAFS, that for zinc sequestered by lichen (a symbiotic microorganism consisting of an algae and a fungi) under similar conditions of contaminant exposure, the dominant product is zinc oxalate.

This experiment demonstrates the capability of making a direct species determination on a very small spatial scale. The results suggest that zinc oxalate is important in the mechanism of contaminant uptake, retention or conversion in its symbiosis with higher plants.

REFERENCES

1. A.A.MacDowell, R.Celestre, C-H.Chang, K.Franck, M.R.Howells, S.Locklin, H.A.Padmore, J.R.Patel and R.Sandler, " Progress towards sub-micron x-ray imaging using Elliptically bent mirrors", *Proc. SPIE,* **3152**, pp.126-135, 1997.
2. "Mechanisms of Lichen resistance to metallic Pollution: An in-situ EXAFS Study". G.Sarret, A.Manceau, D.Cuny, C.Van Haluwyn, M.Imbenotte, S.Derulle, J-L Hazemann, Fourth Int. Conf. Biogeochemistry of Trace Elements. June 23-28, (1997), U.C.Berkeley.

This work was supported by the Director, Office of Energy Research, Office of Basic Energy Sciences, Materials Sciences Division of the U.S. Department of Energy, under Contract no. DE-AC03-76SF00098

Principal Investigator: Geraldine Lamble, Earth and Space Science Division, Lawrence Berkeley National Lab., Berkeley CA 74720. Email: GMLamble@lbl.gov. Tel:510 495 2442

Beamline 12.0.1 Abstracts

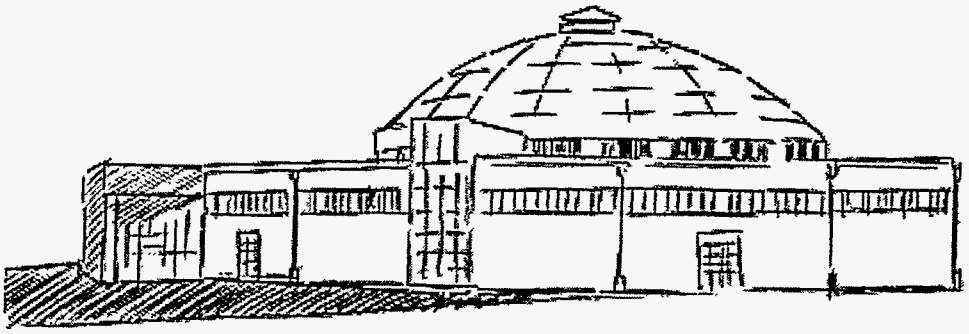

Extreme ultraviolet interferometry: at-wavelength testing of optics for lithography

K. A. Goldberg[1], P. Naulleau[1], C. Bresloff[1], P. Batson[1], P. Denham[1],
S. H. Lee[1,2], C. Chang[1,2], E. Tejnil[2], D. T. Attwood[1,3], J. Bokor[1,3]
[1]Center for X-Ray Optics, Ernest Orlando Lawrence Berkeley National Laboratory, Berkeley, California 94720, USA
[2]Intel Components Research, 2200 Mission College Blvd., Santa Clara, CA, 95052
[3]EECS Department, University of California, Berkeley, California 94720, USA

INTRODUCTION

Extreme ultraviolet (EUV) lithography is a promising and viable candidate for circuit fabrication with 0.1-micron critical dimension and smaller. To achieve this end at 13-nm wavelength, nearly diffraction-limited, multilayer-coated, near-normal-incidence reflective optical systems with 0.1 numerical aperture are required [1]. The suggested wavefront aberration tolerance for these sophisticated, all-reflective systems, composed of aspherical elements, is only 0.02 waves RMS, or 0.27 nm [2]. This places extremely high demands on the fabrication of EUV mirror substrates and multilayer coatings and even higher demands on the metrology tools required to characterize them.

The EUV wavefront is determined by the geometric figure of the mirror surfaces and by the properties of the molybdenum/silicon multilayer coatings, which are deposited across mirror areas of several square centimeters. While advanced visible-light interferometric techniques possessing the required measurement accuracy are being developed [3], optical aberrations arising from multilayer coating defects and thickness errors are measurable only at the EUV operational wavelength. Furthermore, it is widely agreed in the lithography community that final alignment and qualification must be performed at-wavelength in order to successfully predict the imaging performance of an optical system. These factors motivate the development of high-accuracy EUV wavefront-measuring interferometry.

A NOVEL EUV INTERFEROMETER DEVELOPED FOR HIGH-ACCURACY

Researchers from LBNL's Center for X-Ray Optics have built a prototype EUV phase-shifting point-diffraction interferometer (PS/PDI) [4] at ALS Beamline 12.0.1.2. This interferometer incorporates major enhancements over its predecessor, a conventional point-diffraction interferometer [5] implemented for the measurement of diffractive Fresnel zoneplate lenses at 13-nm wavelength.

The PS/PDI is a nearly common-path interferometer that incorporates pinhole diffraction to generate spherical reference wavefronts of extraordinarily high accuracy. Light from an undulator beamline is focused through a pinhole spatial filter to produce a coherent spherical wavefront to illuminate the optical system under test. A coarse grating beamsplitter placed before the test optic divides the beam into multiple diffractive orders that are brought to spatially separated foci in the image-plane. One beam, the *test* beam, containing the aberrations of the test optical system is allowed to pass through a large window in an opaque mask placed in the image-plane. A second beam, the *reference* beam, is spatially filtered by a pinhole smaller than the diffraction-limited resolution of the test optic, and becomes a second spherical wave. These two beams overlap and produce an interference fringe pattern that is detected by an EUV CCD detector. The interference pattern may be interpreted as a coherent comparison of the aberrated test beam, and the nearly-perfect spherical reference beam. The fringe pattern thus reveals the

aberrations in the test optic. Translation of the grating beamsplitter is used to introduce a controlled relative phase-shift between the test and reference beams. This design is optimized for much higher efficiency than the PDI and introduces improved measurement accuracy through its phase-shifting capability.

10X SCHWARZSCHILD OBJECTIVES

The focus of the interferometry research in 1997 was on the measurement of two prototypical EUV lithographic optics, and on the characterization of the performance of the interferometer itself. The reflective, near-normal-incidence, 10x-demagnification Schwarzschild objectives consist of two nested-spherical mirrors. Illumination of an off-axis sub-aperture of 0.08 numerical aperture, these systems are designed for 0.1-μm resolution over a 400-μm^2 field-of-view. The configuration of the interferometry endstation and the important optical components are shown schematically in Fig. 1. The EUV beam illuminates the optic from below reproducing the way it is used in a prototype EUV lithographic system at Sandia National Laboratory [6].

Of the two different optics tested, the measured wavefront aberrations are on the order of 1 nm, or 0.08 waves at 13.4-nm wavelength. A typical interferogram (interference fringe pattern) from one of the optics is shown in Figure 2. Analysis reveals the nearly-diffraction-limited wavefront phasemap shown.

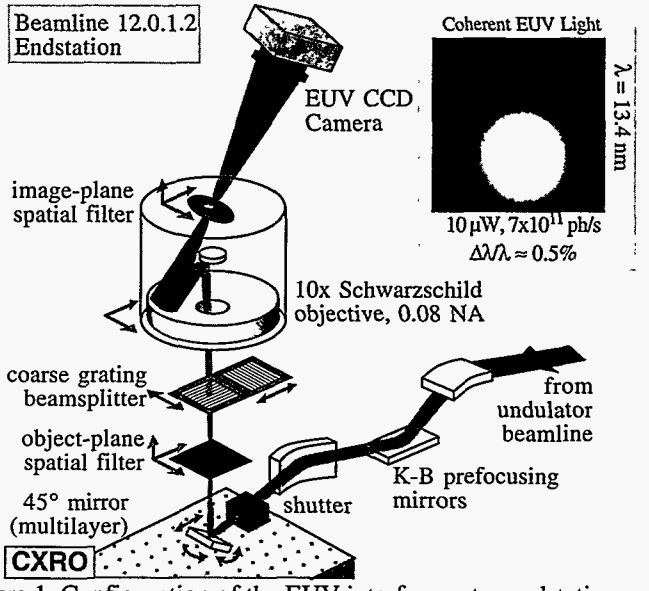

Figure 1. Configuration of the EUV interferometry endstation for the measurement of an EUV 10x Schwarzschild objective. The test optic is designed for use in a prototype EUV lithography system where it is held in a vertical orientation. Interferometric testing is therefore also performed with illumination from below.

INTERFEROMETER CHARACTERIZATION

During 1997, a large number of experiments were conducted to measure the precision and accuracy of the interferometer. Literally thousands of individual interferograms were recorded in the span of a few months. Repeatability tests all indicated measurement precision on the order of 1-2 angstroms in a variety of measurement configurations [7]. Each component of the interferometer was separately examined with *in situ* tests to evaluate its performance and identify potential systematic effects.

The most important function of interferometric optical testing is the prediction of imaging performance. To verify the accuracy of the wavefront measurements, the 10x objectives were used in a series of resolution test pattern printing experiments at Sandia National Laboratory. The results provided excellent agreement between the predicted and the measured performance.

Other tests demonstrated the first direct observation of chromatic effects related to the reflective properties of multilayer-coatings [8]. Figure 3 shows how the measured wavefront changes as the

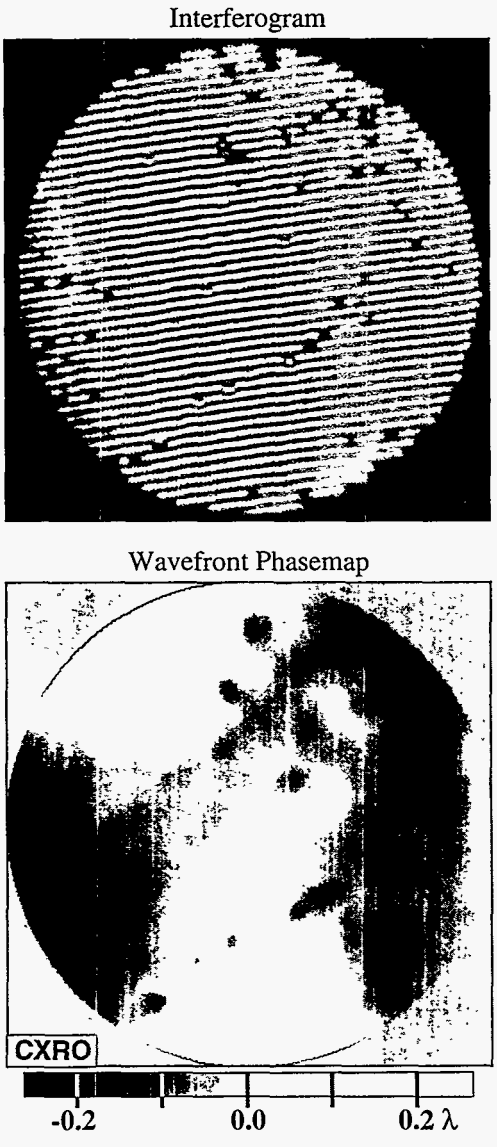

Figure 2. An interferogram recorded during the measurement of an EUV 10x Schwarzschild objective reveals small wavefront aberrations. These aberrations describe the combined effect of the surface figure of the combined two-mirror system plus the phase-effect introduced by the multilayer mirrors.

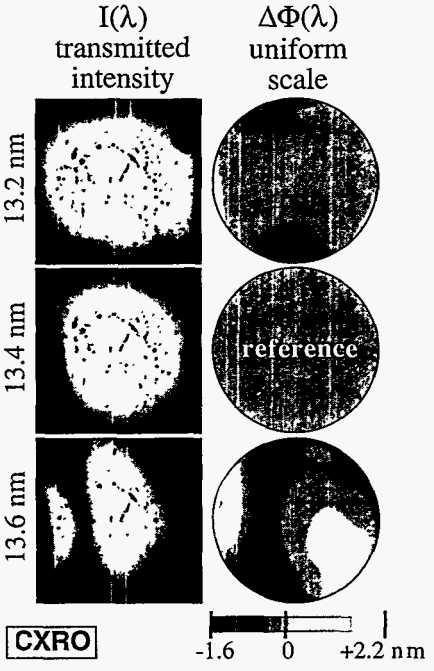

Figure 3. Evidence of the chromatic properties of multilayer mirrors is clearly visible in both the transmitted intensity, and in the changes in the EUV wavefront relative to the 13.4-nm wavelength measurement.

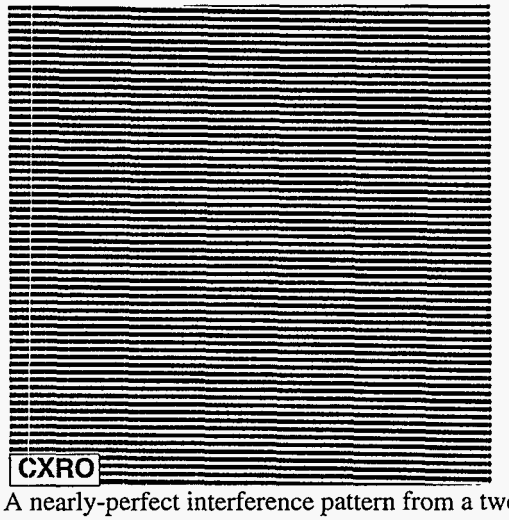

Figure 4. A nearly-perfect interference pattern from a two-pinhole experiment, covering the 1-square-inch area of a CCD detector. Small variations in the fringe contours reveal systematic measurement errors are below l/250, or 0.5 Å, in the PS/PDI.

wavelength is tuned from 13.2 to 13.6 nm. The interferometer is capable of probing the multilayer properties in ways that are invisible to measurements performed using visible light.

To investigate the accuracy of the interferometer, and probe the magnitude of systematic measurement errors, a series of two-pinhole experiments was performed [9]. Similar to Young's famous experiment, both the test and the reference beams were filtered by the tiny image-plane pinholes. A typical interferogram from these measurements is shown in Fig. 4. It was revealed that for pinholes below 120-nm diameter, reference wavefront accuracies below λ/100 waves

(1.3 Å) are achievable. Furthermore, for pinholes of 100-nm diameter, the reference wavefront quality is λ/250 RMS (0.5 Å) on average. Since the pinhole functions as a spatial filter for the aberrated test beam, it is hoped that as higher quality-optics are tested, the wavefront quality can be further improved.

REMARKS FOR FUTURE WORK

With a verified measurement accuracy and precision well beyond the current state-of-the-art in optical fabrication, this interferometer will serve as an important measurement tool in the development of advanced EUV optical systems.

REFERENCES

1. Himel, M. D., "Optic fabrication and metrology for soft x-ray projection lithography," in OSA Proceedings on Soft X-Ray Projection Lithography, Vol. 18, A. M. Hawryluk and R. H. Stulen, Eds., Optical Society of America, Washington, D.C., 1993, pp. 108-9.
2. Williamson, D. M., "The elusive diffraction limit," in OSA Proceedings on Extreme Ultraviolet Lithography, Vol. 23, F. Zernike and D. T. Attwood, Eds., Optical Society of America, Washington, D.C., 1994, pp. 68-76.
3. Sommargren, G. E., "Phase shifting diffraction interferometry for measuring extreme ultraviolet optics," in OSA Trends in Optics and Photonics, Vol. 4, Extreme Ultraviolet Lithography, G. D. Kubiak and D. R. Kania, Eds., Optical Society of America, Washington, D.C., 1996a, pp. 108-12.
4. Medecki, H., et al., "Phase-shifting point diffraction interferometer," Optics Letters, 21 (19), 1526-28 (1996).
5. Goldberg, K. A., et al., "Progress towards λ/20 extreme ultraviolet interferometry," Journal of Vacuum Science & Technology B, 13 (6), 2923-27 (1995).
6. Tichenor, D.A., et al., "Development of a laboratory extreme-ultraviolet lithography tool," Proc. SPIE, 2194, 95-105 (1994).
7. Goldberg, K. A, "Extreme ultraviolet interferometry," *doctoral dissertation*, Physics Department, University of California, Berkeley, 1997.
8. Tejnil, E., et al., "At-wavelength interferometry for EUV lithography," Journal of Vacuum Science & Technology B, 15 (6), pp. 2455-61 (1997).
9. Naulleau, P., et al., "Characterization of the accuracy of EUV phase-shifting point diffraction interferometry," Proc. SPIE, 3331-13, *to be published.*

This research would not have been possible without the generous sponsorship of Intel Corporation, the EUV LLC, and the Virtual National Laboratory, SRC contract no. 96-LC-460, DARPA Defense Advanced Lithography Program, Office of Basic Energy Sciences, and the U. S. Department of Energy under Contract No. DE-AC03-76SF00098

Principal investigator: Jeffrey Bokor, Center for X-Ray Optics, Ernest Orlando Lawrence Berkeley National Laboratory. Email: jbokor@eecs.berkeley.edu. Telephone: 510-642-4134.

First Results on the Spectromicroscopy of AlGaN

G. F. Lorusso[1], H. Solak[1], F. Cerrina[1], J. H. Underwood[2], P. J. Batson[2], Y. Cho[3], C. Kisielowski[3], J. Krueger[3], and E. R. Weber[3]

[1]Center of X-ray Lithography, University of Wisconsin, Madison, WI

[2]Center of X-ray Optics, Lawrence Berkeley Laboratory, Berkeley, CA

[3]Department of Material Science and Mineral Engineering, University of California, Berkeley, CA.

INTRODUCTION

Gallium nitride and related wide band gap semiconductors are an important class of electronic materials because of their potential use in optoelectronic devices operating in the blue range [1]. In the last few years, many efforts have been devoted to investigate the electronic structure of such nitrides, and x-ray photoemission spectroscopy (XPS) has been widely used to study GaN [2]. Among other results, these investigations indicated a substantial band bending due to Fermi level pinning at the sample surface, related to intrinsic localized surface states [3].

XPS has been widely used to study GaN and related compounds, but the technique provides spatially averaged results. Spectromicroscopy [4] can provide spatially resolved information on the chemical composition of the sample surface, as well as standard morphological and chemical analysis. Hence, this technique can provides a deeper insight in the electronic microstructure of these compounds, which is characterized by lateral inhomogeneity and by dislocation densities several order of magnitude above those in other semiconductors.

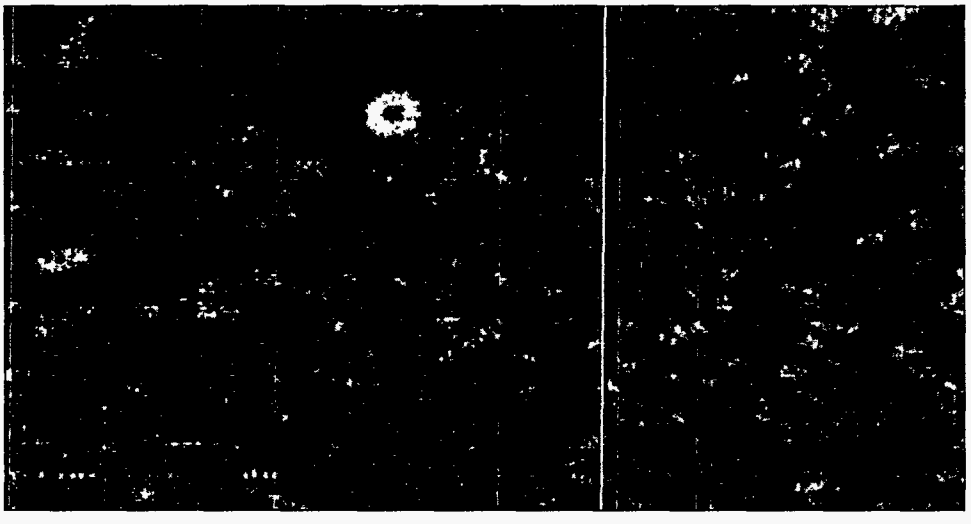

Figure 1: Secondary electron X-ray photoemission micrograph of AlGaN thin film (sample A). The field is 60 μm by 30 μm. The kinetic energy is E_K=5 eV. This image clearly shows the surface morphology of the sample, indicating a mean grain size of about 2 um, in agreement with other atomic force microscopy results.

We report the results of the first investigation of AlGaN films using photoemission spectromicroscopy. The results have been obtained using MAXIMUM [5], a scanning photoemission microscope installed on the 12.0 undulator beamline at the Advanced Light Source (ALS), with a spatial resolution of 100 nm. The AlGaN samples were grown on a sapphire substrate by metal-organic chemical vapor deposition (MOCVD). This preliminary analysis clearly indicates the great potential of spectromicroscopy in investigating chemical inhomogeneity,

impurities and localization in AlGaN films, providing detailed information on the chemistry and on the morphology of the investigated systems in the submicron range.

EXPERIMENTALS

In 1987, the University of Wisconsin, in collaboration with the ALS, started the development of an x-ray microscope system of the scanning type with the goal of reaching a spatial resolution better than 0.1 μm, a spectral resolution better than 300 meV, and a base pressure of 10^{-10} torr. All these goals were achieved in 1992, when the photoemission microscope MAXIMUM was originally installed on Aladdin at the Synchrotron Radiation Center (SRC). During the period from 1992 to 1995, the microscope was successfully used to study semiconductor surfaces, interfaces, biological samples and organic particles. However, during the operation of the microscope it become quickly evident that the microscope performance was severely hampered by the relatively low brightness of Aladdin, which limited the available flux at the microscope's focus and, consequently, the achievable spatial resolution. In order to overcome these problems, the microscope was moved to the ALS in April 1995, where it was temporarily installed on the bend magnet beamline 6.3.2. In August 1997, the installation of the microscope in its final location (beamline 12.0) has been completed. The testing of the microscope demonstrated a spectral resolution of 250 meV, a lateral resolution of 0.1 μm in photoemission mode, and a flux on the pinhole of 4×10^{14} ph/sec.

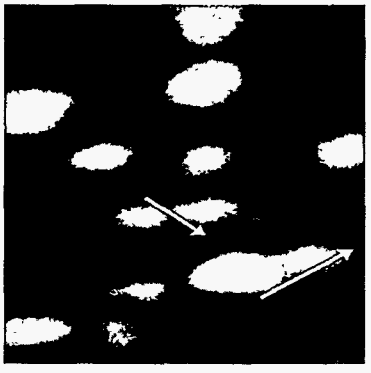

Figure 2: Close-up of the morphological structure of an AlGaN film. The field is 12 mm by 12 mm. The kinetic energy is E_K=5 eV. The grains show a fine structure, related to their crystalline orientation (arrows).

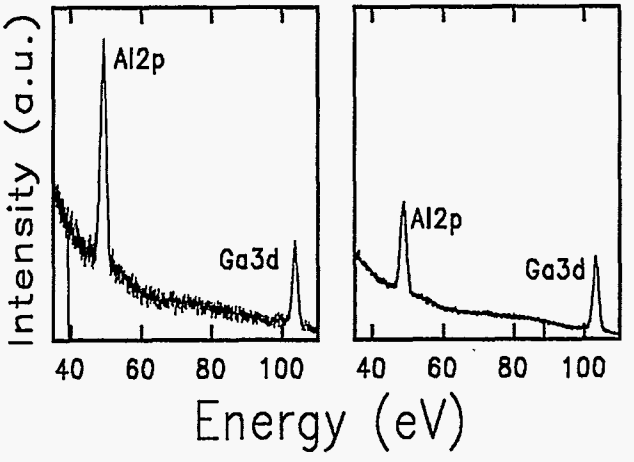

Figure 3: EDCs of the investigated AlGaN films. The results evidence the difference in Al concentration between sample A and B (x=0.23 and x=0.51, respectively).

Radiation from the synchrotron source is monochromatized and then focused by a Kirkpatrick-Baez system to illuminate a pinhole, which serve as spatial filter and source for the microscope optics. A Schwarzschild objective (SO) coated with multilayers for 130 eV produce an image of the pinhole with a 20x demagnification. When a sample is placed at the focus, photoelectrons are collected by a cylindrical mirror analyzed (CMA) electron spectrometer. The sample is mounted on a scanning stage, and by rastering the sample it is possible to produce a 2-d photoemission image.

The MOCVD $Al_xGa_{1-x}N$ thin films had different concentration x of Al and different thickness: sample A (#2922), x=0.23 and 4350 Å thick, and sample B (#2927), x=0.51 and 6540 Å thick.

The chemical composition of the films has been independently analyzed by means of Rutherford backscattering spectrometry (RBS). The results show that both the films have Ga rich surfaces, especially sample A. Sample A shows a top layer ($5x10^{17}$ atoms/cm^2, 550Å thick) with $Al_{0.135}Ga_{0.44}N_{0.425}$. In the case of sample B, the top layer ($2.5x10^{18}$ atoms/cm^2, 2770Å) shows $Al_{0.255}Ga_{0.244}N_{0.50.}$ Standard XPS spectroscopy has also been performed on both the sample.

RESULTS AND DISCUSSION

In Fig. 1 we show a x-ray photoemission micrograph of Sample A. The image evidences the grain structure of the surface morphology. It has been acquired at E_K=5 eV (i.e. imaging secondary electrons) and its size is 60 x 30 μm. The grain size deduced from this image (about 2 μm) is in good agreement with the results of AFM analysis. In Fig. 2 a close-up of the surface grain structure is reported. The image size is 12 x 12 μm, at the same kinetic energy of Fig. 1. The image shows in detail the granular structure of the investigated samples, evidencing also the crystalline orientation of some of the grains (arrows in Fig. 2). These results indicate that photoemission microscopy can give high quality morphological information on the surface of the samples.

In Fig. 3 we report the electron distribution curves (EDCs) of the two samples investigated. The relative intensity of the Al2p at E_K=49.9 eV (E_B=75.8 eV) and the Ga3d at E_K=103.4 eV (E_B=22.4 eV) indicates a change in the Al concentration. By accounting for the x-ray photoemission cross section, it is possible to have a semi-quantitative evaluation of the Al/Ga ratio in the two samples. The results agree quite well with the ones obtained by means of RBS and standard XPS, thus allowing an evaluation *in situ* of the surface composition.
In Fig. 4, we report three XPS microimages of sample B at different kinetic energy. The energies are 5 eV (secondary electrons), 21 eV (Ga 3p), and 50 eV (Al 2p), respectively. The size is 100 x 100 μm. In Fig 4a, the secondary electron images shows the morphology of the sample surface. A rhombohedral feature (dashed line) is evident in the upper part of Fig. 1a. The diagonal line (arrow) is a crystallographic plane at 60 degree with respect to the feature side. The chemical mapping of Ga and Al (Figs. 4b and 4c, respectively) clearly indicate an Al excess and a Ga deficiency in the crystallographic plane.

Figure 4: XPS microimages of sample B at (a) 5 eV (secondary electrons), (b) 21 eV (Ga3p), and (c) 50 eV (Al2p). A rhombohedral feature (dashed line) and a crystallographic plane (arrow) are evident in (a).

CONCLUSION

We have reported some preliminary results on AlGaN using photoemisison spectromicroscopy. The analysis clearly indicates the ability of spectromicroscopy to perform simultaneously morphological and chemical analysis *in situ*, as well as microscopic elemental mapping. Our results

suggest future promising applications of this technique in investigating chemical and morphological inhomogeneity in AlGaN and related materials.

REFERENCES

1. S. Nakamura, M Senoh, N. Iwasa, Jpn. J. Appl. Phys. 34, L797 (1995); S. Nakamura, M Senoh, S. Nagahama, N. Iwasa, T. Yamada, T. Matsushita, K. Kiyoku, and W. Sugimoto, Jpn. J. Appl. Phys. **35**, L74 (1996).
2. G. Martin, S. Strite, A. Botchkarev, A. Agarwal, H. Morkoc, W. R. Lambrecht, and B. Segall, Appl. Phys. Lett. **65**, 610 (1994).
3. V. M. Bermudez, T. M. Jung, K. Doverspike, and A. E. Wickenden, J. Appl. Phys. **79**, 110 (1996).
4. G. Margaritondo and F. Cerrina, Nucl. Instr. and Meth. A**291**, 26 (1990).
5. C. Capasso, A. K. Ray-Chaudhuri, W. Ng, S. Liang, R. K. Cole, J. Wallace, F. Cerrina, G. Margaritondo, J. H. Underwood, J. K. Kortright, and R. C. C. Perera, J. Vac. Sci. Technol. A**9**, 1248 (1991).

This work was supported by the U.S. Department of Energy under Contract No. DE-FG02-96ER45569.

Principal Investigator: Franco Cerrina, Dept of Electrical and Computer Engineering, University of Wisconsin-Madison. Email: cerrina@xraylith.wisc.edu. Telephone: 608/263-4955

In-situ X-ray Photoemission Spectromicroscopy of Electromigration In Patterned Al-Cu Lines with MAXIMUM

H.H. Solak, G.F. Lorusso, S. Singh, and F. Cerrina
Dept. of Electrical and Computer Engineering, University of Wisconsin-Madison, Madison, Wisconsin 53706, USA
J.H. Underwood
Center for X-ray Optics, Ernest Orlando Lawrence Berkeley National Laboratory, Berkeley, California 94720, USA

Electromigration (EM) is the diffusion of atoms in a conductor under the influence of an electric current. This process is one of the major reliability concerns in microelectronics industry because of its damaging effects on metal interconnect lines. Al, which has been the industrial choice for interconnect metallization, is especially susceptible to this damage mechanism. As the interconnect line width and thickness' continue to shrink electrical current densities increase together with the reliability problem. [1] Addition of small amounts of Cu (0.5-4%) to Al has been found to increase the lifetimes of interconnect lines against electromigration damage significantly and it is practiced commonly in industry. [2] However, a consensus still has not been reached upon the mechanism by which Cu slows down electromigration. One great source of difficulty is the low solubility of Cu in Al, and existence of different phases at operation and test conditions. Most of the Cu added to Al lines is found in the (θ) Al_2Cu phase precipitates under equilibrium conditions. In some experiments grain boundaries were also shown to be rich in Cu.[3]

The dominant path for electromigration is through grain boundary networks and Cu must be effective in slowing down the electromigration along grain boundaries to cause the observed effect. [4] Therefore it is essential to obtain information on the Cu content of grain boundaries, its chemical state and the dynamics of Cu distribution between grain boundaries, grains and Al_2Cu precipitates during process, operation and test conditions. MAXIMUM, a spectromicroscope with chemical sensitivity and sub 0.1μm spatial resolution, installed on Beamline 12.0 at the ALS is a suitable tool to study this problem.[5] It can map the distribution of an element and can differentiate chemical states of the same element (like Al or Cu). MAXIMUM is especially powerful in examining the dynamics of the surface electromigration process thanks to its surface sensitivity.

It is essential to do the EM testing *in situ* to preserve the chemical states of newly EM created surfaces, and identify the differences between 'before' and 'after' pictures. For this reason a special stage and a sample holder were constructed for in-situ testing of electromigration samples at accelerated conditions in the UHV chamber of the microscope. We were able to heat the sample above 300°C and bring four separate electrical contacts to the sample with this arrangement.

For the EM test samples, 600nm of Al-Cu alloy was sputter deposited onto thermally oxidized Si wafers. Three different Cu concentrations, 0.5, 2 and 4% (weight) was chosen to observe effect of Cu content in our experiments. Lines were patterned using photolithography and wet etching processes. After patterning wafers were annealed at 450°C for 30 minutes in forming gas to set the microstructure. No passivation was deposited onto the samples. Samples were etched before introducing into the microscope slightly in a solution of Ammonium-oxalate-monohydrate in ammonium hydroxide to reveal the Cu precipitates.[6]

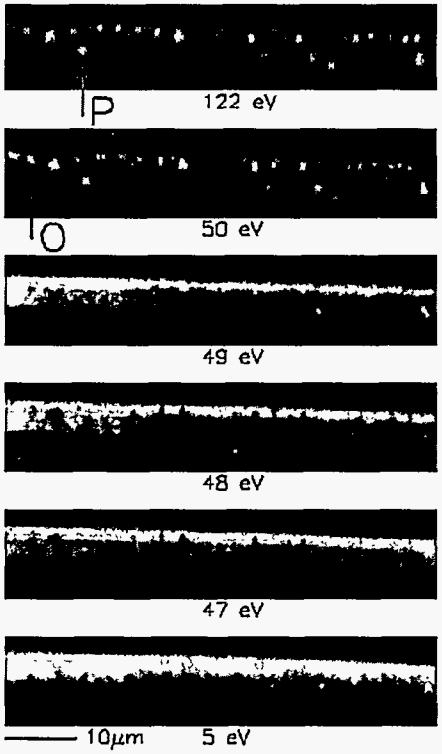

Figure 1. 60 μm X 10 μm images of 5 μm wide Al-4%Cu line *before* electromigration stressing acquired using photoelectrons of indicated energies

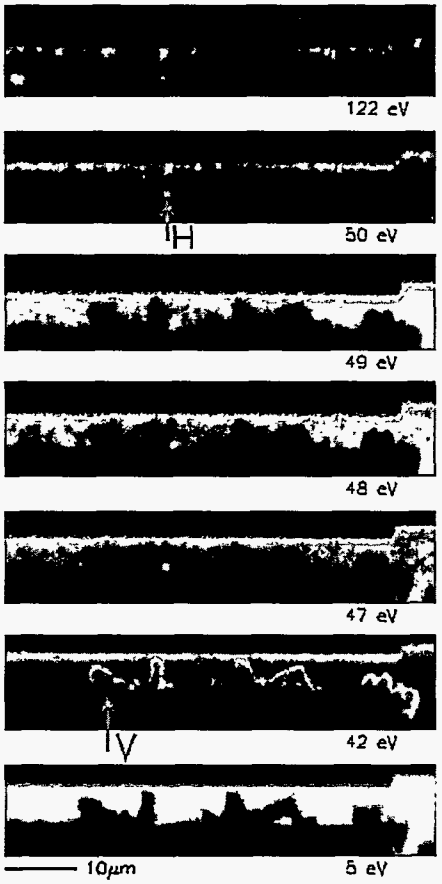

Figure 2. 60 μm X 10 μm images of 5 μm wide Al-4%Cu line *after* electromigration stressing acquired using photoelectrons of indicated energies

Samples were characterized before and after EM testing using the spectromicroscope MAXIMUM. This is done by acquiring images of the sample at interesting photoelectron energies and micro-EDCs (energy distribution curve) on interesting spatial features on the sample. In this way we were able to compare the images and EDCs before and after the EM process and evaluate the changes that has occurred. The stressing was stopped after an open circuit failure was obtained in the line.

Figure 1 shows a typical set of images acquired in an area of sample at six different photoelectron energies before testing for EM. The sample in that case is a 5μm wide Al-4%Cu line. For reference, the image acquired at 5eV kinetic energy (KE) is due to secondary electrons; contrast at this energy arises from sample topography as well as elemental inhomogeneity. Grain boundaries are resolved in that image and they appear darker due to topography. The 122 eV image is acquired at the Cu 3d core level and shows the distribution of Cu in the sample. Bright spots on that image correspond to the Cu-rich precipitates. Figure 3 shows two EDC's acquired at points P (precipitate) and O (ordinary) that are marked in Figure 1. Presence of Cu 3d signal is clearly evident as a shoulder around 121 eV. Images at 47, 48, 49 and 50 eV are acquired around the Al 2p core level. To understand the contrast mechanism in those images let us look at the Al 2p core level EDC's shown in Figure 4. The two micro EDC's shown in this figure are again taken at positions P and O in Figure 1. The Al 2p core level exhibits a shift of 0.45eV towards higher kinetic energy in the Cu ruch area. Going back to the images shown in Figure 1, this core level shift causes Cu rich precipitates to appear bright in the 50 eV image, and dark in the 47 and 48 eV images.

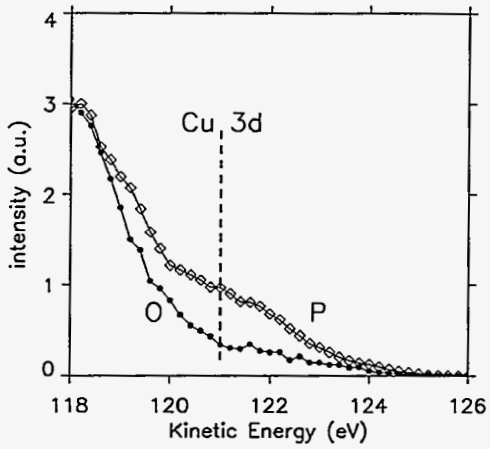

Figure 3. Micro-EDC's acquired at points **P** (precipitate) and **O** (ordinary) in Figure 1 showing the presence of Cu 3d signal at P

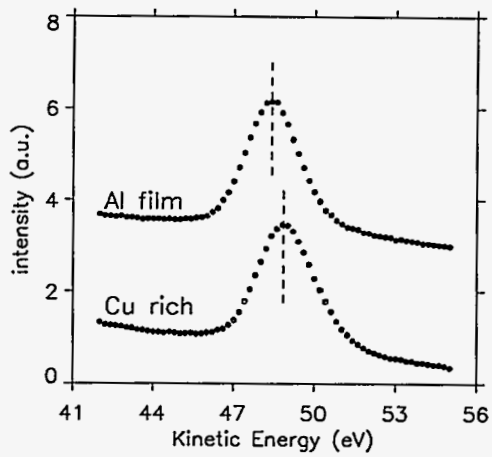

Figure 4. Micro-EDC's acquired at points **P** (precipitate) and **O** (ordinary) in Figure 1 showing the shift of Al 2p core level towards higher kinetic energy due to the presence of Cu at P

Figure 2 shows a set of images taken after electromigration stressing. The images show the *cathode* end of the Al-Cu line. Extensive voiding is apparent in those images which appear as dark regions in all images except the one taken at 42 eV kinetic energy. Figure 5 shows a micro EDC (labeled void) acquired at point V in Figure 2. Here several shifted Al 2p core level components are present near 45 eV. We attribute this energy shift in the void areas to the charging of Al that is left behind on the substrate. The charging is due to the electrical isolation of the left over Al in the voids from the rest of the line. Therefore the void areas appear bright in the 42 eV image. Images acquired at 47 and 48 eV in this set show some grain boundaries as dark areas. Some of the same grain boundaries appear as bright regions in the 50 eV and 122 eV images. This suggests an increased presence of Cu in the grain boundaries after EM.

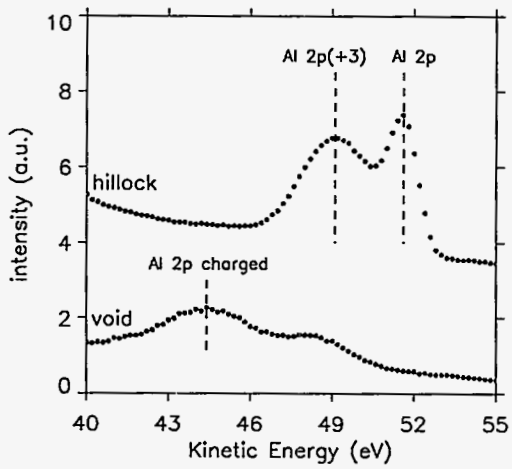

Figure 5. Micro-EDC's of the Al 2p core level acquired at points **H** (hillock) and **V** (void) in Figure 2

Figure 5 shows another micro-EDC (labeled hillock) acquired at point H marked in Figure 2. The narrow peak in that EDC at 51.6 eV is due to metallic Al 2p core level. This is fresh Al that was carried here by the EM flux. Oxidation of Al in that hillock is slowed down by the UHV

environment of the microscope chamber. This area (H) appears bright in images acquired at all phototelectron energies due to high emittance of clean Al surface.The fact that we observe metallic Al only in the hillocks and not anywhere else on the line indicates that surface electromigration did not take place in our experiment. In other words the EM was strictly limited to the grain boundary network.

In conclusion we report here the first photoemission spectromicroscopy study of electromigration in Al-Cu lines. Our preliminary results indicate that we are able to resolve Cu in grain boundaries and precipitates using the Cu 3d emission and the chemical shift of Al 2p core level in the Cu rich phase. We found no evidence of surface electromigration even under favorable conditions of the UHV environment. Finally, MAXIMUM which was installed recently on beamline 12.0 as a permanent endstation is routinely operating with better than 0.1μm spatial resolution which made this experiment possible.

REFERENCES

1. Tom Seidel and Bin Zhao, "0.1μm Interconnect technology challenges and the SIA roadmap," Mat. Res. Soc. Sym. Proc. **427**, 3 (1996)
2. I. Ames, F.M. d'Heurle, and R. Horstman, IBM J. of Res. Develop. **4**, 461 (1970)
3. D.A. Smith, M.B. Small, and A.J. Garratt-Reed. "Segregation of copper in dilute aluminum-copper alloys for interconnects," Mat. Res. Soc. Symp. Proc., **338**, 313 (1994).
4. C-K. Hu, M.B. Small, K.P. Rodbell, C.Stanis, and P. Blauner, "Electromigration failure due to interfacial diffusion in fine Al alloy lines," Appl. Phys. Lett., **62**, 1023 (1993).
5. W. Ng, A.Ray-Chaudhuri, S. Liang, S. Singh, H. Solak, J. Welnak, F.Cerrina, G. Margaritondo, J. Underwood, J. Kortright, and R. Perera, "High resolution spectromicroscopy reaches the 1000 angstrom scale," Nucl. Instr. and Meth. **A347**, 422 (1994).
6. E.G. Colgan, and K.P. Rodbell, "The role of Cu distribution and Al_2Cu precipitation on the electromigration reliability of submicrometer Al(Cu) lines," J. Appl. Phys., **75**, 3423, (1994).

This work was supported by the U.S. Department of Energy under Contract No. DE-FG02-96ER45569.

Principal Investigator: Franco Cerrina, Dept of Electrical and Computer Engineering, University of Wisconsin-Madison. Email: cerrina@xraylith.wisc.edu. Telephone: 608/263-4955

Contact person for Electromigration experiments: Harun H. Solak, Dept of Electrical and Computer Engineering, University of Wisconsin-Madison. Email: solak@xraylith.wisc.edu. Telephone: 608/877-2453

Beam Test Facility Abstracts

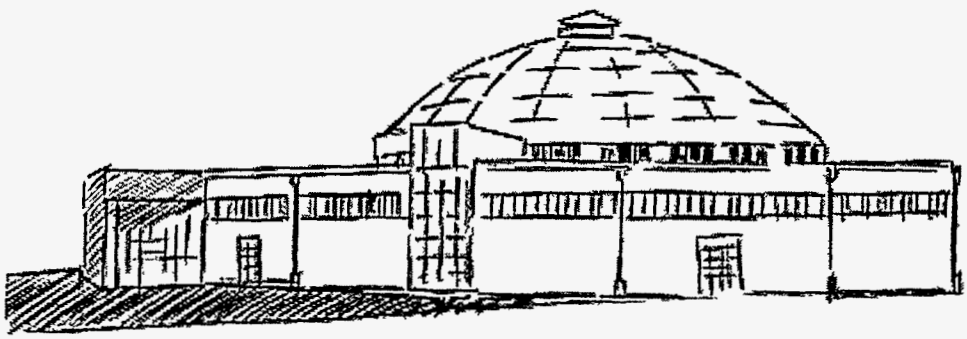

Ultrafast Structural Dynamics in InSb Probed by Time-Resolved X-ray Diffraction

A. H. Chin[1], R. W. Schoenlein[2], T. E. Glover[2], P. Balling[3], W. P. Leemans[4], and C. V. Shank[1,2]
[1]Department of Physics, University of California, Berkeley, California 94720, USA
[2]Materials Sciences Division, Ernest Orlando Lawrence Berkeley National Laboratory, University of California, Berkeley, California 94720, USA
[3]Institute of Physics and Astronomy, University of Aarhus, Ny Munkegade, DK-8000 Aarhus C, Denmark
[4]Accelerator and Fusion Research Division, Center for Beam Physics, Ernest Orlando Lawrence Berkeley National Laboratory, University of California, Berkeley, California 94720, USA

Time-resolved x-ray diffraction is a useful tool for the study of structural dynamics in condensed matter. Until recently, ultrafast atomic motion in solids or molecules has been inferred by observing changes in optical properties [1]. A more direct approach to studying ultrafast structural dynamics is to use x-ray techniques with ultrashort x-ray pulses, as x-rays directly probe atomic core electrons [2,3]. For example, changes in long-range order in crystals may be observed using time-resolved x-ray diffraction. In order to study the ultrafast structural dynamics in laser perturbed InSb, femtosecond time-resolved x-ray diffraction is performed using a novel x-ray source based on 90° Thomson scattering [2,4].

The experiments were carried out in the Center for Beam Physics Beam Test Facility at the Advanced Light Source (ALS). Terawatt laser pulses (~ 100 fs, 800 nm, 100 mJ) are generated using a chirped pulse amplification system based on Ti:Sapphire. These laser pulses Thomson scatter off of relativistic electrons (50 MeV, $\gamma = 98$) produced by the ALS linear accelerator and generate a highly directed (~ 10 mrad divergence) x-ray beam, at a wavelength of 0.4 Å. In the 90° scattering geometry, the x-ray pulse duration (~300 fs) is determined by the transit time of the ultrashort laser pulse across the ~ 90 μm waist of the focused electron beam. The electron beam diameter at the interaction point is measured by imaging optical transition radiation from an aluminum foil placed in the beam path [2,4]. Jitter in the electron beam position (~30 mm sigma) introduces a time uncertainty of ~ 100 fs. The ultrashort x-ray pulses are generated at a 5 Hz repetition rate, limited by the linear accelerator.

Time-resolved x-ray diffraction studies of InSb are performed by using the x-ray pulses along with synchronized femtosecond laser pulses involved in the x-ray generation. The InSb crystal used was cut 3° off the (111) orientation to allow x-ray diffraction in the asymmetric Bragg geometry (the x-ray beam is incident ~ 0.4° relative to the crystal surface). This geometry provides a better match between the penetration depths of the x-rays (~ 500 nm) and laser (~ 100 nm), measured perpendicular to the surface (note that the optical absorption depth remains ~ 100 nm even for angles of incidence close to 90° from normal incidence, due to the large refractive index of InSb.) The asymmetric Bragg diffraction geometry also increases the x-ray diffraction acceptance bandwidth for x-rays incident at shallow angles.

A fraction (10%) of the laser beam used to generate the x-rays is split off and used for sample excitation. The angle between the sample excitation laser beam and the x-rays (~ 4°) is kept small in order to reduce the temporal walkoff (~ 500 fs) between the beams. The temporal zero between the x-ray and laser pulses is obtained by sending unamplified laser pulses through the system. A beamsplitter is placed at the electron-laser interaction point to allow part of the laser beam to follow the x-ray beam path, and cross-correlation techniques are used with the two beams. The estimated uncertainty in the zero position is 200 fs, which is within the x-ray pulse duration.

The p-polarized laser beam is focused by a 75 cm focal length lens to a 3 mm diameter spot at the sample, with the sample positioned before the laser focus. The laser beam illuminates an elliptical spot on the sample at a fluence of 20 mJ/cm^2, which is consistent with the laser fluence needed to see signs of disorder in optical experiments [5]. The laser spot on the sample is slightly larger than the x-ray spot. The sample is moved after multiple laser shots (~10,000). While slight surface damage (monitored while collecting data by observing the scattered laser light from the sample) occurs after multiple shots, no significant degradation in the x-ray diffraction signal is observed. The damaged regions were smaller than the laser and x-ray spots on the sample. Inspection of the slightly damaged areas (visible as a white streak) under an optical microscope revealed flat regions mixed in with smaller raised spots, which may indicate recrystallized areas mixed with amorphous regions. Only the reversible changes in the sample are probed in our experiment.

The x-ray beam is apertured to 200 μrad in the diffraction plane to allow for better spectral resolution and to allow the beam to cover a reasonable area on the InSb crystal. The aperturing reduces the number of diffracted x-ray photons to about 1 every 10 x-ray pulses. This allows for pulse-height analysis of the voltage signal from the diffracted x-ray photons detected by LN2 cooled Ge detector (~ 300 eV resolution at 30 keV) to obtain the diffracted photon energy spectrum. The unused portion of the x-ray beam is used to monitor the x-ray flux, via the phosphor detection system [2,4]. A hole is placed in the phosphor to allow the central portion of the x-ray beam to reach the sample.

Representative x-ray diffraction spectra for –20 ps and +100 ps time delays (positive time delays indicate that x-ray pulses arrive after laser pulses on the sample) are shown in Figure 1. The peak of the diffraction spectrum at +100 ps is slightly shifted towards lower energy relative to the diffraction spectrum at –20 ps. This provides evidence that thermally expanded layers are formed near the surface on this time scale. Laser-induced lattice expansion has also been observed in time-resolved x-ray diffraction experiments on Si [6], and more recently in GaAs [7]. Using the thermal expansion coefficient of InSb (5×10^{-6}/K) and assuming heating up to the melting temperature (803 K), the maximum spectral shift in diffracted x-rays due to increased lattice spacing is ~ 80 eV, which is on the order of the observed ~ 40 eV shift in the Gaussian fits to the spectra in Figure 1.

The x-ray diffraction spectra integrated over the Bragg peak as a function of time delay is shown in Figure 2. We call attention to two features of the data. First, there is a rise in the integrated counts for long time delays. The rise is evidence of an increase in the diffraction bandwidth caused by the growth of a thermally expanded layer near the surface. Second, a delay (~ 10 ps) in the onset of the rise is observed, due to energy relaxation from the electron-hole plasma to acoustic phonons. The absorbed laser pulse energy is initially deposited into the electron-hole plasma. This dense electron-hole plasma may remain dense for a relatively long time (~ 1 ps) due to ambipolar diffusion and bandgap renormalization, which tend to offset hot carrier transport [8]. Consequently, Auger recombination becomes the dominant recombination mechanism for the carriers, resulting in a lowering of carrier density while maintaining the energy in the carriers. This energy is eventually transferred to the lattice via LO phonons. The time scale for this energy relaxation has been recently observed to be ~ 10 ps in GaAs near the ultrafast melting threshold [9]. Because LO phonons involve relative motion between basis atoms in the zinc-blende structure, these phonons do not induce thermal expansion of the lattice. The relaxation of LO phonons into acoustic phonons and the propagation of these acoustic phonons is the likely cause of the lattice expansion. Since the surface is free to move, and most of the energy is deposited closest to the surface, significant lattice

expansion is likely to occur at the surface first. As more LO phonons relax into acoustic phonons, which then propagate into the sample at the speed of sound, lattice expansion moves deeper into the sample. X-rays diffracting off both an expanded layer and an unperturbed layer result in an increase in the bandwidth of the diffracted x-rays. With our collimated, polychromatic Thomson scattering x-ray source, the result is an increase in the integrated x-ray diffraction signal.

X-ray diffraction from a crystal with a strain profile can be calculated using the method in Ref. 6. A simulation of the rise in x-ray diffraction signal is performed using this method, using the source parameters and assuming an expanded layer at the surface. The expanded layer is assumed to be governed by the thermal expansion coefficient and an exponentially decreasing temperature profile (maximum temperature is assumed to be the melting temperature, 803K). The 1/e depth of the temperature profile is assumed to increase at the speed of sound (5×10^5 cm/s), simulating nonequilibrium acoustic phonon transport. With a 7 ps delay in the onset of expansion, the simulation fits the data well, as shown in the curve in Figure 2.

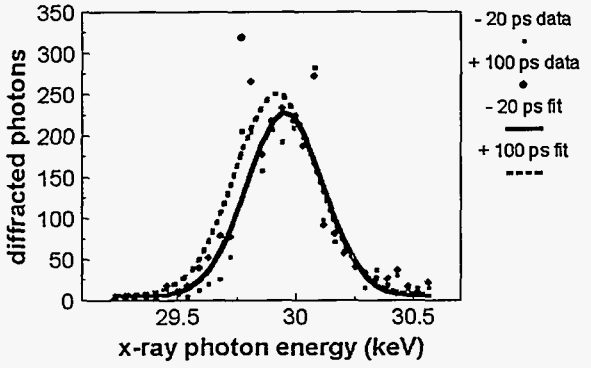

Figure 1. X-ray diffraction spectra at time delays of –20 ps and +100 ps. Solid and dashed lines are Gaussian fits to the data. Note the peak shift and broadening towards lower energy for the +100 ps data, indicating an expansion of the lattice in the volume probed by the x-rays.

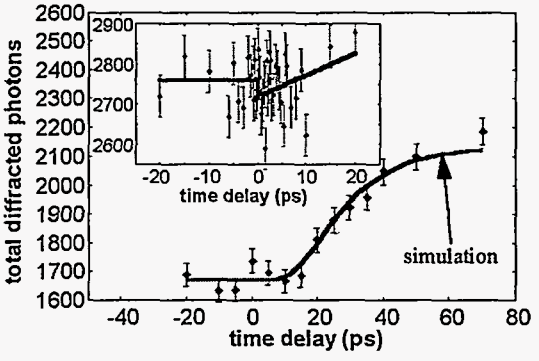

Figure 2. Total diffracted x-ray photons versus time delay. The curve is from a simulation that assumes an expanded layer growing from the surface, with a thickness increasing at the sound velocity. The inset is finer time step data taken around zero time delay. The line is a guide to the eye.

The inset to Figure 2 shows finer time step data taken around zero time delay. The data suggests a very abrupt (< 1 ps) transient reduction in the x-ray diffraction signal, as shown in the fit to the data. A reduction in x-ray diffraction is indicative of disordering. Many optical experiments have been performed on ultrafast disordering in Si [10,11] and GaAs [9,12], all of which indicate that a high electron-hole plasma density induces lattice instability [13,14] as first proposed by Van Vechten [15]. At the laser fluence used in our experiment, a carrier density of ~ 10^{22}/cm^3 is estimated, assuming the linear absorption depth (~ 100 nm) of 800 nm light in InSb. This should be sufficient to induce ultrafast disordering in a thin layer at the surface [5]. This disordered layer does not contribute to the x-ray diffraction signal, but attenuates the number of x-rays entering and diffracting from the sample by photoelectric absorption. The magnitude of the decrease (~ 1.3%) indicates that ultrafast disordering is occurring in a very thin (~ 15 nm) surface layer due to the presence of a dense electron-hole plasma.

In conclusion, time-resolved x-ray diffraction was used to study ultrafast structural dynamics in laser perturbed InSb. A delay in the onset of lattice expansion is observed, due to the time for energy relaxation from electron-hole pairs to acoustic phonons. Lattice expansion is seen to evolve at the speed of sound, as nonequilibrium phonons propagate into the sample. An indication of

subpicosecond disordering of a thin surface layer is also observed. At the laser fluence used, the changes are reversible over multiple laser shots.

The authors wish to acknowledge P. Volfbeyn, M. Zolotorev, K.-J. Kim, S. Chattopadhyay, R. Govil, T. Byrne, and the Advanced Light Source operations crew for help with the x-ray generation. A. H. C. wishes to thank J. Larrson, A. M. Lindenberg, R. W. Falcone, and T. Guo for enlightening discussions.

REFERENCES

1. P.F. Barbara, J.G. Fujimoto, W.H. Knox, W. Zinth, Eds., *Ultrafast Phenomena X,* vol. 62 (Springer-Verlag, Berlin Heidelberg New York, 1996).
2. R.W. Schoenlein, et al., Science 274, 236 (1996).
3. C. Rischel, et al., *Nature* **390**, 490 (1997).
4. W.P. Leemans, et al., *Phys. Rev. Lett.* **77**, 4182 (1996).
5. I.L. Shumay, U. Höfer, *Phys. Rev. B* **53**, 15878 (1996).
6. B.C. Larson, J.Z. Tischler, D.M. Mills, *J. Mater. Res.* **1**, 144 (1986).
7. T. Guo, et al., *SPIE Proc.* **3157**, 84 (1997).
8. H.M. van Driel, *Phys. Rev. B* **35**, 8166 (1987).
9. L. Huang, J.P. Callan, E.N. Glezer, E. Mazur, *Phys. Rev. Lett.* **80**, 185 (1998).
10. C.V. Shank, R. Yen, C. Hirlimann, *Phys. Rev. Lett.* **50**, 454 (1983).
11. C.V. Shank, R. Yen, C. Hirlimann, *Phys. Rev. Lett.* **51**, 900 (1983).
12. E.N. Glezer, Y. Siegal, L. Huang, E. Mazur, *Phys. Rev. B* **51**, 9589 (1995).
13. P. Stampfli, K.H. Benneman, *Appl. Phys. A* **60**, 191 (1995).
14. P.L. Silvestrelli, A. Alavi, M. Parrinello, D. Frenkel, *Phys. Rev. B* **56**, 3806 (1997).
15. J.A. Van Vechten, R. Tsu, F.W. Saris, D. Hoonhout, *Phys. Lett.* **74A**, 417 (1979).

This work was supported by the U.S. Department of Energy under Contract No. DE-AC03-76SF00098 and by the National Science Foundation under grant PHY-9512693.

Principal investigator: Robert Schoenlein, Materials Sciences Division, Ernest Orlando Lawrence Berkeley National Laboratory. Email: robert_schoenlein@ccmail2.lbl.gov. Telephone: 510-486-6557.

Institutions Funding User Research at the ALS

This list is compiled from the funding institutions users listed in their abstracts for work done in 1997.

U.S. Department of Energy

EPSCOR
Office of Energy Research
  Advanced Energy Projects and Technology Research Division
    Laboratory Technology Research Partnership Program
  Office of Basic Energy Sciences
    Chemical Sciences Division
    Materials Sciences Division
  Office of Biological and Environmental Research
    NABIR Program
    Offices of Health and Environmental Sciences
Office of Environmental Management
  Environmental Management Science Program

Other Institutions

Alexander von Humboldt Foundation
American Chemical Society
Amgen, Inc.
Applied Materials, Inc.
BMBF, Germany
Boehringer Ingelheim Fonds, Germany
Bundesminister für Bildung, Wissenschaft, Forschung und Technologie, Germany
Center for Advanced Microstructures and Devices
Centre National de la Recherche Scientifique, France
Commisariat a l'Energie Atomique, France
DAAD
DAM-CEA
Deutsche Forschungsgemeinschaft, Germany
EPSRC, United Kingdom
Extreme Ultraviolet Limited Liability Corporation
Feodor-Lynen-Fellowship
Fukuoka University, Japan
Genentech, Inc.
Göran Gustafsson Foundation for Research in Natural Sciences and Medicine, Sweden
GSI
Hitachi
IBM
INTAS-RFBR
Intel Corporation
Istituto Nazionale per la Fisica della Materia, Italy
Korean Research Foundation
Kyushu University, Japan
Louisiana Education Quality Special Fund
Ministry of Education, Japan
National Aeronautics and Space Administration
National Institutes of Health
National Science Council of Taiwan, R.O.C.

National Science Foundation
National Storage Industry Consortium
NATO Linkage Grant
Natural Sciences and Engineering Research Council of Canada
Osaka Electro-Communication University, Japan
Research Corporation
Research Council of Norway
Rigaku
Russian Science Foundation for Fundamental Research
Russian State Program
Spanish Ministerio de Educación y Ciencia
SRC
Swedish Institute
Swedish Natural Science Research Council (NFR)
Swedish Research Council for Engineering Sciences (TFR)
The Petroleum Research Fund
Tulane University
Université Paris-Sud, France
University of California, Berkeley
University of Nevada, Las Vegas
University of Tennessee
U.S. Department of Defense
    Advanced Research Projects Research Agency
        Advanced Lithography Program
Virtual National Laboratory
Waseda University, Japan

ALS Technical Reports Table of Contents

Introduction

Technical Reports

Report from the ALS Division Director

Brian M. Kincaid

As you can see from the statistics in Table 2-1, the ALS is really hitting its stride. We expect to host over five hundred users this fiscal year. You may have noticed that the numbers for previous years have changed somewhat. We are now using a uniform DOE definition of a user as "a badged researcher who conducts experiments within the user facility (including facility staff)". Another fact that can be gleaned from the table is that in the eighteen months between the Birgeneau Committee site visit (July 1997) and January 1, 1999, the cumulative station-hour totals for the ALS will double. This is a growth rate that would be impressive even for a Silicon Valley start-up company!

We are now seeing the full effect of the Scientific Facilities Initiative, which boosted funding for the ALS and other DOE national user facilities starting in FY 1996. Continuation of this funding during FY 1997 enabled us to maintain the large increase in the number of operating hours for users and build new beamlines. It is an encouraging sign that maintaining scientific facilities utilization is still among the top priorities for the DOE Energy Research Program in FY99, as this will allow us to continue serving our users effectively.

Table 2-1. ALS usage statistics. The impact of the Facilities Initiative in FY 1996 can be seen clearly in this table.

	FY94	FY95	FY96	FY97	FY98 (Projected)
Users	91	182	184	297	500
Independent Investigator Proposals	0	7	43	168	190
User Hours	2,222	2,686	4,461	4,781	4,500
Operating Beamlines	8	11	14	17	23
Station Hours per Year	17,776	29,546	62,454	81,277	103,500
Cumulative Station Hours	17,776	47,322	109,776	191,053	294,553

In Fall 1997 the ALS became a full division of Berkeley Lab. It is part of the Energy Sciences Directorate, which includes the ALS, the Chemical Sciences Division, the Materials Sciences Division, the Earth Sciences Division, and the Environmental Energy Technologies Division. (The Accelerator and Fusion Research Division, its former parent organization, is in the General Sciences Directorate.) The Berkeley Lab organization chart is on the World Wide Web at
http://www.lbl.gov/Workplace/Lab-Support/org-chart.html

In addition, the ALS has been reorganized to have a better balance between operations and the scientific program. The Experimental Systems Group now reports to the Scientific Program Head, and two new groups for user support and scientific support, respectively, have been created. [Note: In July 1998, the ALS organization changed so that all three of the groups mentioned here report directly to the ALS Division Director. —Editor] This rearrangement should provide a more responsive organization and one that is better structured for user support.

The ALS Science Policy Board was reconstituted and held its first meeting in several years.

A major workshop on Scientific Directions at the Advanced Light Source, with more than three hundred participants from around the world, was held March 23-25, 1998. The areas targeted for rapid development at the ALS included environmental science, protein crystallography, the physics of correlated materials, and biological microscopy, among others. We expect to see proposals in these areas funded in the future, leading to new beamlines and instrumentation at the ALS and new scientific output driven by more ALS users. Please see the ALS web site for more details:

http://www-als.lbl.gov

Progress in Performance and Service

Technical progress has continued to be impressive since my last report. Some highlights are mentioned below.

- We now operate at 1.9 GeV about two-thirds of the time, and we have increased the maximum current available in this mode from 340 mA to 400 mA.
- A small-gap vacuum chamber has been installed in Sector 8, along with an improved first optical element for the undulator beamline. This means that the low end of the undulator spectrum can now be reached without requiring 1.0 GeV operation of the ALS.
- The "camshaft" fill pattern provides for a range of timing experiments without interfering with more conventional uses of the beam, minimizing the number of weeks required for time-of-flight experiments using two-bunch filling mode.
- There has been ongoing work to increase the performance of the storage ring, including studies addressing the following: reduction of vertical emittance, a third-harmonic cavity to increase stored beam lifetime, intermediate-field bends and superbends, and small-gap insertion devices.
- Initial microdiffraction (x-ray diffraction) results using Beamline 10.3.2 have demonstrated a sub-micron x-ray spot, and have already stimulated a rapidly expanding user community in environmental science, materials science, and semiconductor applications. A strong user program pursuing micro-XAS measurements, led by the Earth Sciences Division, has started, and we are in the process of commissioning Beamline 7.3.3, dedicated to time-resolved and micro x-ray diffraction.
- Two new programs in atomic, molecular, and optical (AMO) physics and in the physics of correlated electronic materials will start up later this year on the new Beamline 10.0.1. With major funding coming from the Scientific Facilities Initiative, the high-resolution spherical grating monochromator from Beamline 9.0.1 has been moved to sector 10, a new U10 undulator has just been installed, and new endstations have been constructed.
- The extreme-ultraviolet lithography program is growing, with two new bend magnet beamlines in the works: 11.3.2 for mask testing, and 6.3.1 for independent investigator users.
- The new photoelectron microscope on Beamline 7.3.1.1 has recently come on line. This instrument is to be used under a cooperative research and development agreement with IBM and will serve, among others, a growing consortium of users from Arizona State University and the University of California, Berkeley.
- Several new scientific programs investigating the generation and use of femtosecond time-scale x-ray beams have sprung up around the ALS. This is a new area of work in the field of synchrotron radiation, and may lead to a new kind of fourth-generation light source. With funding from Laboratory Directed Research and Development (LDRD) and outside funding agencies, new programs include using the ALS linac beam and a fast laser to make Compton-scattered x rays, a novel project using laser-induced energy modulation of the ALS electron beam in the wiggler to make fast x-ray pulses, a project to make a fast x-ray switch, and Center for Beam Physics work on chirped pulse x-ray generation.
- Beamline 5.0.2 for macromolecular crystallography was completed in the fall of 1997, and in just several months has resulted in a 25% growth in our overall user community. Data sets typically take 2–3 hours to obtain, and high-quality, complete structural data is often taken in

less than 24 hours; a number of important protein structures have been solved. Complete data sets have been taken on crystals as small as 40 x 30 x 5 μm. We expect approximately an order-of-magnitude improvement in performance once our permanent optics are installed later this year. Microfocusing optics have been developed and tested to increase the vertical flux density by a factor of 7, reducing the vertical beam size to 35 μm. We are currently designing and building the next crystallography line, 5.0.1, with a curved crystal focusing monochromator.

- The LIGA lithographic technique is now up and running on Beamline 3.3.2, and a PRT consisting of groups from Sandia National Laboratory, the Jet Propulsion Laboratory, and Berkeley Lab is forming.
- A prototype superconducting bend magnet for the ALS has been successfully completed after a three-year research and development project, paid for with LDRD funds. The idea here, originally due to the ALS's Alan Jackson, is to replace three of the present 36 bend magnets with high-field superconducting magnets. This can be done without compromising the present excellent performance of the ALS, resulting in as many as 12 new beamlines that have excellent high-brightness performance—equivalent to bending magnet sources at the APS, ESRF, and SPRING-8 at considerably lower cost. This innovation would make the ALS a "universal" light source. This project has strong backing from the crystallography community, and will extend the range and applicability of ALS for materials science. The Science Policy Board also gave its blessing to this new direction.
- A working scale model for the EPU insertion device, which shifts rows of magnets to produce light in any polarization from linear to circular (either helicity), was recently measured and found to meet specifications. The first EPU will serve branchline 4.0.1-2, to be dedicated to magnetic spectroscopy , and scheduled to be commissioned in September 1998.

This is really an amazing list of accomplishments, and shows what a talented and well-integrated team we are fortunate to have at the ALS.

Experimental Systems Overview

Many of the projects outlined in this section are also described in more detail in the individual beamline sections of this compendium. The intention here is to give an overview of most of the projects the Experimental Systems Group is working on and to highlight areas of special interest.

BEAMLINE 1.4 is designed for infrared microscopy and spectroscopy. Recently, light was extracted from the 40-mrad-aperture front end and successfully steered into the endstation interferometer and microscope (Fig. 1). Initial work concentrated on reducing vibration-induced intensity noise to an acceptable level, and with a combination of mounting the premirror chamber directly to the lower ALS floor, decoupling the M1/M2 mirror system from the shield wall, and minimizing the rf water pump vibration, the noise has been reduced to an acceptable level. Work is ongoing to reduce noise levels further, by techniques such as remounting the mirror switchyard away from the shield wall, but noise levels now are dominated by high-frequency electron-beam-induced motion. This phenomenon is under active study. The microscope is working well and is in routine use. Two other branchlines are under construction; the first is for surface science using the technique of surface infrared reflection spectroscopy, and it uses a Bruker interferometer. The second is for visible/UV spectroscopy of wide-bandgap materials, and it uses a small normal-incidence monochromator to provide a high-intensity beam. Both of these branchlines and endstations will be completed in the next few months.

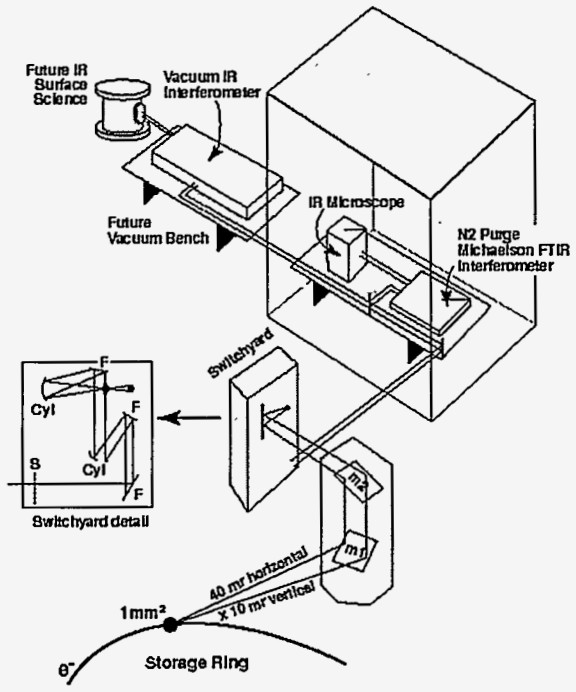

Figure 1. Schematic diagram of Beamline 1.4.

BEAMLINE 3.3.1 is designed for deep-etch lithography (LIGA). An aperture of 7 mrad is extracted through the shield wall and through a thick beryllium filter and window into a nitrogen-flowed end chamber at 16.7 m. The 100-mm-wide beam is used to illuminate a mask and photoresist-coated wafer mounted on a water-cooled carrier. The carrier is itself mounted on a stage that can oscillate up and down, so that the wafer is uniformly illuminated, and can rotate between exposure stations. The whole assembly is mounted in a steel radiation enclosure. The system was recently recommissioned and is now in routine use by a Sandia/Jet Propulsion Laboratory/Berkeley Lab Participating Research Team.

BEAMLINE 4.0.1 is designed for high-resolution soft x-ray spectroscopy of magnetic systems. The source is an elliptically polarizing undulator (EPU) that is in one-half of a chicaned straight section. The other half of the straight will eventually be occupied by a second EPU that will illuminate a second independent beamline, 4.0.2. The light passing down 4.0.1 is first deflected in the horizontal direction by a toroidal mirror, giving a vertical focus on the entrance slits of the monochromator and a horizontal focus in the user end chamber. The light is monochromatized by

an entrance-slitted Peterson-style plane-grating monochromator. This has a vertically reflecting variable-angle plane premirror and plane grating and a horizontally deflecting cylindrical mirror to focus in the vertical direction on the exit slits. The light is then refocused in the vertical direction after the slits by a variable-radius cylindrical mirror. The main challenge in this system is to deal with the extreme power density at the monochromator premirror while maintaining an extremely small slope-error budget. This has necessitated using an internally cooled silicon premirror with aggressive mini-channel multipass cooling. Due to the wide energy range (20–1800 eV) of the monochromator, the variable-angle premirror has to be long (600 mm optical length), and this compounds an already difficult design. The monochromator is being manufactured by Oxford Instruments and is due to be commissioned with light in September 1998. The undulator itself has adjustable phasing so that horizontal, vertical, right- or left-hand circularly polarized light can be selected by the user.

BEAMLINE 5.0.1, a side branch off the 37-pole, 2.1-Tesla wiggler beamline designed for protein crystallography, is under construction. To provide vertical focusing, there will be an upwards-deflecting, 1-m-long, superpolished, Ni-plated Glidcop mirror inside the shield wall, and this will be dynamically bent as well as internally cooled. Light passes through the existing Beamline 5.0.2 monochromator and is deflected horizontally by an asymmetric-cut curved-crystal monochromator. This also will be internally water cooled and will use five separate crystals of differing asymmetric cuts to limit the focal-plane motion to small values. These crystals will be mounted on a linear vertical stage to allow rapid interchange. The monochromator will cover the range from approximately 8.5 keV to 14 keV.

BEAMLINE 5.0.2 was commissioned in November 1997 and is now in routine use. It has the same premirror configuration as 5.0.1, except that in this case the beam is deflected downward. Upstream of the premirrors, a carbon filter system is used to remove unwanted low-energy light to reduce the power load on the components that follow. The beamline uses an Oxford Instruments double-crystal constant-exit-height monochromator, with mini-fin water-cooled Si[111] crystals designed in-house, and is used up to around 14 keV. The endstation is equipped with a Newport Kappa diffractometer and a 2×2-matrix CCD x-ray detector from Area Detector Systems Corporation (Fig. 2). Due to vendor problems, the beamline is currently equipped with temporary mirrors that are shorter than those in the final configuration and do not have the small slope error that is needed to produce a small vertical focus. The beam size at the sample is around 0.5 mm FWHM in both directions; this is correct in the horizontal direction but is too big by about a factor of 2 in the vertical direction. The beamline accepts only 40% of the vertical aperture of the full-length mirrors, and excessive surface roughness reduces the combined reflectivity of the mirrors by a factor of 2. The overall flux density is therefore approximately one order of magnitude what it will be with the final mirror system. Even so, the flux measured in the 0.5-mm focus is approximately 1×10^{12} photons/s at 12.4 keV, and this gives typical data collection times of around 2 hours for 0.3-mm crystals. In addition, microcrystals as small as $30 \times 40 \times 5$ μm have been successfully measured. A further development is that a prototype vertical microfocus mirror has been tested and has successfully demagnified the vertical beam size from 0.5 mm to 0.035 mm FWHM, giving a measured flux density increase of a factor of 7. A dedicated version of this mirror system is currently under construction.

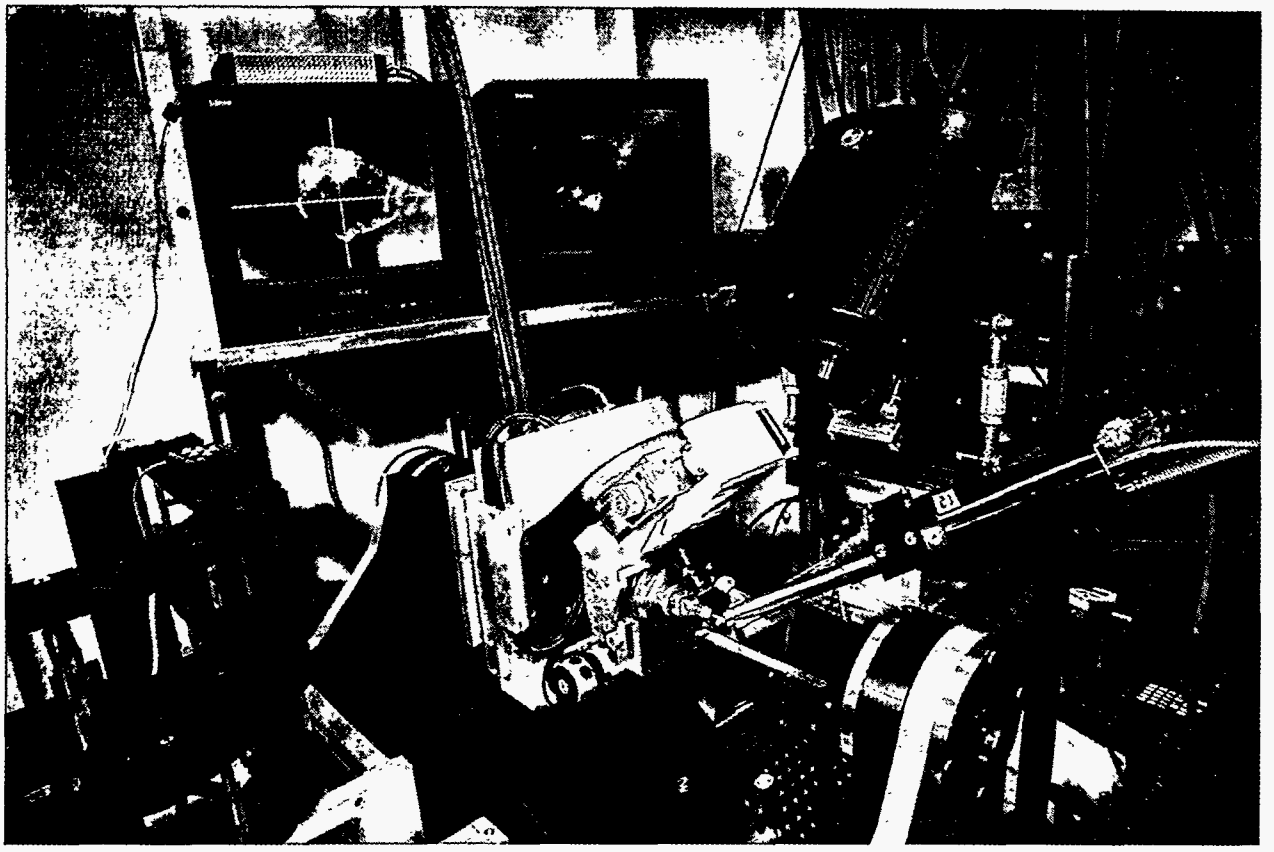

Figure 2. Photograph taken inside the Beamline 5.0.2 hutch.

BEAMLINE 7.0 is in use for Participating Research Team and independent investigator research 24 hours of every operational day. It has also been the site for scanning zone-plate microscope development. Two scanning zone-plate microscopes have been developed for x-ray spectroscopic analysis of materials. A focused x-ray spot is rastered over the sample to make an image, then held on a feature of interest for spectral measurements. The count rates in these microscopes are about ten times higher than previously available. We are currently using zone-plate lenses with a central stop and 80-nm outer zone width, and a corresponding diffraction limit to the spatial resolution of about 100 nm. An order-sorting aperture (OSA) is held in front of the sample and precisely positioned on the optical axis (+/-2 μm) to allow only the first-order diffracted focus to reach the sample. The measured FWHM of the x-ray spot is 150 nm. The Scanning Transmission X-ray Microscope (STXM) provides imaging NEXAFS analysis of samples in transmission at atmospheric pressure. The transmission geometry is the most efficient use of photons for an absorption spectrum, well suited to radiation-sensitive organic samples. Circularly polarized photons have been generated and used for imaging domains at the L edge in Fe, Ni, and Co magnetic films. The Scanning Photo-Electron Microscope (SPEM) provides imaging XPS and NEXAFS analysis of sample surfaces in a UHV environment. Here the sample is stationary during imaging and the zone plate is rastered in the illumination field to carry the focused spot across the sample surface. NEXAFS capability is included by means of a UHV flexure to carry the zone plate 0.5 mm longitudinally to retain the focus condition as the photon energy changes. Different photon energies require different zone-plate/OSA combinations with different built-in focal lengths. So far, we have operated the microscope with three zone-plate/OSAs aligned in this way. SPEM allows us to perform quantitative XPS measurements of atomic concentration and core-level chemical shifts over regions of the sample surface as small as the spatial resolution of the zone-plate lens. The

zone-plate array can be lowered out of the beam, and the sample surface can be observed with a magnifying video system, allowing visible fiducial marks on the sample to be used to position the region of interest within the 100- × 100-μm range of the scan stage. XPS spectra are measured with typical photo-peak count-rates of 70,000 counts/s (Au 4f at 420eV photon energy).

BRANCHLINE 7.3.1.1 uses Beamline 7.3.1's single spherical grating, which provides monochromatic light to two endstations, photoemission electron microscopy (PEEM) on Branchline 7.3.1.1 and micro x-ray photoelectron spectroscopy (μXPS) on Branchline 7.3.1.2. The PEEM beamline accepts 2 mrad of horizontal aperture and uses a 1-m-long horizontally deflecting elliptical mirror to demagnify the source at 10:1 onto the sample (Fig. 3). The grating images at a monochromatic demagnification of 1:1, so with a source size of 250 μm (horizontal) × 22 μm (vertical), we should see a monochromatic image of 25 × 22 μm in the endstation.

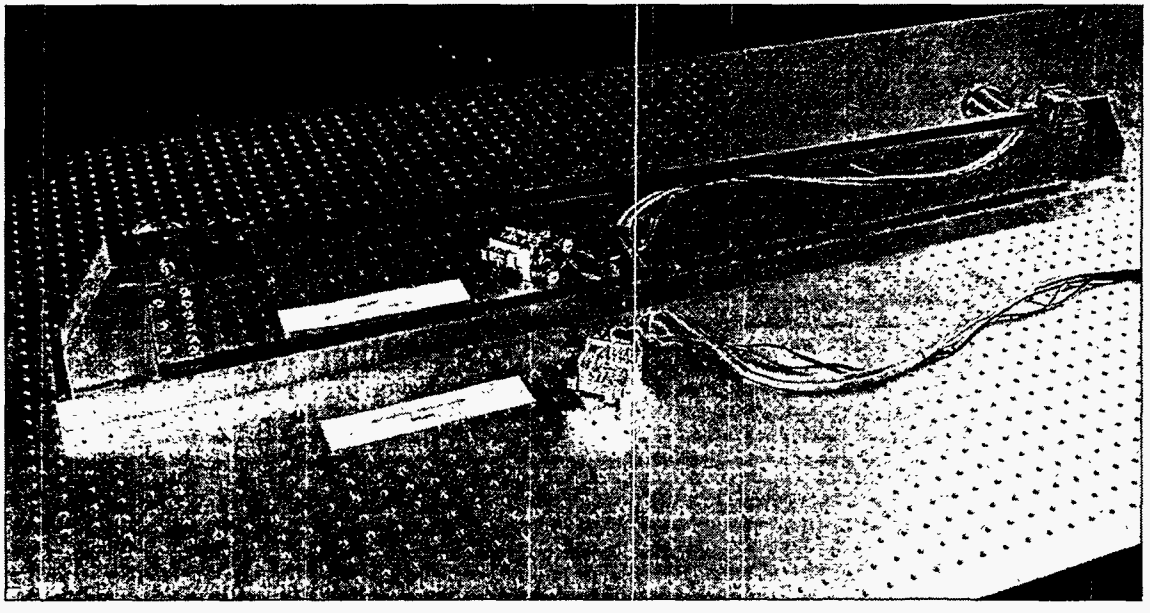

Figure 3. Photograph of the 1-m-long PEEM mirror alongside a smaller Kirkpatrick-Baez mirror for the μXPS experiment.

The measured horizontal width is 30 μm FWHM, and this has to be compared to the 40-mm width of the beam 1.85 m upstream before focusing! This extreme focusing is only possible with elliptical surfaces, and a 1-m-long mirror with the required ellipticity is well beyond the state of the art for conventional optical grinding. We therefore chose to produce the mirror by controlled bending of an initially flat surface by the application of unequal couples to a nonuniform-width beam. This proved to be a challenging project, but as evidenced by the superb focus, we now have developed a very powerful and widely applicable mirror manufacturing method. The 7.3.1.1 PEEM beamline requires as high a flux density as possible in a 20- or 30-μm spot size to enable high-resolution XMCD microscopy to be conducted with reasonable imaging times. Under a cooperative research and development agreement (CRADA) with IBM Almaden, we have constructed a high-voltage PEEM for magnetic imaging using circularly polarized light (Fig. 4). The beamline and PEEM are now complete, and the first magnetic surface images have been recorded. The microscope should be capable of 20-nm resolution, and therefore getting sufficient flux into a 20-nm sample element to correspond to reasonable MCD imaging times is a major challenge. The beamline is performing near its design flux density, so the remaining challenge is to fully commission the microscope to achieve its design resolution target. The 30-kV PEEM

microscope design paid particular attention to thermal and mechanical stability and has several novel features, such as interchangeable back focal plane apertures, direct-conversion imaging, and a V-lens mounting system. The microscope also has a sophisticated sample transfer and preparation system.

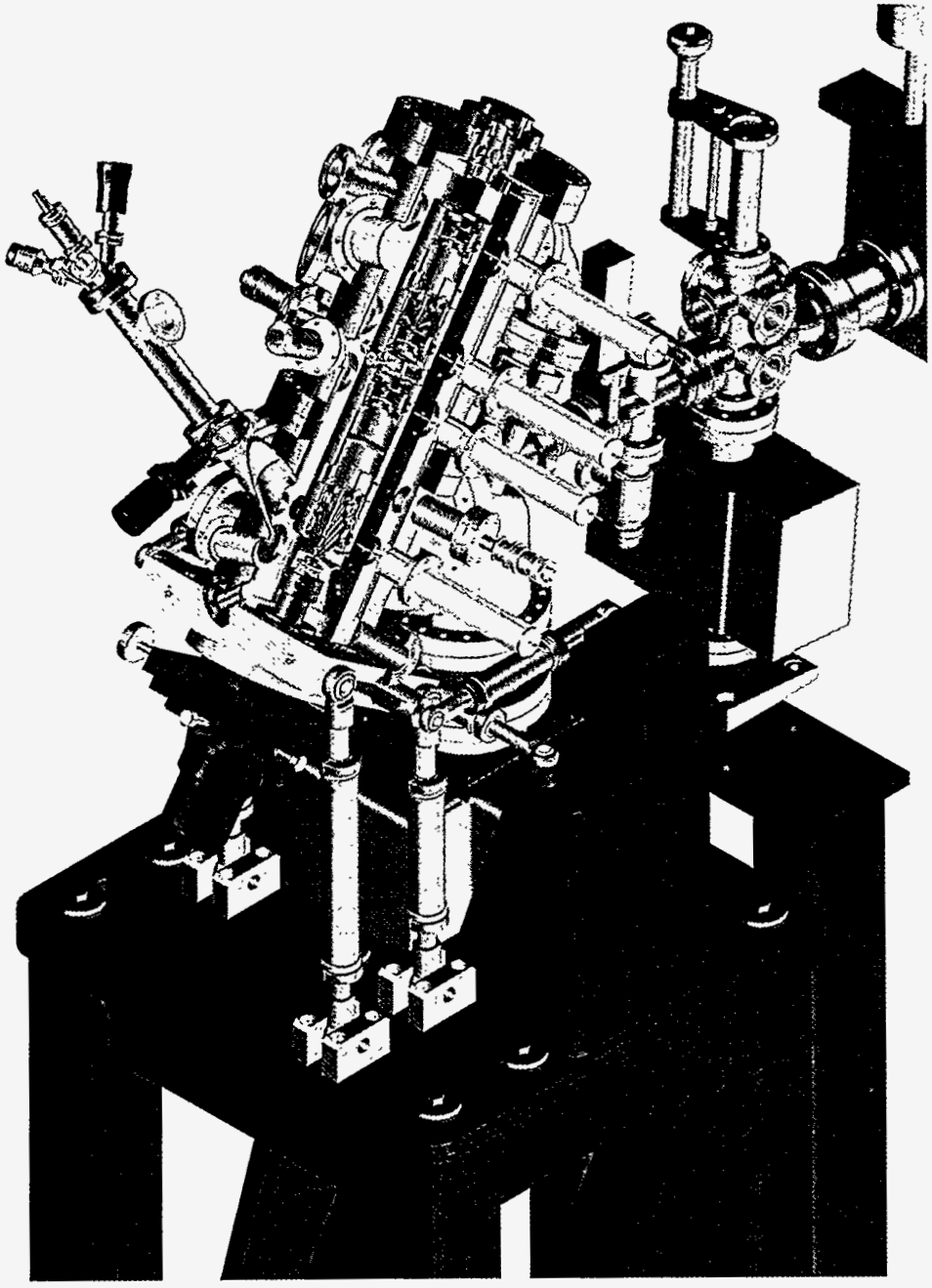

Figure 4. Three-dimensional engineering drawing of the PEEM microscope.

BRANCHLINE 7.3.1.2 is designed for x-ray photoelectron spectroscopy with a spatial resolution of 1 μm (μ-XPS), with tunable photon energies up to 1.3 keV. It uses a horizontal branch mirror just downstream of the Beamline 7.3.1 grating to deflect and focus 0.2 mrad of aperture to the monochromatic focus position of the grating. A pair of bilaterally adjustable slits defines a 20 (v)- × 40 (h)-μm object, and a pair of Kirkpatrick-Baez elliptically bent mirrors is

used to demagnify to a 1-μm focus. These mirrors are particularly challenging, as they have to be inside the main experimental end chamber to achieve the required 20 and 40:1 demagnifications, and they have to be integrated with the sample interchange system, electron analyzer, neutralizer, ion gun, and other surface science equipment. The system now works routinely at 1-μm spatial resolution and, as importantly, wafer samples can be introduced into the chamber and optically refiducialized to the same accuracy. Combined with laser interferometric recording of the sample puck location, we can drive the sample over its 50- × 50-mm size to micron absolute accuracy. This system was developed in collaboration with Intel and Applied Materials and is being applied to a wide range of semiconductor manufacturing issues.

BEAMLINE 7.3.3 is being developed for microfocus x-ray diffraction/spectroscopy and ultra-fast time-resolved x-ray diffraction/spectroscopy. The beamline consists of a grazing-incidence toroidal mirror that collects 3 × 0.2 mrad of bending magnet radiation and focuses it to a ~300- × 200-μm (FWHM) spot in the experimental x-ray hutch. The 0.7-m-long silicon mirror is shown in Figure 5 below. This mirror is bent to the correct major radius of about 3 km by means

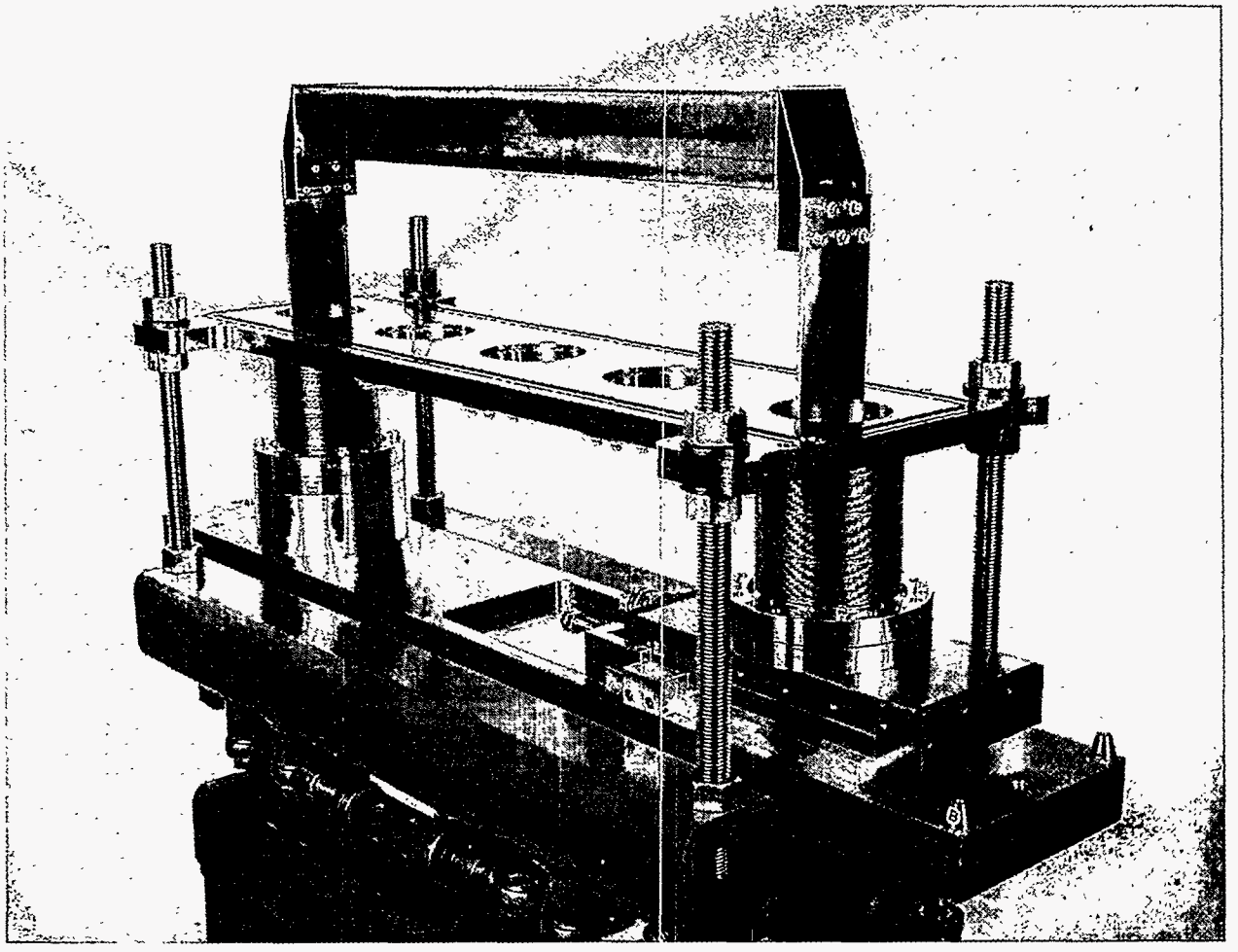

Figure 5. Photograph of the 0.7-m-long bendable mirror for Beamline 7.3.3.

of the flexural springs that support the ends of the mirror. These springs are driven together at the base support structure and provide the necessary force for the mirror bending. The operating angle is 5.4 mrad, which with the platinum coating, allows for useful flux up to 15 keV. There are two

experimental stations in the x-ray hutch. The first experiment station (Roger Falcone, Univ. of Calif., Berkeley) combines x rays with a femtosecond laser system and time-resolved detectors. X-ray diffraction and absorption are utilized as probes of laser-induced phase transitions. The second experiment station is under construction and is designed to carry out x-ray diffraction and x-ray absorption on micron-sized samples. In operation, the grazing-incidence toroidal mirror described above images the source onto some slits at the hutch entrance. These slits provide a source of adjustable size for some Kirkpatrick-Baez (K-B) mirrors that refocus this secondary source onto the sample with spot sizes in the micron range. As the secondary source is adjustable in size, flux can be traded for spot size on the sample. A new custom goniometer with a large-area x-ray CCD is to be installed as the endstation. The operational procedure for carrying out x-ray microdiffraction is to be the same as that established on the development beamline, 10.3.2.

BEAMLINE 10.0.1 is designed for high-resolution spectroscopy in the 20–350 eV range. The beamline will reuse many of the components, including the high-resolution spherical-grating monochromator, from beamline 9.0.1 (which was decommissioned in March, 1998) to provide the high spectral resolution ($E/\Delta E \geq 10{,}000$) and photon flux ($\geq 10^{12}$ photons/s) required by the users. A full-length 10-cm-period undulator built at the ALS will be installed during the spring 1998 shutdown to provide a photon source for the beamline. The horizontal focusing optics from beamline 9.0.1 will be replaced to produce small beam spot sizes (100–400 μm) for the two side branches of the beamline while providing a highly collimated beam with a width of approximately 1 mm for the central branch. Two projects funded by the DOE Scientific Facilities Initiative necessitated the construction of this new undulator beamline: (1) electron spectroscopy of highly correlated materials, and (2) high-resolution atomic, molecular, and optical spectroscopy. Endstations for both projects are under construction and will be permanently positioned at the end of Beamline 10.0.1.

BEAMLINE 10.3.2 is being used in collaboration with the Center for X-ray Optics (CXRO) and Earth Sciences Division (ESD) as the x-ray optics development beamline for the techniques of micro x-ray diffraction and micro x-ray absorption. The beamline arrangement is a 4-crystal monochromator that can pass both white and monochromatic light along the same axis, followed by a pair of K-B mirrors that have been used to image the bending magnet source to spot sizes down to 0.8 μm (FWHM) on the sample. The x-ray microprobe can be switched from white light to monochromatic light whilst illuminating the same micron-sized sample.

Figure 6 shows the Laue pattern from a single aluminum grain in an aluminum wire on a silicon semiconductor wafer recorded in 0.5 seconds. The dominant symmetric pattern is from the silicon substrate, but the asymmetric pattern indicated and indexed is that of the micron-sized aluminum grain of interest. The interest is one of determining the strain within the aluminum grain, as this will provide some insight into the electromigration problem that significantly affects chip reliability in the semiconductor industry. The strain can be measured if one accurately knows the d spacing of the various Laue spots. By switching to monochromatic light and determining the angle of the Laue spot, an accurate measure of the d-spacing can be obtained.

In the case of micro x-ray absorption, the technique is to carry out an elemental scan with either white or monochromatic light, followed by x-ray absorption spectroscopy on the area of interest. Figure 7 shows the micro x-ray absorption spectrum from a live fungus root contaminated with zinc. The elemental map indicates small regions (<5 μm) of high zinc concentration. The absorption spectra show the zinc K edge from the fungus and that from a zinc oxalate standard.

They appear to be very similar, which suggests that zinc oxalate is important in the mechanism of contaminant uptake, retention, or conversion in this fungus metabolism.

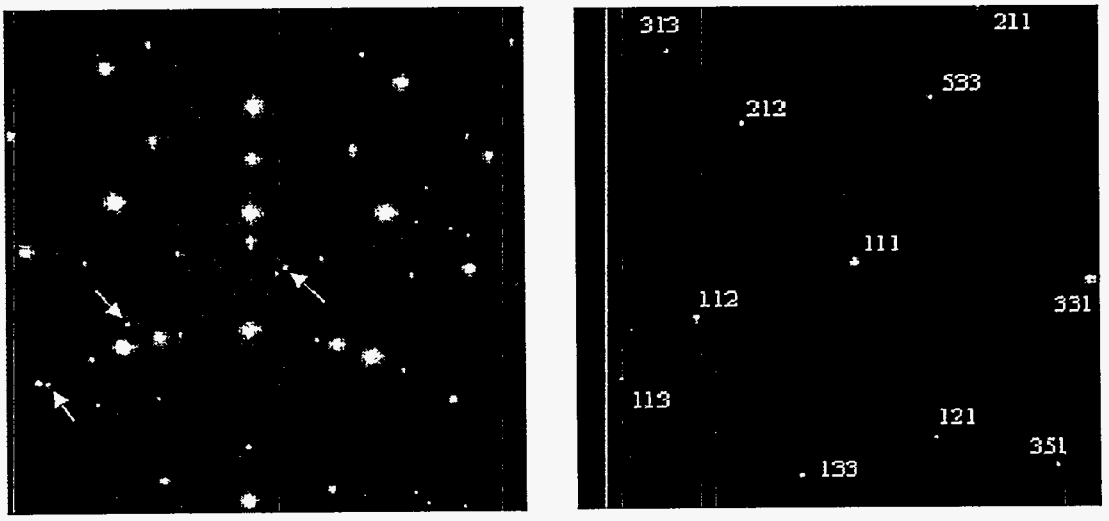

Figure 6. Laue diffraction pattern of a single aluminum grain on a silicon substrate (left, sample provided by Intel). Arrows indicate three of the aluminum diffraction spots. Digitally subtracting the dominant silicon spots shows the entire aluminum Laue pattern that can then be indexed (right).

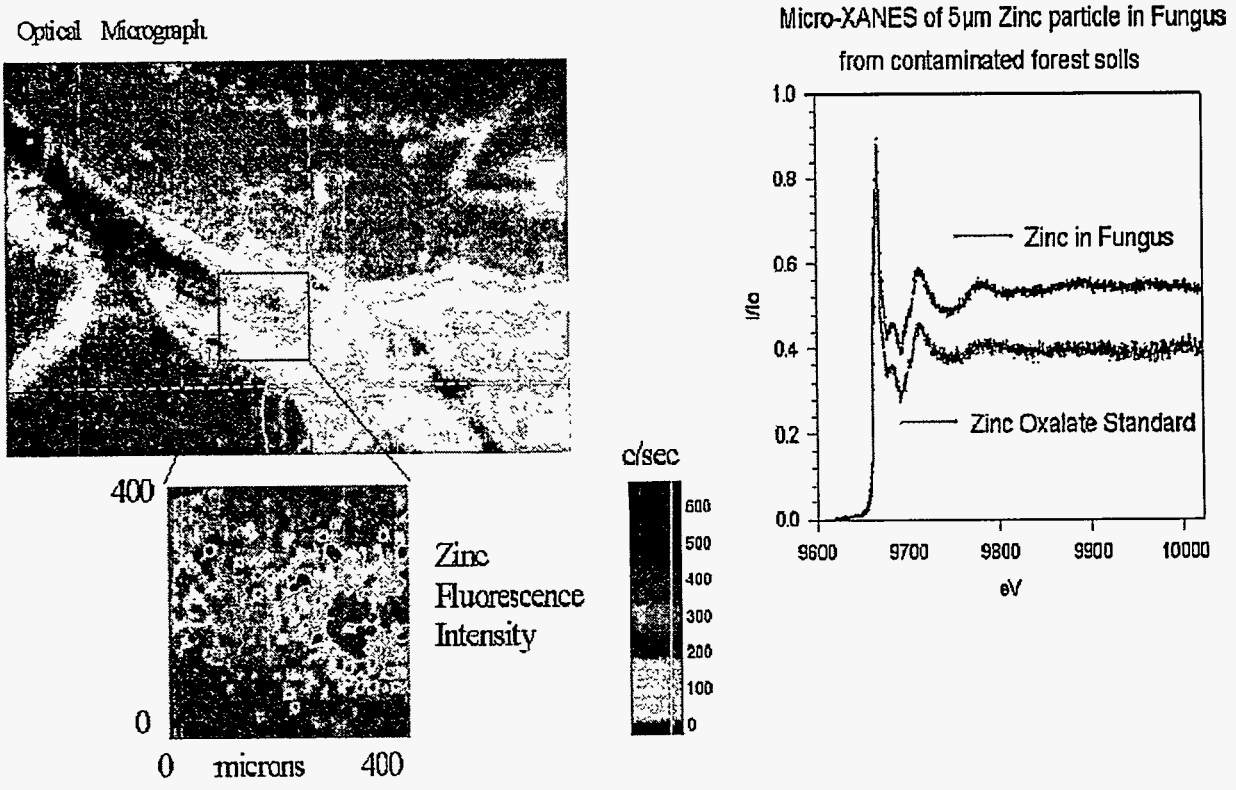

Figure 7. Optical micrograph of fungus in its natural state (top left) with Zinc elemental fluorescence map (lower left). Also included are the near-edge zinc XAS spectra of the high-concentration zinc particles and of a zinc oxalate standard.

Accelerator Physics

Reported by Alan Jackson

For the majority of the ALS user community, 1997 could be characterized as a year of electron-beam stability. The previous year's efforts to master the intricacies of the transverse and longitudinal multibunch feedback systems, together with better control of the temperatures of the low-conductivity cooling water and storage-ring tunnel air, paid immense dividends in the stability of the beam during a fill. From this beginning, the Accelerator Physics Group embarked on the next level of stability—improving the undulator feed-forward system that ensures that the electron beam remains stable as the undulator gaps are changed at the user's request, fine tuning the electron orbit for best transmission of the photon beams to the experimental stations, and ensuring that the beam comes back to the same place, fill after fill, day after day.

To a large extent, as we describe below in the section on Storage Ring Setup, this goal has been achieved. However, since at the micron level we do not have a stable platform, we find it necessary to repeat our setup procedures at regular intervals—typically each week. Experimenters are certainly taking advantage of the enhanced stability by improving the resolution and/or reducing sampling times. In doing so, they are discovering small (but, to some experiments, significant) photon beam motion in the frequency range between 1 and 10 kHz. The Accelerator Physics Group is currently working with several user groups to identify, and hopefully eliminate, the sources of this motion.

Advances have also been made toward delivering higher quality beams for the "single-bunch" user community. During normal multibunch operation, we now offer a fill pattern known as the "camshaft fill." In this pattern, we fill 288 sequential rf buckets to about 1.3 mA/bunch (to a total of 380 mA), plus a single bunch at 20 mA that sits inside a string of 40 empty rf buckets. While this is useful for some experiments, we still operate in two-bunch mode for the traditional time-of-flight spectroscopy experiments. These users require that the unpopulated buckets be truly empty. This has been achieved in the ALS (as at other facilities) by taking advantage of the differences in the betatron oscillation frequency between bunches with different charge densities. Transverse kickers, driven at the discrete frequency of the low-charge bunches, drive out the unwanted electrons without affecting electrons in the two highly populated bunches. In this way, the bunch purity has been improved from about 1:100 to better than 1:10000. Also, the currents that can be accumulated in a single bunch, limited by the transverse mode-coupling instability, have been increased from around 20 mA to 35 mA by the use of active feedback.

In addition to the work aimed directly at improving the quality of beams for users, the Accelerator Physics Group is engaged in a series of investigations to better understand the performance characteristics of the storage ring. As described below, these include investigations of beam lifetime, fast beam motion, reduction of the horizontal and vertical emittance, vacuum-vessel impedance, the fast beam-ion instability, and other non-linear beam dynamics in both transverse and longitudinal planes. Our group has also started work on a series of new initiatives:

- Designing a third-harmonic cavity system to lengthen the electron bunches (without increasing the energy spread of the beam), which will result in longer beam lifetimes.
- Meeting challenges associated with a new storage ring that is designed to have an emittance ten times smaller than that in the ALS (known internally as ALS-N).
- Developing methods for generating x rays in the 1-Å region of the spectrum with a pulse width of 100 fs FWHM.

ALS Storage Ring Setup

The operational parameters of the ALS can be varied over a wide range to meet the needs of the user. The ALS storage ring is capable of operating from 0.75 GeV to 1.9 GeV with almost any fill pattern utilizing from one to 328 rf buckets. The three most common modes of operation are 1.5-GeV multibunch, 1.9-GeV multibunch, and 1.9-GeV two-bunch (4 weeks/year). The multibunch pattern is typically 288 contiguous bunches with a gap for ion clearing. Often one of the empty rf buckets can be filled to high current to create pseudo-one-bunch operation ("camshaft" mode). Substantial progress was made in 1997 toward automating the setup; however, it is still a very machine-time-intensive activity. A full machine setup takes approximately eight hours, which is roughly one-third of the time allotted for accelerator physics studies.

General Storage Ring Setup

Reported by Greg Portmann

Many parameters have to be properly set in order for the storage ring to operate as designed. The storage-ring magnet lattice consists of 36 bends, 48 sextupoles, 72 quadrupoles, 4 skew quadrupoles, 94 horizontal correctors, and 70 vertical correctors. The other major systems include the rf system, the longitudinal-feedback system, and the transverse-feedback system. The main beam diagnostics are the 96 arc-sector beam-position monitors (BPMs), the 20 straight-section BPMs, the tune-measurement system, and the transverse and longitudinal beam-profile monitors (Beamline 3.1). To a large extent the setup and operation of the ALS storage ring has been automated. The setup process consists of accurately setting the parameters in the sequence shown in Figure 2-1. Some steps in the process require iteration.

Special attention was given to the orbit in 1997. A particular orbit, known as the "golden orbit," was defined and then maintained all year. The criteria for defining the golden orbit are the following. First, the orbit is aligned to the center of the QF and QD magnet families. This minimizes the dispersion caused by going off-center in these magnets. Using the electron beam, the quadrupole centers can be measured to the 50-μm level. Second, in order to steer the photon beams down the beamlines, local orbit perturbations (typically displacements of about 100 μm and angles of 30 μrad) are added to the ideal orbit. Lastly, in the straight sections with small-gap vacuum chambers, the optimal orbit is the position that produces the maximum lifetime. Correcting back to the golden orbit every setup has essentially eliminated user requests for local orbit correction.

A simple local-steering feed-forward algorithm to compensate for field errors that change as the insertion device gaps are moved has proved to be extremely effective. The rms orbit distortion due to gap changes after generating a feed-forward table is typically < 10 μm. The difficulty with this method is that the feed-forward tables are strongly orbit dependent, so they need to be regenerated at every setup. Since each table takes about 15 minutes to generate, we are considering replacing this compensation method with one that relies on real-time closed-orbit feedback.

The setup and operation of the ALS storage ring are done using Matlab, a matrix-manipulation language. By connecting Matlab to the ALS control system, the large number of built-in functions for numerical methods in Matlab immediately become available for accelerator optimization. Automating the operation of the storage ring using this one application has improved orbit repeatability considerably by maintaining tight control of the many potential sources of error, such as magnet hysteresis. This has also reduced the time it takes to refill the storage ring and has removed some of the human errors that occasionally creep into day-to-day operation.

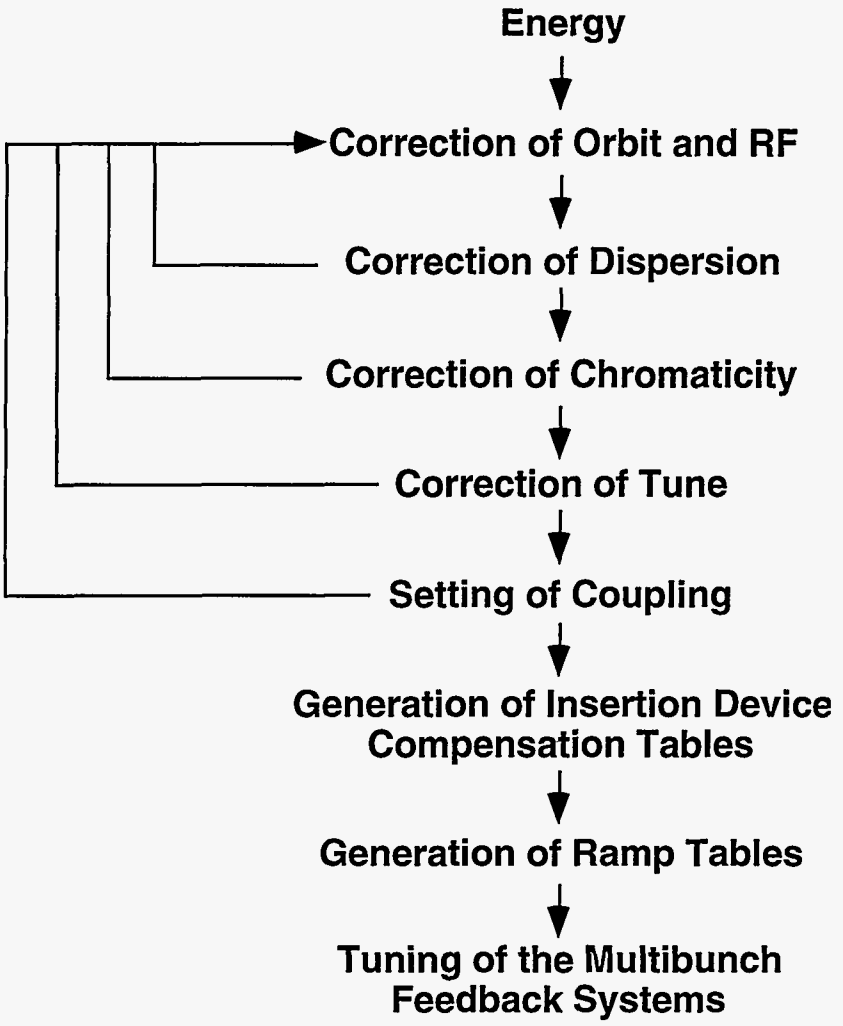

Figure 2-1. Canonical form of the storage ring setup process.

Two-Bunch Setup

Reported by John Byrd

Some synchrotron light users require single pulses of light spaced by at least several hundred nanoseconds. To satisfy this community, the ALS operates in a two-bunch mode about four weeks each year. In this mode, the ALS is filled with two bunches, diametrically opposite in the ring with 328-nanosecond separation. It is also important to the experiments that there be no parasite bunches in the ring. To optimize the machine performance, we are faced with the challenges of reaching high single-bunch current with reasonable lifetime while maintaining the purity of the two-bunch fill.

One limit to high current is a single-bunch effect known as the vertical mode-coupling instability (VMCI), driven by the broadband transverse impedance of the vacuum chamber. The effect is characterized by a sudden increase in vertical oscillations, resulting in a large increase in the effective vertical beam size and corresponding decrease in the brightness and stability of the beam. For the ALS, the threshold of this instability is presently about 16 mA/bunch. To achieve higher currents, we can damp the instability by increasing the lattice chromaticity (variation of betatron tune with electron momentum) from around 0.5 to 5. However, the higher chromaticity lowers the

energy acceptance, thereby increasing the loss of electrons from Touschek scattering, and lowering the lifetime. To avoid a lower lifetime, we have configured the vertical coupled-bunch feedback system to operate in a single bunch mode and tuned it to successfully reach > 30 mA/bunch, thereby doubling the current as compared to that high-chromaticity approach.

The second challenge in two-bunch operation is to achieve high bunch purity. The dominant mechanism through which parasite bunches are filled operates during the injection process. Imperfect bunching of the electron beam in the linac gun leads to a parasite bunch 8 nanoseconds from the main bunch with a charge as large as 1% of the main bunch. A more subtle mechanism, bunch-bunch diffusion, also comes into play (see the description in Figure 2-2). Rather than minimize the parasite filling during injection (which requires lowering the overall injection rate), we have developed a technique for cleaning out the parasite bunches immediately following injection. This technique takes advantage of the current-dependent vertical betatron frequency shift due to the transverse broadband impedance. At around 20 mA/bunch, the vertical betatron frequency has shifted about 15 kHz from the nominal frequency. This provides a selection mechanism for exciting only the low-current parasite bunches. We excite oscillations of the parasite bunches, utilizing the vertical kickers of the multibunch feedback system, to an amplitude large enough for them to be removed by a vertical scraper. Using this technique, we have reached purities (proportion of electrons in parasite bunches) of 10^{-4} and better.

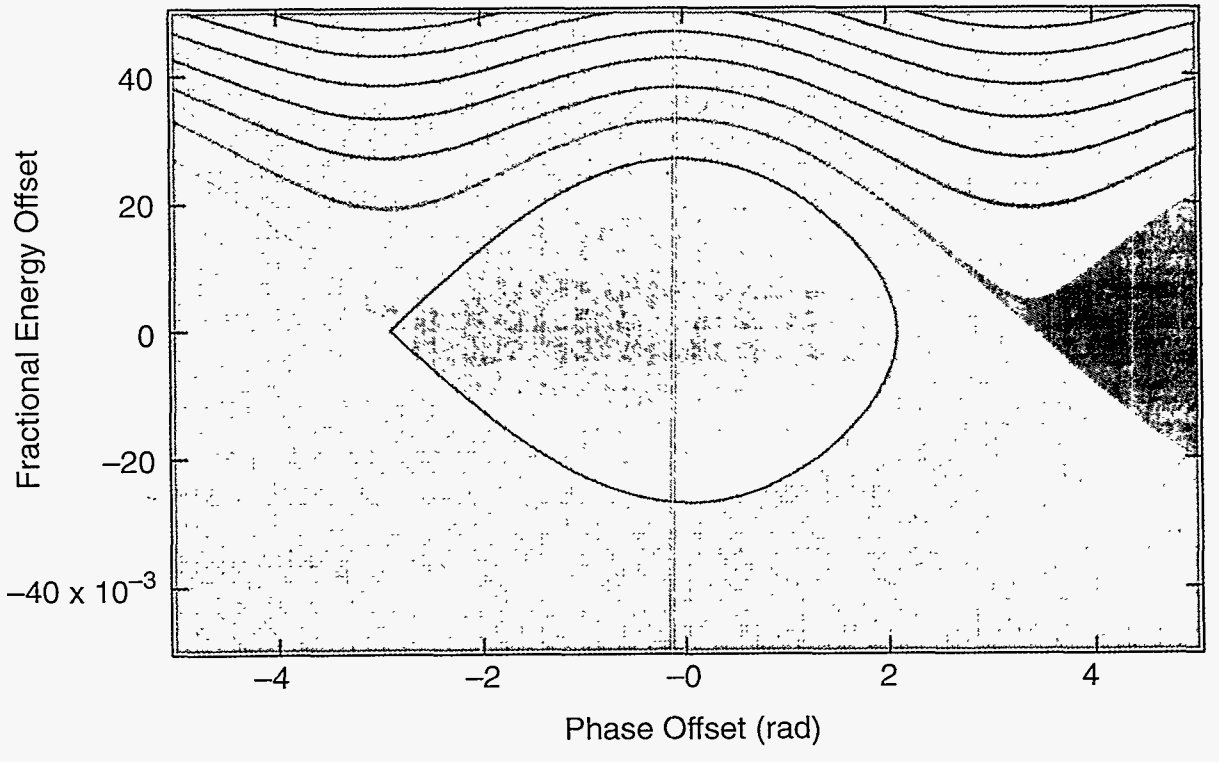

Figure 2- 2. Particle tracking with radiation damping. Ordinarily only the central dark-green region would be stable; electrons scattered out of it would be lost. With radiation damping, such electrons can be captured by the tail of the next bunch (brown, right side), where they are trapped in stable synchrotron orbits.

ALS Storage Ring Characterization

Reported by Greg Portmann

One of the more important user issues in 1997 was electron-beam stability. The stability requirement for the ALS has been steadily growing as each new beamline comes on line and as the more experienced users fine-tune their beamlines. Most ALS users are concerned with orbit motion below 100 Hz. However, beamlines like the infrared line required orbit stability (transverse and longitudinal) up to tens of kHz.

The electron-beam size in an ALS storage-ring straight section is approximately 250 μm horizontally and 16 μm vertically at 1.9 GeV. This small size poses difficult stability requirements for the storage-ring orbit—typically, ALS users would like orbit stability on the order of 10% of the beam size. Fortunately, the ALS storage ring inherently meets this requirement in the 1-Hz to 1000-Hz region. However, maintaining 25-μm horizontal and 1.6-μm vertical stability over the length of a fill (four hours) is very difficult without an orbit-feedback system.

Figure 2-3 shows the orbit and insertion-device gap motion over the length of a fill on March 26, 1998, a typical day. The "fast" orbit motion is only a few microns and the orbit "glitches" caused by errors in the feed-forward system are also only 1–5 μm, with one exception. At approximately 18.8 hours the horizontal orbit changed by about 40 μm because the insertion device in sector 5 (the wiggler) moved to a 14-mm gap. (The wiggler is usually kept at a fixed gap during user shifts to prevent this problem.) The dominant orbit distortions during this fill are slow temperature drifts, ±20 μm horizontally and ±10 μm vertically. Great effort has been spent stabilizing both the storage-ring air temperature and the LCW temperature. To a large extent, this effort has mitigated the orbit drift due to temperature; however, some days are better than others. To eliminate the problem, we are investigating a slow (but real-time) orbit-feedback system. Currently the limiting factor with orbit feedback is the positional stability and current dependence of the BPMs used for feedback.

In Figures 2-4 and 2-5 we take a closer look at the "fast" orbit stability of the storage ring electron beam. Figure 2-4 shows the power spectrum measured from 1 Hz to 300 Hz at insertion-device beam-position monitor (IDBPM) #2 in sector 12 during a 1.9-GeV user shift. The integral of the power spectrum, the rms displacement, amounts to 2.5 μm horizontally and 1.4 μm vertically. The shape of the power spectrum compares quite well with the shape of the ground-motion power spectrum calculated when including the structural bending modes of the ALS girders. Figure 2-5 shows a waterfall display of the power spectrum over eight hours. The change in rms displacement over the eight-hour period is very small; however, there is one anomalous peak that appears to migrate (usually in the 90-Hz to 300-Hz region). The cause of this peak is being investigated.

Very slow orbit motion (on a time scale of days) can cause misalignment of the photon beam through the photon-beamline optics. As shown in Figures 2-6 and 2-7, the day-to-day repeatability of the orbit can be quite good—remember that no orbit correction is done after the setup has been completed. The solid line in the plot shows the data from the upstream IDBPM, and the dashed line that of the downstream IDBPM, for each of the insertion device straight sections. Typically, the orbit stays within ±150 μm horizontally and ±50 μm vertically over a week's time. However, the ALS orbit clearly has good days and bad days when considering stability over such long time periods. Table 2-2 summarizes orbit stability for different time durations. For frequencies below 1 Hz, it is very difficult to assign one number to the orbit stability when considering an entire year

because the day-to-day fluctuations can be reasonably large. The numbers in this table are conservative estimates.

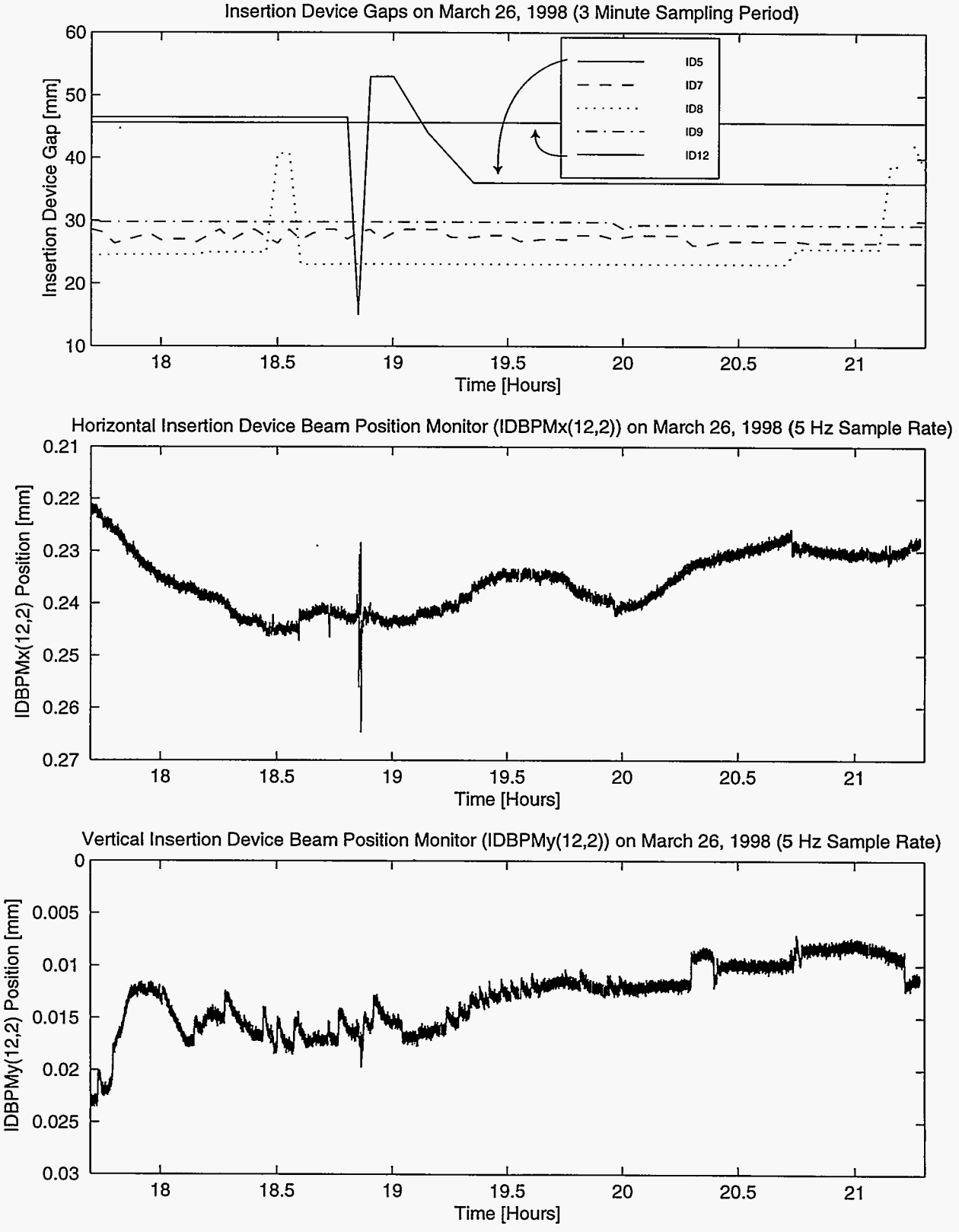

Figure 2-3. Plot of orbit motion over the course of a typical day shows the kind of long-term stability achievable with feedback.

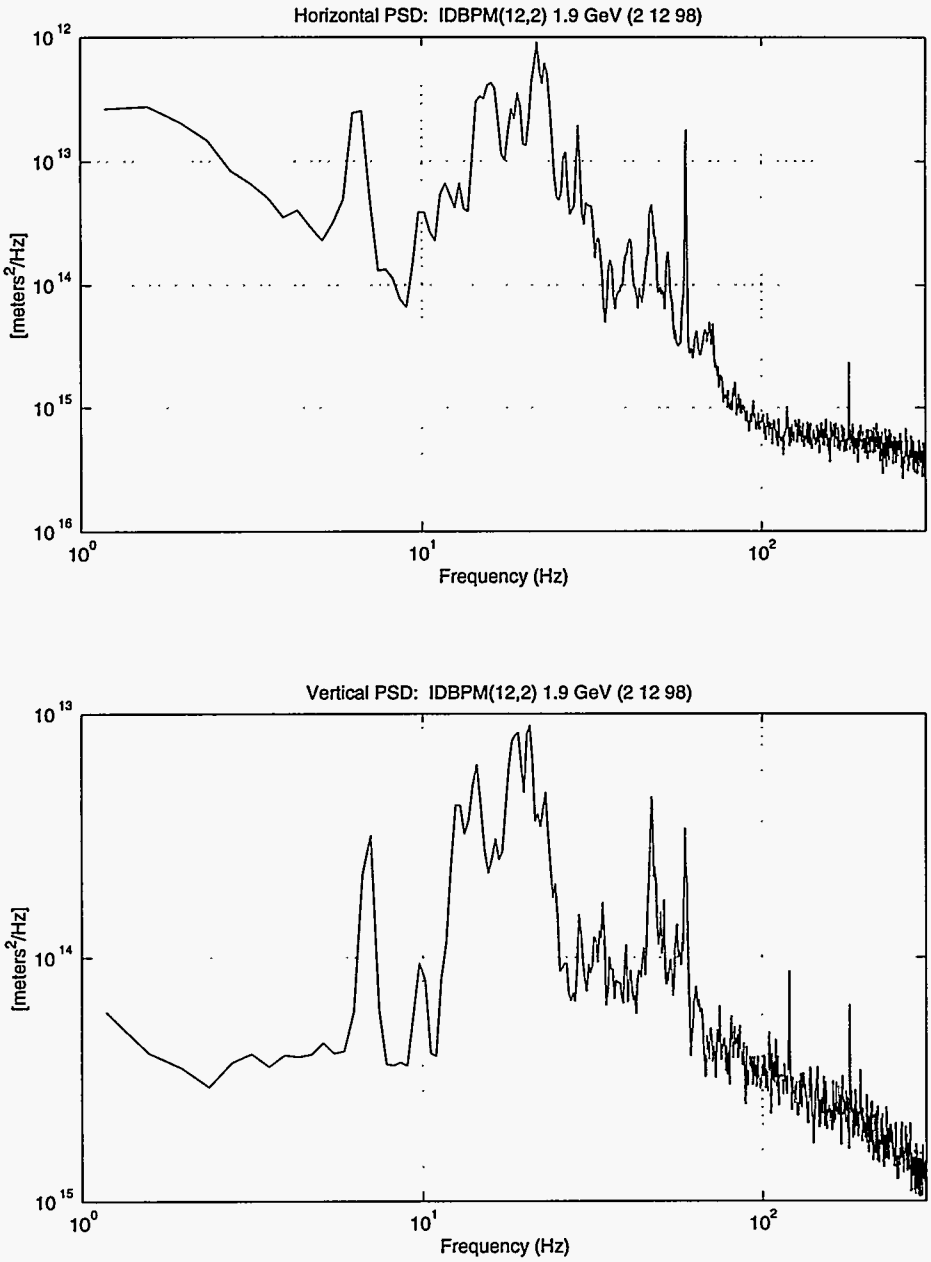

Figure 2-4. Power spectrum at insertion-device beam position monitor #2, sector 12.

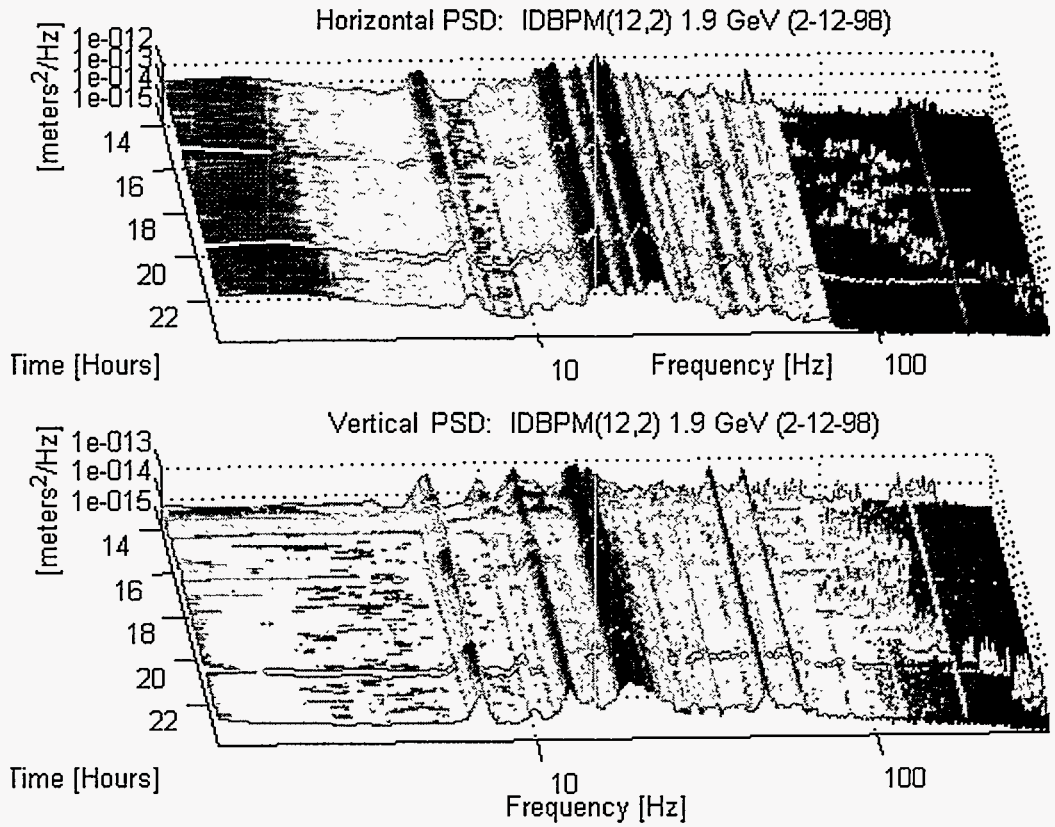

Figure 2-5. "Waterfall display" of the power spectrum shown in Figure 2-4 over an 8-hour period.

Table 2-2. ALS Storage Ring Stability.

"Frequency" Range	Magnitude[1]	Dominant Cause	Cure
Months	Difficult to measure	1. ALS floor setting 2. Seasonal temp. variation	Storage ring setup
Setup to setup repeatability	±200 μm Horizontally ±75 μm Vertically	1. Magnet hysteresis 2. Temperature fluctuations 3. Component heating between 1.5 and 1.9 GeV	Orbit correction
Days	±150 μm Horizontally ±50 μm Vertically	1. Temperature fluctuations	Orbit correction and/or improved temp. regulation
Length of a fill (4 Hours)	±50 μm Horizontally ±25 μm Vertically	1. Temperature fluctuations 2. Feed forward errors	Slow orbit feedback and/or improved temp. regulation
Minutes	5 to 10 μm	1. Feedforward errors	Slow orbit feedback
1 to 300 Hz	1 to 3 μm rms	1. Ground vibration	"Fast" orbit feedback
> 300 Hz	To be determined	To be determined	To be determined

[1] These are typical (and approximate) numbers that have been observed over the last year. The actual orbit fluctuations may vary depending on the day or new environmental conditions that arise. The orbit measurements were made at the straight-section beam-position monitors (IDBPMs).

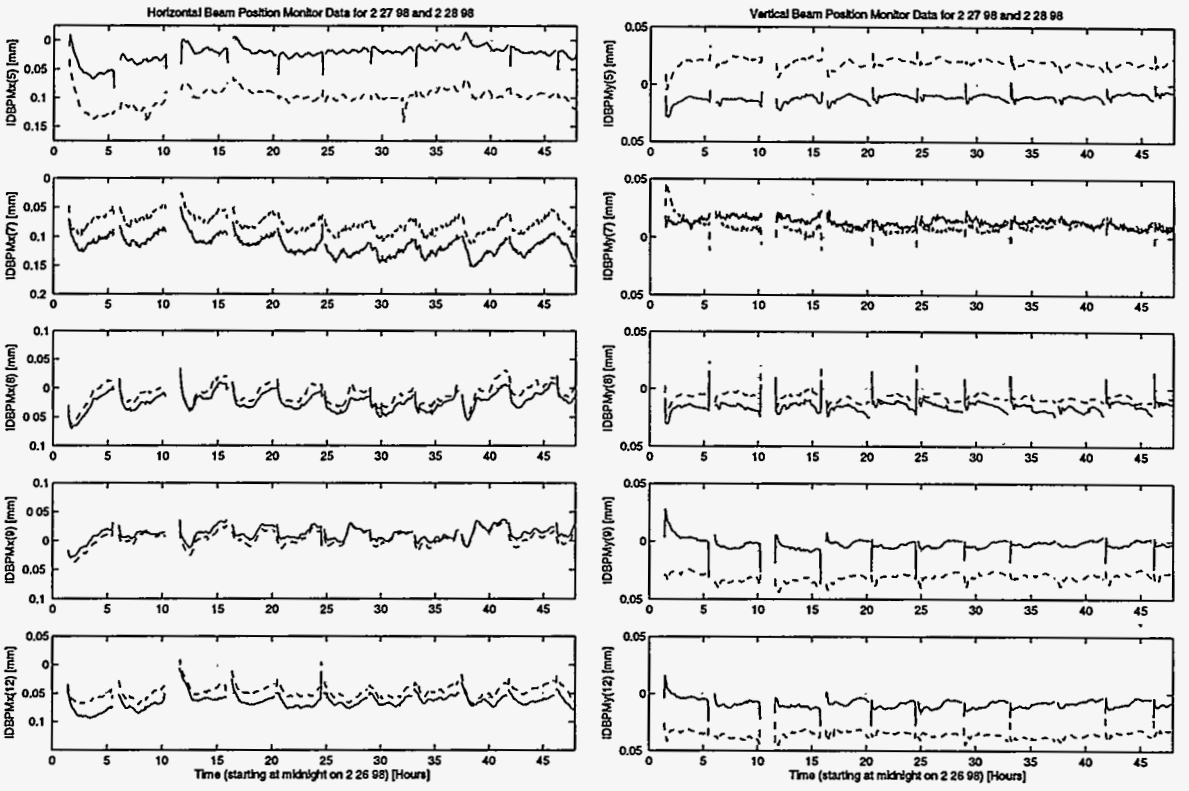

Figures 2-6 (left) and **2-7**. Orbit stability. Measurements of the beam position upstream (solid line) and downstream (dashed line) of insertion devices in the ALS storage ring show that the day-to-day reproducibility of the electron orbit can be quite good. Horizontal position is shown in Figure 2-6 at left, vertical position in Figure 2-7 at right.

Lifetime Measurements

Reported by Winfried Decking

The lifetime of the stored beam is one of the more important parameters of ALS storage-ring operation. For several reasons a long lifetime is desirable:

- The users have longer time spans in which to set up and run their experiments.
- A slower decay of the current leads to lower thermal variations in the vacuum chamber and beamline optics components.
- Higher average stored-beam current means, on average, more photons for the experimenters.

Several experiments were performed to obtain a better understanding of the effects that limit the lifetime in the ALS. The results of these measurements allowed us to differentiate between the various effects and pointed towards possible solutions to improve the lifetime.

The lifetime in an electron storage ring is usually determined by the following effects: the quantum lifetime (τ_q), elastic (τ_{el}) and inelastic scattering (τ_{inel}) of electrons by the residual gas atoms, scattering of electrons within the bunch (Touschek effect) (τ_{tou}), and trapping of charged particles in the beam potential (τ_{ion}). The total lifetime is given by:

$$\frac{1}{\tau_t} = \frac{1}{\tau_q} + \frac{1}{\tau_{inel}} + \frac{1}{\tau_{el}} + \frac{1}{\tau_{tau}} + \frac{1}{\tau_{ion}}$$

The functional dependencies of the lifetime effects on different machine parameters are as follows.

Quantum Lifetime:

$$\frac{1}{\tau_q} = \frac{1}{\tau_D}\frac{\Delta_{x,y,s}^2}{\sigma_{x,y,s}^2}\exp\left(-\frac{\Delta_{x,y,s}^2}{2\sigma_{x,y,s}^2}\right)$$

Elastic Scattering:

$$\frac{1}{\tau_{el}} = C_{el}\frac{1}{E^2}\left(\langle P\beta_x\rangle\frac{\beta_x}{\Delta_x^2} + \langle P\beta_y\rangle\frac{\beta_y}{\Delta_y^2}\right)$$

Inelastic Scattering:

$$\frac{1}{\tau_{inel}} = C_{inel}\langle P\rangle 1n\left(-\frac{1}{\Delta_s} + \frac{5}{8}\right)$$

Touschek Lifetime:

$$\frac{1}{\tau_{tou}} \approx C_{tou}\frac{1}{E^3}\frac{I_{bunch}}{\text{Volume}\,\Delta_s^2} f\left(\Delta_s\sigma_x', E\right)$$

In these equations, $\Delta_{x,y}$ is the transverse aperture, $\beta_{x,y}$ the β-functions, and $\sigma_{x,y}$ the beam size at the position of the aperture. σ_s is the width of the longitudinal particle distribution, and Δ_s the longitudinal acceptance of the storage ring. The longitudinal acceptance can be determined by the size of the rf bucket or by the dynamic acceptance.

The damping time τ_D is a known function of the storage ring parameters (between 13 and 17 ms at the ALS). C_{el} and C_{inel} depend on the constitution of the residual gas. Assuming that the gas consists of 100% nitrogen, $C_{el} = 38.88$ GeV^2/mbar h, and $C_{inel} = 4.2 \times 10^6$/mbar h at 300 K. We will refer the gas pressure P to this "standard" atmosphere. <P> is the average gas pressure around the ring and <P $\beta_{x,y}$> is the average product of the local pressures and β-functions around the ring. The gas pressure (and distribution) varies with total beam current because of desorption effects:

$$\langle P\rangle = \langle P_0\rangle + \frac{dP}{dI} I_{total}$$

where *dP/dI* is the gas desorption coefficient and I_{total} is the total beam current.

The quantum lifetime is only important for transverse apertures smaller than ≈ 6 σ, which corresponds to 1.2 mm horizontally and 0.08 mm vertically (for standard 1.5-GeV operating conditions) at the position of the scraper.

When electrons scatter within a bunch, they may transfer enough momentum from transverse oscillations into longitudinal motion, to be outside the momentum acceptance of the storage ring. This effect is proportional to the electron density within a bunch. Assuming a flat beam, so that the main contribution to the velocity spread comes from horizontal motion, gives the Touschek lifetime shown above. In this equation, I_{bunch} is the bunch current and Volume is the bunch volume. The bunch volume varies around the ring, thus the Touschek lifetime has to be averaged around the ring. The function *f* varies slowly with Δ_s and σ_x'. For this investigation we only use the fact that τ_{tou} is inversely proportional to the bunch current.

Recent work at the ALS extended the classical one-dimensional theory to the general three-dimensional case, taking into account the velocity spread in all three dimensions. For standard ALS operating conditions, the new theory agrees with the classical one to within 10%.

Transverse Scraper Measurements

The quantum lifetime and the elastic-scattering lifetime directly depend on the available transverse aperture, which can be varied with beam scrapers. The dependency of the lifetime on the scraper position reveals information about the gas pressure at the beam position, the transverse beam sizes, and the limiting transverse aperture.

The Touschek and inelastic scattering lifetime depend only indirectly on the scraper position. Inserting a scraper can also reduce the longitudinal acceptance of a storage ring, which is the defining aperture for these lifetime effects. The scraper measurements were thus done at a low bunch current. This minimizes the contribution from the Touschek effect.

Results of several measurements with horizontal and vertical scrapers are shown in Figure 2-8. The measured lifetime as function of horizontal scraper position was fitted to the following curve:

$$\frac{1}{\tau}(\Delta_x)=\begin{cases} \text{const.} & \text{if } \Delta_x > A_x \\ \dfrac{1}{\tau_{tou+inel}} + C_{el}\dfrac{1}{E^2}\langle P\rangle\left(\langle\beta_x\rangle\dfrac{\beta_x}{\Delta_x^2}+\langle\beta_y\rangle\dfrac{\langle\beta_y\rangle}{\Delta_y^2}\right) & \text{if } \Delta_x < A_x \end{cases}$$

where $A_{x,y}$ is the real aperture of the storage ring. Exchanging x and y allows us to fit the lifetime for the vertical scraper position. As the real aperture of the storage ring is not known, this fitting procedure is done iteratively to determine the apertures that best fit the measurements.

The average pressure around the ring was determined to be $\langle P\rangle(5\text{ mA}) \approx 5\times10^{-10}$ mbar from the horizontal-scraper measurement and $\langle P\rangle(5\text{ mA}) \approx 2\times10^{-10}$ from the vertical-scraper measurements. This discrepancy could be due to higher pressure at locations where the ratio of the horizontal to the vertical β-functions is 5/2, as for example in the straight sections. Assuming these β-functions, the average pressure is $\langle P\rangle(5\text{ mA}) \approx 3\times10^{-10}$ mbar.

We define the acceptance $A_{x,y}$ of the ALS as the point where the lifetime stays constant with changing scraper positions. The horizontal acceptance is thus $A_x \approx 10$ mm to 12 mm, which is much smaller than what we expect from tracking calculations. The vertical acceptance is $A_x \approx$ 3.5 mm to 4 mm, which is in agreement with the free aperture of the narrow-gap chambers.

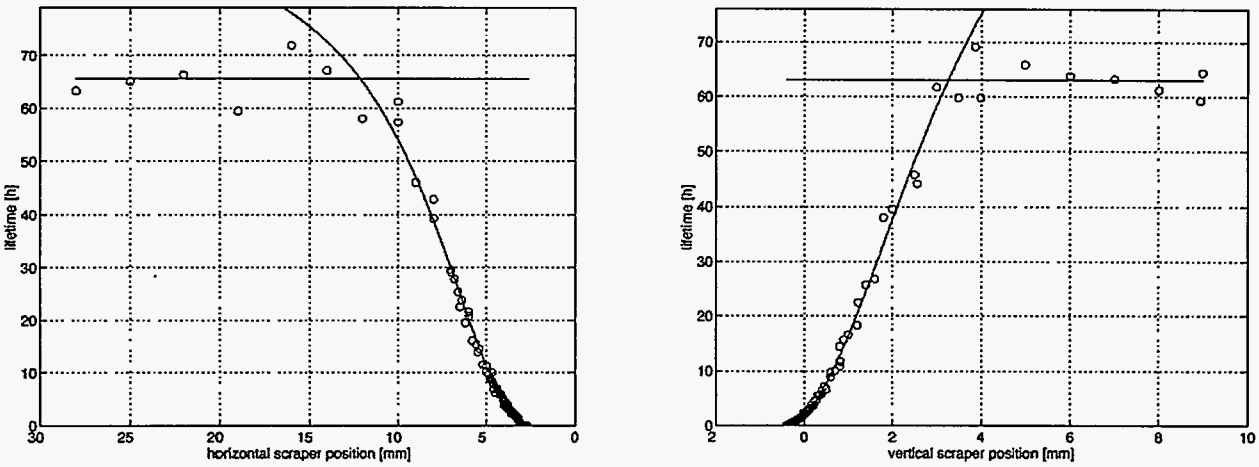

Figure 2-8. Lifetime as a function of the horizontal (left) and vertical (right) scraper position. The storage-ring parameters were beam current 5 mA in 288 bunches, beam energy 1.5 GeV, and multibunch feedback off.

This information allows one to calculate the contributions of the different lifetime effects to the total lifetime at 5 mA in 288 bunches. As the current per bunch is very small, the Touschek lifetime is very large. A measurement of the lifetime at the same total current but with varying bunch currents (i.e. number of bunches) is shown in Figure 2-9.

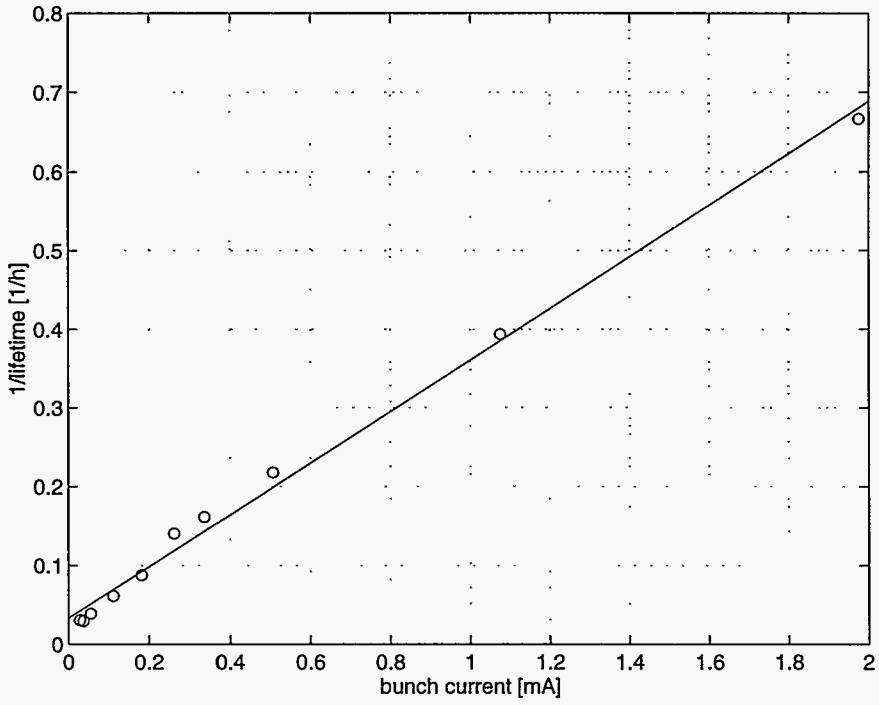

Figure 2-9. Inverse life-time versus bunch current. The total current is held constant in this measurement.

As the gas pressure does not change in this experiment, the slope of the curve gives the change of the Touschek lifetime with bunch current at 1.5 GeV:

$$\frac{1}{\tau_{tou}} = 0.33\left[\frac{1}{\mathrm{h}\cdot\mathrm{mA}}\right] I_{bunch}$$

Remember, the Touschek lifetime changes with the bunch volume, thus any variations of this parameter will change the coefficient given above.

Table 2-3 summarizes the different contributions to the total beam lifetime for 1.5 GeV and 288 bunches (i.e., standard operating conditions). We assumed that the gas is distributed more uniformly for the 400 mA case, as the gas desorption probably takes place in the arcs rather than in the straight sections.

Table 2-3. Contributions of the lifetime limiting effects to the total lifetime at 5 mA and 400 mA in 1.5 GeV operation.

	5 mA	400 mA
quantum lifetime τ_q	∞	∞
elastic scattering lifetime τ_{el}	85 hours	>18 hours
inelastic lifetime τ_{inel}	265 hours	>55 hours
Touschek lifetime τ_{tou}	≈200 hours	2.2 hours
total lifetime τ_t	50 hours	>1.9 hours

Table 2-3 shows that, at standard operating conditions, the Touschek lifetime dominates the total beam lifetime. But even with a fully coupled beam, the lifetime would not exceed 16 hours, which is in agreement with measurements showing a 15-hour lifetime under these conditions.

As the Touschek lifetime is the limiting effect for ALS operations, several options are available to increase it. The most obvious is to increase the bunch volume, which is currently done by increasing the vertical beam size with the help of skew quadrupoles. This leads to a reduction in the brightness. A better way is to elongate the beam with the help of a third-harmonic cavity, which we plan to install in the near future.

Another possibility is to increase the longitudinal acceptance, Δ_s. At a beam energy of 1.5 GeV, the measured longitudinal acceptance is smaller than we expect. The reason for this is currently under investigation. However, at a beam energy of 1.9 GeV, the momentum acceptance is limited by the available rf power. Plans are under way to increase the rf power.

Lower Beam Emittances

Reported by Alan Jackson

Recently it has been recognized that the bend-magnet radiation from the center bends of the ALS triple-bend achromat lattice is extremely bright, primarily because of the small beam sizes at these source points. The beam sizes can be made smaller yet by reducing the horizontal and vertical beam emittances, and/or reducing the β-functions at the source points, and/or reducing the dispersion function at the source points. In practice, all three conditions tend to go together, as we see from the equation below, the emittance ε is a function of the lattice functions (β, α, η, η') in the bend magnets.

$$\varepsilon \propto \int_{\text{dipoles}} \left(\gamma_x \eta_x^2 + 2\alpha_x \eta_x \eta_x' + \beta_x \eta_x'^2 \right) ds$$

The values of these functions can be manipulated by adding quadrupoles in the achromatic arcs or by permitting the dispersion function to be non-zero in the long straight sections. We are currently simulating these possibilities using the lattice design and analysis code TRACY-V.

In the upper panel of Figure 2-10, we show an example in which the natural (zero-beam limit) emittance is reduced from 3.6 nm·rad to 2.1 nm·rad simply by increasing the strengths of the QFA family of quadrupole magnets (the so-called "momentum quads"). Analysis of the dynamic aperture (Figure 2-10, lower panel), with the usual complement of alignment-error terms included, suggested that there is sufficient aperture for injection and acceptable beam lifetime.

Four hours of accelerator beam time were allocated for a "trial run" to check the predictions of the simulation (e.g., the tune change as QFA is varied), and in this time we were able to stack beam at the new working point—a true testament to the predictive capabilities of TRACY-V. A measurement of the beam-size at the diagnostic beamline (Beamline 3.1), confirmed that the emittance was reduced to the expected value (within a measurement error of ± 20%). It is unlikely that this new working point will be offered to users any time soon, since the beam lifetime (through Touschek scattering) suffers significantly. However, it is an operating mode that may well become desirable after the lifetime is enhanced by implementation of the third-harmonic cavity system.

Vertical beam sizes are determined mainly through field errors in the lattice magnets that result in coupling of transverse energy from the horizontal plane to the vertical plane (a process known as betatron oscillation coupling) and in generating vertical dispersion in the bend magnets. We are now trying to reduce the coupling and vertical dispersion using skew quadrupoles and vertical correctors.

Observation and Characterization of the Fast Beam-Ion Instability

Reported by John Byrd

A new regime of ion trapping has been predicted, first described by Raubenheimer and Zimmerman [*Phys. Rev. E* **52**, 5487-5498 (1995)], where ions generated and trapped during the passage of a *single* train lead to a fast instability. In this case, a gap in the bunch train does not help because the instability develops over a single passage of the beam. As a bunch train passes through the storage ring, it ionizes residual gas. A small oscillation of the electron beam drives oscillations of the ions, which in turn drive subsequent bunches in the electron beam. Through this amplification mechanism, small oscillations at the head of the bunch train drive large oscillations at the tail. In many future rings, this transient instability is predicted to have very fast growth rates, much faster than the damping rates of existing and proposed transverse-feedback systems, and thus is a potential limitation.

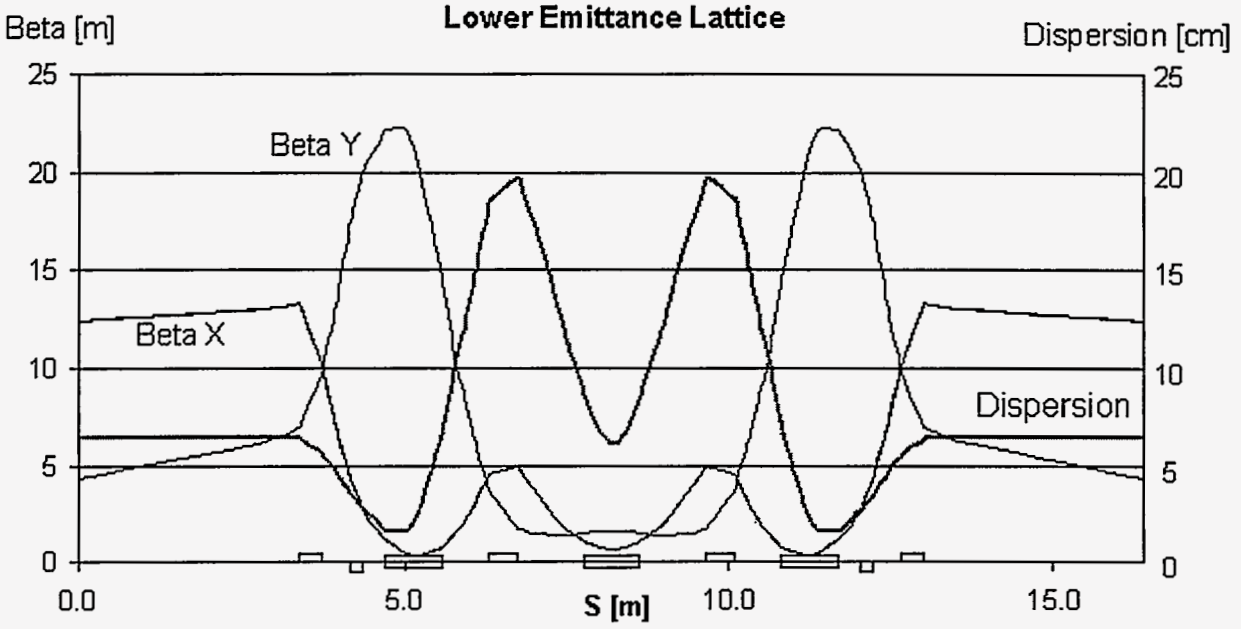

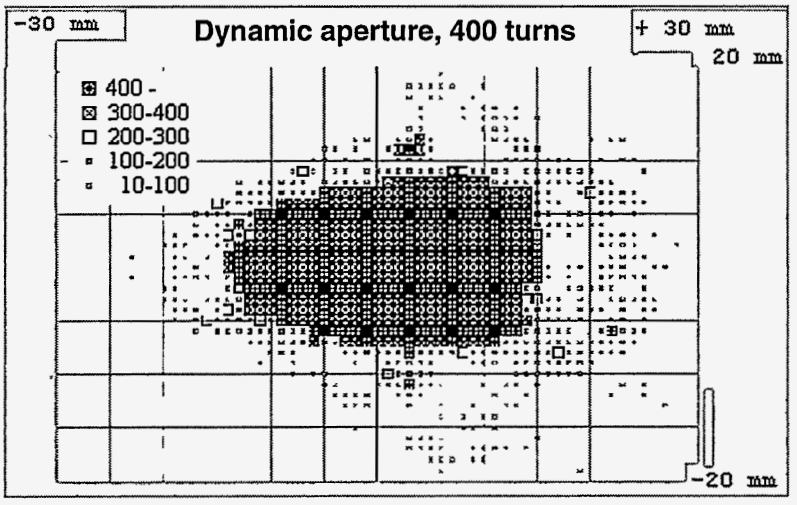

Figure 2-10. TRACY-V plots of how emittance could be reduced with adequate dynamic aperture simply by increasing the strengths of the QFA or "momentum" quadrupoles.

A collaboration between the ALS Accelerator Physics Group and physicists from Stanford Linear Accelerator Center was the first to observe and characterize this potentially important instability [J. M. Byrd, A. Chao, S. Heifets, M. Minty, T. O. Raubenheimer, J. Seeman, G. Stupakov, J. Thomson, F. Zimmermann, *Phys. Rev. Lett.* **79**, 79-82 (1997)]. Since the initial experiments, further measurements have tested methods proposed to cure the instability, such as filling the storage ring with short bunch trains and gaps larger than the ion wavelength. The short length of the bunch train allows very little time for the amplification mechanism to occur, and the gap allows collected ions to drift away. Comparison of the beam stability with a continuous bunch train and a series of short trains indicated that this technique is successful in avoiding the fast instability.

Single-Bunch Instabilities

Reported by John Byrd

Single-bunch instabilities are driven by short-range wakefields, which typically decay over the length of the bunch. Longitudinal effects include distortion of the longitudinal bunch distribution and increase of the energy spread. Transverse effects include the mode-coupling instability in the vertical direction which limits the single-bunch current to about 16 mA (at zero chromaticity.) We have begun an effort (in collaboration with M. Migliorati, University of Rome-La Sapienza) to characterize the longitudinal short-range wakefields by measurements of the bunch length and energy spread as a function of single bunch current. Shown below (Figures 2-11 and 2-12) are examples of such measurements at a beam energy of 1.5 GeV. The longitudinal bunch profile was measured using a streak camera on the diagnostic beamline (Beamline 3.1). The lengthening of the bunch is evident, as well as a distortion of the shape where the front of the bunch becomes steeper than the rear.

Preliminary analysis of the measurements indicates that the measurements are consistent with a simple resistive/inductive impedance model of the ring with a resistance of 580 ohms and an inductance of 80 nanohenries. This model is currently being refined and compared with numerical computation of the wakefield, as well as computer simulations of the beam dynamics.

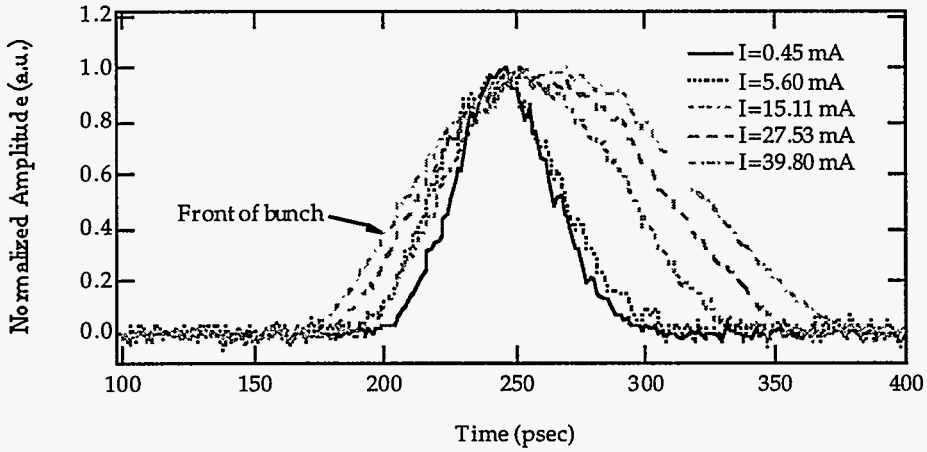

Figure 2-11. Bunch shape, measured as a function of bunch current.

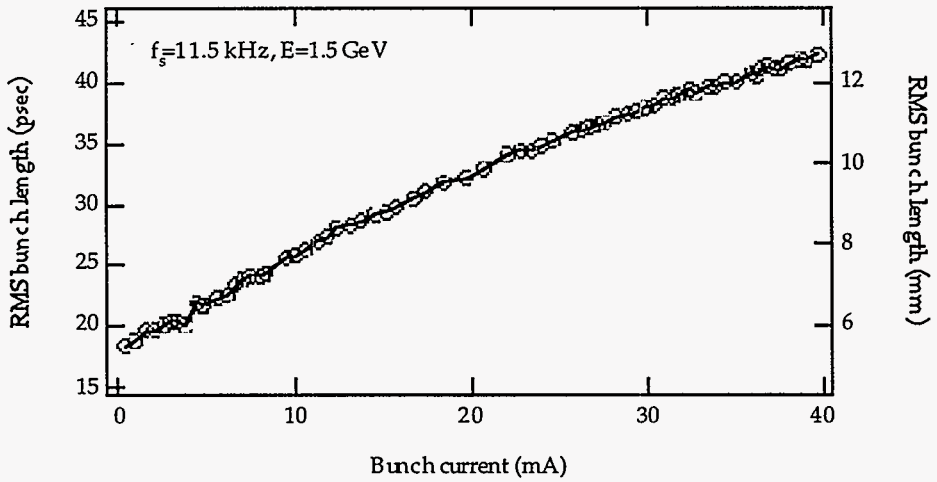

Figure 2-12. Bunch length as a function of bunch current. Imagine each of the circles in this figure being expanded to a shape distribution like the one in Figure 2-11.

Longitudinal Beam-Transfer-Function Diagnostics in an Electron Storage Ring

Reported by John Byrd

Beam-transfer-function (BTF) diagnostics are used in almost all storage rings for measuring the betatron and synchrotron frequencies. In the simplest case, a swept frequency drive excites either betatron or synchrotron oscillations while a beam signal is observed on a spectrum analyzer. In other applications, BTF techniques have been used for measuring beam impedance and feedback-loop stability. In recent studies at the ALS, we have used the BTF technique to measure the distribution of synchrotron frequencies within a single bunch at low beam- current modulation [J.M. Byrd, *Particle Accelerators* **57** (No. 3), 159 (1997)]. By taking advantage of the Gaussian distribution in the energy spread within the bunch, resulting from the quantum nature of the emission of synchrotron radiation and the sinusoidal rf voltage, we can use these measurements to derive a precise measure of the nominal synchrotron frequency, the longitudinal radiation damping rate, and the bunch length.

Although these parameters can be measured using other techniques, the BTF method has the advantage of being relatively simple and inexpensive, as it typically uses equipment that is already available in the control room. The BTF technique can potentially be used to study the effects of short-range wakefields and the longitudinal beam dynamics of more complicated situations, such as double-rf systems and low-momentum compaction. Shown below (Figure 2-13) is a measurement of the longitudinal BTF of the storage ring, along with a fit using the theoretical parameters of the BTF. For ALS conditions, the width of the synchrotron resonance is determined by a combination of the spread in synchrotron frequencies within the bunch and the width of the response of individual electrons due to radiation damping.

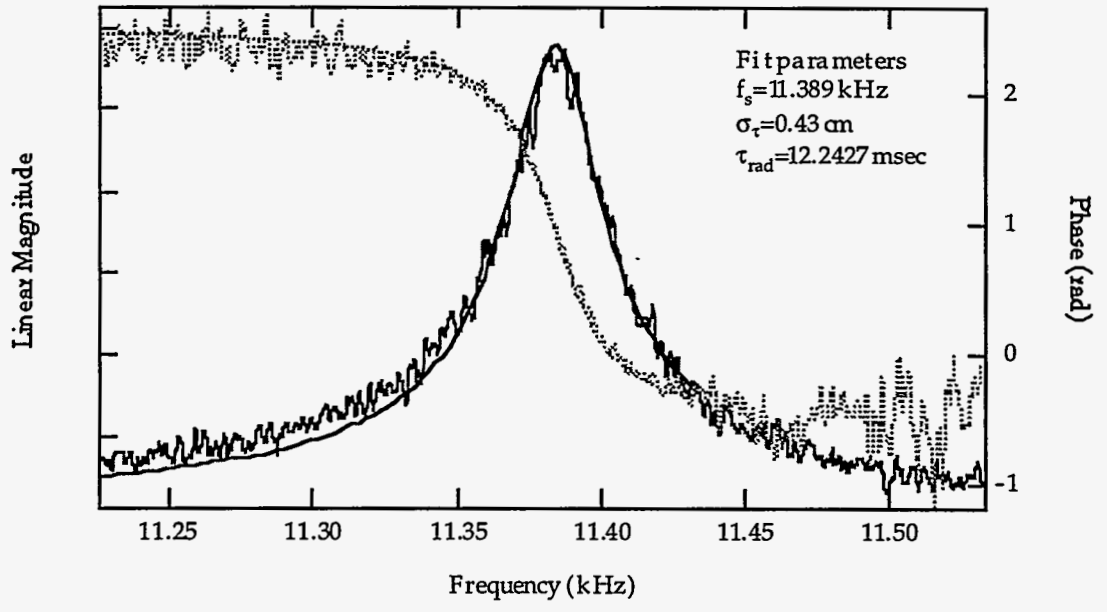

Figure 2-13. A measurement of the longitudinal BTF of the storage ring, along with a fit using the theoretical parameters of the BTF.

Nonlinear Longitudinal Dynamics with Phase Modulation

Reported by John Byrd

The ALS has suffered from longitudinal and transverse coupled-bunch instabilities since it was commissioned. In the case of longitudinal instabilities, the beam oscillations grow to a certain level and stop, probably due to a nonlinear saturation mechanism. As a first step in understanding this saturation mechanism, as well as nonlinear dynamics in general, we have performed a series of experiments to study nonlinear synchrotron oscillations in the presence of strong phase modulation [J. M. Byrd, W.-H. Cheng and F. Zimmermann, *Phys. Rev. E* **48**, 4678 (1998)].

We studied this phenomenon using a dual-scan streak camera in synchroscan mode. This allowed us to observe the time evolution of the longitudinal distribution of a single bunch as the modulation frequency is swept through the synchrotron frequency. Shown below (Figure 2-14) is an example of the longitudinal distribution for three modulation frequencies. The vertical axis is time with respect to a synchronous bunch (i.e., a bunch not executing synchrotron oscillations), where positive displacement indicates early arrival. The horizontal axis represents the relatively slow sweep time of the streak camera. For these images, the horizontal time scale is about 530 turns. The darker area in the image represents higher intensity. The sinusoidal pattern of the distribution is due to the phase modulations (the nominal RMS bunch length is 15 ps to 20 ps.) At this level of excitation, the bunch has oscillation amplitude of about 100 ps to 300 ps peak-to-peak. At the bifurcation frequency, the bunch appears to split into two separate beamlets, oscillating with different amplitudes and out of phase by 180 degrees. The charge in the second beamlet increases while the first decreases. Above the bifurcation frequency, the original beamlet disappears and only the second remains. The time at which the second beamlet appears depends on the modulation sweep rate and the bunch current. We observe similar effects for downward sweeps of the modulation frequency, which are also dependent on sweep rate and bunch current.

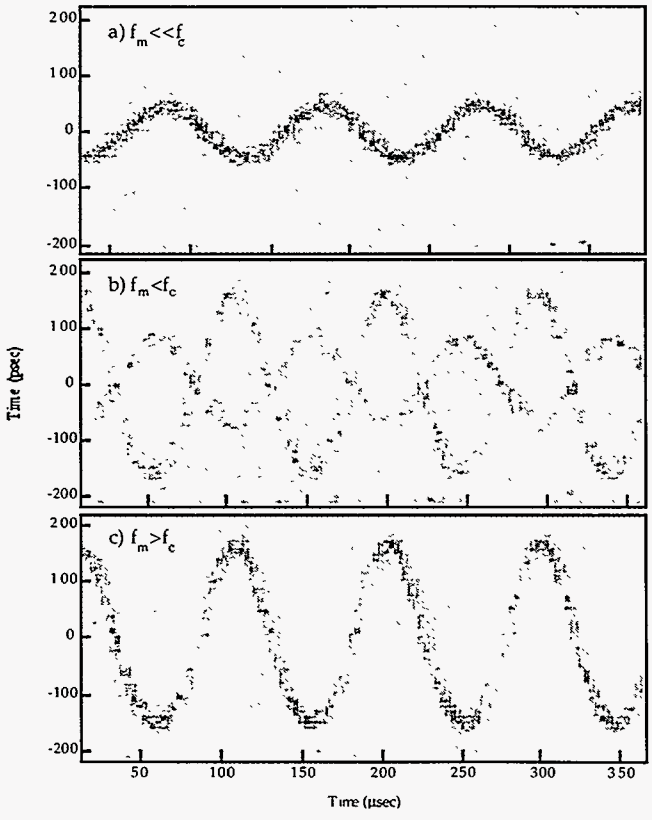

Figure 2-14. Time evolution of the longitudinal distribution of a single bunch at modulation frequencies much less than (top), slightly less than, and slightly greater than the synchrotron frequency.

New Initiatives: The Accelerator Physics Group and the Next Generation of Light Sources

Reported by Alan Jackson

During 1997 the Accelerator Physics Group began discussions with the ALS user community as to what parameters should define a next-generation light source. Since free-electron laser systems are being pursued at the three other DOE light source facilities [(Stanford Synchrotron Radiation Laboratory (SSRL), Advanced Photon Source (APS), and National Synchrotron Light Source (NSLS)], we chose to follow different alternatives. Two areas of opportunity came out of these discussions. The first was to push the beam sizes and emittances even smaller in a ring based system.

The drivers for this type of facility are: (1) potential for many users, particularly on high brightness bend-magnet beamlines; (2) small-gap, short period insertion devices to get to high photon energies at relatively low (≈ 2 GeV) electron-beam energy; and (3) enhanced performance for users of transverse coherence, particularly at higher photon energies. The results of the accelerator physics study are presented below. However, when these capabilities were discussed further with the user community, we discovered that the market for such a machine was not yet developed—clearly the community is still learning how to deal with the beam brightnesses presented by the third-generation machines.

This chicken-and-egg situation can also be used to describe the second area that we pursued—generation of femtosecond pulses of x rays. However, in this case we found more immediate interest. Users are already performing proof-of-principle experiments on the ALS, at very low photon fluxes, and are desperate for more photon intensity. Our initial discussions with local users led to an informal workshop attended by users from outside Berkeley Lab, and by accelerator physicists from Berkeley Lab's Center for Beam Physics, Stanford Linear Accelerator Center (SLAC), and Lawrence Livermore National Laboratory (LLNL). A discussion of the workshop findings is given below.

ALS-N

ALS-N is conceived as an ultrahigh-brightness source of synchrotron radiation (natural emittance ≈ 0.5 nm·rad) at an energy of 2 GeV to 2.5 GeV, with a circumference in the range of 350 to 400 m so that it could fit on a site at Berkeley Lab. The main issues associated with such a facility are lattice design and dynamic aperture, the influence on the emittances of intrabeam scattering, and Touschek lifetime. Other considerations are beam stability and cost. To address this last issue, we borrowed an idea from the Fermilab recycler ring, which is to use permanent magnets for most of the magnet lattice. With the small aperture anticipated for the ring, around 20 mm (horizontal) × 10 mm (vertical), such magnets could be relatively small and inexpensive. Further, the magnets would be light in weight and have inexpensive support systems. Another advantage is that the magnets have no power requirements, and therefore do not require cooling water, further reducing cost and also sources of vibration and temperature variation.

A sample lattice was developed based on the concept of compact minimum-theoretical-emittance lattice cells, matched into long straight sections for insertion devices. The layout (on the site of the Bevatron) and a list of parameters are given in Figure 2-15 and Table 2-4, respectively. This lattice was used to investigate the issues described above. Dynamic aperture is indeed an issue, and a

satisfactory sextupole distribution has not yet been worked out. Both the electron-beam emittance and the bunch length suffer from intrabeam scattering. Even so, significant improvements in beam brightness could be achieved over those available at the ALS, as shown in Figure 2-16. Assuming 1% coupling and use of a third-harmonic rf system (to increase the bunch length), the Touschek lifetime was estimated at more than 4 hours.

More information on this work is reported in LBNL-39799 (A. Jackson et al., "ALS-N - A Candidate for a Next-Generation Light Source") or in the proceedings of the 1997 Particle Accelerator Conference.

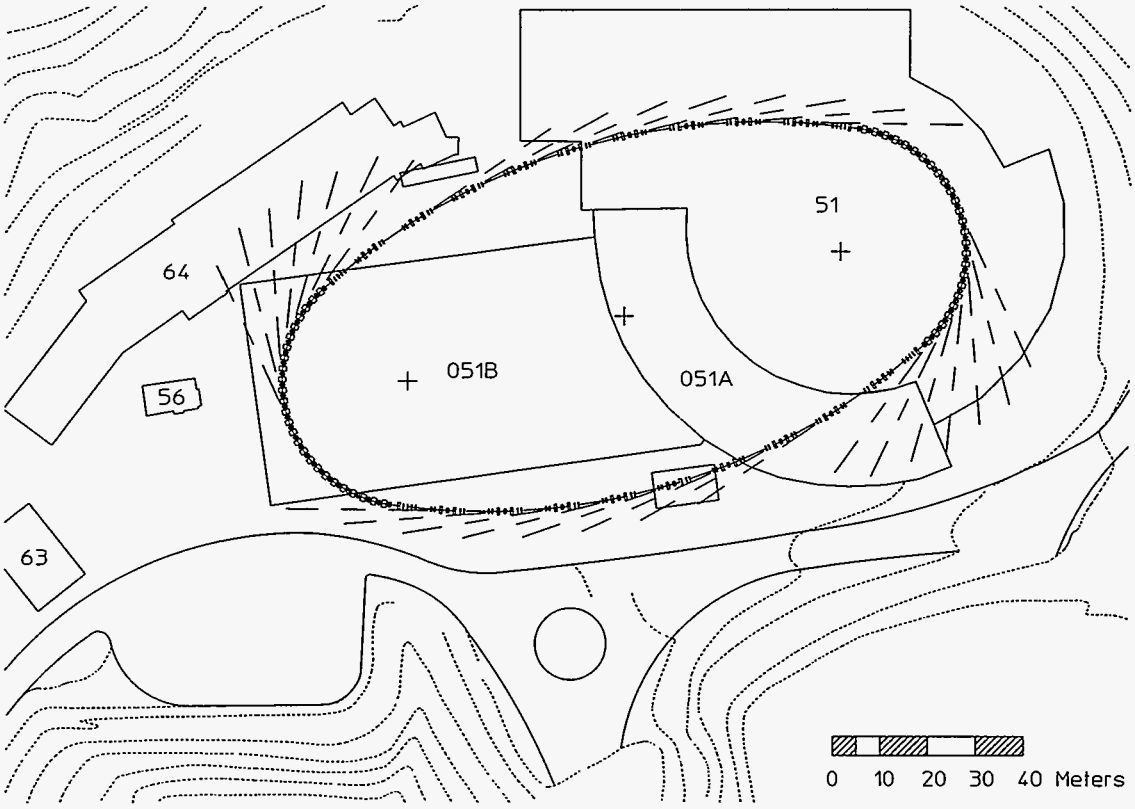

Figure 2-15. Footprint of the ALS-N on the Bevatron site. The straight-section beamlines are 40 m long.

Table 2-4. Parameters of ALS-N.

Energy	2 GeV
Circumference	380 m
Natural emittance	5.5×10^{-10} mrad
Natural energy spread	8×10^{-4}
Momentum compaction	6.7×10^{-4}
Tunes x, y	33.18, 23.73
Chromaticities x, y	–46, –76
Free straight	16, each 5 m long
β_x, β_y in straight	3 m, 3.2 m
β_x, β_y in arc bend	0.8 m, 4 m
Maximum current	400 mA

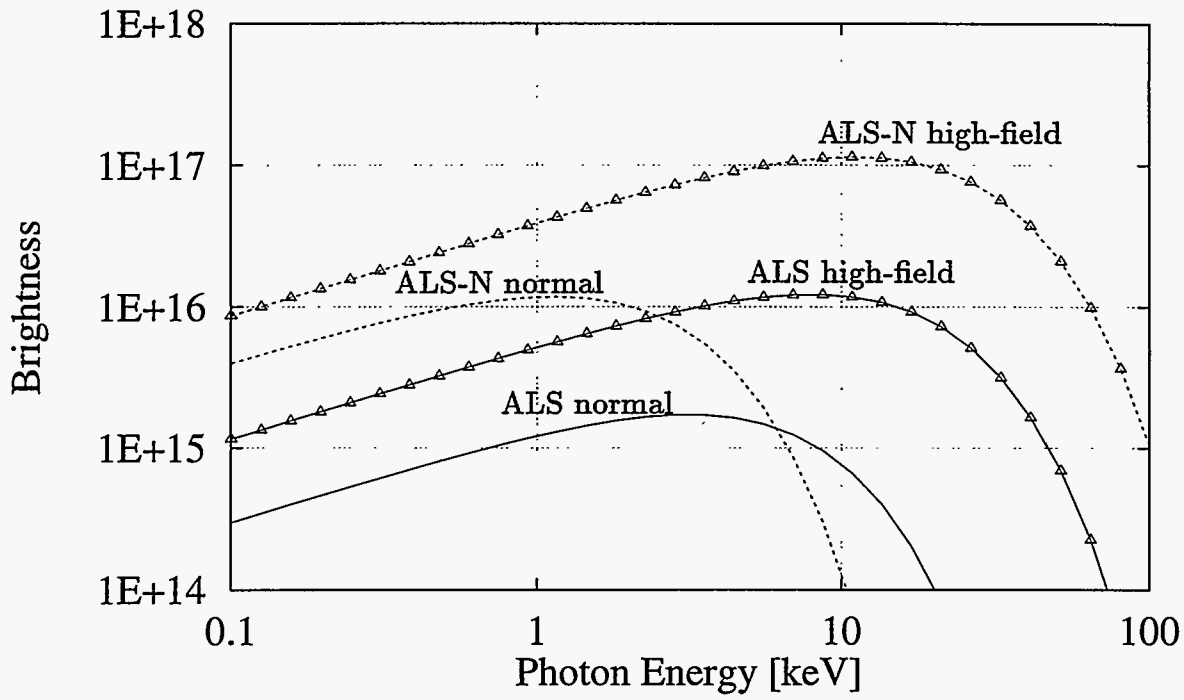

Figure 2-16a. Brightness [photons/(s mm^2 mrad^2 0.1%b.w.)] from normal (1.2 T) and high-field (5 T) dipoles at the present ALS and the ALS-N.

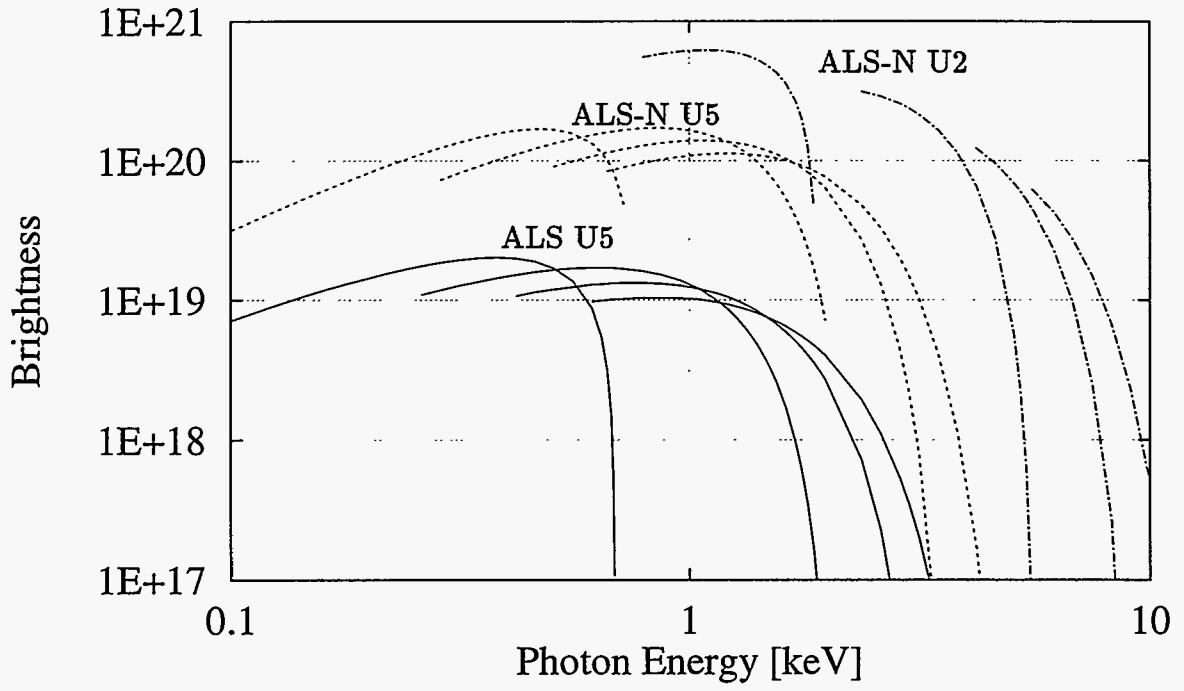

Figure 2-16b. Brightness [photons/(s mm^2 mrad^2 0.1%b.w.)] from insertion devices (U5 = 5 cm undulator period, U2 = 2 cm undulator period) at the present ALS and the ALS-N.

Workshop on the Uses and Generation of Femtosecond Radiation

The goal of the workshop, held at Berkeley Lab in February 1998, was to develop a set of parameters that would be useful for specific experiments and to describe to the user community the different techniques that might eventually be used to meet their requirements. The workshop was indeed informative and very useful. Certainly, the cross-discipline interactions were very successful. However, it became clear during the discussion period that the experimenters present had not thought much beyond the extremely demanding experiments that they are doing right now, and we did not come away from the workshop with the hoped-for set of parameters that could be the basis for a new source. The workshop did however spur a number of investigators to think further about what they would need to push forward with their experiments; the types of experiments and the parameters required are:

- Order-disorder transitions in ordered solids, e.g., silicon melting (using Bragg diffraction).
- Order-disorder transitions in amorphous materials, e.g., the molten carbon insulator-metal transition (using EXAFS).
- Chemical dynamics at surfaces or in solution, e.g., in laser desorption of CO from metal surfaces (using EXAFS).
- Protein-chromophore dynamics, e.g., bacteriorhodopsin isomerization (using diffraction).

The photon parameters required for these experiments are typically:

- Energy: 1–20 keV.
- Bandwidth: 10^{-3}.
- Pulse width: <100 fs.
- Flux: $>10^4$ photons/pulse.
- Repetition rate: ~100 kHz.
- Sample size: 100 μm.
- Angle subtended: <1 mrad.
- Synchronization: to within 100 fs.

Some novel source concepts also evolved during and immediately after the workshop, involving both linac- and ring-based systems. These will be pursued in the coming year.

Operations

Reported by Bob Miller

ALS operations continued with 21 weekly shifts as follows: 16 user shifts, three accelerator physics shifts, one maintenance shift, and one startup and test shift per week. In addition, we continued to insert one two-day maintenance period per month during 1997. The maintenance period helped keep the time needed for major installation shutdowns to a minimum.

Figure 2-16 shows that the beam reliability (actual/scheduled beam time) during the year was 92.3% overall and 92.1% during user shifts (a total of 6483 hours scheduled for users and 5976 hours delivered). The time-accounting algorithm for the ALS was changed beginning October 1, 1997 so that the two normally scheduled storage ring refills per shift are not included as downtime. This was done, with DOE concurrence, in part to make our reporting more consistent with that of some other comparable facilities. The result is an average increase of about 4% in apparent uptime that will show up fully in next year's statistics but that is not reflected in the data shown for the first three quarters of 1997, which were calculated using the old algorithm.

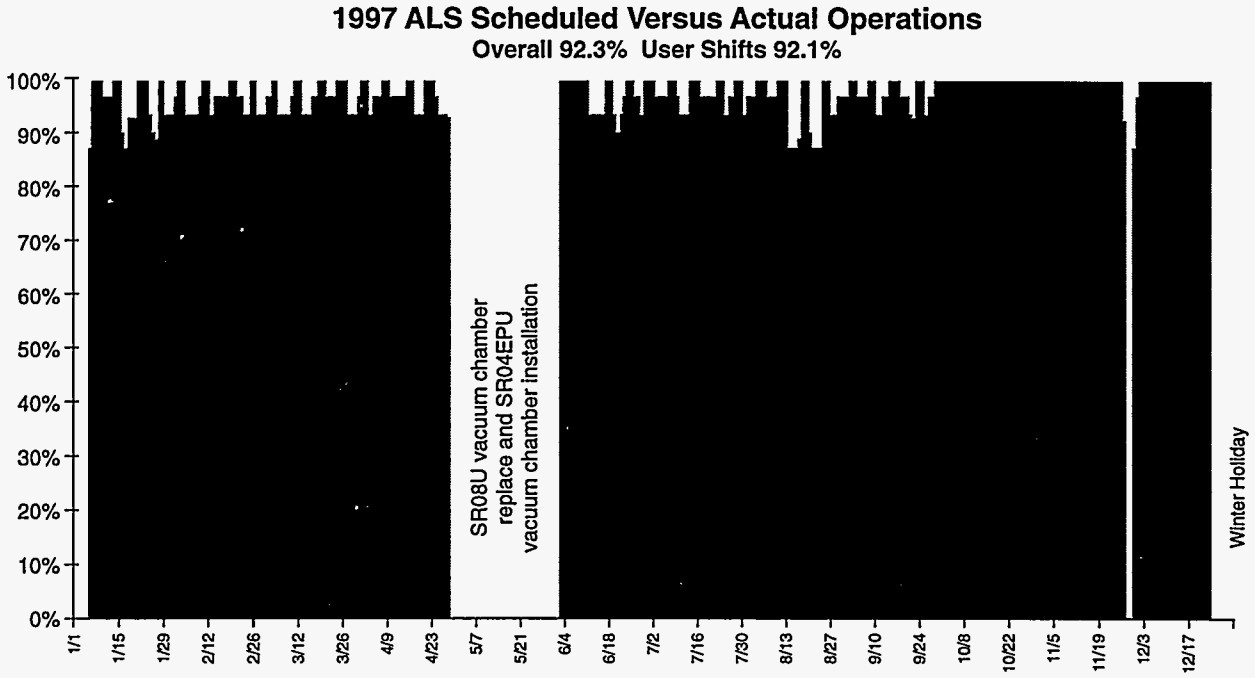

Figure 2-16. ALS scheduled versus actual operations during 1997.

Scheduling for user operations is done at least six months in advance with input from users, the Users' Executive Committee (UEC), and ALS management. Weekly scheduling meetings are held to fine-tune the two-week rolling schedule.

1997 Operations Highlights

User operations fit the general pattern of one-third of the time for 1.5-GeV and two-thirds of the time for 1.9-GeV beam energy. The default multibunch fill pattern is 288 contiguous bunches, which allows a sufficient gap so that a single 20-mA bunch (camshaft) spike can be provided in the gap when requested by users for time-resolved measurements. Special operations included

1.3-GeV multibunch (1 week) and 1.9-GeV two-bunch (4 weeks). There were no major outages during 1997.

Beam current for 1.9-GeV multibunch operation was increased to 400 mA after tests and rf-system tuning to allow increasing the power limit with the existing rf-cavity windows. Beam stability fill-to-fill was improved by the development and implementation of a "one button fill routine" using Matlab, which carries out a set of pre-determined routines, as well as setup at the beginning of each week, to insure that all the critical steps for storage ring refill are carried out exactly the same to maintain fill-to-fill beam-orbit stability.

Storage-ring thermal stability remains good as a result of the work done in 1996. A new 450-ton chiller unit will be installed in 1998 to supply all the chilled water needs for the ALS complex. This will further improve temperature stability of the storage ring by eliminating the need to switch on an additional chiller during warm weather.

The storage ring RF water system was identified as a source of vibration that was observed at the infrared beamline (Beamline 1.4). A team of ALS physicists and mechanical and operations staff, in collaboration with the users, carried out tests to characterize the vibration frequencies, resulting in recommendations to reduce the vibration; the recommendations are being implemented. This work will continue in 1998.

Publications and Preprints Based on Work Done at the ALS

These publications date from January 1997 to April 1998. If a publication is associated with a particular beamline, the beamline number appears to the left of the reference.

Refereed Journal Articles

9.0.2 Ahmed, M., D. Blunt, D. Chen, and A. Suits, "UV photodissociation of oxalyl chloride yields four fragments from one photon absorption," *J. Chem. Phys.* (May 1997).

Alders, D., T. Hibma, G.A. Sawatzky, K.C. Cheung, G.E van Dorssen, H.A. Padmore, M. D. Roper, G. van der Laan, J. Vogel, and M. Sacchi, "Grazing incidence reflectivity and total electron yield effects in soft x-ray absorption spectroscopy," *J. Appl. Phys.* **82** (September 1997), pp. 3120-3124.

9.0.1 Berrah, N., and B. Langer, "Probing electron correlations using third generation synchrotron radiation sources," *Comments on Atomic and Molecular Physics* **33**, 1997, p. 325.

9.0.1 Berrah, N., B. Langer, and A.H. Farhat, "High resolution excitation and photoionization using synchrotron radiation from the Advanced Light Source," *Indian Journal of Physics* **B71B** (1997), p. 223.

8.0.1 Bozek, J.D., T.X. Carroll, J.A. Hahne, L.J. Saethre, J.E. True, and T. Thomas, "High-resolution carbon 1s photoelectron spectrum of ethene. *Ab initio* calculation of vibrational structure with dynamic localization of the core hole," *Phys. Rev. A* (in press).

7.0.1 Braeuning, H., R. Doerner, C.L. Cocke, and M.H. Prior, "Recoil and electronic angular asymmetry parameters for photo double ionization of helium at 99 eV," *J. Phys. B* **30** (July 1997), pp. 649-655.

Byrd, J., "Longitudinal beam transfer function diagnostics in an electron storage ring," *Particle Accelerators* (in press).

Byrd, J., J.A. Thomson, A. Chao, M. Minty, T. Raubenheimer, S. Heifets, J. Seeman, G. Stupakov, and F. Zimmermann, "First observation of the fast beam-ion instability," *Phys. Rev. Lett.* **79**, 1 (July 1997), pp. 79-82.

Byrd, J., W.-H. Cheng, and F. Zimmermann, "Nonlinear effects of phase modulation in an electron storage ring," *Phys. Rev. E* **57**, 4 (April 1998), p. 1500.

7.0.1 Cesar, A., F. Gel'mukhanov, Y. Luo, H. Agren, P.I. Skytt, P.N. Glans, J. Guo, K.M. Gunnelin, and J.E. Nordgren, "Resonant x-ray scattering beyond the Born-Oppenheimer approximation: Symmetry breaking in the oxygen resonant x-ray emission spectrum of carbon dioxide," *J. Chem. Phys.* **106**, 9 (March 1997), pp. 2448-2451.

9.3.2 Chambers, S.A., S. Thevuthasan, Y.J. Kim, G.S. Herman, Z. Wang, E. Tober, R. Ynzunza, J. Morais, C. Peden, K. Ferris, and C.S. Fadley, "Chemisorption geometry of formate on TiO_2(110) by photoelectron diffraction," *Chem. Phys. Lett.* **267**, 1-2 (May 1997), pp. 51-57.

8.0.1 Curioni, A., W. Andreoni, R. Treusch, F. Himpsel, E. Haskal, P. Seidler, C. Heske, S. Kakar, A. van Buuren, and L.J. Terminello, "Atom-resolved electronic spectra for Alq_3 from theory and experiment," *Appl. Phys. Lett.* **72**, 13 (February 1998), pp. 1575-1577.

8.0.1 Dias, E., H. Chakraborty, P. Deshmukh, S.T. Manson, O.A. Hemmers, P.N. Glans, D.L. Hansen, H. Wang, S. Whitfield, D.W. Lindle, R. Wehlitz, J.C. Levin, I.A. Sellin, and R.C. Perera, "Breakdown of the independent particle approximation in high-energy photoionization," *Phys. Rev. Lett.* **78**, 24 (June 1997), pp. 4553-4556.

9.0.1 Diehl, S., D. Cubaynes, E.T. Kennedy, F. Wuilleumier, J. Bizau, L. Journel, L. Voky, P. Faucher, A. Hibbert, C.P. Blancard, N. Berrah, T.J. Morgan, J.D. Bozek, and A.S. Schlachter, "Hollow atom-hollow ion decay routes of triply-excited lithium: First auger results and comparison with R-matrix calculations," *J. Phys. B* **30** (1997), p. 595.

9.0.1 Diehl, S., D. Cubaynes, F. Wuilleumier, J. Bizau, L. Journel, E.T. Kennedy, C.P. Blancard, L. Voky, P. Faucher, A. Hibbert, N. Berrah, T.J. Morgan, J.D. Bozek, and A.S. Schlachter, "Experimental observation and theoretical calculations of Rydberg Series in hollow lithium atomic states," *Phys. Rev. Lett.* **79** (1997), p. 1241.

9.0.1 Diehl, S., D. Cubaynes, K.T. Chung, F. Wuilleumier, E.T. Kennedy, J. Bizau, L. Journel, C.P. Blancard, L. Voky, P. Faucher, A. Hibbert, N. Berrah, T.J. Morgan, J.D. Bozek, and A.S. Schlachter, "Photoelectron spectroscopy measurements and theoretical calculations of the lowest doubly hollow lithium state," *Phys. Rev. A* **56**, R1171 (1997).

9.0.1 Diehl, S., D. Cubaynes, K.T. Chung, F. Wuilleumier, J. Bizau, L. Journel, E.T. Kennedy, C.P. Blancard, L. Voky, P. Faucher, A. Hibbert, N. Berrah, T.J. Morgan, J.D. Bozek, and A.S. Schlachter, "First measurement and theoretical calculations of doubly-hollow lithium states," *Phys. Rev. A* **56** (1997), p. 1.

7.0.1 Doerner, R., H. Braeuning, J.M. Feagin, V. Mergel, O. Jagutzki, L. Spielberger, T. Vogt, H. Khemliche, M.H. Prior, J.H. Ullrich, C.L. Cocke, and H. Schmidt-Böcking, "Photo double ionization of He: Fully differential and absolute electronic and ionic momentum distributions," *Phys. Rev. A* **57** (July 1997), p. 1074.

Doerner, R., H. Braeuning, J. Feagin, V. Mergel, C.L. Cocke, M.H. Prior, B. Kraessig, A. Braeuning-Demian, K. Carnes, S. Dreuil, V. Mergel, P. Richard, J.H. Ullrich, and H. Schmidt-Boecking, "Asymmetry parameters of electrons and recoil ion for photo double ionization of helium at 99 eV," *J. Phys. B* **30**, L649 (1997).

9.0.1 Doerner, R., H. Braeuning, O. Jagutzki, V. Mergel, M. Achler, R. Moshammer, J. Feagin, A. Braeuning-Demian, L. Spielberger, J.H. McGuire, M.H. Prior, N. Berrah, J.D. Bozek, C.L. Cocke, and H. Schmidt-Boecking, "Double photoionization of spatially aligned D_2," *Phys. Rev. Lett.* (in press).

Doerner, R., V. Mergel, L. Spielberger, M. Achler, K. Khayyat, T. Vogt, H. Braeuning, O. Jagutzki, J.H. Ullrich, R. Moshammer, M. Unverzagt, T. Schmitt, H. Khemliche, M.H. Prior, C.L. Cocke, J. Feagin, R.E. Olson, and H. Schmidt-Boecking, "Kinematically complete experiments using cold target recoil ion momentum spectroscopy," *Nucl. Instrum. Methods* **B124** (1997), p. 225.

7.0.1 Droubay, T.C., G. Mursky, and B.P. Tonner, "High resolution x-ray absorption micro-spectroscopy of lamellar phases in natural ilmenite," *J. Electron Spectros. Relat. Phenom.* **84**, 1-3 (March 1997), pp. 159-169.

7.0.1 Duda, L.C., P. Isberg, Ph. Andersson, B. Hjörvarsson, J. Guo, C. Såthe, and J.E. Nordgren, "Hydrogen induced changes of the electronic states in ultra-thin single crystal vanadium layers," *Phys. Rev. B* **55** (May 1997), pp. 12914-12917.

9.0.2 Evans, M.D., C.Y. Ng, C. Hsu, and P.A. Heimann, "A high resolution energy-selected kinetic energy release study of the process $SF_6 + h\nu \rightarrow SF_5^+ + F + e^-$: Heat of formation of SF_5^+," *Chem. Phys. Lett.* **106** (January 1997), pp. 978-981.

9.0.1 Farhat, A.H., M.A. Humphrey, B. Langer, N. Berrah, J.D. Bozek, and D. Cubaynes, "Angle-resolved study of Ar $2p_{1/2,3/2}^{-1}$ ns, d resonant auger decay," *Phys. Rev. A* **56** (1997), p. 501.

7.0.1 Gammon, W.J., S.R. Mishra, K.W. Goodman, J.G. Tobin, F.O. Schumann, R.F. Willis, J. Denlinger, E. Rotenberg, T. Warwick, and N.V. Smith, "A comparison of magnetic linear dichroism in 4f photoemission and 4d-4f photoemission from Gd on Y(0001)," *J. Vac. Sci. Technol.* (in press).

8.0.1 Grush, M.M., Y. Muramatsu, D.L. Ederer, R.C. Perera, and T.A. Callcott, "Soft x-ray emission and absorption: A comparative study on the sensitivity and oxidation state and ligand environment of transition metal complexes," *J. Electron Spectros. Relat. Phenom.* (in press).

8.0.1 Gunnelin, K.M., P.N. Glans, P.I. Skytt, J. Guo, J.E. Nordgren, and H. Agren, "Combined analysis of x-ray emission and adsorption for spectral assignments: The O-K spectra of CO_2," *Phys. Rev. A* **57**, 1 (January 1998).

7.0.1 Gunnelin, K.M., P.N. Glans, P.I. Skytt, J. Guo, J.E. Nordgren, and H. Agren, "Assigning x-ray absorption spectra by means of soft-x-ray emission spectroscopy," *Phys. Rev. A* (in press).

7.0.1 Guo, J., M. Magnuson, C. Såthe, J.E. Nordgren, L. Yang, Y. Luo, K.Z. Xing, N. Johansson, W.R. Salaneck, and W.J. Feast, "Resonant and non-resonant x-ray scattering spectra of some poly(phenylene-vinylene)s," *J. Chem. Phys.* (in press).

8.0.1 Hemmers, O.A., G. Fisher, P.N. Glans, D.L. Hansen, H. Wang, S. Whitfield, D.W. Lindle, R. Wehlitz, J.C. Levin, I.A. Sellin, R.C. Perera, E.W.B. Dias, H.S. Chakraborty, P.C. Deshmukh, and S.T. Manson, "Beyond the dipole approximation: Angular-distribution effects in valence photoemission," *J. Phys. B* **30** (September 1997), pp. 727-733.

Hemmers, O.A., R. Wehlitz, G. Fisher, P.N. Glans, D.L. Hansen, H. Wang, S. Whitfield, J.C. Levin, I.A. Sellin, and D.W. Lindle, "Electric-quadrupole and magnetic-dipole angular distribution effects on Ne 2s and 2p valence photoemission," *Phys. Rev.* **78** (1997), p. 4553.

9.0.2 Hemmi, N., and A. Suits, "Photodissociation of oxalyl chloride at 193 nm probed via synchrotron radiation," *J. Phys. Chem.* **106** (September 1997), pp. 7617-7624.

8.0.1 Himpsel, F.J., R. Treusch, I. Jimenez, A. Jankowski, D.G. Sutherland, L.J. Terminello, C. Heske, R.C.C. Perera, D.K. Shuh, W.M. Tong, J.H. Underwood, J.A. Carlisle, T.A. Callcott, J. Jia, D.L. Ederer, D.M. Gruen, A.R. Krauss, D.C. Zuiker, and G.L. Doll, "Core level spectroscopy for surface analysis," *Critical Reviews of Optical Science and Technology* **CR 69** (September 1997), p. 357.

9.0.1 Hitchcock, A.P., S.G. Urquhart, A.T. Wen, A.L.D. Kilcoyne, T. Tyliszczak, E. Rühl, N. Kosugi, J.D. Bozek, J. Spencer, D.N. McIlroy, and P.A. Dowben, "Inner-shell excitation spectroscopy of closo-carboranes," *J. Phys. Chem.* **101**, 18 (November 1997), pp. 2267-2276.

Howells, M., J. Anspach, and J. Bender, "An assessment of approximating aspheres with more easily manufactured surfaces," *Journal of Synchrotron Radiation* (in press).

9.0.2.2 Hsu, C.-H., M.D. Evans, S.L. Stimson, and C.Y. Ng, "Rotationally resolved photoelectron study of O_2: Identification of vibrational progressions for $O_2^+(2\ ^2\Pi_u, {}^2\Sigma_u^-)$ at 19.6–21.0 eV," *J. Chem. Phys.* **108**, 4701 (1998).

9.0.2.2 Hsu, C.-H., P.A. Heimann, M.D. Evans, S.L. Stimson, and C.Y. Ng, "High resolution photoelectron spectroscopy using multibunch synchrotron radiation: Rotational-resolved photoelectron bands of O_2^+ $(b^4\Sigma_g^-, v^+)$," *Chem. Phys.* (in press).

9.0.2 Hsu, C.-W., M.D. Evans, C.Y. Ng, and P.A. Heimann, "High resolution threshold and pulsed field ionization photoelectron spectroscopy using multibunch synchrotron radiation source," *Rev. Sci. Instrum.* **68** (April 1997), pp. 1694-1702.

9.0.2.2 Hsu, C.-W., M.D. Evans, S.L. Stimson, and C.Y. Ng, "High resolution pulsed field ionization photoelectron sudy of O_2: Predissociation lifetimes and high-n Rydberg lifetimes converging to O_2^+ $(c^4\Sigma_u^-, v^+=0,1)$," *J. Chem. Phys.* (in press).

9.0.2 Hsu, C.-W., M.D. Evans, S.L. Stimson, C.Y. Ng, and P.A. Heimann, "A high resolution pulsed field ionization photoelectron study of O_2 using third generation undulator synchrotron radiation," *J. Chem. Phys.* **106** (June 1997), p. 8931.

9.0.2 Huang, J.-C., Y.-S. Cheung, M.D. Evans, C.-X. Liao, C.Y. Ng, C.-W. Hsu, P.A. Heimann, H. Lefebvre-Brion, and C. Cossart-Magos, "A high resolution VUV photoionization, photoelectron, and pulsed field ionization study of CS_2 near the CS_2^+ $(2p_{3/2,1/2})$ thresholds," *J. Chem. Phys.* **106** (January 1997), p. 864.

8.0.1 Jimenez, I., A. Jankowski, L.J. Terminello, D.G. Sutherland, J.A. Carlisle, G.L. Doll, W.M. Tong, D.K. Shuh, and F.J. Himpsel, "Core level photoabsorption study of defects and metastable bonding configurations in boron nitride," *Phys. Rev. Lett.* **55**, 18 (May 1997), pp. 12025-12037.

8.0.1 Jimenez, I., L.J. Terminello, D.G. Sutherland, J.A. Carlisle, E.L. Shirley, and F.J. Himpsel, "The band width of diamond," *Phys. Rev. B* **56** (October 1997), p. 7215.

7.0.1.2 Kawakami, R.K., E. Rotenberg, E.J. Escoria-Aparicio, H.J. Choi, T.R. Cummins, J.G. Tobin, N.V. Smith, and Z.Q. Qiu, "Photoemission detection of the quantum well interference in magnetic nanostructures," (in press).

9.0.2 Keister, J.W., T. Baer, M.D. Evans, C.Y. Ng, and C.-W. Hsu, "Methyl loss kinetics of energy-selected butadiene radical photocations," *J. Phys. Chem.* **101**, 10 (March 1997), pp. 1866-1872.

7.0.1 Kortright, J., S.K. Kim, T. Warwick, and N.V. Smith, "Soft x-ray circular polarizer using magnetic circular dichroism at the Fe L_3 line," *Appl. Phys. Lett.* **71** (September 1997), pp. 1446-1448.

6.3.2 Kosugi, N., R.G. Cavell, and A.P. Hitchcock, "(LS) versus (jj) coupling in P 2p inner-shell excited states of PF_3," *Chem. Phys. Lett.* **265** (November 1997), pp. 490-496.

7.0.1 Kuiper, P., J. Guo, C. Såthe, L.C. Duda, J.E. Nordgren, J.J.M. Pothuizen, F.M.F. de Groot, and G.A. Sawatzky, "X-ray resonant raman spectra of Cu dd excitations in $Sr_2CuO_2Cl_2$," *Phys. Rev. Lett.* (in press).

Kukk, E., A.A. Wills, N. Berrah, B. Langer, J.D. Bozek, O.Y. Nayandin, M.A. Alshehri, A.H. Farhat, and D. Cubaynes, "Angle-resolved two-dimensional mapping of electron emission following Cl 2p excitations in the HCl molecules," *Phys. Rev. A* (in press).

8.0.1 Kurmaev, E.Z., S. Stadler, D.L. Ederer, I. Hase, Y.M. Yarmoshenko, M. Neumann, D.A. Zatsepin, A. Fujimori, M. Sato, R.C. Perera, M.M. Grush, and T.A. Callcott, "Excitation energy dependence of S $L_{2,3}$ x-ray fluorescent emission of $BaNiS_2$ near S 2p threshold," *Phys. Rev. A* **235**, 2 (October 1997), pp. 191-194.

6.1.2 Kurtis, K., P. Monteiro, J.T. Brown, and W. Meyer-Ilse, "Imaging of AAR gel by soft x-ray microscopy," *Cem. Concr. Res.* (in press).

6.3.2 Lambrecht, W.R.L., S.N. Rashkeev, B. Segall, K. Lawniczak-Jablonska, T. Suski, E. Gullikson, J.H. Underwood, R.C. Perera, J.C. Rife, I. Graegory, S. Porowski, and D. Wickenden, "X-ray absorption, glancing-angle reflectivity, and theoretical study of the N-K and Ga-M edge spectra in GaN," *Phys. Rev. B* **55** (January 1997), p. 2612.

9.0.1 Langer, B., N. Berrah, A.H. Farhat, M.A. Humphrey, J.D. Bozek, and U. Becker, "Angular distributions of resonant and non-resonant auger electrons as a test case for the validity of the spectator model: The argon L_2MM case," *J. Phys. B* **30** (1997), p. 4255.

10.3.2 Larsson, J., P.A. Heimann, A.M. Lindenberg, P.J. Schuck, P.H. Bucksbaum, R.W. Lee, H.A. Padmore, J.S. Wark, and R.W. Falcone, "Ultrafast structural changes measured by time resolved x-ray diffraction," *Opt. Lett.* (in press).

10.3.2 Larsson, J., P.A. Heimann, Z. Chang, P.H. Bucksbaum, E. Judd, H.C. Kapteyn, R.W. Lee, X. Liu, A. Manchacek, and M.M. Murnane *et al* ., "Ultrafast x-ray diffraction using a streak camera in averaging mode," *Opt. Lett.* (in press).

6.3.2 Lawniczak-Jablonska, K., J. Jia, L. Lin, T.A. Callcott, A. Asfaw, J.A. Carlisle, L.J. Terminello,
8.0.1 F.J. Himpsel, D.L. Ederer, J.H. Underwood, and R.C. Perera, "Resonant inelastic scattering in dilute magnetic semiconductors by soft x-ray fluorescence spectroscopy," *Appl. Phys. A* **65**, 2 (August 1997), pp. 173-177.

6.3.2 Lawniczak-Jablonska, K., R.C. Perera, J.H. Underwood, E. Gullikson, and R. Iwanowski, "Hybridization of the 3d states of transition metals with the states of the ZnS matrix," *Phys. Rev. B* **55**, 16 (April 1997), pp. 10376-10381.

6.3.2 Lawniczak-Jablonska, K., T. Suski, Z. Liliental-Weber, E. Gullikson, J.H. Underwood, T. Drummond, and R.C. Perera, "Anisotropy of the nitrogen conduction states in the group III nitrides studied by polarized x-ray absorption," *Appl. Phys. Lett.* **70**, 20 (May 1997), pp. 2711-2713.

BTF Leemans, W., R. Schoenlein, P. Volfbeyn, A.H. Chin, T.E. Glover, P. Balling, M. Zolotorev, K.-J. Kim, S. Chattopadhyay, and C.V. Shank, "Interaction of relativistic electrons with ultrashort laser pulses: Generation of femtosecond x-rays and microprobing of electron beams," *IEEE J. Quantum Electron.* **33**, 11 (November 1997), pp. 1925-1934.

9.3.2 Len, P.M., S. Thevuthasan, A.P. Kaduwela, M.A. Van Hove, and C.S. Fadley, "Optimal atomic imaging in photoelectron holography," *J. Electron Spectros. Relat. Phenom.* **85**, 1-2 (April 1997), pp. 145-158.

9.3.2 Len, P.M., T. Gog, C.S. Fadley, and G. Materlik, "X-ray fluorescence holography and multiple energy holography: A critical comparison of atomic images," *Phys. Rev. B* **55**, 6 (February 1997), pp. 3323-3991.

9.3.2 Len, P.M., T. Gog, D. Novikov, R.A. Eisenhower, G. Materlik, and C.S. Fadley, "Multiple energy x-ray holography: Incident-radiation polarization effects," *Phys. Rev. B* **56**, 3 (July 1997), pp. 1529-1539.

8.0.1 Lindle, D.W., O.A. Hemmers, P.N. Glans, D.L. Hansen, H. Wang, S. Whitfield, R. Wehlitz, J.C. Levin, I.A. Sellin, and R.C. Perera, "The x-ray atomic and molecular spectroscopy program at the Advanced Light Source," *Indian Journal of Physics* **B71**, 3 (1997), pp. 325-334.

7.0.1 Ma, Q., R.A. Rosenberg, C. Kim, J. Grepstat, P.A. Pianetta, T.C. Droubay, D.J. Dunham, and B.P. Tonner, "Comparative magnetic-field imaging, electric-field imaging, and scanning Auger microscopy study of metal-matrix composites," *J. Electron Spectros. Relat. Phenom.* **84** (March 1997), pp. 99-107.

7.0.1 Magnuson, M., N. Wassdahl, and J.E. Nordgren, "Energy dependence of Cu L_2, L_3 satellites using synchrotron excited x-ray-emission spectroscopy," *Phys. Rev. B* **56** (November 1997), pp. 12238-12242.

6.1.2 Magowan, C., J.T. Brown, J. Liang, J. Heck, R.L. Coppel, N. Mohandas, and W. Meyer-Ilse, "Intracellular structures of normal and aberrant *Plasmodium falciparum* malaria parasites imaged by soft x-ray microscopy," *Proc. Natl. Acad. Sci. U.S.A.* **94** (June 1997), pp. 6222-6227.

8.0.1 Martensson, N., M.G. Weinelt, O. Karis, N. Wassdahl, A. Nilsson, J. Stöhr, M.G. Samant, and M. Magnuson, "Coherent and incoherent processes in resonant photoemission," *Appl. Phys. A* (August 1997).

9.0.2 Mayer, P.M., J.W. Keister, T. Baer, C.-W. Hsu, M.D. Evans, and C.Y. Ng, "The fragmentation of dimethylamine dimer ions: Accurate neutral and ionic dimer binding energies by a combined TPEPICO, variation RRKM, and *ab initio* approach," *J. Phys. Chem.* **101**, 7 (February 1997), pp. 1270-1276.

10.3.1 McHugo, S., "Release of metal impurities from structural defects in polycrystalline silicon," *Appl. Phys. Lett.* **71**, 14 (October 1997), pp. 1984-1986.

9.3.2 Moler, E., Y. Feng, T. Huff, S.A. Kellar, Z. Hussain, and D.A. Shirley, "Evidence of the nature of core level photoemission satellites using angle-resolved photoemission fine structure," *Phys. Rev. B* (August 1997).

8.0.1 Nelson, A.J., G. Berry, A. Rocket, D.K. Shuh, J.A. Carlisle, D.G. Sutherland, and L.J. Terminello, "Observation of core-level binding energy shifts between the (100) surface and bulk atoms of epitaxial $CuInSe_2$," *Appl. Phys. Lett.* **70** (April 1997), pp. 1873-1875.

8.0.1 Nilsson, A., M.G. Weinelt, T. Wiell, P. Bennich, O. Karis, N. Wassdahl, J. Stöhr, and M.G. Samant, "Local probing of the surface chemical bond using x-ray emission spectroscopy," *Appl. Phys. Lett.* **65**, 2 (August 1997), pp. 147-154.

7.0.1 Nordgren, J.E., P.N. Glans, K.M. Gunnelin, J. Guo, P.I. Skytt, C. Såthe, and N. Wassdahl, "Resonant soft x-ray fluorescence spectra of molecules," *Appl. Phys. A* **65**, 2 (August 1997), pp. 97-105.

10.3.1 Perry, D.L., A.C. Thompson, R.E. Russo, X.L. Mao, and K.L. Chapman, "Characterization of quaternary metal oxide films by synchrotron x-ray fluorescence microprobe," *Appl. Spectrosc.* **51**, 12 (June 1997), pp. 1781-1783.

7.0.1 Rightor, E.G., A.P. Hitchcock, H. Ade, R.D. Leapman, S.G. Urquhart, A.P. Smith, G.E. Mitchell, D. Fischer, H.J. Shin, and T. Warwick, "X-ray absorption and electron energy loss spectroscopy of poly(ethylene terephthalate) and dimethylterephthalate," *J. Phys. Chem.* **B 101** (1997), pp. 1950-1961.

6.3.2 Sacchi, M., C.F. Hague, E. Gullikson, and J.H. Underwood, "Resonant magnetic scattering of polarized soft x-rays: Specular reflectivity and Bragg diffraction from multilayers," *Phys. Rev. B* **57** (January 1998), pp. 108-111.

9.0.1 Samson, J.A., W.C. Stolte, Z.-X. He, J.N. Cutler, Y. Lu, and R.J. Bartlett, "Double photoionization of helium," *Phys. Rev. A* (in press).

9.0.1 Samson, J.A., Y. Lu, and W.C. Stolte, "Aspects of postcollision interactions near the Ar L shell," *Phys. Rev. A* **56**, 4 (October 1997), pp. 2530-2532.

7.0.1 Schumann, F.O., R.F. Willis, K.W. Goodman, and J.G. Tobin, "On the magnetic instability of ultrathin fcc Fe_xNi_{1-x} films grown on Cu(100)," *Phys. Rev. Lett.* (in press).

9.0.2.2 Shiell, R.C., M.D. Evans, S.L. Stimson, and C.Y. Ng, "A high resolution study of the low lying correlation satellites in xenon," *Phys. Rev. Lett.* **80**, 472 (1998).

7.0.1 Shin, H.J., K. Jeong, D.C. Johnson, S.D. Kevan, M. Noh, and T. Warwick, "Study of $TiSe_2/NbSe_2$ superlattice with use of scanning transmission x-ray microscope," *J. Korean Phys. Soc.* **30** (June 1997), pp. 575-579.

8.0.1 Singh, S., H. Solak, N. Krasnoperov, F. Cerrina, A. Cossy-Gantner, J. Diaz, J. Stöhr, and M.G. Samant, "An x-ray spectromicroscopic study of the local structure of patterned titanium silicide," *Appl. Phys. Lett.* **71** (July 1997), pp. 55-57.

7.0.1 Skytt, P., P. Glans, K.M. Gunnelin, J. Guo, and J.E. Nordgren, "Lifetime-vibrational interference effects in the resonantly excited x-ray-emission spectra of CO," *Phys. Rev. A* **55**, 1 (January 1997), pp. 146-154.

7.0.1 Skytt, P.I., P.N. Glans, K.M. Gunnelin, J. Guo, J.E. Nordgren, Y. Luo, and H. Agren, "Role of screening and angular distributions in resonant x-ray emission of CO," *Phys. Rev. A* **55**, 1 (January 1997), pp. 134-145.

6.3.2 Soufli, R., and E. Gullikson, "Reflectance measurements on clean surfaces for the determination of optical constants of silicon in the EUV/soft x-ray region," *Appl. Opt.* **369**, 221 (August 1997), pp. 5499-5507.

6.3.2 Soufli, R., and E. Gullikson, "Absolute photoabsorption measurements of molybdenum in the range 60 to 930 eV for optical constant determination," *Appl. Opt.* (in press).

7.0.1 Stagarescu, C.B., L.C. Duda, K.E. Smith, D.-K. Seo, M.-H. Whangbo, D. Jeromé, R.C. Haddon, J.S. Brooks, J. Guo, and J.E. Nordgren, "C 2p valence band structure of the organic superconductors k-$ET_2Cu(SCN)_2$ and k-$ET_2CU[N(CN_2)]Br$," *Phys. Rev. B* (in press).

9.0.2.2 Stimson, S., Y.-J. Chen, M.D. Evans, C.-L. Liao, C.Y. Ng, C.-W. Hsu, and P.A. Heimann, "A high resolution pulsed ionization photoelectron study of H_2 using multibunch synchrotron radiation," *Chem. Phys. Lett.* (in press).

9.0.2.2 Stimson, S.L., M.D. Evans, C.Y. Ng, C. Destandau, G. Chambaud, P. Rosmus, C.-W. Hsu, and P. Heimann, "High resolution vacuum ultraviolet pulsed field ionization photoelectron band for $OCS^+(X^2\Pi)$: An experimental and theoretical study," *J. Chem. Phys.* **108**, 6205 (1998).

6.3.2 Stolte, W.C., Y. Lu, J.A. Samson, O.A. Hemmers, D.L. Hansen, S. Whitfield, H. Wang, P.N. Glans, and D.W. Lindle, "The K-shell auger decay of atomic oxygen," *J. Phys. B* **30** (April 1997), pp. 4489-4497.

6.3.2 Stolte, W.C., Z.X. He, J.N. Cutler, and J.A. Samson, "Dissociative photoionization cross sections of N_2 and O_2 from 100 to 800 eV," *Atomic Data and Nuclear Data Tables* (in press).

8.0.1 Sutherland, D.G., L.J. Terminello, J.A. Carlisle, I. Jimenez, F.J. Himpsel, K.M. Baines, D.K. Shuh, and W.M. Tong, "The chemisorption of $H_2C[Si(CH_3)_3]_2$ and $Si_6(CH_3)_{12}$ on Si(100) surfaces," *J. Appl. Phys.* **82** (October 1997), pp. 3567-3571.

12.0.1 Tejnil, E., K. Goldberg, S-H. Lee, H. Medecki, P.J. Batson, P.E. Denham, A.A. MacDowell, J. Bokor, and D.T. Attwood, "At-wavelength interferometry for EUV lithography," *J. Vac. Sci. Technol. B* **15**, 6 (Nov/Dec. 1997), pp. 2455-2461.

9.3.2 Thevuthasan, S., G.S. Herman, Y.J. Kim, S.A. Chambers, C. Peden, Z. Wang, R.X. Ynzunza, E.D. Tober, J. Morais, and C.S. Fadley, "The structure of formate on TiO_2(110) by scanned-energy and scanned-angle photoelectron diffraction," *Surf. Sci.* (in press).

9.3.2 Tober, E., R.X. Ynzunza, J. Palomares, Z. Wang, Z. Hussain, M.A. Van Hove, and C.S. Fadley, "Interface structures of ordered Fe and Gd overlayers on W(110) from photoelectron diffraction," *Phys. Rev. Lett.* **79**, 11 (September 1997), pp. 2085-2088.

9.3.2 Tober, E., J. Palomares, R. Ynzunza, R. Denecke, Z. Wang, J. Morais, J. Liesegang, Z. Hussain, and C.S. Fadley, "Observation of a ferromagnetic-to-paramagnetic phase transition on a ferromagnetic surface using spin-polarized photoelectron diffraction: Gd(0001)," *Phys. Rev. Lett.* (in press).

7.0.1 Tobin, J.G., K.W. Goodman, F.O. Schumann, R.F. Willis, J. Kortright, J. Denlinger, E. Rotenberg, T. Warwick, and N.V. Smith, "Direct extraction of exchange splittings from magnetic x-ray dichroism in photoelectron spectroscopy," *Surf. Sci.* **395** (January 1998), pp. 227-235.

7.0.1 Tobin, J.G., K.W. Goodman, F.O. Schumann, R.F. Willis, J. Kortright, J. Denlinger, E. Rotenberg, T. Warwick, and N.V. Smith, "Generalized description of magnetic x-ray circular dichroism in Fe 3p photoelectron emission," *J. Vac. Sci. Technol.* **A15**, 3 (May/June 1997), pp. 1766-1769.

7.0.1 Tonner, B.P., D.J. Dunham, and T.C. Droubay, "A photoemission microscope with a hemispherical capacitor energy filter," *J. Electron Spectros. Relat. Phenom.* **84** (March 1997), pp. 211-229.

6.3.2 Uehara, Y., D.W. Lindle, T.A. Callcott, L.J. Terminello, F.J. Himpsel, D.L. Ederer, J.H. Underwood,
8.0.1 E. Gullikson, and R.C. Perera, "Resonant inelastic scattering at the L edge of Ti in barium strontium titanate by soft x-ray fluorescence spectroscopy," *Appl. Phys. A* **65**, 2 (August 1997), pp. 179-182.

7.0.1 Urquhart, S.G., A.P. Hitchcock, A.P. Smith, H. Ade, and E.G. Rightor, "Inner-shell excitation spectroscopy of polymer and monomer isomers of dimethyl phthalate," *J. Phys. Chem.* **101**, 13 (January 1997), pp. 2267-2276.

7.0.1 Warwick, T., H. Ade, S. Cerasari, J. Denlinger, K. Franck, A.L. Garcia, S. Hayakawa, A.P. Hitchcock, J. Kikuma, S. Klinger, J. Kortright, G. Morrison, M.M. Moronne, E.G. Rightor, E. Rotenberg, S. Seal, H.-J. Shin, W. Steele, and B.P. Tonner, "Development of scanning x-ray microscopes for materials science spectromicroscopy at the Advanced Light Source," *Journal of Synchrotron Radiation* (in press).

7.0.1 Warwick, T., H. Ade, A.P. Hitchcock, H.A. Padmore, and B.P. Tonner, "Soft x-ray spectromicroscopy development for materials science at the Advanced Light Source," *J. Electron Spectros. Relat. Phenom.* **84** (January 1997), pp. 85-98.

8.0.1 Wehlitz, R., I.A. Sellin, O.A. Hemmers, S. Whitfield, P.N. Glans, H. Wang, D.W. Lindle, B. Langer, N. Berrah, J. Viefhaus, and U. Becker, "Photon energy dependence of ionization-excitation in helium at medium energies," *J. Phys. B* **30**, 2 (January 1997), pp. 51-58.

8.0.1 Weinelt, M.G., A. Nilsson, M. Magnuson, T. Wiell, N. Wassdahl, O. Karis, A. Föhlisch, N. Martensson, M.G. Samant, and J. Stöhr, "Resonant photoemission at the 2p edges of Ni: Resonant raman and interference effects," *Phys. Rev. Lett.* **78** (February 1997), pp. 967-970.

Wills, A.A., N. Berrah, T.W. Gorczyca, B. Langer, Z. Felf, M.A. Alshehri, O.Y. Nayandin, and J.D. Bozek, "Breakdown of LS coupling for a parity unfavored transition in Ne: Angle resolved 2d imaging of two electron processes," *Phys. Rev. Lett.* (in press).

Wuilleumier, F., S. Diehl, D. Cubaynes, J. Bizau, and E.T. Kennedy, "Photoelectron spectroscopy studies of hollow lithium states," *J. Electron Spectros. Relat. Phenom.* (in press).

8.0.1 Zhou, L., T.A. Callcott, Q.Y. Dong, K.E. Miyano, D.L. Ederer, and R.C. Perera, "Sulphur $L_{2,3}$ and zinc $M_{2,3}$ soft x-ray fluorescence spectra in CdS and ZnS," *Phys. Rev. B* **55**, 8 (February 1997), pp. 5051-5061.

8.0.1 Zhou, L., T.A. Callcott, Q.Y. Dong, J. Jia, K.E. Miyano, D.L. Ederer, and R.C. Perera, "A study of the electronic structure of CdS and ZnS using soft-x-ray emission spectroscopy," *Phys. Rev. B* **55** (February 1997), pp. 5051-5061.

Refereed Conference Proceedings

10.3.2 Heimann, P.A., J. Larsson, A. Lindenberg, P.J. Schuck, E. Judd, P.H. Bucksbaum, R.W. Lee, H.A. Padmore, J.S. Wark, and R. Falcone, "Melting of a semiconductor crystal (InSb) with a short laser pulse (100 fs)," in Proceedings of High Heat Flux Engineering, July 31, 1997, San Diego, CA, USA.

10.3.2 Heimann, P.A., J. Larsson, Z. Chang, A. Lindenberg, P.J. Schuck, E. Judd, H.A. Padmore, P.H. Bucksbaum, R.W. Lee, and M. Murnane, "Ultra-fast x-ray diffraction of laser-irradiated crystals," in Proceedings of U.S. National Synchrotron Radiation Instrumentation Conference, June 17-20, 1997, Ithaca, NY, USA.

Martynov, V., H.A. Padmore, A. Yakshin, and A. Agafonov, "Lamellar multilayer gratings with very high diffraction efficiency," in *SPIE Proceedings*, Proceedings of Gratings and Grating Monochromators for Synchrotron Radiation, July 31, 1997, San Diego, CA, USA.

1.4 McKinney, W.R., C. Hirschmugl, H.A. Padmore, T. Lauritzen, N. Andresen, G. Andronaco, R. Patton, and M. Fong, "The first infrared beamline at the Advanced Light Source: Design, construction and initial commissioning," in *SPIE Proceedings*, Proceedings of Accelerator-Based Infrared Sources and Applications, July 31, 1997, San Diego, CA, USA.

McKinney, W.R., M. Howells, and H.A. Padmore, "Aberration analysis calculations for synchrotron radiation beamline design," in *SPIE Proceedings*, Proceedings of Gratings and Grating Monochromators for Synchrotron Radiation, July 31, 1997, San Diego, CA, USA.

7.3.1.1 Renner, T.R., M. Howells, H.A. Padmore, S.-Y. Rah, and K. Franck, "The construction and performance of a one meter long elliptically bent steel mirror," in *SPIE Proceedings*, Proceedings of Materials Manufacturing and Measurements for Synchrotron Radiation Mirrors, July 31, 1997, San Diego, CA, USA.

9.0.1 Samson, J.A., Y. Lu, and W.C. Stolte, "Postcollision interactions in the auger decay of the Ar L shell," in Proceedings of International Symposium on (e,2e), Double Photoionization and Related Topics, July 31-August 2, 1997, Rome, Italy.

Conference Proceedings

Anderson, D.E., and G. Stover, "Design of quasi-traveling wave pinger magnet for beam diagnostics on the Advanced Light Source," in Proceedings of 1997 IEEE Particle Accelerator Conference, May 12-16, 1997, Vancouver, Canada.

7.0.1 Brundle, R., T. Warwick, et al, "Particle analysis on silicon wafers by microXANES," in Proceedings of 42nd National Symposium of the American Vacuum Society.

Byrd, J., "Longitudinal measurements via single bunch beam transfer functions," in Proceedings of 1997 IEEE Particle Accelerator Conference, May 12-16, 1997, Vancouver, Canada.

Byrd, J., "Controlling the vertical mode coupling instability with feedback in the Advanced Light Source," in Proceedings of 1997 IEEE Particle Accelerator Conference, May 12-16, 1997, Vancouver, Canada.

Byrd, J., J.A. Thomson, A. Chao, S. Heifets, M. Minty, J. Seeman, G. Stupakov, F. Zimmerman, and T.O. Raubenheimer, "A study of single-pass ion effects at the Advanced Light Source," in Proceedings of 1997 IEEE Particle Accelerator Conference, May 12-16, 1997, Vancouver, Canada.

Byrd, J., W.H. Cheng, and F. Zimmerman, "Longitudinal nonlinear dynamics studies at the Advanced Light Source," in Proceedings of 1997 IEEE Particle Accelerator Conference, May 12-16, 1997, Vancouver, Canada.

9.0.1 Diehl, S., D. Cubaynes, F. Wuilleumier, J. Bizau, L. Journel, K.T. Chung, L. Voky, P. Faucher, A. Hibbert, N. Berrah, T.J. Morgan, E.T. Kennedy, C.P. Blancard, J.D. Bozek, and A.S. Schlachter, "First observation of a hollow lithium state with two empty inner-shells," in *Bull. Am. Phys. Soc.*, Proceedings of DAMOP Meeting of the American Physical Society, April 18-21, 1997, Washington, D.C., USA.

7.0.1 Goodman, K.W., J.G. Tobin, F.O. Schumann, R.F. Willis, W.J. Gammon, D.P. Pappas, J. Kortright, J. Denlinger, E. Rotenberg, T. Warwick, and N.V. Smith, "Effects of symmetry on circular and linear magnetic dichroism in angle-resolved photoemission spectra of GD/Y(001) and Fe/Ni/Cu(001)," in *Proceedings of the Spring 1997 Materials Research Society Meeting*, March 31-April 4, 1997, San Francisco, CA, USA.

7.0.1 Guo, J., C. Såthe, A. Föhlisch, J.E. Nordgren, L. Yang, and H. Agren, "Soft x-ray emission study of chromium hexacrabonyl," in Proceedings of 2nd German-Russian Symposium on Electron and X-Ray Spectroscopy, November 2-5, 1997.

7.0.1 Guo, J., M. Magnuson, C. Såthe, J.E. Nordgren, L. Yang, Y. Luo, H. Agren, K. Xing, N. Johansson, W.R. Salaneck, R. Daik, and W.J. Feast, "How the phenyl rings (benzene) act as building blocks in the π conjugated polymers," in Proceedings of 2nd German-Russian Symposium on Electron and X-Ray Spectroscopy, November 2-5, 1997.

7.0.1 Guo, J., W.T. Zheng, C. Såthe, N. Hellgren, A. Agui, J.-E. Sundgren, and J.E. Nordgren, "Spectroscopic study of CN_x films grown by magnetron sputter deposition," in Proceedings of 2nd German-Russian Symposium on Electron and X-Ray Spectroscopy, November 2-5, 1997.

6.3.2 Harris, S., A.J. Burek, J.J. Fitch, D. Graessle, D.A. Schwartz, R.L. Blake, and E. Gullikson, "Determination of optical constants for AXAF mirrors from 0.05-1.0 keV through reflectance measurements," in *Materials, Manufacturing and Measurement for Synchrotron Radiation Mirrors*, Proceedings of SPIE Conference, August 30-31, 1997, San Diego, CA, USA.

10.3.2 Heimann, P.A., B. Larsson, Z. Chang, A.M. Lindenberg, P.J. Schuck, E. Judd, H.A. Padmore, P.H. Bucksbaum, R.W. Lee, M.M. Murnane, H.C. Kapteyn, J.S. Wark, and R. Falcone, "Ultrafast x-ray diffraction of laser-irradiated crystals," in Proceedings of National Synchrotron Radiation Instrumentation '97, June 17-20, 1997, Ithaca, NY, USA.

Hinkson, J., R. Keller, R. Alvis, and A. Lumpkin, "Commissioning of the Advanced Light Source dual-axis streak camera," in Proceedings of 1997 IEEE Particle Accelerator Conference, May 12-16, 1997, Vancouver, Canada.

7.0.1 Hitchcock, A.P., "Ionic fragmentation of inner-shell excited molecules," in Proceedings of 7th International Conference on Electron Spectroscopy, September 8-12, 1997, Chiba, Japan.

7.0.1 Hitchcock, A.P., "Inner-shell excitation and fragmentation of molecules," in Proceedings of Workshop on Opportunities for Synchrotron Light in Materials and Manufacturing: Focus on X-Ray Spectromicroscopy of Polymers, February 10, 1998, Sheridan Park.

7.0.1 Hitchcock, A.P., "Overview of synchrotron light applications in materials and manufacturing," in Proceedings of Workshop on Opportunities for Synchrotron Light in Materials and Manufacturing: Focus on X-Ray Spectromicroscopy of Polymers, February 10, 1998, Sheridan Park.

7.0.1 Hitchcock, A.P., S.G. Urquhart, E.G. Rightor, A.P. Smith, H. Ade, and T. Warwick, "Microanalysis of polymers using inner-shell excitation in scanning x-ray transmission microscopes," in Proceedings of 7th International Conference on Electron Spectroscopy, September 8-12, 1997, Chiba, Japan.

7.0.1 Hitchcock, A.P., S.G. Urquhart, E.G. Rightor, W. Lidy, H. Ade, A.P. Smith, and T. Warwick, "Quantitative chemical analysis of sub-micron phase segregation in polyurethane polymers by soft x-ray spectromicroscopy," in *Proceedings of Microscopy and Microanalysis '97 Conference*, August 11-14, 1997, Cleveland, OH, USA.

7.0.1 Hitchcock, A.P., S.G. Urquhart, E.G. Rightor, W. Lidy, H. Ade, A.P. Smith, and T. Warwick, "Quantitative chemical analysis of sub-micron phase segregation in polyurethane polymers by soft x-ray spectromicroscopy," in *Proceedings of Microscopy and Microanalysis '97 Conference*, August 11-14, 1997, Cleveland, OH, USA.

Howells, M., and R.A. Paquin, "Optical substrate materials for synchrotron radiation beamlines," in *Advanced Materials for Optics and Precision Structures*, Proceedings of SPIE Conference, July 27-28, 1997, San Diego, CA, USA.

Jackson, A., "Improving and extending performance at synchrotron radiation facilities," in Proceedings of 1997 IEEE Particle Accelerator Conference, May 12-16, 1997, Vancouver, Canada.

Jackson, A., J. Byrd, W. Decking, R. Keller, C. Kim, D. Massoletti, H. Nishimura, D. Robin, and H. Zyngier, "Advanced Light Source-N — a candidate for a next-generation synchrotron light source," in Proceedings of 1997 IEEE Particle Accelerator Conference, May 12-16, 1997, Vancouver, Canada.

Keller, R., "Tune-split effects at the Advanced Light Source ring," in Proceedings of 1997 IEEE Particle Accelerator Conference, May 12-16, 1997, Vancouver, Canada.

Keller, R., "Transfer functions for the Advanced Light Source lattice magnets," in Proceedings of 1997 IEEE Particle Accelerator Conference, May 12-16, 1997, Vancouver, Canada.

Keller, R., H. Nishimura, and Stability Task Force, "Orbit stability of the Advanced Light Source ring," in Proceedings of 1997 IEEE Particle Accelerator Conference, May 12-16, 1997, Vancouver, Canada.

Kim, C., "A code for calculating intrabeam scattering and beam lifetime," in Proceedings of 1997 IEEE Particle Accelerator Conference, May 12-16, 1997, Vancouver, Canada.

Kim, C., "A modified ZAP code for calculating initial value problems and effects of harmonic cavities," in Proceedings of 1997 IEEE Particle Accelerator Conference, May 12-16, 1997, Vancouver, Canada.

Kim, C., A. Jackson, and T. Warwick, "Beam brightness and beam lifetime in the Advanced Light source," in Proceedings of 1997 IEEE Particle Accelerator Conference, May 12-16, 1997, Vancouver, Canada.

Krebs, G.F., "Measurement of storage ring motion at the Advanced Light Source," in Proceedings of 1997 IEEE Particle Accelerator Conference, May 12-16, 1997, Vancouver, Canada.

Krebs, G.F., and M. Holmes, "Measurement of the radiation incident on NbFeB insertion devices at the Advanced Light Source," in Proceedings of 1997 IEEE Particle Accelerator Conference, May 12-16, 1997, Vancouver, Canada.

8.0.1 Kurmaev, E.Z., S. Bartkowski, M. Neumann, S. Stadler, D.L. Ederer, V.R. Galakhov, Y.M. Yarmoshenko, I.V. Solovyev, S.N. Shamin, V.A. Trofinova, and D.A. Zatsepin, "Electronic structure of ternary transition metal oxides and sulphides: X-ray of photoelectron and x-ray emission spectroscopy study," in Proceedings of 7th International Conference on Electron Spectroscopy, September 8-12, 1997, Chiba, Japan.

Lawniczak-Jablonska, K., T. Suski, W.R.L. Lambrecht, S.N. Rashkeev, B. Segall, and J. Rife, "X-ray edge spectra of III-nitrides," in Proceedings of American Physical Society, March 17-21, 1997, Kansas City, MO, USA.

9.3.2 Len, P., C.S. Fadley, and G. Materlik, "Atomic holography with electrons and x-rays," in Proceedings of 17th International Conference on X-Ray and Inner Shell Processes, September 9-13, 1996, Hamburg, Germany.

MacDowell, A.A., "Progress in elliptical bender mirror adjustment using the long trace profiler," in *Materials, Manufacturing and Measurement for Synchrotron Radiation Mirrors*, Proceedings of SPIE Conference, August 30-31, 1997, San Diego, CA, USA.

MacDowell, A.A., R. Celestre, C.-H. Chang, K. Franck, M. Howells, S. Locklin, H.A. Padmore, J.R. Patel, and R. Sandler, "Progress towards sub-micron hard x-ray imaging using elliptically bent mirrors," in *Materials, Manufacturing and Measurement for Synchrotron Radiation Mirrors*, Proceedings of SPIE Conference, August 30-31, 1997, San Diego, CA, USA.

Marks, S., C. Cortopassi, J. DeVries, E.H. Hoyer, R. Leinbach, Y. Minamihara, H.A. Padmore, P. Pipersky, D. Plate, R. Schlueter, and A.T. Young, "The Advanced Light Source elliptically polarizing undulator," in Proceedings of 1997 IEEE Particle Accelerator Conference, May 12-16, 1997, Vancouver, Canada.

10.3.1 McHugo, S., A.C. Thompson, M. Imaizumi, H. Hieslmair, and E.R. Weber, "Rate limiting mechanism of transition metal gettering in multicrystalline silicon," in *ICDS-19*, Proceedings of 19th International Conference on Defects in Semiconductors, July 1-5, 1997, Aveiro, Portugal.

10.3.1 McHugo, S., and M. Imaizumi, "Release of impurities from structural defects in polycrystalline silicon solar cells," in *Proceedings of the Spring 1997 Materials Research Society Meeting*, March 31-April 4, 1997, San Francisco, CA, USA.

6.1.2 Meyer-Ilse, W., H. Medecki, J. Brown, J. Heck, E.H. Anderson, C. Magowan, A.D. Stead, T.W. Ford, and D.T. Attwood, "High resolution soft x-ray microscopy," in Proceedings of International Conference on Soft X-Rays in the 21st Century, January 13-17, 1997, Orem, UT, USA.

Robin, D., H. Nishimura, W. Decking, and J. Safranek, "Global beta-beating compensation of the Advanced Light Source W16 wiggler," in Proceedings of 1997 IEEE Particle Accelerator Conference, May 12-16, 1997, Vancouver, Canada.

7.0.1 Rotenberg, E., "High resolution photoemission investigation of quasiparticle lifetimes," in Proceedings of 42nd National Symposium of the American Vacuum Society.

9.0.1 Samson, J.A., Y. Lu, and W.C. Stolte, "Photoelectron capture and reemission in post-collision interactions in the Ar L-shell," in *Bull. Am. Phys. Soc.*, Proceedings of DAMOP Meeting of the American Physical Society, April 18-21, 1997, Washington, D.C., USA.

Sasaki, S., "Crossed elliptical polarization undulator," in Proceedings of 1997 IEEE Particle Accelerator Conference, May 12-16, 1997, Vancouver, Canada.

7.0.1 Seal, S., T. Warwick, A.L. Garcia, H. Ade, J. Denlinger, B.P. Tonner, T.L. Barr, and N. Sobczark, "Soft x-ray spectromicroscopy in application to materials science problems," in *Proceedings of the 2nd International Conference on High Temperature Capillarity*, June 16-20, 1997, Krakow, Poland.

6.3.2 Soufli, R., and E. Gullikson, "Optical constants of materials for multilayer mirror applications in the EUV/soft x-ray region," in *SPIE Proceedings,* Proceedings of SPIE's 42nd Annual Meeting on Optical Engineering and Instrumentation - Conference on Grazing Incidence and Multilayer X-Ray Optical Systems, July 27-29, 1997, San Diego, CA, USA.

9.3.2 Thevuthasan, S., G.S. Herman, Y.J. Kim, S.A. Chambers, Z. Wang, E. Tober, R. Ynzunza, J. Morais, C. Peden, and C.S. Fadley, "The structure determination of formate on TiO_2(110) by low-energy photoelectron diffraction," in Proceedings of Gordon Research Conference on Chemical Reactions at Surfaces, February 16-20, 1997, Ventura, CA, USA.

Thur, W., J. Guigli, A. Gavidia, and J. Akre, "Mechanical design of a pinger system for the Advanced Light Source accelerator," in Proceedings of 1997 IEEE Particle Accelerator Conference, May 12-16, 1997, Vancouver, Canada.

Thur, W., T. Lauritzen, R. DeMarco, B. Baldock, and K. Rex, "Rigid, adjustable support of aligned elements via six struts," in Proceedings of Fifth International Workshop on Accelerator Alignment, October 13-17, 1997, Argonne, IL, USA.

Timossi, C., and H. Nishimura, "Accelerator control software construction based on software object components," in Proceedings of 1997 IEEE Particle Accelerator Conference, May 12-16, 1997, Vancouver, Canada.

7.0.1 Tobin, J.G., D. Chambliss, D. Kubinski, K. Barmak, P. Dederichs, W. de Jonge, T. Katayama, and A. Schuhl, "Ultrathin films, multilayers, and surfaces 1997," in *Proceedings of the Spring 1997 Materials Research Society Meeting*, March 31-April 4, 1997, San Francisco, CA, USA.

7.0.1 Tobin, J.G., "Probing Ni/Fe nanoscale alloy films with photoemission magnetic x-ray linear dichroism," in Proceedings of 42nd National Symposium of the American Vacuum Society.

7.0.1 Urquhart, S.G., A.P. Hitchcock, E.G. Rightor, H. Ade, and A.P. Smith, "Chemical speciation by NEXAFS spectro-microscopy: Insights from molecular modeling of polymers," in *CSC-97*, Proceedings of Chemical Society of Canada, June 1-3, 1997, Windsor, Canada.

7.0.1 Warwick, T., H. Ade, S. Cerasari, J. Denlinger, A.L. Garcia, S. Hayakawa, A.P. Hitchcock, J. Kikuma, J. Kortright, M.M. Moronne, E.G. Rightor, E. Rotenberg, S. Seal, H. Shin, W. Steele, and B.P. Tonner, "Scanning zone-plate x-ray microscopes for materials analysis at the Advanced Light Source," in Proceedings of 9th International Conference on Modern Materials Technology, January 1-5, 1998, Italy.

7.0.1 Warwick, T., H. Ade, S. Cerasari, J. Denlinger, A.L. Garcia, S. Hayakawa, A.P. Hitchcock, J. Kikuma, J. Kortright, M.M. Moronne, E.G. Rightor, E. Rotenberg, S. Seal, H. Shin, W. Steele, and B.P. Tonner, "Scanning zone-plate x-ray microscopes for materials science spectromicroscopy at the Advanced Light Source," in Proceedings of Synchrotron Radiation Instrumentation-97, September 1-4, 1997, Himeji, Japan.

8.0.1 Wehlitz, R., I.A. Sellin, O.A. Hemmers, S. Whitfield, P.N. Glans, H. Wang, D.W. Lindle, B. Langer, N. Berrah, J. Viefhaus, et al., "Making a link from ionization-excitation to the double photoionization of helium," in *XX. ICPEAC*, Proceedings of Twentieth International Conference on the Physics of Electronic and Atomic Collisions, July 23-29, 1997, Vienna, Austria.

8.0.1 Wehlitz, R., I.A. Sellin, O.A. Hemmers, S. Whitfield, P.N. Glans, H. Wang, D.W. Lindle, B. Langer, N. Berrah, J. Viefhaus, and U. Becker, "Partial photoionization cross-sections of helium satellites at medium photon energies," in *Bull. Am. Phys. Soc.*, Proceedings of DAMOP Meeting of the American Physical Society, April 18-21, 1997, Washington, D.C., USA.

8.0.1 Wehlitz, R., I.A. Sellin, O.A. Hemmers, S. Whitfield, P. Glans, H. Wang, D.W. Lindle, B. Langer, N. Berrah, J. Viefhaus, et al., "Partial photoionization cross-sections of helium satellites at medium energies," in Proceedings of American Physical Society, March 17-21, 1997, Kansas City, MO, USA.

9.0.1 Wuilleumier, F., S. Diehl, D. Cubaynes, J. Bizau, L. Journel, E.T. Kennedy, N. Berrah, T.J. Morgan, C.P. Blancard, J.D. Bozek, and A.S. Schlachter, "Experimental evidence of Rydbergs series within the hollow states of lithium," in *Bull. Am. Phys. Soc.*, Proceedings of DAMOP Meeting of the American Physical Society, April 18-21, 1997, Washington, D.C., USA.

Zholents, S. et al., "Modification of the Advanced Light Source booster synchrotron for an experiment on optical stochastic cooling," in Proceedings of 1997 IEEE Particle Accelerator Conference, May 12-16, 1997, Vancouver, Canada.

Books and Book Chapters

Duarte, R., M. Howells, Z. Hussain, T. Lauritzen, R. McGill, E. Moler, and J.A. Spring, "A linear motion machine for soft x-ray interferometry," in *Optomechanical Design and Precision Instruments*, Hatheway, A.E., ed., Vol. 3132, Society of Photo-Optical Instrumentation Engineers, Bellingham, 1997.

Howells, M., and J. Casstevens, "Achievement of a superpolish on bare stainless steel," in *Materials, Manufacturing, and Measurement for Synchrotron Radiation Mirrors*, Takacs, P.Z, and T.W. Tonnessen, eds.; Vol. 3152, Society of Photo-Optical Instrumentation Engineers, Bellingham, 1997, pp. 35-40.

Howells, M., and R.A. Pacquin, "Optical substrate materials for synchrotron radiation beamlines," in *Advanced Materials for Optics and Precision Structures*, Ealey, M. and R. Paquin, eds., Vol. CR67, Critical Reviews of Optical Science and Technology, Bellingham, 1997, pp. 339-372.

Kennedy, E.T., S. Diehl, D. Cubaynes, J. Bizau, and F. Wuilleumier, "Triply-excited lithium: Recent experimental and theoretical developments," in *Physics of Atomic and Electronic Collisons*, Aumayr, F. and H. Peter Winter, eds., World Science, 1998.

McKinney, W.R., M. Howells, and H.A. Padmore, "Aberration analysis calculations for synchrotron radiation beamline design,"*Gratings and Grating Monochromators for Synchrotron Radiation*, Vol. 3150, Society of Photo-Optical Instrumentation Engineers, Bellingham, 1997.

Moler, E., R.M. Duarte, M. Howells, Z. Hussain, C. Oh, and J.A. Spring, "First measurements using the Advanced Light Source soft x-ray Fourier transform spectrometer," in *Coherent Electron-Beam X-Ray Sources and Applications*, Freund, A.K., H.P. Freund, and M.R. Howells, eds., Vol. 3154, Society of Photo-Optical Instrumentation Engineers, Bellingham, 1997.

Padmore, H.A., "Optimization of soft x-ray monochromators,"in *VUV Synchrotron Radiation Instrumentation: Beamline and Instrument Development.*

Padmore, H.A., M. Howells, and W.R. McKinney, "Grazing incidence monochromators for third generation synchrotron radiation sources,"in *Techniques of Vacuum Ultraviolet Physics*, Academic Press, Orlando, 1997.

Paquin, R.A., and M. Howells, "Mirror materials for synchrotron radiation optics," in *Materials Manufacturing and Measurement for Synchrotron Radiation Mirrors*, Takacs, P.Z., and T. Tonnessen, eds., Vol. 3152, Society of Photo-Optical Instrumentation Engineers, Bellingham, 1997.

Rah, S., S. Locklin, S.C. Irick, and M. Howells, "New schemes in the adjustment of bendable elliptical mirrors using a long trace profiler," in *Materials, Manufacturing and Measurement for Synchrotron Radiation Mirrors*, Takacs, P.Z., and T. Tonnessen, eds., Vol. 3152, Society of Photo-Optical Instrumentation Engineers, Bellingham, 1997.

Renner, T.R., K. Franck, M. Howells, S.C. Irick, H.A. Padmore, and S. Rah, "The construction and performance of a one meter long elliptically bent steel mirror," in *Materials, Manufacturing and Measurement for Synchrotron Radiation Mirrors*, Takacs, P.Z., and T. Tonnessen, eds., Vol. 3152, Society of Photo-Optical Instrumentation Engineers, Bellingham, 1997.

Spielberger, L., O. Jagutzki, R. Doerner, V. Mergel, U. Meyer, K. Khayyat, T. Vogt, M. Achler, H. Schmidt-Boecking, J.H. Ullrich, M. Unverzagt, B. Kraessig, M.B. Jung, E.P. Kanter, D.S. Gemmell, M.H. Prior, H. Khemliche, and C.L. Cocke, "Studies of photoabsorbtion and Compton scattering using cold target recoil ion momentum spectroscopy," in *Applications of Accelerators in Research and Industry*, Duggan, J.L., and I.L. Morgan, eds., AIP Press, New York, 1997, p. 213.

Thorne, A., and M. Howells, "Interferometric spectrometers," in *Techniques of Vacuum Ultraviolet Physics*, Samson, J.A.R., and D. Ederer, eds., Academic Press, Orlando, 1998.

Vogt, T., R. Doerner, O. Jagutzki, C.L. Cocke, J. Feagin, M.B. Jung, E.P. Kanter, H. Khemliche, S.D. Kravis, V. Mergel, L. Spielberger, J.H. Ullrich, M. Unverzagt, H. Braeuning, U. Meyer, and H. Schmidt-Boecking, "From gamma, 2e to gamma, eR: Kinematically complete experiments with COLTRIMS," in *Proceedings of the Euroconference Ionization and Coincidence Spectroscopy*, Whelan, C.T., and H.R.J. Walters, eds., Plenum, 1997.

Theses Based on Work Done at the ALS

7.0.1 Gunnelin, K.M., "Soft X-Ray Emission Studies of the Electronic Structure of Molecules," licenciat dissertation, Uppsala University, Uppsala, Sweden, 1997, Advisor: Joseph Nordgren.

9.3.2 Len, P., "Atomic Holography with Electrons and X-Rays," doctoral dissertation, University of California, Davis, CA, 1997, Advisor: Prof. Charles Fadley.

9.0.1 Schulz, K., "High-Resolution Absorption Spectroscopy Autoionization Resonance of Helium and Neon," doctoral dissertation, Freie Universität Berlin, Berlin, Germany, 1997, Advisor: Prof. Dr. Günter Kaindl.

6.3.2 Soufli, R., "Optical Constants of Materials in the EUV/Soft X-ray Region for Multilayer Mirror Applications," doctoral dissertation, Department of Electrical Engineering and Computer Sciences, University of California, Berkeley, CA, 1997, Advisors: Dr. Eric M. Gullikson and Prof. David T. Attwood.

9.3.2 Tober, E., "The Interfacial and Surface Properties of Thin Fe and Gd Films Grown on W(110) as Studied by Scanning Tunneling Microscopy, Site-Resolved Photoelectron Diffraction, and Spin Polarized Photoelectron Diffraction," doctoral dissertation, University of California, Davis, CA, 1997, Advisor: Prof. Charles Fadley.

9.3.2 Wang, Z., "Short-Range Magnetic Order from Spin-Polarized Photoelectron Diffraction and Holography: Experiment and Theory for MnO(001)," doctoral dissertation, University of California, Davis, CA, 1997, Advisor: Prof. Charles Fadley.

Contributed News Articles

9.0.1 Berrah, N., A.A. Wills, B. Langer, and J.D. Bozek, "Two-dimensional imaging of atoms and molecules using angle-resolved, electron time-of-flight spectroscopy," *Synchrotron Radiation News*.

8.0.1 Hemmers, O.A., P.N. Glans, D.L. Hansen, H. Wang, S. Whitfield, D.W. Lindle, R. Wehlitz, J.C. Levin, I.A. Sellin, and R.C. Perera, "Photoelectron spectroscopy and the dipole approximation," *Synchrotron Radiation News* **10**, 3, 1997, p. 21.

10.3.2 Padmore, H.A., G. Ackerman, R. Celestre, C.-H. Chang, M. Howells, Z. Hussain, S.C. Irick, S. Locklin, A.A. MacDowell, and J.R. Patel, "Sub-micron white beam focusing using elliptically bent mirrors," *Synchrotron Radiation News* **10**, 6, December 1997, pp. 18-26.

Robinson, A., "Workshop on molecular environmental science in the soft x-ray region," *Synchrotron Radiation News* **10**, 6, November 1997, pp. 2-4.

5.0.2 7.3.1.2 Robinson, A., "ALS light to two new beamlines," *Synchrotron Radiation News* **10**, 3 (May 1997), pp. 36-38.

Robinson, A., "ALS Users' Association Tenth Annual Meeting," *Synchrotron Radiation News* **11**, 1, January 1998, pp. 2-7.

Robinson, A., "Advanced Light Source Users' Association Tenth Annual Meeting," *Synchrotron Radiation News* **11**, 1 (January/February 1998), pp. 2-7.

12.0 Robinson, A., "New at-wavelength interferometer tests EUV optics," *Synchrotron Radiation News* **10**, 4 (July 1997), pp. 10-12.

BTF Robinson, A., "Laser techniques for generating femtosecond x-rays at the Advanced Light Source," *Synchrotron Radiation News* **10**, 1 (Jan/Feb 1997), pp. 32-33.

Robinson, A., "Advanced Light Source Users' Association Ninth Annual Meeting," *Synchrotron Radiation News* **10**, 1 (Jan/Feb 1997), pp. 4-7.

6.1.2 Robinson, A., "Biological x-ray microscopy at the Advanced Light Source," *SIM News* **47**, 1 (Jan/Feb 1997), pp. 5-11.

Robinson, A., "Making light work of spectroscopy," *Chemistry in Britain* (April 1997), p. 50.

Becoming an ALS User

The ALS, a Department of Energy national user facility, welcomes researchers from universities, industry, and government laboratories. Qualified users have access either as members of participating research teams (PRTs) or as independent investigators. PRTs (groups of researchers with related interests from one or more institutions) construct and operate beamlines and have primary responsibility for experiment endstation equipment. They are entitled to a certain percentage of their beamline's operating time according to the resources contributed by the PRT. Through a proposal process, the remaining beamtime is granted to independent investigators, who may provide their own endstation or negotiate access to a PRT-owned endstation.

Anyone wishing to explore the potential of synchrotron radiation in their research should review the beamline information given in the next section to gain some familiarity with the beamlines' photon energy ranges and other individual capabilities. To inquire more specifically about a particular beamline, use the contact information given in the individual beamline tables.

The ALS Quick Guide for Users on the Internet (http://www-als.lbl.gov/quickguide) provides the most up-to-date information on beamlines and the process of becoming an ALS user.

Independent Investigator Program

Independent researchers may propose experimental programs or single experiments to be performed on existing beamlines. Proposals may involve bringing experiment chambers to the ALS from other locations, or they may involve the use of chambers provided by the ALS facility or by a PRT. Independent investigators may also establish collaborations with PRT members.

The ALS has two semesters per year for soliciting independent investigator proposals: April–September and October–March. After the proposals are submitted, they are reviewed by ALS personnel for technical feasibility and safety, and PRT members from the appropriate beamline check the proposal for conformance to the beamline's capabilities. If a particular beamline is specified in the proposal, it is strongly recommended that the independent investigator contact the appropriate PRT spokesperson before submitting the proposal. Contact information for the PRT spokespersons and local contacts for each beamline are given in the beamline information tables on pp. 469–505. For information on beamlines available to independent investigators, contact the ALS Program Support Coordinator; for information on the submission process and deadlines, contact the ALS User Administrator (see inside back cover for ALS contact information).

After the ALS and PRT review, the proposals undergo peer review by a five-member Proposal Study Panel, which rates the proposals and makes recommendations on the requisite beam time. Highly rated proposals are allocated beam time by the User Services Office in consultation with the spokesperson of the host PRT.

Non-Proprietary Research

The ALS does not charge users for beam access if their research is non-proprietary. However, they must sign a user agreement which, among other things, requires the experimenter to send the ALS a copy of all publications resulting from data collected at the ALS. For research to be considered non-proprietary, the research results must be published in the open literature. All users are responsible for the day-to-day costs of research (e.g., supplies, phone calls, and technical support).

Proprietary Research

Proprietary research can also be performed at the ALS. Users performing proprietary research will be charged a fee based on cost recovery for ALS usage. In return, the user may choose to take title to any inventions made during the proprietary research program and treat as proprietary all technical data generated during the program. Contact the ALS User Services Administrator for information on proprietary research proposals (see inside back cover for contact information).

Table of Beamlines at the ALS

Up-to-date information is on the Web at http://www-als.lbl.gov/als/als_users_bl/bl_table.html

No.	Source *	Areas of Research	Energy Range	Avail.	Pages for Abstracts/ Technical Info.
1.4.1	Bend	Ultraviolet photoluminescence	1.6–6.2 eV	1998	1/469
1.4.2	Bend	Visible and infrared Fourier transform spectroscopy	0.006–3 eV	Now	1/470
1.4.3	Bend	Infrared spectromicroscopy	0.05–1 eV	Now	1/471
3.1	Bend	Diagnostic beamline	200–280 eV	Now	– /–
3.3.2	Bend	Deep-Etch X-Ray Lithography (LIGA)	3–12 keV	Now	–/472
4.0.1-2	EPU5	Magnetic spectroscopy	100–2000 eV	1998	–/473
5.0.1	W16	Monochromatic protein crystallography	7–14 keV	1998	–/474
5.0.2	W16	Multiple-wavelength (MAD) and monochromatic protein crystallography	3.5–14 keV	Now	15/475
6.1.2	Bend	High-resolution zone-plate microscopy	500–800 eV	Now	31/476
6.3.1	Bend	Calibration and standards, EUV/soft x-ray optics testing, solid-state chemistry	100–2000 eV	1998	–/477
6.3.2	Bend	Calibration and standards; EUV optics testing; atomic, molecular, and materials science	50–1300 eV	Now	51/478
7.0.1	U5	Surface and materials science, spectromicroscopy, spin resolution, photon-polarization dichroism	60–1000 eV	Now	99/479
7.0.2	U5	Coherent optics experiments	200–650 eV	1998	175/483
7.3.1.1	Bend	Magnetic microscopy, spectromicroscopy	260–1500 eV	Now	179/484
7.3.1.2	Bend	Surface and materials science, micro x-ray photoelectron spectroscopy	260–1500 eV	Now	179/485
7.3.3	Bend	Micro x-ray diffraction, micro x-ray absorption spectroscopy	3–12 keV	Now	–/486
8.0.1	U5	Surface and materials science, spectromicroscopy, imaging photoelectron spectroscopy	60–1000 eV	Now	195/488
9.0.2.1	U10	Chemical reaction dynamics, photochemistry	5–30 eV	Now	305/490
9.0.2.2	U10	High-resolution photoelectron and photoionization spectroscopy	5–30 eV	Now	305/491
9.3.1	Bend	Atomic, molecular, and materials science	2.2–6 keV	Now	337/492
9.3.2	Bend	Chemical and materials science, circular dichroism, spin resolution	30–1500 eV	Now	349/495
10.0.1	U10	High-resolution atomic, molecular, and optical physics; photoemission of highly correlated materials	20–320 eV	Now	–/497
10.3.1	Bend	X-ray fluorescence microprobe	3–20 keV	Now	371/500
10.3.2	Bend	X-ray optics development, materials science	3–12 keV	Now	377/501
11.3.2	Bend	Inspection of EUV lithography masks	50–1000 eV	1998	–/502
12.0.1.1	U8	Surface and materials science, spectromicroscopy	60–320 eV	Now	395/503
12.0.1.2	U8	EUV lithography optics testing, interferometry	60–320 eV	Now	395/504
BTF	ALS linac	Beam Test Facility	50 MeV electrons	Now	409/505

* Bend = bend magnet; EPU5 = 5-cm-period elliptical polarization undulator; W16 = 16-cm-period wiggler; Ux = x-cm-period undulator

Beamline 1.4.1

Ultraviolet Photoluminescence (Abstracts begin on page 1)

Operational	1998
Source characteristics	Bend magnet
Energy range	1.6–6.2 eV
Frequency range	750–200 nm
Spectrometer resolution	Depends on slit size
Endstation	Optical table
Spatial resolution	Diffraction limited
Detector	Photomultiplier tube
Spot size at sample	Diffraction limited
Samples Preparation	 ALS user wet lab available
Sample environment	Air, cryostat, high pressure
Scientific applications	UV-visible photoluminescence
Local contact	Name: Joel W. Ager Phone: (510) 486-6715 Fax: (510) 486-4114 Email: jwager@lbl.gov
Spokesperson	Name: Eugene E. Haller Affiliation: Materials Science Division, Berkeley Lab; MSME Department, U. California Berkeley Phone: (510) 486-5294 Fax: (510) 486-5530 Email: eehaller@lbl.gov

Beamline 1.4.2

Visible and Infrared Fourier Transform Spectroscopy (FTIR)
(Abstracts begin on page 1)

Operational	Now
Source characteristics	Bend magnet
Energy range	0.006–3 eV
Frequency range	50 cm^{-1} to 25,000 cm^{-1}
Interferometer resolution	0.125 cm^{-1}
Endstations	Bruker IFS66v/S FTIR (vacuum), Surface Science UHV Chamber
Characteristics	Rapid- and Step-Scan FTIR, up to 5 nsec time resolution, transmission and reflection modes
Spatial resolution	Diffraction limited (≈ wavelength)
Detectors	Silicon Bolometer (LHe cooled) Wide-range MCT (mercury cadmium telluride) Gap Diode Silicon Diode Fast Silicon Diode DTGS Mid-IR DTGS Far-IR
Spot size at sample	1 mm (varies with coupling optics)
Samples Preparation	 Stereo microscope and table available UHV surface science chamber
Sample environment	10^{-2} Torr vacuum in main FTIR bench or 10^{-9} Torr vacuum in surface science chamber
Scientific applications	Sub-monolayers on surfaces, polymers, semiconductors, superconductors, environmental samples, forensic studies, etc.
Local contact	Name: Michael C. Martin Phone: (510) 495-2231 Fax: (510) 486-7696 Email: mcmartin@lbl.gov
Spokesperson	Name: Wayne R. McKinney Affiliation: Advanced Light Source, Berkeley Lab Phone: (510) 486-4395 Fax: (510) 486-7696 Email: wrmckinney@lbl.gov

Beamline 1.4.3

Infrared Spectromicroscopy (Abstracts begin on page 1)

Operational	Now
Source characteristics	Bend magnet
Energy range	0.05–1 eV
Frequency range	450 cm^{-1} to 10,000 cm^{-1}
Interferometer resolution	0.125 cm^{-1}
Endstations	Nicolet 760 FTIR, Nic-Plan IR microscope (N_2 purged)
Characteristics	Motorized sample stage, micron resolution, transmission and reflection modes
Spatial resolution	Diffraction limited (≈ wavelength)
Detectors	Extended-range MCT (mercury cadmium telluride)
Spot size at sample	10 μm (diffraction limited)
Samples Preparation	 Stereo microscope and table available
Sample environment	N_2 purged, minimal clean area (no particle specification)
Scientific applications	Particulate contamination, biological samples, forensic studies, laminates, polymers, fibers, environmental samples
Local contact	Name: Michael C. Martin Phone: (510) 495-2231 Fax: (510) 486-7696 Email: mcmartin@lbl.gov
Spokesperson	Name: Wayne R. McKinney Affiliation: Advanced Light Source, Berkeley Lab Phone: (510) 486-4395 Fax: (510) 486-7696 Email: wrmckinney@lbl.gov

Beamline 3.3.2

Deep-Etch X-Ray Lithography

Operational	Now
Source characteristics	Bend magnet (7 horizontal mrad at 17 m from bend magnet)
Energy range	3–12 keV
Monochromator Calculated flux (1.9 GeV, 400 mA)	None 2.7×10^{13} photons/sec/0.1%BW
Endstation	Deep-etch x-ray lithography
Characteristics	Hutchless, self-contained scanner and shutter endstation
Spot size at sample	10 cm × 1.3 mm
Scientific applications	Research and development on deep-etch x-ray lithography such as LIGA (micromachining of high-aspect-ratio microstructures)
Local contact	Name: Cheryl Hauck Phone: (510) 486-7885 Fax: (510) 486-4102 Email: cahauck@lbl.gov
Spokesperson	Name: Jill Hruby Affiliation: Sandia National Laboratories Phone: (925) 294-2596 Fax: (925) 294-3410 Email: jmhruby@sandia.gov

Beamline 4.0.1-2

Magnetic Spectroscopy

Operational	1998
Source characteristics	5.0-cm-period elliptical polarization undulator (EPU5.0), EPU7.5 (planned)
Energy range	20–1800 eV
Monochromator Calculated flux (1.9 GeV, 400 mA) Resolving power (E/ΔE)	Variable included angle PGM 1×10^{13} photons/sec/0.1%BW at 800 eV* 5,000–10,000
Endstations	Total yield, XPS, and fluorescence detectors in UHV chambers with magnets generating fields up to 6 T
Local contact	Name: Anthony T. Young Affiliation: Advanced Light Source, Berkeley Lab Phone: (510) 486-7746 Fax: (510) 486-7696 Email: atyoung@lbl.gov

* Polarization is user selectable, from horizontal to vertical and left and right elliptical (or circular) polarization. Value reported is the merit function flux = total flux × (degree of circular polarization)^2.

Beamline 5.0.1

Monochromatic Protein Crystallography

Operational	1998
Source characteristics	16-cm-period wiggler (W16)
Energy range	7–14 keV
Monochromator Calculated flux (1.9 GeV, 400 mA) Resolving power (E/ΔE)	Single crystal, cylindrically bent 8.5×10^{13} photons/sec/0.1%BW at 12 keV (energy dependent) ≈6000 with Si(111) at 10° asymmetry angle
Endstation	Macromolecular crystallography facility
Detectors	CCD (planned)
Spot size at sample (FWHM)	0.7 mm (h) × 0.3 mm (v)
Samples Format Preparation	 Single crystals of biological molecules Support labs available
Sample environment	Ambient or ≈100°K
Special notes	Computers for data processing and analysis are available
Scientific applications	Biological crystallography; monochromatic
Local contact/spokesperson	Name: Thomas Earnest Affiliation: Physical Biosciences Division, Berkeley Lab Phone: (510) 486-4603 Fax: (510) 486-5664 Email: tnearnest@lbl.gov

Beamline 5.0.2

Multiple-Wavelength Anomalous Diffraction (MAD) and Monochromatic Protein Crystallography (Abstracts begin on page 15)

Operational	Now
Source characteristics	16-cm-period wiggler (W16)
Energy range	3.5–14 keV
Monochromator Calculated flux (1.9 GeV, 400 mA) Resolving power (E/ΔE)	Double crystal 2.3×10^{13} photons/sec/0.1%BW into 1.5 mrad at 12.4 keV 15,000 for Si(111)
Endstation	Macromolecular crystallography facility
Characteristics	Kappa-geometry camera, CCD detector, low-temperature system
Detectors	2 × 2 array CCD detector
Spot size at sample (FWHM)	0.4 mm (h) × 0.4 mm (v)
Samples Format Preparation	 Single crystals of biological molecules Support labs available
Sample environment	Ambient or ≈100°K
Special notes	Computers for data processing and analysis are available
Scientific applications	Biological crystallography; multiple-wavelength anomalous diffraction (MAD); monochromatic
Local contact/spokesperson	Name: Thomas Earnest Affiliation: Physical Biosciences Division, Berkeley Lab Phone: (510) 486-4603 Fax: (510) 486-5664 Email: tnearnest@lbl.gov

Beamline 6.1.2

High-Resolution Zone-Plate Microscopy (Abstracts begin on page 31)

Operational	Now
Source characteristics	Bend magnet
Energy range	500–800 eV (extended range 250–950 eV)
Monochromator Calculated flux (1.9 GeV, 400 mA) Resolving power (E/ΔE)	Zone plate linear Images with 1000 × 1000 pixels, 1000 photons/pixel are recorded in 3 sec at 517 eV/0.3%BW 200–500 (with 20–5 μm field of view)
Endstation	X-ray microscope (XM-1)
Characteristics	Conventional-type (full-field) soft x-ray microscope
Spatial resolution	40 nm
Detectors	Back-thinned CCD camera
Field of view	5 to 20 μm single field; larger areas can be tiled together like a mosaic
Samples Format Preparation	 Thin samples (up to 10 μm thick) on silicon nitride or other foils, wet chamber provided Sample dependent
Sample environment	Helium at atmospheric pressure, wet or dry, low temperature (cryo) (in preparation)
Special notes	Mutual indexing system with visible-light microscopy provided to position and focus sample
Scientific applications	Biology, environmental sciences, material sciences, polymers
Local contact/spokesperson	Name: Werner Meyer-Ilse Affiliation: Center for X-Ray Optics, Berkeley Lab Phone: (510) 486-6892 Fax: (510) 486-4550 Email: w_meyer-ilse@lbl.gov

Beamline 6.3.1

Calibration and Standards, EUV/Soft X-Ray Optics Testing, Solid State Chemistry

Operational	1998
Source characteristics	Bend magnet
Energy range	500–2000 eV
Monochromator Calculated flux (1.9 GeV, 400 mA) Resolving power (E/ΔE)	Double crystal 10^{11} photons/sec/0.01%BW at 1000 eV 5000
Endstation	Reflectometer
Characteristics	VLS-PGM monochromator with fixed exit slit and refocusing mirror; 2-circle goniometer with x, y, z, θ sample mirror
Spatial resolution	Can position to 1 μm
Detectors	Si diode, CEM, MCP, total yield
Spot size at sample	5 × 200 μm
Samples Format	Solid-state, gas phase Foils, powders, etc.
Sample environment	High vacuum or UHV
Scientific applications	Solid-state chemistry to the Al and Si K edges, atomic physics reflectometry, scattering
Local contact/spokesperson	Name: Jim H. Underwood Affiliation: Center for X-Ray Optics, Berkeley Lab Phone: (510) 486-4958 Fax: (510) 486-4550 Email: jhunderwood@lbl.gov

Beamline 6.3.2

Calibration and Standards; EUV Optics Testing; Atomic, Molecular, and Materials Science (Abstracts begin on page 51)

Operational	Now
Source characteristics	Bend magnet
Energy range	50–1300 eV
Monochromator Calculated flux (1.9 GeV, 400 mA) Resolving power (E/ΔE)	VLS-PGM 10^{11} photons/sec/0.01%BW at 100 eV 7000
Endstation	Reflectometer
Characteristics	2-circle goniometer with x, y, z, θ movement of sample
Spatial resolution	Can position to 1 μm
Detectors	Si diode, CEM, MCP, total yield
Spot size at sample	5 μm (v) × 300 μm (h)
Samples Format	Solid state, gas phase Foils, powders, films
Sample environment	High vacuum or UHV
Scientific applications	Solid-state chemistry, gas phase, atomic physics, reflectometry, scattering
Local contact/spokesperson	Name: Eric Gullikson Affiliation: Center for X-Ray Optics, Berkeley Lab Phone: (510) 486-6646 Fax: (510) 486-4550 Email: emgullikson@lbl.gov

Beamline 7.0.1

Surface and Materials Science, Spectromicroscopy, Spin Resolution, Photon-Polarization Dichroism (Abstracts begin on page 99)

Operational	Now
Source characteristics	5-cm-period undulator (U5) (first, third, and fifth harmonics)
Energy range	60–1000 eV
Monochromator Calculated flux (1.9 GeV, 400 mA) Resolving power (E/ΔE)	SGM (gratings: 150, 380, 925 l/mm) $\approx 10^{12}$ photons/sec/0.01%BW (resolution dependent) 3000 typical, 8000 optimized
Endstations	UltraESCA Scanning transmission x-ray microscope (STXM) Scanning photoemission microscope (SPEM) Fluorescence spectrometer

Endstation identifier	**UltraESCA**
Characteristics	High-resolution, angle-resolved XPS spectroscopy; capable of making images by rastering the sample through a fixed spot; sample is rotated for angle-resolved measurements
Spatial resolution	50 μm
Detectors	Hemispherical electron energy analyzer; total electron yield detector
Spot size at sample	50 μm
Samples Format Preparation	 Solid samples, 1" maximum diameter Preparation chamber with sputtering is provided
Sample environment	UHV
Special notes	LEED and in-situ sample heating and cooling available
Scientific applications	XPS, XPD, NEXAFS of solids and surfaces
Local contact	Name: Eli Rotenberg Phone: (510) 486-5975 Fax: (510) 486-2930 Email: erotenberg@lbl.gov
Spokesperson	Name: James Tobin Affiliation: Lawrence Livermore National Laboratory Phone: (510) 422-7247 Fax: (510) 423-7040 Email: tobin1@llnl.gov

Beamline 7.0.1, cont.

Endstation identifier	Scanning transmission x-ray microscope (STXM)
Characteristics	Used to make x-ray images and NEXAFS spectra of thin samples in transmission in the photon energy range 180–900 eV
Spatial resolution	Scanning microscope with focusing by means of Fresnel zone plates; resolution determined by spot size, which is 150 nm with current zone plates but will improve with new zone plates
Detectors	Gas proportional counter, silicon photodiode
Spot size at sample	150 nm with current zone plates
Samples Format Preparation	Solids Thin sections or thin films (100 nm thick) typically 3 × 3 mm in area No preparation chamber available
Sample environment	Helium at 1 atm
Special notes	Samples may be wet or dirty; thin films may be deposited on silicon nitride widows; optical alignment is provided by looking at the back side of the sample to locate regions of interest from optical micrographs
Scientific applications	Imaging, NEXAFS in small spots
Local contact	Name: Tony Warwick Phone: (510) 486-5819 Fax: (510) 486-7696 Email: t_warwick@lbl.gov
Spokesperson	Name: James Tobin Affiliation: Lawrence Livermore National Laboratory Phone: (510) 422-7247 Fax: (510) 423-7040 Email: tobin1@llnl.gov

Beamline 7.0.1, cont.

Endstation identifier	**Scanning photoemission microscope (SPEM)**
Characteristics	Designed for sub-micron XPS in the photon energy range 200–800 eV
Spatial resolution	Scanning microscope with focusing by means of Fresnel zone plates; resolution determined by spot size, which is 150 nm with current zone plates but will improve with new zone plates
Detectors	Hemispherical electron energy analyzer; total electron yield detector
Spot size at sample	150 nm with current zone plates
Samples Format Preparation	Solids 1" maximum diameter Preparation chamber with sputtering and annealing provided
Sample environment	UHV
Special notes	Optical alignment equipment provided so that visible marks on the sample surface can be used to find an area of interest prior to x-ray measurements; in-situ heating and cooling.
Scientific applications	Imaging, XPS and NEXAFS in small spots
Local contact	Name: Tony Warwick Phone: (510) 486-5819 Fax: (510) 486-7696 Email: t_warwick@lbl.gov
Spokesperson	Name: James Tobin Affiliation: Lawrence Livermore National Laboratory Phone: (510) 422-7247 Fax: (510) 423-7040 Email: tobin1@llnl.gov

Beamline 7.0.1, cont.

Endstation identifier	Fluorescence spectrometer
Characteristics	Grating spectrometer for high-resolution (1:3000) photon-in/photon-out spectroscopy in the 50–1200 eV range
Detectors	Channel-plate photon counter in spectrometer focal plane
Spot size at sample	50 μm
Samples Format Preparation	 Solids or gases in windowed cell No preparation chamber provided
Sample environment	UHV
Special notes	This spectrometer is installed by the group from the University of Uppsala, Sweden. Potential users are asked to contact Professor Nordgren to explore possible collaborations.
Scientific applications	Photon-in/photon-out spectroscopy
Local contact	Name: Tony Warwick Phone: (510) 486-5819 Fax: (510) 486-7696 Email: t_warwick@lbl.gov
Spokesperson	Name: Professor Joseph Nordgren Affiliation: University of Uppsala, Sweden Phone: +46 (0)18 183554 Fax: +46 (0)18 183524 Email: joseph@fysik.uu.se

Beamline 7.0.2

Coherent Optics Experiments (Abstracts begin on page 175)

Operational	1998
Source characteristics	5-cm-period undulator (U5)
Energy range	200–650 eV
Monochromator Calculated flux (1.9 GeV, 400 mA) Resolving power (E/ΔE)	None 2.8×10^{15} photons/sec/1%BW/central cone at 457 eV 70
Endstations	General purpose
Detectors	Resist and CCD
Samples Format Preparation	Any Mount on thin membrane Can be cryo
Sample environment	Clean high vacuum
Special notes	Endstation separated from beamline by cooled window
Scientific applications	Coherent scattering, holography, diffraction, correlation spectroscopy
Local contact/spokesperson	Name: Malcolm Howells Affiliation: Advanced Light Source, Berkeley Lab Phone: (510) 486-4949 Fax: (510) 486-7696 Email: howells@lbl.gov

Beamline 7.3.1.1

Magnetic Microscopy, Spectromicroscopy (Abstracts begin on page 179)

Operational	Now
Source characteristics	Bend magnet
Energy range	260–1500 eV
Monochromator Calculated flux (1.9 GeV, 400 mA) (linearly polarized) Resolving power (E/ΔE)	SGM 3×10^{12} photons/sec/0.1%BW at 800 eV 1800 at 800 eV
Endstation	Photoemission electron microscope (PEEM2)
Characteristics	Imaging of electron emission
Spatial resolution	200 x 200 Å (designed)
Detectors	Slow scan CCD
Spot size at sample	$\leq 50 \times 50$ μm
Samples Format Preparation	Conductive solids up to 1 cm^2 in area Solid Sputtering, heating, evaporation transfer capability
Sample environment	UHV
Special notes	Choice of linearly or circularly polarized radiation (flux of circularly polarized radiation is reduced)
Scientific applications	Real-time study of magnetic, elemental, chemical, and topological properties of materials
Local contact	Name: Simone Anders Phone: (510) 486-5928 Fax: (510) 486-7696 Email: sanders@lbl.gov
Spokesperson	Name: Joachim Stöhr Affiliation: IBM Almaden Research Center Phone: (408) 927-2461 Fax: (408) 927-2100 Email: stohr@almaden.ibm.com

Beamline 7.3.1.2

Surface and Materials Science, Micro X-Ray Photoelectron Spectroscopy

(Abstracts begin on page 179)

Operational	Now
Source characteristics	Bend magnet
Energy range	260–1500 eV
Monochromator Calculated flux (1.9 GeV, 400 mA) Resolving power (E/ΔE)	SGM 1×10^{10} photons/sec/0.1%BW at 800 eV 1800 at 800 eV
Endstation	Micro-XPS
Characteristics	X-ray photoelectron spectroscopy study of 50×50 mm sample with 1-μm^2 spot size
Spatial resolution	1×1 μm (designed)
Spot size at sample	1.5×1.5 μm (now)
Detectors	Electron energy analyzer detector
Samples Format Preparation	Up to 50×50 mm Solid Heating, sputtering
Sample environment	UHV
Special notes	In-vacuum fiducialization of sample using optical visible-light microscope; high-precision 2" × 4.5" x-y stage; laser interferometer encoding
Experimental techniques	Micro-XPS, NEXAFS, MCD
Scientific applications	Study of microstructures and interfaces in integrated circuits
Local contact	Name: Zahid Hussain Phone: (510) 486-7591 Fax: (510) 486-7696 Email: hussain@lbl.gov
Spokesperson	Name: Baylor Triplett Affiliation: Intel Corporation Phone : (408) 765-2069 Fax: (408) 765-2949 Email: baylor_b_triplett@ccm.sc.intel.com

Beamline 7.3.3

Micro X-Ray Diffraction, Micro X-Ray Absorption Spectroscopy

Operational	1998
Source characteristics	Bend magnet
Energy range	See endstation tables
Monochromator	See endstation tables
Endstations	Micro x-ray diffraction/micro x-ray absorption Femtosecond laser-driven x-ray diffraction and absorption

Endstation identifier	**Micro x-ray diffraction/micro x-ray absorption**
Characteristics	Designed for microprobe, white light, and monochromatic experiments
Energy range	4–12 keV
Monochromator	White light and monochromatic [Four-crystal Ge (111)]
Calculated flux (1.9 GeV, 400 mA)	Monochromatic (8.5 keV): 1×10^{9} photons/sec/μm^2/3×10^{-4}BW (1×1 μm spot) 1×10^{12} photons/sec/3×10^{-4}BW (100×300 μm spot)
Resolving power (E/ΔE)	3500 at 8.5 keV (monochromatic)
Spot size at sample	100×300 μm down to 1×1 μm
Detectors	X-ray CCD, fluorescence SiLi detector
Samples Format	 Typically < 1 $cm^2 \times 1$ mm thick
Sample environment	Typically air
Scientific applications	Measurement of strain, micro-XAS, environmental science
Local contact/spokesperson	Name: A.A. MacDowell Affiliation: Advanced Light Source, Berkeley Lab Phone: (510) 486-4276 Fax: (510) 486-7696 Email: aamacdowell@grace.lbl.gov

Beamline 7.3.3, cont.

Endstation identifier	**Femtosecond laser-driven x-ray diffraction**
Characteristics	Designed for time-resolved x-ray diffraction and absorption
Energy range	0.1–12 keV
Monochromator Flux (1.9 GeV, 400 mA) Resolving power (E/ΔE)	White light and monochromatic, with various monochromatizing elements ~1×10^{12} photons/sec/3×10^{-4}BW Dependent on monochromatizing element
Spot size at sample	50×300 μm
Detectors	Femtosecond streak camera
Samples Format	 Typically < 1 $cm^2 \times 1$ mm thick
Sample environment	Typically 10^{-5} Torr vacuum
Scientific applications	Sub-picosecond diffraction/absorption
Local contact/spokesperson	Name: Phil Heimann Affiliation: Advanced Light Source, Berkeley Lab Phone: (510) 486-7628 Fax: (510) 486-7696 Email: paheimann@lbl.gov

Beamline 8.0.1

Surface and Materials Science, Spectromicroscopy, Imaging Photoelectron Spectroscopy (Abstracts begin on page 195)

Operational	Now
Source characteristics	5-cm-period undulator (U5) (first, third, and fifth harmonics)
Energy range	95–1200 eV (1.5 GeV); 210–1200 eV (1.9 GeV)
Monochromator Flux (1.9 GeV, 400 mA) Resolving power (E/ΔE)	SGM (gratings: 150, 380, 925 l/mm) 10^{10}–10^{14} photons/sec (resolution and energy dependent) 3000 typical, 8000 optimized
Endstations	Ellipsoidal-mirror electron energy analyzer Soft x-ray fluorescence spectrometer

Endstation identifier	**Ellipsoidal-mirror electron energy analyzer (EMA)**
Characteristics	Measures 84° of electron emission angles from solid samples with 80 meV resolution
Spot size at sample	100 μm
Samples Format Preparation	Solids < 1 × 1 cm *In-situ* resistive heating; *in-situ* evaporation
Sample environment	UHV
Special notes	Sample transfer capabilities; preparation chamber
Scientific applications	XPS, ARPES, NEXAFS of solids and surfaces
Local contact	Name: Clemens Heske Phone: (510) 486-7249 Fax: (510) 486-4299 Email: ctheske@lbl.gov
Spokesperson	Name: Franz Himpsel Affiliation: University of Wisconsin, Madison Phone: (608) 263-5590 Fax: (608) 263-2334 Email: himpsel@comb.physics.wisc.edu

Beamline 8.0.1, cont.

Endstation identifier	**Soft x-ray fluorescence spectrometer**
Characteristics	Measures the soft x-ray emission from solid samples with a dispersive grating spectrometer
Spot size at sample	100 μm
Samples Format	Solids Samples up to 4" (10.1 cm) in diameter
Sample environment	UHV
Special notes	Sample transfer capabilities
Scientific applications	SXF, fluorescence-yield XAS of solids
Local contact	Name: Melissa Grush Phone: (510) 486-6645 Fax: (510) 486-4773 Email: mmgrush@lbl.gov
Spokesperson	Name: Thomas Callcott Affiliation: University of Tennessee Phone: (423) 974-6765 Fax: (423) 974-3949 Email: tomc@utkux.utcc.utk.edu

Beamline 9.0.2.1

Chemical Reaction Dynamics, Photochemistry (Abstracts begin on page 305)

Operational	Now
Research program	Chemical reaction dynamics, photochemistry
Source characteristics	10-cm-period undulator (U10) (fundamental)
Energy range	5–30 eV
Monochromator Calculated flux (1.9 GeV, 400 mA) Resolving power (E/ΔE)	None $\approx 10^{16}$ photons/sec/2.5%BW 40
Endstation	Crossed molecular beam
Characteristics	Designed for photofragmentation spectroscopy and reactive scattering; two rotatable molecular-beam sources
Detectors	Time-of-flight spectroscopy by quadrupole mass analyzer
Spot size at sample (calculated)	170 μm (h) × 50 μm (v)
Samples Format Preparation	 Gas sample Molecular beam, seeded in rare gas
Sample environment	Vacuum $\approx 10^{-6}$ Torr
Scientific applications	Photofragmentation spectroscopy, reactive scattering
Local contact/spokesperson	Name: Arthur Suits Affiliation: Chemical Sciences Division, Berkeley Lab Phone: (510) 486-4754 Fax: (510) 486-5311 Email: arthur@leea.cchem.berkeley.edu

Beamline 9.0.2.2

High-Resolution Photoelectron and Photoionization Spectroscopy
(Abstracts begin on page 305)

Operational	Now
Source characteristics	10-cm-period undulator (U10) (fundamental)
Energy range	5–30 eV
Monochromator Calculated flux (1.9 GeV, 400 mA) Resolving power (E/ΔE)	Off-plane Eagle $\approx 10^{11}$ photons/sec/0.01%BW 70,000
Endstation	Molecular-beam photoelectron/photoion spectroscopy
Characteristics	Multipurpose design for high-resolution photoelectron spectroscopy and photoelectron/photoion coincidence experiments
Detectors	Time-of-flight and quadrupole ion and pulse field ionization electron detector
Spot size at sample (calculated)	360 μm (h) by 240 μm (v)
Samples Format Preparation	 Gas sample Molecular beam, seeded in rare gas
Sample environment	Vacuum $\approx 10^{-6}$ Torr
Scientific applications	Pulse field ionization photoelectron spectroscopy, threshold photoelectron/photoion coincidence
Local contact	Name: Gary Jarvis Phone: (510) 495-2092 Fax: (510) 486-6665 Email: gkjarvis@lbl.gov
Spokesperson	Name: Cheuk Ng Affiliation: Iowa State University Phone: (515) 294-4225 Fax: (515) 294-5825 Email: cyng@pop.ames.lab.gov

Beamline 9.3.1

Atomic, Molecular, and Materials Science (Abstracts begin on page 337)

Operational	Now
Source characteristics	Bend magnet
Energy range	2200–6000 eV with Si(111) crystals
Monochromator Measured flux (1.9 GeV, 300 mA) Resolving power (E/ΔE)	Double crystal $> 10^{11}$ photons/sec/2200–5000 eV 3000–8000
Endstations	X-ray absorption cell Ion time-of-flight spectrometer Angle-resolved time-of-flight electron spectrometer Angle-resolved hemispherical electron analyzer Polarized-x-ray emission spectrometer

Endstation identifier	**X-ray absorption cell**
Detectors	Photodiode
Spot size at sample	< 0.5 mm
Samples	Powder, 1/2" diameter; gases
Sample environment	UHV, gas cell
Scientific applications	NEXAFS
Local contact	Name: Rupert Perera Phone: (510) 486-5680 Fax: (510) 486-4550 Email: rupert@lbl.gov
Spokesperson	Name: Dennis Lindle Affiliation: University of Nevada, Las Vegas Phone: (702) 895-4426 Fax: (702) 895-4072 Email: lindle@nevada.edu

Beamline 9.3.1, cont.

Endstation identifier	**Ion time-of-flight spectrometer**
Characteristics	Timing resolution ≈200 ps; capable of coincidence measurement (ion–ion, ion–ion–ion, electron–ion, electron–ion–ion, etc.)
Detectors	Microchannel plates for ions, channeltron for electrons
Spot size at sample	< 0.5 mm
Samples	Gases
Sample environment	Gas-phase flow system
Scientific applications	Ion spectroscopy, total and partial ion yields, PIPICO, PEPICO, PEPIPICO, etc.
Local contact	Name: Wayne Stolte Phone: (510) 486-5538 Fax: (510) 495-2111 Email: wstolte@unlinfo.unl.edu
Spokesperson	Name: Dennis Lindle Affiliation: University of Nevada, Las Vegas Phone: (702) 895-4426 Fax: (702) 895-4072 Email: lindle@nevada.edu

Endstation identifier	**Angle-resolved time-of-flight electron spectrometer**
Characteristics	Timing resolution ≈200 ps; chamber rotates about x-ray beam (±100°)
Detectors	4 time-of-flight electron analyzers (0.5 m long)
Spot size at sample	< 0.5 mm
Samples	Gases
Sample environment	Gas-phase flow system
Scientific applications	Photoelectron and Auger spectroscopy, electron–electron coincidence
Local contact	Name: Honghong Wang Phone: (510) 486-5804 Fax: (510) 495-2111 Email: wangh@nevada.edu
Spokesperson	Name: Dennis Lindle Affiliation: University of Nevada, Las Vegas Phone: (702) 895-4426 Fax: (702) 895-4072 Email: lindle@nevada.edu

Beamline 9.3.1, cont.

Endstation identifier	**Angle-resolved hemispherical electron analyzer**
Characteristics	High energy resolution ($E/\Delta E \leq 5000$) and high electron kinetic energies (≤ 5 keV); chamber rotates about x-ray beam and analyzer rotates about a perpendicular axis, allowing coverage of $\approx 1\pi$ steradians
Detectors	2-D position-sensitive detector (microchannel plates plus resistive anode)
Spot size at sample	< 0.5 mm
Samples	Gases
Sample environment	Gas-phase flow system
Scientific applications	Photoelectron and Auger spectroscopy
Local contact	Name: Honghong Wang Phone: (510) 486-5804 Fax: (510) 495-2111 Email: wangh@nevada.edu
Spokesperson	Name: Dennis Lindle Affiliation: University of Nevada, Las Vegas Phone: (702) 895-4426 Fax: (702) 895-4072 Email: lindle@nevada.edu

Endstation identifier	**Polarized-x-ray emission spectrometer (available in 1998)**
Characteristics	High x-ray energy resolution ($E/\Delta E \approx 3000$). Curved-crystal Rowland-circle spectrometer
Detectors	2-D position-sensitive detector (microchannel plates plus resistive anode)
Spot size at sample	< 0.5 mm
Samples	Gases
Sample environment	Static gas cell with windows
Scientific applications	X-ray emission
Local contact	Name: Wayne Stolte Phone: (510) 486-5538 Fax: (510) 495-2111 Email: wstolte@unlinfo.unl.edu
Spokesperson	Name: Dennis Lindle Affiliation: University of Nevada, Las Vegas Phone: (702) 895-4426 Fax: (702) 895-4072 Email: lindle@nevada.edu

Beamline 9.3.2

Chemical and Materials Science, Circular Dichroism, Spin Resolution
(Abstracts begin on page 349)

Operational	Now
Source characteristics	Bend magnet
Energy range	30–1500 eV
Monochromator Calculated flux (1.9 GeV, 400 mA) Resolving power (E/ΔE)	SGM (gratings: 100, 600, 1200 l/mm) $\approx 10^{11}$ photons/sec/0.1%BW at 400 eV 3000 typical, 8000 max (with 10-μm slits) Capability for circularly polarized radiation
Endstations	Advanced materials chamber (AMC) Advanced photoelectron spectrometer/diffractometer (APSD) Users may bring their own endstation

Endstation identifier	**Advanced materials chamber (AMC)**
Characteristics	PHI analyzer, sample preparation with LEED, XPS, evaporation, sputtering, precision manipulator
Spatial resolution	0.5×1 mm^2
Detectors	16-element multichannel detector, partial electron yield detector
Spot size at sample	0.5×1 mm^2
Samples Format Preparation	Solid 5–10 mm diameter Sputtering, evaporation, XPS, LEED, heating up to 2000°C; cooling down to 80°K
Sample environment	UHV
Special notes	Sample transfer capability
Experimental techniques	Photoelectron diffraction, XPS, NEXAFS, MCD
Scientific applications	Studies of atomic and electronic structure of surfaces
Local contact	Name: Zhou Xin Phone: (510) 486-7633 Fax: (510) 486-4299 Email: xin@ux8.lbl.gov
Spokesperson	Name: Eddie Moler Affiliation: Advanced Light Source, Berkeley Lab Phone: (510) 486-7637 Fax: (510) 486-4299 Email: ejmoler@lbl.gov

Beamline 9.3.2, cont.

Endstation identifier	**Advanced photoelectron spectrometer/diffractometer (APSD)**
Characteristics	High-resolution rotatable Scienta analyzer, sample preparation with LEED, evaporator, high-precision sample manipulator, sputtering
Spatial resolution	5 μm with pre-lens
Detectors	Multichannel detector and spin-resolved mini Mott
Spot size at sample	0.5 × 1.0 mm
Samples Format Preparation	Solid 5–10 mm diameter, 1–2 mm thick Sputtering, evaporation, LEED, XPS, heating up to 2000°C; cooling down to 150°K
Sample environment	UHV
Special notes	Capability of using either a multichannel detector or a spin detector, analyzer rotatable in horizontal plane
Experimental techniques	Photoelectron diffraction, high-resolution XPS, UPS; MCD
Scientific applications	Studies of the atomic, electronic, and magnetic structure of surfaces, interfaces, and nanostructures
Local contact	Name: Zahid Hussain Phone: (510) 486-7591 Fax: (510) 486-7696 Email: hussain@lbl.gov
Spokesperson	Name: Professor C. S. Fadley Affiliation: Material Sciences Division, Berkeley Lab; and U. California, Davis Phone: (510) 486-5774; (916) 752-8788 Fax: (510) 486-4680 Email: fadley@lbl.gov

Beamline 10.0.1

High-Resolution Atomic, Molecular, and Optical Physics; Photoemission of Highly Correlated Materials

(Beamline 9.0.1 was moved to Sector 10 in 1998 and with some modifications became Beamline 10.0.1. Abstracts for Beamline 9.0.1 begin on page 273.)

Operational	Now
Source characteristics	10-cm-period undulator (U10) (first and third harmonics)
Energy range	20–350 eV
Monochromator Calculated flux (1.9 GeV, 400 mA) Resolving power (E/ΔE)	SGM (gratings: 380, 925, 2100 l/mm) $\approx 10^{13}$ photons/sec/0.01%BW (resolution dependent) ≈10,000 (selectable by slit width)
Endstations	High-energy-resolution spectrometer (HERS) High-resolution gas-phase electron spectrometer Ion-beam endstation

Endstation identifier	**High-energy-resolution spectrometer (HERS)**
Scientific applications	Studies of highly correlated electron systems using angle-resolved photoemission of solids
Characteristics	Optimized for high-resolution studies of highly correlated electron systems at low temperature
Detectors	Scienta SES-200 hemispherical electron energy analyzer with angular mode LEED Partial-yield detector
Spot size at sample	100 μm (h) × <100 μm (v) depending on exit slit setting
Samples	Solids in UHV
Local contact	Name: Scot Kellar Phone: (510) 486-4989 Fax: (510) 486-4299 Email: sakellar@lbl.gov
Spokesperson	Name: Prof. Z.X. Shen Affiliation: Stanford University Phone: (650) 725-8254 Fax: (650) 725-5457 Email: shen@ee.stanford.edu

Beamline 10.0.1, cont.

Endstation identifier	**Ion-beam endstation (available fall 1998)**
Scientific applications	Photoionization of ions
Characteristics	The charged ion beam from the ion accelerator is merged with the photon beam (counter propagating) for approximately 0.5 m. An analyzing magnet disperses the ion beam based on charge state following the interaction region.
Spot size at sample	1.5 mm (h) × 1.5 mm (v)
Samples	Beam of positively charged ions
Sample environment	Differential pumping permits gas pressures of up to 10^{-5} Torr
Local contact	Name: Fred Schlachter Phone: (510) 486-4892 Fax: (510) 486-6499 Email: fred_schlachter@lbl.gov
Spokespersons	Name: Nora Berrah Affiliation: Western Michigan University Phone: (616) 387-4955 Fax: (616) 387-4939 Email: berrah@wmich.edu Name: Prof. Ronald A. Phaneuf Affiliation: University of Nevada–Reno Phone: (702) 784-6816 Fax: (702) 784-1398 Email: phaneuf@physics.unr.edu

Beamline 10.0.1, cont.

Endstation identifier	**High-resolution gas-phase electron spectrometer (available summer 1998)**
Scientific applications	High-resolution atomic and molecular electron spectroscopy
Characteristics	The electron spectrometer uses a gas cell on the beam axis to form the interaction region between the sample and the photon beam. The analyzer rotates from 0° to 90° relative to the polarization vector of the photon beam, permitting angle-resolved measurements.
Detector	Scienta electron spectrometer
Spot size at sample	0.4 mm (h) × 0.1–0.5 mm (v) depending on exit slit setting
Samples	Gas cell
Sample environment	Differential pumping permits gas pressures of up to 10^{-5} Torr
Special notes	Vented gas cabinets are available for hazardous samples
Local contact	Name: John D. Bozek Phone: (510) 486-4967 Fax: (510) 486-7696 Email: jdbozek@lbl.gov
Spokesperson	Name: Nora Berrah Affiliation: Western Michigan University Phone: (616) 387-4955 Fax: (616) 387-4939 Email: berrah@wmich.edu

Beamline 10.3.1

X-Ray Fluorescence Microprobe (Abstracts begin on page 371)

Operational	Now
Source characteristics	Bend magnet
Energy range	3–20 keV (without multilayer mirrors) 6–15 keV (with multilayer mirrors)
Monochromator Calculated flux (1.9 GeV, 400 mA) Resolving power (E/ΔE)	 Multilayer mirrors in Kirkpatrick-Baez configuration 3×10^{10} photons/sec 25 at 12.5 keV
Endstation	Large hutch with optical table
Characteristics	X-ray fluorescence analysis of samples with high elemental sensitivity and high spatial resolution
Spatial resolution	1.0 × 1.2 μm
Detectors	Si (Li)
Spot size at sample	1.0 × 1.2 μm
Samples Format Preparation	 Samples are usually mounted between two layers of super-clean polypropylene. Standard sample holders are available for samples less than 2 cm in diameter. Almost any sample can be measured since samples are measured in air.
Sample environment	Air
Special notes	By special arrangement, the focusing mirrors can be removed and then the white-light beam can be used for experiments that require white radiation (e.g., testing capillary optics or evaluating x-ray collimators)
Scientific applications	Trace element analysis with high spatial resolution, for example silicon solar cells, GaN, environmental soil samples, and biological samples; testing of x-ray capillary optics and new x-ray detectors
Local contact/spokesperson	Name: Al Thompson Affiliation: Center for X-Ray Optics, Berkeley Lab Phone: (510) 486-5590 Fax: (510) 486-4550 Email: thompson@lbl.gov

Beamline 10.3.2

X-Ray Optics Development, Materials Science (Abstracts begin on page 377)

Operational	Now
Source characteristics	Bend magnet (2 horizontal mrad at 32 m from bend magnet)
Energy range	3–20 keV
Monochromator Calculated flux (1.9 GeV, 400 mA)	None 2.7×10^{13} photons/sec/0.1%BW A Si(111) 4-bounce monochromator is also available for high-energy-resolution experiments.
Endstation	Large hutch with optical table for experimental equipment
Characteristics	A large 10 cm × 1 cm white radiation beam is available. At present a silicon monochromator and a pair of grazing-incidence focusing mirrors are installed to produce a 1.5 × 2-μm spot that can be either white radiation or monochromatic ($E/\Delta E = 10^4$).
Scientific applications	Many different experiments have been done which use x-ray energies above 3 keV: past experiments include x-ray microdiffraction, micro-XAFS, LIGA, TXRF of silicon wafers, femtosecond timing, and testing of x-ray optical elements
Local contact/spokesperson	Name: Al Thompson Affiliation: Center for X-Ray Optics, Berkeley Lab Phone: (510) 486-5590 Fax: (510) 486-4550 Email: thompson@lbl.gov

Beamline 11.3.2

Inspection of EUV Lithography Masks

Operational	1998
Source characteristics	Bend magnet
Energy range	50–1000 eV
Monochromator Calculated flux (1.9 GeV, 400 mA) Resolving power (E/ΔE)	VLS-PGM 10^{11} photons/sec/0.01%BW at 100 eV 7000
Endstation system	Scanning bright field and dark field mask inspection
Spot size at sample	4 × 6 μm
Local contact/spokesperson	Name: Jim H. Underwood Affiliation: Center for X-Ray Optics, Berkeley Lab Phone: (510) 486-4958 Fax: (510) 486-4550 Email: jhunderwood@lbl.gov

Beamline 12.0.1.1

Surface and Materials Science, Spectromicroscopy
(Abstracts begin on page 395)

Operational	Now
Source characteristics	8-cm-period undulator (U8)
Energy range	95–130 eV
Monochromator Calculated flux (1.9 GeV, 400 mA) Resolving power (E/ΔE)	VLG-PGM $\approx 6 \times 10^{11}$ photons/sec/1%BW after 1-μm pinhole 200–1000
Endstation	MAXIMUM
Characteristics	Scanning photoelectron microscope with multilayer optics at 95 eV or 130 eV
Spatial resolution	0.1 μm
Detectors	CMA-MCP
Spot size at sample	0.1 μm
Samples Format Preparation	 15 × 15 mm maximum sample size Deposition, cleaving, ion beam sputtering, annealing
Sample environment	UHV; in-situ heating and electrical testing
Scientific applications	Semiconductor surfaces and interfaces, microelectronics, metallization, silicides
Local contact	Name: Gian Franco Lorusso Phone: (510) 486-6853 Fax: (510) 486-4550 Email: glorusso@grace.lbl.gov
Spokesperson	Name: Jim H. Underwood Affiliation: Center for X-Ray Optics, Berkeley Lab Phone: (510) 486-4958 Fax: (510) 486-4550 Email: jhunderwood@lbl.gov

Beamline 12.0.1.2

EUV Lithography Optics Testing, Interferometry (Abstracts begin on page 395)

Operational	Now
Source characteristics	8-cm-period undulator (U8)
Energy range	60–320 eV
Monochromator Calculated flux (1.9 GeV, 400 mA) Resolving power (E/ΔE)	VLG-PGM $\approx 5 \times 10^{13}$ photons/sec/1%BW at 134 eV 200–1000
Endstation	EUV interferometer
Detectors	GaAsP flux monitor, silicon 1000 × 1000 CCD array
Samples Format	 All-reflective, multilayer-coated EUV optics
Sample environment	10^{-7} Torr or 10^{-4} Torr of O_2
Scientific applications	Interferometric wavefront measurement of optics designed for EUV lithography
Local contact	Name: Kenneth A. Goldberg Phone: (510) 486-2261 Fax: (510) 486-4550 Email: kagoldberg@lbl.gov
Spokesperson	Name: Jeffrey Bokor Affiliation: U.C. Berkeley; Center for X-Ray Optics, Berkeley Lab Phone: (510) 642-4134 Fax: (510) 642-2739 Email: jbokor@light.eecs.berkeley.edu

Beam Test Facility

(Abstracts begin on page 409)

Operational	Now
Electron beam energy	50 MeV
Charge/bunch	1–1.5 nC
Bunch length	25–35 ps
Emittance	0.2–0.5 mm-mrad
Number of bunches/macropulse	1–8
Repetition rate	1, 2 Hz
Minimum spot size	35 μm
Lasers	Ti: Al_2O_3 Nd:YAG λ = 800 nm λ = 1.064 μm, 0.532 μm, 0.266 μm ε =150 mJ ε = 1 J, 0.5 J, 0.1 J τ = 60 fs τ = 9 ns, 7 ns, 4–5 ns Rep. rate: 10 Hz
Local contact/spokesperson	Name: Wim Leemans Affiliation: Center for Beam Physics, Berkeley Lab Phone: (510) 486-7788 Fax: (510) 486-7981 Email: leemans@lbl.gov

Table of Beamlines at the ALS

Up-to-date information is on the Web at http://www-als.lbl.gov/als/als_users_bl/bl_table.html

No.	Source *	Areas of Research	Energy Range	Avail.	Pages for Abstracts/ Technical Info.
1.4.1	Bend	Ultraviolet photoluminescence	1.6–6.2 eV	1998	1/469
1.4.2	Bend	Visible and infrared Fourier transform spectroscopy	0.006–3 eV	Now	1/470
1.4.3	Bend	Infrared spectromicroscopy	0.05–1 eV	Now	1/471
3.1	Bend	Diagnostic beamline	200–280 eV	Now	–/–
3.3.2	Bend	Deep-Etch X-Ray Lithography (LIGA)	3–12 keV	Now	–/472
4.0.1-2	EPU5	Magnetic spectroscopy	100–2000 eV	1998	–/473
5.0.1	W16	Monochromatic protein crystallography	7–14 keV	1998	–/474
5.0.2	W16	Multiple-wavelength (MAD) and monochromatic protein crystallography	3.5–14 keV	Now	15/475
6.1.2	Bend	High-resolution zone-plate microscopy	500–800 eV	Now	31/476
6.3.1	Bend	Calibration and standards, EUV/soft x-ray optics testing, solid-state chemistry	100–2000 eV	1998	–/477
6.3.2	Bend	Calibration and standards; EUV optics testing; atomic, molecular, and materials science	50–1300 eV	Now	51/478
7.0.1	U5	Surface and materials science, spectromicroscopy, spin resolution, photon-polarization dichroism	60–1000 eV	Now	99/479
7.0.2	U5	Coherent optics experiments	200–650 eV	1998	175/483
7.3.1.1	Bend	Magnetic microscopy, spectromicroscopy	260–1500 eV	Now	179/484
7.3.1.2	Bend	Surface and materials science, micro x-ray photoelectron spectroscopy	260–1500 eV	Now	179/485
7.3.3	Bend	Micro x-ray diffraction, micro x-ray absorption spectroscopy	3–12 keV	Now	–/486
8.0.1	U5	Surface and materials science, spectromicroscopy, imaging photoelectron spectroscopy	60–1000 eV	Now	195/488
9.0.2.1	U10	Chemical reaction dynamics, photochemistry	5–30 eV	Now	305/490
9.0.2.2	U10	High-resolution photoelectron and photoionization spectroscopy	5–30 eV	Now	305/491
9.3.1	Bend	Atomic, molecular, and materials science	2.2–6 keV	Now	337/492
9.3.2	Bend	Chemical and materials science, circular dichroism, spin resolution	30–1500 eV	Now	349/495
10.0.1	U10	High-resolution atomic, molecular, and optical physics; photoemission of highly correlated materials	20–320 eV	Now	–/497
10.3.1	Bend	X-ray fluorescence microprobe	3–20 keV	Now	371/500
10.3.2	Bend	X-ray optics development, materials science	3–12 keV	Now	377/501
11.3.2	Bend	Inspection of EUV lithography masks	50–1000 eV	1998	–/502
12.0.1.1	U8	Surface and materials science, spectromicroscopy	60–320 eV	Now	395/503
12.0.1.2	U8	EUV lithography optics testing, interferometry	60–320 eV	Now	395/504
BTF	ALS linac	Beam Test Facility	50 MeV electrons	Now	409/505

* Bend = bend magnet; EPU5 = 5-cm-period elliptical polarization undulator; W16 = 16-cm-period wiggler; Ux = x-cm-period undulator

* U.S. GOVERNMENT PRINTING OFFICE: 1998-685-271/99129